Physics of Atomic Nuclei, Vol. 66, No. 8, 2003, pp. 1399–1406. From Yadernaya Fizika, Vol. 66, No. 8, 2003, pp. 1445–1452.

The ALTO Project at IPN Orsay*

F. Ibrahim**

Institut de Physique Nucléaire, Orsay, France

Received December 15, 2002

Abstract—In order to probe neutron-rich radioactive noble gases produced by photofission, a PARRNe 1 experiment (Production d'Atomes Radioactifs Riches en Neutrons) has been carried out at CERN. The incident electron beam of 50 MeV was delivered by the LIL machine (LEP Injector Linac). The experiment allowed one to compare under the same conditions two production methods of radioactive noble gases: fission induced by fast neutrons and photofission. The obtained results show that the use of the electrons is a promising mode to obtain intense neutron-rich ion beams. Thereafter, with the success of this photofission experiment, a conceptual design for the installation at IPN Orsay of a 50-MeV electron accelerator close to the PARRNe 2 device has been worked out: the ALTO project. This work has started within a collaboration between IPNO, LAL, and CERN groups. © *2003 MAIK "Nauka/Interperiodica"*.

1. INTRODUCTION

There is currently in the nuclear physics community a strong interest in the use of beams of accelerated radioactive ions. Although a fast glance at the nuclide chart immediately shows the vast unknown territories on the neutron-rich side of the valley of beta stability (see Fig. 1), only few projects are concerned with the neutron-rich nuclides.

The availability of intense neutron-rich ion beams will open new perspectives in the study of nuclei very far away from the valley of stability. It would allow one to apprehend the behavior of the nuclear matter under extreme conditions [1, 2]. Several laboratories have concentrated their efforts in studies aiming to produce beams intense enough for the next generation of experiments (SPIRAL II and EURISOL projects). To get such beams, a large R&D effort is required. Uranium fission is a very powerful mechanism to produce such radioactive beams. A substantial part of the PARRNe program (Production d'Atomes Radioactifs Riches en Neutrons) at the IPN Orsay is dedicated to the development of neutron-rich isotope beams by the ISOL (Isotopes Separator On-Line) method.

2. INVESTIGATION OF FAST NEUTRON PRODUCTION MODE

The aim of the PARRNe program is to establish the feasibility of producing neutron-rich radioactive beams for the SPIRAL II project at GANIL and to determine the optimum conditions for the production of such beams. The neutron-rich radioactive nuclides are to be produced by fissioning a heavy nuclide, such as ^{238}U. The technique originally proposed [3] is the use of energetic neutrons to induce fission of depleted uranium. The neutrons are generated by the breakup of deuterons in a thick target, a so-called converter, of sufficient thickness to prevent charged particles from escaping. The energetic forward-going neutrons impinge on a thick production target of fissionable material. The resulting fission products accumulate in the target, diffuse to the surface from which they evaporate, are ionized, mass-selected, and finally postaccelerated. An ISOL device has been developed to carry out various R&D projects [4] (see Fig. 2).

This method has several advantages. The highly activated converter can be kept at low temperature without affecting the neutron flux. The target is bombarded by neutral projectiles losing energy only by useful nuclear interactions and having a high penetrating power allowing very thick targets.

One of the main objectives of the R&D program was to determine the energy of the primary deuteron beam giving the best yields of radioactive nuclides of interest for radioactive beams while taking into account beam power evacuation and safe operation of the facility. The approach has consisted in carrying out simulations with various codes available or developed by different task groups of the SPIRAL II project and performing a number of key experiments to validate the simulations. In this way, confidence is gained about the predictive power of the codes for situations where experiments could not be set up within the allocated time for the study.

*This article was submitted by the author in English.

**e-mail: ibrahim@ipno.in2p3.fr

1063-7788/03/6608-1399$24.00

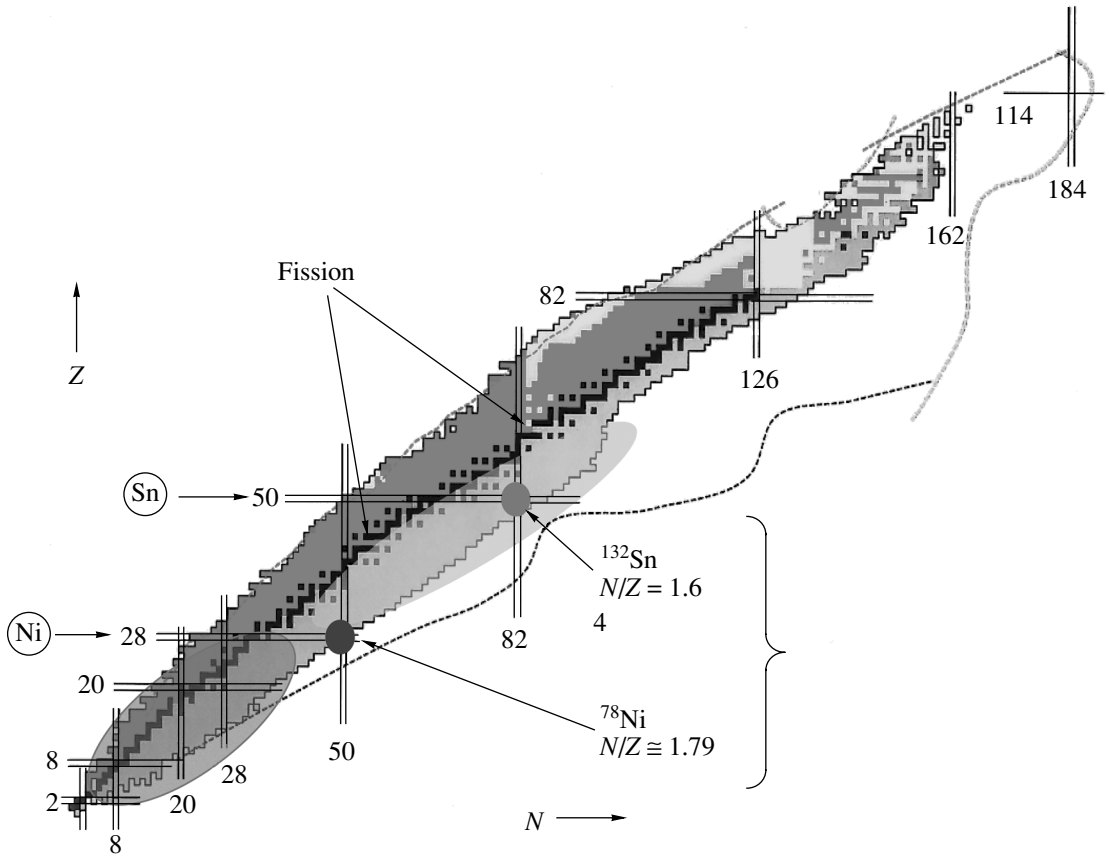

Fig. 1. The production of fission fragments (upper light gray part) in comparison with the production for SPIRAL (dark gray part).

The concept of using neutrons generated by deuteron breakup implies a study of the production yields, energy spectrum, and angular distributions of neutrons in converters made of various materials and as a function of deuteron energy. Experiments were performed at IPN Orsay, KVI Groningen, and SATURNE at Saclay. They explored a deuteron energy range between 14 and 200 MeV. The main features of neutron spectra are listed below.

At forward angles, the energy distribution has a broad peak centered at about 0.4 times the deuteron energy. The angle of emission becomes narrower with increasing energy. For 100-MeV deuterons, the energy width (FWHM) of the neutron spectrum is about 30 MeV and the FWHM opening angle of the cone of emission is about 10° [5, 6].

There is a rather isotropic distribution of neutrons of a few MeV due to evaporation in the fusion reaction.

The angular distributions and energy spectra are in fair agreement with calculations with an extended version of the Serber model [7] and with the LAHET code. The Serber model reproduces the distributions of high-energy neutrons but not of the low-energy neutrons since evaporation is not implemented in the code. LAHET reproduces the low-energy neutron spectrum, while it tends to slightly underestimate (less than a factor of 2) the neutron distributions at very forward angles.

A strong increase in neutron production is observed for deuteron energy between 14 and 100 MeV. It is much less pronounced between 100 and 200 MeV (see Fig. 3). Among converters tested, Be is slightly more productive than C. It has, however, disadvantages related to its physical and chemical properties.

Productions of radioactive noble gases on a cryogenic finger have been measured for different deuteron energy in the same experimental conditions with the so-called PARRNe 1 setup [8] in the framework of the European RTD program SPIRAL II. The PARRNe 1 setup has been designed to be compact and portable to enable its installation at various accelerators. The search of the optimal energy of the deuterons was done by installing this setup successively at IPN Orsay (20 MeV) [9], at CRC Louvain La Neuve (50 MeV), and at KVI Groningen (80 and 130 MeV) [10].

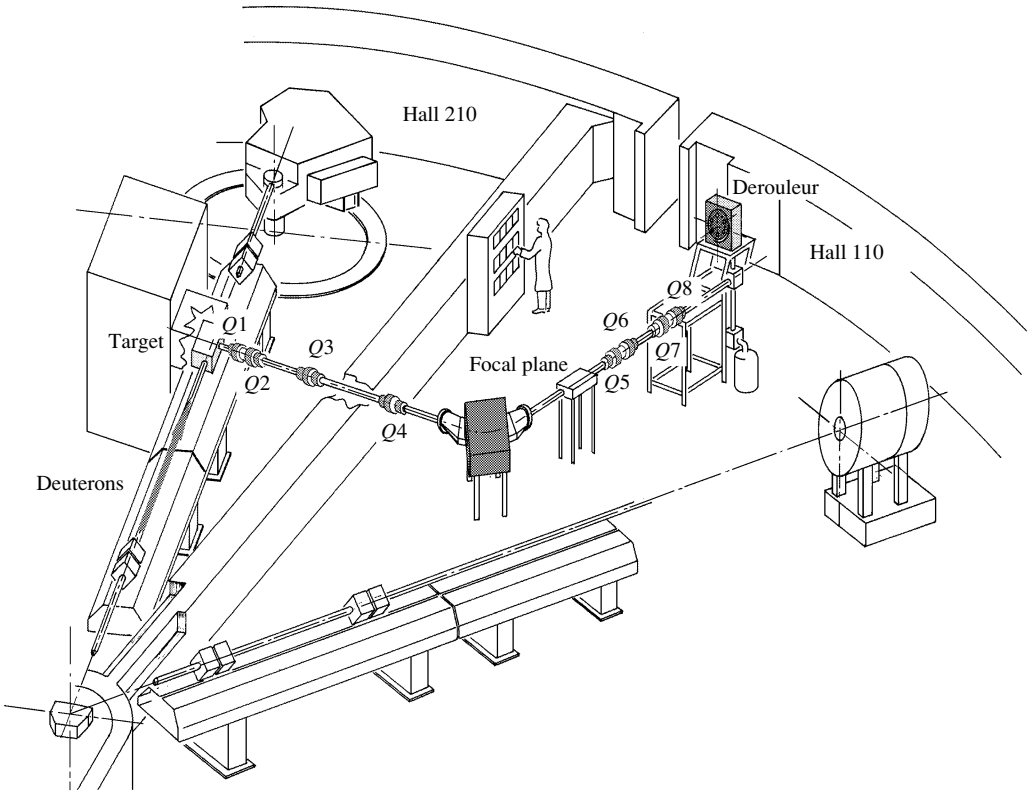

Fig. 2. Schematic view of the ISOL device PARRNe 2 at the Tandem of IPN Orsay.

3. INVESTIGATION OF PHOTOFISSION PRODUCTION MODE

It has recently appeared that photofission could be an alternative to neutron-induced fission [11, 12]. We have therefore initiated a study of photofission induced by bremsstrahlung generated by electrons.

With an electron driver, electron interaction with matter will radiate bremsstrahlung photons inside the target. Fission will then be induced by those photons exciting the giant dipolar resonance (GDR) of the nucleus at the right energy. This well-known process is called photofission.

The GDR cross section for ^{238}U is shown in Fig. 4. A maximum fission probability of 160 mb is obtained for photons having energy around 15 MeV. At that energy, the photoelectric and the Compton and Rayleigh scattering cross sections start to fall off rapidly, so the main contributions to gamma absorption are e^+e^- pair production and the photonuclear reactions (γ, f), (γ, n), and $(\gamma, 2n)$. Although the absolute fission cross section is rather small (compared to normal fission with neutrons), its contribution is not negligible as even a pair production reaction may in a thick target eventually lead to a fission through the resulting photon produced. In the same manner, the neutrons produced by (γ, n) and $(\gamma, 2n)$ reactions as well as the (γ, f) itself can also induce fission, this time by the regular (n, f) high cross section (0.5 b for fast neutrons). Therefore, in a thick target, photofission may be a rather interesting way of creating radioactive fission fragments.

Unfortunately, no efficient monochromatic sources of 15-MeV photons are available. The most common way for producing high gamma fluxes is the bremsstrahlung radiated by passage of electrons through matter. This process has a cross section rising linearly with energy. It will dominate the ionization process above a critical energy (around 20 MeV). But the resulting bremsstrahlung spectrum is widely spread in energy from zero up to the full initial electron energy (Fig. 4). Although each single electron may ultimately produce as many as 20 photons, only a small fraction of them (0.5 to 0.7 gamma per e^-) are "useful" photons lying in the GDR range (15 ± 5 MeV).

A simple calculation including the main electron interactions (bremsstrahlung and ionization) and the

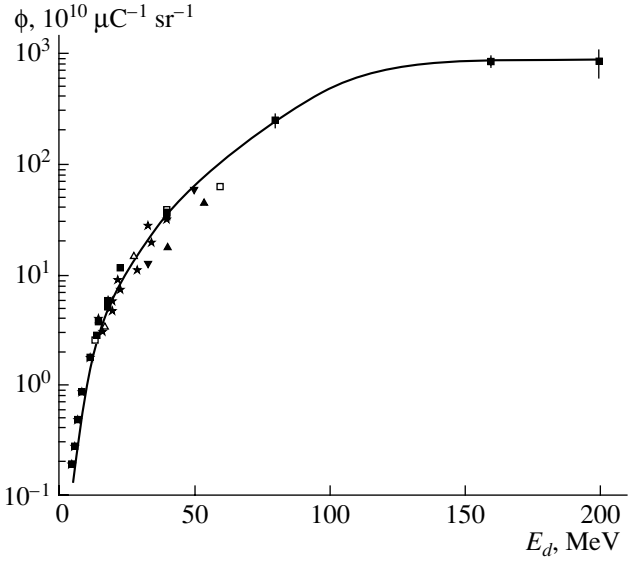

Fig. 3. Neutron yield at 0° as a function of the incident deuteron energy for a Be converter.

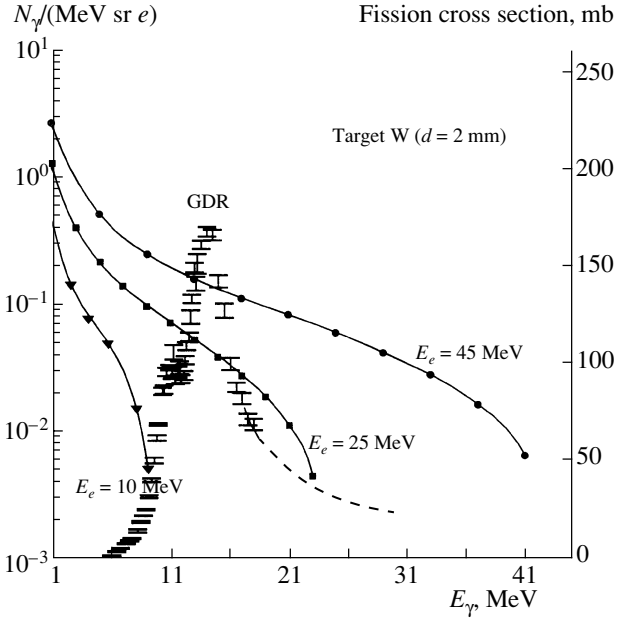

Fig. 4. The GDR cross section for ^{238}U. The solid curves are the γ spectrum produced by electrons with various energies. The experimental points correspond to the ^{238}U photofission cross section.

main nuclear reactions of interest (pair production and fission cross section) in a thick depleted uranium target can give the expected number of fissions per incident electron. In Fig. 5, the number of fissions produced by the (γ, f) reaction is plotted as a function of the electron energy [12]. This result is a complete Monte Carlo calculation performed with an MCNP code also offering photonuclear capability (full electron, photon, and neutron transport). The obtained result is in accordance with simple analytic calculations. For comparison, fission production is also given when using a tungsten converter (5 mm thick) in front of the ^{238}U target. It appears that, when using a converter in the electron driver option, less than 30% of the beam power is lost inside the converter (in contrast to the deuteron driver option). In the direct method, one will produce about 25% more fissions per electron (and probably more when taking in account neutron-induced fission). Fission production is almost linear above a threshold energy of 10 MeV. High production is obtained above 40 MeV.

In order to compare rapid-neutron-induced fission and photofission, measurements of Kr and Xe isotopic distributions produced by photofission and diffused out of a thick UCx target have been performed using the same PARRNe 1 device in the same conditions as those with deuterons beams and with the same target [13]. The setup of the experiment is presented in Fig. 6.

The incident electron beam of 50 MeV was delivered by the LIL machine (LEP Injector Linac). The electrons are slowed down in a W converter or directly in the target, generating bremsstrahlung γ rays which may induce fission.

The PARRNe 1 setup consists in measuring the activity of produced radioactive noble gases by trapping them on a cold finger (13 K) in front of which is placed a germanium detector. The cold finger is connected to the target by an 8-m-long tube at room temperature. This device allows one to shield the detection system from the irradiation point. All other

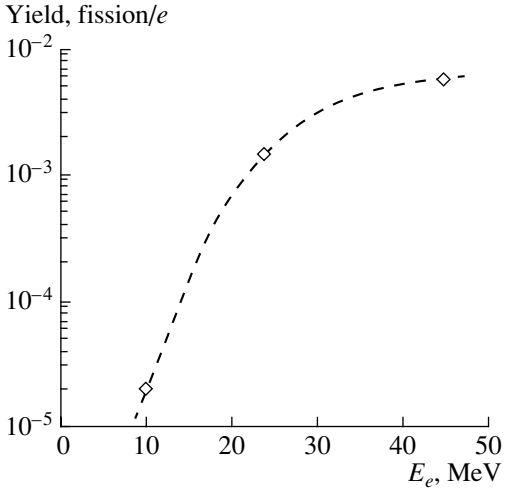

Fig. 5. The fission yield per electron for ^{238}U as a function of the electron energy [12] (curve).

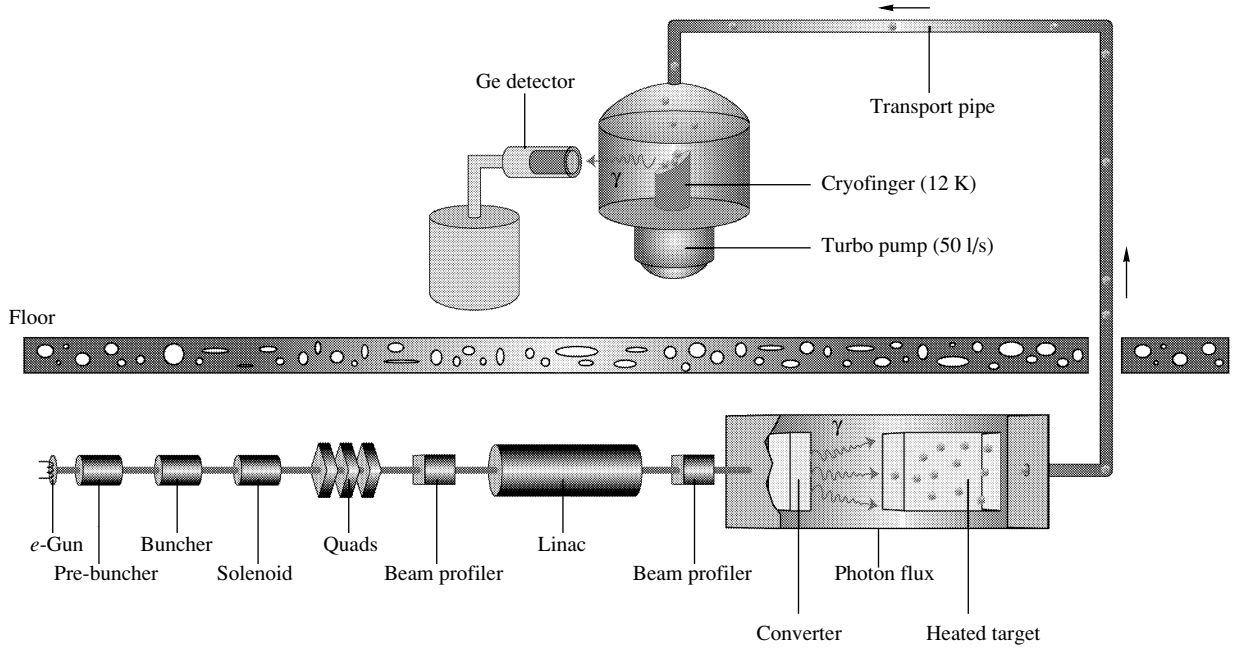

Fig. 6. The PARRNe 1 setup at LIL CERN.

produced elements are condensed at the entrance of the long tube.

The measurements have been made with a 4-mm W converter in different positions (8 and 4 mm from the target), and one measurement has been made without the W converter. Comparison with the 80-MeV deuteron-induced fission measurements are presented in Fig. 7. The results obtained are well understood taking into account the percentage of photons between 11 and 17 MeV emitted in the cone subtended by the target that is the solid angle [13].

The extrapolation of the obtained results indicates that the use of a 50-MeV electron beam of 10 μA would allow a gain in production of at least 100 in comparison with PARRNe 2 results (using a 26-MeV deuteron beam of 1 μA). Such a situation would offer the possibility of providing, for example, $\sim 4 \times 10^7$ ^{132}Sn/s and $\sim 2 \times 10^5$ ^{78}Zn/s with the PARRNe 2 device at Orsay.

4. THE ALTO PROJECT

It has been decided to start a conceptual project for the installation at IPN Orsay of a 50-MeV electron accelerator [14]: the ALTO project (Accélérateur Linéaire auprès du Tandem d'Orsay). The accelerator will be installed in the experimental area of the Tandem, to deliver beams mainly to the PARRNe 2 device. After the photofission experiment success, the CERN scientific authorities interested in the ALTO project have decided to offer the LIL front end to the IPN Orsay.

The linac is composed of a thermionic gun, a bunching system, and a matching section to the linac. The schematic layout in Fig. 8 presents an overall view of the main components of ALTO.

The gun is a thermionic source held to 90 kV; it is designed to provide beam pulses up to ~ 2 μs in length and peak current of 50 mA. The operating frequency is 100 Hz.

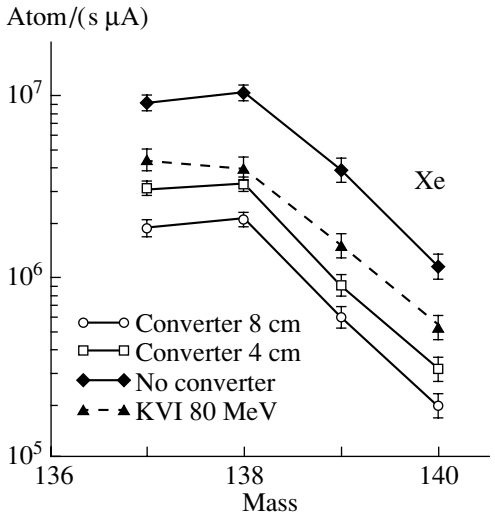

Fig. 7. Results obtained for Xe isotopes using photofission.

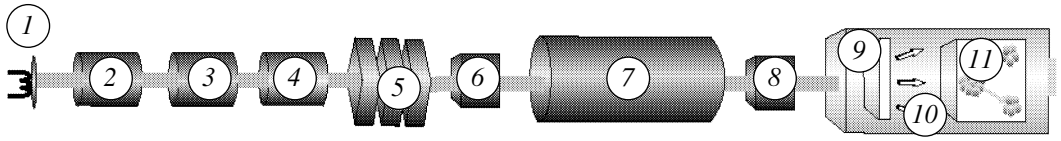

Fig. 8. Layout of the ALTO: (*1*) *e* gun, (*2*) prebuncher, (*3*) buncher, (*4*) solenoid, (*5*) quads, (*6*) beam profiler, (*7*) acceleration section, (*8*) beam profiler, (*9*) converter, (*10*) photon flux, and (*11*) heated target.

The prebuncher is an RF cavity 15 mm long working in the standing wave mode at 3 GHz. It is mounted at a distance of 100 mm from the buncher. For the transverse focusing of the beam, three solenoids are installed downstream of the gun.

The buncher is a triperiodic RF structure cavity working in the standing wave mode at 3 GHz. The cavity structure is surrounded by a solenoid producing a 0.2-T magnetic field. The buncher provides an output energy of about 4 MeV.

The accelerating section is a 4.5-m-long RF cavity operating in the traveling wave mode at 3 GHz. The section output energy is 46 MeV. In order to match the beam from the buncher exit to the accelerating section entrance, we use one solenoid and one quadrupole triplet.

The whole RF structure (prebuncher, buncher, and accelerating section) is powered by only one 35-MW klystron TH 2100. The operation of the accelerator at 50 MeV needs an HF power less than 20 MW.

The transport beam line consists of two 65° dipole magnets ($R = 0.4$ m) and seven magnetic quadrupoles. The first Q-triplet placed behind the accelerating section allows the control of the beam envelop at the entrance of the first magnet. To make the achromatism in the deviation, a quadrupole will be placed between the two magnets. The spot beam dimension is adjusted on the PARRNe target by using the last Q-triplet. The expected energy resolution is less than 5×10^{-3}. The beam line is equipped by instruments for the beam diagnostic: measurement of current, beam position, energy, and energy dispersion.

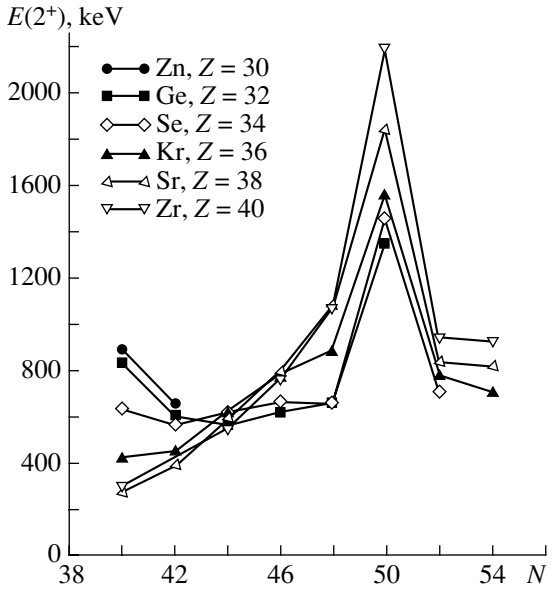

Fig. 9. Evolution of the 2^+ energies in the $N = 50$ region.

The installation cost of ALTO is estimated to be €1.4 million without including the cost of the LIL front end (from CERN), the HF material (from LAL), and all the infrastructure and manpower (from IPNO). After acceptation of the financial plan before the end of 2002, the ALTO project planning will be extended for a maximum period of 18 months.

The expected intensities for the 30-keV mass-separated beams at ALTO will give the opportunity for nuclear spectroscopy of very neutron-rich nuclei in various regions of interest. Properties such as the modification of shell closures are predicted for a wide range of extremely neutron-rich nuclei. Nuclei in the vicinity of the doubly magic nucleus ^{78}Ni are amongst the best candidates to study the evolution of nuclear structure far from stability. In particular, the question of whether the $N = 50$ shell gap persists so far away from stability might be studied. The study of the position of the first excited 2^+ state in even–even isotopes can give a first indication on the collectivity of these nuclei. With counting rates as low as a few particles per second the position of the first excited 2^+ state can be determined [15]. This type of experiments allow for a rather quick "mapping" of a region of interest. As an example, Fig. 9 shows the evolution of the 2^+ state energy for neutron-rich isotopes in the $N = 50$ region. Similar studies must be continued toward ^{78}Ni.

The study of γ rays emitted following spontaneous fission has recently been a precious source of information about the structure of neutron-rich nuclei and about the fission process itself; "in-beam" experiments as described in [16, 17] can be very useful. Prompt γ rays following photofission can be ob-

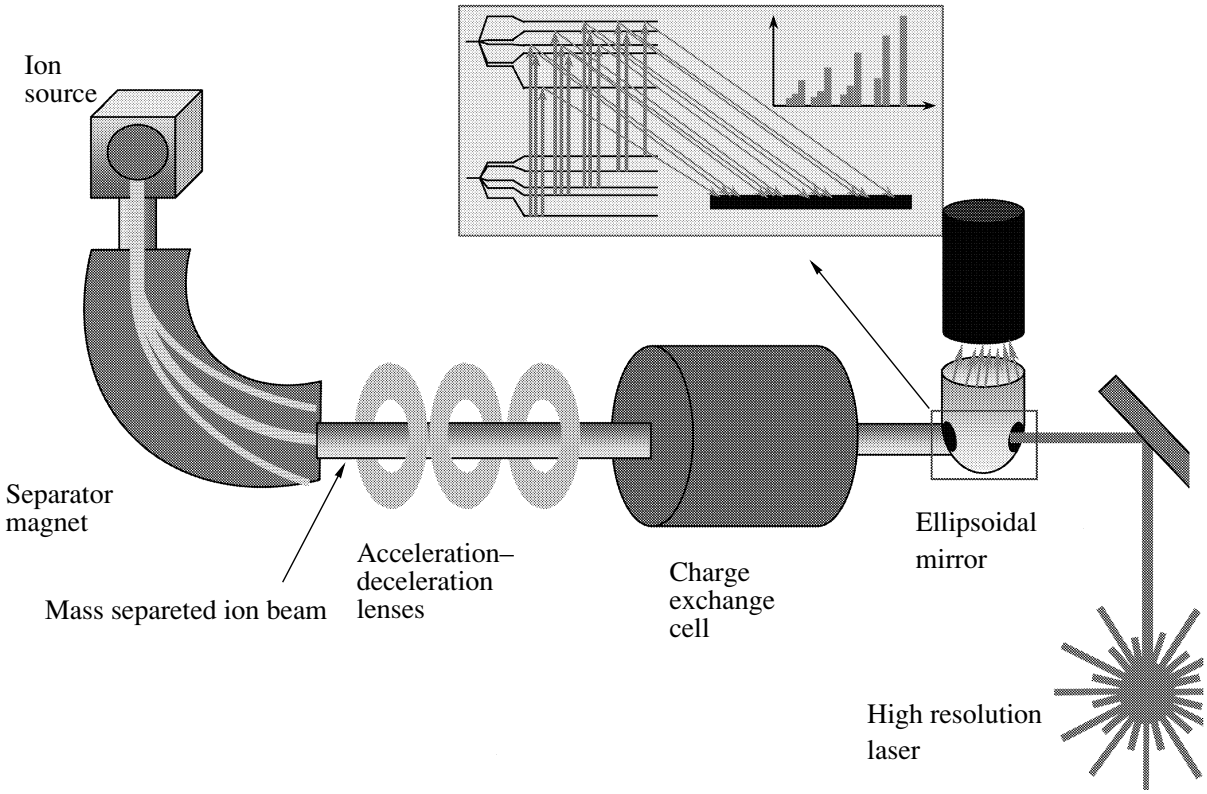

Fig. 10. Setup for collinear laser spectroscopy at ALTO.

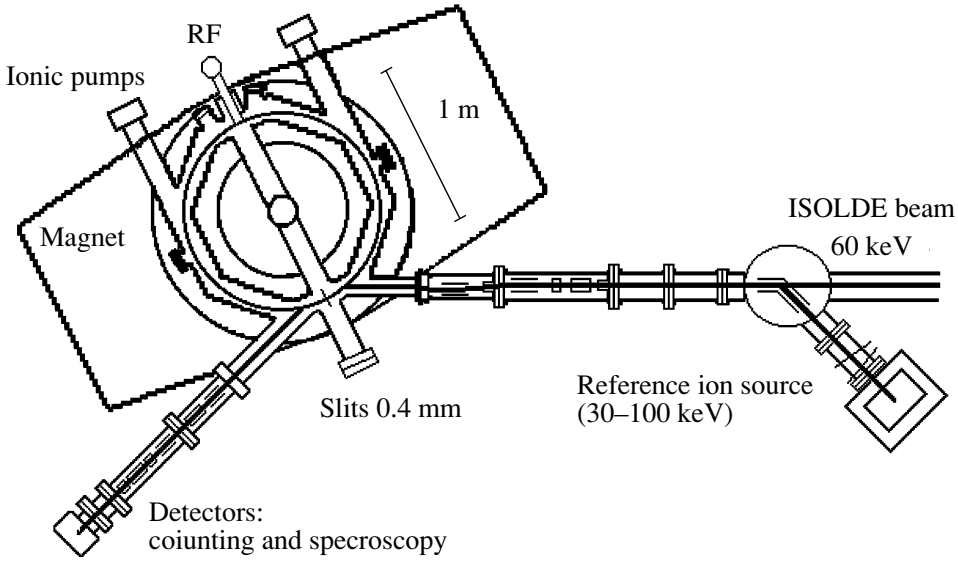

Fig. 11. Layout of the MISTRAL spectrometer (overhead view).

served with γ-ray facilities. The multiplicity requirement strongly suppresses events associated with the beta decay of fission products. The production of fission fragments by photofission with ALTO can be an interesting opportunity to study prompt γ rays in the region of $N = 50$.

Laser spectroscopic studies at ALTO can be used to measure isotope shift and hyperfine structure in atomic spectra. These quantities are used to determine nuclear spins, magnetic dipole, and electric spectroscopic quadrupole moments, and to follow the changes in nuclear mean-square charge radius

through isotopic sequences. Figure 10 illustrates the setup that could be used for laser spectroscopic measurements at ALTO. With this setup, a beam from a tunable laser is made to overlap the beam of ions or atoms produced by ALTO. Measurements could be performed at ALTO for the heavy Ge isotopes, lying above the $N = 50$ shell closure.

To understand stellar evolution and the production of the elements in the Universe, extensive model calculations are used to describe and simulate the different processes occurring in the stars. Especially for violent processes like supernovae explosions or x-ray bursts, mainly properties of unstable nuclei are the most important inputs to the models. In neutron-rich stellar environments, the rapid-neutron-capture process produces heavy elements by a sequence of neutron captures and nuclear beta decays. To correctly model this r process, the model inputs needed are masses of very neutron-rich nuclei, their beta-decay half-lives, and their neutron capture cross sections. However, up to now, these properties are only known for a few isotopes involved in the r process. Neutron-rich fission fragments from ALTO will allow one to perform measurements of half-lives and masses for some of the key nuclei. Mass measurements of high precision could be performed at ALTO for ~ 100 new nuclei using the MISTRAL RF transmission spectrometer from CSNSM at Orsay [18]. MISTRAL is currently installed at the ISOLDE mass separator facility at CERN [19]. The layout of MISTRAL is shown in Fig. 11. A production greater than 10^3 ions per second is needed for the mass measurement program.

REFERENCES

1. *NuPECC Report on Radioactive Nuclear Beams Facilities* (2000), http://www.nupecc.org
2. *OECD Report of the Study Group on RNB*, OECD (Paris, 1999), http://www.ganil.fr/eurisol
3. *Concept for an Advance Exotic Beam Facility Based on Atlas*, Working Paper, Physics Division, Argonne National Laboratory (1995).
4. B. Roussière, F. Ibrahim, *et al.*, Nucl. Instrum. Methods Phys. Res. B **194**, 151 (2002).
5. S. Ménard *et al.*, Phys. Rev. ST Accel. Beams **2**, 033501 (1999).
6. N. Pauwels *et al.*, Nucl. Instrum. Methods Phys. Res. B **160**, 315 (2000).
7. M. Mirea *et al.*, Eur. Phys. J. A **11**, 59 (2001).
8. S. Kandri-Rody *et al.*, Nucl. Instrum. Methods Phys. Res. B **160**, 1 (2000).
9. F. Clapier *et al.*, Phys. Rev. ST Accel. Beams **1**, 013501 (1998).
10. Ch. Lau, Thesis (Université Paris, 2000).
11. W. T. Diamond, Nucl. Instrum. Methods Phys. Res. A **432**, 471 (1999).
12. Yu. Ts. Oganessian *et al.*, Nucl. Phys. A **701**, 87 (2002).
13. F. Ibrahim *et al.*, Eur. Phys. J. A (in press).
14. S. Essabaa *et al.*, IPNO Report (2002).
15. O. Perru *et al.*, this Proceedings.
16. J. H. Hamilton *et al.*, Prog. Part. Nucl. Phys. **35**, 635 (1995).
17. A. Bauchet *et al.*, Eur. Phys. J. A **10**, 145 (2001).
18. D. Lunney *et al.*, Phys. Rev. C **64**, 054311 (2001).
19. B. Jonson, H. L. Ravn, and G. Walter, Nucl. Phys. News **3**, 5 (1993).

Physics of Atomic Nuclei, Vol. 66, No. 8, 2003, pp. 1407–1412. From Yadernaya Fizika, Vol. 66, No. 8, 2003, pp. 1453–1458.

Physics with Fission Fragments: Project DRIBs-2*

Yu. E. Penionzhkevich**

Flerov Laboratory of Nuclear Reactions, Joint Institute for Nuclear Research, Dubna, Moscow oblast, 141980 Russia

Received September 17, 2002

Abstract—Phase II of the Dubna radioactive beam factory is described, together with the possibilities that it opens for fundamental and applied physics research. © *2003 MAIK "Nauka/Interperiodica".*

The Dubna radioactive beam factory (DRIBs) [1] will make use of two possibilities for producing secondary beams of radioactive nuclei (Fig. 1). During the first phase of the project (phase I), the possibility for obtaining radioactive nuclei in fragmentation reactions of stable nuclei, accelerated by the cyclotron U400M to intermediate energies ($\sim$50 MeV/A), will be realized. The fragmentation products, obtained in a special ion source, will be converted into singly charged ions, which after transportation to the second cyclotron (U400) will be accelerated up to energies of $\sim$20–25 MeV/A. This method will make it possible to obtain mainly beams of light radioactive nuclei with $Z \leq 30$ with intensities of up to 10^8 pps (e.g., nuclei such as ^{6}He). In the second phase of the project (phase II), it is supposed to produce and accelerate radioactive neutron-rich nuclei in the mass region $80 \leq A \leq 140$. This mass region corresponds to the fragments of low-energy fission of heavy nuclei. For this reason, use will be made of the photofission of ^{238}U. The γ quanta will be produced by the electron accelerator (the microtron MT-25), where the electron beam with an intensity of about 20 μA has an energy of 25 MeV. With the help of a special converter, the electron beam is transformed into a beam of γ quanta with an energy of up to 25 MeV and a flux of 10^{14} s^{-1}. This beam, focused into a narrow angle, will fall onto a ^{238}U target weighing 100 g. It is well known that the photofission cross section has a maximum corresponding to the giant dipole resonance at an energy of the γ quanta equal to $E_\gamma = 13.5$–14 MeV [2] (see Fig. 2). This brings forth an increase in the photofission probability. The yield of the fission fragments will increase as a result of the interaction of the secondary neutrons (γn and fission neutrons) with the U target. When the above-mentioned parameters of the beam and target are realized, one can get as much as 10^{11} fission fragments/s.

1. PRODUCTION OF FISSION-FRAGMENT BEAMS

The MT-25 microtron electron accelerator generates electron beams with an energy of $E_{\max} =$ 25 MeV with an intensity of about 20 μA (full beam power: $W = 0.5$ kW). The limiting intensity is determined by the power of a magnetron-type 1.6-kW RF generator, operating with a duty factor of 10^{-3} (the peak current in a pulse of 1 μs is 20 mA). In principle, the beam intensity can be increased to a level of 100 μA by designing a new RF generator of a klystron type with a power of 13.5 kW. A generator of this type and all the accompanying upgrading of the RF path could be introduced into the existing scheme of the MT-25 microtron.

The electron beam produces in the converter bremsstrahlung spectra of γ rays with a maximum energy of 25 MeV. The yield of ^{238}U fission fragments is determined by the absorption of γ rays by a ^{238}U nucleus in the region of the giant dipole resonance (GDR) located at an energy of 13.5 MeV with a width of about 5 MeV. The angular spread of γ rays for this energy region is $\alpha_{1/2} = 2.5°$. To choose the optimum size of the ^{238}U target, a special experiment defining the yield of the fission fragments and their spatial distribution in the longitudinal and radial directions with respect to the γ-ray beam has been carried out.

More than 80% of the γ quanta located in the GDR region are absorbed in a metallic uranium target with a thickness of 30 g/cm^2. The size of the electron beam spot on the converter determines the cross-sectional size of the target. For a beam with a diameter of $d_e = 6$ mm (experiments were carried out under these conditions), the target volume has a shape of a cylinder with $d = 8$ mm and $l = 15$ mm (corresponding to total weight of about 15 g). When the

*This article was submitted by the author in English.

**e-mail:pyuer@nrsun.jinr.ru

1063-7788/03/6608-1407$24.00

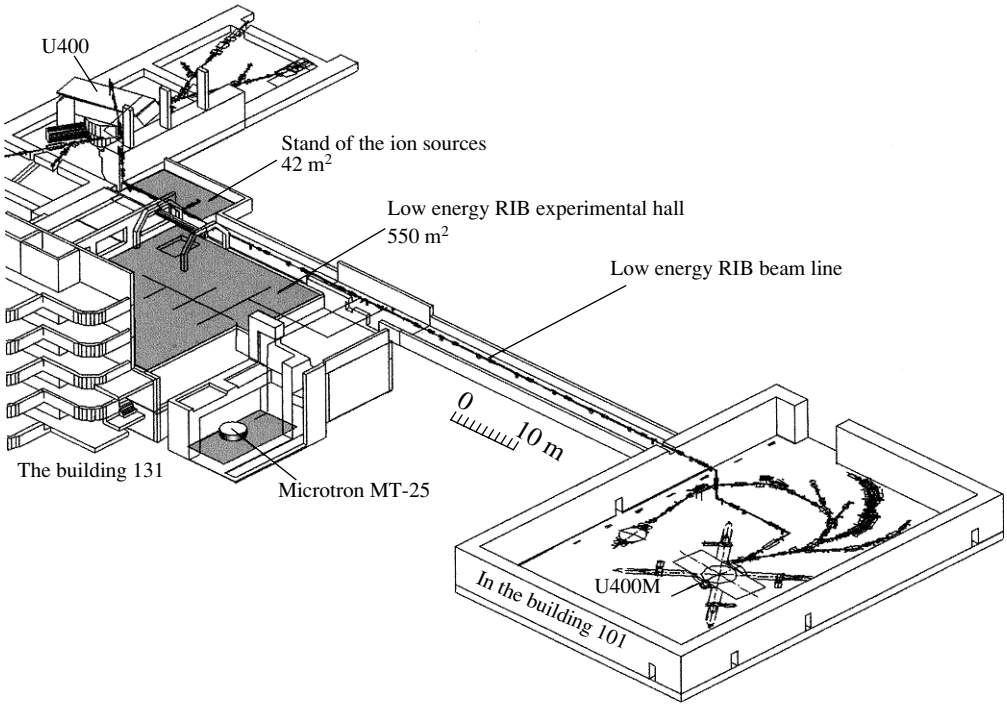

Fig. 1. Layout of the Dubna radioactive ion beams facility (DRIBs).

beam is focused on the converter to $d_e = 3$ mm, the target weight decreases to 4 g. In order to increase the diffusion rate, it is planned to use a composite material in which uranium atoms are implanted into a UC_x structure ($x = 5$–7) (the density is about 1.5 g/cm^3).

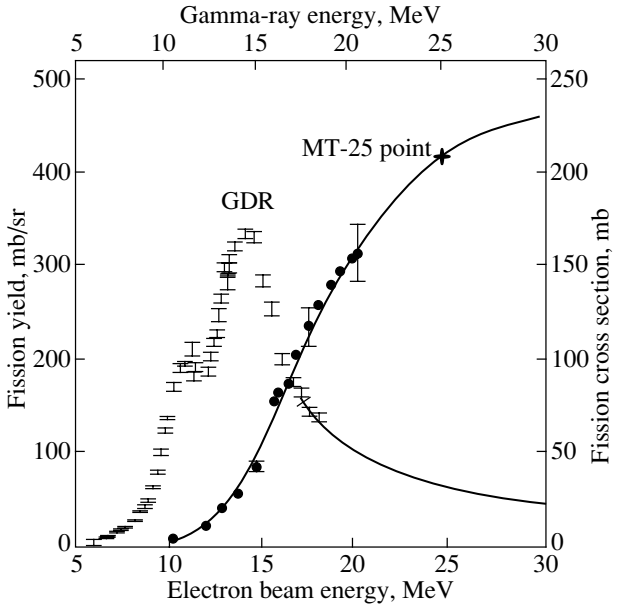

Fig. 2. Dependence of the ^{238}U fission cross section on the γ-quanta energy and the fission fragment yield taken from works indicated in the figure.

According to the tests performed at the Institute of Nuclear Physics (St. Petersburg), such a structure may contain up to 80% uranium by atomic weight. In this case, at a transversal cross section of the electron beam of $d_e = 5$ mm, the target configuration will look like a truncated cone with diameters $d_1 = 5$ mm and $d_2 = 15$ mm and a length of about 120 mm. When passing the target, the γ-ray-intensity loss due to absorption by carbon does not exceed 10%. To produce relatively long-lived radioactive atoms, which include, for example, the magic nuclides ^{132}Sn ($T_{1/2} = 40$ s), ^{133}Sb (2.5 min), and ^{134}Te (42 min), the target can be manufactured of a more solid type of uranium carbide (with a density of about 12 g/cm^2). In this case, the target volume can be decreased to 1.3–1.5 cm^3.

Atoms leaving the heated target are transported into an isobar separator directly connected to the working volume of the target. The separation is performed using the difference of the properties of elements at different temperature gradients of a moving collector. After the isobar separator, the atomic pairs reach an isotope separator source, designed in analogy with well-known sources operating in CSNSM (Orsay) and (GSI) (Darmstadt). After magnetic separation ($m/\Delta m \sim 1000$), the ion beam is to be transported by a special device to the laboratory of low-energy RIBs and via the beamline connecting the U400M and U400 accelerators.

Exotic fragments from photofission

Fragment and its characteristics	Y, 1/f	Y, 1/f (DRIBs)
^{78}Ni—doubly magic nucleus, $Z = 28$, $N = 50$	10^{-8}	10^{3}
^{80}Zn—closed shell at $N = 50$	10^{-6}	10^{5}
^{81}Ge—closed shell at $N = 50$	3×10^{-5}	3×10^{6}
^{131}In—closed shell at $N = 50$	10^{-3}	10^{8}
^{132}Sn—doubly magic nucleus, $Z = 50$, $N = 82$	3×10^{-3}	3×10^{8}
^{134}Sn—two neutrons above the closed shell	8×10^{-4}	10^{7}
^{100}Zr—beginning of deformation region	10^{-2}	10^{9}
^{104}Zr—strongly deformed nucleus	5×10^{-4}	5×10^{7}
^{160}Sm—strongly deformed nucleus	10^{-4}	10^{7}
^{134}Sb—delayed two-neutron decay	10^{-6}	10^{5}
^{140}I—delayed α decay	10^{-5}	10^{6}

Taking into account the widths of the mass and charge distributions of the fission fragments, the yields of definite fission fragments can be estimated. We have studied the yields of Kr ($A = 87$–93) and Xe ($A = 138$–143) isotopes formed as fission fragments in the photofission of ^{232}Th, ^{238}U, and ^{244}Pu. The distributions of xenon isotopes produced in the fission of ^{244}Pu, ^{232}Th, and ^{238}U induced by γ quanta are shown in Fig. 3. The largest cross sections for producing neutron-rich xenon isotopes are observed for the case of the plutonium target. The cross sections for the uranium target are a few times lower. The yield of neutron-rich xenon isotopes from the thorium target is almost an order of magnitude lower than for the uranium target. The isotopic distributions of fission fragments from the 14-MeV neutron-induced fission of uranium are presented in Fig. 4. The points denote the experimental data in the case of γ quanta of 25 MeV. As can be seen, the yields of Kr and Xe isotopes are almost equal in the two reactions using a uranium target. In the table, the yields of different exotic fragments are shown relative to the total number of fission fragments. From the table, it follows that, when the efficiency of the ion source and the transport system amounts to some 20–30%, it is possible to obtain beams of fission fragments in the region of Sn with an intensity of up to 10^{8} s^{-1}. Simultaneously with the fragments situated close to the maxima of the mass distribution ($A = 90$ and 130), asymmetric fission fragments are formed with a rather high yield. These are neutron-rich nuclei, which are of interest in connection with the studies of the structure of exotic nuclei. For the isotopes situated at the "tails" of the fragment mass distribution (for instance, for ^{80}Zr, ^{78}Ni), the yields are 10^{5}–10^{3} s^{-1}. This allows producing them in sufficiently large amounts to permit precise measurement of their decay characteristics. The problem lies only in the possibility of creating a relatively fast ion source having a diffusion time for these elements not longer than 0.1–0.2 s. The obtained ions, corresponding to the exotic nuclei with energies up to 10 keV, will be transported to a special experimental hall, where investigations will be carried out with low-energy radioactive nuclear beams. Low-energy radioactive beams of light elements obtained in fragmentation reactions at the U400M cyclotron will also be transported to the same area. In the low-energy radioactive beam laboratory (LERIS), investigations of the properties of exotic nuclei will be performed in the following directions.

2. NUCLEAR STRUCTURE

The data on the structure of neutron-rich nuclei with $30 \leq Z \leq 60$ is rather scarce, in spite of the fact that many interesting features have been predicted for them—new deformation regions, inversion of the energy levels, change of the sign of the deformation when going from neutron-deficient to neutron-rich nuclei [3], shape isomerism [4], etc. Figure 5 presents the systematics of the low-energy levels of the Sn isotopes. A sharp change in the energy is observed in the transition to the neutron-rich isotopes. Thus, for the 2^{+} states of the isotopes $^{120-130}$Sn, this value

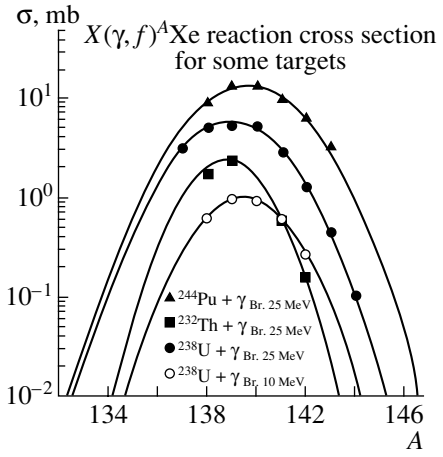

Fig. 3. Distributions of xenon isotopes produced in the fission of ^{244}Pu, ^{232}Th, and ^{238}U induced by γ quanta. The points denote the experimental data.

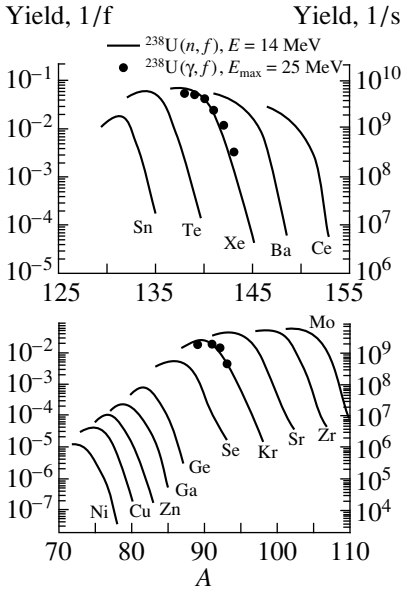

Fig. 4. Isotopic distributions of fission fragments from the 14-MeV neutron-induced fission of uranium. The points denote the experimental data.

amounts to ~1.2 MeV, while, for the isotope ^{132}Sn, it is already about 4 MeV. This can be explained by different factors, including the deformation close to the closed shell $N = 82$. In the framework of the given project, it is planned to study energy level schemes using 4π γ spectroscopy (gamma balls), the nuclear deformation, and root-mean-square radii—using the methods of collinear laser spectroscopy [5]. From this point of view, also interesting are nuclei with neutron magic numbers, e.g., $N = 82$, such as ^{131}In, ^{130}Cd, and ^{129}Ag, which will also be formed with yields

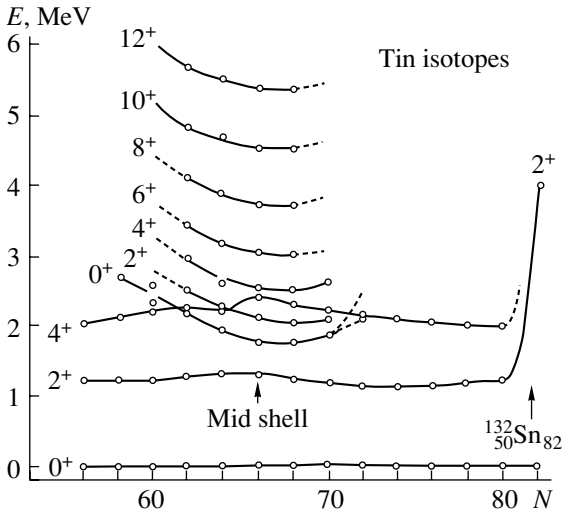

Fig. 5. The γ-quanta energies (E) for different Sn isotopes (N).

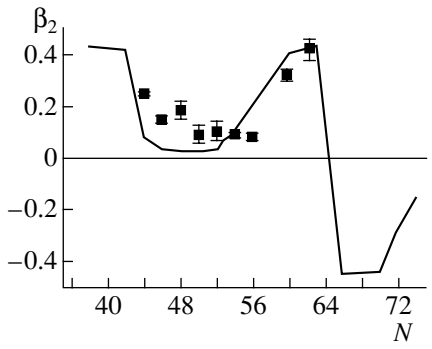

Fig. 6. Quadrupole deformation β_2 as a function of the neutron number of Zr isotopes.

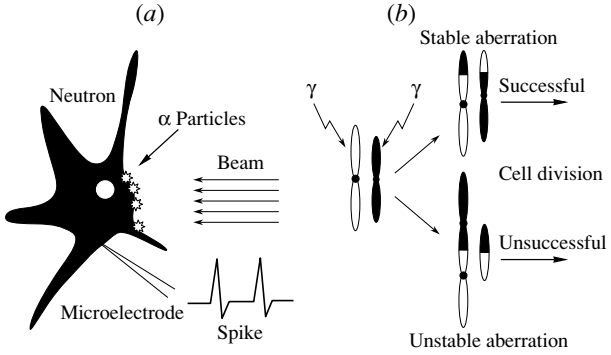

Fig. 7. (a) Neutron excitation. (b) Stable and chromosome aberration.

sufficient to allow investigating them with the above-mentioned methods.

As has been mentioned in some articles (e.g., [6]), because of the large deformation of the fission fragments, high-spin isomers can be formed. It is in-

teresting to study isomers such as ^{99m}Nb ($I = 5^+$), ^{125m}Cd ($I = 11/2^+$), ^{128m}In ($I = 8^-$), ^{130m}In ($I = 10^-$), ^{131m}Sn ($I = 11/2^-$), and ^{131m}Sn ($I = 19/2^-$). It is of additional interest within the DRIBs project to produce also isomeric beams.

The prospects are good for studying oriented nuclei using the methods of low-temperature nuclear orientation [7]. These methods allow a high-precision determination of the quadrupole moments of nuclei, including those of isomers. For odd-neutron nuclei, the LMR method has proven to be highly efficient [8]. It should also be mentioned that the low-temperature nuclear orientation method could be used for the production of polarized beams of fission fragments.

It is also interesting to study the neutron decay of fission fragments. Because of the relatively high β-decay energy of neutron-rich nuclei in this mass region, β-delayed $2n$- and $3n$-decay modes of nuclei such as ^{100,102}Rb, $^{131-133}$Cd, and $^{135-137}$Sn are possible. By investigating the correlation between the two neutrons emitted in the decay, it is possible to look for possible dineutron configurations in these nuclei. Estimation shows that, for neutron-rich fission fragments, exotic decay modes such as cluster decay are also energetically possible. Moreover, after β decay (for these nuclei $Q_\beta \geq 15$ MeV), the excitation of giant resonances at energies $E_{GR} \geq 15$ MeV is also possible.

Low-energy beams of fission fragments are expected to be very useful for high-precision measurements of nuclear masses. The exact determination of the mass excess of nuclei far from the line of β stability is a very important issue in nuclear physics. On the basis of the mass values, conclusions can be drawn about the stability of nuclei close to the nucleon drip lines as well as about the location of the drip lines themselves. The low-energy nuclides could be used in special high-frequency traps [8]. Also, the nuclei stored in such traps can be used for the determination of the charge radii and quadrupole moments using the methods of nuclear spectroscopy. Figure 6 presents the quadrupole deformation of different Zr isotopes. The experimental points obtained by means of nuclear spectroscopic methods are for isotopes up to ^{101}Zr. It can be seen that, for the two neutron-rich isotopes ^{100,101}Zr, the value of the deformation rapidly increases up to $\beta \approx 0.4$. The theoretical calculations within the shell model predict, for the Zr isotopes with $A > 101$, an abrupt change in the deformation and, moreover, a change in its sign. In order to reveal this interesting effect it is necessary to investigate all Zr isotopes including ^{106}Zr. All of them are produced with a rather high yield as fission fragments.

Thus, beams of fission fragments open new possibilities in the investigation of neutron-rich nuclei with Z in the range $30 < Z < 60$, which are, for the most part, poorly studied.

3. APPLIED RESEARCH WITH LOW-ENERGY FISSION-FRAGMENT BEAMS

When using low-energy radioactive beams for investigations in the field of condensed matter physics and biology, we should stress one very important advantage, namely, that they can be implanted in the studied object without causing any radiation damage, as is usually the case in the interaction of high-energy beams, where a large part of the imported energy is deposited at the end of the Bragg curve.

In the investigation of the structure of a crystal, the implanted radioactive nuclei emitting penetrating radiation (e.g., γ radiation) can experience a blocking effect inside the crystal lattice [9]. This radiation can be measured with special position-sensitive detectors. This allows determining with high resolution the structure of the crystal and its changes as a result of the radiation effects.

The use of low-energy radioactive beams opens new possibilities in radiobiological investigations. The usual methods in studying neurons and neuron meshes consist in exciting and measuring the signals using special microelements. In the case of implantation of a radioactive nucleus in the region of the studied neuron, the latter is subjected to excitation by the radiation, e.g., by α particles emitted by the implanted nucleus. Such a method allows excitation of a definite group of neurons without affecting or destroying the adjacent regions of biological tissues (Fig. 7*a*).

A fundamental problem of biology is the investigation of chromosomal aberrations, which can cause different illnesses, including oncological ones. Figure 7*b* shows a scheme of the interaction of radiation with chromosomes [10]. The chromosomes fission into two types and further they form new chromosomes. At this point, stable and unstable aberrations can be realized. The unstable aberrations can lead to the creation of new degenerated cells, which are the cause of different illnesses at a genetic level. The modeling of such processes can be carried out efficiently by implanting radioactive nuclei in the region of the investigated cells.

ACKNOWLEDGMENTS

This work has been carried out with financial support from INTAS (grant no. 00-00463) and from the Russian Foundation for Basic Research (project no. 01-02-22001).

REFERENCES

1. Yu. Ts. Oganessian, *Brief Description of the Dubna Radioactive Ion Beams Project "DRIBs"* (Dubna, 1998).
2. J. T. Caldwall *et al.*, Phys. Rev. C **21**, 1215 (1980).
3. J. L. Wood *et al.*, Phys. Rep. **102** (3–4) (1983).
4. K. Neergard *et al.*, Nucl. Phys. A **262**, 61 (1976).
5. Yu. P. Gangrsky, Part. Nucl. **23**, 1616 (1992).
6. H. Kudo *et al.*, in *Proceedings of the VI International School–Seminar on Heavy Ion Physics, Dubna, 1997,* Ed. by Yu. Ts. Oganessian and R. Kalpakchieva (World Sci., Singapore, 1998), p. 675.
7. *Proceedings of the International Workshop on Symmetry and Spin, Prague, 1998,* Ed. by M. Finger, Czech J. Phys. **49** (1999).
8. N. Hermanspahn *et al.*, Acta Phys. Pol. B **27**, 357 (1996).
9. M. Morjean *et al.*, in *Proceedings of the VI International School–Seminar on Heavy Ion Physics, Dubna, 1997,* Ed. by Yu. Ts. Oganessian and R. Kalpakchieva (World Sci., Singapore, 1998), p. 683.
10. E. A. Krasavin and S. Kozulek, *Mutagenetic Influence of Radiation with Different Linear Energy Transfer* (Énergoizdat, Moscow, 1991).

Physics of Atomic Nuclei, Vol. 66, No. 8, 2003, pp. 1413–1420. From Yadernaya Fizika, Vol. 66, No. 8, 2003, pp. 1459–1466.

Isotopic Production Cross Sections of Residues in Reactions Induced by Relativistic Heavy Ions with Protons and Deuterons*

E. Casarejos[1)], P. Armbruster[2)], L. Audouin[3)], J. Benlliure[1)], M. Bernas[3)], A. Boudard[4)], R. Legrain[4)], S. Leray[4)], B. Mustapha[3)], S. Czajkowski[5)], T. Enqvist[6)], B. Fernandez[4)], J. Pereira[1)], M. Pravikoff[5)], F. Rejmund[3)], K.-H. Schmidt[2)], C. Stephan[3)], J. Taieb[3)], L. Tassan-Got[3)], C. Villagrasa[4)], C. Volant[3)], and W. Wlazlo[2)]**

[1)] *Universidad de Santiago de Compostela, Spain*
[2)] *GSI, Darmstadt, Germany*
[3)] *Institut de Physique Nucléaire, Orsay, France*
[4)] *DAPNIA/SPhN, CEA/Saclay, Gif-sur-Yvette, France*
[5)] *CENBG, France*
[6)] *University of Jyväskylä, Finland*

Received December 15, 2002

Abstract—The isotopic production cross sections of heavy residues in relativistic heavy-ion collisions have been investigated in inverse kinematics. The primary reaction products were fully identified in mass and atomic number prior to beta decay using the fragment separator FRS. The huge collection of data obtained helps in the understanding of the two main reaction mechanisms involved: fragmentation and fission. These data provide basic information for future radioactive ion beam facilities and for technical applications like intense neutron sources by means of spallation targets. © *2003 MAIK "Nauka/Interperiodica".*

INTRODUCTION

A large experimental program was initiated at GSI in 1996 to determine the production cross sections of heavy residues in relativistic heavy-ion collisions [1–9]. The project aimed to study the fission and fragmentation reaction mechanisms involved in relativistic heavy-ion collisions, defining a large benchmark data collection. Already, these data are relevant for accelerator-driven reactor systems (ADS) [10, 11]. The residues investigated are a result of so-called spallation reactions, understood as a two-step process [12]. The impact of a light nucleus (or nucleon) into a heavy target nucleus induces a certain preequilibrium emission and the formation of an excited prefragment. The further deexcitation of the prefragment by either particle emission or fission, the second step, defines the reaction mechanism leading to the residue.

These data provide basic information for intense neutron sources, needed for materials science investigation, and in technical application as those of the ADS. The production of intense radioactive ion beams is nowadays feasible using isotope separation on-line ISOL techniques, based on spallation reactions [13]. The production of either neutron deficient or neutron-rich nuclides depends on the reaction mechanisms involved, determining the available intensities. A better understanding of the mechanisms will allow a correct evaluation of the productions and improve the expected intensities. Additionally, spallation produces excited nuclear matter at normal densities while keeping the angular momentum low. Those are the conditions allowing one to investigate the onset of thermal multifragmentation.

The experiments were performed in inverse kinematics, using a relativistic heavy-ion beam and a cryogenic target of liquefied hydrogen or deuterium. The primary reaction products were fully identified in mass and atomic number prior to beta decay, using the fragment separator FRS. This technique allows an unambiguous identification of the residues. This kind of study gives access directly to the primary reaction production, thus allowing the study of the reaction mechanisms. The following list shows the reactions studied so far:

$$^{197}\mathrm{Au}(0.8\,A\ \mathrm{GeV}) + p \quad [4, 5],$$

$$^{208}\mathrm{Pb}(1,\ 0.8,\ 0.5\,A\ \mathrm{GeV}) + p \quad [1, 2],$$

*This article was submitted by the authors in English.

** e-mail: casarejo@usc.es

$$^{208}\mathrm{Pb}(1\,A\ \mathrm{GeV}) + d \quad [3],$$
$$^{238}\mathrm{U}(1\,A\ \mathrm{GeV}) + p \quad [6, 7],$$
$$^{238}\mathrm{U}(1\,A\ \mathrm{GeV}) + d \quad [8],$$
$$^{57}\mathrm{Fe}(1.0,\ 0.7, 0.5\,A\ \mathrm{GeV}) + p \quad [9].$$

The list of reactions studied is representative of the chart of nuclides, covering from the heaviest stable isotope to intermediate-mass nuclides. The additional study of Xe, foreseen before 2003, will close the program. Lead is a very interesting reaction since it is the first candidate to be the spallation target in ADS projects. Uranium, the heaviest, is also a highly fissile nuclide, thus showing the strength of that reaction mechanism. Iron is interesting from the point of view of nuclear astrophysics, since it is a very valuable element to understand the observed abundances, but also for ADS projects since it represents structural materials. The studies with proton and deuteron help to understand the reactions induced by protons and neutrons in collisions of heavy ions.

These data will also allow one to improve our understanding of the two reaction mechanisms involved. The different production after, e.g., ^{238}U and ^{208}Pb allows one to investigate the influence of the fissility and nucleus deformation in the reaction process. The studies with proton and deuteron shows the extension from a single-nucleon to double-nucleon collision, as well as the influence of the wide spatial distribution of the nuclear matter. Thus, we can discuss topics such as the energy deposition in the collision, the geometry of the impact, or the strength of the fission channel.

EXPERIMENTAL TECHNIQUE

The experiments were performed at GSI by shooting the heavy-ion beam accelerated in the SIS synchrotron into a cryogenic liquefied hydrogen (deuterium) target with a thickness of about 80 (200) mg/cm^2. The cryogenic target was used for the first time in this kind of experiments, allowing access to proton- and deuteron-induced reactions. The liquid is encapsulated within a vessel made of Al and Ti to preserve the vacuum of the beam and residues line. The beam intensities, up to 10^8 particles/s, were measured continuously by a secondary electron transmission monitor (SEETRAM) [14], as well as the dead time of the acquisition (<30%). The produced residual nuclides were fully identified in mass and atomic numbers, while flying forward, using the FRS [15], a 70-m-long zero-degree magnetic spectrometer, and a dedicated detection setup. This technique, so-called inverse kinematics, allowed us to measure a large amount of high-quality data in a single experiment. The separation of the heavy residues with good resolution, $A/\Delta A \sim 400$, is a very exigent technique, being possible with the FRS, which has an angular acceptance of 15 mrad, a longitudinal-momentum acceptance of 3%, and a resolving power of 1600, and was used as an achromatic energy-loss spectrometer.

Two plastic scintillators, two ionization chambers, and two multiwire proportional chambers, were used to provide information on position and energy losses of the residues in flight. The short times of flight involved (<200 ns) allowed us to observe the primary production of the reaction, overcoming the radioactive decay drawback present in direct kinematic experiments [16]. Only a few extremely short lived alpha emitters with 128 neutrons, having half-lives around 100 ns, partly decayed inside the spectrometer. For all other nuclides, the production cross sections were determined prior to their radioactive decay.

The beam allowed the calibration of the involved detectors (for velocity, energy loss, and particle counting), the ion-optical parameters of the FRS, and the thicknesses of the layers of matter present in the path of the residues. The measurement of the magnetic fields of the FRS and the position of the particles in the magnetic dispersion coordinate at the focal planes of the FRS defines the magnetic rigidity $B\rho$ of each residue. Its time of flight, after the calibration and correction of the flying path along the FRS, defines the relativistic $\beta\gamma$ value. The definition of the ionic charge Q to mass A ratio of each residue is made according to the relationship $B\rho = (A/Q)(u/e)\beta\gamma$, where u and e are the atomic mass and charge units, respectively. The FRS provides the power to separate with enough accuracy the rigidities involved in our experiments. The setup must be adequate to determine the time of flight and atomic and nuclear charges.

The rigidity distributions measured in the intermediate focal plane of the FRS can be linked to the longitudinal momentum of the nuclide, as far as the ion has been identified. Actually and due to the limited longitudinal momentum acceptance of the FRS, the production and momentum of each nuclide are measured in several overlapping steps, which is possible by adequate tuning of the FRS. The limitation in angular acceptance determines the final FRS transmission for each nuclide (see [17]). The transmission is close to 100% for the heavier spallation-evaporation residues, decreasing with mass. In the case of spallation-fission residues, the kinematic changes drastically lead to more reduced transmissions.

Thus, our technique allows us to measure not only the production but also the momentum distribution of the residue. That information is very valuable for the model describing the reaction mechanisms as well

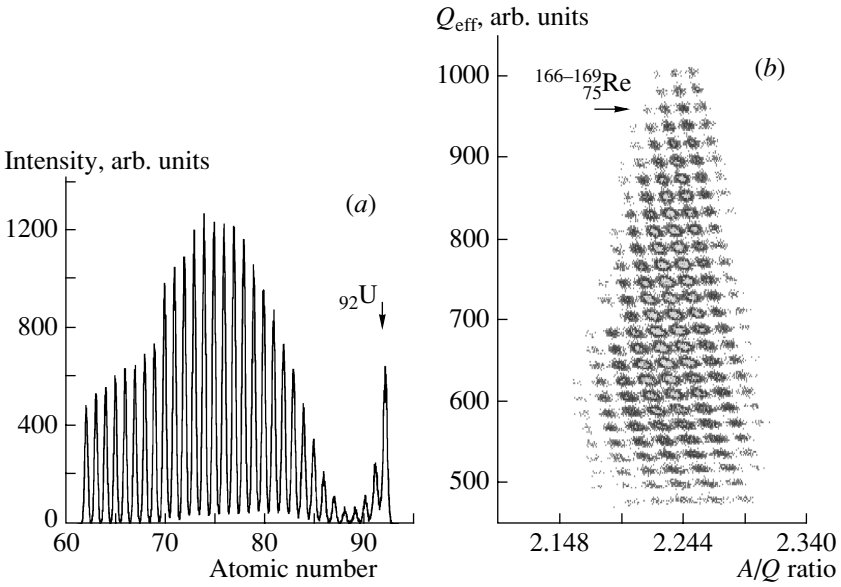

Fig. 1. (*a*) Energy loss Q_{eff} measured in one ionization chamber at the exit of the spectrometer. The beam allows the calibration to define the atomic charge of the ion. (*b*) Energy loss Q_{eff} vs. the A/Q ratio defined with the magnetic rigidity. Each spot corresponds to one isotope: some of element Re is indicated.

as for technical applications in ADS. What is more valuable, it allows us to disentangle the two reaction mechanisms present there: fission and evaporation (see, e.g., [3]).

If the produced ions were fully stripped, the atomic and nuclear charges would be the same, and a measurement of the energy loss, with enough resolution, would determine Z. The beam allows the calibration of the energy loss to determine the charge of the ion. Since the magnetic rigidity and time of flight measured in the FRS determine the A/Q ratio, the identification is completed. In Fig. 1*a*, we show an energy loss distribution: the peak corresponding to the beam (U case) is marked. Since the bare ions have been selected as explained above, the atomic number can be determined. The resolution can be appreciated better in Fig. 1*b*: the energy loss is plot as a function of the A/Q ratio for bare ions. Each spot corresponds to one isotope: the separation achieved is clearly stated.

In general, at the energies of our experiments, the heavier ions are not fully stripped, some of them carrying one or even two electrons, the distribution depending strongly on Z number. Our collaboration has developed a dedicated technique to disentangle and measure both Q and Z with enough resolution so that the identification is fully unambiguous (see [1–9]). The method is based in the use of a profile achromatic energy degrader [18].

CROSS SECTIONS

To determine the production cross sections, we had to correct the measured counting rates of each identified nuclide for the different effects inherent to our method, previous to the normalization to the target thickness and beam intensity. The dead time of the whole acquisition system was monitored with an accuracy within 1%. The uncertainty in beam intensity was 4% after the calibration of the SEETRAM. The uncertainty in the target thickness was calculated including the deformation of the target walls and alignment of beam-target axis, resulting in 3%. The statistical accuracy aimed for in the project was a limit of 10% for productions above 0.1 mb. For most spallation-evaporation residues, that accuracy is usually better. However, in the case of spallation-fission residues, due to the limited production, the accuracy limit is reached, e.g., in the reaction of lead with deuterium, for productions above 1 mb. The statistical accuracy was investigated by comparing the measured cross sections of nuclides along paths of the chart of nuclides with a softer change than that of the isotopic chains. We have used, e.g., the chains following the $N - Z =$ const relationship. The deviation of any measured production from the smoothed trend observed induces a correction. The statistical quality of the data is shown in the smoothness of the isotopic cross sections in Fig. 2.

The limited longitudinal momentum acceptance of the spectrometer is overcome by overlapping several magnetic settings, which scan the whole momentum distribution for each nucleus. The transversal distributions, of few mrad, maybe are not fully accepted. A dedicated study of that problematic allowed us to evaluate the correction to apply with an accuracy

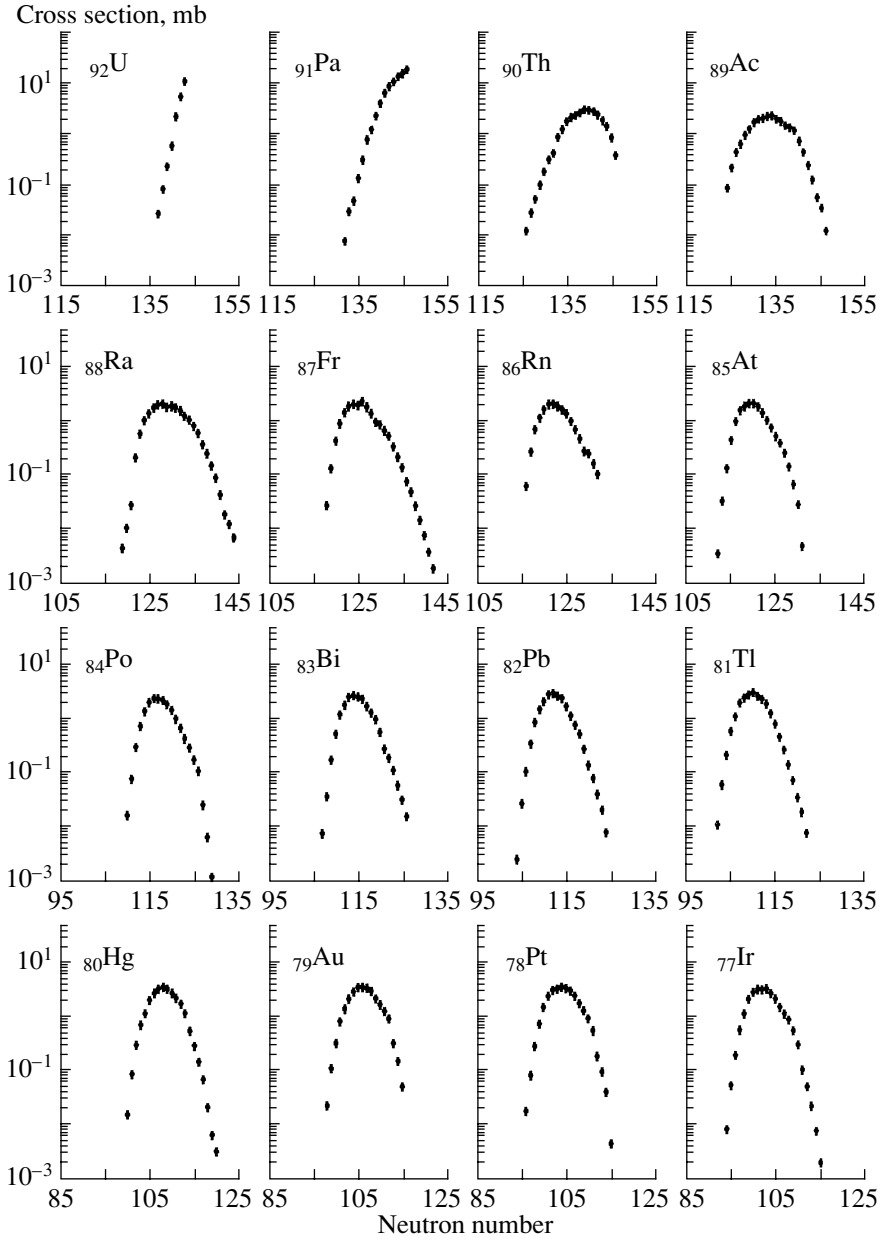

Fig. 2. Isotopic production cross sections of elements $_{77}$Ir to $_{92}$U, measured in the reaction ^{238}U(1 A GeV) + d [8]. The error bars are visible if larger than the symbol size.

better than 10%. The correction depends on the kinematics of the reaction mechanisms involved, resulting in a factor below 15% for evaporation residues and increasing very fast with decreasing masses for fission residues.

The momentum scanning was designed to recover the momentum distributions of all the bare nuclides produced. To correct the observed production, we had to evaluate the probability of having bare ions along the FRS, as well as within the ionization chambers. The evaluation was done according a three-states method [19], since at our energies the bare hydrogen-like and helium-like states are the only populated states. The calculations were cross checked with values that we measured in our system, and the uncertainty established was 5%.

The secondary reactions in any layer of matter along the path of the detection change the production intensity of any nuclide. The setup and identification method guarantee that this secondary production does not contaminate any other residue. Thus, we have to correct the production of each nucleus according the losses in all the matter traversed. Both nuclear [20, 21] and electromagnetic-

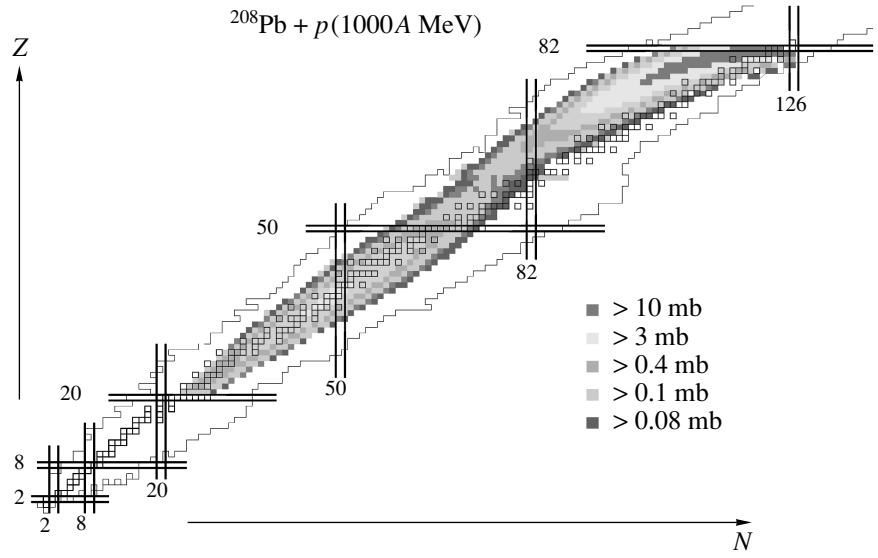

Fig. 3. Production cross section of residues measured in the reaction of ^{208}Pb (1 A GeV) with proton [1] plotted on a gray-scale on top of a chart of nuclides.

dissociation [22, 23] processes have been considered in the evaluation of the total reaction cross section. The former process is evaluated with a microscopic Glauber-like method that we have modified to deuteron density. The later process is evaluated by considering the virtual photon field equivalent to the target nucleus and the photon absorption cross section of the projectile. The losses in the degrader amount up to 40% for the heavier residues, since we have used a degrader thickness above 4 g/cm^2, adjusted to the range of the ions detected (see [18]). The cross section values for these processes were obtained with an accuracy of 10%.

With the former corrections, we can evaluate the production of the whole target assembly. To subtract the production related to the Al (19 mg/cm^2), Ti (41 mg/cm^2), and Nb (60 mg/cm^2) components present at the target area either as layers of the target structure or as strippers, we have performed the same measurements but with an empty target container. The productions observed due to those additional materials were typically below 3% of the total for the heavy spallation-evaporation residues. In some cases, the whole collection of residue data after the empty target was not measured, but partially. Then, we evaluated the production with reliable simulation codes, and the results were compared with the available data to estimate the accuracy.

The observed yields suffer additionally from multiple reactions happening within the target itself. The resulting production we have observed is then a redistribution of the primary production we aimed to measure. The possibility of correcting the measured values relies in a realistic evaluation of the production cross section values of any residue within the target material, according to the method described, e.g., in [1]. This correction includes both the attenuation of the beam (and residue) flux within the target and the additional contributions from other nuclides (increasing for lower masses). The resulting uncertainty of the cross-section values was 8–30%, depending on the mass.

RESULTS

Within our project, we have already measured several thousand isotopic cross sections. The quality and quantity of data now available allow us to discuss the most salient features of each reaction. In Fig. 3, we can see the isotopic production cross sections of residues of ^{208}Pb (1A GeV) induced by a proton [1] plotted on top of a chart of nuclides. The production of any residue is determined by the competition among the two open deexcitation channels: neutron or light-charged particle emission (evaporation), and fission. An excited prefragment with more than 80 protons has a large probability of undergoing fission, thus limiting the production of evaporation residues with Z above 80. Below that limit, the fission channel is weakly populated, and the residue production lies in the so-called fragmentation corridor or evaporation attractor line, defined by the competition of proton and neutron emission, thus along the neutron-deficient side. The residues we observe in Fig. 3 on the neutron-deficient side with atomic masses above 20 are the result of evaporation processes. Those residues with intermediate masses and populating the

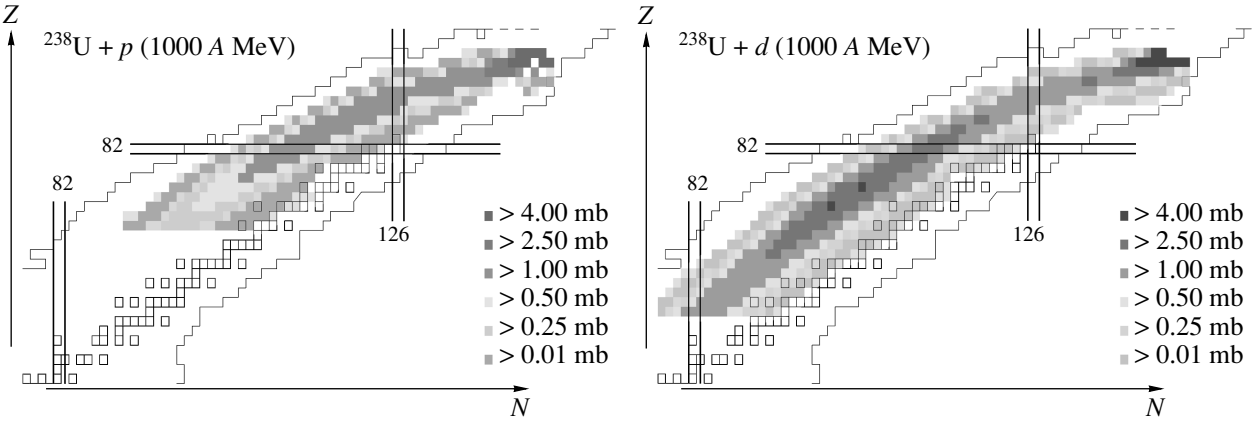

Fig. 4. Production cross sections measured in the reaction ^{238}U (1 A GeV) with proton (left panel, [6]) and deuteron (right panel, [8]), plotted on a gray-scale on top of a chart of nuclides.

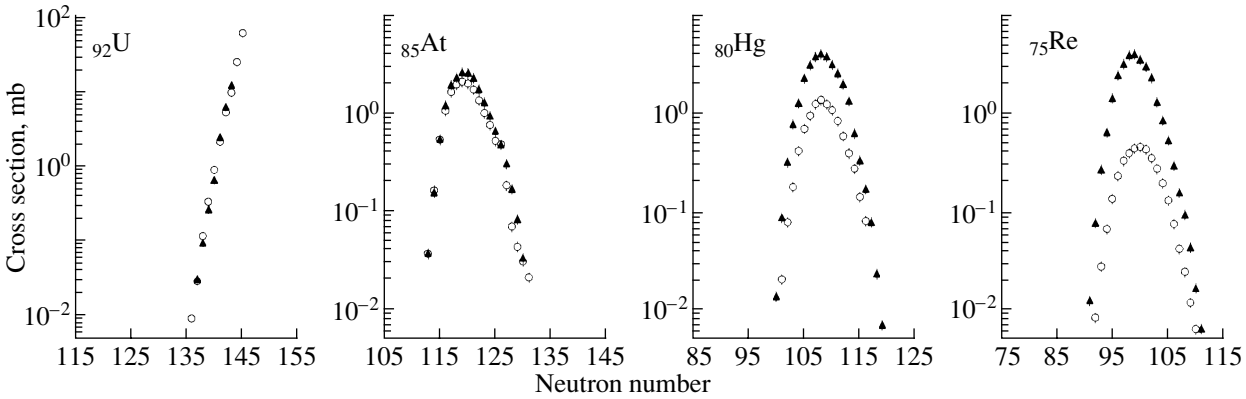

Fig. 5. Isotopic production cross sections measured in the reaction ^{238}U (1 A GeV) with proton (open symbols, [6]) and deuteron (full symbols, [8]) for elements $_{92}$U, $_{85}$At, $_{80}$Hg, and $_{75}$Re. The error bars are visible if larger than the symbol size.

neutron-rich side are fission residues, clearly seen in the case of the deuteron reaction. Both productions overlap in many isotopic chains. The possibility of disentangling the mechanisms relies on the different kinematic result after each process. The measurement of the longitudinal momentum distribution of each isotope allows us to separate both contributions, as mentioned before.

Energy Deposition

In Fig. 4, we show the isotopic cross sections measured in the reactions of ^{238}U (1A GeV) induced on a proton (left panel, [6]) and deuteron (right panel, [8]). We can observe that the position of the corridor is common to proton and deuteron systems, as expected in the limiting fragmentation regime. It is also the same position for gold or lead residues. However, the length of the corridor is larger in the case of the deuteron residues than those of the proton. This effect is due to the additional available excitation energy in the system just after the collision. The deexcitation process can proceed thorough larger evaporation chains, reaching lighter residues.

In Fig. 5, we show the isotopic distribution of residues from the reactions induced by ^{238}U (1A GeV) on a proton (open symbols, [6]) and deuteron (full symbols, [8]) for some elements. Residues close to the projectile show a rather similar production in both reactions. This observation can be explained if we consider that the heaviest residues result from the most peripheral collisions. Due to the large spatial distribution of the deuteron, many of the impacts involve a single nucleon. Thus both reactions, with deuteron and proton, result in the same production. Consequently, no differences between neutron and proton impacts were found. For elements with Z below 80, the production by a deuteron increases with respect to that of a proton.

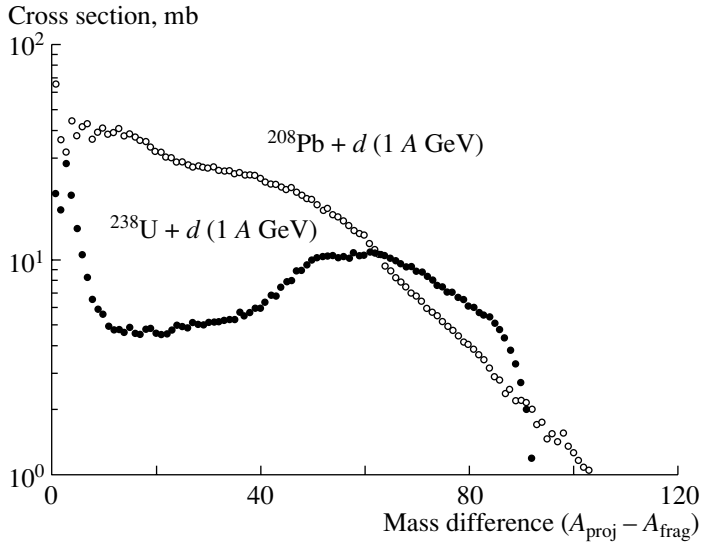

Fig. 6. Mass distribution of production of residues in the reactions induced by ^{208}Pb [3] and ^{238}U [8] on deuteron as a function of the difference in mass of the residue in respect to the projectile.

Fission Influence

In Fig. 6, we compare the residual isobaric distribution, that is, the production added for a given mass of the residue, in the reactions induced by ^{208}Pb [3] and ^{238}U [8] on a deuteron, as a function of the difference in mass of the residue with respect to the projectile. As is known from other spallation reactions [4], the results are expected to be similar, just scaled by the ratio of the total reaction cross sections: that is the case of gold or lead. However, large differences in the production of heavy residues were observed, due to the fission channel. This channel largely dominates the reaction mechanism in the neighborhood of the projectile ^{238}U, depopulating the production of residues close to the projectile and populating medium-mass residues.

The strength of this process causes the production of the neutron-deficient isotopes of the heaviest elements to be drastically reduced, due to the drop of the fission barrier. That imposes requirements of beam intensities to reach the proton drip line efficiently and produce, e.g., heavy proton emitter candidates.

CONCLUSIONS

The experimental effort developed within this project has already resulted in a huge data collection of residue production cross sections of relativistic heavy-ion reactions with protons and deuterons. This collection allows a systematic study of the reaction mechanisms that are present in these processes.

The deuteron data showed the influence of the larger energy available in the system, with respect to nucleon-induced reactions. Longer deexcitation chains populated lower mass isotopes, extending the fragmentation production to masses 100 units below that of the projectile. The difference in energy deposition between nucleon and ion collisions can also be investigated. We also showed how the strength of the fission mechanisms determines the production of heavy spallation residues. The range of impact parameters that enhance the probability of a single-nucleon collision of deuterium showed (i) no difference between proton and neutron impact and (ii) that proton- and deuteron-induced reactions share a common wide range of production due to the large spatial distribution of the deuterium.

The comparison of the results from proton- and deuteron-induced reactions will allow one to improve the description of the impact of several nucleons, since the deuteron is the simplest extension after the collision of a single nucleon. The comparison of reactions involving ions with very different fissilities helps to determine the accuracy of the competition of the fission and particle emission. The projects for production of intense radioactive ion beams or neutron sources for ADS depend on complex models describing also the basic processes involved, such as evaporation and fission. A satisfactory description of the two steps of the reaction by the available or future models definitely depends on the collections of measured data used as a benchmark. This work has contributed largely to the success of that project.

ACKNOWLEDGMENTS

This work was partially supported by the European Commission under projects EC-HPRI-CT-1999-00001 and FIS5-1999-00150.

REFERENCES

1. T. Enqvist *et al.*, Nucl. Phys. A **686**, 481 (2001).
2. B. Fernandez *et al.*, in *Proceedings of the XL International Winter Meeting on Nuclear Physics, Bormio, Italy, 2002*.
3. T. Enqvist *et al.*, Nucl. Phys. A **903**, 93 (2002).
4. F. Rejmund *et al.*, Nucl. Phys. A **683**, 540 (2001).
5. J. Benlliure *et al.*, Nucl. Phys. A **683**, 513 (2001).
6. J. Taieb, Ph.D. Dissertation, Univ. de Paris Sud, U. F. R. Scientifique d'Orsay (France, Sept. 2000), IPN report IPNO-T-00-10.
7. V. Ricciardi *et al.*, in *Proceedings of the XXXIX International Winter Meeting on Nuclear Physics, Bormio, Italy, 2001*.
8. E. Casarejos, Ph.D. Dissertation, Univ. of Santiago de Compostela (Spain, June 2001), GSI Diss-04-2002.
9. C. Villagrasa *et al.*, in *Proceedings of the XL International Winter Meeting on Nuclear Physics, Bormio, Italy, 2002*.
10. C. Rubbia *et al.*, Report CERN-AT/95-44 (ET) (Geneva, 1995).
11. C. D. Bowman, Annu. Rev. Nucl. Part. Sci. **48**, 1029 (1998).
12. R. Serber, Phys. Rev. **72**, 1114 (1947).
13. See, e.g., the *Proceedings of the 5th Conference on Radioactive Nuclear Beams, Divonne, France, 2000*, Nucl. Phys. A **701** (2002).
14. B. Jurado, K.-H. Schmidt, and K.-H. Behr, Nucl. Instrum. Methods Phys. Res. A **483**, 603 (2002).
15. H. Geissel *et al.*, Nucl. Instrum. Methods Phys. Res. B **70**, 286 (1992).
16. R. Michel *et al.*, Nucl. Instrum. Methods Phys. Res. B **103**, 183 (1995); **129**, 153 (1997).
17. J. Pereira *et al.*, Nucl. Instrum. Methods Phys. Res. A **478**, 493 (2002).
18. J. P. Dufour *et al.*, Nucl. Instrum. Methods Phys. Res. A **248**, 267 (1986).
19. Ch. Scheidenberger *et al.*, Nucl. Instrum. Methods Phys. Res. B **142**, 441 (1998).
20. P. J. Karol, Phys. Rev. C **11**, 1203 (1975).
21. T. Brohm and K.-H. Schmidt, Nucl. Phys. A **569**, 821 (1994).
22. Th. Rubehn *et al.*, Z. Phys. A **353**, 197 (1995).
23. K.-H. Schmidt *et al.*, Nucl. Phys. A **665**, 221 (2000).

Physics of Atomic Nuclei, Vol. 66, No. 8, 2003, pp. 1421–1427. From Yadernaya Fizika, Vol. 66, No. 8, 2003, pp. 1467–1473.

Decay of Neutron-Rich Ga Isotopes near $N = 50$ at PARRNe*

O. Perru**, **F. Ibrahim, O. Bajeat, C. Bourgeois, F. Clapier, E. Cottereau, C. Donzaud, M. Ducourtieux, S. Galès, D. Guillemaud-Mueller, C. Lau, H. Lefort, F. Le Blanc, A. C. Mueller, J. Obert, N. Pauwels, J. C. Potier, F. Pougheon, J. Proust, B. Roussière, J. Sauvage, O. Sorlin, and D. Verney**

Institut de Physique Nucléare, Orsay, France

Received January 9, 2003

Abstract—The PARRNe facility has been used to produce neutron-rich isotopes ^{83,84}Ga by the ISOL method. Their decay has been studied, and β–γ coincidence and γ–γ coincidence data were collected as a function of time. The first two excited levels in ^{83}Ge and the first excited level in ^{84}Ge have been measured for the first time. © *2003 MAIK "Nauka/Interperiodica".*

1. INTRODUCTION

The existence of magic numbers is the basis of the nuclear shell model. Testing the persistence of magic numbers near the drip line allows one to improve the validity of this model far from stability. To do so, measuring the lowest excited states energies provides a clear signature of shell persistence since, in nuclei with magic numbers of either protons or neutrons, these energies are very high as compared to their neighbors. In particular, in even–even nuclei, the first excited state is nearly always a 2^+ state and its energy is much higher in magic nuclei.

In this context, the $N = 50$ shell closure is interesting to study, near the $Z = 28$ shell closure. It has been shown that, when the neutron shells are filled up to 50, 40 can be considered as magic for protons [1]. In Fig. 1 are represented the 2^+ energies of nuclei with $N = 50$, and with even Z from 32 to 40, the two shell closures are marked with black lines, and the midshell is marked with a dashed line. It is interesting to note that, although the behavior of this systematic is expected to be symmetric with respect to the midshell, the 2^+ energy of ^{82}Ge lies lower than that of ^{84}Se.

The status of our present knowledge of the first 2^+ state in this region is represented in Fig. 2 [2–30]. The $N = 50$ shell closure is marked for Zr, Sr, Kr, and Se: the 2^+ energy at $N = 50$ is much higher than the 2^+ energy at $N = 48$ and $N = 52$. For Ge, data at $N = 52$ are missing; the goal of our experiment was to measure the first excited level in ^{84}Ge.

We have produced ^{84}Ga and ^{83}Ga and studied their β decay. In this region, nuclei also decay by β–n: β–n decay of ^{83}Ga feeds excited levels in ^{82}Ge, while excited levels in ^{83}Ge are fed by β decay (see Fig. 3). Since the transitions in ^{82}Ge are well known [31], the new transitions identified in the decay of ^{83}Ga are then attributed to ^{83}Ge. Then, the rays associated with the decay of excited levels in ^{83}Ge, fed by β–n decay of ^{84}Ga, can be isolated in the spectra when one would expect any unidentified line to belong to ^{84}Ge.

2. EXPERIMENTAL PROCEDURE AND RESULTS

The aim of the experiment is to study the decay of neutron-rich ^{83,84}Ga isotopes which feed excited levels of the nuclei of interest ^{83,84}Ge by β and β–n decay. The Ga isotopes were obtained from the fission of ^{238}U at the PARRNe mass separator (Production d'Atomes Radioactifs Riches en Neutrons), installed at the tandem at Orsay. The aim of the PARRNe program is to produce neutron-rich radioactive beams by the ISOL method. The 25-MeV deuteron beam delivered by the 15-MV tandem hits a 12-mm-thick graphite converter placed 40 mm upstream from the center of the target. The fast neutrons produced in the breakup of the deuterons irradiate a UC_x target heated in a graphite oven up to 2200°C. The fission fragments released from the target flow to a MK5 ISOLDE-type ion source to be ionized. The ions are extracted under 30 kV, then mass separated by a magnet, and finally collected on a mylar/aluminium tape (see Fig. 4). The production rate for ^{83,84}Ga was on the order of 1 to 0.1 nucleus/s.

*This article was submitted by the authors in English.

**e-mail: perru@ipno.in2p3.fr

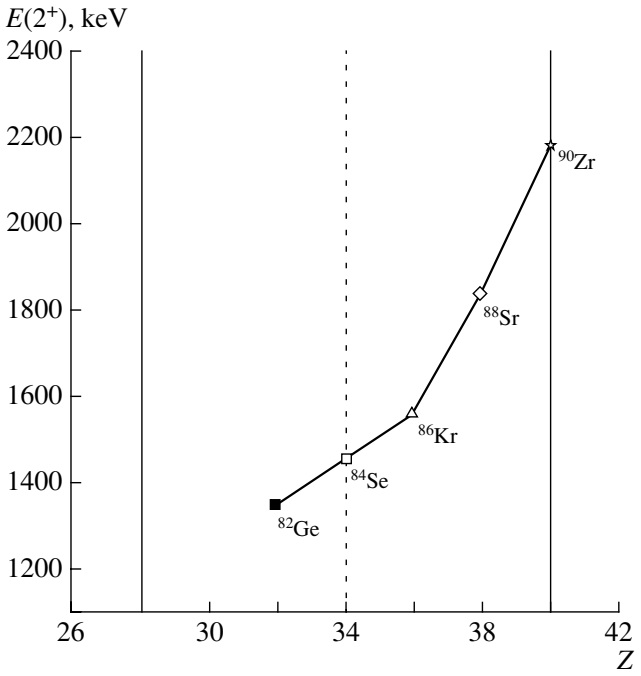

Fig. 1. 2^+ energies for $N = 50$ isotones. The lines at $Z = 28$ and $Z = 40$ show the shell closures, and the dashed line represents the midshell.

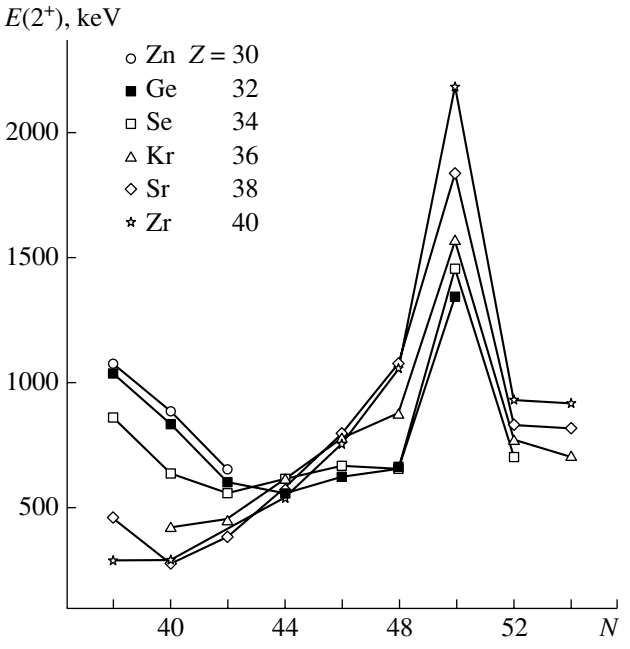

Fig. 2. 2^+ energies for different isotopes. The $N = 50$ shell closure is clearly marked.

The detection setup consisted in a 4π plastic scintillator detector surrounding the tape and two Ge detectors very close to the tape to obtain a better efficiency: direct γ spectra from the two Ge were added. The two Ge detectors were used to perform γ–γ coincidences. With this setup, we can also detect β and γ in coincidence. The selected beam is collected on the tape for one second, and then the beam is deflected for another one second. At the end of the two seconds, the tape moves, and we again start the same collection–decay operation. The coding is suspended by a coding enable signal when the tape moves, and starts at the beginning of a new cycle of collection–decay.

Each event is labeled with absolute time by using an electronic module of the COMET type [32]. This allows us to look for coincidences on-line but also off-line by soft computing with the appropriate time window. During the experiment, we looked for β–γ coincidences in a 400-ns window. For the analysis of the data, we felt it necessary to reduce the background by reducing this window down to 70 ns.

We have built a bidimensional spectrum γ energy vs. β time for β and γ in coincidence. This allows us to see the time evolution of each γ line between two coding enable signals and to perform a Z identification by measuring their half-lives. This is the way we have attributed levels to ^{83}Ge and ^{84}Ge. As an example, the spectrum in Fig. 5 represents the projection on the time axis of the β events in coincidence with 1348-keV γ rays from a coding enable signal to another. The growth corresponds to the collection, and we observe the decay when the beam is deflected. The measured half-life for the decay is 376 ± 74 ms, which corresponds to the half-life of ^{83}Ga (310 ± 10 ms [30]). For comparison, the same spectrum in coincidence with background γ rays, displays no distinct time structure (Fig. 6). We have also built a bidimensional γ–γ energy spectrum for γ in coincidence with a β.

With such a setup, we were able to distinguish between transitions from β decay of ^{84}Ga and ^{83}Ga.

2.1. ^{83}Ge

What happens for the decay of ^{83}Ga is illustrated in Fig. 3: the β decay of this nucleus feeds the excited levels of ^{83}Ge whose γ are detected in coincidence with the β; the β–n decay feeds the excited levels of ^{82}Ge; its γ are also detected in coincidence with a β. Therefore, in the $A = 83$ γ spectrum, γ lines from transitions in both ^{82}Ge and ^{83}Ge are present. Since the neutron emission is very quick it does not contribute to the measured decay time of peaks in ^{82}Ge. Then, in our measurements, γ transitions of ^{83}Ge and ^{82}Ge have the same time spectrum, and their decay time is 310 ± 10 ms, which is the ^{83}Ga half-life. The ^{82}Ge transitions are well known, a detailed

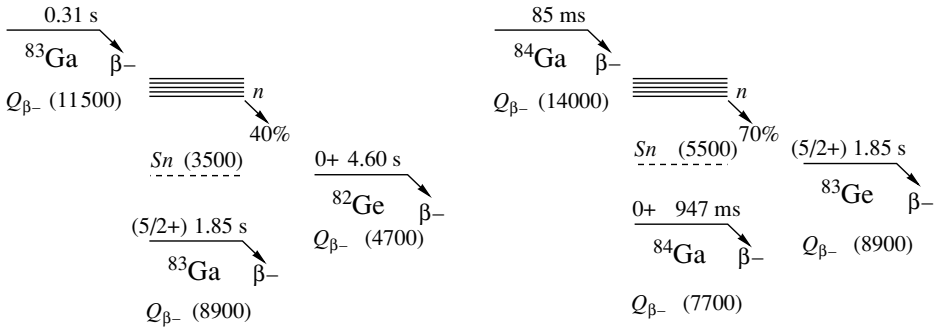

Fig. 3. Decay schemes for ^{83}Ga and ^{84}Ga.

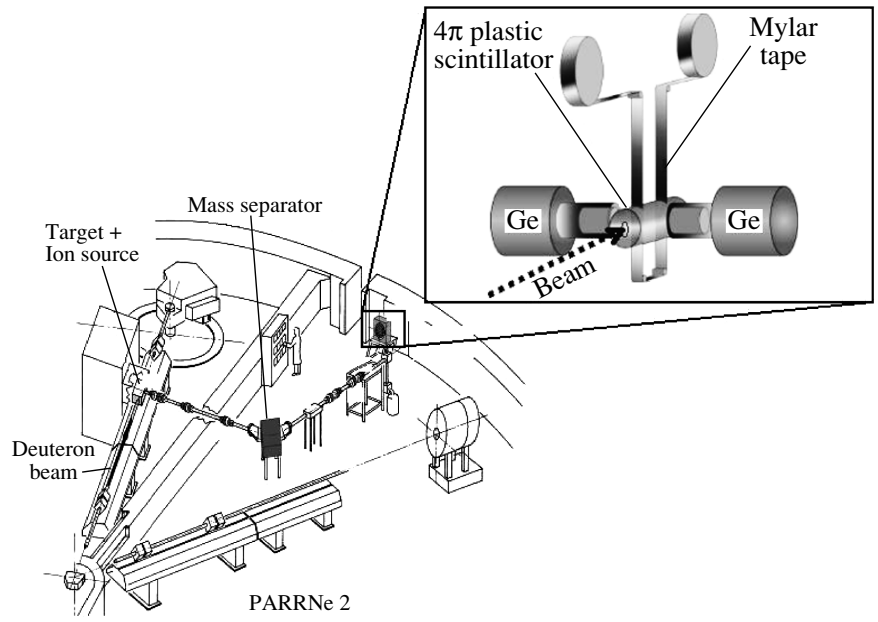

Fig. 4. Experimental setup at the Tandem at Orsay. The two rooms are separated by concrete walls to isolate the production place (with ^{238}U target and ion source) from the separation and detection place and therefore reduce the background. A more detailed scheme of the experimental setup is shown in the inset. A hole in the plastic scintillator lets the beams be collected on the mylar tape. The light emitted from the detection of a β in the plastic is collected with a photomultiplicator (not represented here) placed at the back of the plastic detector.

level scheme has been obtained, and the most intense transition is the $2^+ - 0^+$ at 1348 keV. Therefore, we assume that the intense unknown γ rays, with a measured half-life consistent with 310 ± 10 ms, belong to ^{83}Ge transitions.

In Fig. 7 is represented a part of the γ spectrum obtained for mass 83. We can see three peaks of interest: the $2^+ - 0^+$ transition of ^{82}Ge at 1348 keV and the two peaks that we have attributed to ^{83}Ge, 1238 keV and 866 keV, which have a decay time in agreement with the half-life of ^{83}Ga. All other peaks in the picture belong to identified transitions, essentially in ^{83}Br, ^{83}As, and other transitions in ^{82}Ge.

The 1238-keV line. When we fit the background-subtracted decay part of the time spectrum of the 1238-keV transition (Fig. 8), we find a half-life of 260 ± 140 ms, which is in agreement with the ^{83}Ga half-life. All other elements present in mass 83 are identified: we have ^{83}Br($T_{1/2} = 2.40$ h), ^{83}Se($T_{1/2} =$ 22.3 min), ^{83m}Se($T_{1/2} = 70.1$ s), ^{83}As($T_{1/2} =$ 13.4 s), and ^{83}Ge($T_{1/2} = 1.85$ s) [30]. They all have half-lives very different from ^{83}Ga. Then, there is no ambiguity to attribute the 1238-keV transition to an excited level of ^{83}Ge. The time structure of this transition can be seen in Fig. 9, in which one can also see the time structure of the 1348-keV transition (transition $2^+ - 0^+$ in ^{82}Ge) and the 1092-keV transition (transition in ^{83}As). The 1348-keV transition has the same time structure

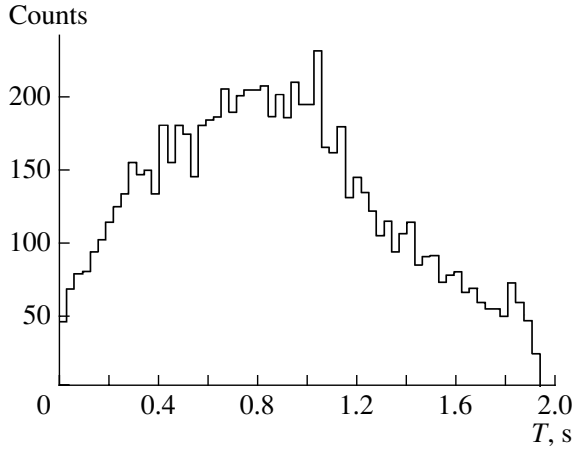

Fig. 5. Time spectrum for the 1348-keV transition in ^{82}Ge. The growth corresponds to acquisition with the beam on, and the decay starts when the beam is deflected. The collection time is 1 s and the decay time is 1 s.

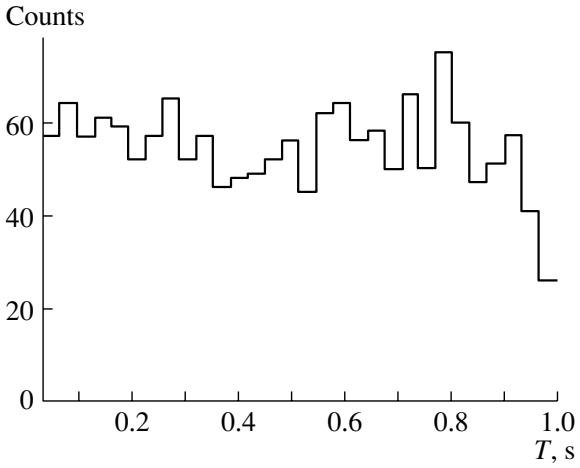

Fig. 6. Time spectrum of the γ background (obtained with the $A = 84$ γ spectrum).

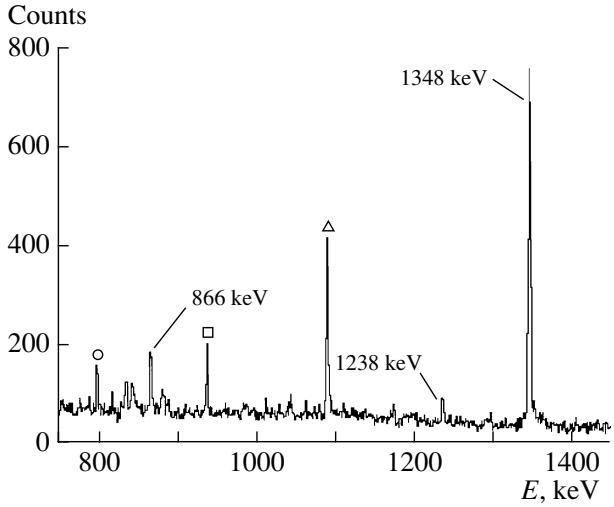

Fig. 7. Part of the γ spectrum for $A = 83$. The two peaks attributed to ^{83}Ge (866 and 1238 keV) are indicated, as well as the $2^+ - 0^+$ transition in ^{82}Ge at 1348 keV. Other peaks are transitions in ^{83}Br at 799 keV (○), in ^{82}Ge at 938 keV (□), and in ^{83}As at 1092 keV (△).

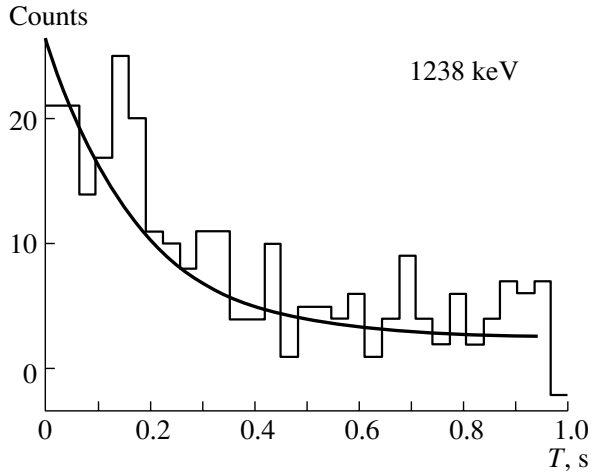

Fig. 8. Time spectrum background subtracted for the γ line at 1238 keV observed in the $A = 83$ spectrum. The fit gives a half-life of 260 ± 140 ms.

as the 1238-keV transition as explained above, and the 1092-keV transition has a totally different time structure since it is fed by the decay of ^{83}Ge.

The 866-keV line. The other peak situated at 866 keV is a little bit more tricky as long as it corresponds to two known γ transitions which belong to β decay from ^{83}Se to ^{83}Br and to β–n decay from ^{83}Ga to ^{82}Ge. On the other hand, it will be shown here from time and γ–γ spectrum analysis that this peak must contain mainly γ coming from a transition in ^{83}Ge.

The half-life of ^{83}Se is 22.3 min, which can be considered as infinite in our time basis; its contribution to the time spectrum is flat all over the spectrum. This can be seen in the background-subtracted time spectrum for the 866-keV transition (Fig. 10): there is a constant component that does not disappear with the background subtraction.

In the β-decay level scheme of ^{82}Ga to ^{82}Ge, the 866-keV transition is in coincidence with the 1348-keV transition. In the γ–γ spectrum, if we make a gate on the 1348-keV peak to look at the transitions in coincidence, the 866-keV transition is not present, whereas the 938-keV transition, which is also in coincidence with the 1348-keV transition, is present (see Fig. 11). We deduce from this analysis that the 866-keV transition may be only fed by the β decay of

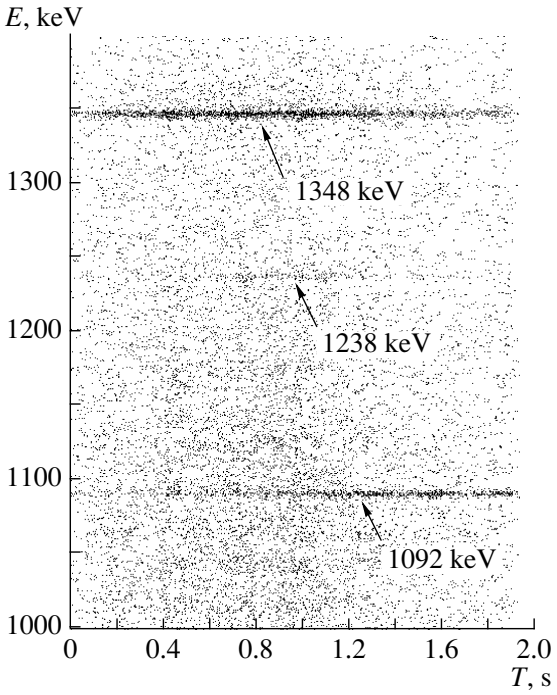

Fig. 9. Part of the bidimensional spectrum filled with γ energies (y axis) and time (x axis) for γ in coincidence with a β. The 1238-keV transition attributed to ^{83}Ge is clearly seen. The most intense transition in ^{82}Ge (at 1348 keV) is also present in the spectrum, as well as the γ line of the ^{83}Ge daughter (^{83}As) at 1092 keV; the two lines have two different time behaviors since ^{83}As is fed by the decay of ^{83}Ge.

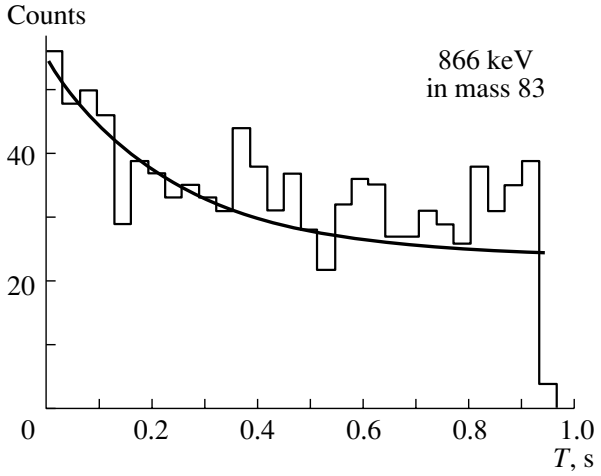

Fig. 10. Time spectrum background subtracted for the γ line at 866 keV observed in the $A = 83$ spectrum. The fit gives a half-life of 250 ± 160 ms.

^{82}Ga to ^{82}Ge and not fed by the β–n decay of ^{83}Ga to ^{82}Ge.

Moreover, this 866-keV transition is also seen in the $A = 83$ spectrum. This is another reason why it may belong to ^{83}Ge. Then, we may attribute this energy to an excited level of ^{83}Ge. The measured half-life for this peak is 250 ± 161 ms, which is also in agreement with the ^{83}Ga half-life.

2.2. ^{84}Ge

Now we have found two peaks for ^{83}Ge, identified thanks to their decay. We can look at the $A = 84$ spectrum to identify the lines corresponding to transitions in ^{84}Ge and at least the one associated with the 2^+–0^+ transition.

Similarly to what has been observed in the $A = 83$ spectrum, in the $A = 84$ spectrum, transitions from both β decay and β–n decay of ^{84}Ga are present. From β–n decay, only the 866-keV transition, previously attributed to the ^{83}Ge excited level, could be seen. When we fit the time spectrum associated with this transition (Fig. 12), we obtain 65 ± 28 ms; this is in agreement with the half-life of ^{84}Ga, which is 85 ± 10 ms [16].

In the energy spectrum, we have identified a peak at 820 keV (Fig. 13) with a short half-life. A fit of its time spectrum gives a half-life of 65 ± 36 ms, which is in agreement with the known half-life of ^{84}Ga. Therefore, we may attribute this 820-keV peak to a β-decay transition from ^{84}Ga to ^{84}Ge, and as it is the only one, it is most likely to be the 2^+–0^+ transition of ^{84}Ge.

3. CONCLUSION

We have studied the decay of ^{83}Ga to identify the most intense γ transitions in ^{83}Ge. Two transitions at 866 keV and 1238 keV were found which can be attributed to excited levels in ^{83}Ge. Then, we have studied the decay of ^{84}Ga. In the γ spectrum, only the 866-keV transition corresponding to the β–n decay could be identified. A γ line at 820 keV was found which could be attributed to the first excited level decay in ^{84}Ge.

This experiment was a very first step in a systematic in the $N = 50$ region to get closer and closer to ^{78}Ni. The measurement could have been done with neutron detectors; this would have allowed us to distinguish directly in the $A = 84$ spectrum between β decay and β–n decay of ^{84}Ga.

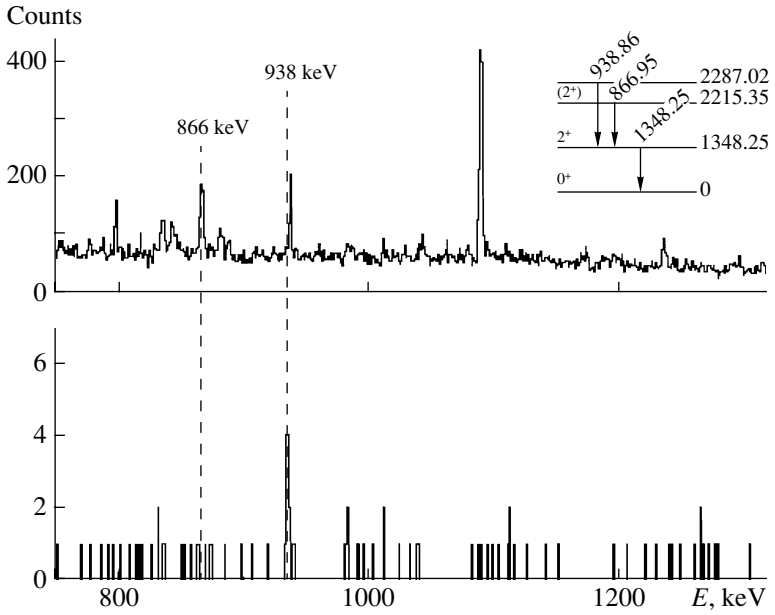

Fig. 11. Top: part of the γ spectrum in $A = 83$. Bottom: same spectrum gated on the 1348-keV peak; only the γ line at 938 keV is present. In the inset is shown a part of the decay scheme for ^{82}Ge.

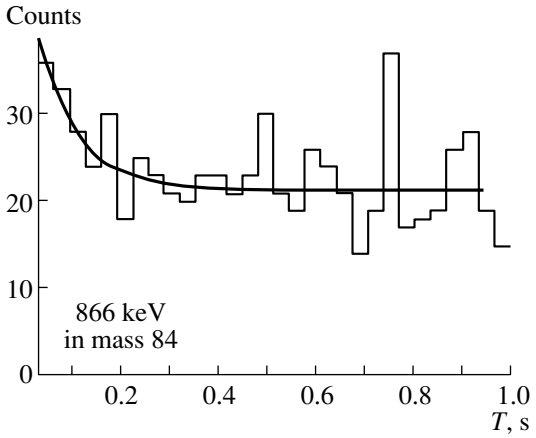

Fig. 12. Time spectrum background subtracted for the γ line at 866 keV observed in the $A = 84$ spectrum. The fit gives a half-life of 65 ± 28 ms.

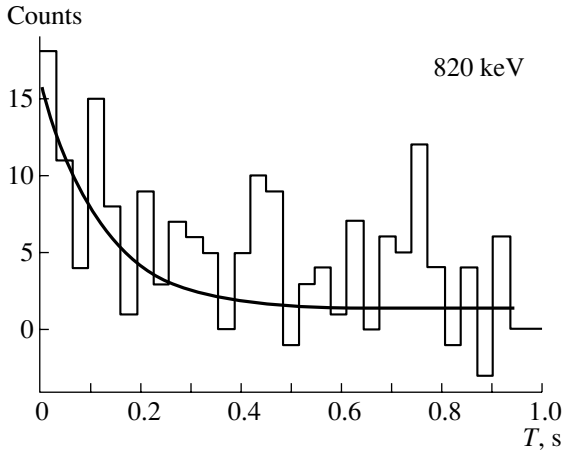

Fig. 13. Time spectrum background subtracted for the γ line at 820 keV observed in the $A = 84$ spectrum. The fit gives a half-life of 65 ± 36 ms.

REFERENCES

1. O. Sorlin, private communication.
2. F. R. Hudson and R. N. Glover, Nucl. Phys. A **189**, 264 (1972).
3. M. Kregar and B. Elbek, Nucl. Phys. A **93**, 49 (1967).
4. D. C. Camp, Nucl. Phys. A **121**, 561 (1968).
5. D. C. Camp *et al.*, Nucl. Phys. A **163**, 145 (1971).
6. D. C. Camp and B. P. Foster, Nucl. Phys. A **177**, 401 (1971).
7. W.-T. Chou *et al.*, Phys. Rev. C **47**, 157 (1993).
8. P. Hoff and B. Fogelberg, Nucl. Phys. A **368**, 210 (1981).
9. R. M. Lieder and J. E. Draper, Phys. Rev. C **2**, 531 (1970).
10. D. K. McMillan and B. D. Pate, Nucl. Phys. A **174**, 593 (1971).
11. M. Karras, T. E. Ward, and H. Ihochi, Nucl. Phys. A **147**, 120 (1970).
12. J. V. Kratz *et al.*, Nucl. Phys. A **250**, 13 (1975).
13. D. M. Moltz *et al.*, Nucl. Phys. A **427**, 317 (1984).
14. R. Broda *et al.*, Nucl. Phys. A **216**, 493 (1973).
15. M. M. King and W.-T. Chou, Nucl. Data Sheets **76**, 285 (1995).
16. J. K. Tuli, Nucl. Data Sheets **81**, 331 (1997).
17. E. Achterberg *et al.*, Phys. Rev. C **5**, 1587 (1972).
18. G. Skarnemark *et al.*, Z. Phys. A **323**, 407 (1986).
19. P. Hoff *et al.*, Z. Phys. A **300**, 289 (1981).

20. C. J. Lister *et al.*, Phys. Rev. Lett. **49**, 308 (1982).
21. C. J. Lister *et al.*, Phys. Rev. C **24**, 260 (1981).
22. M. M. King, Nucl. Data Sheets **80**, 567 (1997).
23. G. Ardisson, S. Laribi, and C. Marsol, Nucl. Phys. A **223**, 616 (1974).
24. W. L. Talbert, Jr. *et al.*, Phys. Rev. C **23**, 1726 (1981).
25. R. J. Olson, W. L. Talbert, Jr., and J. R. McConnell, Phys. Rev. C **5**, 2095 (1972).
26. C. J. Lister *et al.*, Phys. Rev. Lett. **59**, 1270 (1987).
27. K. Oxorn and S. K. Mark, Z. Phys. A **316**, 97 (1984).
28. E. Brown, Nucl. Data Sheets **82**, 379 (1997).
29. W. L. Talbert, Jr. *et al.*, Nucl. Phys. A **146**, 149 (1970).
30. J. K. Tuli, Nucl. Data Sheets **66**, 1 (1992).
31. J. C. Hill *et al.*, in *Proceedings of the V International Conference on Nuclei Far from Stability, Rosseau Lake, Ontario, Canada, 1987*, Ed. by I. S. Towner (AIP Conf. Proc., 1988), p. 375.
32. http://ipnweb.in2p3.fr/activitech/frame_actech.html

Physics of Atomic Nuclei, Vol. 66, No. 8, 2003, pp. 1428–1433. From Yadernaya Fizika, Vol. 66, No. 8, 2003, pp. 1474–1479.

A Study of γ Decays and Octupole Bands in ^{21}Ne and ^{21}Na*

S. Thummerer[1)], W. von Oertzen[1),2)], Tz. Kokalova[1),2)], H. G. Bohlen[1)], B. Gebauer[1)], A. Tumino[1)], T. N. Massey[3)], G. de Angelis[1),4)], M. Axiotis[4)], A. Gadea[4)], Th. Kröll[4)], N. Marginean[4)], D. R. Napoli[4)], M. De Poli[4)], C. Ur[4)], D. Bazzacco[5)], S. M. Lenzi[5)], C. Rossi Alvarez[5)], S. Lunardi[5)], R. Menegazzo[5)], P. G. Bizzeti[6)], and A. M. Bizzeti-Sona[6)]**

[1)] *Hahn-Meitner-Institut, Berlin, Germany*

[2)] *Freie Universität Berlin, Fachbereich Physik, Germany*

[3)] *Department of Physics and Astronomy, Ohio University, Athens, OH 45701, USA*

[4)] *Laboratóri Nazionali di Legnaro, Istituto Nazionale di Fisica Nucleare (INFN), Legnaro (Padova), Italy*

[5)] *Dipartimento di Fisica and INFN, Padova, Italy*

[6)] *Dipartimento di Fisica and INFN, Firenze, Italy*

Received December 10, 2002

Abstract—The reactions ^{16}O(^{7}Li, $2n$) and ^{16}O(^{7}Li, np) populating ^{21}Na and ^{21}Ne have been studied at $E_L = 27$ MeV using the GASP γ-detector array. The level schemes for ^{21}Na and ^{21}Ne have been extended to higher spin. The population of the bands with $K = 3/2$ and $1/2$, forming parity doublets, are compared. Preferential $E1$ decay between bands of opposite parity is observed in agreement with the octupole scenario. The structure of these bands can be interpreted as consisting of an instrinsic asymmetric (^{4}He + ^{16}O) structure with octupole deformation. © *2003 MAIK "Nauka/Interperiodica".*

1. INTRODUCTION

Reflection asymmetric shapes have often been suggested for the structure of the lightest nuclei in the *sd* shell based on the observation of negative parity states [1]. Such shapes, characterized by bands of opposite parity connected by strong $E1$ transitions, have also been interpreted as an indication of possible evidence for molecular structures [2]. In odd nuclei, reflection asymmetric shapes give rise to the observation of parity doublets with an energy splitting depending on the height of the internal barrier separating the two opposite parity states. This is schematically illustrated in Fig. 1, where two octupole shapes with $\beta_3 < 0$ and $\beta_3 > 0$ are separated by a potential barrier. A high internal barrier gives a small splitting of the bands with opposite parity. A particular interesting case, which has been recently discussed in the context of the octupole scenario, is ^{21}Ne [2]. The well-known doublet structure of ^{20}Ne is mirrored there in two doublets of bands with $K = 3/2$ and $1/2$ in ^{21}Ne. Although mixing of the corresponding positive parity states with states of quadrupole deformation is to be expected, the negative parity states are difficult to relate to simple Nilsson orbitals, and in most papers on the structure of light *sd*-shell nuclei, the negative parity states have generally been omitted in the discussion of the level structure [3].

We have investigated the rotational structure of the opposite parity bands in ^{21}Ne. The results reported here also show the comparison of the level structure of these nuclei in a mirror symmetry concept and the related decay properties. They are consistent with the formation of a reflection asymmetric molecular structure. An estimate of the intrinsic dipole moment, based on branching ratios of γ decays, gives a limit value in agreement with the present interpretation.

2. STRUCTURE OF ^{20,21}Ne AND THE α + ^{16}O POTENTIAL

In the context of the covalently bound molecular structures in nuclei, the ^{21}Ne nucleus can be described as $^{16}\mathrm{O} + \alpha + n$. The cluster (molecular) structure of ^{21}Ne will therefore be based on the underlying structure of ^{20}Ne. The cluster structure in ^{20}Ne has been discussed extensively (see [1, 4]).

The structure of ^{20}Ne has also been discussed in the framework of the deformed Nilsson model suggesting stable octupole deformation [1, 5]. Similar

*This article was submitted by the authors in English.

**e-mail: thummerer@hmi.de

results have also been obtained for other light nuclei such as ^{18}O [6] and ^{19}F [7, 8].

Two bands, "inversion doublets," of an instrinsic reflection asymmetric octupole with $K = 0$ and parities $\pi = (+ \text{ and } -)$ are observed in ^{20}Ne, the negative parity band starting with a 1^- state at 5.787 MeV.

Other bands in ^{20}Ne are obtained in the cluster model by considering higher nodal wave functions in the relative motion [4, 9].

For ^{21}Ne, the concept of octupole deformation and a weak coupling of an extra valence neutron leads to parity doublets with $K = 3/2$ and $1/2$. The properties of these doublets can be described well in a molecular orbital concept as discussed in [2].

The present experiment was done to contribute to the establishment of the band structure in ^{21}Ne and its comparison to ^{21}Na observed simultaneously in the same experiment.

In light nuclei like neon, octupole shapes cannot be explained by a mixing of shell model configurations with $\Delta l = 3$, but must be due to cluster structures [1].

Parity doublet bands with $K = 1/2$ show a significant effect due to the Coriolis interaction. The excitation energy of the levels with spin J is influenced by the Coriolis interaction depending on the value of the decoupling parameter a:

$$E = \frac{\hbar^2}{2\theta}\left[J(J+1) + a(-1)^{J+1/2}(J+1/2)\right]. \quad (1)$$

The consideration of the variation of the level energies compared to the prediction with $E = \hbar^2/2\theta\,[J(J+1)]$ is a good fingerprint for a cluster structure: assuming a shell model configuration of the parity doublet bands, the decoupling parameter a is expected to be very different (even having a different sign) for the two members, resulting in nonparallel bands for the same K value, but different parity. In the case of parity doublets based on cluster structures, the decoupling parameter a is similar and, therefore, the parity split bands should show a more or less parallel behavior. This was shown by Jolos and von Brentano for octupole-deformed nuclei for the actinide nuclei [10]. Dufour and Descouvemont [8] have performed microscopic multicluster model calculations for parity split bands in ^{19}F. The ^{19}F nucleus was built up as a $^{15}\text{N} + \alpha$ system in the calculations. Figure 2 shows the positive and negative parity bands. The energies of the $K = 1/2^{\pm}$ bands show a alternating behavior, pointing to a strong Coriolis decoupling. Even if the parity split bands are not exactly parallel, the systematics show the same sign of a.

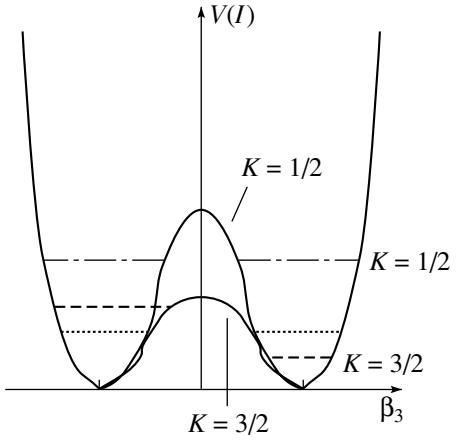

Fig. 1. The potential $V(\beta_3, I)$ for fixed angular momentum I as a function of β_3 showing the two symmetric minima. For the $K = 3/2$ bands (dashed lines), the lower barrier induces a large energy splitting; for $K = 1/2$ (dash-dotted lines), the higher internal barrier gives degenerated positive and negative parity bands.

3. GAMMA DECAYS IN ^{21}Ne AND ^{21}Na OBSERVED IN THE ^{7}Li + ^{16}O REACTION

A. Experimental Procedure

We report here on the results of the ^{7}Li + ^{16}O reaction at a ^{7}Li beam energy of 27 MeV obtained in an experiment using a ^{10}BeO target deposited on a thick backing (4 mg/cm^2 Pt and 35 mg/cm^2 Au). ^{21}Ne is formed in the $(^7\text{Li}, 2n)$ reaction, and ^{21}Na is formed in the $(^7\text{Li}, np)$ reaction. The γ spectra have been obtained using the GASP-detector array [11] at the Tandem Accelerator of LNL. Events with γ rays in at least two Ge detectors were recorded. For additional channel selection, the emitted light charged particles were detected with the ΔE–E Si-ball ISIS [12].

The relevant parts of the spectra for γ decays observed in ^{21}Ne and ^{21}Na are shown in Figs. 3 and 4; both are gated on the $5/2^+ \to 3/2^+$ transition. The Doppler shift correction has been done by an optimization procedure of the recoil velocity since, in both ^{21}Ne and ^{21}Na, the lifetimes of the states, except for the $5/2^+$ and the $1/2^-$ state, are shorter than the stopping time of the nuclei in the backing material. For background substraction, the automatic procedure of the program XTRACKN [13] was used, which results in a very low background level of only a very few counts, as seen in Figs. 3 and 4.

B. Level Structure of ^{21}Ne

In this work, we discuss the γ decay of the negative parity states, assuming as a fingerprint of octupole correlations the existence of strong $E1$ transi-

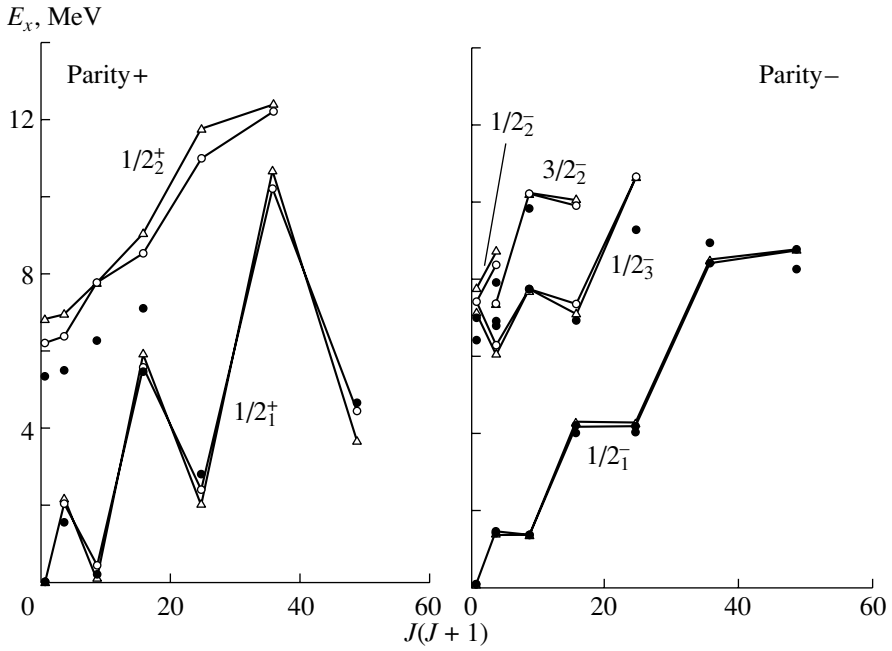

Fig. 2. Energy spectra of ^{19}F showing strong Coriolis decoupling (from [8]). The left-hand side shows the positive parity bands and the right-hand side shows the negative parity bands. The symbols correspond to experimental and theoretical data as follows: full circles, experiment; open circles, GCM with the Volkov force; triangles, GCM with the Minnesota force.

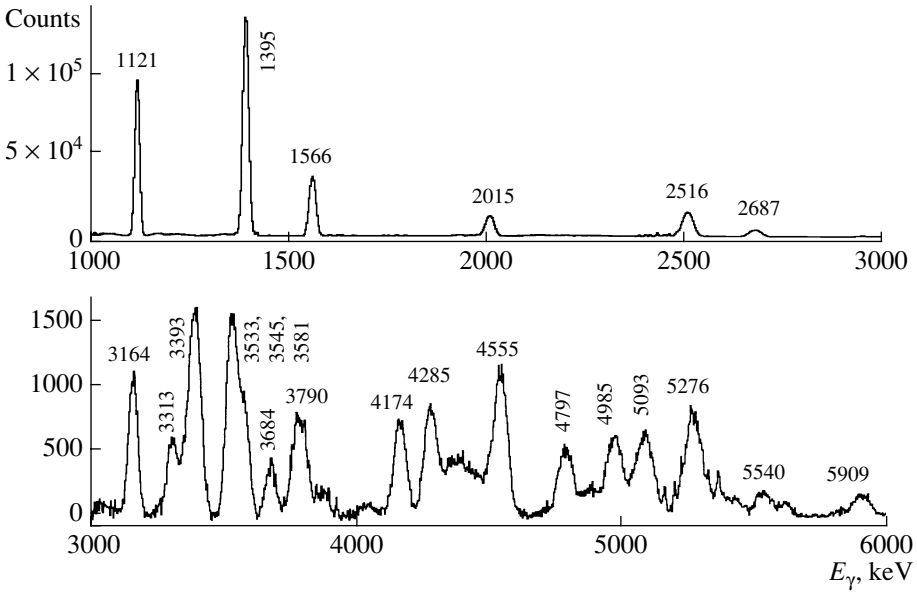

Fig. 3. γ spectrum for ^{21}Ne obtained by gating on the 351-keV ($5/2^+ \to 3/2^+$) γ transition.

tions connecting rotational bands with opposite parity, whereas the innerband $E2$ transitions are expected to be weak. In Fig. 5, we have selected the opposite parity states of the proposed octupole character and have arranged them in parity doublets with K values of 1/2 and 3/2 (see details in [2]). In the figure, we have not included additional levels associated with structures corresponding to the "normal" quadrupole deformation and discussed in previous studies, which have established the main features of the γ decay in this nucleus [3, 14–16].

The most striking characteristic of the $K = 1/2^-$ band is, besides the small energy splitting of the $K = 1/2^\pm$ bands, the long lifetime (110 ps) of the $1/2^-$ state ($K = 1/2^-$) at 2.79 MeV decaying into

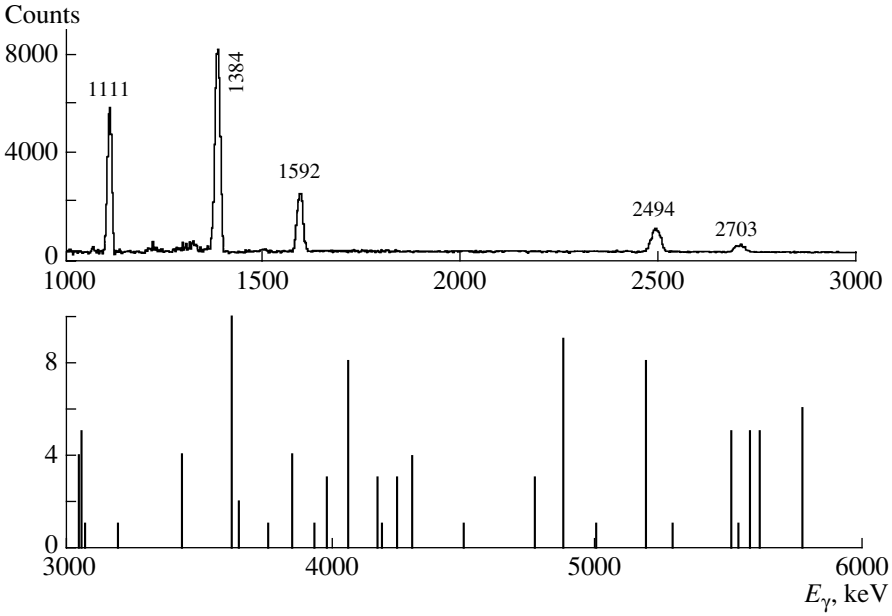

Fig. 4. γ spectrum for ^{21}Na obtained by gating on the 332-keV ($5/2^+ \to 3/2^+$) γ transition.

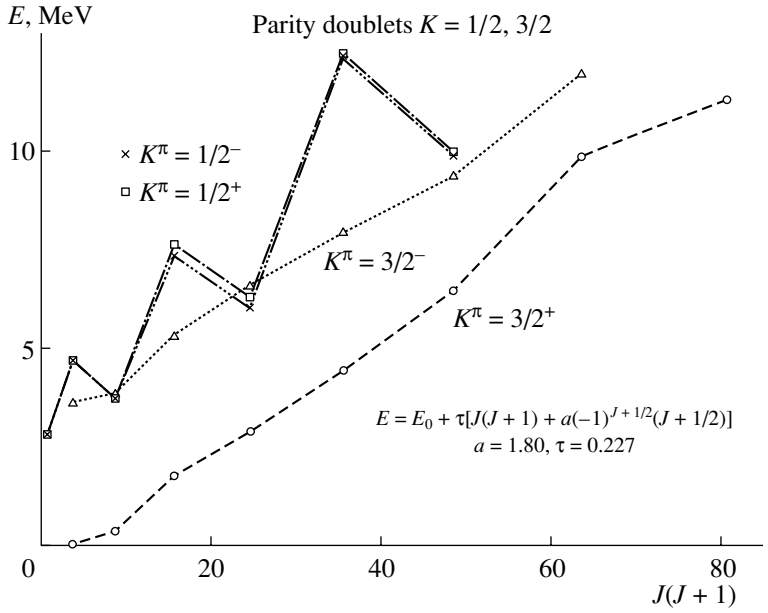

Fig. 5. Plot of the proposed rotational band structure of ^{21}Ne showing the parity doublet bands (based on Fig. 4 of [2]). The spins are given as $J(J+1)$ and the parity of the states follow from the band description below each band.

the $K = 3/2^+$ ground-state band, which in the cluster picture requires a re-arrangement from a π-type to a σ-type bond [2]. Therefore, the transitions connecting the $1/2^-$ state to the $5/2^+$ and the $3/2^+$ state of the $K = 3/2^+$ band appear to be retarded by more than three orders of magnitude. The intensity ratio of the two transitions with 2789 keV ($E1$) and 2438 keV ($M2$) is 1 : 3 from our experimental data. Similarly, Warbuton *et al.* [14] have measured this ratio at 15% : 85%. Using the common systematics of the relative strength of $E1$ and $M2$ transitions, we would expect that the $E1$ transition is stronger than the $M2$ transition by a factor of 10^6, and not even weaker. Two possible explanations were already discussed in [14]. In our understanding, the reason to prefer an $M2$ transition in this case is that two quantum numbers have to be changed to go from the $1/2^-$ state ($K = 1/2^-$ band) to the $5/2^+$ or the $3/2^+$

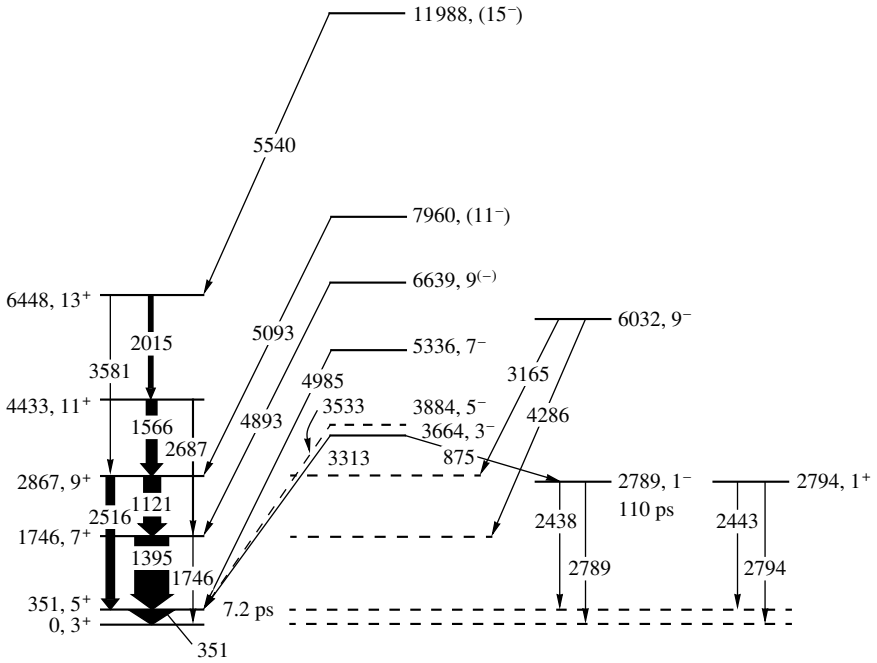

Fig. 6. γ decays of the $K = 3/2$ and $1/2$ bands of ^{21}Ne in the ^{16}O(^{7}Li, np) reaction as obtained in the present work. All energies are given in keV and spins as $J(J+1)$. The intensities (widths) of the right-side arrows are not to scale.

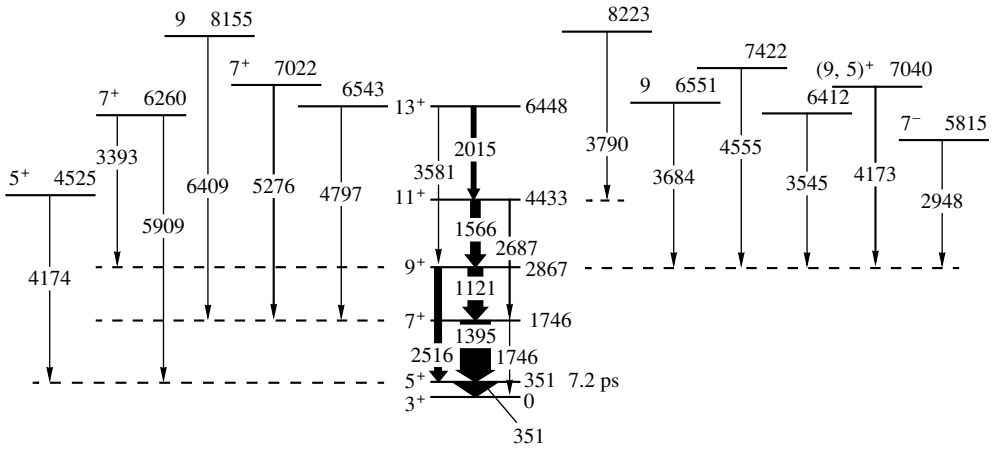

Fig. 7. Decay scheme of ^{21}Ne showing the levels not forming rotational structures together with the $K = 3/2^+$ ground-state band as obtained in the present work. All energies are given in keV and spins as $J(J+1)$. The given spins and parities are taken from adopted levels. The intensities (widths) of the arrows outside the ground-state band are not to scale.

state ($K = 3/2^+$ band), namely, the orbital angular momentum l and the spin s. Changing both (i.e., Δl and Δs) favors an $M2$ transition rather than an $E1$, resulting in an enhanced $M2$ strength.

The small energy splitting in the $K = 1/2$ bands suggests that the internal barrier between $\beta_3 < 0$ and $\beta_3 > 0$ is quite high (see Fig. 1).

In Fig. 6, we show the observed transitions between states of octupole character classified in the newly ordered band structure. Figure 7 shows, together with the ground-state band, the observed γ transitions of excited levels of ^{21}Ne not connected to the present band structure.

The γ transitions within the $K = 3/2^+$ yrast band were seen up to the $13/2^+$ state.

The states in the $K = 3/2^-$ band have been identified through their interband decay to the $K = 3/2^+$ band. No intraband γ transistions have been observed. The lowest state in this band ($3/2^-$, 3664 keV) also feeds the $1/2^-$ state of the $K = 1/2^-$ band, with an intensity, however, reduced by a factor

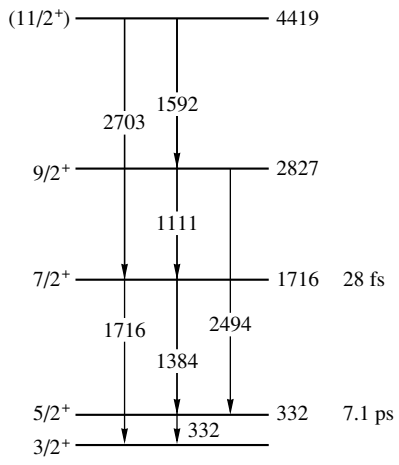

Fig. 8. Ground-state band and γ transitions of ^{21}Na as obtained in the present work. All energies are given in keV.

of three when compared to its transition to the $K = 3/2^+$ band. The fact that the members of the $K = 3/2^-$ band decay predominantly into states of the $K = 3/2^+$ band points to the fact that we are dealing with strongly enhanced $E1$ transitions. The existence of an $E1$ transition connecting the band head $3/2^-$ to the ground state could not be clearly established due to the absence of a feeding transition to gate on and due to the poor selectivity of the ungated spectra.

The nonobservation of the intraband $E2$ transitions allows one to extract a limit on the $B(E1)/B(E2)$ ratios, which can be used, in the framework of the rotational model, to constrain the value of the intrinsic dipole moment D_0 [17]. Assuming for ^{21}Ne the same value of the measured charge intrinsic quadrupole moment of ^{20}Ne, $Q_0 = 58(3)\ e$ fm^2 [18], the intrinsic dipole moment from the considerations explained above results in $D_0 > 0.1\ e$ fm, in good agreement with previous calculation [19].

The $K = 1/2^+$ band was visible in the data only by its weak transitions from the band head to the lowest states ($3/2^+$ and $5/2^+$) in the $K = 3/2^+$ band. No feeding of the $K = 1/2^+$ band head could be identified.

For the $K = 1/2^-$ band, we observed the transitions depopulating the band head ($1/2^-$), which was fed by the $K = 3/2^-$ ($3/2^-$) state.

A more detailed discussion of the obtained level scheme is given in [20].

The reaction seems to populate directly the individual states with negative parity and is not the usual type of compound reaction with a statistical feeding of all states.

C. Level Structure of ^{21}Na

The corresponding mirror nucleus to ^{21}Ne is ^{21}Na. Figure 8 shows the level scheme and γ-decay pattern of ^{21}Na as observed in the present experiment. We found two new transitions extending the ground-state band ($K = 3/2^+$) up to a state at 4419 keV, which we tentatively assign to the $11/2^+$ state.

ACKNOWLEDGMENTS

This work was supported by the EU (contract ERBFMGECT 980110) and the BMBF (Verbundforschung, contract 06 OB 900). Tz. Kokalova was supported by the DAAD (contract A/99/08070). G. de Angelis was supported by the Humboldt foundation with the Wilhelm-Bessel-Preis.

REFERENCES

1. P. A. Butler and W. Nazarewicz, Rev. Mod. Phys. **68**, 349 (1996).
2. W. von Oertzen, Eur. Phys. J. A **11**, 403 (2001).
3. A. Hoffmann, P. Betz, H. Roepke, and B. H. Wildenthal, Z. Phys. A **332**, 289 (1989).
4. S. Ohkubo *et al.*, Prog. Theor. Phys. Suppl. **132**, 1 (1998).
5. B. Buck, C. B. Dover, and J. P. Vary, Phys. Rev. C **11**, 1803 (1975).
6. G. Reidemeister and F. Michel, Phys. Rev. C **47**, R1846 (1993).
7. H. J. Krappe and U. Wille, Nucl. Phys. A **124**, 641 (1969).
8. M. Dufour and P. Descouvemont, Nucl. Phys. A **672**, 153 (2000) (and refs. therein).
9. H. Horiuchi, K. Ikeda, and Y. Suzuki, Prog. Theor. Phys. Suppl. **52**, Chap. 3 (1972).
10. R. V. Jolos and P. von Brentano, Nucl. Phys. A **587**, 377 (1995).
11. D. Bazzacco, in *Proceedings of the International Conference on Nuclear Structure at High Angular Momentum, Ottawa, 1992*, Report No. AECL 10613, Vol. II (AECL Research, Ottawa, 1992), p. 376.
12. E. Farnea *et al.*, Nucl. Instrum. Methods Phys. Res. A **400**, 87 (1997).
13. N. Marginean, C. A. Ur, and D. Bazzacco, INFN LNL (Padova, Italy, 1991–2001).
14. E. K. Warbuton *et al.*, Phys. Rev. C **3**, 2344 (1971).
15. G. Andritsopoulos *et al.*, Nucl. Phys. A **372**, 281 (1981).
16. A. A. Pilt, R. H. Speak, R. V. Elliott, *et al.*, Can. J. Phys. **50**, 1826 (1972).
17. P. A. Butler *et al.*, Nucl. Phys. A **533**, 249 (1991).
18. Y. Horikawa *et al.*, Phys. Lett. B **36B**, 9 (1971).
19. G. Leander and S. E. Larsson, Nucl. Phys. A **239**, 93 (1975).
20. S. Thummerer *et al.*, to be published.

Physics of Atomic Nuclei, Vol. 66, No. 8, 2003, pp. 1434–1438. From Yadernaya Fizika, Vol. 66, No. 8, 2003, pp. 1480–1484.

Separable Skyrme Interactions and Quasiparticle RPA*

A. P. Severyukhin[1)], V. V. Voronov[1)], Ch. Stoyanov[2)], and Nguyen Van Giai[3)]**

[1)] *Bogolyubov Laboratory of Theoretical Physics, Joint Institute for Nuclear Research, Dubna, Moscow oblast, 141980 Russia*

[2)] *Institute for Nuclear Research and Nuclear Energy, Sofia, Bulgaria*

[3)] *Institut de Physique Nucléaire, Université Paris-Sud, Orsay, France*

Received August 28, 2002

Abstract—A finite rank separable approximation for the quasiparticle random phase approximation with Skyrme interactions is applied to study the low-lying quadrupole and octupole states in some S isotopes and giant resonances in some spherical nuclei. It is shown that characteristics calculated within the suggested approach are in good agreement with available experimental data. © *2003 MAIK "Nauka/Interperiodica".*

1. INTRODUCTION

The random phase approximation (RPA) [1–4] with the self-consistent mean field derived with the use of Gogny interaction [5] or Skyrme-type interactions [6, 7] is nowadays one of the standard tools to perform nuclear structure calculations. Many properties of the nuclear collective states can be described successfully within such models [7–14].

Due to the anharmonicity of vibrations, there is a coupling between one-phonon and more complex states [2, 4]. The main difficulty is that the complexity of calculations beyond the standard RPA increases rapidly with the size of the configuration space and one has to work within limited spaces. It is well known that, using simple separable forces, one can perform calculations of nuclear characteristics in very large configuration spaces since there is no need to diagonalize matrices whose dimensions grow with the size of configuration space. For example, the well-known quasiparticle-phonon model (QPM) [4] belongs to such a model. Very detailed predictions can be made by QPM for nuclei away from closed shells [15–17].

That is why a finite rank approximation for the particle–hole (p–h) interaction resulting from Skyrme-type forces has been suggested in our previous work [18]. Thus, the self-consistent mean field can be calculated in the standard way with the original Skyrme interaction, whereas the RPA solutions would be obtained with the finite rank approximation to the p–h matrix elements. It was found that the finite rank approximation reproduces reasonably well the dipole and quadrupole strength distributions in Ar isotopes [18].

Recently, we extended the finite rank approximation to p–h interactions of Skyrme type to take into account pairing [19]. We tested our approach to calculate characteristics of the low-lying quadrupole and octupole states in some spherical nuclei. In this paper, we apply our approach to study the low-lying quadrupole and octupole states in some S isotopes. Choosing as examples some spherical nuclei, we demonstrate an ability of the method to describe correctly the strength distributions in a broad excitation energy interval.

2. BASIC FORMULAS AND DETAILS OF CALCULATIONS

We start from the effective Skyrme interaction [6] and use the notation of [20] containing explicit density dependence and all spin-exchange terms. The single-particle spectrum is calculated within the Hartree–Fock (HF) method. The continuous part of the single-particle spectrum is discretized by diagonalizing the HF Hamiltonian on the harmonic oscillator basis [21]. The p–h residual interaction $\tilde{V}_{\rm res}$ corresponding to the Skyrme force and including both direct and exchange terms can be obtained as the second derivative of the energy density functional with respect to the density [22]. Following our previous papers [18, 19], we simplify $\tilde{V}_{\rm res}$ by approximating it by its Landau–Migdal form. For Skyrme interactions, all Landau parameters F_l, G_l, F'_l, G'_l with $l > 1$ are zero. Here, we keep only the $l = 0$ terms in $V_{\rm res}$, and

*This article was submitted by the authors in English.

** e-mail: sever@thsun1.jinr.ru

in the coordinate representation, one can write it in the following form:

$$V_{\rm res}(\mathbf{r}_1,\mathbf{r}_2) = N_0^{-1}[F_0(r_1) + G_0(r_1)\sigma_1\sigma_2 + (F_0'(r_1) + G_0'(r_1)\sigma_1\sigma_2)\tau_1\tau_2]\delta(\mathbf{r}_1 - \mathbf{r}_2), \quad (1)$$

where σ_i and τ_i are the spin and isospin operators, and $N_0 = 2k_{\rm F}m^*/\pi^2\hbar^2$ with $k_{\rm F}$ and m^* standing for the Fermi momentum and nucleon effective mass. The expressions for F_0, G_0, F_0', and G_0' in terms of the Skyrme force parameters can be found in [20]. Because of the density dependence of the interaction, the Landau parameters of Eq. (1) are functions of the coordinate $\mathbf{r}$.

The p–h residual interaction can be represented as a sum of N separable terms. To illustrate a procedure for making the finite rank approximation, we examine only the contribution of the term F_0. In what follows, we use the second quantized representation and $V_{\rm res}$ can be written as

$$\hat{V}_{\rm res} = \frac{1}{2}\sum_{1234} V_{1234} : a_1^+ a_2^+ a_4 a_3 :, \quad (2)$$

where a_1^+ (a_1) is the particle creation (annihilation) operator and 1 denotes the quantum numbers $(n_1 l_1 j_1 m_1)$,

$$V_{1234} = \int \phi_1^*(\mathbf{r}_1)\phi_2^*(\mathbf{r}_2)V_{\rm res}(\mathbf{r}_1,\mathbf{r}_2)\phi_3(\mathbf{r}_1)\phi_4(\mathbf{r}_2)d\mathbf{r}_1 d\mathbf{r}_2, \quad (3)$$

$$V_{1234} = \sum_{JM} \hat{J}^{-2}\langle j_1||Y_J||j_3\rangle\langle j_2||Y_J||j_4\rangle I(j_1j_2j_3j_4) \times (-1)^{J+j_3+j_4-M-m_3-m_4}\langle j_1 m_1 j_3 - m_3|J-M\rangle\langle j_2 m_2 j_4 - m_4|JM\rangle. \quad (4)$$

In the above equation, $\langle j_1||Y_J||j_3\rangle$ is the reduced matrix element of the spherical harmonics $Y_{J\mu}$, $\hat{J} = \sqrt{2J+1}$, and $I(j_1j_2j_3j_4)$ is the radial integral:

$$I(j_1j_2j_3j_4) = N_0^{-1} \times \int_0^\infty F_0(r)u_{j_1}(r)u_{j_2}(r)u_{j_3}(r)u_{j_4}(r)\frac{dr}{r^2}, \quad (5)$$

where $u(r)$ is the radial part of the HF single-particle wave function. As is shown in [18, 19], the radial integrals can be calculated accurately by choosing a sufficiently large cutoff radius R and using an N-point integration Gauss formula with abscissas r_k and weights w_k:

$$I(j_1j_2j_3j_4) \simeq N_0^{-1}\frac{R}{2} \times \sum_{k=1}^{N}\frac{w_k F_0(r_k)}{r_k^2}u_{j_1}(r_k)u_{j_2}(r_k)u_{j_3}(r_k)u_{j_4}(r_k). \quad (6)$$

Thus, we employ the Hamiltonian including an average nuclear HF field, pairing interactions, and the isoscalar and isovector p–h residual forces in the finite rank separable form [19]. This Hamiltonian has the same form as the QPM Hamiltonian with N separable terms [4, 23], but in contrast to the QPM, all parameters of this Hamiltonian are expressed through parameters of the Skyrme forces.

In what follows, we work in the quasiparticle representation defined by the canonical Bogolyubov transformation:

$$a_{jm}^+ = u_j\alpha_{jm}^+ + (-1)^{j-m}v_j\alpha_{j-m}. \quad (7)$$

The single-particle states are specified by the quantum numbers (jm). The quasiparticle energies, the chemical potentials, the energy gap, and the coefficients u,v of the Bogolyubov transformations (7) are determined from the BCS equations.

We introduce the phonon creation operators

$$Q_{\lambda\mu i}^+ = \frac{1}{2}\sum_{jj'}\left(X_{jj'}^{\lambda i}A^+(jj';\lambda\mu) - (-1)^{\lambda-\mu}Y_{jj'}^{\lambda i}A(jj';\lambda-\mu)\right), \quad (8)$$

where

$$A^+(jj';\lambda\mu) = \sum_{mm'}\langle jmj'm'|\lambda\mu\rangle\alpha_{jm}^+\alpha_{j'm'}^+. \quad (9)$$

The index λ denotes total angular momentum and μ is its z projection in the laboratory system. One assumes that the QRPA ground state is the phonon vacuum $|0\rangle$, i.e., $Q_{\lambda\mu i}|0\rangle = 0$. We define the excited states for this approximation by $Q_{\lambda\mu i}^+|0\rangle$.

Making use of the linearized equation-of-motion approach [1], one can derive the QRPA equations [3, 4]:

$$\begin{pmatrix} \mathcal{A} & \mathcal{B} \\ -\mathcal{B} & -\mathcal{A} \end{pmatrix}\begin{pmatrix} X \\ Y \end{pmatrix} = w\begin{pmatrix} X \\ Y \end{pmatrix}. \quad (10)$$

Table 1. Energies, $B(E2)$ values, and $(M_n/M_p)/(N/Z)$ ratios for up-transitions to the first 2^+ states

Nucleus	Energy, MeV		$B(E2\uparrow)$, e^2 fm^4		$(M_n/M_p)/(N/Z)$	
	exp.	theor.	exp.	theor.	exp.	theor.
^{32}S	2.23	3.34	300 ± 13	340	0.94 ± 0.16	0.92
^{34}S	2.13	2.48	212 ± 12	290	0.85 ± 0.23	0.87
^{36}S	3.29	2.33	104 ± 28	130	0.65 ± 0.18	0.40
^{38}S	1.29	1.55	235 ± 30	300	1.09 ± 0.29	0.73

Table 2. Energies, $B(E3)$ values, and $(M_n/M_p)/(N/Z)$ ratios for up-transitions to the first 3^- states

Nucleus	Energy, MeV		$B(E3\uparrow)$, e^2 fm^6		$(M_n/M_p)/(N/Z)$
	exp.	theor.	exp.	theor.	theor.
^{32}S	5.01	7.37	12700 ± 2000	8900	0.89
^{34}S	4.62	5.66	8000 ± 2000	8500	1.06
^{36}S	4.19	3.86	8000 ± 3000	7200	1.15
^{38}S	–	5.68	–	6200	1.01

In QRPA problems, there appear two types of interaction matrix elements, the matrix related to forward-going graphs $\mathcal{A}^{(\lambda)}_{(j_1j_1')(j_2j_2')}$ and the matrix related to backward-going graphs $\mathcal{B}^{(\lambda)}_{(j_1j_1')(j_2j_2')}$. Solutions to this set of linear equations yield the eigenenergies and the amplitudes X, Y of the excited states. The dimension of the matrices $\mathcal{A}$, $\mathcal{B}$ is the space size of the two-quasiparticle configurations. Expressions for $\mathcal{A}$, $\mathcal{B}$ and X, Y are given in [19].

Using the finite rank approximation, we need to invert a matrix having a dimension $4N \times 4N$ independently of the configuration space size. One can find a prescription of how to solve the system (10) within our approach in [18, 19]. The QRPA equations in the QPM [4, 23] have the same form as the equations derived within our approach [18, 19], but the single-particle spectrum and parameters of the p–h residual interaction are calculated making use of the Skyrme forces.

In this work, we use the standard parametrization *SIII* [24] of the Skyrme force. Spherical symmetry is assumed for the HF ground states. It is well known [11, 12] that the constant gap approximation leads to an overestimation of occupation probabilities for subshells that are far from the Fermi level, and it is necessary to introduce a cutoff in the single-particle space. Above this cutoff, subshells do not participate in the pairing effect. In our calculations, we choose the BCS subspace to include all subshells lying below 5 MeV. The pairing constants are fixed to reproduce the odd–even mass difference of neighboring nuclei. In order to perform RPA calculations, the single-particle continuum is discretized [21] by diagonalizing the HF Hamiltonian on a basis of twelve harmonic oscillator shells and cutting off the single-particle spectra at the energy of 160 MeV. This is sufficient to exhaust practically all the energy-weighted sum rule. Our investigations [19] enable us to conclude that $N = 45$ is sufficient for multipolarities $\lambda \leq 3$ in nuclei with $A \leq 208$. Increasing N, for example, up to $N = 60$ in ^{208}Pb, changes the results for energies and transition probabilities by no more than 1%, so all calculations in what follows have been done with $N = 45$. Our calculations show that, for the normal parity states, one can neglect the spin-multipole interactions as a rule and this reduces by a factor 2 the total matrix dimension. For example, for the octupole excitations in ^{206}Pb [19], we need to invert a matrix having a dimension $2N = 90$ instead of diagonalizing a 1376×1376 matrix as would be the case without the finite rank approximation. For light nuclei, the reduction of matrix dimensions due to the finite rank approximation is 3 or 4. Thus, for heavy nuclei our approach gives a large gain in comparison with an exact diagonalization. It is worth pointing out that, after solving the RPA problem with a separable interaction, to take into account the coupling with two-phonon configurations requires one to diagonalize a matrix having a size that does not exceed 40 for the giant resonance calculations in heavy nuclei, whereas one would need to diagonalize a matrix with a dimension

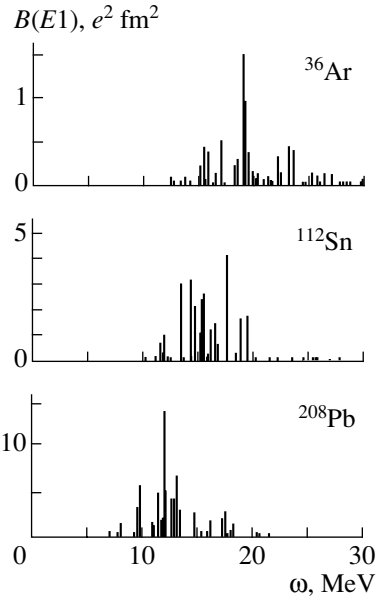

Fig. 1. Strength distributions of the GDR in ^{36}Ar, ^{112}Sn, and ^{208}Pb.

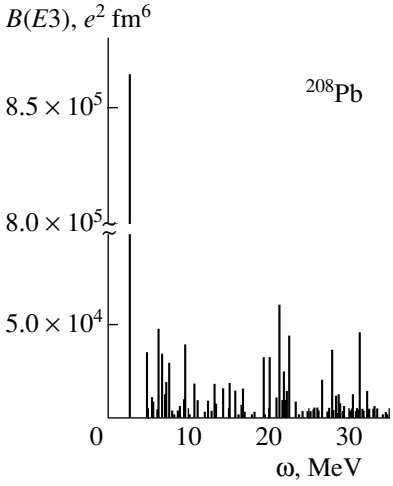

Fig. 2. The octupole strength distribution in ^{208}Pb.

of the order of a few thousand at least for a nonseparable case.

3. RESULTS OF CALCULATIONS

As a first example, we examine the 2_1^+ and 3_1^- state energies and transition probabilities in some S isotopes. The results of our calculations for the energies and $B(E2)$ values and the experimental data [25] are shown in Table 1. One can see that there is rather good agreement with experimental data. Results of our calculations for S isotopes are close to those of QRPA with Skyrme forces [26]. The evolution of the $B(E2)$ values in the S isotopes demonstrates clearly the pairing effects. The experimental and calculated $B(E2)$ values in ^{36}S are lower by a factor of two than those in ^{34,38}S. The neutron shell closure leads to the vanishing of the neutron pairing and a reduction of the proton gap. As a result, there is a remarkable reduction of the $E2$ transition probability in ^{36}S. Some overestimate of the energies in ^{34,38}S indicates that there is room for two-phonon effects. The study of the influence of two-phonon configurations on properties of the low-lying states within our approach is in progress now.

Results of our calculations for the 3_1^- energies and the transition probabilities $B(E3)$ are compared with experimental data [27] in Table 2. Generally, there is good agreement between theory and experiment.

Additional information about the structure of the first $2^+, 3^-$ states can be extracted by looking at the ratio of the multipole transition matrix elements M_n/M_p that depend on the relative contributions of the proton and neutron configurations. In the framework of the collective model for isoscalar excitations, this ratio is equal to $M_n/M_p = N/Z$, and any deviation from this value can indicate an isovector character of the state. The M_n/M_p ratio can be determined experimentally by using different external probes [28–30]. Recently [26], QRPA calculations of the M_n/M_p ratios for the 2_1^+ states in some S isotopes have been done. The predicted results are in good agreement with experimental data [26]. Our calculated values of the M_n/M_p ratios for the 2_1^+ and 3_1^- states are shown in Tables 1 and 2, respectively. Our results support the conclusions of [26] about the isovector character of the 2_1^+ states in ^{36}S. As one can see from Table 2, our calculations predict that the M_n/M_p ratios for the 3_1^- states are rather close to N/Z, thus indicating their isoscalar character.

To test our approach for high-lying states, we examine the dipole strength distributions. The calculated dipole strength distributions (GDR) in ^{36}Ar, ^{112}Sn, and ^{208}Pb are displayed in Fig. 1. For the energy centroids (m_1/m_0), we get 19.9, 15.8, and 12.7 MeV in ^{36}Ar, ^{112}Sn, and ^{208}Pb, respectively. The calculated energy centroid for ^{208}Pb is in a satisfactory agreement with the experimental value [31] (13.4 MeV). The values of energy centroids for ^{36}Ar, and ^{112}Sn are rather close to the empirical systematics [32] $E_c = 31.2A^{-1/3} + 20.6A^{-1/6}$ (MeV). For ^{36}Ar, the QRPA gives results that are very similar to our previous calculations with the particle–hole RPA [18] because the influence of pairing on the giant resonance properties is weak. It is worth mentioning that experimental data for the giant resonances in light nuclei are very scarce.

The octupole strength distribution in ^{208}Pb is rather well studied in many experiments [33, 34]. The calculated octupole strength distribution up to the excitation energy 35 MeV is shown in Fig. 2. According to experimental data [33] for the 3_1^- state in ^{208}Pb, the excitation energy equals $E_x = 2.62$ MeV and the energy-weighted sum rule (EWSR) is exhausted by 20.4%, which can be compared with the calculated values $E_x = 2.66$ MeV and EWSR = 21%. For the low-energy octupole resonance below 7.5 MeV, our calculation gives the centroid energy $E_c = 5.96$ MeV and EWSR = 12% and the experimental values are 5.4 MeV and 15.2%, accordingly. For the high-energy octupole resonance, we get values $E_c = 20.9$ MeV and EWSR = 61%, which are in good agreement with experimental findings $E_c = 20.5 \pm 1$ MeV and EWSR = (75 ± 15)% [34]. One can conclude that present calculations reproduce correctly not only the 3_1^- characteristics but also the whole octupole strength distribution in ^{208}Pb.

4. CONCLUSION

A finite rank separable approximation for the QRPA calculations with Skyrme interactions that was proposed in our previous work is applied to study the evolution of dipole, quadrupole, and octupole excitations in several nuclei. It is shown that the suggested approach enables one to reduce remarkably the dimensions of the matrices that must be inverted to perform structure calculations in very large configuration spaces.

As an illustration of the method, we have calculated the energies and transition probabilities of the 1^-, 2^+, and 3^- states in some S, Ar, Sn, and Pb isotopes. The calculated values are very close to those that were calculated in QRPA with the full Skyrme interactions. They are in agreement with available experimental data.

REFERENCES

1. D. J. Rowe, *Nuclear Collective Motion, Models and Theory* (Barnes and Noble, 1970).
2. A. Bohr and B. Mottelson, *Nuclear Structure* (Benjamin, New York, 1975), Vol. 2.
3. P. Ring and P. Schuck, *The Nuclear Many Body Problem* (Springer, Berlin, 1980).
4. V. G. Soloviev, *Theory of Atomic Nuclei: Quasiparticles and Phonons* (IOP, Bristol, Philadelphia, 1992).
5. D. Gogny, in *Nuclear Self-Consistent Fields*, Ed. by G. Ripka and M. Porneuf (North-Holland, Amsterdam, 1975).
6. D. Vautherin and D. M. Brink, Phys. Rev. C **5**, 626 (1972).
7. A. B. Migdal, *Teoriya konechnykh Fermi-sistem i svoistva atomnykh yader* (Nauka, Moscow, 1983), 2nd ed.
8. H. Flocard and P. Quentin, Annu. Rev. Nucl. Part. Sci. **28**, 523 (1978).
9. J. Dobaczewski, W. Nazarewicz, T. R. Werner, *et al.*, Phys. Rev. C **53**, 2809 (1996).
10. G. Colò, N. Van Giai, P. F. Bortignon, and R. A. Broglia, Phys. Rev. C **50**, 1496 (1994).
11. E. Khan and N. Van Giai, Phys. Lett. B **472**, 253 (2000).
12. G. Colò and P. F. Bortignon, Nucl. Phys. A **696**, 427 (2001).
13. S. A. Fayans *et al.*, Nucl. Phys. A **676**, 49 (2000).
14. E. E. Saperstein, S. A. Fayans, and V. A. Khodel, Fiz. Élem. Chastits At. Yadra **9**, 221 (1978) [Sov. J. Part. Nucl. **9**, 91 (1978)].
15. V. V. Voronov and V. G. Soloviev, Fiz. Élem. Chastits At. Yadra **14**, 1380 (1983) [Sov. J. Part. Nucl. **14**, 583 (1983)]
16. A. I. Vdovin, V. V. Voronov, V. G. Soloviev, and Ch. Stoyanov, Fiz. Élem. Chastits At. Yadra **16**, 245 (1985) [Sov. J. Part. Nucl. **16**, 105 (1985)].
17. S. Galès, Ch. Stoyanov, and A. I. Vdovin, Phys. Rep. **166**, 127 (1988).
18. N. Van Giai, Ch. Stoyanov, and V. V. Voronov, Phys. Rev. C **57**, 1204 (1998).
19. A. P. Severyukhin, Ch. Stoyanov, V. V. Voronov, and N. Van Giai, nucl-th/0206059.
20. N. Van Giai and H. Sagawa, Phys. Lett. B **106B**, 379 (1981).
21. J. P. Blaziot and D. Gogny, Nucl. Phys. A **284**, 429 (1977).
22. G. F. Bertsch and S. F. Tsai, Phys. Rep. **18C**, 126 (1975).
23. V. G. Soloviev, Yad. Fiz. **50**, 40 (1989) [Sov. J. Nucl. Phys. **50**, 25 (1989)].
24. M. Beiner, H. Flocard, N. Van Giai, and Ph. Quentin, Nucl. Phys. A **238**, 29 (1975).
25. S. Raman, C. W. Nestor, Jr., and P. Tikkanen, At. Data Nucl. Data Tables **78**, 1 (2001).
26. E. Khan *et al.*, Nucl. Phys. A **694**, 103 (2001).
27. T. Kibedi and R. H. Spear, At. Data Nucl. Data Tables **80**, 35 (2002).
28. A. M. Bernstein, V. R. Brown, and V. A. Madsen, Comments Nucl. Part. Phys. **11**, 203 (1983).
29. M. A. Kennedy, P. D. Cottle, and K. W. Kemper, Phys. Rev. C **46**, 1811 (1992).
30. J. K. Jewell *et al.*, Phys. Lett. B **454**, 181 (1999).
31. S. S. Dietrich and B. L. Berman, At. Data Nucl. Data Tables **38**, 199 (1988).
32. A. van der Woude, Prog. Part. Nucl. Phys. **18**, 217 (1987).
33. Y. Fujita *et al.*, Phys. Rev. C **32**, 425 (1985).
34. T. Yamagata *et al.*, Phys. Rev. C **23**, 937 (1981).

Physics of Atomic Nuclei, Vol. 66, No. 8, 2003, pp. 1439–1444. From Yadernaya Fizika, Vol. 66, No. 8, 2003, pp. 1485–1490.

Clustering in the Region of Nuclear Surface*

V. G. Kartavenko[1),2)], K. A. Gridnev[2),3)], J. Maruhn[2)], and W. Greiner[2)]**

[1)] *Joint Institute for Nuclear Research, Dubna, Moscow oblast, 141980 Russia*
[2)] *J. W. Goethe-Universität, Frankfurt am Main, Germany*
[3)] *Institute of Physics, St. Petersburg State University, Petrodvorets, Russia*

Received August 28, 2002

Abstract—The aim of this report is to formulate the approach to describe evolution of a localized density fluctuation in the region of a nuclear surface. © *2003 MAIK "Nauka/Interperiodica".*

1. MOTIVATION

Recent progress in modern experimental techniques gives new experimental data confirming that the following collective modes, heavy cluster radioactivity, bimodal fission, cold fission, and inverse processes, such as (subbarier) fusion, could belong to the general phenomena of cold nuclear fragmentation (see, e.g., [1, 2]). Cold fragmentation leads to a large density redistribution and indicates the formation of a binary or possibly multicenter quasistationary nuclear system, which lives $\sim 10^{-21}$ s without reaching statistical equilibrium. Since the lifetime of this nonequilibrium system is an order of magnitude greater than the time of a nucleon traveling at Fermi velocity to pass through the total system, a mean field can be formed in the composite system. Fragmentation in the surface and between nuclear surfaces, especially the neck region, is an object of special interest due to the following reasons.

The existence of a central region of constant density and a well-shaped surface region makes it possible to describe a clustering in the region of a nuclear surface, including the neck region [3]. Nuclear density falls considerably in the region of a nuclear surface. This fact is very important due to the possibility of clustering and other fluctuations of the nuclear density leading to instability in the surface region [4].

Different types of instability may develop in the surface region and lead to fragmentation processes at low (cold fragmentation) and high (multifragmentation, breakup) energies [5–9].

Nuclear scission can be described by random neck rupture, which could be traced back to a series of instabilities [10, 11]. The fragmentation phenomenon can be understood as an evolution by instabilities.

The study of droplet breakup has a distinguished history, beginning with the work of Lord Rayleigh in the 19th century [12, 13]. Recently, there has been a rebirth of interest, largely motivated by the recent experimental progress in investigation of droplet breakup in a Hele-Shaw cell [14], the rupture of soap films [15], and experiment on the space shuttle *Columbia* [16] (see also review [17]).

The dynamics of shapes of any complicated systems inevitably leads to a mathematical problem of describing global geometric quantities such as the surface and the enclosed volume in different dimensions (polymer, cell membranes, 3D droplets, etc.). The important feature of nonlinear dynamics is that, after scale transformations, the same dimensionless nonlinear differential equations can be used in very different micro- and macrosystems.

Recently, we suggested the general formalism to describe nonlinear evolution of the nuclear surface without additional assumptions about the shape of a nuclear system in the framework of nonlinear nuclear quantum hydrodynamics [18]. The aim of this report is to formulate an approach to describe evolution of a localized density fluctuation in the region of a nuclear surface.

The plan of our exposition is as follows. The basic framework is given in Section 2. The main mathematical formulas needed for subsequent calculations and the preliminary numerical results are presented in Section 3. A brief discussion of the results obtained is given in Section 4.

2. GENERAL SCHEME

General fluid dynamical concepts [19] yield a traditional way to classify nuclear collective modes, for it provides a natural set of variables (collective currents

*This article was submitted by the authors in English.

**e-mail: kart@thsun1.jinr.ru

and densities) describing nuclear collective excitations. Out of the many formulations of the nuclear hydrodynamical approach, we will follow here a way based on the algebra of current and density operators [3].

For nuclear systems, a usual second-quantized form of a nonrelativistic theory is defined by introducing canonically conjugated nucleon fields $\psi(\mathbf{x}, \sigma, q)$, where (q) denotes (n, p) for neutrons and protons and $\sigma = \pm$ is the spin index, which satisfy the equal-time canonical anticommutation relations

$$\{\psi^+(1), \psi(2)\}_+ = \delta(1-2), \qquad (1)$$
$$\{\psi^+(1), \psi^+(2)\}_+ = \{\psi(1), \psi(2)\}_+ = 0.$$

In terms of these operators, a nonrelativistic Hamiltonian $\hat{H}_{\rm nucl}[\psi^+, \psi; U_{\rm nucl}(\mathbf{x})]$ could be defined from a general two-body nuclear interaction $U_{\rm nucl}(\mathbf{x})$.

The term "hydrodynamics" means here that we will describe the dynamical behavior of the nuclear system in a restricted space of collective variables representing the density and the nucleon current of the system:

$$(\psi^+(\mathbf{x}), \psi(\mathbf{x})) \Longrightarrow (\hat{n}(\mathbf{x}), \hat{j}_k(\mathbf{x})), \qquad (2)$$

where the index k stands for the Cartesian vector components. To do so, one should use commutation relations of the collective current and density operators [3, 20] between themselves,

$$[\hat{n}(\mathbf{x}), \hat{j}_k(\mathbf{y})], \quad [\hat{n}(\mathbf{x}), \hat{n}(\mathbf{y})], \quad [\hat{j}_k(\mathbf{x}), \hat{j}_l(\mathbf{y})], \quad (3)$$

and their commutation relations with the nuclear Hamiltonian $\hat{H}_{\rm nucl}$:

$$\frac{\partial \hat{n}(\mathbf{x})}{\partial t} = \frac{1}{i\hbar}[\hat{n}(\mathbf{x}), \hat{H}_{\rm nucl}], \qquad (4)$$
$$\frac{\partial \hat{j}_k(\mathbf{x})}{\partial t} = \frac{1}{i\hbar}[\hat{j}_k(\mathbf{x}), \hat{H}_{\rm nucl}].$$

These commutation relations (3), (4) can be obtained from the initial commutation relations (1) for the nucleon quantum fields and the existing formal representation for the kinetic energy density tensor operator

$$\hat{K}_{nk}(\mathbf{x}) \equiv \nabla_n \psi^+(\mathbf{x}) \cdot \nabla_k \psi(\mathbf{x}) + \nabla_k \psi^+(\mathbf{x}) \cdot \nabla_n \psi(\mathbf{x}) \qquad (5)$$

in terms of collective density and currents $\hat{K}^{\rm hyd}_{nk}[n; \mathbf{j}]$ satisfying Eqs. (4) as well [11].

As a result, one gets a collective hydrodynamical Hamiltonian

$$\hat{H}_{\rm nucl}\big[\psi^+; \psi; U_{\rm nucl}(\mathbf{x})\big] \qquad (6)$$
$$\Longrightarrow \hat{H}_{\rm hyd}\big[n; \mathbf{j}; K^{\rm hyd}, \mathcal{E}[n, \mathbf{j}]\big]$$

which is equivalent to the initial nuclear Hamiltonian $\hat{H}_{\rm nucl}$ as far as the equations of motion (4) are concerned and where $\mathcal{E}[n, \mathbf{j}]$ denotes an effective nucleon–nucleon interaction.

In classical hydrodynamics [21], the fundamental variables are the local density $n(\mathbf{x})$ and the fluid velocity $\mathbf{v}(\mathbf{x})$, from which the quantum current density can be defined by the anticommutator [22]

$$\hat{j}_i(\mathbf{x}) = \frac{m}{2\hbar}\{\hat{n}(\mathbf{x}), \hat{v}_i(\mathbf{x})\}_+, \qquad (7)$$

where a symmetrized form has been chosen to anticipate the transition to quantum mechanics.

Using the commutation relations (3) and the definition (7), one derives the following velocity–density and velocity–velocity commutators:

$$[\hat{v}_k(\mathbf{x}), \hat{n}(\mathbf{y})] = -i\frac{\hbar}{m}\frac{\partial}{\partial x_k}\delta(\mathbf{x}-\mathbf{y}), \qquad (8)$$
$$[\hat{n}(\mathbf{x}), \hat{n}(\mathbf{y})] = 0,$$

$$\hat{n}(\mathbf{x})\hat{n}(\mathbf{y})[\hat{v}_i(\mathbf{x}), \hat{v}_j(\mathbf{y})] \qquad (9)$$
$$= i\frac{\hbar}{m}\epsilon_{ijk}\hat{n}(\mathbf{x})\mathrm{curl}_k\hat{v}(\mathbf{y})\delta(\mathbf{x}-\mathbf{y}).$$

Since the order of the operators $\mathrm{curl}\hat{v}_k(\mathbf{y})$ and $\hat{n}(\mathbf{x})$ is not important because $\hat{n}(\mathbf{x})$ commutes with $\mathrm{curl}\hat{v}_k(\mathbf{y})$, we finally get

$$[\hat{v}_i(\mathbf{x}), \hat{v}_j(\mathbf{y})] = i\frac{\hbar}{m}\epsilon_{ijk}\frac{\mathrm{curl}\hat{v}_k(\mathbf{y})}{\hat{n}(\mathbf{y})}\delta(\mathbf{x}-\mathbf{y}). \qquad (10)$$

Following the well-known Helmholtz theorem, we will use the decomposition of a velocity operator into potential and pure rotational currents:

$$\hat{v}_k(\mathbf{x}) = \frac{\partial\hat{\Phi}(\mathbf{x})}{\partial x_k} + \hat{R}_k(\mathbf{x}), \qquad (11)$$
$$\mathrm{div}\mathbf{R} = 0, \qquad \hat{\boldsymbol{\zeta}} = \mathrm{curl}\hat{\mathbf{R}}.$$

Commutation relations between the density and the potential velocity are then reduced to the canonical bosonic form

$$[\hat{n}(\mathbf{x}), \hat{\Phi}(\mathbf{y})] = i\delta(\mathbf{x}-\mathbf{y}), \quad [\hat{\Phi}(\mathbf{x}), \hat{\Phi}(\mathbf{y})] = 0, \quad (12)$$
$$[\hat{n}(\mathbf{x}), \hat{n}(\mathbf{y})] = 0,$$

allowing us thus to treat (in the absence of any rotation ($R_k = 0$)) the evolution via $H_{\rm mod}$ within an anharmonical picture. Commutation relations for the rotational part of a current are more complicated [23],

$$[\hat{R}_i(\mathbf{x}), \hat{R}_j(\mathbf{y})] = i\epsilon_{ijk}\delta(\mathbf{x}-\mathbf{y})\frac{\hat{\zeta}_k(\mathbf{y})}{\hat{n}(\mathbf{y})}, \qquad (13)$$
$$[\hat{\zeta}_k(\mathbf{x}), \hat{n}(\mathbf{y})] = 0,$$

$$[\hat{\zeta}_i(\mathbf{x}), \hat{R}_j(\mathbf{y})] = i\delta_{ij} \sum_k \frac{\partial}{\partial x_k} \left(\frac{\hat{\zeta}_k(\mathbf{y})}{n(\mathbf{y})} \delta(\mathbf{x}-\mathbf{y}) \right) - i\frac{\partial}{\partial x_j} \left(\frac{\hat{\zeta}_i(\mathbf{y})}{n(\mathbf{y})} \delta(\mathbf{x}-\mathbf{y}) \right). \quad (14)$$

It is, however, possible to separate, as far as commutation relations are concerned, rotational and vibrational modes,

$$[\hat{R}_i(\mathbf{x}), \hat{n}(\mathbf{y})] = 0, \qquad [\hat{R}_k(\mathbf{x}), \hat{\Phi}(\mathbf{y})] = 0, \quad (15)$$
$$[\hat{\zeta}_k(\mathbf{x}), \hat{\Phi}(\mathbf{y})] = 0,$$

which remain, of course, connected via the equations of motion.

3. SIMPLE MODEL

The general quantum scheme presented in the previous section gives the principal possibility of analyzing the large amplitude vibrational and vortical modes and their coupling. Let us consider the simple model case.

3.1. Model Hamiltonian

$$H_{\mathrm{mod}} \equiv \frac{m}{2} \int \mathbf{v} n \mathbf{v} d^3x + \mathcal{W}[n], \quad (16)$$
$$\mathcal{W}[n] \equiv \mathcal{W}_s[n] + \mathcal{W}_v[n],$$
$$\mathcal{W}_s[n] \equiv \int \mathcal{E}_s[n] d^3x,$$
$$\mathcal{E}_s[n] \equiv \frac{\hbar^2\xi^2}{2m} \frac{|\nabla n|^2}{n} + \gamma |\nabla n|^2,$$
$$\mathcal{W}_v[n] \equiv \int \mathcal{E}_v[n] d^3x,$$
$$\mathcal{E}_v[n] \equiv A_1 n^2 + A_7 n^{2+\alpha} + \kappa n^{5/3}(1+\beta n),$$
$$A_1 = 3t_0/8, \qquad A_7 = t_3/16, \quad (17)$$
$$\kappa \equiv \frac{3\hbar^2}{10m} \left(\frac{3\pi^2}{2} \right)^{2/3}, \qquad \beta = \frac{2m}{\hbar^2} A_3, \quad (18)$$
$$A_3 = \frac{3t_1}{16} + \frac{5t_2}{16} + \frac{t_2 x_2}{4}.$$

For symmetric infinite nuclear matter (without Coulomb interaction), one obtains from Eq. (16) for the binding energy per nucleon

$$(E/A)_\infty = \mathcal{E}_v[n]/n = \kappa n^{2/3}(1+\beta n) + A_1 n + A_7 n^{1+\alpha}. \quad (19)$$

The saturation density n_0 is fixed by the condition

$$\left. \frac{d(E/A)_0}{dn} \right|_{n_0} = 0. \quad (20)$$

The infinite nuclear matter incompressibility is

$$K_0 \equiv 9n_0^2 \left. \frac{d^2(\mathcal{E}_v[n]/n)}{dn^2} \right|_{n_0} = -2\kappa n_0^{2/3} + 10\kappa\beta n_0^{5/3} + 9\alpha(\alpha+1) n_0^{1+\alpha}, \quad (21)$$

$$K_0 = 9m^* c_s^2, \quad c_s \equiv \left(\frac{1}{m^*} n^2 \left. \frac{d^2(\mathcal{E}_v[n]/n)}{dn^2} \right|_{n_0} \right)^{1/2},$$

and the isoscalar effective nucleon mass m_0^* is given by

$$m/m_0^* \equiv 1 + \beta n_0. \quad (22)$$

The Weitzsäcker term in the variational equation leads to an asymptotic falloff of the density with the correct exponential form (in the spherical case without any vorticity terms)

$$n(r)_{r\to\infty} \Rightarrow \frac{\mathrm{const}}{r^2} \exp(-r/a). \quad (23)$$

The range a is given by the Fermi energy $(E/A)_0$ and the coefficient of the Weitzsäcker term:

$$a = \sqrt{\frac{-1}{(E/A)_0} \frac{\hbar^2\xi^2}{2m}}. \quad (24)$$

This range is too small by a factor of ~ 2–3 compared with realistic nuclear surfaces if one uses the semiclassical value $\xi = 1/6$. Consequently, the densities fall off too quickly in the outer surface and lead to an overestimate of the kinetic energy. Direct derivation of this coefficient from commutation relations leads to the more correct value $\xi = 1/2$. Finally, we will use the original Weitzsäcker term and the surface coefficient from effective Skyrme interaction without any renormalization,

$$\xi = 1/2, \qquad \gamma = -A_5, \quad (25)$$
$$A_5 = \frac{-9t_1}{64} + \frac{5t_2}{64} + \frac{t_2 x_2}{16},$$

and the Skyrme forces SkM^* with the parameters [24] $t_0 = -2645$ MeV fm^3, $t_1 = 410$ MeV fm^5, $t_2 = -135$ MeV fm^5, $t_3 = 15\,595$ MeV fm$^{3+3\alpha}$;

$$x_0 = 0.09, \quad x - 1 = x_2 = x_3 = 0, \quad \alpha = 1/6.$$

This gives

$$n_0 = 0.16\ \mathrm{fm}^{-3}, \quad (E/A)_0 = -15.77\ \mathrm{MeV},$$
$$K_0 = 216.4\ \mathrm{MeV}, \quad m_0^*/m = 0.79.$$

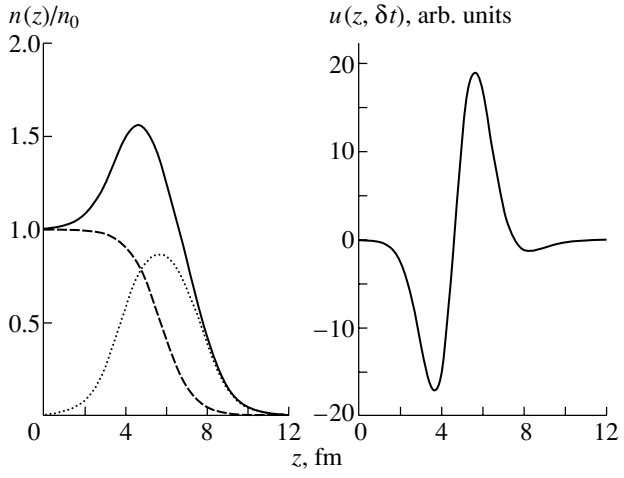

Fig. 1. The initial one-dimensional density distribution simulating the three-dimensional system with α particle ($\bar{A} = 4$) in the surface region of a large nucleus ($\bar{A} = 100$) for $z_0 = R_{\bar{A}}$. The corresponding velocity distribution at the beginning of evolution (in arbitrary units).

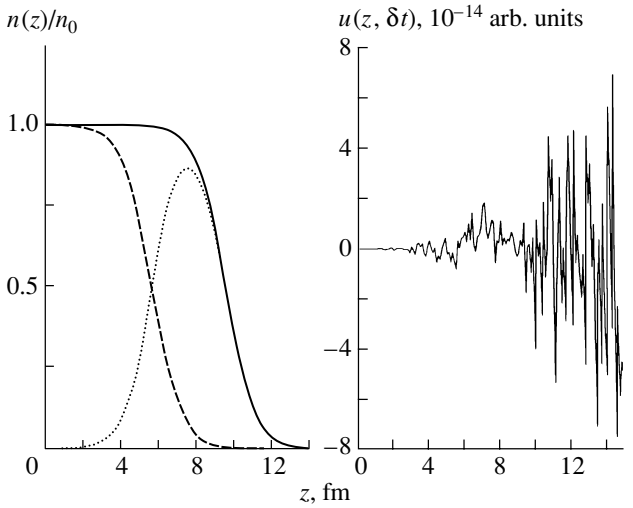

Fig. 2. The same as Fig. 1 for the $z_0 = R_{\bar{A}} + R_{\tilde{A}}$. One can see the practically negligible flux in the case of the touching distance.

3.2. Equations of Motion

The main hydrodynamical set of Eqs. (4) can be recast in the following form in spherical polar coordinates:

$$\frac{\partial n}{\partial t} + \nabla \cdot (\mathbf{u}n) = 0, \tag{26}$$

$$\frac{\partial u_r}{\partial t} + \mathbf{u} \cdot \nabla u_r - \frac{u_\theta^2}{r} - \frac{u_\phi^2}{r} = -\frac{\partial}{\partial r}\left(\frac{1}{m}\frac{\delta \mathcal{W}}{\delta n}\right),$$

$$\frac{\partial u_\theta}{\partial t} + \mathbf{u} \cdot \nabla u_\theta + \frac{u_r u_\theta}{r} - \frac{u_\phi^2 \cot\theta}{r} = -\frac{1}{r}\frac{\partial}{\partial \theta}\left(\frac{1}{m}\frac{\delta \mathcal{W}}{\delta n}\right),$$

$$\frac{\partial u_\phi}{\partial t} + \mathbf{u} \cdot \nabla u_\phi + \frac{u_r u_\phi}{r} - \frac{u_\theta u_\phi \cot\theta}{r} = -\frac{1}{r\sin\theta}\frac{\partial}{\partial \phi}\left(\frac{1}{m}\frac{\delta \mathcal{W}}{\delta n}\right),$$

$$\frac{\delta \mathcal{W}}{\delta n} = \frac{\hbar^2 \xi^2}{2m}\left(-2\frac{\Delta n}{n} + \frac{|\nabla n|^2}{n^2}\right) - 2\gamma\Delta n + 2A_1 n + (2+\alpha)A_7 n^{1+\alpha} + \frac{5}{3}\kappa n^{2/3} + \frac{8}{3}\kappa\beta n^{5/3}. \tag{27}$$

Stationary solutions are given by

$$\sum_\alpha \frac{\partial}{\partial x_\alpha}(\bar{n}(\mathbf{x})\bar{v}_\alpha(\mathbf{x})) = 0, \tag{28}$$

$$\frac{\partial}{\partial x_\alpha}\left(\frac{\bar{\mathbf{v}}(\mathbf{x})^2}{2} + \frac{1}{m}\frac{\overline{\delta \mathcal{W}}(\mathbf{x})}{\delta n}\right) + \sum_{\beta\gamma} \epsilon_{\alpha\beta\gamma}\bar{v}_\beta(\mathbf{x})\mathrm{curl}_\gamma \bar{\mathbf{v}}(\mathbf{x}) = 0. \tag{29}$$

The density distribution of an isolated spherically symmetric nucleus without any vortical flux ($\bar{n}(r)$) may be found from the following equations:

$$\bar{\mathbf{v}}(r) = 0, \qquad \frac{\overline{\delta \mathcal{W}}(r)}{\delta n} = \bar{\lambda}, \tag{30}$$

where $\bar{\lambda}$ is defined by the nucleon number $\bar{A}$.

The initial state with the density fluctuation in the surface region could be simulated via the following simplest way:

$$n(\mathbf{r}; t = 0) \equiv \bar{n}(r) + \tilde{n}(r, \theta), \tag{31}$$

$$\tilde{n}(r, \theta) \equiv \frac{\Lambda n_0}{\cosh^2(\tilde{r}/b)}, \quad \tilde{r} \equiv \sqrt{r^2 - 2rz_0\cos\theta + z_0^2},$$

where z_0 controls the distance between centers of the two density waves. The corresponding nucleon numbers and other parameters in (31) may be found from the simple relations

$$A = \bar{A} + \tilde{A} = \int n d^3 r, \tag{32}$$

$$\bar{A} = \int \bar{n} d^3 r, \quad \tilde{A} = \int \tilde{n} d^3 \tilde{r} = \Lambda n_0 \frac{\pi^3 b^3}{3};$$

if $\tilde{A} = 4$ and $\Lambda \leq 1/2$, then $\pi b \geq (24/n_0)^{1/3}$,

$$\langle \tilde{r}^2 \rangle = \frac{\int \tilde{r}^2 \tilde{n} d^3 \tilde{r}}{\int \tilde{n} d^3 \tilde{r}} = \frac{7b^2\pi^2}{20}.$$

The equations of motion (26), (28) give the possibility of analyzing the evolution of the density fluctuation (31), (32) in the framework of semiclassical nuclear hydrodynamics.

3.3. Numerical Results

Our preliminary calculations show that the existing three-dimensional hydrodynamical codes should be rebuilt to deal correctly with the gradient terms. Therefore, we limited ourselves, in this paper, to the simplest case: a small time at the beginning of the evolution of the effective one-dimensional system.

We selected the initial state with nonmoving density waves ($u(z,0)=0$). Therefore, at the beginning of the evolution at the first small time step δt, the density distribution is the same as the initial one, and the corresponding velocity distribution is proportional to the effective "force"

$$n(z,\delta t)\approx n(z,0),\quad u(z,\delta t)\approx\frac{d}{dz}\left(\frac{1}{m}\frac{\delta\mathcal{W}}{\delta n}\right)\delta t.$$

The initial one-dimensional density distribution simulating the three-dimensional system with α particle ($\tilde{A}=4$) in the surface region of a large nucleus ($\bar{A}=100$) is presented in Fig. 1 for $z_0=R_{\bar{A}}$ and in Fig. 2 for $z_0=R_{\bar{A}}+R_{\tilde{A}}$, respectively. The dashed curve describes the initial large nucleus $\bar{n}(z,0)$, and the dotted curve describes the density fluctuation $\tilde{n}(z,0)$. The solid curve corresponds to the total density. The respective velocity distributions $u(z,\delta t)$ are presented (in the same arbitrary units) in the right panels of these figures. One can see the complicated flux leading to dispersion of an initial density bump in the case of large overlapping densities (Fig. 1) and the practically negligible flux at the touching distance (Fig. 2). These preliminary results can be considered only as the first estimates. The complete three-dimensional calculations are in progress.

4. SUMMARY

The existence of a central region of constant density and a well-shaped surface region makes it possible to describe a clustering in the region of a nuclear surface, including the neck region. Nuclear density falls considerably in the region of a nuclear surface, and fluctuations of the nuclear density may develop and lead to fragmentation processes.

In this report, we suggest one possible way to describe the density fluctuation in the framework of nonlinear nuclear hydrodynamics. The general quantum scheme to analyze the large amplitude vibrational and vortical modes and their coupling is given. In the semiclassical limit, one derives the semihydrodynamical equations of motion, allowing one to use the existing codes. The initial conditions have been formulated. The preliminary numerical results have been presented.

This investigation is the further development of the general formalism, suggested by us recently, to describe nonlinear evolution of the nuclear surface without additional assumptions about the shape of a nuclear system [18]. A nonlinear approach to fragmentation of α particles on the nuclear surface is suggested and applied to analysis of the elastic scattering of α particles from ^{28}Si [25, 26]. The existence of resonances in the scattering of α particles from $2s$–$1d$ targets is established without dispute by experimental evidence. Bands of resonance states at excitation energies over 13 MeV in ^{28}Si and ^{32}S are explained in terms of a model of three and four α particles orbiting around an ^{16}O core. This model is deduced from the systematics of resonances of highest spins. The dynamic properties of these particles have been discussed referring to published theoretical models. A vibrational degree of freedom [27, 28] and solitonic or bosonic quantum numbers [8, 25, 29, 30] have been mentioned as exciting issues. They hint at the occurrence of new kinds of nuclear dynamics [31]. New measurements on elastic and inelastic scattering that cover large energy ranges scanned in small energy and angular steps are needed to promote the understanding of the current experimental results. Here, we have the confirmation that the investigation of the scattering of α particles at large angles gives us some feeling of the quasicrystalline structure of light nuclei. The energy band structure of the rotational bands is some signature of the crystalline structure. It is one of the keys to the understanding of such phenomena as fragmentation.

ACKNOWLEDGMENTS

This work was supported in part by Deutsche Forschungsgemeinschaft, the Russian Foundation for Basic Research, and the Heisenberg–Landau Program.

REFERENCES

1. *Proceedings of the International Conference "Perspectives in Nuclear Physics," Paradise Island, Bahamas, USA, 1998,* Ed. by J. H. Hamilton, H. K. Carter, and R. B. Piercey (World Sci., Singapore, 1999).
2. *Proceedings of the International Workshop "Fusion Dynamics at the Extremes," Dubna, Russia, 2000,* Ed. by Yu. Ts. Oganessian and V. I. Zagrebaev (World Sci., Singapore, 2001).
3. V. G. Kartavenko, Fiz. Élem. Chastits At. Yadra **24**, 1469 (1993) [Phys. Part. Nucl. **24**, 619 (1993)].
4. V. G. Kartavenko, Yad. Fiz. **56** (8), 38 (1993) [Phys. At. Nucl. **56**, 1013 (1993)].
5. V. G. Kartavenko, K. A. Gridnev, and W. Greiner, Int. J. Mod. Phys. E **3**, 1219 (1994).
6. V. G. Kartavenko, K. A. Gridnev, J. Maruhn, and W. Greiner, J. Phys. G: Nucl. Part. Phys. **22**, L19 (1996).

7. M. Freer and A. C. Merchant, J. Phys. G: Nucl. Part. Phys. **23**, 261 (1997).
8. V. G. Kartavenko, K. A. Gridnev, and W. Greiner, Int. J. Mod. Phys. E **7**, 287 (1998).
9. V. G. Kartavenko, A. Sandulescu, and W. Greiner, Int. J. Mod. Phys. E **7**, 449 (1998).
10. U. Brosa, S. Grossmann, A. Müller, and E. Becker, Nucl. Phys. A **502**, 423c (1989).
11. V. G. Kartavenko, Yad. Fiz. **40**, 377 (1984) [Sov. J. Nucl. Phys. **40**, 240 (1984)].
12. W. S. Rayleigh, Proc. R. Soc. London **29**, 71 (1879).
13. Lord Rayleigh, *Scientific Papers. Article 58* (Dover, New York, 1964), p. 361.
14. R. E. Goldstein, A. I. Pesci, and M. J. Shelley, Phys. Rev. Lett. **70**, 3043 (1993).
15. M. Cryer and P. Steen, J. Colloid Interface Sci. **154**, 276 (1992).
16. R. E. Apfel *et al.*, Phys. Rev. Lett. **78**, 1912 (1997).
17. J. Eggers, Rev. Mod. Phys. **69**, 865 (1997).
18. V. G. Kartavenko, K. A. Gridnev, and W. Greiner, Yad. Fiz. **65**, 669 (2002) [Phys. At. Nucl. **65**, 637 (2002)].
19. E. Madelung, Z. Phys. **40**, 332 (1926).
20. R. F. Dashen and D. H. Sharp, Phys. Rev. **165**, 1857 (1968).
21. H. Lamb, *Hydrodynamics* (Dover, New York, 1932).
22. B. T. Geilikman, Dokl. Akad. Nauk USSR **94**, 199 (1954).
23. V. G. Karnavenko and P. Quentin, in *Proceedings of the International Conference NSRS'97, Dubna, Russia, 1997,* Ed. by S. N. Ershov, R. V. Jolos, and V. V. Voronov, Preprint No. E4-97-327, Joint Inst. Nucl. Res. (Dubna, 1997), p. 303.
24. P. Bonche, H. Flocard, and P. H. Heenen, Nucl. Phys. A **467**, 115 (1987).
25. K. A. Gridnev, M. W. Brenner, S. E. Belov, *et al.*, in *Proceedings of the XV Workshop on High Energy Physics and Quantum Field Theory, Tver, Russia, 2000,* Ed. by M. Dubinin and V. Savrin (Moscow, 2001), p. 406.
26. K. A. Gridnev, M. W. Brenner, S. E. Belov, *et al.*, in *Proceedings of the 1st Eurasian Conference on Nuclear Science and Its Application (I EC 2000), Izmir, Turkey, 2000,* p. 897.
27. M. Brenner, E. Indola, K.-M. Källman, *et al.*, Heavy Ion Phys. **7**, 355 (1998).
28. U. Abbondano, N. Cindro, and P. M. Milazzo, Nuovo Cimento A **110**, 955 (1997).
29. K. A. Gridnev, M. W. Brenner, K. V. Ershov, *et al.*, in *Proceedings of the International Symposium on Clustering Aspects of Quantum Many-Body Systems, Kyoto, Japan, 2001,* Ed. by A. Ohnishi *et al.* (World Sci., Singapore, 2002), p. 293; http://www.yukawa.kyoto-u.ac.jp/postyk01/proc/gridnev.pdf.
30. A. Ludu, A. Sandulescu, W. Greiner, *et al.*, J. Phys. G **21**, L41 (1995).
31. M. Brenner, in *Proceedings of the International Workshop on Fission Dynamics, Luso, Portugal, 2000* (in press).

Physics of Atomic Nuclei, Vol. 66, No. 8, 2003, pp. 1445–1449. From Yadernaya Fizika, Vol. 66, No. 8, 2003, pp. 1491–1495.

Study of Giant Pairing Vibrations with Neutron-Rich Nuclei*

L. Fortunato**

Dipartimento di Fisica and INFN, Padova, Italy

Received December 12, 2002

Abstract—We investigate the possible signature of the presence of giant pairing states at an excitation energy of about 10 MeV via two-particle transfer reactions induced by neutron-rich weakly bound projectiles. Performing particle–particle RPA calculations on ^{208}Pb and BCS + RPA calculations on ^{116}Sn, we obtain the pairing strength distribution for two-particle addition and removal modes. Estimates of two-particle transfer cross sections can be obtained in the framework of the macroscopic model. The weak-binding nature of the projectile kinematically favors transitions to high-lying states. In the case of the (^{6}He, ^{4}He) reaction, we predict a population of the Giant Pairing Vibration with cross sections of the order of a millibarn, dominating over the mismatched transition to the ground state. © *2003 MAIK "Nauka/Interperiodica"*.

1. PAIRING FIELD AND REACTION MECHANISMS

1.1. Introduction

Nuclei in interaction with external fields display a wide variety of collective vibrations known as giant resonances, associated with various degrees of freedom and multipolarities. The giant isovector dipole resonance and the giant isoscalar quadrupole resonance are the most studied examples in this class of phenomena. A particular mode that is associated with vibrations in the number of particles was predicted in the 1970s [1] and discussed, under the name of Giant Pairing Resonance, in the middle of the 1980s in a number of papers [2]. This phenomenon, despite some early efforts aimed at resolving some broad bump in the high-lying spectrum in (p, t) reactions [3], is still without any conclusive experimental confirmation. For a discussion, in particular, in connection with two-particle transfer reactions, on many aspects of pairing correlations in nuclei, we refer to a recent review [4].

We have studied the problem of collective pairing modes at high-excitation energy in two-neutron transfer reactions with the aim to prove the advantage of using an unstable beam as a new tool to enhance the excitation of such modes [5]. The main point is that, with standard available beams, one is faced with a large energy mismatch that strongly hinders the excitation of high-lying states and favors the transition to the ground state of the final system. Instead, the optimum Q-value condition in the (^{6}He, ^{4}He) stripping reaction suppresses the ground state and should allow the transition to the energy region of 10–15 MeV. We have performed particle–particle RPA calculations on lead and BCS + RPA on tin, as paradigmatic examples of normal and superfluid systems, evaluating the response to the pairing operator. Subsequently the two-neutron transfer form factors have been constructed in the framework of the macroscopic model [6] and used in DWBA computer codes. We have estimated cross sections of the order of some millibarns, dominating over the mismatched transition to the ground state. Recently we added similar calculations on other much studied targets to give some guide for experimental work.

1.2. The Giant Pairing Vibrations (GPV)

The formal analogy between particle–hole and particle–particle excitations is very well established both from the theoretical side [7] and from the experimental side for what concerns low-lying pairing vibrations around closed shell nuclei and pairing rotations in open shells. The predicted concentration of strength of an $L = 0$ character in the high-energy region (8–15 MeV for most nuclei) is understood microscopically as the coherent superposition of $2p$ (or $2h$) states in the next major shell above the Fermi level. We have roughly depicted the situation in Fig. 1. In closed shell nuclei, the addition of a pair of particles (or holes) to the next major shell, with a total energy $2\hbar\omega$, is expected to have a high degree of collectivity. Also, in the case of open shell nuclei, the same is expected for the excitation of a pair of particles with $2\hbar\omega$ energies.

*This article was submitted by the author in English.

**e-mail: fortunat@pd.infn.it

1063-7788/03/6608-1445$24.00

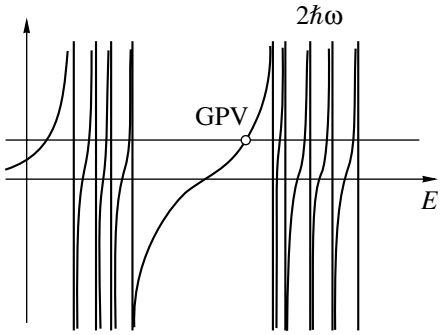

Fig. 1. Raw picture of the dispersion relation. The two bunches of vertical lines represent the unperturbed energy of a pair of particles placed in a given single-particle-energy level. The graphical solution of the secular equation is the intersection of the horizontal line with the curves. The GPV is the collective state relative to the second major shell.

2. DETAILS OF CALCULATIONS

For normal nuclei, the Hamiltonian with a monopole strength interaction reads

$$H = \sum_j \epsilon_j a_j^\dagger a_j - 4\pi G P^\dagger P, \qquad (1)$$

where P annihilates a pair of particles coupled to zero total angular momentum.

Getting rid of all the technicalities of the solution of the pp-RPA equations (which may be found in the already cited work by the author), we merely state that the pairing phonon may be expressed as a superposition of $2p$ (or $2h$) states with proper forward and backward amplitudes (X_n and Y_n). The pair transfer strength, which is a measure of the amount of collectivity of each state n, is given by

$$\beta_{Pn} = \sum_j \sqrt{2j+1}[X_n(j) + Y_n(j)]. \qquad (2)$$

This quantity is plotted in Fig. 2 for the removal (Fig. 2a) and addition mode (Fig. 2b). In the same figure are reported the pairing strength parameters for the states of ^{116}Sn. To obtain these last quantities for superfluid spherical nuclei, one has to rewrite the Hamiltonian according to the BCS transformation and solve more complex RPA equations. In this case, the pairing strength for the addition of two particles is given, for each state n, by

$$\beta_P(2p) = \sum_j \sqrt{2j+1}\langle n|[a_j^\dagger a_j^\dagger]_{00}|0\rangle \qquad (3)$$
$$= \sum_j \sqrt{2j+1}[U_j^2 X_n(j) + V_j^2 Y_n(j)],$$

where U and V are the usual occupation probabilities. The amount of collectivity is a clear signal of the structural existence of GPV in the high-lying energy region. We also report in Fig. 3 a number of analogous results for other commonly studied targets with the aim of giving some indications to experimentalists on the reasons why we think that lead and tin are some of the most promising candidates. We have studied two isotopes of calcium with closed shells. Even if the absolute magnitudes of β_P is lower, it is worthwhile to note that some enhancement is seen in the more neutron-rich ^{48}Ca with respect to ^{40}Ca. An important role in this change is certainly due to the different shell structure of the two nuclei as well as to the scheme that we implemented to obtain the set of single-particle levels. The latter is responsible for the collectivity of the removal modes in both Ca isotopes and also for the difficulty in finding a collective state in the addition modes. We also display results for ^{90}Zr, where the strength is much more fragmented and the identification of the GPV is more difficult. In the work of Bes and Broglia [7], estimates for the energy of the pairing resonance are given as $68/A^{1/3}$ MeV and $72/A^{1/3}$ MeV for normal and superfluid systems, respectively. Our figures follow roughly these prescriptions based on simple arguments (and much better grounded in the case of normal nuclei), as evident from Table 1.

Table 1. Comparison of the position (in MeV) of GPV between our calculation and the Bes and Broglia estimate

Nucleus	Our calculation	Bes and Broglia estimate
Sn	12.68	14.76
Pb	11.81	11.47

3. MACROSCOPIC MODEL FOR TWO-PARTICLE TRANSFER REACTIONS

The starting point of the macroscopic model for two-particle transfer reactions is to push further the analogy of the vibrations of the nuclear surface with the vibrations across different mass partitions. If one imagines an idealized space in which a discrete coordinate (the number of particles of the system) labels different sections of the space, it is plausible to give an interpretation of pairing modes as back and forth oscillations in the number of particles. The role of macroscopic variable in this game is played by the quantity ΔA, which is the difference in mass from the initial mass partition. Exploiting the analogy with inelastic modes leads us to construct a macroscopic guess for the pairing transition density $\delta\rho_P$ modeled on the surface transition density $\delta\rho_S$:

$$\delta\rho_S = \frac{\partial\rho}{\partial\alpha}\alpha = \frac{\partial\rho}{\partial r}R_0\alpha, \qquad (4)$$

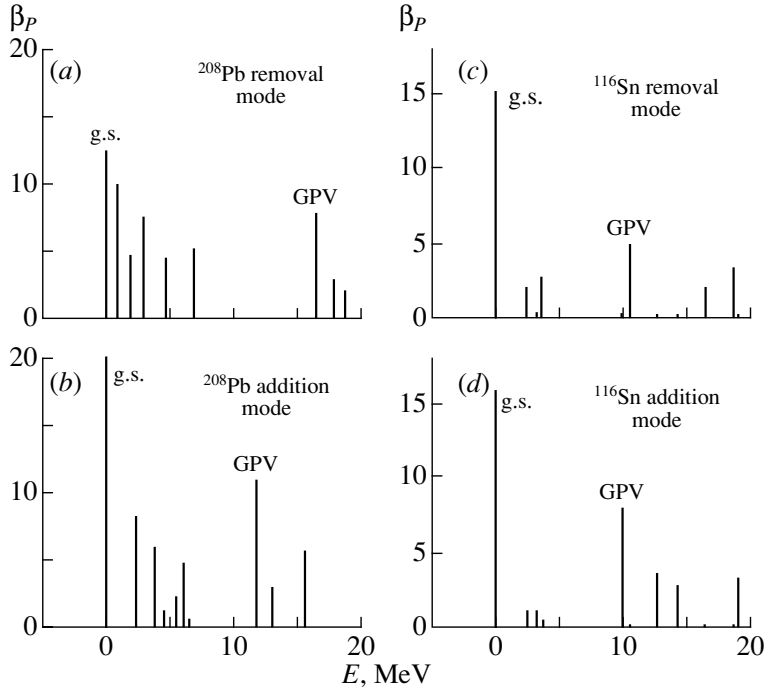

Fig. 2. Pairing response for removal and addition mode in ^{208}Pb and ^{116}Sn. The ground-state transition and the candidate for the GPV are marked.

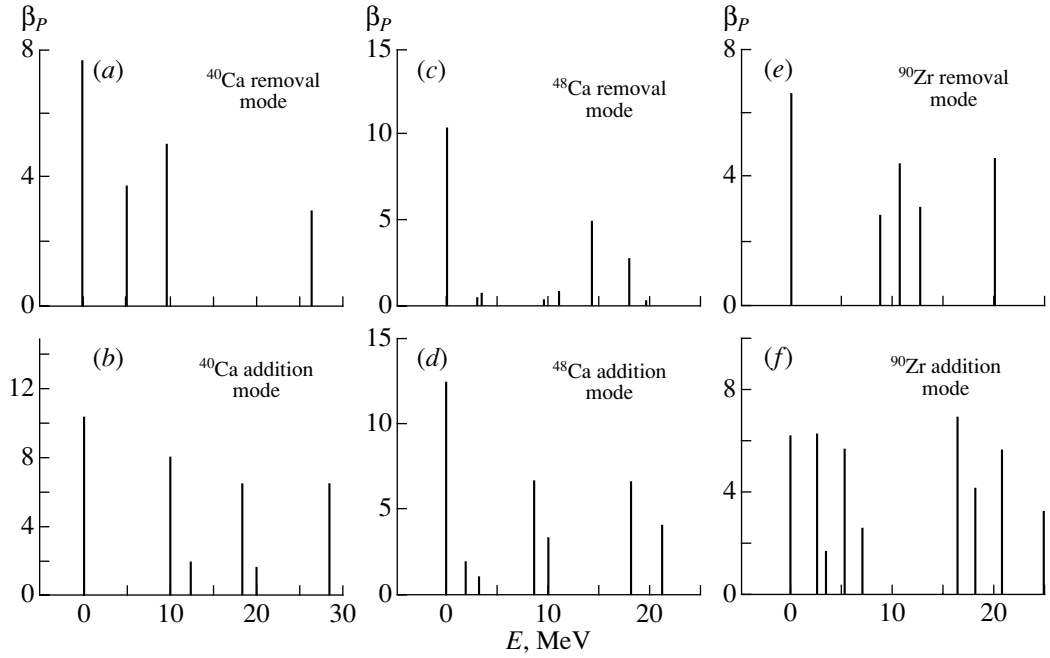

Fig. 3. Pairing response for removal and addition mode in ^{40}Ca, ^{48}Ca, and ^{90}Zr.

$$\delta\rho_P = \frac{\partial\rho}{\partial\Delta A}\Delta A = \left(\frac{R_0}{3A}\right)\frac{\partial\rho}{\partial r}\Delta A. \qquad (5)$$

One usually identifies α with the deformation parameter β_S, and the formal analogy suggests the correspondence with a pairing deformation parameter $\beta_S \Leftrightarrow \beta_P/(3A)$. This scheme implies the assumption that nuclear density is saturated and that a change in the number of particles is strictly related to a change of volume. The two-particle transfer form factors may

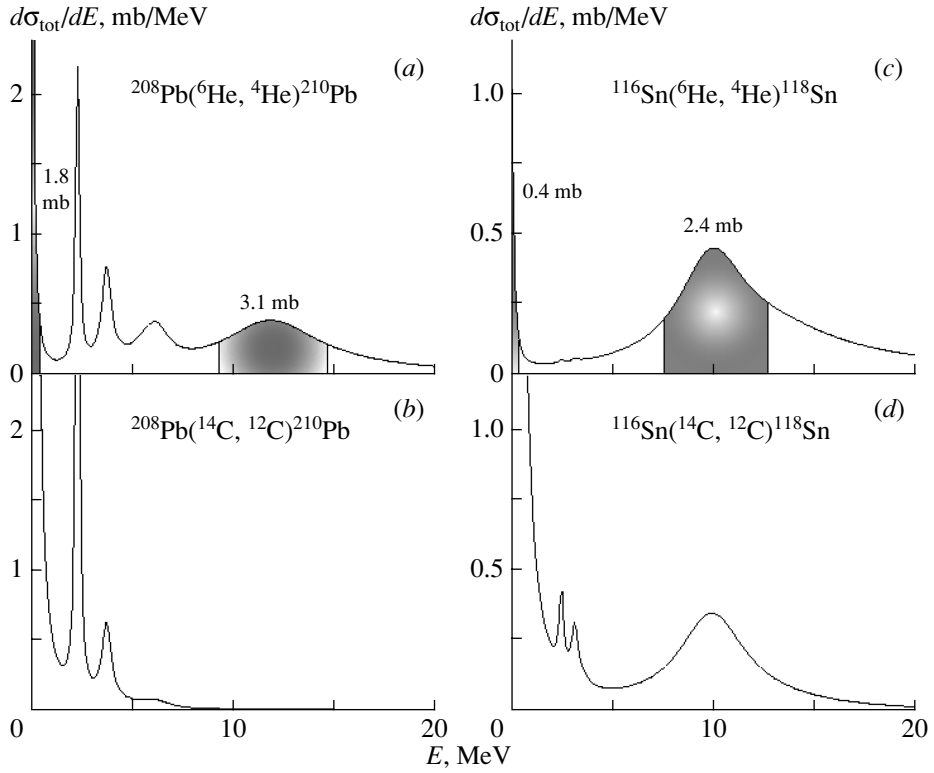

Fig. 4. Differential cross sections as function of the excitation energy. The shaded areas for the (^{6}He, ^{4}He) reactions allows a comparison between the transition to the ground states and to the GPVs. Note that the vertical scale is changed in Sn with respect to Pb.

then be connected to the ion–ion potential $U(r)$ as

$$F_P(r) = \left(\frac{\beta_P}{3A}\right) R_0 \frac{\partial U(r)}{\partial r}. \qquad (6)$$

This formalism has been applied to many low-energy aspects of two-particle transfer reactions [8, 9]. Certainly, the macroscopic approach is liable to improvements when one turns to a microscopic description, but the predictions may be considered robust enough to give order-of-magnitude evaluations.

Table 2. Cross sections (in mb) for ground-state and GPV transitions obtained with the DWBA code Ptolemy [the target (column) and projectile (row) are specified]

	^{14}C → ^{12}C	^{6}He → ^{4}He
^{116}Sn → ^{118}Sn$_{g.s}$	19.4	0.4
^{208}Pb → ^{210}Pb$_{g.s}$	15.3	1.8
^{116}Sn → ^{118}Sn$_{GPV}$	0.14	2.4
^{208}Pb → ^{210}Pb$_{GPV}$	0.04	3.1

4. RESULTS FOR Pb, Sn, AND OTHER TARGETS

DWBA calculations have been performed for two-neutron transfer reactions on the two cited targets either with usually available beams (^{14}C, ^{12}C) or with new unstable ones (^{6}He, ^{4}He). The last reaction has been chosen since it has optimal matching conditions: the Q values for the transition to the ground states of both targets are strongly positive, with the consequence of Q values to the GPV close to the optimum Q value ($Q_{opt} \sim 0$ MeV). This should favor the excitation of the pairing mode, while the situation with carbon beam is reversed, having large (and negative) Q values for the high-lying energy region and small Q values for the low-lying region. In Table 2, we report the angle-integrated cross sections obtained with standard DWBA computer codes.

These cross sections have been derived for sharp states, and we refer to the numbers in the last table when speaking of order-of-magnitude estimates. Obviously, cross sections in the high-lying energy region have a finite (and large) width that should be inserted for a more realistic description of the spectrum. We have chosen a simple scheme that gives a Lorentzian distribution with a width that grows quadratically with the excitation energy, $\Gamma = kE_x^2$,

with k adjusted to give a width of 4 MeV for the GPV. This might seem rather arbitrary since there is no reason for an a priori assignment of this quantity. We have been brought to this simple prescription because other collective states (of different nature) lying in the same energy region display similar values for their width, and it is reasonable to assume some rule to narrow the low-energy states and to broaden the high-energy ones.

5. FINAL REMARKS

The final achievements for the four reactions studied in detail are presented in Fig. 4, where the areas corresponding to the cross sections given above have been shaded to give a feeling of the relative magnitudes of the transition to the ground states and to the GPVs. It is worthwhile to note that, in the case of Pb, there is a considerable gain in using unstable beams, while in Sn it is much less evident. One sees the need for unstable helium when one compares the magnitude for the pairing resonance in the (c) and (d) panels with the peak at zero energy: in the first panel, the transition to the ground state is extremely hindered.

A ^{6}He beam is currently available (or it will be available in the very near future) in many radioactive ion-beam facilities around the world, and the calculations that we have presented could allow planning for future experiments aimed at studying the not yet completely unraveled role of pairing interaction in common nuclei, using exotic weakly bound nuclei as useful tools.

ACKNOWLEDGMENTS

I wish to gratefully acknowledge discussions with Andrea Vitturi, Hugo Sofia, and Wolfram von Oertzen on various aspects of theoretical and experimental nuclear physics. The participation at the VII International School–Seminar on Heavy-Ion Physics, Dubna, Russia, 2002, has been supported by the INFN.

REFERENCES

1. R. A. Broglia and D. R. Bes, Phys. Lett. B **69B**, 129 (1977).
2. M. W. Herzog, R. J. Liotta, and L. J. Sibanda, Phys. Rev. C **31**, 259 (1985).
3. G. M. Crawley *et al.*, Phys. Rev. Lett. **39**, 1451 (1977).
4. W. von Oertzen and A. Vitturi, Rep. Prog. Phys. **64**, 1247 (2001).
5. L. Fortunato, W. von Oertzen, H. M. Sofia, and A. Vitturi, Eur. J. Phys. A **14**, 37 (2002).
6. *Collective Aspects in Pair Transfer Phenomena*, Ed. by C. H. Dasso and A. Vitturi, SIF Proc. **18**, (Editrice Compositori, Bologna, 1987).
7. D. R. Bes and R. A. Broglia, Phys. Rev. C **3**, 2349 (1971).
8. C. H. Dasso and G. Pollarolo, Phys. Lett. B **155B**, 223 (1985).
9. C. H. Dasso and A. Vitturi, Phys. Rev. Lett. **59**, 634 (1987).

Physics of Atomic Nuclei, Vol. 66, No. 8, 2003, pp. 1450–1453. From Yadernaya Fizika, Vol. 66, No. 8, 2003, pp. 1496–1499.

New Experimental Results on Emission and Reaction Barriers*

N. Rowley**

Institut de Recherches Subatomiques, Université Louis Pasteur, Strasbourg, France

Received December 16, 2002

Abstract—The use of the method of experimental barrier distributions is now commonplace in the interpretation of heavy-ion fusion excitation functions. The application of a similar technique to the α emission from a hot compound nucleus will be briefly discussed. Less well known than the fusion-barrier distribution is the one obtained from quasi-elastic scattering. Some details of this method will be discussed with particular emphasis on possible advantages for its exploitation with radioactive beams.

1. INTRODUCTION

It is now well known that an experimental fusion-barrier distribution $D_f(E)$ can be obtained from the fusion excitation function $\sigma_f(E)$, where E is the incident c.m. energy, by applying the following formula:

$$D_f(E) = \frac{d^2(E\sigma_f)}{dE^2}. \quad (1)$$

This equation was first proposed in [1] and a detailed review of its significance and its applications has been given in [2].

The usefulness of this equation depends on the approximate validity of an eigenchannel formalism for the important channel couplings (collective excitations) for the problem in question. That is, one should be able to write approximately the total fusion cross section as a weighted sum of the fusion cross section for a number of uncoupled eigenchannels:

$$\sigma_f(E) \approx \sum_\alpha w_\alpha \sigma_f(E, B_\alpha), \quad (2)$$

where w_α and B_α are the weights and barrier heights in these channels. In certain limits, this equation can be derived analytically, the mapping between physical coupled channels and uncoupled eigenchannels taking place through a unitary transformation depending only on the coupling matrix [2]. The relevant approximations are as follows:

(a) The centrifugal potential in the final channel should be little different from its entrance-channel value (isocentrifugal approximation).

(b) The form factors for the couplings should all have a similar radial dependence.

(c) The excitation energies E^* of the strongly coupled excited states of the target and projectile should be negligible (adiabatic approximation).

The first approximation is rather good for heavy-ion reactions, since the reduced mass of such systems is large. The second is good for the most important collective excitations in question. The third is good for strongly deformed nuclei having a large moment of inertia but not good for phonon excitations, where E^* can be large. Despite this, however, some of the most interesting effects can be found in highly vibrational nuclei (see, for example, [3]). One finds that the barrier structures still exist but that the weights of the different barriers can be strongly influenced by nonadiabatic effects. It should be stressed that, even well outside the validity of Eq. (2), the representation of fusion data afforded by Eq. (1) is still useful, giving a stringent test of whether or not a theoretical calculation correctly reproduces the important features of an experiment.

Later in this paper, we shall compare the method of Eq. (1) with a similar technique for obtaining a distribution of reaction barriers from the total quasi-elastic excitation function $\sigma_{\rm qe}(E)$. Let us first, however, discuss the possible consequences of barrier distributions on the inverse problem of charged-particle decays.

2. EMISSION BARRIERS FOR HOT NUCLEI

The eigenchannel formalism for subbarrier fusion with statically deformed nuclei has been extended to the α decay of the even–even actinide nuclei in [4]. An interesting feature of this problem is that it is not possible to extract any energy dependence, since the α decay takes place at a unique energy. However, for a strongly deformed nucleus, the decay may proceed to different final rotational states of the daughter, and

*This article was submitted by the author in English.

** e-mail: Neil.Rowley@IReS.in2p3.fr

the same eigenchannel transformation can still yield valuable information (on the α-particle internal wave function) when applied to the relevant branching ratios.

There exists, however, a problem concerning charged-particle emission where energy dependence is still a valid concept, that is, the α decay of a hot compound nucleus. An experiment was performed at the IReS Laboratory in 2000 exploiting the EUROBALL γ-ray multidetector and aimed at measuring the barrier distribution for α-particle evaporation.

In order to see whether the high temperature of the compound nucleus leads to a different potential barrier than for α-particle scattering from a cold nucleus, it is essential to know that the α particle was emitted in the first step of the cooling process. Thus, two reactions were studied, $^{30}\mathrm{Si} + {}^{170}\mathrm{Er}$ at 165 MeV and $^{29}\mathrm{Si} + {}^{170}\mathrm{Er}$ at 147 MeV, in order to populate very similar compound nuclei but at different excitation energies. By using EUROBALL to gate on the same (strongest) evaporation-residue channel (^{191}Hg) in each case, it was possible to extract the first-chance α emission for the system [5].

Figure 1 shows the α-particle energy spectra for the two reactions obtained in this way, and normalized to give the same values at low energies. The difference then gives the required first-chance probability. Unfolding the effects of the nuclear temperature and of the nuclear level density, one finds transmission coefficients consistent with an α-particle Coulomb barrier around 2 MeV lower than that found in scattering experiments, a strong indication that, at high temperature, the nuclear surface is more diffuse than at $T = 0$.

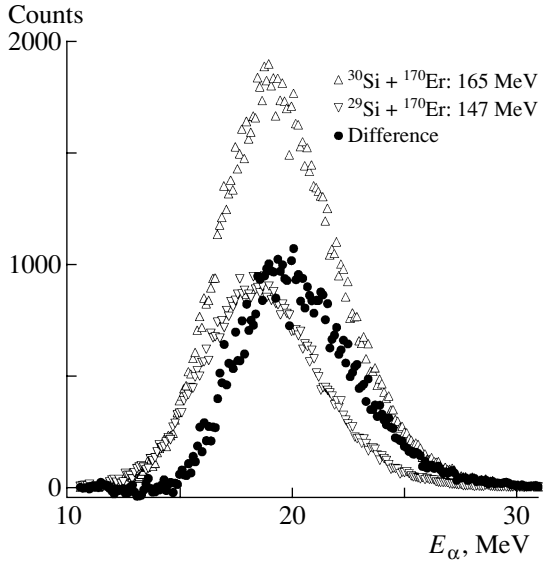

Fig. 1. Spectra of α particles emitted in the two reactions indicated. The difference of the spectra (normalized to be equal at low energies) gives the probability of first-chance α emission.

3. QUASI-ELASTIC BARRIER DISTRIBUTIONS

Under the same approximations outlined above for the validity of Eq. (2), one can also prove the following relation for the total quasi-elastic excitation function at any angle θ:

$$\sigma_{\mathrm{qe}}(E,\theta) \approx \sum_{\alpha} w_\alpha \sigma_{\mathrm{el}}(E, B_\alpha, \theta), \qquad (3)$$

with the same weights that appear in the fusion problem. Here, the σ_{el} are the elastic cross sections for scattering in the eigenchannels having barriers of height B_α.

We must now ask what the significance is of Eq. (1) in the context of Eq. (2). In other words, why does taking a second derivative of $E\sigma_f$ lead to such insights into the dynamics of the reaction? The answer is that when applied to the basic fusion cross section for a single barrier, this second derivative gives a function with particularly useful and simple properties. Consider the single-barrier fusion cross section σ_f^{W} in the Wong approximation:

$$E\sigma_f^{\mathrm{W}} = \frac{\hbar\omega R^2}{2}\ln(1+e^x), \qquad (4)$$

where ω is the oscillator frequency of the inverted potential barrier and $x = 2\pi(E-B)/(\hbar\omega)$. This leads to

$$\frac{1}{\pi R^2}\frac{d^2(E\sigma_f^{\mathrm{W}})}{dE^2} = \left[\frac{2\pi}{\hbar\omega}\frac{e^x}{(1+e^x)^2}\right] = G_f(E-B), \qquad (5)$$

where the function $G_f(E-B)$ has the following properties:

(a) It is symmetric.

(b) It is centered on $E = B$.

(c) Its integral over E is unity.

(d) It has a relatively narrow width of around $0.56\hbar\omega$.

The function G_f plays, therefore, the role of a test function and the expression

$$\frac{1}{\pi R^2}D_f(E) = \frac{1}{\pi R^2}\frac{d^2(E\sigma_f)}{dE^2} = \sum_{\alpha} w_\alpha G_f(E-B_\alpha) \qquad (6)$$

is a distribution in the mathematical sense of the term. We must now ask the question of how best to define a

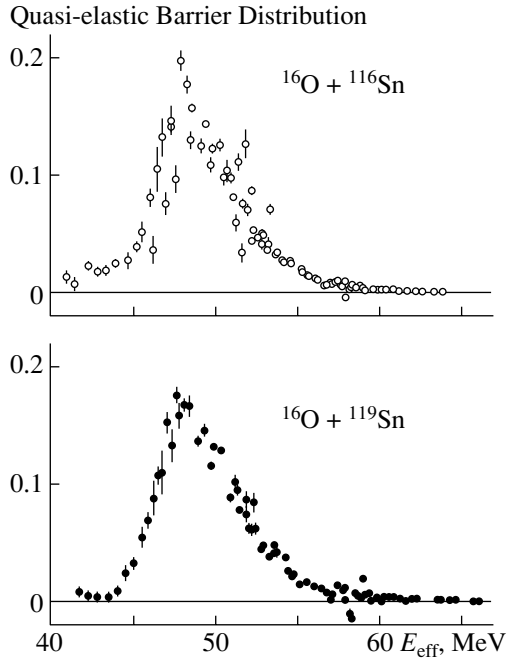

Fig. 2. Quasi-elastic barrier distributions for the two systems indicated, measured at the Warsaw cyclotron. The structures at the very lowest energies are probably related to Fresnel diffraction.

similar test function for Eq. (3) relating to the quasi-elastic case, in order to be able to extract the same information on the weights w_α.

A difficulty with this task is that σ_{el} may possess oscillations in some angular regions. However, for heavy-ion systems, it is well known that, for reasonably large angles (though not too close to π), the single-barrier elastic cross section falls off smoothly from a value close to that for Rutherford scattering at low energies to very small values at energies high above the barrier. Thus, the appropriate test function for our current problem is

$$G_{\text{qe}} = -\frac{d}{dE}\left(\frac{\sigma_{\text{el}}}{\sigma_{\text{R}}}\right), \qquad (7)$$

and the quasi-elastic barrier distribution may be defined by

$$D_{\text{qe}} = -\frac{d}{dE}\left(\frac{\sigma_{\text{qe}}}{\sigma_{\text{R}}}\right). \qquad (8)$$

The quasi-elastic test function G_{qe} has similar properties to the fusion test function:

(a) It is reasonably symmetric.

(b) Its integral over E is unity.

(c) It has a similar relatively narrow width.

It is, however, no longer centered on $E = B$ due to the intervention of a different centrifugal potential E_{cent} corresponding to the different grazing angular momenta at different angles. The function is, therefore, centered on an energy:

$$B^* = B + E_{\text{cent}}(\theta) = \frac{1 + \text{cosec}(\theta/2)}{2}B. \qquad (9)$$

Thus, at an energy E and an angle θ, one obtains the barrier distribution at an effective energy:

$$E_{\text{eff}} = \frac{2}{1 + \text{cosec}(\theta/2)}E. \qquad (10)$$

This may seem like an inconvenience, but in fact it means that several effective energies can be obtained for a single-beam energy. This opens up the possibility of performing barrier distribution experiments with a cyclotron accelerator, achieving the relatively small energy steps required for such work by an astute choice of the scattering angles at which σ_{qe} is measured.

This fact was recently exploited for the first time at the Warsaw cyclotron [6]. Figure 2 shows the results of the first experiments for $^{16}\text{O} + {}^{116,119}\text{Sn}$. (Of course, earlier experiments with a tandem accelerator, where the fine energy steps could be obtained simply by changing-beam energy, have also exploited the possibility of obtaining multiple effective energies. See, for example, [7].) The figure shows the quasi-elastic barrier distributions obtained by the usual point-difference method from the experimental data. However, the paper [6] also discusses in some detail the possibility of obtaining a better behaved distribution by employing smoothing techniques (for example, spline fitting) before taking the appropriate derivative analytically. We shall not discuss this further here, since our main interest is to elaborate possible advantages of the quasi-elastic barrier distribution for radioactive beams.

4. RADIOACTIVE BEAMS

Certain advantages in measuring σ_{qe} rather than σ_f are immediately obvious from the above discussions:

(a) Less accuracy is required in the data for taking the first derivative of Eq. (8) rather than the second derivative of Eq. (1).

(b) Whereas measuring the fusion cross section requires specialized recoil separators (electrostatic deflector/velocity filter) usually of low acceptance and efficiency, the measurement of σ_{qe} needs only very simple charged-particle detectors, not necessarily possessing good resolution either in energy or in charge. By having rings of such detectors, high efficiency can be achieved.

(c) Several effective energies can be measured at a single-beam energy. This not only improves the

efficiency of the experiment, but also allows the use of a cyclotron accelerator where the relatively small energy steps required cannot be obtained from the machine itself.

These all point to greater ease of measurement with low-intensity exotic beams.

There is a further advantage to D_{qe} when studying very heavy systems. Entrance-channel models calculate the total capture cross section with no reference as to whether the composite system will go on to produce long-lived evaporation resides or whether it will rapidly fission. Thus, in order to measure what these theories calculate, it would be necessary to measure fusion–evaporation and fusion–fission cross sections simultaneously for heavy systems where the compound nucleus is fissile. (Alternatively one may try to reconstruct the total capture cross section from the evaporation-residue results, using an evaporation model code which takes fission into account [8].) Since, however, the quasi-elastic cross section is the complementary part of the flux scattered from the barrier (and related to capture by unitarity), this measurement will always be related to the total capture cross section, irrespective of what happens once the barrier is crossed. Though of course in such a case, the other reaction channels (fission, quasi-fission, deep-inelastic) could complicate matters by contaminating the quasi-elastic measurements.

There are, of course, some possible disadvantages to measuring σ_{qe}. For example with a heavy exotic beam such as ^{132}Sn, one should consider the consequences of the inverse kinematics. For a light target, the quasi-elastic flux will be forward focused and this will require particle detectors at forward angles. Since energy resolution is now related to angular resolution through Eq. (10), the ensuing problems are obvious.

Other disadvantages are intrinsic in the theoretical approach to this problem. For example, although the global shapes of D_{qe} and D_f have been shown to be very similar for many systems, certain structural details appear to be lost in the quasi-elastic case [7]. This seems to be due to a dephasing of the different amplitudes contributing to Eq. (3). Also, as pointed out above, the quasi-elastic test function has less good properties than its fusion counterpart. In particular, for light ions, the single-barrier elastic cross sections can be strongly oscillatory, making the method unsuitable. Even for heavy ions, a possible problem may arise from the appearance of Fresnel oscillations at energies below the effective barrier energy for a given angle.

Despite these negative aspects, however, we believe that quasi-elastic barrier distributions have been rather underexploited and that further studies with stable beams should be undertaken in anticipation of possible future experiments with exotic beams. This is particularly true for systems where the isospin degree of freedom could be pushed to greater limits, for example, with a ^{132}Sn beam, and where neutron transfers could play a dominant role [9].

REFERENCES

1. N. Rowley, G. R. Satchler, and P. H. Stelson, Phys. Lett. B **254**, 25 (1991).
2. M. Dasgupta, D. J. Hinde, N. Rowley, and A. M. Stefanini, Annu. Rev. Nucl. Part. Sci. **48**, 401 (1998).
3. A. M. Stefanini, D. Ackermann, L. Corradi, *et al.*, Phys. Rev. Lett. **74**, 864 (1995).
4. T. L. Stewart, M. W. Kermode, D. J. Beachey, *et al.*, Nucl. Phys. A **611**, 332 (1996); T. L. Stewart, M. W. Kermode, N. Rowley, and D. J. Beachey, J. Phys. G **5**, 1057 (1999).
5. G. Viesti, V. Rizzi, D. Fabris, *et al.*, Phys. Lett. B **521**, 165 (2001).
6. E. Piasecki, F. Carstoiu, W. Czarnacki, *et al.*, Phys. Rev. C **65**, 054611 (2002).
7. H. Timmers, J. R. Leigh, M. Dasgupta, *et al.*, Nucl. Phys. A **584**, 190 (1995).
8. A. B. Quint, W. Reisdorf, K.-H. Schmidt, *et al.*, Z. Phys. A **346**, 119 (1993).
9. H. Timmers, D. Ackermann, S. Beghini, *et al.,* Nucl. Phys. A **633**, 421 (1998).

Physics of Atomic Nuclei, Vol. 66, No. 8, 2003, pp. 1454–1459. From Yadernaya Fizika, Vol. 66, No. 8, 2003, pp. 1500–1505.

Dynamics of Superheavy System in ^{86}Kr + ^{208}Pb Reaction*

V. A. Rubchenya[1),2)], A. A. Alexandrov[3)], S. V. Khlebnikov[2)], V. G. Lyapin[2),4)], V. A. Maslov[3)], Yu. E. Penionzhkevich[3)], G. Prete[5)], Yu. V. Pyatkov[3)], Yu. G. Sobolev[3)], G. P. Tiourin[1),2)], W. H. Trzaska[1),4)], D. N. Vakhtin[2)], and J. Äystö[1),4)]**

[1)] *Department of Physics, University of Jyväskylä, Juväskylä, Finland*

[2)] *Khlopin Radium Institute, St. Petersburg, Russia*

[3)] *Flerov Laboratory of Nuclear Reactions, Joint Institute for Nuclear Research, Dubna, Moscow oblast, 141980 Russia*

[4)] *Helsinki Institute of Physics, Helsinki, Finland*

[5)] *INFN Laboratori Nazionali di Legnaro, Legnaro, Italy*

Received December 20, 2002

Abstract—The dynamics of the excited superheavy system with $Z = 118$ in the reaction ^{86}Kr + Pb at $E_{Kr} = 600$ MeV has been investigated. The mass and kinetic energy of binary fragments were measured by the time-of-flight method. Double differential distributions of neutrons and α particles were measured in coincidence with fragments. Neutron and α-particle probes were used for determination of the fragmentation time scale. Evidence of the neck fragmentation was obtained from analysis of double differential α spectra. Properties of the α-particle neck fragmentation component are close to those known from the ternary fission of actinide nuclei, but the multiplicity is much larger. The total kinetic energy distribution of fragments tagged by neutrons or α particles shifts towards lower energies. Fragment yields in the symmetric region increase substantially when fragments are tagged by α particles. © *2003 MAIK "Nauka/Interperiodica".*

1. INTRODUCTION

During the last decade, a number of new superheavy nuclides have been synthesized using cold and hot fusion reaction methods [1, 2]. The main problem in planning future experiments is predicting the formation of the compact compound superheavy nucleus which transits into the ground state by neutron and γ-ray emission with very strong fission competition. This, in turn, depends on the interplay of reaction channels and, ultimately, on the dynamics of the fusion–fission process. The reaction of 449-MeV ^{86}Kr with ^{208}Pb was used in an attempt to produce new superheavy nuclei with $Z = 118$ [3]. Fragment mass and kinetic energy distributions for this reaction near Bass barrier energies have been measured in Dubna, and the fission probability of the compact compound system was estimated [4].

In the present paper, results of investigation of the dynamics of the excited superheavy system with $Z = 118$ in the reaction ^{86}Kr + Pb at $E_{Kr} = 600$ MeV using neutron and α-particle probes are presented. In principle, the method of nuclear clock and nuclear thermometer [5] can be applied for this reaction, though the contribution of fusion–fission channels is small. Alpha particles can also be used as a clock for the neck fragmentation process. According to the neck double-rupture model of ternary fission [6], the probability of light charged particle (LCP) emission depends on the lifetime of the dinuclear system (DNS) with a well-developed neck. In addition, mass and kinetic energy distributions of fragments tagged by neutrons or α particles can give more information about relative contributions of main gross reaction channels: deep inelastic, fast fission, and decay of compact compound configuration. Neutron and α-particle double differential distributions were analyzed within the multiple-source model, which includes four sources: two fragments, a compound nucleus, and fragmentation of the neck region. To describe α-particle yields, one has to assume relatively high probability for the neck fragmentation.

2. EXPERIMENT

Measurements were carried out using the HENDES (High Efficiency Neutron DEtection System) facility [7] at the Department of Physics, University of Jyväskylä. The cyclotron provided a ^{86}Kr^{20+}

*This article was submitted by the authors in English.

** e-mail: rubchen@phys.jyu.fi

beam with diameter on target about 3 mm. Beam intensity was limited to 1 pnA to avoid overloading the data acquisition system. Two 100-μg/cm^2-thick lead targets were used: natural ^{nat}Pb and isotopic ^{208}Pb, each evaporated on identical 70-μg/cm^2 Al_2O_3 backings. The target was mounted in the center of the 75-cm-in-diameter HENDES reaction chamber, which also housed the fragment and LCP detection system.

Masses and energies of fragments were determined by the time-of-flight (TOF) technique using a two-shoulder TOF spectrometer consisting of two microchannel plate (MCP) start detectors and two 24.3-cm-in-diameter position-sensitive avalanche counters (PSAC) of the type developed for the FOBOS facility at FLNR, Dubna [8]. The angles from beam direction to centers of two PSACs were $-60°$ and 56°, and the flight bases in each shoulder were 22.6 cm. Mass resolution of the spectrometer was determined mostly by time resolution of PSACs and was about 1.5%.

LCPs were detected by 21 pin diodes placed inside the HENDES reaction chamber at distances of 21 to 29 cm from the target in- and out-of-plane determined by two directions to the centers of fragment detectors. The dimensions of each pin diode were 2 cm $\times$ 2 cm $\times$ 380 μm and they were arranged in groups of three. To suppress fragments and scattered heavy particles, the surfaces of all LCP detectors were covered by aluminum foil with thickness from 10 to 20 μm depending on the position of the detector. Each LCP detector provided energy and time signals used to distinguish between different types of light particles by the TOF-E technique. The energy resolution of LCP detectors was FWHM $\approx$ 1.5%, and the time resolution for monochromatic α particles was estimated to be $\approx$100 ps.

The reaction chamber was surrounded by four 1-m-long position-sensitive neutron detectors (PSND) [9] which covered angles from $\pm30°$ to $\pm150°$ in the reaction plane. Signals from two photomultipliers attached to opposite edges of the 5.5-cm-in-diameter quartz tube filled with NE-213 liquid scintillator provided time of arrival and coordinate for each neutron, as well as allowed separating neutrons from γ rays by means of pulse-shape analysis. The time resolution of each PSND was better than 1 ns, which led to a position resolution of 10 cm and error of neutron energy determination from 2 to 6% for energies of 1 and 10 MeV, respectively. The PSND's intrinsic efficiency varied from 30 to 20% in the energy range from 1 to 10 MeV.

During in-beam experiments, the data acquisition was triggered by coincidences in two shoulders of the fragment TOF spectrometer. Throughout the experiment, the count rate was kept around 1000 double coincidences per second. The total number of collected double events exceeded 2×10^8, most of which corresponded to projectile-like and target-like fragments. The total number of neutrons detected in four PSNDs in coincidence with fragments was about one million. The full α-particle statistics collected from all LCP detectors in coincidence with fragments was about 6000.

Before and after in-beam measurements, the whole system was calibrated using a very thin ^{252}Cf source and several standard α sources. Data analysis was carried out to obtain well-known mass and energy characteristics of fission fragments of ^{252}Cf to make sure the work of the setup is fully understood. Measurements with ^{252}Cf were also used to extract the efficiency of PSNDs at neutron energies close to the threshold ($\approx$ 0.7 MeV), where calculations are unreliable. Relative positions of PSNDs and PSACs during the calibration were the same as during the in-beam experiment, so that the experimental efficiencies also incorporated the influence of scattering of neutrons on the material of PSACs and surrounding supporting constructions.

3. RESULTS AND DISCUSSION

3.1. Fragment Mass and Kinetic Energy Distributions

Masses and energies of fragments were extracted from TOF using an iterative procedure to account for energy losses in the target and in START detector. Energy losses in START were mostly responsible for mass resolution ($\sigma_M \approx 2$), while uncertainty in determining width of the total kinetic energy distribution (σ_{TKE}) was mainly due to variation of the interaction position and consecutive energy loss by fragments in the material of the target. The energy loss by the beam in the backing was accounted for in calculations of collision energy in the center of mass.

In the analysis, the velocity of the compound nucleus V^{cm} was assumed to be an unknown value and was determined for each event from fragment velocity vectors. Following the recipe similar to that proposed in [10], components of V^{cm} parallel ($V_{\parallel}^{\mathrm{cm}}$) and perpendicular ($V_{\perp}^{\mathrm{cm}}$) to the beam direction were constructed, and a gate

$$\sqrt{(V_{\parallel}^{\mathrm{cm}} - V_0^{\mathrm{cm}})^2 + (V_{\perp}^{\mathrm{cm}})^2} < 3\sigma_{V_{\perp}^{\mathrm{cm}}}$$

was applied to suppress nonbinary events. Here, V_0^{cm} is the velocity of the compound nucleus in the case of LMT = 100%.

The two-dimensional plot of the mass–energy distribution (M-TKE matrix) of fragments for the

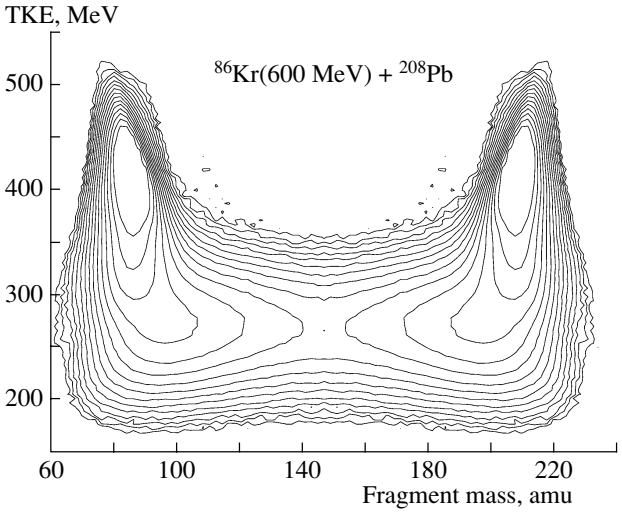

Fig. 1. The fragment mass–total kinetic energy distribution in ^{86}Kr+^{208}Pb reaction at $E_{Kr} = 600$ MeV.

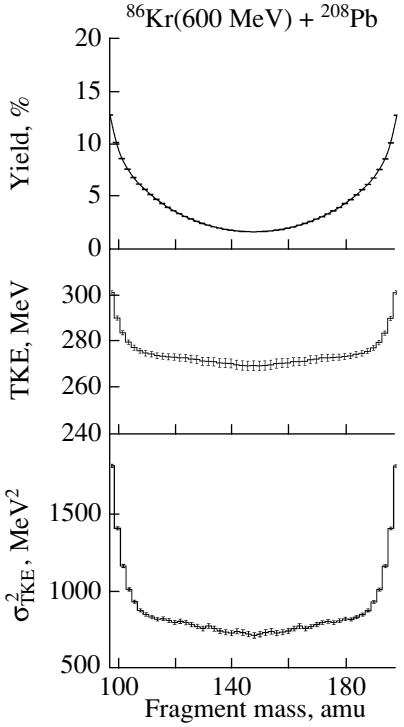

Fig. 2. Averaged mass yields, TKE, and width of TKE as functions of the fragment mass.

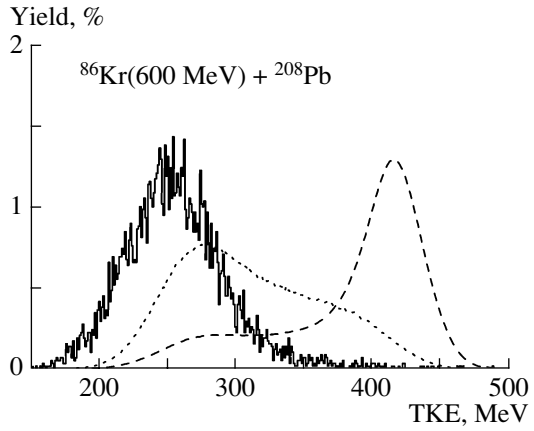

Fig. 3. Measured TKE distribution for all fragmentation events (dashed curve) and in coincidence with neutrons (dotted curve) and α particles (solid curve).

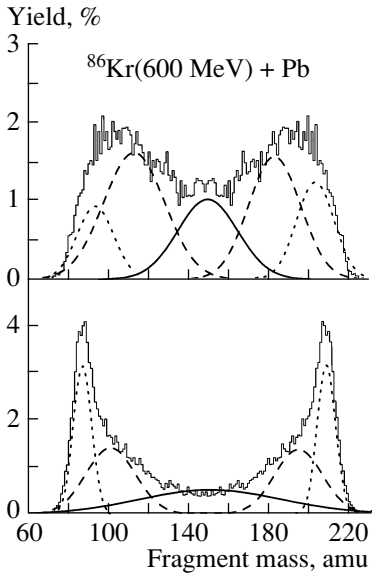

Fig. 4. The fragment mass distribution measured in coincidence with neutrons (lower part) and α particles (upper part) and contributions from compound nucleus fission (solid curve), deep-inelastic collisions (dotted curve), and fast fission (dashed curve).

studied reaction corresponding to the total excitation energy of the compound system of ^{294}118 about 125 MeV is presented in Fig. 1. One can see from Fig. 1, apart from an elastic–quasi-elastic scattering peak, a broad distribution formed mainly by the fast-fission process. Averaged mass yields, TKE, and variance of TKE as functions of fragment mass are shown in Fig. 2. It is impossible to determine the contribution of the compound nucleus fission from these inclusive distributions. The mass dependence of averaged TKE in the fragment mass region between 110 and 190 amu is nearly flat (≈270 MeV), while this dependence for compound nucleus fission should be parabolic with a maximum at symmetric mass division about 230 MeV.

Total kinetic energy distributions of fragments tagged by neutrons or α particles tend to shift towards lower energies, as one can see in Fig. 3, where the TKE distributions for all fragmentation events (dashed curve) and in coincidence with neutrons

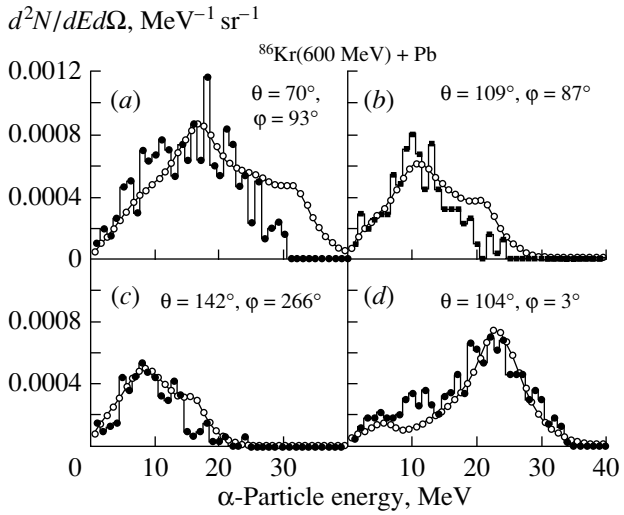

Fig. 5. The comparison of the measured α-particle spectra (histogram) with calculated spectra (open circles) at four different angles.

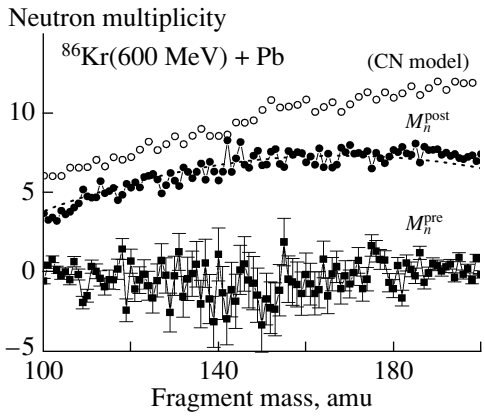

Fig. 6. Pre- and postscission neutron multiplicities as functions of the fragment mass. The values of postscission neutron multiplicities predicted for compound nucleus fission are shown by open circles.

(dotted curve) and α particles (solid curve) are shown. The fragmentation accompanied by α particles corresponds to a strongly damped collision which leads to formation of compound configurations, further evolving into elongated prescission shapes.

Fragment mass distributions measured in coincidence with neutrons (lower part) and α particles (upper part) are displayed in Fig. 4. Fragment yields in the symmetric region increase substantially when fragments are tagged by α particles. These mass distributions can be decomposed into a symmetric and two asymmetric components. The symmetric component can be attributed to compound nucleus fission. The asymmetric components correspond to deep-inelastic scattering (dotted curve) and fast or quasi-fission (dashed curve).

3.2. α-Particle Emission

Double differential spectra of α particles have been analyzed within the multiple-source model, which included four sources: two fragments, a compound nucleus, and a neck region between fragments (NF—neck fragmentation). Corresponding α-particle multiplicities and spectrum parameters in the c.m. frame were extracted from fitting the experimental spectra by the expression

$$\frac{d^2N}{dEd\Omega} = \sum_{A_F}\int P(\Omega^{\rm FR})d\Omega^{\rm FR} \times \sum_{{\rm TKE}(A_F)}\left[\frac{M^{\rm CN}}{4\pi}\sqrt{\frac{E}{\varepsilon}}W^{\rm CN}(\varepsilon) + M^{\rm NF}P^{\rm NF}(\theta^{\rm NF}_{\rm cm\,fr})W^{\rm NF}(\varepsilon) + \frac{M^F(A_F)}{4\pi}\sqrt{\frac{E}{\varepsilon}}W^F(\varepsilon)\right]Y(A_F, {\rm TKE}(A_F)). \quad (1)$$

Here $M^{\rm CN}$, $M^{\rm NF}$, and M^F are α-particle multiplicities from the compound nucleus, neck fragmentation, and fragment sources, respectively. The first term in brackets corresponds to evaporation from the composite nucleus, and the third term describes the contribution from fragments. Particle evaporation is assumed to be isotropic in both of these cases. The kinetic energy in the c.m. frame ε is transformed to the laboratory energy E using the velocity of corresponding sources. The second term describes particle emission from the neck region. In this case, the angular distribution of α particles in the c.m. frame is mainly perpendicular to the fragmentation axis, which is oriented into solid angle $\Omega^{\rm FR}$. The interval of integration over orientation angle of the fragmentation axis is determined by the fragment detector geometry and detection efficiency $P(\Omega^{\rm FR})$. Multiplicities $M^{\rm CN}$ and $M^{\rm NF}$ were assumed to be independent of the fragment mass asymmetry. For the fragment mass dependence of postscission multiplicity M^F, the following linear approximation was used:

$$M^F(A_F) = 0.085 - 0.00008A_F. \quad (2)$$

The α-particle Coulomb barrier dependence on the fragment mass was approximated by a linear function which reflects increasing fragment charge with mass,

$$B^F_\alpha(A_F) = 3.0 + 0.075A_F. \quad (3)$$

The c.m. spectra $W^{\rm CN}(\varepsilon)$ and $W^F(\varepsilon)$ are of evaporation nature with some temperature considered as a fitted parameter. The averaged Coulomb barrier of α particles evaporated from the composite system was taken equal to 28.0 MeV.

The spectrum $W^{NF}(\varepsilon)$ was described by a Gaussian form with parameters of the averaged energy $\overline{\varepsilon}_{NF} = 22.0$ MeV and energy width $\sigma_{\varepsilon}^{NF} = 6.0$ MeV. The angular distribution of NF—component $P^{NF}(\theta_{cm\,fr}^{NF})$—was approximated by a Gaussian form relative to the plane which is perpendicular to the fragmentation axis with angular dispersion $\sigma_{\theta_{cm\,fr}^{NF}} = 20°$. These parameters of the NF component differ from parameters extracted from ternary fission data in the Th–Cf region [11]. The fragment mass–energy yields were taken from the experiment (see Fig. 1) and summation over the fragment mass was done in the interval $A_F = 100$–200 amu.

A comparison between experimental spectra (histogram) and calculated spectra (open symbols) at four angles with $M^{CN} = 0.015$, $M^{NF} = 0.05$, and temperature $T = 2$ MeV is shown in Fig. 5. To describe spectra of α particles, one has to assume a high multiplicity for the neck fragmentation which exceeds by about a factor of four the yields for the $^{294}118$ compound nucleus predicted by the model of ternary fission [6].

3.3. Neutrons

Each PSND was treated as five independent 20-cm-long segments. For each segment, the neutron energy spectrum was constructed from TOF data. Pulse-shape analysis was used for n–γ discrimination. Pre- and postscission neutron multiplicities were extracted from 20 (four detectors × five segments) experimental spectra by a multiple-source model fit. Pre- and postscission neutron spectra were assumed to have a Maxwell form. Errors were determined from the behavior of χ^2 near the minimum. The procedure was described in detail in our recent publication [12].

Experimental pre- (solid squares) and postscission (solid circles) neutron multiplicities together with the theoretical values of postscission neutron multiplicities (open circles) calculated for compound nucleus fission, using our model for description of the fusion–fission process [12], are presented in Fig. 6. Here, the following gates on TKE were applied to suppress elastic events: $|\mathrm{TKE} - \overline{\mathrm{TKE}}| < 70$ MeV. One can conclude that the averaged prescission neutron multiplicity is close to zero, but that the error is large, $M_n^{pre} = 0.0 \pm 0.9$.

The fragment mass dependence of the postscission multiplicity is very well fitted by the second-order polynomial (dashed curve in Fig. 6)

$$M_n^{post}(A_F) = -13.86 + 0.254A_F - 0.00076A_F^2. \quad (4)$$

Deviation of the experimental $M_n^{post}(A_F)$ from the calculated values reflects the fact that the contribution of the fast-fission process is high. The experimental value of the averaged postscission neutron multiplicity is equal to $M_n^{post} = 13.7 \pm 0.4$ in the symmetrical mass region.

4. TIME SCALE AND NECK FRAGMENTATION

The application of the theoretical models usually used for extraction of the time scale in fusion–fission reactions meets serious diffilculties in the case under consideration because the heated compound nucleus has no fission barrier and contributions from fast-fission and deep-inelastic processes are high. Estimates of the time scale of the mass-symmetric fragmentation were made using our model and a computer code for fusion–fission reactions [12]. Emission of particles near the compact compound configuration is small, and this emission was considered during some time interval which depends on the internal excitation through the energy dependence of friction strength {see formula (4.3) in [12]}. The initial internal excitation energy is assumed to be equal to the sum of the compound nucleus excitation energy and half of the difference of potential energies between the saddle and scission point configuration, and fragment kinetic energy at the scission point was subtracted. By comparing the calculated prescission multiplicity with the experimental limit of $M_n^{pre} < 0.9$, an estimate of the lifetime of the composite system for symmetric fragmentation $T_{FF}^{pre} \leq 10^{-21}$ s was obtained. The prescission α-particle multiplicity was predicted to be $M_\alpha^{CN} \leq 0.01$, which is close to the value extracted from the multiple-source fit.

Alpha particles emitted from the neck region between fragments can be used as a probe for dynamics near the scission point. Using the value of the averaged energy of these α particles, $\overline{\varepsilon}_\alpha^{NF} = 22$ MeV, equal to the Coulomb energy of ternary configuration consisting of spherical nuclei, one can make a crude estimate of the distance between the centers of fragments, $D_{FF} = 30.4$ fm. More statistics for α particles are needed to investigate the probability of neck fragmentation for different fragment mass and kinetic energy. The multiplicity of light particles emitted from the neck region between fragments can be used to determine the lifetime of a dinuclear system with a well-developed neck [6],

$$M_\alpha^{NF} \sim \tau_{sc}/\tau_{DNS}. \quad (5)$$

Here, M_α^{NF} is used instead of the total light-particle multiplicity because α emission is overwhelming. The neck rupture time τ_{sc} is on the order of 10^{-23} s. Using

the experimental value of $M_\alpha^{\mathrm{NF}} = 0.053$, one can get the estimate $\tau_{\mathrm{DNS}} \sim 2 \times 10^{-22}$ s. The value of the light-particle multiplicity emitted in ternary fission of the compound nucleus of $^{294}118$ calculated according to [6] is equal to 0.013, which is much lower than the experimental value of M_α^{NF}.

5. CONCLUSIONS

Fragment mass and kinetic energy distributions and double differential neutron and α-spectra have been measured in the reaction $^{86}\mathrm{Kr} + \mathrm{Pb}$ at $E_{\mathrm{Kr}} =$ 600 MeV, which is well above the interaction barrier. Inclusive fragment mass and kinetic energy distributions show a pattern which is typical of the fast-fission process. Average total fragment kinetic energy is about 270 MeV, which is considerably higher than the value predicted for fission of the compound nucleus (about 235 MeV). Fragment mass and kinetic energy distributions tagged by neutrons or α particles correspond to more damped collisions, when the mass-symmetric component is enhanced.

It was determined that prescission neutron multiplicity is close to zero and the time scale is of the order of 10^{-21} s. To describe α particle spectra, one has to assume the high multiplicity of α-particles $M_\alpha^{\mathrm{NF}} \approx 0.05$ emitted from the neck region between fragments. Thus, evidence of the neck fragmentation in heavy-ion collisions at low energy was obtained. A new experiment to investigate the neck fragmentation process more deeply is planned in the nearest future.

ACKNOWLEDGMENTS

This work was supported by the Access to Large Scale Facility Program under the Training and Mobility of Researchers Program of the European Union, by the Access to Large Scale Facility Program under the TMR Program of the EU, and by the Academy of Finland under the Finnish Center of Excellence Programme 2000–2005 (project no. 44875, Nuclear and Condensed Matter Physics Programme at JYFL). One of us (V.A.M.) would like to acknowledge a CIMO Fellowship for financial support.

REFERENCES

1. Yu. Ts. Oganessian, Yad. Fiz. **63**, 1391 (2000) [Phys. At. Nucl. **63**, 1315 (2000)].
2. S. Hofmann and G. Münzenberg, Rev. Mod. Phys. **72**, 733 (2000).
3. V. Ninov, K. E. Gregorich, W. Loveland, *et al.*, Phys. Rev. Lett. **83**, 1104 (1999).
4. M. G. Itkis, Yu. Ts. Oganessian, E. M. Kozulin, *et al.*, in *Proceedings of the Second International Conference "Fission and Properties of Neutron-Rich Nuclei," St. Andrews, Scotland, 1999*, Ed. by J. H. Hamilton, W. R. Philips, and H. K. Carter (World Sci., Singapore, 2000), p. 268.
5. D. Hilscher and H. Rossner, Ann. Phys. (Paris) **17**, 471 (1992).
6. V. A. Rubchenya and S. G. Yavshits, Z. Phys. A **329**, 217 (1988).
7. W. Trzaska, J. Äystö, Z. Radivojevic, *et al.*, in *Proceedings of the 4th International Conference "Dynamical Aspect of Nuclear Fission", Časta-Papiernička, Slovak Republic, 1998*, Ed. by Yu. Ts. Oganessian, J. Kliman, and Š. Gmuca (World Sci., Singapore, 2000), p. 283.
8. W. Wagner *et al.*, Nucl. Instrum. Methods Phys. Res. A **403**, 65 (1998).
9. A. V. Kuznetsov, I. D. Alkhazov, D. N. Vakhtin, *et al.*, Nucl. Instrum. Methods Phys. Res. A **346**, 259 (1994).
10. D. J. Hinde, M. Dasgupta, J. R. Leigh, *et al.*, Phys. Rev. C **53**, 1290 (1996).
11. M. Mutterer and J. P. Theobald, *Nuclear Decay Modes*, Ed. by D. Poenaru (IOP Publ., Bristol, 1996), p. 487.
12. V. A. Rubchenya *et al.*, Phys. Rev. C **58**, 1587 (1998).

Physics of Atomic Nuclei, Vol. 66, No. 8, 2003, pp. 1460–1470. From Yadernaya Fizika, Vol. 66, No. 8, 2003, pp. 1506–1516.

Isospin Effects in Nuclear Fragmentation*

V. Baran[1)], M. Colonna[1)], M. Di Toro[1)], V. Greco[1)], M. Zielinska-Pfabe[2)], and H. H. Wolter[3)]**

[1)] *LNS, Catania, Italy*
[2)] *Smith College, Northampton, MA, USA*
[3)] *University of Munich, Germany*

Received August 28, 2002

Abstract—The availability of radioactive heavy-ion beams has driven a large interest in studies of nuclear structure of unstable nuclei. Some essential information in this field can come from investigations of charge asymmetry effects on nonequilibrium dynamics. It is therefore very important to understand the properties of the symmetry term in the nuclear matter equation of state. The purpose of this work is to extract valuable information about the symmetry term in the nuclear equation of state by studying the multifragmentation processes occurring during intermediate-energy heavy-ion reactions. We will concentrate on those observables in fragment production that are particularly sensitive to the symmetry term. The calculations are performed within the semiclassical Boltzmann–Uehling–Uhlenbeck approach with the inclusion of nuclear density fluctuations. We consider neutron-poor and neutron-rich Sn + Sn reactions at 50 MeV/A, with the N/Z ratio varying from 1.24 to 1.48. Both central and peripheral collisions are investigated. Some comparison with the experimental data obtained in the National Superconducting Cyclotron Laboratory at Michigan State University is presented. © *2003 MAIK "Nauka/Interperiodica".*

1. INTRODUCTION

The knowledge of the nuclear equation of state (EOS) and especially the density dependence of the symmetry (isospin) term is of great importance for many issues in nuclear physics and in astrophysics. It is relevant for studies of neutron star structure and stability, for any investigation of phase transition in low-density asymmetric nuclear matter, for fission of extremely asymmetric systems, and for level densities of nuclei far from the beta stability line.

This important and fundamental property of nuclear matter is still not well understood and its investigation is quite crucial.

The density and asymmetry dependence of energy for asymmetric nuclear matter is frequently parameterized in the following way:

$$E(\rho,\delta) = E(\rho,0) + S(\rho)\delta^2. \qquad (1)$$

Here, the density $\rho = \rho_n + \rho_p$ with ρ_n and ρ_p denoting the neutron and proton densities, respectively, and $\delta = (\rho_n - \rho_p)/\rho$.

Various functional dependences have been suggested for $S(\rho)$. Some of them are shown in Fig. 1. In the present work, we will consider the "asy-soft" EOS, where a potential symmetry term increases linearly with nuclear density and the "asy-stiff" EOS, where the symmetry term shows a saturation (even a slight decrease) at higher densities. Our goal is to extract the density behavior of the symmetry term from a study of the process of multifragmentation in intermediate-energy heavy-ion reactions.

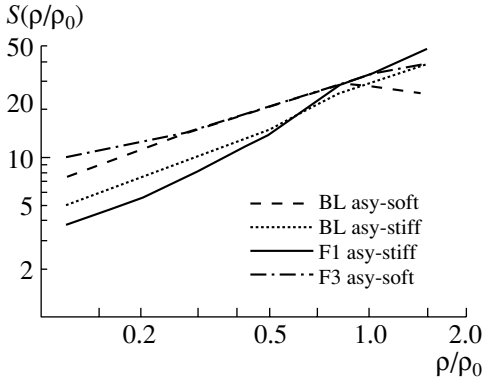

Fig. 1. Symmetry function $S(\rho/\rho_0)$ [see Eq. (1)] as a function of ρ/ρ_0 (data taken from Bao-An Li *et al.*, Phys. Rev. Lett. **78,** 1644 (1997) and M. Colonna *et al.*, Phys. Rev. C **57,** 1410 (1998)).

*This article was submitted by the authors in English.

**e-mail: mpfabe@smith.edu

1063-7788/03/6608-1460$24.00

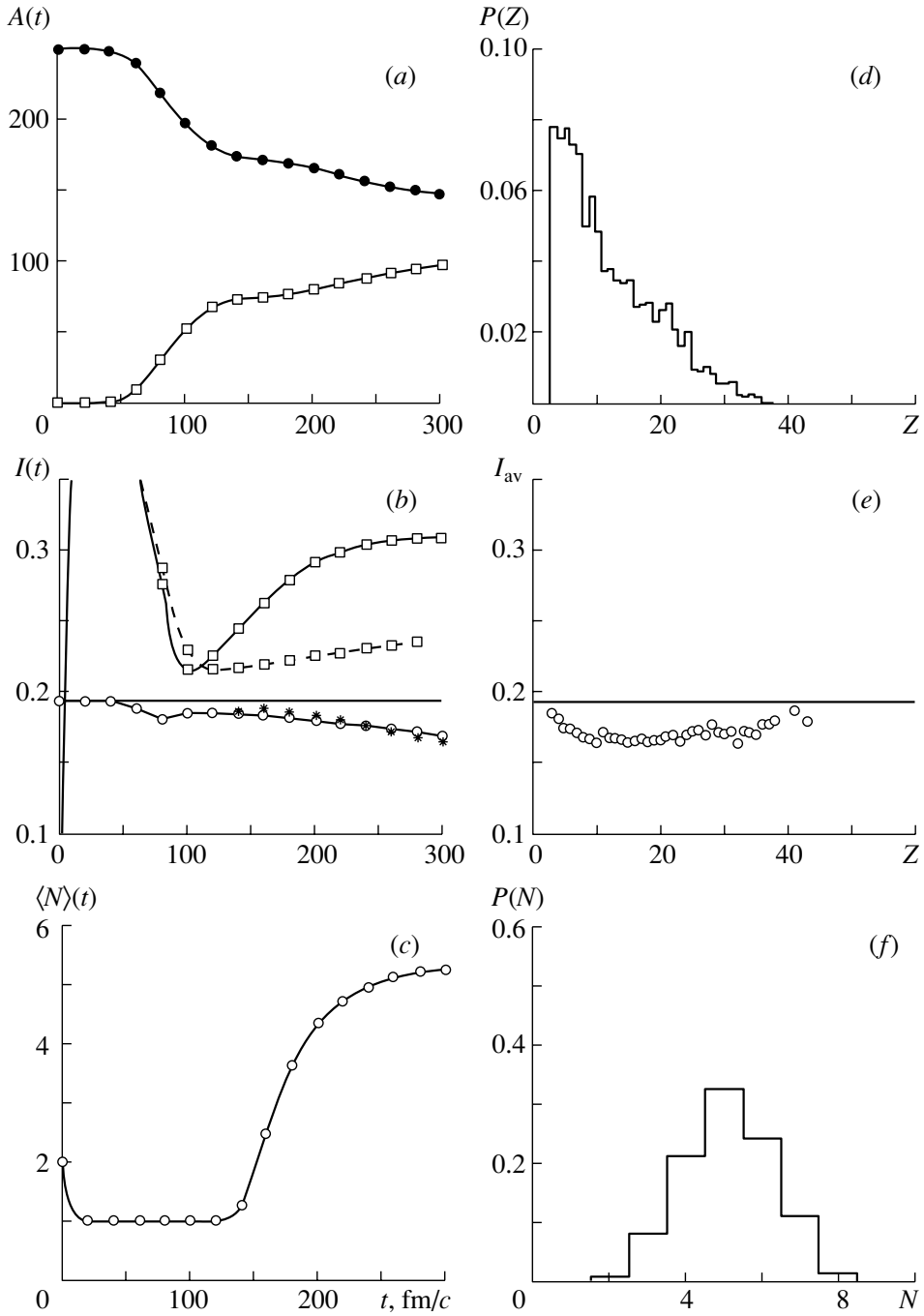

Fig. 2. $^{124}\mathrm{Sn} + {}^{124}\mathrm{Sn}$ collision at $b = 2$ fm, asy-stiff EOS.

2. THE MODEL

The dynamical evolution of collisions between heavy ions has been successfully described by semiclassical microscopic mean field theories like Boltzmann–Uehling–Uhlenbeck (BUU). The starting point for this approach is the time-dependent Hartree–Fock equation for the single-particle-density matrix. When the Wigner transform is applied and only the first term in the $\hbar$ expansion is kept, one gets an equation for the average value $\bar{f}$ of the distribution function $f(\mathbf{r}, \mathbf{p})$. After adding a Boltzmann collision term, it reads

$$\frac{d\bar{f}}{dt} = \frac{\partial \bar{f}}{\partial t} + \frac{\mathbf{p}}{m}\boldsymbol{\nabla}_{\mathbf{r}}\bar{f} - \boldsymbol{\nabla}_{\mathbf{r}}U\boldsymbol{\nabla}_{\mathbf{p}}\bar{f} = I_{\mathrm{coll}}(\bar{f}). \quad (2)$$

Here, U is a mean field potential. This equation is in principle deterministic. The influence of the neglected higher order terms can be considered as a fluctuation of the stochastic distribution function $f(\mathbf{r}, \mathbf{p})$ around

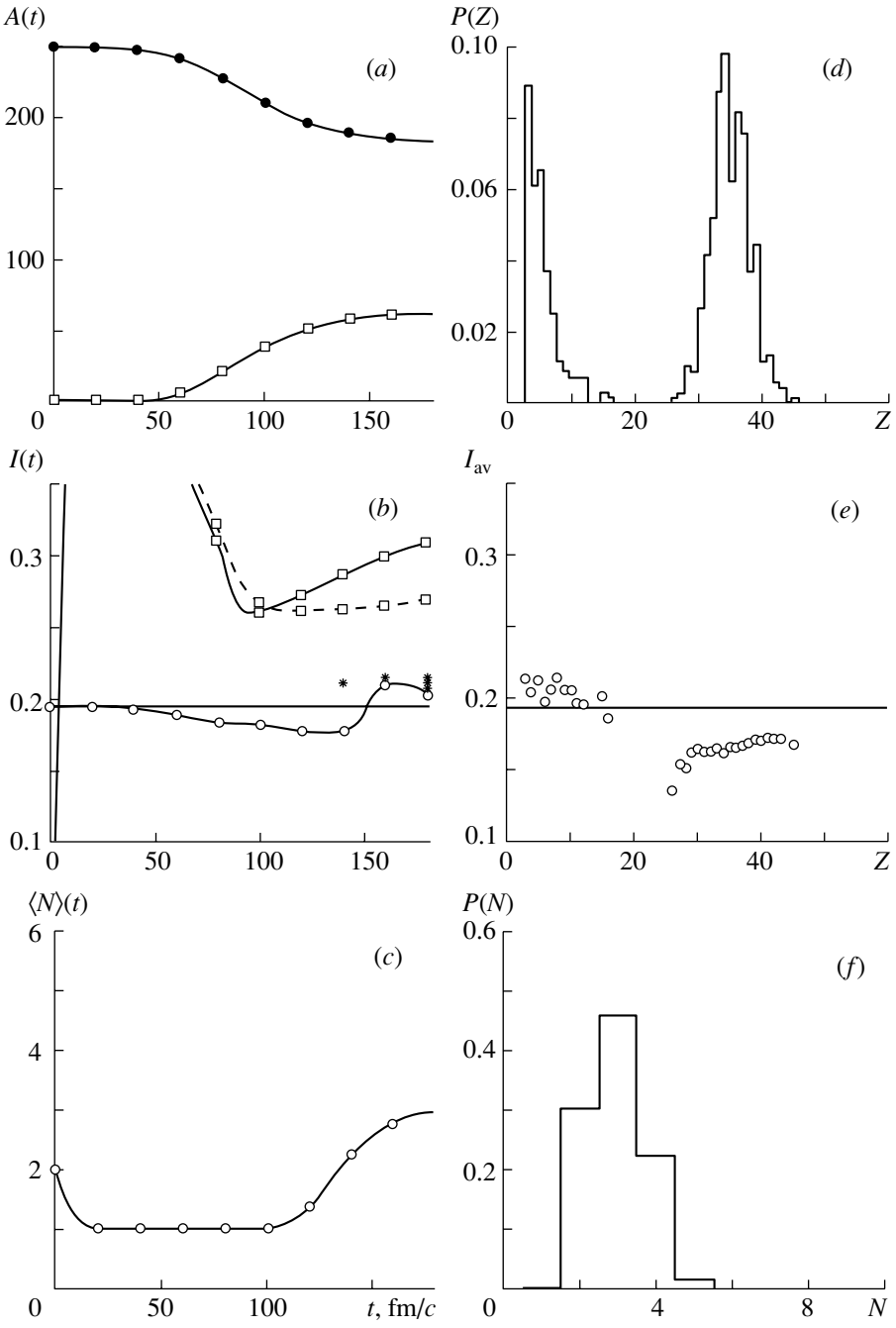

Fig. 3. The same as Fig. 2, but at $b = 6$ fm.

its average value $\bar{f}$, so f is equal to $\bar{f} + \delta f$. The evolution of the system with the fluctuating density is described by the Boltzmann–Langevin equation [1, 2]:

$$\frac{df}{dt} = I_{\text{coll}}(f) + \delta I(f). \tag{3}$$

However, this equation is very difficult to solve, so approximate methods of introducing fluctuations must be considered. One possible way is based on a projection of the fluctuations in the distribution function on coordinate space [3] and considering local density fluctuations, which will then be evolved by the mean field.

To introduce density fluctuations having correct statistical properties near equilibrium, we need to evaluate variances of density in coordinate space cells of volume V and then randomly distribute the particles according to these variances. We assume a free Fermi quantum gas. Then, the variances in the

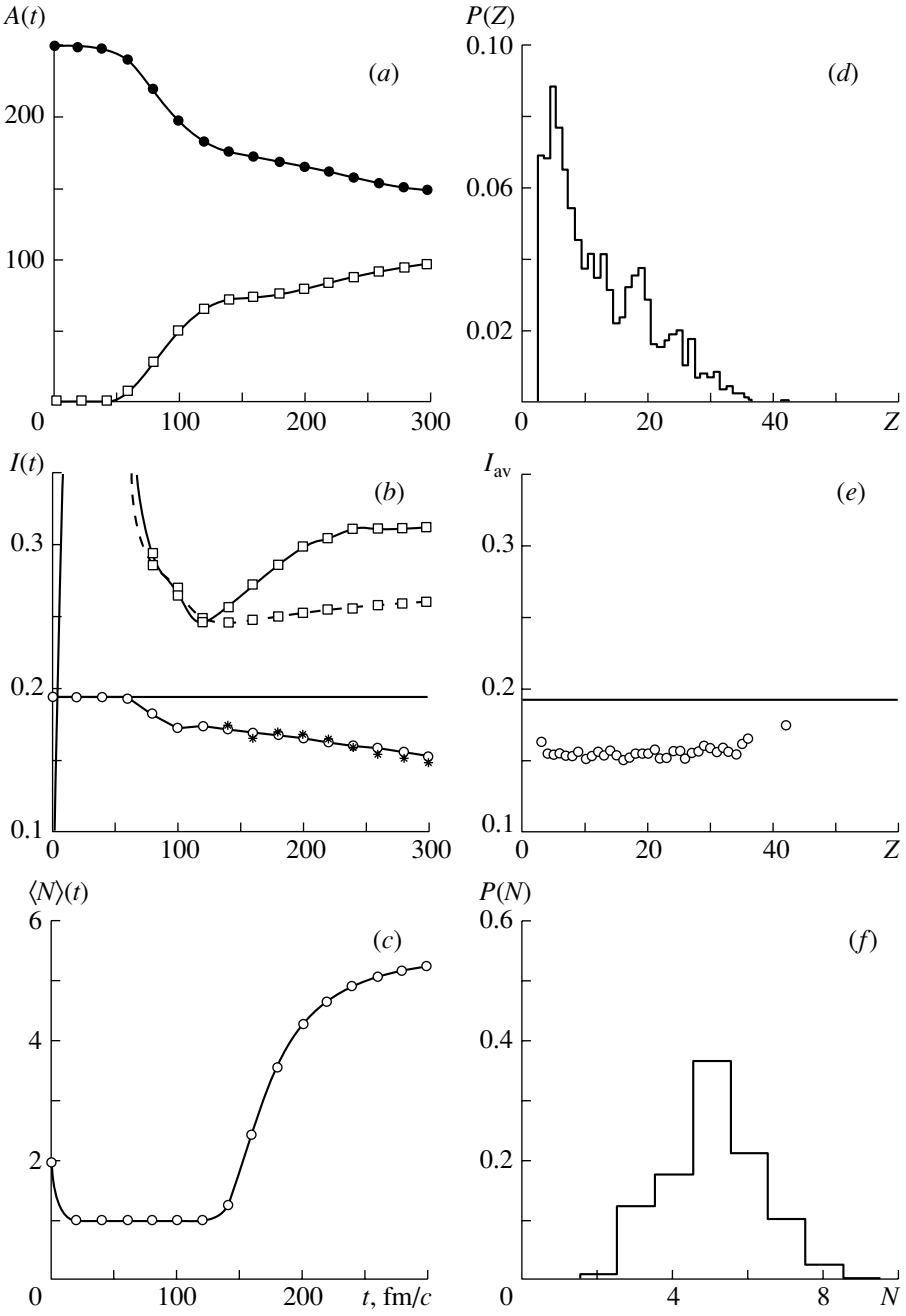

Fig. 4. $^{124}\mathrm{Sn} + {}^{124}\mathrm{Sn}$ collision at $b = 2$ fm, asy-soft EOS.

number of particles N in volume V are

$$\langle (\Delta N)^2 \rangle = T \left(\frac{\partial N}{\partial \mu} \right)_{T,V}, \qquad (4)$$

where μ is a chemical potential. The variance of density can be written as

$$\sigma_\rho^2 = \langle (\Delta \rho)^2 \rangle = \frac{T}{V^2} \left(\frac{\partial N}{\partial \mu} \right)_{T,V}. \qquad (5)$$

Since

$$N = \frac{4Vm^{3/2}}{\pi^2 \hbar^3 \sqrt{2}} \int_0^\infty \frac{\sqrt{\varepsilon}}{e^{(\varepsilon-\mu)/T} + 1} d\varepsilon, \qquad (6)$$

where ε is the energy and m is the mass of the particle, the variance

$$\sigma_\rho^2 = \frac{16\pi m \sqrt{2m}}{V\hbar^3} \sqrt{\varepsilon_\mathrm{F}} T \left(1 - \frac{\pi^2}{12} \frac{T^2}{\varepsilon_\mathrm{F}^2} + \ldots \right). \qquad (7)$$

The variance in a cell is determined by the local

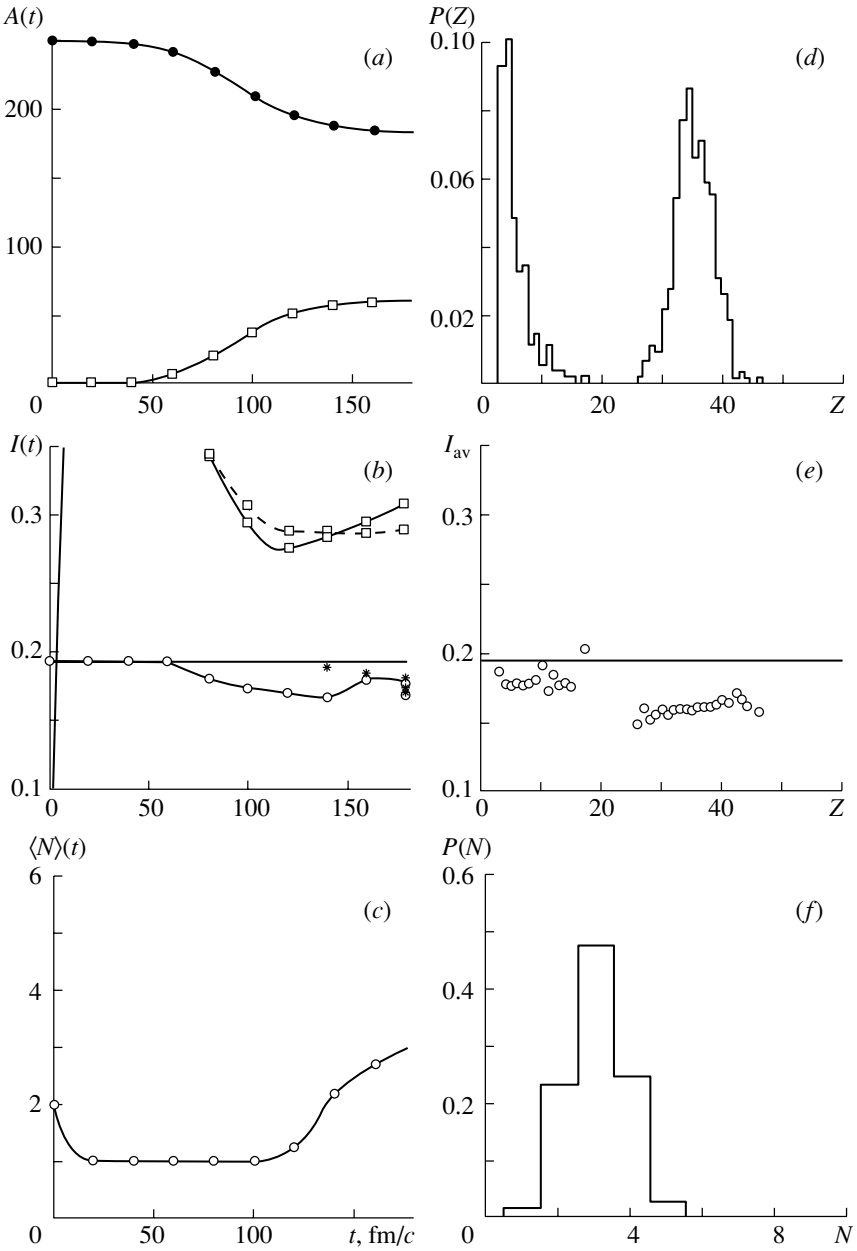

Fig. 5. The same as Fig. 4, but at $b = 6$ fm.

density $\rho(\mathbf{r})$ and the temperature T in the cell. The temperature is calculated from the local kinetic energy density for the noncollective motion

$$\tilde{e} = \frac{3}{5}\varepsilon_{\mathrm{F}}\left(1 + \frac{5\pi T^2}{12\varepsilon_{\mathrm{F}}^2} + \ldots\right). \tag{8}$$

The collective part of the momentum is the average momentum

$$\bar{\mathbf{p}} = \frac{1}{N_{\mathrm{G}}}\sum_{\mathrm{cell}} \mathbf{p}_i. \tag{9}$$

Here, N_{G} is the number of Gaussian test particles in a cell and $\mathbf{p}_i$ is the momentum of a test particle. The collective energy in the cell is then

$$E_{\mathrm{coll}} = \frac{N_{\mathrm{G}}}{N_t}\frac{\bar{\mathbf{p}}^2}{2m} \tag{10}$$

(N_t is the number of Gaussians per nucleon).

Another way to determine the collective energy is related to the nuclear current:

$$E_{\mathrm{coll}} = \frac{m}{2}\int \frac{\mathbf{j}^2(\mathbf{r})}{\rho(\mathbf{r})}d^3\mathbf{r}. \tag{11}$$

The nuclear current

$$\mathbf{j}(\mathbf{r}) = \rho(\mathbf{r})\mathbf{v}(\mathbf{r}), \tag{12}$$

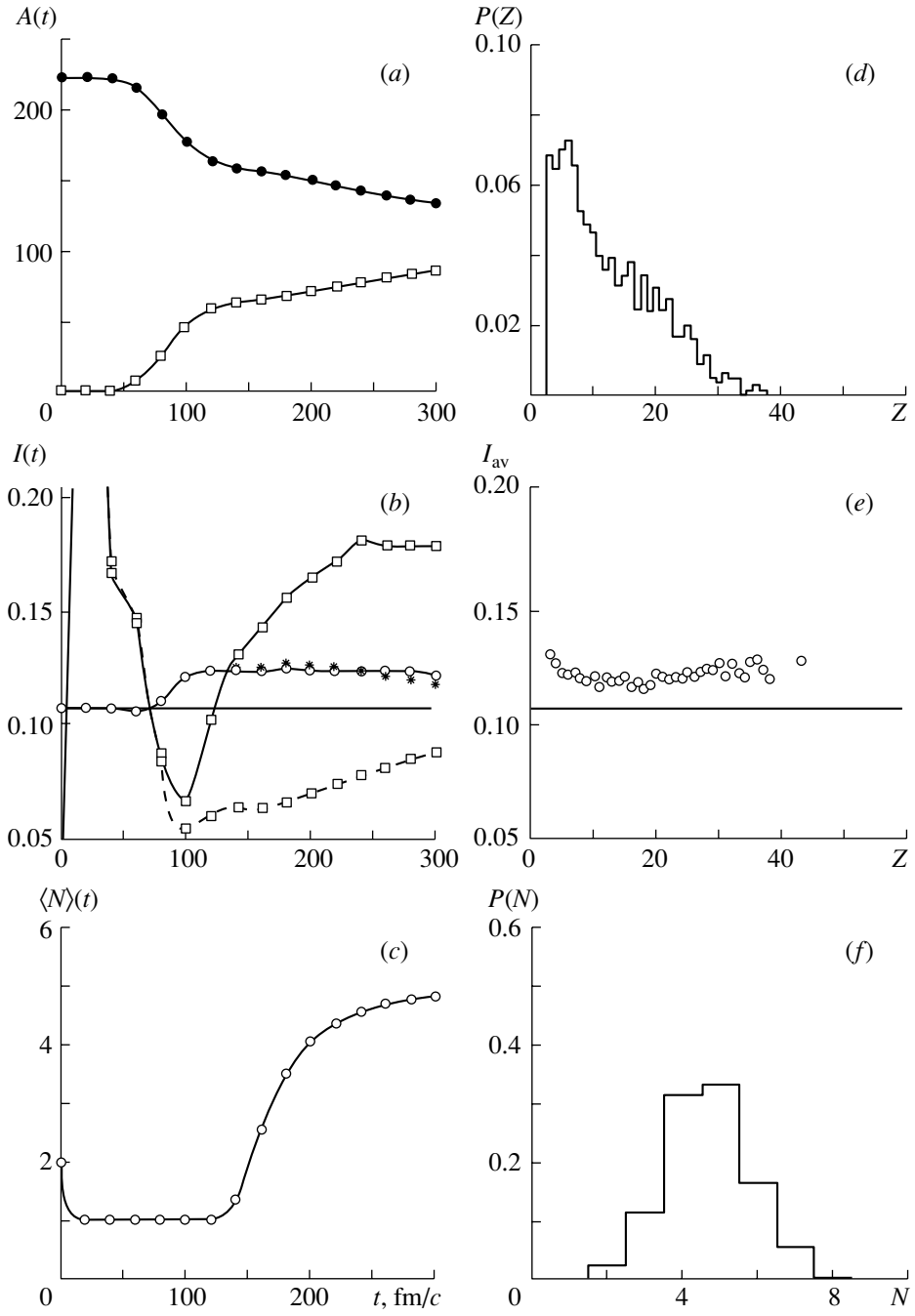

Fig. 6. ^{112}Sn + ^{112}Sn collision at $b = 2$ fm, asy-stiff EOS.

with $\mathbf{v}(\mathbf{r})$ denoting the local velocity.

This method of including density fluctuations in the BUU calculations has been successfully tested [3] first for the case of stable dynamics, namely, for the incomplete fusion of ^{58}Ni + ^{58}Ni at $b = 0$. Here, the fluctuations were not evolved by the mean field. The second case was a deep inelastic reaction of Ni and Zr at $E = 40$ MeV/u. The density fluctuations were introduced before the system reached a region of volume instabilities. The mean field caused a growth of fluctuations leading to a variety of final configurations. The mass and charge distributions for this reaction compared well with experimental data. This method of introducing fluctuations has been used in the present work.

3. CALCULATIONS AND RESULTS

The BUU formalism with density fluctuations has been used to study the reactions of ^{112}Sn + ^{112}Sn

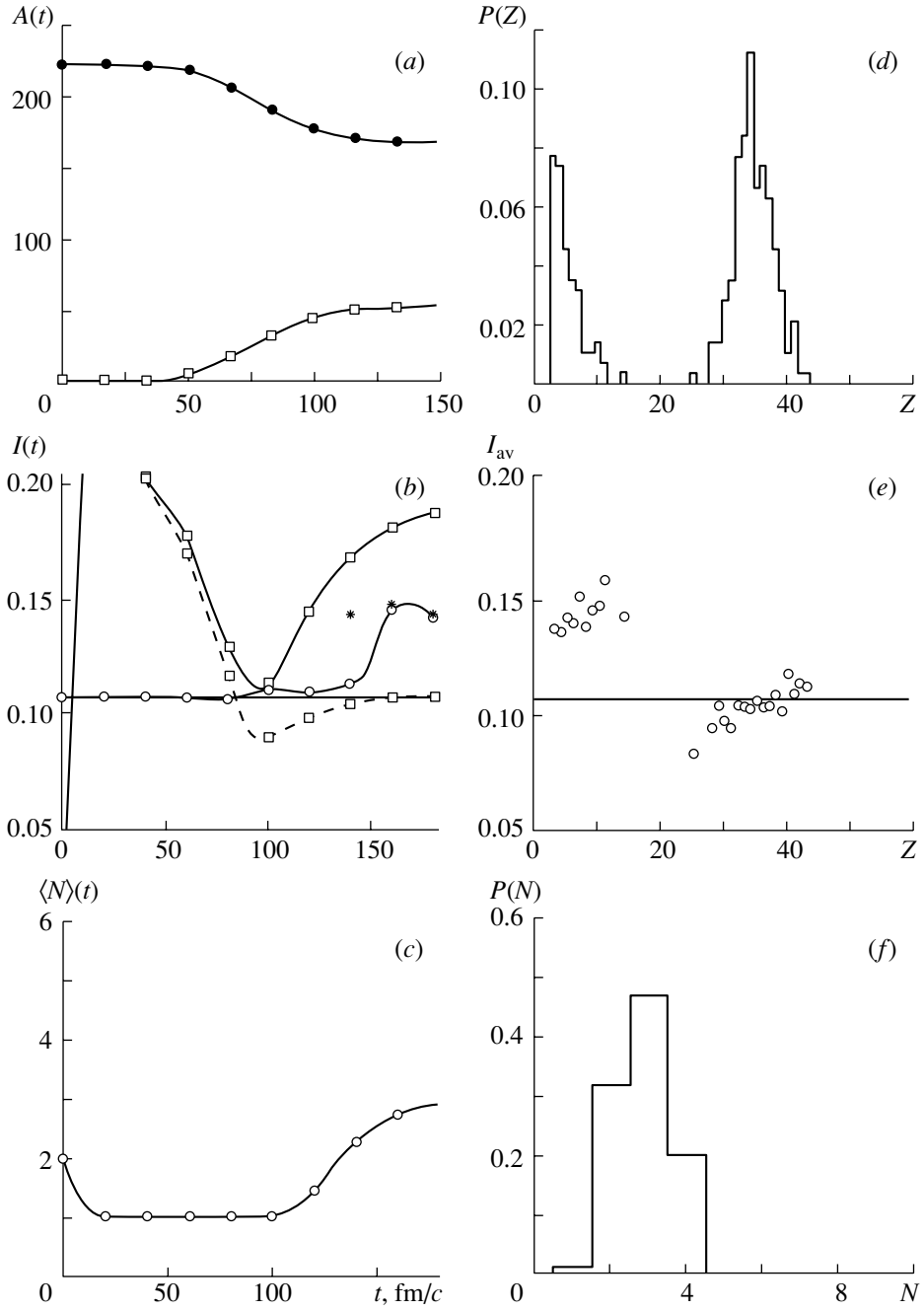

Fig. 7. The same as Fig. 6, but at $b = 6$ fm.

and $^{124}\mathrm{Sn} + {}^{124}\mathrm{Sn}$ at $E = 50$ MeV/u. We considered central and more peripheral collisions at impact parameter values of 2 and 6 fm. The Skyrme interaction with the compressibility of 200 MeV was used, and the density dependence of the symmetry term corresponds to an asy-stiff and an asy-soft equation of state [4]. The Skyrme interactions used in this paper are given below:

$$U(\rho) = A\left(\frac{\rho}{\rho_0}\right) + B\left(\frac{\rho}{\rho_0}\right)^{\sigma} + C\left(\frac{\rho_n - \rho_p}{\rho_0}\right)\tau, \tag{13}$$

where $A = -356$ MeV, $B = 303$ MeV, $\sigma = 7/6$,

$$\tau = \begin{cases} +1 & n, \\ -1 & p, \end{cases}$$

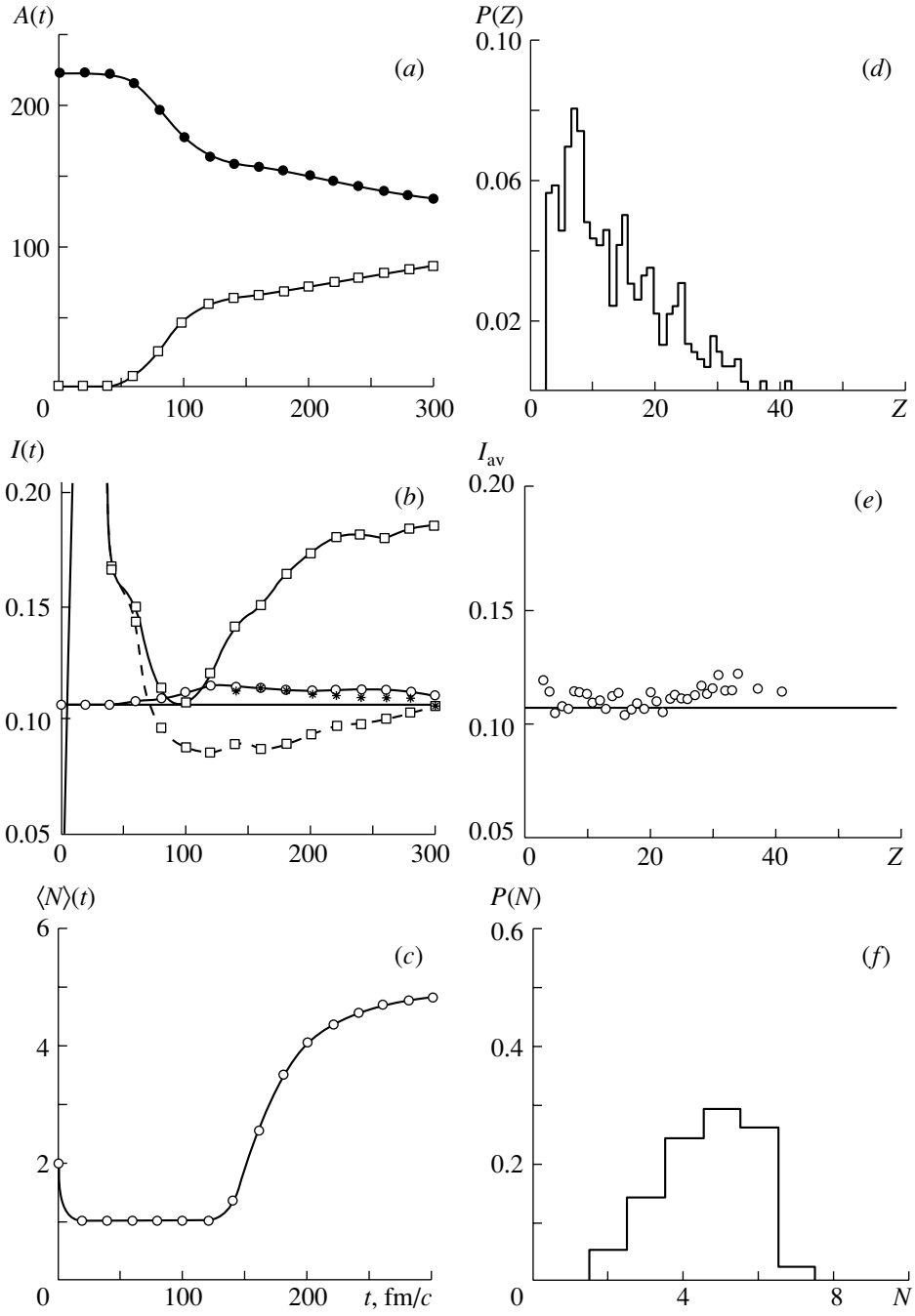

Fig. 8. ^{112}Sn + ^{112}Sn collision at $b = 2$ fm, asy-soft EOS.

ρ_0 is the normal nuclear matter density, $C = 32$ MeV for the asy-stiff case, and $C/\rho_0 = 481$ MeV fm^3–1638.2 MeV fm$^6\rho$ for the asy-soft case.

The test particle method of solving the BUU equation was applied [3] with 100 test particles per nucleon.

When, after the initial compression, the system started to expand, the fluctuations were introduced by a random redistribution of the test particles in the coordinate space cells according to the calculated variances of density. They were introduced at three times during the evolution in steps of 30 fm/c. The redistribution conserves energy, momentum, and mass of the system. The pattern of the collective energy is kept unchanged as discussed above [3]. After the fluctuations have been introduced, the dynamics of the reaction is governed again by the mean field only.

The reactions considered here lead to a bulk fragmentation of the system in the case of the low impact

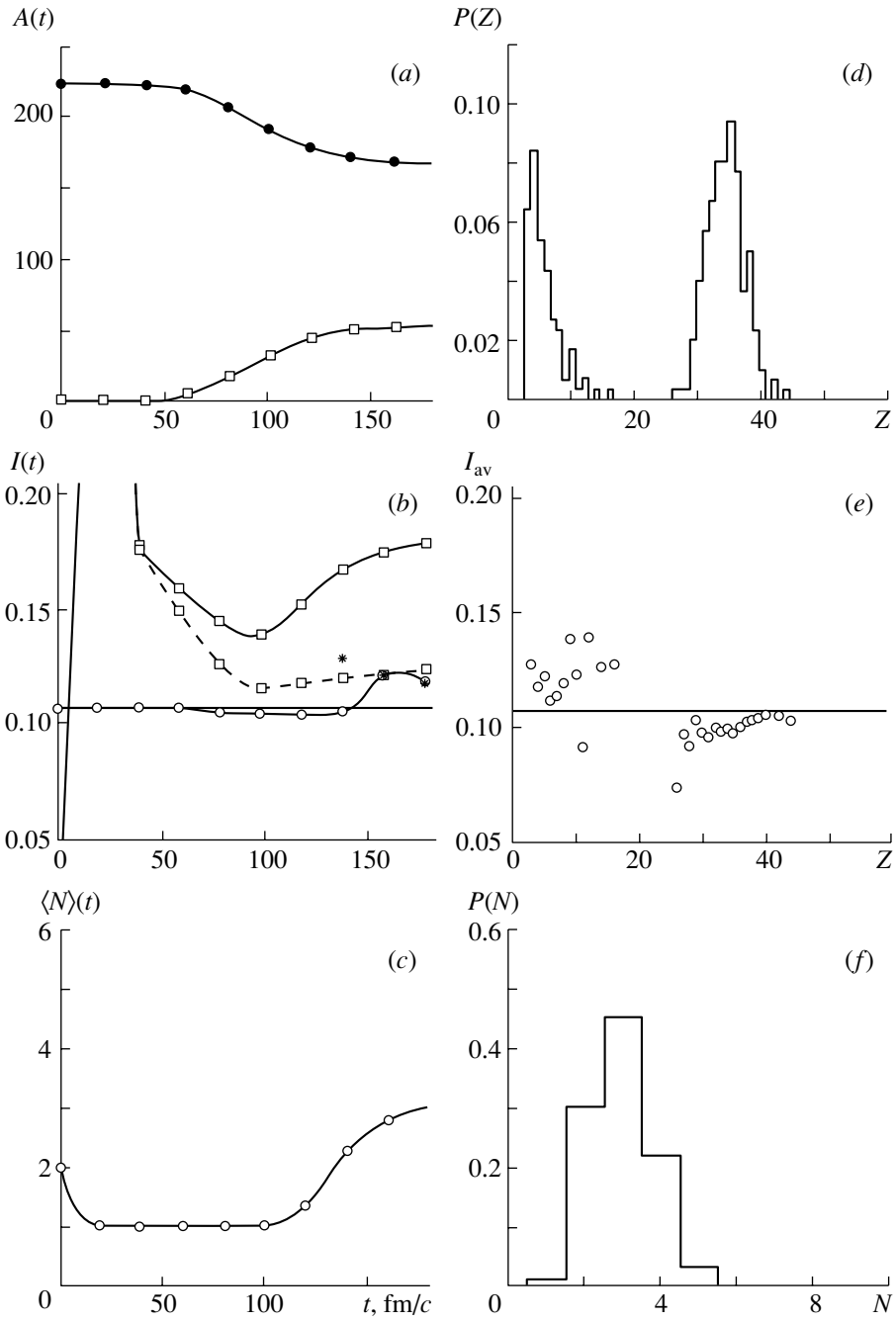

Fig. 9. The same as Fig. 8, but at $b = 6$ fm.

parameter and to a neck production of light fragments in the case of more peripheral collisions [4].

The detailed results obtained with asy-soft and asy-stiff symmetry terms for both semicentral ($b = 2$ fm) and semiperipheral ($b = 6$ fm) collisions for $^{112}\mathrm{Sn} + {}^{112}\mathrm{Sn}$ and $^{124}\mathrm{Sn} + {}^{124}\mathrm{Sn}$ are presented in Figs. 2–9. In each of these figures, the left column shows the time evolution of (*a*) mass in the liquid phase, $Z \geq 3$ (solid curve and dots), and the gas phase, $Z < 3$ (solid curve and squares); (*b*) asymmetry $I = (N - Z)/(N + Z)$ in the gas "central" (solid curve and square) (where central means in a cubic box of side 20 fm around CM), gas total (dashed curve and squares), and liquid central (solid curve and dots) phase and for intermediate-mass fragments (IMF) ($3 < Z < 15$, stars); the horizontal line shows the initial symmetry; and (*c*) mean fragment multiplicity $Z \geq 3$; the saturation of this curve defines the freeze-out time and configuration. The right column gives the distribution of the "primary" fragments in the

freeze-out configuration; (d) charge distribution; (e) asymmetry distribution as a function of the fragment charge; (f) fragment multiplicity distribution (normalized to 1).

Figures 2, 4, 6, and 8 show the semicentral collisions ($b = 2$), while Figs. 3, 5, 7, and 9 present the semiperipheral ($b = 6$) reactions. Comparing parts (d) of these figures, we see that, for more central collisions, the charge distribution decreases rapidly, while in peripheral collisions there is a second maximum. We are dealing with the bulk fragmentation and neck fragmentation, respectively. The average number of fragments produced in central collisions is significantly larger than in semiperipheral [parts (c)]. In the case of central collisions, fragments are produced in very dilute asymmetric nuclear matter. The neck matter, relevant for more peripheral collisions, ruptures starting from densities close to saturation values in the presence of normal density spectators. A study of fragmentation in semicentral and semiperipheral collisions probes the symmetry term in different regions of density.

To see the effect of the symmetry term, we will first look at the neutron-rich system and compare parts (b) and (e) of Figs. 2–5.

A large number of particles are emitted during the expansion phase, 50–120 fm/c [see parts (a)]. At these subnuclear densities, for the asy-soft EOS, neutrons are less bound than for the asy-stiff case. It is opposite for protons. Therefore, more neutrons and neutron-rich particles are emitted in this phase of the reaction for the asy-soft case.

Comparing the symmetry of the IMF ($3 \leq Z \leq 20$), we observe that the asy-soft EOS produces the most symmetric IMF for semicentral collisions, with the symmetry below the initial one for the colliding system. The asy-stiff equation of state leads to very neutron-rich IMF originating in the neck area for the semiperipheral collisions, with the asymmetry above the initial one. These opposite trends are due to the behavior of the symmetry term in various regions of subnormal nuclear densities. A more detailed analysis of the behavior of the symmetry term can be found in [4].

For the reaction $^{112}\mathrm{Sn} + {}^{112}\mathrm{Sn}$, the initial asymmetry is on the proton-rich side, so the general trend is to move towards higher asymmetries. As for the neutron-rich case, we see that, for the IMF emitted from the neck, the asymmetry is larger than the initial one. As opposed to the neutron-rich system, there is a larger emission of protons during the expansion phase, especially for semicentral collisions [parts (b)]. For the case of the neutron-poor system, the protons are less bound at subnuclear densities and this effect is larger for a stiffer case. As a result of the enhanced proton emission, the asymmetry of IMF is larger than the initial one. The neutron enrichment of the neck IMF in the asy-soft case is mostly due to neutron migration towards the lower density region.

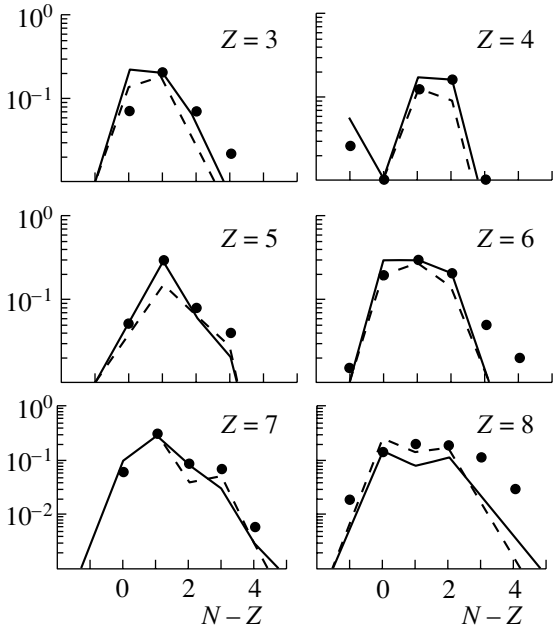

Fig. 10. Isotopic distribution for $Z = 3$–8 fragments. The differential multiplicities $dM/d\Omega(\mathrm{sr}^{-1})$ are shown as functions of neutron excess N–Z. The continuous line corresponds to the asy-stiff EOS, while the dashed line shows the asy-soft case. Points represent preliminary experimental data.

The above analysis shows that the characteristics of the primary multifragmentation products, especially the asymmetries of the IMF, depend on the stiffness of the equation of state. Similarly, there are differences between the asy-soft and asy-stiff EOS in the emission of prompt neutrons and protons.

Therefore, a comparison with experimental data could shed some light on the density dependence of the symmetry term in the nuclear equation of state.

It is, however, important to realize that the calculations described above lead to primary fragments that are excited and will undergo a statistical decay leading to different final fragments. Unfortunately the distributions of the final fragments are less sensitive to the symmetry term.

Recently, the reaction $^{124}\mathrm{Sn} + {}^{124}\mathrm{Sn}$ at $E =$ 50 MeV/u and low-impact parameter has been studied at the National Superconducting Cyclotron Laboratory at MSU [5]. A preliminary comparison of isotopic distribution for $Z = 3$–8 is presented in Fig. 10. It shows that there is weak evidence for an asy-stiff equation of state. It definitely leads to a final conclusion that more sensitive observables

[5] must be used in the future in order to find the appropriate density dependence of the symmetry term in the equation of state for asymmetric nuclear matter.

ACKNOWLEDGMENTS

We would like to thank Marc-Jan van Goethem for his help in comparing our results with experimental data. One of us (M. Z-P.) is grateful to the National Science Foundation for its support of her research.

REFERENCES

1. S. Ayik and C. Gregoire, Phys. Lett. B **121B**, 269 (1983); Nucl. Phys. A **513**, 187 (1990).
2. J. Randrup and B. Remaud, Nucl. Phys. A **514**, 339 (1990).
3. M. Colonna, M. Di Torro, A. Guarnera, *et al.*, Nucl. Phys. A **642**, 449 (1998).
4. V. Baran, M. Colonna, M. Di Toro, *et al.*, Nucl. Phys. A **703**, 603 (2002).
5. T. X. Liu, X. D. Liu, and W. G. Lynch, to be published.

Physics of Atomic Nuclei, Vol. 66, No. 8, 2003, pp. 1471–1477. From Yadernaya Fizika, Vol. 66, No. 8, 2003, pp. 1517–1522.

Determination of the Freeze-Out Temperature by the Isospin Thermometer*

P. Napolitani[1),2)], K.-H. Schmidt[1)], P. Armbruster[1)], A. S. Botvina[1),3)], M. V. Ricciardi[1)], L. Tassan-Got[2)], F. Rejmund[2)], and T. Enqvist[4)]**

[1)] *Gesellschaft für Schwerionenforschung, Darmstadt, Germany*

[2)] *Institut de Physique Nucléaire, Orsay, France*

[3)] *Institute for Nuclear Research, Russian Academy of Sciences, pr. Shestidesyatiletiya Oktyabrya 7a, Moscow, 117312 Russia*

[4)] *University of Jyväskylä, Jyväskylä, Finland*

Received August 28, 2002

Abstract—The high-resolution spectrometer FRS at GSI, Darmstadt, provides the full isotopic and kinematical identification of fragmentation residues in relativistic heavy-ion collisions. Recent measurements of the isotopic distribution of heavy projectile fragments led to a very surprising new physical finding: the residue production does not lose memory of the N/Z of the projectile ending up in a universal deexcitation corridor; an ordering of the residues in relation to the neutron excess of the projectile has been observed. These unexpected features can be interpreted as a new manifestation of multifragmentation. We have found that, at the last stage of the reaction, the temperature of the big clusters subjected to evaporation is limited to a universal value. The thermometer to measure this limiting temperature is the neutron excess of the residues. © *2003 MAIK "Nauka/Interperiodica".*

1. INTRODUCTION

Different mechanisms of fragment production can be studied within peripheral nucleus–nucleus collisions. Spallation and fission have been under investigation for many years. In the last decade, a so-called multifragmentation reaction, which leads to the total disintegration of heavy nuclei into light and intermediate-mass fragments (IMF), has aroused large interest [1–3]. Originally, it was motivated by studying the liquid–gas-type phase transition in nuclear matter [4, 5], as well as the role of thermal and spinodal instabilities in the disintegration of finite nuclei. In high-energy collisions, the multifragmentation share was found to correspond to 10–20% of the total reaction cross section, and its contribution to the yield of the IMF (with charges $Z = 3$–30) is crucially important. With increasing excitation energy of the thermal source, the transition from the evaporation and fission decay mechanisms to the multifragmentation is smooth: The probability for the formation of one compound nucleus decreases, whereas the multifragmentation appears first as a freeze-out state with two hot fragments and progressively involves three, four, and many fragment channels with increasing excitation. In this mechanism, a considerable part of the available excitation energy goes into the disintegration of the system, but not into increasing the temperature of the fragments [5].

2. EXPERIMENTAL INVESTIGATION OF THE REACTION MECHANISM

Multifragmentation is a field of intense investigation by the ALADIN (GSI, Darmstadt) collaboration [1], with an instrument whose total acceptance allows for the full counting of the produced fragments and their correlations. This precious information could be analyzed as in Fig. 1 (left), where a study of ^{238}U impinging on a copper target at 1 A GeV [1, 6] is shown: for each collision we have a collection of fragments of different Z; we chose the two residues having the highest Z and plotted one against the other for each event. The fission products, individuated by two fragments of about half the projectile charge, are well separated. The region of multifragmentation, characterized by high multiplicity and small impact parameter and identified in the low-Z corner, shows a gradual transition towards more and more peripheral collisions, where fragments of about half the projectile charge are correlated to very light

*This article was submitted by the authors in English.

**e-mail: napolita@ipno.in2p3.fr

1063-7788/03/6608-1471$24.00

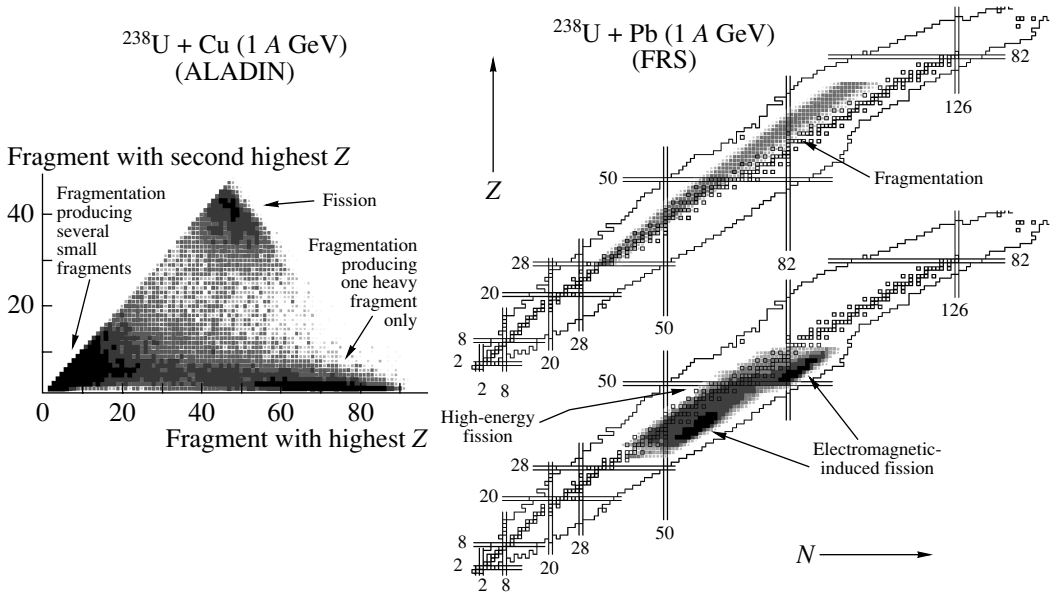

Fig. 1. Comparison between the experimental investigations that could be performed with ALADIN and with FRS. (Left) ALADIN provides the measurement of the multiplicity and the correlation between the emitted particles for each event. (Right) FRS provides the full isotopic and kinematical identification of one fragment for each event: it is possible to reconstruct the reaction process.

residues like lithium, beryllium, or boron. The aim of this paper is to discuss the possibility that the heavy fragments could provide complementary information on the multifragmentation process.

By concentrating on the heavy residue, we can take advantage of the high-resolution spectrometer FRS (GSI, Darmstadt) [7], which was designed to obtain exclusive information on the heavy fragments. The precise kinematical identification of the FRS provides unambiguous information on the deexcitation process that generated the observed residues: the measurement of the velocity distribution of each fragment enables one to disentangle fragmentation and fission products clearly. In addition, the measurements of the energy loss and the mass to charge ratio lead to the full isotopic identification. A very systematic overview is shown in Fig. 1 (right) for the collision of ^{238}U with lead at 1 *A* GeV [8]: we can clearly recognize the region of electromagnetic-induced fission: this process originates from low-excited projectile-like prefragments and, consequently, produces very neutron-rich residues. The area of high-energy fission, generated by more excited prefragments, is less neutron rich. Fragmentation products, expected to originate from a long evaporation process starting from very highly excited prefragments, populate the neutron-deficient side of the isotopic chart. This analysis, based on the knowledge of the reaction process, establishes a connection between the isotopic distribution of the residues and the excitation energy introduced at the beginning of the evaporation. In the following, we will restrict this analysis to fragmentation only and continue to study how the neutron excess can provide indications of the reaction mechanism.

3. STUDY OF THE NEUTRON EXCESS OF THE FRAGMENTATION RESIDUES

The classical model describes fragmentation as a two-stage process [9]: highly excited prefragments are generated in an initial fast stage, usually described as an abrasion process (e.g., for nucleus–nucleus collisions), or an intranuclear cascade process (mostly for hadron–nucleus collisions). The time required by the fast stage is of the order of 20 to 50 fm/*c*. The resulting prefragment, whose neutron to proton ratio is initially close to the projectile, will then experience a sequential decay (or evaporation) dominated by neutron emission. The role of the second process is to change the neutron to proton ratio and to guide the isotopic production towards a universal evaporation corridor, where the initially more favorable neutron emission is finally balanced by proton emission. If the excitation energy introduced by the fast stage were entirely removed by sequential decay, the evaporation would be long enough for the residues to end up in the universal corridor and lose memory of the projectile.

This classical picture is in contradiction with recent experimental data on fragmentation of neutron-rich projectiles. The isotopic cross sections of ^{238}U fragments produced in a lead target at 1 *A* GeV [8]

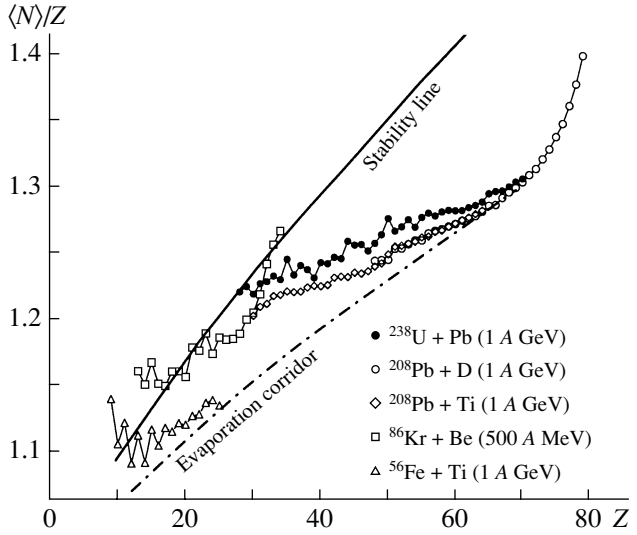

Fig. 2. Collection of experimental data showing a deviation from the evaporation corridor. The projectiles have different neutron excess. ^{56}Fe [10] is not neutron rich and its residues approach the evaporation corridor. ^{86}Kr [11] does not reach the corridor. The lead system, ^{208}Pb on deuterons [12] and ^{208}Pb on Ti [13], shows a clear deviation from the corridor. The ^{238}U system [8] deviates and is more neutron rich than ^{208}Pb. The evaporation corridor has been reproduced with the two-stage model (the abrasion code ABRA coupled with the evaporation code ABLA).

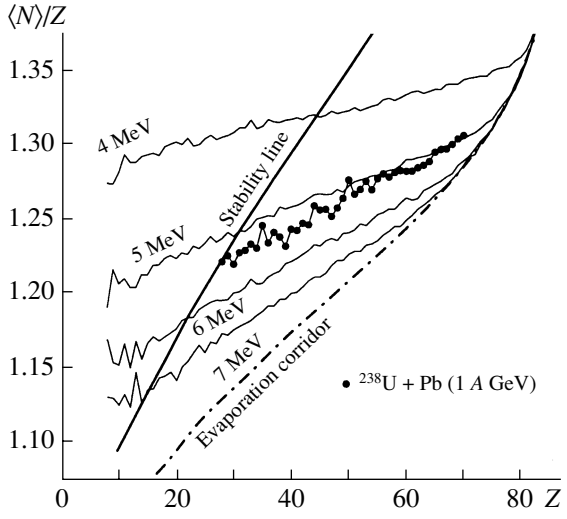

Fig. 3. The principle of the "isospin thermometer." The value of the freeze-out temperature is changed as a parameter of a three-stage model [9] calculation (ABRA followed by a breakup simulation and later by ABLA). The experimental data of fragmentation of ^{238}U are reproduced for a freeze-out temperature between 5 and 6 MeV.

show an increasing deviation from the corridor (represented by the two-stage model calculation [9] in Fig. 2) for decreasing Z towards higher neutron numbers. As presented in Fig. 2, the measured fragmentation residues of ^{238}U even have the tendency to cross the stability line; this is very surprising because, with respect to β stability (equal Fermi levels of protons and neutrons), the evaporation of protons is suppressed by the Coulomb barrier.

The increasing deviation from the evaporation corridor indicates that, for collisions expected to be more and more violent, less and less excitation energy is available for the evaporation stage; evidently, in the classic picture of the fragmentation mechanism, an intermediate process that removes this excess of energy is missing.

Figure 2 presents the evolution of the mean neutron to proton ratio of the residues produced by the fragmentation of different systems. We infer that there is an ordering of the residues in relation to the neutron excess of the projectile: the isotopic distributions of different fragmenting systems do not collapse on the same universal evaporation corridor, but they are more neutron rich for more neutron-rich projectiles, showing an evident memory effect related to the neutron-to-proton ratio of the projectile.

4. A THERMOMETER BASED ON THE NEUTRON EXCESS

We can infer that the present data (Fig. 2) are closely related to the observation of multifragmentation. We will analyze the data with two models. First, a three-stage model is used, which describes the multifragmentation as an intermediate breakup stage after the high-energy nucleon–nucleon collisions and before the sequential decay in a rather schematic way. Secondly, we have chosen the Statistical Multifragmentation Model (SMM) as a dedicated model for multifragmentation, which is very effective in the description of the experimental data (see, e.g., [5, 14]). The most intensively investigated signature for the onset of multifragmentation is the production of several about equal-size fragments. However, also in accordance with SMM, the fragments do not necessarily need to be about equal size. In peripheral collisions, we could expect a disassembly of the hot primary fragment into a heavy residue, accompanied by clusters and very light nuclei: in this case, when one heavy fragment is observed in the FRS, we still have indication of the onset of the multifragmentation phenomenon [5].

The experimental data can be reproduced through introduction of an intermediate process that, right after the fast stage, removes part of the mass and energy. This stage can be described as a breakup process: the compression caused by the high excitation energy and, eventually, by the collision dynamics provides a high internal pressure. A consequent expansion and disassembly of the system will remove part of

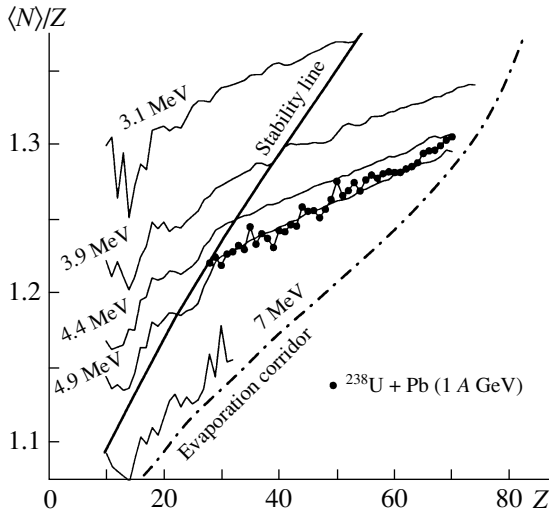

Fig. 4. Set of calculations performed with SMM [5] for different values of the excitation energy at breakup corresponding to mean temperatures of 3.1, 3.9, 4.4, 4.9, and 7 MeV.

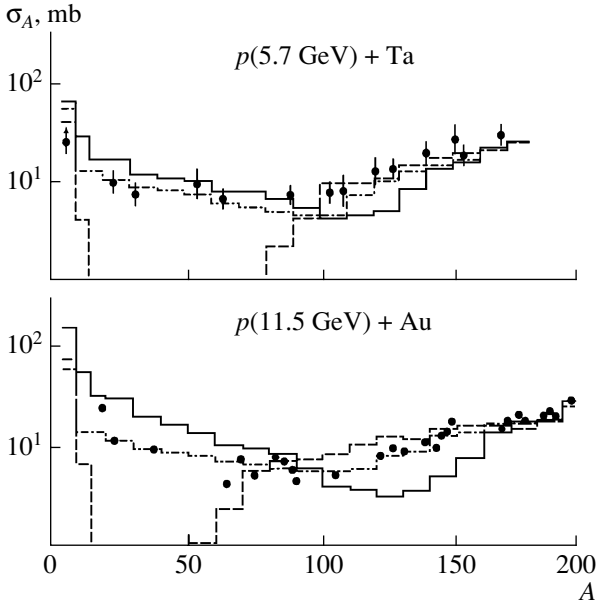

Fig. 5. Mass yields of fragments from tantalum and gold targets. The points denote the experimental data [18] (tantalum) and [19] (gold). The histograms correspond to calculations. Dashed lines: cascade-evaporation model (breakup was disregarded). Solid line: calculation where the breakup is included. Dash-dotted line: calculation with breakup included, with the addition of a preequilibrium process.

the initial excitation energy. This process might be related to a liquid–gas-like phase transition. A fundamental assumption for the process is the conservation of the mean neutron to charge number ratio $\langle N\rangle/Z$. The nearly complete conservation of the $\langle N\rangle/Z$ ratio is also predicted by SMM [15]. The breakup stage ends when the system reaches the freeze-out transition, and recondenses in an ensemble of cooled fragments. If we assume that thermodynamic equilibrium is established in the system at the transition point, we can consider a freeze-out temperature as a major parameter of the reaction process. This parameter can in fact be defined as a limiting temperature, since no more than the corresponding excitation energy will be available for the sequential decay. As a result, also the length of the evaporation process will be limited and determined by this value. We assume that the sequential decay will start from an excitation energy corresponding to the freeze-out temperature.

The deviation of the experimental data from the universal corridor suggests a new tool to measure the length of the sequential decay and, consequently, the value of the freeze-out temperature. Between the fast stage and the evaporation stage, a new step has been added in order to describe the effect of the breakup. We should observe that the treatment of the partitioning of the spectator into breakup products affects the final cross section, but has no effect on the neutron excess of the isotopic distribution of the residues; the quantity $\langle N\rangle/Z$ of the residues is only sensitive to the value of the freeze-out temperature. This assumption motivates the calculation shown in Fig. 3, where the experimental data of fragmentation of ^{238}U on a lead target are compared with a set of calculations. The treatment of the partitioning was simplified by a parametrization; the description of the neutron excess of the residues is determined by the freeze-out temperature as the only free parameter of the calculation: when this parameter has low values, the breakup dominates and the residues are too neutron rich. Inversely, for high values, the breakup tends to be suppressed and the isotopic production ends up in the evaporation corridor.

The measurement fixes the freeze-out temperature in a range between 5 and 6 MeV. Missing the complete data for systems covering a wide range of the neutron excess, we still cannot determine whether the freeze-out temperature is a constant value or a function of N/Z. However, the choice of around 5 MeV provides a very satisfactory reproduction of the available data [16].

A more elaborate physical description of the partitioning is provided by SMM. In Fig. 4, we present the results of a series of SMM calculations for the disintegration of a ^{238}U source. The excitation energy at breakup was taken as a parameter. The calculation was performed for excitation energies of 1, 1.5, 2, 2.5, and 8 MeV, corresponding to mean temperatures of 3.1, 3.9, 4.4, 4.9, and 7 MeV, respectively. With increasing temperature, the breakup generates more excited fragments, and the mean neutron excess

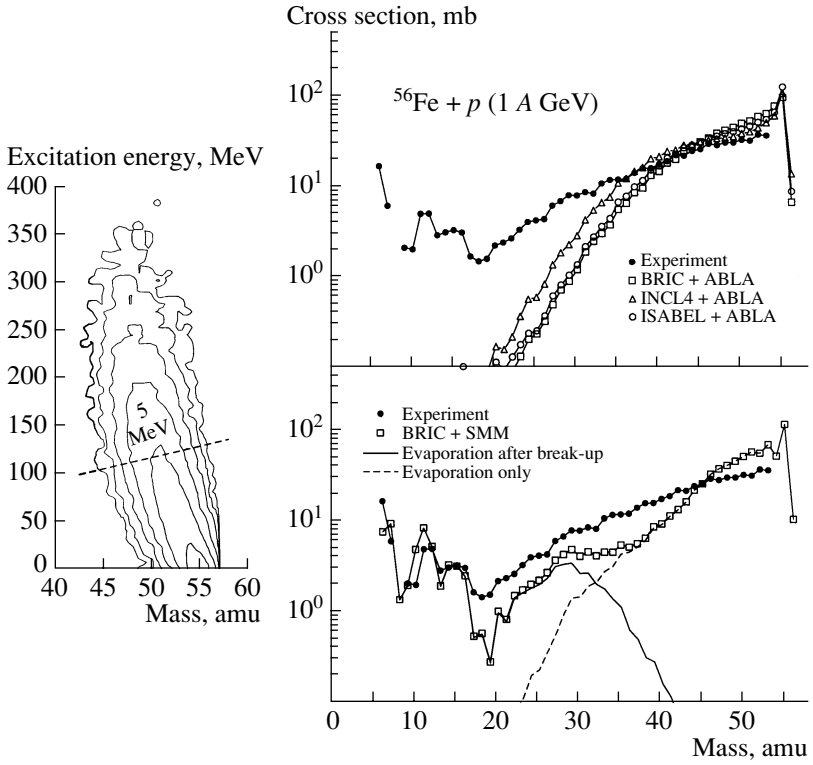

Fig. 6. (Left) Prefragments produced right after the intranuclear-cascade stage in the reaction of ^{56}Fe on a proton at 1 A GeV (calculation performed with INCL4 [21]). The dashed line indicates the excitation energy corresponding to a freeze-out temperature of 5 MeV. (Right, top) Three intranuclear-cascade codes (BRIC [20], INCL4 [21], ISABEL [22]) coupled with the evaporation code ABLA do not reproduce the experimental data of ^{56}Fe on a proton at 1 A GeV [10]. (Right, bottom) The experimental data are reproduced if the breakup is considered. The calculation is performed coupling the intranuclear-cascade code BRIC with SMM.

of the residues approaches the evaporation corridor. This calculation led to about the same results as presented in Fig. 3: also, in this case, a remarkable agreement with the data is obtained for a freeze-out temperature of around 5 MeV. An important finding is the independence of the temperature from the mass of the residues. The observed universality is an indication that the limiting freeze-out temperature is rather independent of the initial conditions.

5. EFFECT OF THE BREAKUP ON THE MASS DISTRIBUTION

We now investigate the effect of the breakup in recent data of fragmentation of ^{56}Fe [10] in a proton target at 1 A GeV, measured in inverse kinematics at the FRS. This is an interesting case to study the generality of the breakup process and its extension to cases where the excitation energy of the system is neither high enough to be dominated by thermal instability nor too low to exclude some breakup events. However, ^{56}Fe is not neutron rich and the isotopic distribution is not expected to deviate from the evaporation corridor. To observe the effect of thermal instability, we should then look for a different signature like, for instance, the mass distribution.

As was established in previous studies (see, e.g., references in [5]), in reactions where considerable energy is transferred to the thermal source, the multifragmentation substantially influences the yield of the residues. The ALADIN fragmentation data provide a typical example of multifragmentation obtained in peripheral nucleus–nucleus collisions at high energy [14]. It was also found that this process takes place in reactions induced by high-energy protons. In Fig. 5, we present the results of the analysis performed in [17] concerning inclusive yields of fragments from tantalum [18] and gold [19] targets. The theoretical calculations were done within cascade, evaporation, and fission models which ignore the multifragment breakup stage and, alternatively, with the same models including the multifragmentation additionally. In the last case, the INC (Dubna version) and SMM were used. We can clearly see that fragments with $A = 10$–60 can be explained only by multifragmentation. However, the yield is not fully reproduced with the INC + SMM calculations. An additional correction of the

parameters (masses and excitation energies) of the aftercascade residual nuclei is necessary. We can attribute this additional preequilibrium process to the expansion of the residues toward the freeze-out volume [5].

We applied the same investigation to study the reaction of ^{56}Fe on a proton at 1 A GeV. Such a system is expected to produce a broad distribution of the residues in excitation energy depending on the impact parameter and fluctuations during the preequilibrium process. In general, nucleus–proton reactions at about 1 A GeV generate too low an excited system to undergo a multifragmentation event, but, nevertheless, ^{56}Fe is still light enough to reach the breakup temperature. A very indicative way to discriminate the possible breakup events is presented in Fig. 6 (left): the plot shows a collection of calculated prefragments, generated by the fast stage, distributed according to their mass and excitation energy. The region above the energy corresponding to a freeze-out temperature of 5 MeV is hot enough to undergo a breakup stage. The region below collects the prefragments expected to start the sequential decay immediately after the fast stage.

As shown in Fig. 6 (top), three intranuclear-cascade codes (BRIC [20], INCL4 [21], ISABEL [22]) coupled with the same evaporation code (ABLA) appear to severely underpredict the experimental data for the lighter half of the mass distribution (Fig. 6, top). In contrast, the introduction of a breakup stage (calculation performed with BRIC coupled with SMM) provides a satisfactory reproduction of the measurement. A slight discrepancy in the yields of fragments with mass numbers $A > A_{\text{target}}/2$ is probably caused by the discussed uncertainty of the parameters of the excited residues produced after the intranuclear-cascade stage: the hybrid model used to reproduce the data is still too simple to describe correctly the transition from the fast stage to the breakup, and the inclusion of a preequilibrium process could be needed. In Fig. 6 (bottom), it is possible to observe that the light part of the mass distribution is mainly populated by breakup events. A very interesting result revealed by the experiment is the tendency for the cross sections to increase in the region of light masses: the only mechanism able to reproduce this characteristic seems to be a series of breakup events.

6. CONCLUSIONS

The analysis of recent experimental data revealed the influence of multifragmentation to be more general than expected. In nucleus–nucleus reactions, the signature for the onset of multifragmentation not only is carried by the lightest fragments, but it also extends towards the intermediate-mass fragments. The breakup process does not describe only the reactions at small impact parameter, but it should be taken into account in peripheral collisions as well. Moreover, the memory of the N/Z of the projectile reflected in the neutron excess of the residues is not only experimental evidence of the generality of multifragmentation, but it is also a new tool to study the reaction mechanism. The study of the relation between the isotopic distribution of the residues and the breakup process opens up new possibilities of investigation: the combination between the isotopic identification (FRS) and the measurement of the multiplicity (ALADIN) can provide new insight into the role of the impact parameter on multifragmentation.

In the case of nucleon–nucleus reactions, the impact of thermal instability is also more general than expected. We have experimental evidence that the fragmentation of light nuclei like ^{56}Fe in a proton target at 1 A GeV shows similar features as in the case of proton-induced fragmentation of heavy nuclei at high energy (5–10-GeV range). Disregarding the breakup process in the complete description of nucleon–nucleus collisions could lead to an underprediction of the yields of the light residues by several orders of magnitude, even at beam energies around 1 A GeV.

REFERENCES

1. A. Schüttauf, W. D. Kunze, A. Worner, *et al.*, Nucl. Phys. A **607**, 457 (1996).
2. N. Marie, A. Chbihi, J. B. Natowitz, *et al.*, Phys. Rev. C **58**, 256 (1998).
3. R. P. Scharenberg, B. K. Srivastava, S. Albergo, *et al.*, Phys. Rev. C **64**, 054602 (2001).
4. J. Pochodzalla, T. Mohlenkamp, T. Rubehn, *et al.*, Phys. Rev. Lett. **75**, 1040 (1995).
5. J. P. Bondorf, A. S. Botvina, A. S. Iljinov, *et al.*, Phys. Rep. **257**, 133 (1995).
6. A. Schüttauf, PhD Thesis (Frankfurt am Main, 1996).
7. H. Geissel, P. Armbruster, K. H. Behr, *et al.*, Nucl. Instrum. Methods B **70**, 286 (1992).
8. T. Enqvist, J. Benlliure, F. Farget, *et al.*, Nucl. Phys. A **658**, 17 (1999).
9. J.-J. Gaimard and K.-H. Schmidt, Nucl. Phys. A **531**, 709 (1991).
10. P. Napolitani, Diploma-work, DEA, IPN (Orsay, 2001).
11. M. Weber, C. Donzaud, J. P. Dufour, *et al.*, Z. Phys. A **343**, 67 (1992).
12. T. Enqvist, P. Armbruster, J. Benlliure, *et al.*, Nucl. Phys. A **703**, 435 (2002).
13. T. Enqvist, W. Wlazlo, P. Armbruster, *et al.*, Nucl. Phys. A **686**, 481 (2001).

14. A. S. Botvina, I. N. Mishustin, M. Begemann-Blaich, *et al.*, Nucl. Phys. A **584**, 737 (1995).
15. A. S. Botvina and I. N. Mishustin, Phys. Rev. C **63**, 061601(R) (2001).
16. K.-H. Schmidt, M. V. Ricciardi, A. S. Botvina, and T. Enqvist, Nucl. Phys. A **710**, 157 (2002).
17. A. S. Botvina, A. S. Iljinov, and I. N. Mishustin, Nucl. Phys. A **507**, 649 (1990).
18. J. Robb Grover, Phys. Rev. **126**, 1540 (1962).
19. S. B. Kaufman, M. W. Weisfield, E. P. Steinberg, *et al.*, Phys. Rev. C **14**, 1121 (1976).
20. H. Duarte, in *Proceedings of the SARE-5 Workshop on Models and Codes for Spallation Neutron Sources, Paris, 2000*.
21. A. Boudard, J. Cugnon, S. Leray, and C. Volant, Phys. Rev. C **66**, 044615 (2002).
22. Y. Yariv and Z. Fraenkel, Phys. Rev. C **20**, 2227 (1979).

Physics of Atomic Nuclei, Vol. 66, No. 8, 2003, pp. 1478–1488. From Yadernaya Fizika, Vol. 66, No. 8, 2003, pp. 1523–1533.

Nuclear Rainbow in Scattering and Reactions and Nucleus–Nucleus Interaction at Small Distances*

A. A. Ogloblin[1)], S. A. Goncharov[2)], Yu. A. Glukhov[1)], A. S. Dem'yanova[1)], M. V. Rozhkov[1)], V. P. Rudakov[1)], and W. H. Trzaska[3)]**

[1)] *Russian Research Centre Kurchatov Institute, pl. Kurchatova 1, Moscow, 123182 Russia*

[2)] *Institute of Nuclear Physics, Moscow State University, Vorob'evy gory, Moscow, 119992 Russia*

[3)] *University of Jyväskylä, Jyväskylä, Finland*

Received August 28, 2002

Abstract—A review of recent experiments on the study of the nuclear rainbow phenomenon in scattering and some reactions induced by light heavy ions is given. It includes (i) the study of the differential cross sections of the $^{16}O + {}^{12}C$ elastic scattering at seven ^{16}O energies between 130 and 281 MeV; (ii) finding of the phenomenological potential deeper than that of folding model; (iii) the first data on $^{16}O + {}^{14}C$ elastic scattering; (iv) dispersion relation analysis of the obtained data and observation of abnormal nuclear dispersion; and (v) use of the charge-exchange $^{14}C(^6Li,^6He)^{14}N$ reaction to search for pion-condensation effects. © *2003 MAIK "Nauka/Interperiodica"*.

1. INTRODUCTION

The term "nuclear rainbow" is applied to some special behavior of the scattering and reaction differential cross sections. Nuclear rainbow is a phenomenon of the same origin as the well-known optical rainbow. They both result from the refraction of the incident waves in a drop of nuclear liquid or water, correspondingly. Qualitatively, a nuclear rainbow can be identified by the resemblance of the angular distribution shape to the square of the Airy function followed by exponential falloff, just as in the case of semiclassical rainbow scattering.

The main features of nuclear elastic rainbow scattering are determined by the refraction index of nuclear matter, which is directly connected with the nucleus–nucleus potential. In the case of nuclear reactions, the scattering amplitude is modulated by the reaction form factor, which is determined by nuclear wave functions. The very fact of the dominance of the refraction means that the interaction in the nuclear interior is important, contrary to more common diffraction scattering, which is sensitive only to the nuclear periphery. If observed, nuclear rainbows become a unique instrument for studying nucleus–nucleus interactions at small distances.

One of the most important consequences of the deep interpenetration of the colliding nuclei is that the overlap of nucleon densities can be achieved. This follows from the fact that the collision time in the processes demonstrating nuclear rainbow patterns is typically shorter (in some cases, much shorter) than the characteristic time of the nuclear internal movement. This qualitative argument is supported by very good agreement between experiment and folding model (FM) calculations. The latter intrinsically include the assumption of a frozen nucleon density during the collision. The comparisons show that the data are sensitive to the density dependence of the nucleon–nucleon interaction in nuclear media, and this opens the way to extract the nuclear equation of state of cold nuclear matter from the nuclear rainbow experiments. Of special importance becomes the study of the nuclear rainbow phenomenon in some light-nucleus collisions in which the region of nuclear compression can contain quite a large amount of nucleons providing a piece of nuclear matter.

Valuable information on rainbow elastic scattering of light heavy ions has been obtained by investigation of $^{16}O + {}^{16}O$ and $^{12}C + {}^{12}C$ systems ([1, 2] and references therein). However, due to the fact that these systems are symmetric, the meaningful angular distributions are limited by angles less than 90°, and some important parts of rainbow structures sometimes cannot be observed. This paper is mainly dedicated to our studies of asymmetrical combination of the neighboring nuclei $^{16}O + {}^{12}C$, which is free from the above limitation. The first results on the investigation of another asymmetrical system,

*This article was submitted by the authors in English.

**e-mail: aoglob@dni.polyn.kiae.su

1063-7788/03/6608-1478$24.00

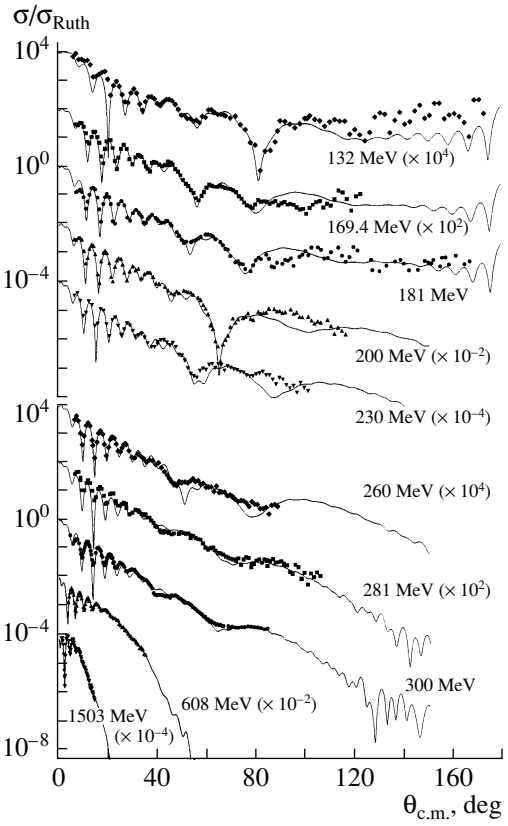

Fig. 1. $^{16}O + {}^{12}C$ elastic-scattering differential cross sections at 132, 169, 200, 230, and 260 MeV [4], 181 and 281 MeV [10], 300 MeV [8], 608 and 1503 MeV [5]. The curves correspond to optical model calculations with the potentials WS-2 (see text).

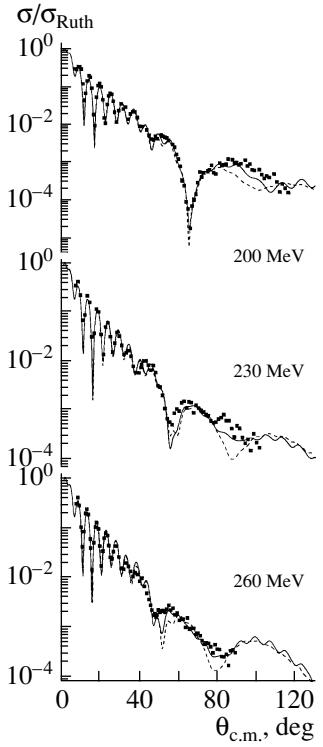

Fig. 2. $^{16}O + {}^{12}C$ elastic-scattering differential cross sections at 200, 230, and 260 MeV (data from [4]) and optical model calculations with the potentials WSD-2 and WS-2 (solid and dashed curves, respectively).

$^{16}O + {}^{14}C$, are also presented. As for rainbows in nuclear reactions, some new features of the charge-exchange (^{6}Li, ^{6}He) reactions will be discussed.

2. $^{16}O + {}^{12}C$ ELASTIC SCATTERING

Recent measurements undertaken by our group in the ^{16}O energy interval 132–260 MeV [3, 4] really led to the observation of well-developed rainbow patterns including the supernumerary Airy structures. The potential parameters obtained from both phenomenological (WS1 in [4]) and FM calculations have smoothly connected the results at higher [5] and lower [6, 7] energies. The authors of a recent paper [8] presented data at 300 MeV and claimed that their results also are consistent with the previous studies. Thus, the general understanding of the main features of $^{16}O + {}^{12}C$ elastic scattering seemed to be quite satisfactory.

However, the first steps in a more detailed theoretical analysis started in [9] revealed some problems, and new measurements at ^{16}O energies of 181 and 281 MeV were fulfilled (the data without any calculations were published in [10]).

The whole collection of existing data taken at energies of 132 MeV and above is presented in Fig. 1. An unexpected and the most interesting result of the measurements at 281 MeV was the observation of an additional rainbow-like structure (the minimum at ~70°) in the angular range, where only exponential falloff was expected from the previous systematics [4]. The latter has predicted the location of the primary rainbow minimum in the region of ~45° just at the position of the second observed minimum. The 300-MeV data [8] look very much alike in all important details, including the Airy-like minima under discussion.

This finding pushed us to perform anew the optical model analysis of all existing data in the energy interval from 132 to 1503 MeV. This was done using the phenomenological potential with an ordinary Woods–Saxon (WS) form. At the first stage, we deliberately used a six-parametric potential in order to get a general picture, which could then be compared with the results obtained in [4].

At energies from 181 to 281 MeV, two potential sets WS-1 and WS-2 were found, being the analogs of WS1 and WS2 from [4], respectively. They both

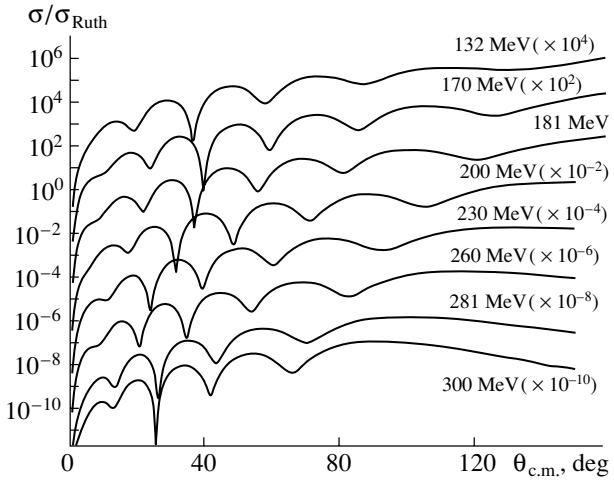

Fig. 3. The far-side $^{16}O + {}^{12}C$ elastic-scattering cross sections calculated using the WS-2 potential with zero absorption ($W = 0$).

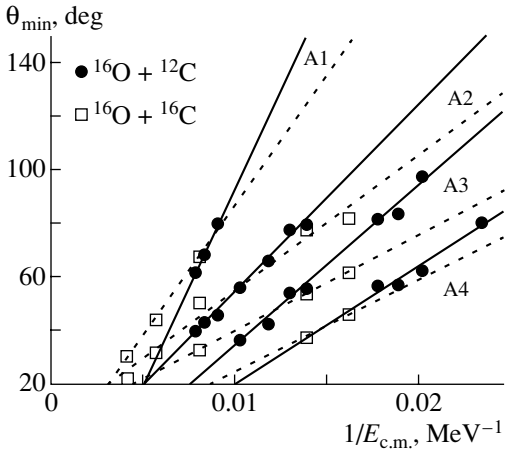

Fig. 4. The positions of the experimentally observed minima, interpreted as Airy ones, in the $^{16}O + {}^{12}C$ (and $^{16}O + {}^{16}O$ [2] differential cross sections as a function of the inverse c.m. energies. A1–A4 denote the numerical order of the minima. The straight lines (solid for $^{16}O + {}^{12}C$ and dashed for $^{16}O + {}^{16}O$) are drawn through the calculated minima (not shown) obtained by fitting the data.

have similar imaginary parts, but the real part of WS-2 is deeper (the difference in volume integrals is ~25%). As to the 300-MeV data, we found only one χ^2 minimum, which corresponded to the set WS-2. As was expected, we got excellent fits to the higher energy data exhibiting only the exponential falloff of the cross section in the rainbow region. The calculated curves shown in Fig. 1 were obtained with the WS-2 potential.

The previous analysis [4] did not include the data at 181, 281, and 300 MeV and gave some preference to the set WS1. We recall that the volume integral of the real part of the WS1 (WS-1) potential is very close to that of the FM potential from [4]. This fact was considered in [4] as an additional argument in favor of the potentials of the WS-1 set. However, the 70° minima at 281 and 300 MeV could not be reproduced by too shallow a WS-1 potential, and just this particular feature required the use of a deeper potential WS-2. In this case, the 70° minima become the first ones, and the structures at ~45° should be interpreted as the secondary minima, contrary to the expectation based on the former analysis.

Brandan *et al.* [8] considered the minimum at 45° as the first one. The ~70° structure in their calculations is generated by the imaginary part of the potential taken as a combination of a volume and a surface term. However, the description of the angular distribution beyond 60° is obtained only on average, and the 70° minimum actually is not reproduced (see Fig. 2 in [8]). As to our deeper WS-2 potential, it reproduces the 300-MeV data quite well. We emphasize that this better agreement was achieved with a fewer number of parameters because the imaginary part of the WS-2 potential included only the volume term having quite traditional geometry.

Nevertheless, the crucial question is whether the WS-2-type potential is able to give fits of the same quality to the data of other energies as the WS1 one in [4] did. Though the refractive behavior of the differential cross sections was observed in the whole ^{16}O energy range 60–1500 MeV studied up to now, only the data at 200–300 MeV are really useful for the determination of the numerical order of Airy extremes. For energies higher than 600 MeV, the rainbow patterns are located at overly small angles and obscured by the diffraction oscillations. On the other hand, the nonpotential mechanism of alpha-particle elastic transfer strongly contributes in the whole back hemisphere as the 132- and 181-MeV data show.

We recall that the analog of the WS-2 potential (WS2) was rejected in [4] due to worse fitting to the data just in the energy range from 200 to 260 MeV. One can see this from Fig. 1.

In order to improve the agreement with the experiment in this energy region, we made calculations with the WSD-2 potential. The latter includes both the volume absorption term and the surface one using the standard derivative WS form factor

$$W_D(r) = -4a_D W_D \frac{d}{dr} f_D(r). \qquad (1)$$

The results are shown in Fig. 2, where the data are compared with WS-2 and WSD-2 calculations. One can see that the WSD-2 calculations reproduce the data much better, particularly at the energy of

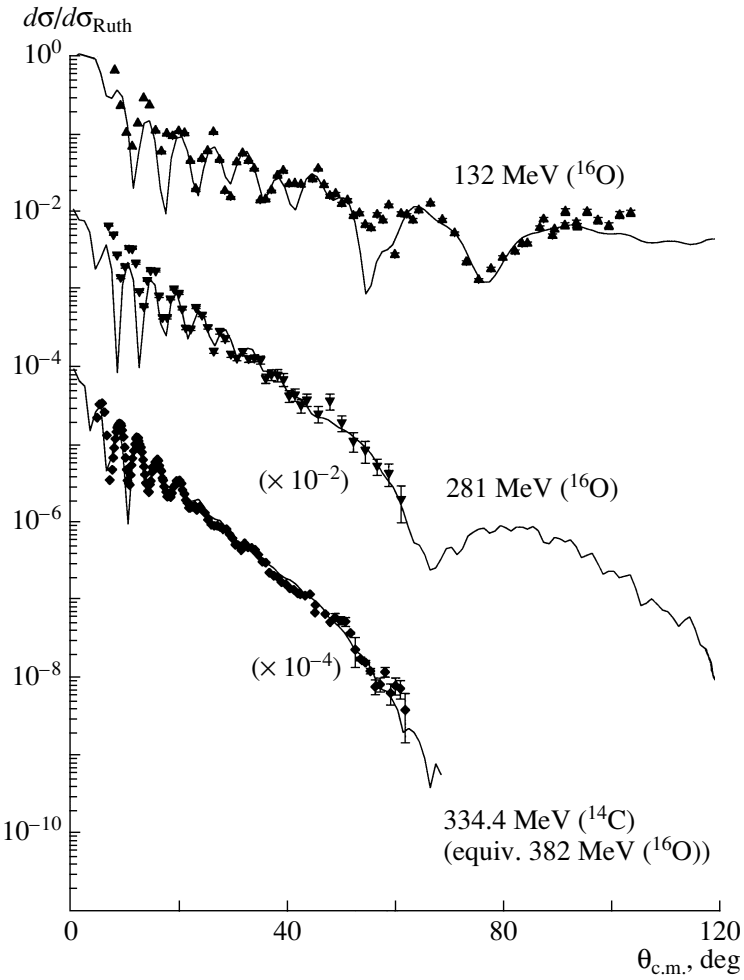

Fig. 5. $^{16}O + {}^{14}C$ elastic-scattering differential cross sections. Theoretical curves were calculated with the WS-2-type potentials.

260 MeV. Some minor disagreements at 200 and 230 MeV still remain in the refraction region; however, one cannot be sure that the interference with the alpha-particle transfer is completely excluded. We did not make WSD-2 calculations for the other energies because it is evident that the use of more free parameters can only improve the agreement.

In order to check that the new WS-2 potential really generates the rainbow patterns in the angular distributions, the cross sections were decomposed into far-side and near-side components. The cross sections in the expected rainbow regions really are exhausted by the far-side component. If the latter is calculated with zero absorption ($W = 0$) (Fig. 3), clear Airy structures are revealed, and they correspond to those observed experimentally. The largest angle minima at 281 and 300 MeV evidently can be identified as the first Airy minima, and the expected shift to the smaller angles with the energy is clearly seen.

Thus, we come to the conclusion that the WS-2 potential, a deeper one than was required before, is able to reproduce all existing data on the $^{16}O + {}^{12}C$ elastic scattering. The other arguments in favor of a deeper potential come from the energy dependence of the values characterizing the refractive properties of the nucleus–nucleus potential. First, we shall analyze the positions of Airy minima.

A semiclassical nuclear rainbow angle θ_{NR} is connected with the depth of the potential in a way similar to that of the refraction index. It was shown [11] that, for the WS potential,

$$\theta_{NR} \approx \text{const}(V/E_{c.m.})^{1/2}, \qquad (2)$$

where const depends on the geometry factors.

The refraction index for a particle with the energy E entering a half plane with the potential V from vacuum is

$$n = (1 + V/E)^{1/2}. \qquad (3)$$

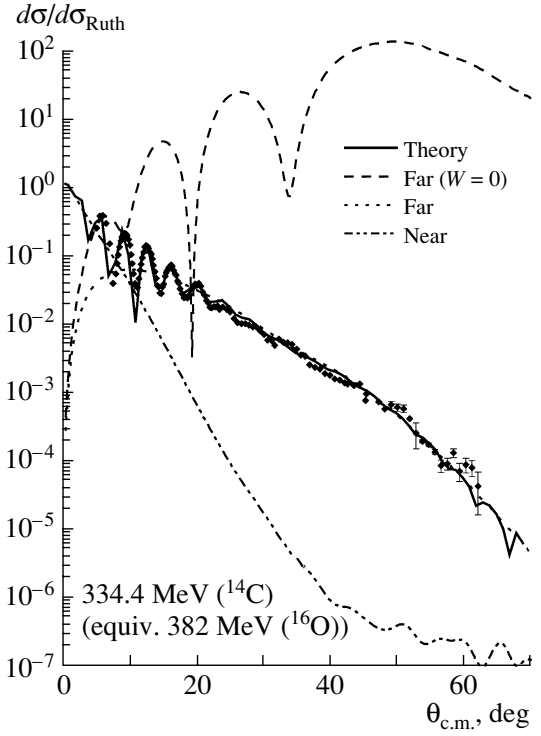

Fig. 6. Near–far decomposition of $^{16}O + {}^{14}C$ elastic-scattering cross sections at the equivalent ^{16}O energy of 382 MeV.

Thus, we see from (2) and (3) that the nuclear rainbow angle to some extent can play a role of the effective refraction index of nuclear matter. Of course, this statement makes sense only if expression (2) can be related to some observables, say, to the positions of Airy minima θ_{min}. The latter really lie on the straight lines in the plane θ_{min} vs. $1/E_{c.m.}$ corresponding to their numerical order as was shown in [4].

The new systematics of Airy minima of the measured angular distributions including the data at 181, 281, and 300 MeV is shown in Fig. 4. We also used some of the data from [6]. We took into account only the minima that were actually observed in the measured angular distributions. One can see that the minima identified at 281 and 300 MeV as the first ones form a new straight line marked A1 together with the previously ignored minimum in the 260-MeV data. The Airy minima recognized in [4] as the first ones now become the second ones and are located on the straight line A2. Newly determined secondary Airy minima at 281 and 300 MeV also fit the straight line A2 quite well. A similar change happens for the lines of higher numbers. Some lower energy data [6] also form a straight line but should be attributed to the Airy minima one number higher than was claimed in [6, 7].

Thus, the observation of the large-angle structures at 281 and 300 MeV requires some modification of the previously determined systematics of Airy minima but is consistent with the assumption of their nuclear rainbow scattering origin.

The other arguments in favor of the deeper WS-2 potential come from the comparison of $^{16}O + {}^{12}C$ scattering with that of $^{16}O + {}^{16}O$ and $^{12}C + {}^{12}C$. The refraction properties of the potentials of these neighboring systems are expected to be similar because the effective nucleon–nucleon interaction, which determines the real parts of the potentials, is known to be an attribute of nuclear matter. This means that the nuclear rainbow angles and the volume integrals of the real parts of the potentials should be more or less the same.

The positions of the primary and supernumerary Airy minima up to the fourth number are shown in Fig. 4. For comparison, the $^{16}O + {}^{16}O$ data [2] also are presented. One can see that the positions of minima in both systems are very close in the overlapping energy regions. On the contrary, a definite discrepancy would appear if one uses the shallower WS-1 potential (in this case the full A2 line should be compared with the dashed line A1).

The volume integral of some potential $u(r)$ is

$$J_u = -\frac{4\pi}{A_P A_T}\int_0^\infty u(r) r^2 dr. \qquad (4)$$

For the real part of the optical model potential, it is considered to be a measure of its refractive strength.

The values of the real volume integrals J_V of the WS-2 potential are quite close ($\sim$350 MeV fm^3 in the low-energy region $<$20 MeV per nucleon) to those obtained from the analysis of the $^{16}O + {}^{16}O$ and $^{12}C + {}^{12}C$ data. On the contrary, the WS-1 potentials and those obtained at lower energies [6] give real volume integrals significantly smaller (310–280 MeV fm^3). This discrepancy, not understood earlier, is now eliminated by introducing the WS-2 potentials.

Thus, Airy systematics and the values of the volume integrals support the conclusion that the real potential for $^{16}O + {}^{12}C$ system is deeper than was thought before [4, 6]. This means that the particular variant of the FM used in [4] is not completely adequate to the scattering dynamics. We shall come back to this problem later on.

3. $^{16}O + {}^{14}C$ ELASTIC SCATTERING

The study of $^{16}O + {}^{12}C$ elastic scattering demonstrated some serious advantages of the asymmetric systems for the investigation the rainbow phenomenon. However, the back-angle scattering in this

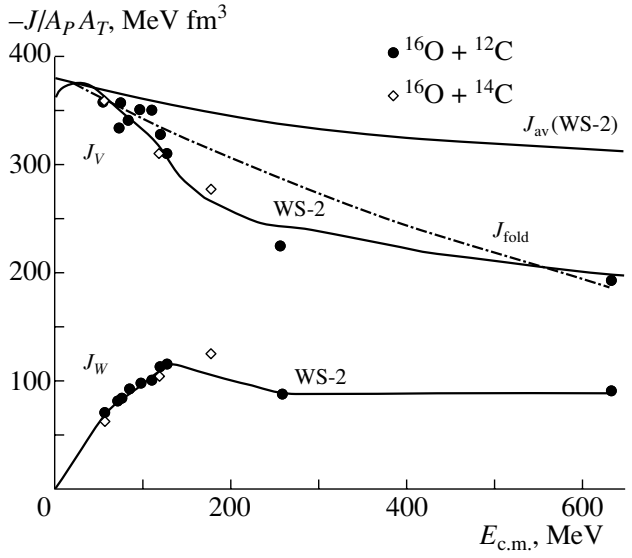

Fig. 7. Energy dependence of the real and imaginary volume integrals obtained with WS-2 potentials and dispersion relation analysis. Fitting to J_V requires the average potentials J_{av} (see text). For comparison, the energy dependence of the volume integrals J_{fold} of the nonrenormalized FM potentials from [4] is plotted.

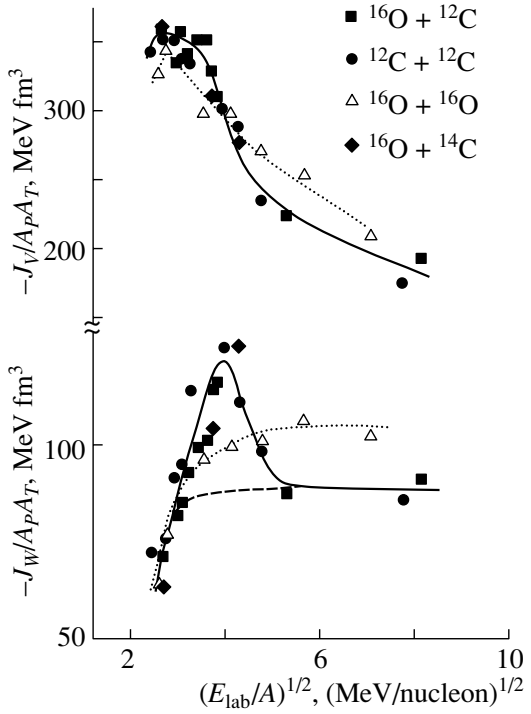

Fig. 8. The real (upper part) and imaginary (bottom part) volume integrals vs. $(E_{lab}/A)^{1/2}$, the value proportional to the relative velocity of the colliding nuclei (for explanation of the curves see the text).

particular combination of nuclei is strongly influenced by alpha-particle transfer. The latter was observed not only at relatively low energies but even in the 181-MeV data. This pushed us to look for another neighboring asymmetric system, ^{16}O + ^{14}C. One can expect that the elastic transfer process, namely, that of two protons, is much less probable here. On the other hand, the preliminary measurements taken at the ^{14}C energy of 334 MeV (which is equivalent to the 382 MeV of ^{16}O) [12] indicated that the absorption is quite strong, and the rainbow structures are not seen at all.

We measured ^{16}O + ^{14}C elastic scattering at two more energies, 132 and 281 MeV. The whole set of data is presented in Fig. 5. The theoretical curves were calculated with the real part of the potential practically identical to the WS-2. One can see that 132-MeV data demonstrate well-developed rainbow-like minima just at the angles where the corresponding structures were observed in ^{16}O + ^{12}C scattering. Some change of the slopes in the differential cross sections at 281 and 382 MeV could be considered as the residual rainbow minima of the second and first orders, respectively. In order to check this, we decompose the 382-MeV cross section into near and far components (Fig. 6). One can see that the cross section beyond the region of the diffraction oscillations is completely exhausted by the far component. Therefore, although the absorption in the ^{16}O + ^{14}C system really is stronger than that in the ^{16}O + ^{12}C one, the scattering still preserves its refractory nature.

4. ENERGY DEPENDENCE OF THE VOLUME INTEGRALS AND ABNORMAL NUCLEAR DISPERSION

Important information on nuclear dynamics can be obtained from the analysis of the energy dependences of the real and imaginary parts of the potentials. They characterize the evolution of the refractory and absorptive properties of the nuclear field. Being a powerful theoretical technique, the dispersion relations can be used for the data analysis.

The energy dependence of the real and imaginary volume integrals for ^{16}O + ^{12}C and ^{16}O + ^{14}C scattering is shown in Fig. 7. Some important features should be noted. First, both systems have very similar refraction and absorptive properties. Secondly, the absorption goes up with the energy in the low-energy region as the number of open channels increases. Some broad maximum appears at the c.m. energy ~150 MeV. Thirdly, the energy dependence of the refraction also is not monotonic, demonstrating a steep change just in the energy region where the J_W maximum is located.

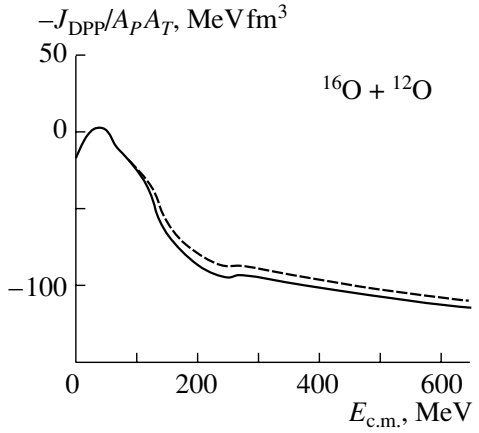

Fig. 9. The volume integrals of the real part of dynamical polarization potential J_{P,E_S} calculated by the dispersion relation. The solid and dashed curves refer to the WS-2 and WS-1 potentials, respectively.

The nonmonotonic behavior of the energy dependence of the real volume integrals $J_V(E)$ correlated with a broad maximum in $J_W(E)$ was first observed [13] in ^{6}Li elastic scattering on ^{12}C targets. It resembles the dependence of the real and imaginary parts of the refraction index on the frequency of light in the presence of a strong absorption line (optical abnormal dispersion). Analogously, the effect was called [13] abnormal nuclear dispersion. A kindred effect of influence of additional absorption on refraction is well known in low-energy nuclear scattering (so-called "threshold anomaly" [14]). However, its occurrence in the vicinity of 15–20 MeV per nucleon was quite unexpected.

Some interesting conclusions can be made if the volume integrals are plotted as a function of the relative velocity of the colliding nuclei (Fig. 8) instead of the energy. For comparison, we included the values of the volume integrals for the ^{12}C + ^{12}C and ^{16}O + ^{16}O scattering [1, 2]. First, the maximum in the J_W, being rather expressionless in the energy dependence, now becomes very prominent. The J_W for ^{12}C + ^{12}C happen to behave in a way similar to that for the ^{16}O + ^{12}C system (solid curve, Fig. 8). Moreover, the ^{12}C + ^{12}C data are complementary to the latter, outlining the right slope of the maximum and confirming its existence unambiguously. The real volume integrals for all three systems also form a unique curve.

Secondly, it becomes evident that the positions of the $J_W(E)$ maxima and, correspondingly, the jumps in $J_V(E)$ occur at quite different c.m. energies in the ^{16}O + ^{12}C, ^{12}C + ^{12}C and ^{6}Li + ^{12}C systems but at similar energies per nucleon (velocities). This finding hints at the possible existence of some resonance process coming from the nearness of the interaction time and the time of some high-frequency internal motion. Rough estimates show that the interaction time is close to the half-period of the giant resonances in light nuclei, which is the classical condition for the resonance excitation of an oscillator. It is tempting to suggest that the observed additional resonance absorption is connected with the excitation of the isoscalar dipole giant resonance (ISGDR). As was already mentioned, the nuclear rainbow phenomenon corresponds to the strong density overlap of the colliding nuclei. On the other hand, the ISGDR can be treated as some oscillation of a compression wave.

It is seen from Fig. 8 that the imaginary volume integrals from ^{16}O + ^{16}O scattering behave differently and do not demonstrate any resonance structure (dotted curve). The J_W rise fast at low energies and then level off. Correspondingly, the ^{16}O + ^{16}O real volume integrals also do not show the dispersion jump, contrary to what was observed for the other systems. Using optical language, one can say that, in this case, the energy (or velocity) dependence is similar to normal dispersion. It is seen from Fig. 8 that the two other nucleus–nucleus combinations also contain the normal component (dashed curve).

The reason for such a difference is unclear. The only visible one could be connected with the structure of ^{12}C. From this point of view, it would be interesting to take measurements of ^{16}O + ^{14}C scattering at an energy of ~600–700 MeV: the existing data allow both resonance or nonresonance extrapolation.

The dispersion relations were applied to the analysis of the energy dependences of the volume integrals. The effective nucleus–nucleus potential (see, e.g., [14] and references therein) depends on the energy $E_{c.m.}$, is complex and nonlocal, and can be written as

$$U(r, r', E_{c.m.}) = V_{av}(r, r') + \Delta U(r, r', E_{c.m.}), \quad (5)$$
$$\Delta U(r, r', E_{c.m.}) = V_P(r, r', E_{c.m.}) + iW(r, r', E_{c.m.}).$$

Here, V_{av} is referred to as an average potential. ΔU is often called a dynamic polarization potential (DPP). It contains information on all possible inelastic channels of the nucleus–nucleus interaction. Its real part is determined by the virtual transitions, and the imaginary part takes into account the absorption.

The dispersion relation connects the real V_P and imaginary W parts of the model DPP:

$$V_P(r, E) = \frac{P}{\pi} \int_0^\infty \frac{W(r, E')}{E' - E} dE'. \quad (6)$$

Here, P stands for principal value. The expression (6) is an analog of the Kramers–Kronig relation for a complex refraction index in optics.

Usually, the dispersion relation is applied not to the components of the potential but to the corresponding volume integrals. In practice, the subtracted dispersion relation [14] is used:

$$J_P(E) - J_P(E_S) \tag{7}$$
$$= (E - E_S)\frac{P}{\pi}\int_0^\infty \frac{J_W(E')}{(E' - E_S)(E' - E)}dE'.$$

Here, E_S is some "reference energy." Thus, relation (7) determines $J_P(E)$ up to a constant. The advantage of using (7) is that the sensitivity of the value $J_P(E) - J_P(E_S) \equiv J_{P,E_S}(E)$ to the assumed energy dependence of $J_W(E)$ at energies no longer of interest is greatly reduced.

To calculate the integral (7), $J_W(E)$ should be approximated in some way. Following the usual practice, we used a linear schematic model [14]. The details of the calculations have been published elsewhere [9]. We took the value $E_S = 20$ MeV.

The obtained energy dependence of the volume integrals of the real part of DPP $J_{P,E_S}(E)$ is shown in Fig. 9. It turns out to be nonmonotonic. A steep change takes place in the c.m. energy region 50–150 MeV, and the difference between its low- and high-energy values reaches ~80 MeV fm^3. The origin of such behavior and the location of the region of steep change are directly connected with the maximum in the E dependence of J_W (Fig. 7).

A total real volume integral is a sum of the volume integrals of the average potential and the real part of DPP (dispersion correction):

$$J_V(E) = J_{\text{av}}(E) + J_P(E). \tag{8}$$

The usual philosophy is that the average potential can be associated with the FM potential. In this case, J_V can be written as a sum of the nonrenormalized FM potential volume integral J_{fold} and J_P:

$$J_V(E) = J_{\text{fold}}(E) + J_P(E). \tag{9}$$

In order to get better agreement with the experimental data, the renormalization factors N_R are used as a rule in FM calculations, that is, $J_V = N_R J_{\text{fold}}$. The renormalization factors N_R obtained in [4] for the ^{16}O + ^{12}C scattering are approximately constant (~0.8) for the whole energy interval. Strong disagreement between the results of dispersion analysis and normal folding model procedure is clearly seen. Note that J_{P,E_S} obtained from the dispersion relation practically does not depend on the choice of the potential, WS-1 or WS-2.

In order to reproduce the energy dependence of the real volume integrals by the expressions (7) and (8), one has to select some energy dependence of the average potential $J_{\text{av}}(E)$. It can be of different origin and mostly spurious due to the effects of nonlocality. Often, a constant value of J_{av} is chosen in the dispersion relations calculations. Another possibility could be taking $J_{\text{fold}}(E)$ for $J_{\text{av}}(E)$.

Our choice was to extract an empirical $J_{\text{av}}(E)$. The parametrization was performed in the form $J_{\text{av}}(E) = a + b\exp(-cE_{\text{c.m.}})$, which is well known from nucleon–nucleus scattering. The reference-energy value of $E_S = 20$ MeV was adopted in order to make J_{av} equal to the nonrenormalized FM potential volume integral J_{fold} at $E_{\text{c.m.}} = 0$. This corresponds to our selection of the reference energy $E_S = 20$ MeV.

The results of the analysis of dispersion relations using the expressions (7)–(9) are shown in Fig. 7. The energy dependence of J_V obtained from the optical model analysis is reproduced quite well. One can see that the energy dependence of the empirical $J_{\text{av}}(E)$ is required to be much slower than that of $J_{\text{fold}}(E)$.

Thus, we came to the conclusion that the FM calculations, at least in the form accepted in our previous paper [4], cannot explain some important features of the ^{16}O + ^{12}C elastic-scattering data. From a general point of view, this is not too surprising. The FM potential represented as the first-order term of the effective potential in Feshbach reaction theory [15] does not contain contributions from the coupling to the inelastic channels, which could be quite significant. A lot of virtual excitations can take place during the nucleus–nucleus interaction, and the results of our dispersion analysis show that they really influence the scattering process. In addition, more complicated exchange effects possibly play an important role.

Of course, we do not exclude the possibility of improving the FM itself, but discussion of this problem is beyond the scope of this paper. Moreover, we think that new measurements at higher energies (300–400 MeV) and at sufficiently large angles are desirable for deeper understanding of the above-discussed problems. We plan to perform these measurements in the nearest future.

5. RAINBOWS IN THE CHARGE-EXCHANGE REACTIONS AND SEARCH FOR PION-CONDENSATION EFFECTS

Nuclear rainbow effects are observed not only in elastic scattering but also in some inelastic processes. In previous years, we extensively studied its manifestation in the charge-exchange reactions (^{3}He, t) [16] and (^{6}Li,^{6}He) [17]. In this paper, we shall dwell only on a previously unpublished indication of possible observation in the ^{14}C(^{6}Li,^{6}He)^{14}N reaction of some

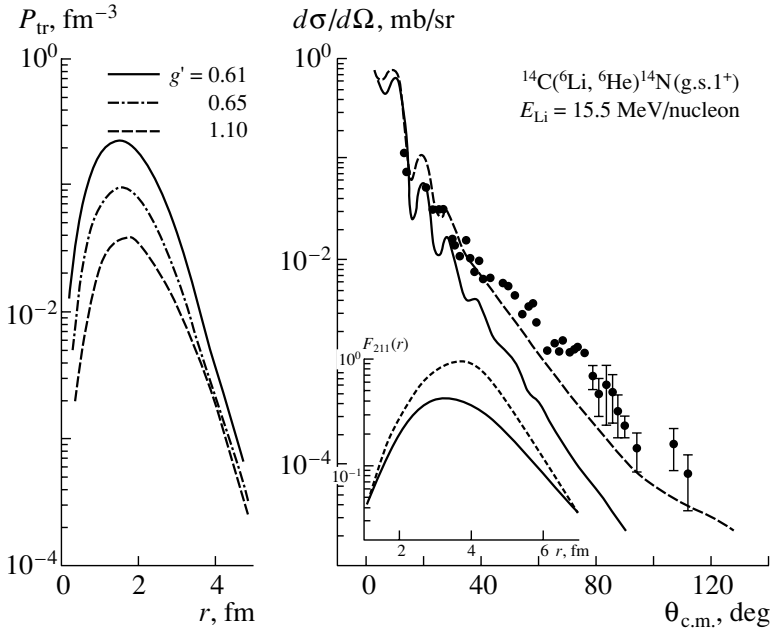

Fig. 10. (Left) Transition densities for different values of the g' constant ($g' = 0.61$ corresponds to the phase transition to the pion condensation state). (Right) Differential cross section of the reaction $^{14}C(^6Li,^6He)^{14}N_{gr}$. The solid curve corresponds to the theoretical form factor, and the dashed curve, to the empirical one. Both form factor are shown in the inset.

signatures of phase transition to the state of pion condensation.

The problem of pion condensate was widely discussed in the 1970s. Migdal's original idea was that the spontaneous generation of the pion field in nuclear matter occurs if nucleon density exceeds some critical value ρ_c. Estimates [18] predict that ρ_c is about $(2–2.5)\rho_0$ ($\rho_0 = 0.17$ n/fm) for cold nuclear matter. Though such compression can be achieved in central heavy-ion collisions, all attempts to observe any signatures of the phase transition or approaching this state failed.

Without discussing here the theoretical problems concerning pion condensation phenomenon, we only note that a possible reason for the negative results could be connected with the fact that nuclear matter compression obtained in central nucleus–nucleus collisions is inevitably connected with strong heating in the interaction zone. Thus, a pion condensate has little chance of survival even if it was actually formed.

The heating of nuclear media while the nuclear density in the overlap region increases can be avoided if the nuclear rainbow mechanism is used. Some time ago, the $^{14}C(^6Li, ^6He)^{14}N$ reaction was proposed [19] for this purpose. Strong enhancement of the charge-exchange reaction cross sections was predicted for the excitation of the states of so-called abnormal parity (0^-, 1^+, etc.) if the point of phase transition is approached. An especially strong effect was expected for the transition between the ^{14}C and ^{14}N ground states ($0^+ \to 1^+, T = 1$).

The study of the $^{14}C(^6Li, ^6He)^{14}N$ reaction at 90 MeV was carried out [17]. The refractory behavior of the reaction was established. The experimental data were sensitive to the distances between the centers of the colliding nuclei of about 2.5–3.0 fm. The total nucleon density at these distances exceeds the equilibrium density by a factor of 1.5.

The data reveal some features that could be interpreted as a hint at manifestation of pion-condensation effects (Fig. 10). The measured differential cross sections for the ground-state transition exceed the calculated ones at large angles by approximately an order of magnitude, though in all other (^{6}Li, ^{6}He) reactions studied in [17] the data were well reproduced by normal theoretical form factors. All attempts to improve the calculations with shell-model wave functions (inclusion of tensor forces in the effective interaction, use of different potentials in the entrance and exit channels) produced no agreement with the data. The contribution of multistep mechanisms can be reliably evaluated from the cross section of the reaction to the first excited state of ^{14}N (its population is strictly forbidden in a one-step process) and could not exceed 15–20%.

The only way to approach the experiment was to modify the reaction form factor. This modification (Fig. 10) had to be done in the direction just as was

predicted for the case when the influence of pion-condensation effects becomes considerable.

Of course, one cannot rely on the results of a single experiment, which still could contain some uncertainties. The best and most direct way to eliminate them is to make measurements at higher energies. The relative role of multistep processes diminishes with energy, and, on the other hand, the interpenetration of the colliding nuclei will increase, making the compression slightly higher. In addition, Pirner and Voskresensky [20] predicted some specific effect that could provide some additional enhancement of the cross section with energy if approach to the point of phase transition takes place.

6. CONCLUSIONS

We performed a wide study of the elastic scattering in asymmetric light heavy-ion systems $^{16}O + {}^{12}C$ and $^{16}O + {}^{14}C$ at several ^{16}O energies. The nuclear rainbow nature of the differential cross sections beyond the diffraction patterns was proved. Airy minima up to the fourth order were identified. The angular distribution of $^{16}O + {}^{12}C$ scattering at 281 MeV revealed an unexpected rainbow minimum from the point of view of the previous analyses. A new analysis of the whole set of the $^{16}O + {}^{12}C$ data was done, and it required a real potential (WS-2) deeper than was thought before on the basis of the phenomenological and folding model calculations.

The refractory properties of the WS-2 potential turn out to be very similar to those of the potentials describing $^{12}C + {}^{12}C$ and $^{16}O + {}^{16}O$ scattering. This concerns both the positions of the Airy minima at the same c.m. energies and values of the real volume integrals. It was shown that Airy minima of different order are located in the $\theta_{\min}-1/E_{\text{c.m.}}$ plane on straight lines. This feature allows treatment of $\theta_{\min}$ as a rough analog of the nuclear matter refraction index.

The energy dependence of the volume integrals of the real and imaginary parts of the potentials was studied. The energy dependence of the imaginary volume integrals reveals a broad maximum in the vicinity of 20 MeV per nucleon. The position of the maximum is correlated with a fast change in the energy dependence of the real volume integrals. Such a correlation resembles an abnormal dispersion in optics where it is connected with the appearance of a strong absorption line at some particular light frequency. The abnormal nuclear dispersion becomes especially prominent if the volume integrals are represented as functions of the relative velocities of the colliding nuclei. It gives a hint that some resonance absorption influences the elastic scattering. The comparison with the neighboring systems showed that a similar effect is present in $^{12}C + {}^{12}C$ scattering and absent in $^{16}O + {}^{16}O$ scattering.

We fulfilled the dispersion relation analysis of the energy dependences of the volume integrals. The energy dependence of the dynamical polarization potential was obtained. It turns out to be nonmonotonic and changes steeply in the c.m. energy range 50–150 MeV. The analysis results in the extraction of an empirical average potential. To fit the real volume integral energy dependence, it needs to have a much slower fall with energy in comparison with the folding model potential.

Our results indicate that the folding model calculations, at least in the form accepted in our previous paper [4], cannot explain some important features of the $^{16}O + {}^{12}C$ elastic-scattering data.

The rainbow mechanism in the charge-exchange reactions as a possible instrument to search for pion-condensation effects was discussed. Some unexplained features observed in the previously studied $^{14}C(^{6}Li, {}^{6}He)^{14}N$ reaction [17] require further investigation of this process.

ACKNOWLEDGMENTS

We are indebted to H. Bohlen, Dao T. Khoa, and W. von Oertzen for useful discussions.

This work was partly supported by the Russian Foundation for Basic Research (project nos. 01-02-16667 and 00-15-96534), by the Academy of Finland, and by the Access to the Large Scale Facility Program under the Training and Mobility of Researchers Program of the European Union.

REFERENCES

1. M. E. Brandan and G. R. Satchler, Phys. Rep. **285**, 143 (1997).
2. Dao T. Khoa, W. Von Oertzen, H. G. Bohlen, and F. Nuoffer, Nucl. Phys. A **672**, 387 (2000).
3. A. A. Ogloblin, Dao T. Khoa, Y. Kondo, *et al.*, Phys. Rev. C **57**, 1797 (1998).
4. A. A. Ogloblin, Yu. A. Glukhov, W. H. Trzaska, *et al.*, Phys. Rev. C **62**, 044601 (2000).
5. M. E. Brandan, A. Menchaca-Rocha, M. Buenerd, *et al.*, Phys. Rev. C **34**, 1484 (1986).
6. M. P. Nicoli, F. Haas, R. M. Freeman, *et al.*, Phys. Rev. C **61**, 034609 (2000).
7. S. Szilner, M. P. Nicoli, Z. Basrak, *et al.*, Phys. Rev. C **64**, 064614 (2001).
8. M. E. Brandan, A. Menchaca-Rocha, L. Trache, *et al.*, Nucl. Phys. A **688**, 659 (2001).
9. S. A. Goncharov, Yu. A. Glukhov, A. S. Dem'yanova, *et al.*, Izv. Ross. Akad. Nauk, Ser. Fiz. **65**, 651 (2001).
10. Yu. A. Glukhov, S. A. Goncharov, A. S. Dem'yanova, *et al.*, Izv. Ross. Akad. Nauk, Ser. Fiz. **65**, 647 (2001).
11. J. Knoll and R. Schaeffer, Ann. Phys. (N.Y.) **97**, 307 (1976).

12. H. G. Bohlen, B. Gebauer, Ch. Langner, *et al.*, HMI Annual Report HMI-B-507 (Berlin, Germany, 1992), p. 57.
13. S. A. Goncharov, A. S. Dem'yanova, and A. A. Ogloblin, in *Proceedings of the Conference ENAM'98, Bellaire, Michigan, USA, 1998,* Ed. by B. M. Sherrill, D. J. Morrissey, and C. N. Davids (AIP, Woodbury, New York, 1998), p. 510.
14. C. Mahaux, H. Ngo, and G. R. Satchler, Nucl. Phys. A **449**, 354 (1986).
15. H. Feshbach, *Theoretical Nuclear Physics* (Wiley, New York, 1992).
16. A. S. Dem'yanova, A. A. Ogloblin, S. N. Ershov, *et al.*, Phys. Scripta **32**, 89 (1990).
17. A. S. Dem'yanova, J. M. Bang, F. A. Gareev, *et al.*, Nucl. Phys. A **501**, 336 (1989).
18. A. B. Migdal, E. E. Saperstein, M. A. Troitsky, and D. N. Voskresensky, Phys. Rep. **192**, 179 (1990).
19. D. V. Alexandrov, Yu. A. Glukhov, A. S. Dem'yanova, *et al.*, Nucl. Phys. A **436**, 338 (1985).
20. H. J. Pirner and D. N. Voskresensky, Phys. Lett. B **343**, 25 (1995).

Physics of Atomic Nuclei, Vol. 66, No. 8, 2003, pp. 1489–1493. From Yadernaya Fizika, Vol. 66, No. 8, 2003, pp. 1534–1538.

Rainbow, Airy Structure, and Molecular Structure in the $^{16}O + {}^{16}O$ System*

S. Ohkubo**

Department of Applied Science and Environment, Kochi Women's University, Kochi, Japan

Received August 28, 2002

Abstract—Rainbow, Airy structure, and molecular structure in the $^{16}O + {}^{16}O$ system are investigated from the viewpoint of a unified description of the composite system. The potential for the $^{16}O + {}^{16}O$ system determined from rainbow scattering is applied to low-energy scattering near the Coulomb barrier. Quasi-bound and bound molecular states are calculated in the complex scaling method. Evidence for the existence of the lowest $N = 24$ and $N = 28$ molecular bands with the $^{16}O + {}^{16}O$ structure in ^{32}S is shown.

1. INTRODUCTION

Recently, rainbow and Airy structure in heavy-ion scattering attracted much attention [1]. In the 1990s, great progress was made experimentally and theoretically, and the interaction potential for the light heavy-ion systems such as $^{16}O + {}^{16}O$, $^{16}O + {}^{12}C$, and $^{12}C + {}^{12}C$ was determined up to the internal region. Especially for the $^{16}O + {}^{16}O$ system, the potential was thoroughly investigated above $E_L = 75$ MeV from the systematic analysis of rainbow scattering [2, 3].

In the literature, the mechanism of the Airy structure was investigated by decomposing the scattering amplitude into two subamplitudes of far-side and near-side components [1–3]. Although in this traditional approach the Airy structure is shown to be due to the far-side component, it was not clear what kind of interference causes the oscillatory Airy structure. Very recently, we have shown [4] that the far-side amplitude can be further decomposed into barrier-wave and internal-wave subamplitudes in a straightforward and rigorous way. It is found that the Airy structure is caused by the interference between the far-side internal wave and the far-side barrier wave. Thus, the global deep potential describes well the mechanism of the rainbow and Airy structure above $E_L = 75$ MeV for the $^{16}O + {}^{16}O$ system. The real physical meaning of the Airy structure as well as its terminology is discussed by the present author with Michel and Reidemeister [5].

It is important to investigate whether the potential determined from rainbow scattering can describe the lower energy scattering and the quasi-bound and bound molecular states of the composite system. In this paper, we show that the potential which describes the Airy structure in rainbow scattering can also describe the molecular structure of the quasi-bound and bound states in a unified way.

2. LONG-STANDING PROBLEM OF THE $^{16}O + {}^{16}O$ MOLECULAR STRUCTURE

The $^{16}O + {}^{16}O$ system is the most typical heavier cluster analog to the $\alpha + \alpha$ cluster in ^{8}Be. A large number of investigations [6] have been devoted to the system, and $^{16}O + {}^{16}O$ molecular resonances have been observed in elastic scattering, fusion reactions, and transfer reactions. To reveal the $^{16}O + {}^{16}O$ cluster structure in ^{32}S, many theoretical approaches, such as the microscopic cluster-model calculations with the Resonating Group Method (RGM) and the Generator Coordinate Method (GCM) [7–9], have been made. Up to now, in spite of many efforts, the band structure with the $^{16}O + {}^{16}O$ configuration in ^{32}S has not been established. For example, the problems concerning at what energy the lowest $^{16}O + {}^{16}O$ cluster band starts and how many rotational bands exist have not been solved yet.

Ikeda's threshold rule has been a useful guide in knowing at what energy the lowest cluster structure appears in nuclei. However, as for the $^{16}O + {}^{16}O$ cluster structure in ^{32}S, the cluster band has not been clearly confirmed experimentally. On the other hand, theoretical studies using GCM and RGM located the lowest cluster band at different energies depending on the effective force used. According to [7], which uses

*This article was submitted by the author in English.

** e-mail: shigeo@cc.kochi-wu.ac.jp

Optical potential parameters in the standard notation and volume integrals per nucleon pair

$E_{\text{c.m.}}$, MeV	V_0, MeV	R_V, fm	a_R, fm	J_V, MeV fm^3	W_0, MeV	R_I, fm	a_I, fm	J_W, MeV fm^3
12.5	410	4.03	1.35	332	95	3.10	0.275	4.2
14.0	410	4.03	1.25	325	95	3.10	0.275	4.2
15.5	410	4.03	1.35	332	95	3.10	0.275	4.2
20.5	408.5	3.99	1.552	340	90	3.15	0.275	4.2
24.5	410	3.99	1.55	341	90.5	3.65	0.275	6.7
29.5	410	4.08	1.2	333	90.5	3.28	0.365	4.6
31.5	410	4.08	1.2	333	85	3.63	1.62	14.9

Volkov force no. 1, and [8], which uses the Brink–Boeker force, each theory gives only one rotational band, which starts at $E_{\text{c.m.}} = 10.36$ and 6.6 MeV, respectively, and the gross structure of the 90° excitation function for ^{16}O + ^{16}O scattering is due to the band. On the other hand, according to [9], which uses density-dependent forces as well as the Volkov force, its theory gives more than two rotational bands: the first band starts near the threshold energy and the second one is responsible for the gross structure. The energy surface of the GCM calculation [8] or the equivalent potential of the RGM [9] was consistent with the phenomenological shallow potential [10–12] obtained from the systematic analysis of elastic ^{16}O + ^{16}O scattering. Many other theoretical models also supported the shallow potential.

It was shown in [13] that the ^{16}O + ^{16}O elastic scattering and fusion cross sections can be described by a J-dependent deep real potential with $J_V = 307$ MeV fm^3, which is consistent with the RGM result, $J_V = 306$ MeV fm^3 [14] (this belongs to a shallower family as discussed below). However, the calculated rms radius of the potential, 4.45 fm, was inconsistent with the RGM result, 3.8 fm. (Kondō *et al.* [15] also considered the depth of the potential by taking into account the dispersion relation.) Using the inversion technique, Ait-Tahar *et al.* [16] pointed out that this inconsistency is due to its J-dependent character of the potential. They also suggested that the potential for the ^{16}O + ^{16}O system must not necessarily have J dependence. In fact, in the α + ^{40}Ca and α + ^{16}O systems, the global potentials did not need any J dependence [17]. Therefore, it was important to make clear whether J dependence is essential for the ^{16}O + ^{16}O system, unlike the α + nucleus systems, or a J-independent deep potential can describe the heavy-ion system in a wide range of energies.

3. UNIFIED DESCRIPTION OF BOUND AND SCATTERING STATES OF THE ^{16}O + ^{16}O SYSTEM

In the 1990s, rainbow scattering of ^{16}O + ^{16}O scattering was measured systematically and higher energy data could solve the discrete ambiguities of the deep potential. Systematic analysis of the higher energy data between $E_L = 124$ and 1120 MeV by Khoa *et al.* [3] showed clearly that the angular distributions can be described well by a folding-type diffuse deep potential (no J dependence) with the family of $J_V = 340$ MeV fm^3. Recent Strasbourg data of ^{16}O + ^{16}O elastic scattering between $E_L = 75$–124 MeV [2] also showed that this potential was successful. Thus, the global potential for the ^{16}O + ^{16}O system has been uniquely established. This situation is very similar to the one for α + ^{40}Ca in the 1980s, where the unique global potential was determined from the systematic analysis of elastic α scattering from ^{40}Ca: the potential was also shown to describe the fusion data as well. The unified description of bound and scattering states of the α + ^{40}Ca system predicted the existence of the $N = 13$, $K = 0^-$ α-cluster band [17], which is a parity doublet partner of the ground band of ^{44}Ti and was observed later in the α-transfer experiment [18, 19].

However, for the ^{16}O + ^{16}O system, different from the ^{44}Ti case, the ground state of the composite system ^{32}S, which is 16.54 MeV below the ^{16}O + ^{16}O threshold, does not have the ^{16}O + ^{16}O configuration. Furthermore, the lowest band with the ^{16}O + ^{16}O configuration has not been confirmed in experiment. This situation seems to have hampered attempts to try to unify bound and scattering states of the ^{16}O + ^{16}O system to reveal the cluster structure in ^{32}S. However, recent understanding of the Airy oscillations [2, 3, 5] observed in ^{16}O + ^{16}O elastic scattering urges us to study whether the viewpoint of unified understanding is applicable to ^{32}S like

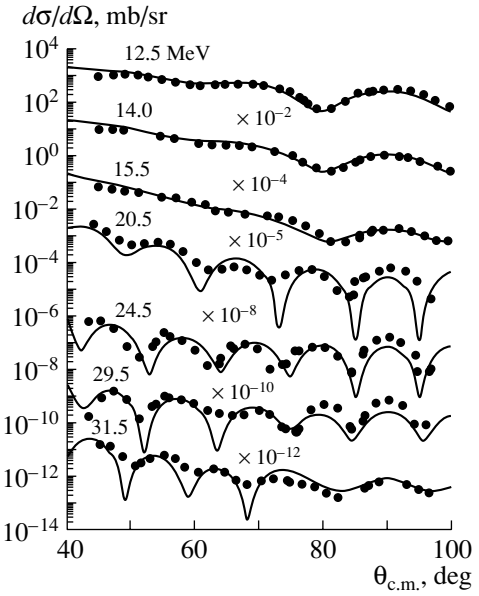

Fig. 1. Calculated angular distributions of $^{16}O + {}^{16}O$ scattering are compared with the experimental data [11].

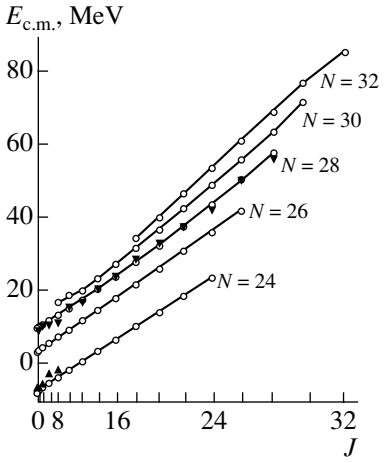

Fig. 2. $^{16}O + {}^{16}O$ cluster bands (circles) calculated in the complex scaling method are compared with the experimental data (triangles).

^{44}Ti and ^{20}Ne or not. This is a very important long-standing problem to be solved because, if it is shown to be successful in this typical system, it means that this unification cannot be limited only to the $^{16}O + {}^{16}O$ system and could be applicable to other heavy-ion systems such as the $^{16}O + {}^{12}C$ cluster structure in ^{28}Si.

To see how the potential obtained in the energy range of $E_{c.m.} = 37.5$ MeV ($E_L = 75$ MeV) to 560 MeV ($E_L = 1120$ MeV) can describe the low-energy data between $E_{c.m.} = 12.5$ and 31.5 MeV, which have usually been described by shallow potentials or a J-dependent deep potential [13], we have analyzed the $^{16}O + {}^{16}O$ scattering starting from a potential determined by Nicoli [20] at $E_{c.m.} = 37.5$ MeV ($V_0 = 412$ MeV, $R_V = 3.97$ fm, $a_R = 1.492$ fm), which has a Woods–Saxon squared form factor for real and imaginary parts. The calculated angular distributions are shown in Fig. 1 in comparison with the experimental data. The potential parameters in the table do not change very much from the original one at $E_{c.m.} = 37.5$ MeV [20] and belong to the same family. This shows that the deep potential is valid up to the very low energy near the Coulomb barrier.

4. $^{16}O + {}^{16}O$ CLUSTER BANDS IN THE COMPLEX SCALING METHOD

In order to know the properties of the resonances and bound states supported by this deep potential, the complex scaling method [21] has been used. In Fig. 2, the energy levels calculated with the potential at $E_{c.m.} = 37.5$ MeV are shown in comparison with the experimental data. The $N = 24$ band, which is located about 8 MeV below the threshold, is the lowest Pauli-allowed band. The rotational constant k estimated from the lowest spin to the highest one is $k = 52$ keV. The second, $N = 26$, rotational band with $k = 55$ keV, which starts from about 3 MeV, has a width of less than 5 keV. The $N = 28$ band with $k = 59$ keV, which starts from about 10 MeV, has a width of 0.19–1.7 MeV. The three $N = 24$, 26, and 28 bands have almost the same rotational constant. The $N = 30$ band with $k = 68$ keV starts near the Coulomb barrier and is in broad resonance with a width of several MeV. The $N = 32$ band has a width of about 10–20 MeV.

The three gross structures of the 90° excitation function at $E_{c.m.} = 20$–30 MeV in Fig. 3, which was assigned to the $N = 24$ band resonances in [7, 8] and the $N = 26$ band resonances in [9], are found to be due to the 14^+, 16^+, and 18^+ resonances of the $N = 28$ band. As indicated in Fig. 3, the peaks of the 90° excitation function [11, 22] are assigned as follows: 12^+ (17.5 MeV), 14^+ (21 MeV), 16^+ (24.5 MeV), 18^+ (29 MeV), 20^+ (33.5 MeV), 22^+ (38 MeV), 24^+ (43 MeV), 26^+ (51 MeV), and 28^+ (57 MeV), which show the $J(J+1)$ behavior with $k = 50$ keV and correspond well to our $N = 28$ band as seen in Fig. 2. The lower spin states observed in transfer reactions (also in precise elastic scattering) [23, 24], 2^+ (9.7 MeV), 4^+ (10.7 MeV), 6^+ (11.3 MeV), 8^+ (12.0 MeV), and 10^+ (15.8 MeV), correspond well to our band (Fig. 2). It is surprising that the calculated energies of the $N = 28$ band correspond well to the experimental data without any adjustment. Although the band head 0^+ state has not been reported in

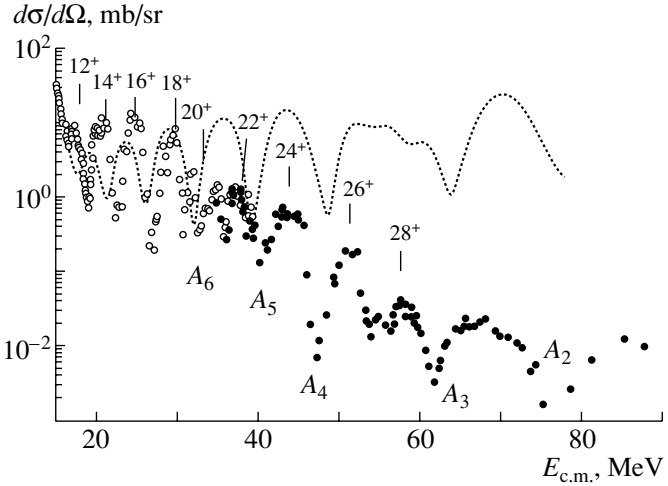

Fig. 3. Candidates of the $N = 28$ band are indicated for the experimental data (open [11] and closed circles [22]) of 90° excitation function for $^{16}O + {}^{16}O$ elastic scattering. Airy minima are also shown.

experiment, it seems that there is an indication of a peak in the experimental 90° excitation function near $E_{c.m.} = 9.6$ MeV [23]. Because our calculation predicts the band head 0^+ state around this energy region, 10.1 MeV, we hope that it will be searched for in experiment.

5. FRAGMENTATION OF THE BAND STATES

It is recalled that, in ^{40}Ca and ^{44}Ti, the observed α-cluster $N = 13$, $K = 0^-$ band states and the higher nodal $N = 14$ band states are fragmented [19]. The fragmentation will become more significant in heavier systems like the $^{16}O + {}^{16}O$ bands. In fact, many states considered to have the $^{16}O + {}^{16}O$ molecular resonances have been reported [25]: 10^+ (14.35, 14.57, 14.79, 15.1, 15.2, 15.8, 15.83, 15.9, 16.32, 17.31, 17.67 MeV), 12^+ (16.9, 17.3, 17.9 MeV), and 14^+ (19.8 MeV). Recently, Curtis *et al.* [26] observed new states: 16.42 MeV (10^+ or 12^+), 18.15 MeV (12^+ or 14^+), 19.10 MeV (12^+ or 14^+), 21.01 MeV (14^+ or 16^+), and 21.78 MeV (14^+ or 16^+). The centroids of the above 10^+, 12^+, and 14^+ states are located on the $N = 28$ band and agree well with the corresponding resonance energies marked in Fig. 3. The observed $k = 42$–49 keV is in agreement with that of the $N = 28$ rather than that of the $N = 30$ band. The molecular states, 10^+, 12^+, 14^+ and 16^+ observed by Curtis may be fragmented from the $N = 28$ band.

In Fig. 3, the deep Airy minima (A_2–A_6) caused by the interference between the far-side internal wave, to which high-spin members of the $N = 30$ and $N = 32$ bands contribute, and the far-side barrier wave are clearly seen (A_1 is located at 100 MeV). We notice in Fig. 3 that, below the A_3 Airy minimum at 62 MeV, where both the $N = 28$ and $N = 30$ bands are involved, the broad peaks are fragmented and the spacing between the peaks becomes narrower. The spin states of the $N = 30$ and $N = 32$ bands, which have a width of more than several MeV, are difficult to be seen as a clear peak in the excitation function.

The lowest Pauli-allowed cluster band with $N = 24$ appears at 7.5 MeV below the threshold, i.e., $E_x = 9.0$ MeV in excitation energy. Experimentally, the band has not been established. In [27], three $^{16}O + {}^{16}O$ quasi-molecular bands with $k = 91$–109 keV, which show the $J(J + 1)$ behavior, were suggested in $E_x = 11$–17 MeV. The $k = 52$ keV of our $N = 24$ band disagrees with the ones extracted from the data. Also, theory cannot give three $K = 0^+$ bands with the $^{16}O + {}^{16}O$ configuration in this energy region. In [27], it was argued that the band obtained in the RGM could correspond to the observed band because the calculated $k = 60$–70 keV by Ando *et al.* [9] is not far from the experimental data: However, as mentioned already, we know that the RGM calculation [9] adopted an interaction that belongs to a wrong shallower family, giving $J_V = 302$ MeV fm^3 at $E_L/A = 10$ MeV for its equivalent local potential [14]. Kondō *et al.* [13] have discussed the possible $N = 24$ band of [27] using a J-dependent real potential, whose J_V of the equivalent J-independent local potential ranges from 291 to 326 MeV fm^3 [16]. However, it is difficult to reconcile the k with the J-dependent potential.

How one can reconcile the $k = 91$–109 keV of the experimental data with the present cluster model prediction? We note that many 0^+, 2^+, 4^+, and 6^+ states have been observed in this energy region [27, 28]: 0^+; $E_x = 8.507$, 9.983, 10.457, 10.787 MeV

(centroid 9.93 MeV): 2^+; $E_x = 8.690$, 8.861, 9.464, 9.711, 9.992, 10.104, 10.510, 10.520, 10.696, 10.757, 10.792, and 10.827 MeV (centroid 10.131 MeV): 4^+; $E_x = 9.065$, 10.276, 11.70, and 13.04 MeV (centroid 11.020 MeV): 6^+; $E_x = 12.76$, 13.76, and 15.20 MeV (centroid 13.91 MeV). (In Fig. 2, the centroids are plotted by triangles.) As for the 8^+ state, only one is observed at 14.81 MeV [27]. The derived $k = 33$–64 keV (average $k = 49$ keV) for the centroid of the observed states agrees well with the present prediction $k = 52$ keV. The observed states may be considered to be fragmented from the $N = 24$ $^{16}O + {}^{16}O$ cluster band in Fig. 2. The $N = 26$ higher nodal band is inevitably predicted between the $N = 24$ and $N = 28$ bands, just above the threshold energy. As no experimental counterpart has been observed, it is highly desired to observe the band.

6. SUMMARY

It was shown that rainbow scattering, Airy structure, and molecular structure of the $^{16}O + {}^{16}O$ system are described in a unified way with a global deep potential. The Airy minima are caused by the interference between the far-side internal wave and far-side barrier wave. It was shown that the lowest $N = 24$ $^{16}O + {}^{16}O$ molecular band exists and starts at $E_x \sim 8$ MeV with $k \sim 50$ keV, being fragmented. Furthermore, the existence of the higher nodal $N = 26$ band was predicted and the $N = 28$ band was also shown to appear in experiment.

ACKNOWLEDGMENTS

I thank Ms. K. Yamashita for collaboration in the initial stage of this work. This work has been supported by a grant-in-Aid for Scientific Research of the Japan Society for Promotion of Science (no. 12640288). I also thank Prof. F. Michel, Prof. W. Von Oertzen, and Prof. H.G. Bohlen for their interests in this work.

REFERENCES

1. M. E. Brandan and G. R. Satchler, Phys. Rep. **285**, 143 (1997).
2. M. P. Nicoli, F. Haas, R. M. Freeman, *et al.*, Phys. Rev. C **60**, 064608 (1999).
3. Dao T. Khoa, W. Von Oertzen, H. G. Bohlen, and F. Nuoffer, Nucl. Phys. A **672**, 387 (2000).
4. F. Michel, F. Brau, G. Reidemeister, and S. Ohkubo, Phys. Rev. Lett. **85**, 1823 (2000); F. Michel, G. Reidemeister, and S. Ohkubo, Phys. Rev. C **63**, 034620 (2001).
5. F. Michel, G. Reidemeister, and S. Ohkubo, Phys. Rev. Lett. **89**, 152701 (2002).
6. P. E. Hodgson, *Nuclear Heavy Ion Reactions* (Clarendon, Oxford, 1978); R. Bock, *Heavy Ion Collisions* (North-Holland, Amsterdam, 1979, 1980), Vols. 1, 2.
7. H. Friedrich, Nucl. Phys. A **224**, 537 (1974).
8. D. Baye and G. Reidemeister, Nucl. Phys. A **258**, 157 (1976); D. Baye and D.-H. Heenen, Nucl. Phys. A **276**, 354 (1977).
9. T. Ando, K. Ikeda, and A. Tohsaki-Suzuki, Prog. Theor. Phys. **61**, 101 (1979); **64**, 1608 (1980).
10. R. H. Siemssen, J. V. Maher, A. Weidinger, and D. A. Bromley, Phys. Rev. Lett. **19**, 369 (1967); **20**, 175 (1968).
11. J. V. Maher, M. W. Sachs, R. H. Siemssen, *et al.*, Phys. Rev. **188**, 1665 (1969).
12. A. Gobbi, R. Wieland, L. Chua, *et al.*, Phys. Rev. C **7**, 30 (1973).
13. Y. Kondō, B. A. Robson, and R. Smith, Phys. Lett. B **227**, 310 (1989).
14. T. Wada and H. Horiuchi, Prog. Theor. Phys. **80**, 488 (1988).
15. Y. Kondō, F. Michel, and G. Reidemeister, Phys. Lett. B **242**, 340 (1990).
16. A. Ait-Tahar, S. G. Cooper, and R. S. Mackintosh, Nucl. Phys. A **542**, 499 (1992).
17. F. Michel, G. Reidemeister, and S. Ohkubo, Phys. Rev. Lett. **57**, 1215 (1986); F. Michel, S. Ohkubo, and G. Reidemeister, Prog. Theor. Phys. Suppl. **132**, 7 (1998).
18. T. Yamaya, S. Oh-ami, M. Fujiwara, *et al.*, Phys. Rev. C **42**, 1935 (1990).
19. T. Yamaya, K. Katori, M. Fujiwara, *et al.*, Prog. Theor. Phys. Suppl. **132**, 73 (1998).
20. M. P. Nicoli, PhD Thesis (Strasbourg, 1998), Int. Rep. IReS 98-16.
21. J. Aguilar and J. M. Combes, Commun. Math. Phys. **22**, 269 (1971); E. Balslev and J. M. Combes, Commun. Math. Phys. **22**, 280 (1971); B. Simon, Commun. Math. Phys. **27**, 1 (1971).
22. M. L. Halbert, C. B. Fulmer, S. Raman, *et al.*, Phys. Lett. B **51B**, 341 (1974).
23. G. Gaul, W. Bickel, W. Lammer, and R. Santo, *Resonances in Heavy Ion Reactions*, Lecture Note in Physics (Springer-Verlag, Berlin, 1982), Vol. 156; G. Gaul and W. Bickel, Phys. Rev. C **34**, 326 (1986).
24. M. Gai, E. C. Schloemer, J. E. Freedman, *et al.,* Phys. Rev. Lett. **47**, 1878 (1981).
25. N. Cindro, Ann. Phys. (Paris) **13**, 289 (1988).
26. N. Curtis, A. St. J. Murphy, N. M. Clarke, *et al.*, Phys. Rev. C **53**, 1804 (1996).
27. K. Morita, S. Kubono, M. H. Tanaka, *et al.*, Phys. Rev. Lett. **55**, 185 (1985).
28. R. B. Firestone, V. S. Shirley, C. M. Baglin, *et al.*, *Table of Isotopes* (Wiley, New York, 1996).

Physics of Atomic Nuclei, Vol. 66, No. 8, 2003, pp. 1494–1500. From Yadernaya Fizika, Vol. 66, No. 8, 2003, pp. 1539–1545.

Structure of Neutron-Rich Be and C Isotopes*

H. G. Bohlen[1)], W. von Oertzen[1)]***, R. Kalpakchieva[2)]****, B. Gebauer[1)], S. M. Grimes[3)], A. Lenz[1)], T. N. Massey[3)], M. Milin[1)], Ch. Schulz[1)], Tz. Kokalova[1)], S. Torilov[1)], and S. Thummerer[1)]**

[1)] *Hahn-Meitner-Institut GmbH, Berlin, Germany*

[2)] *Flerov Laboratory of Nuclear Reactions, Joint Institute for Nuclear Research, Dubna, Moscow oblast, 141980 Russia*

[3)] *Department of Physics and Astronomy, Ohio University, Athens, OH 45701-2979, USA*

Received August 28, 2002

Abstract—The structure of neutron-rich beryllium isotopes has been investigated using different heavy-ion-induced transfer reactions. In neutron transfer reactions, the population of final states shows a strong sensitivity to the chosen core nucleus, i.e., the target nuclei ^{9}Be or ^{10}Be, respectively. Molecular rotational bands up to high excitation energies are observed with ^{9}Be as the core due to its pronounced 2α-cluster structure, whereas only a few states at low excitation energies are populated with ^{10}Be as the core. For ^{11}Be, a detailed investigation has been performed for the three states at 3.41, 3.89, and 3.96 MeV, which resulted in the most probable spin-parity assignments $3/2^{+}$, $5/2^{-}$, and $3/2^{-}$, respectively. Furthermore, we have studied particle–hole states of ^{16}C using the ^{13}C(^{12}C, ^{9}C)^{16}C reaction and found 14 previously unknown states. Using the ^{12}C(^{12}C, ^{9}C)^{15}C reaction, five new states were observed for ^{15}C.

1. INTRODUCTION

Neutron-rich Be isotopes can form pronounced cluster structures and even molecular structures with two α particles as a core and additional neutrons for the binding [1]. Alpha-cluster structures have already been investigated extensively in light nuclei by many authors [2], mostly in $A = 4N$ nuclei. Nuclear molecules can be characterized as structures consisting of at least two heavier particles (e.g., α particles), which have at relatively large distance a minimum in their effective interaction potential. The minimum is mediated by an attractive exchange interaction at large distances and a repulsion at small distances, as is the case for the α–α interaction potential of Ali and Bodmer [3]. In the ^{8}Be ground state, the α particles have an equilibrium distance of about 3 fm, which corresponds roughly to a touching configuration.

For the ground state of ^{9}Be, calculations with the two-center shell model [4], the antisymmetrized molecular dynamics (AMD) model [5], and the generator coordinate method [6] find a minimum energy at α–α distances of 3.0–3.4 fm and, at the same time, reproduce the ground state properties known from experiment. The cited references given above for theoretical calculations represent only a selection; there are many other calculations. Experimentally the α–α distance in ^{9}Be can be estimated from the moment of inertia of the ground-state band ($K^{\pi} = 3/2^{-}$), which is derived from excitation energies and spins of the band members: a distance of about 3.1(2) fm is found (see Section 2). ^{9}Be can be considered as the best example for a particle-stable nuclear molecule.

Cluster and molecular structures have also been found in the heavier beryllium isotopes ($A = 10$–12) [1, 7–10]; the results will be discussed in the next section. It is, however, important to understand also the structure of states with different character, e.g., with single-particle or core-excited configurations. There exists, for example, a controversy of spin assignments for the three low-lying states in ^{11}Be at excitation energies of 3.41, 3.89, and 3.96 MeV. The latter state is considered as the band head of the $K^{\pi} = 3/2^{-}$ molecular rotational band [1, 7], whereas $5/2^{-}$ is also used in the literature [11]. In this investigation, we used the two-neutron stripping reaction ^{9}Be(^{16}O, ^{14}O), which has the special feature of a $0^{+} \rightarrow 0^{+}$ transition in the projectile. In this case, the angular distributions directly reflect the parity of the

*This article was submitted by the authors in English.

** e-mail: bohlen@hmi.de

*** Also Freie Universität Berlin, Fachbereich Physik, Germany.

**** Also Institute for Nuclear Research, Bulgarian Academy of Sciences, Sofia.

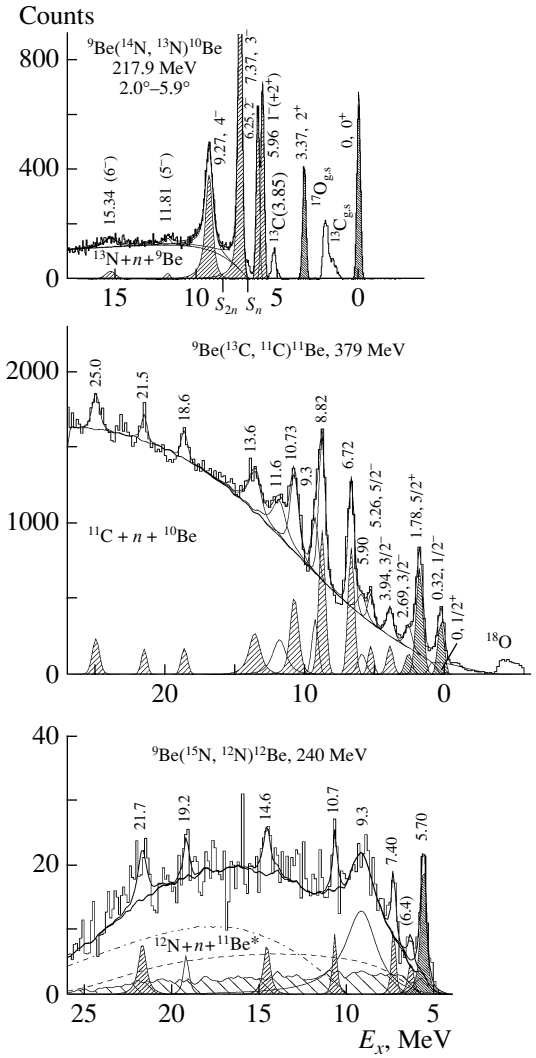

Fig. 1. Spectra of one-neutron (upper panel), two-neutron (middle panel), and three-neutron (lower panel) transfer reactions on ^{9}Be. In each spectrum, the states, which form a rotational band, are marked by 45° upward hatched areas. The numbers correspond to excitation energies in MeV. The broad background corresponds to three-body distributions. In the lower panel, the background from ^{16}O contaminations in the target is indicated by the wide hatched area.

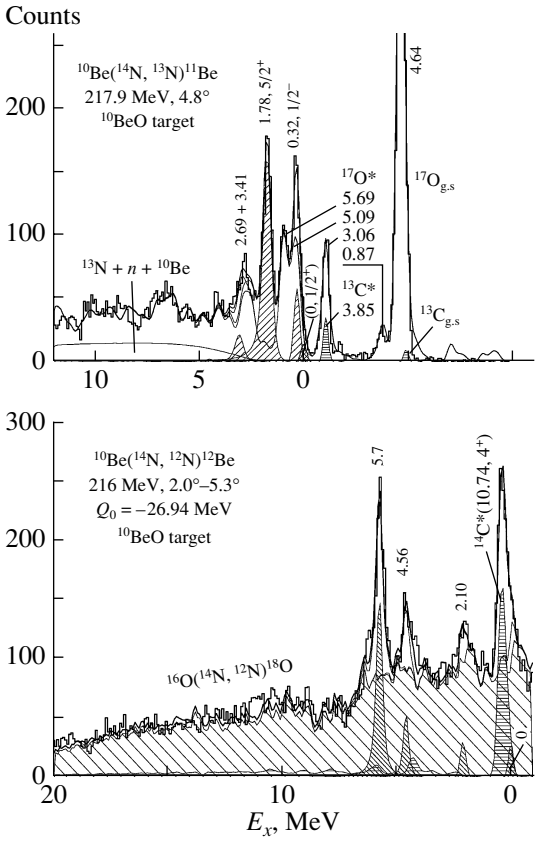

Fig. 2. Spectra of one-neutron (upper panel) and two-neutron (lower panel) transfer reactions on ^{10}Be showing the population of states in ^{11}Be and ^{12}Be, respectively. Strong background contributions result from oxygen, since the target material is beryllium oxide (lines indicated by horizontal hatched areas result from carbon contaminations).

ℓ transfers to the different final states of the target transitions. The same is also true for the two-proton pickup reaction ^{13}C(^{12}C, ^{14}O), but now states of very different character are populated. The states of ^{10}Be have also been studied in this way.

Cluster structures and possible molecular structures are also expected for neutron-rich carbon isotopes; however, the latter, at relatively high excitation energy [1]. For ^{15}C and ^{16}C, excited states are known only up to excitation energies of 11.8 and 6.1 MeV, respectively. We observed in the (^{12}C, ^{9}C) reaction on ^{12}C and ^{13}C excited states up to 16 MeV in ^{15}C and up to 17.4 MeV in ^{16}C. This three-neutron transfer reaction populates in ^{15}C and ^{16}C states of particle–hole character with one hole (for ^{16}C) or two holes (for ^{15}C) in the 1p shell and two or one particle in the sd shell, respectively. The population of the configurations in this transfer reaction can be related to the observed cross sections by using dynamical matching conditions. Partial angular distributions have been obtained for the strongest transitions. These results are presented in Section 3.

2. NEUTRON-RICH BERYLLIUM ISOTOPES

2.1. Comparison of Neutron Transfer Reactions on ^{9}Be and ^{10}Be

In our investigations of the structure of neutron-rich beryllium isotopes, we used one-, two-, and three-neutron transfer reactions on ^{9}Be and as well as one- and two-neutron transfer reactions on ^{10}Be

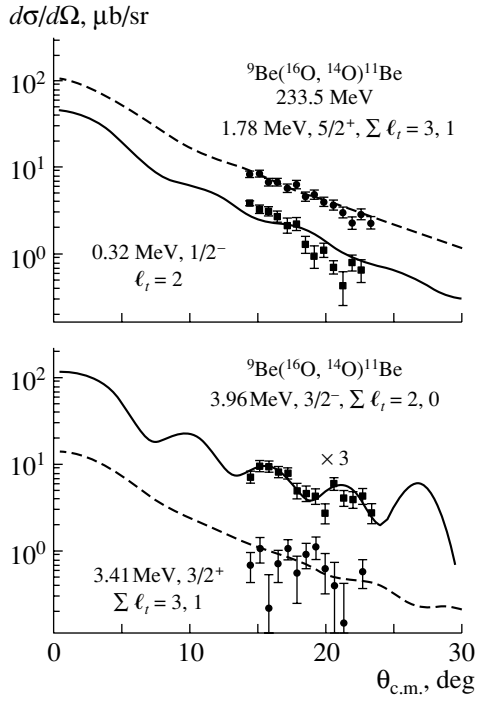

Fig. 3. Partial angular distributions of the ^{9}Be(^{16}O,^{14}O) reaction for the ^{11}Be states at 1.78 MeV ($5/2^{+}$) and 0.32 MeV ($1/2^{-}$) (upper panel), and 3.96 MeV ($3/2^{-}$) and 3.41 MeV ($3/2^{+}$) (lower panel). The solid and dashed curves correspond to DWBA calculations with the code Ptolemy [21]. The transferred angular momenta are indicated by the given l_t values.

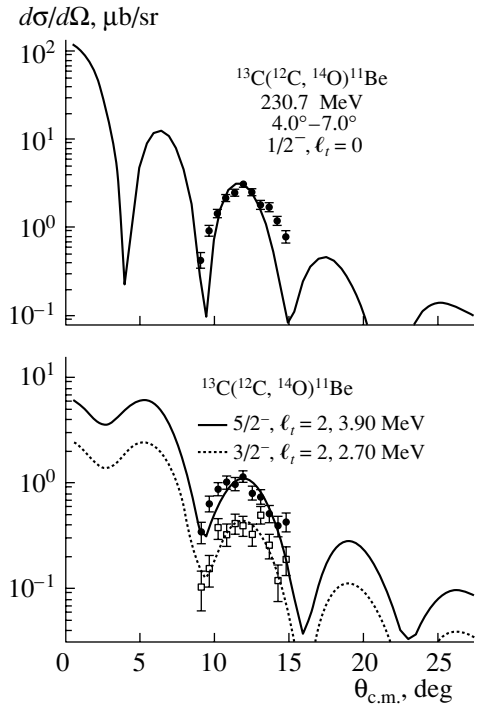

Fig. 4. Partial angular distributions of the ^{13}C(^{12}C,^{14}O) reaction for the ^{11}Be states at 0.32 MeV ($1/2^{-}$, upper panel) and at 2.70 MeV ($3/2^{-}$) (open squares) and 3.90 MeV, ($5/2^{-}$), (closed circles) (lower panel). The curves correspond to DWBA calculations with the code Ptolemy [21].

to study the structure of ^{10}Be, ^{11}Be, and ^{12}Be. The measurements have been performed at the Q3D magnetic spectrograph of the Hahn-Meitner-Institut. In these reactions, the target nuclei ^{9}Be and ^{10}Be can be considered in the first order as cores for the neutron configurations populated in the final nucleus. Characteristic differences can be expected, since ^{9}Be already has in its ground state a well-developed 2α structure, whereas the ^{10}Be ground state has a more compact shape. In fact, a striking difference is observed in the spectra on ^{9}Be (Fig. 1) and ^{10}Be (Fig. 2).

On ^{9}Be, the neutron transfer reactions populate states up to high excitation energies in
^{10}Be: 8 states up to 15.34 MeV;
^{11}Be: 15 states up to 25.0 MeV;
^{12}Be: 7 states from 5.5 to 21.7 MeV (states at lower excitation energies did not fall into the focal plane).

Most of the states of the three isotopes show a linear dependence between excitation energies and $J(J+1)$ (J is spin of the states), which is characteristic for a rotational band. These states are marked in Fig. 1 by 45° upward hatched areas. The spin assignments have been made tentatively in this way for those states which show this characteristic dependence [7, 8] (for 2 states in ^{10}Be, for 7 states in ^{11}Be, and for 5 states in ^{12}Be). The spins of a few states, mostly at low excitation energies, were known from the literature [15]. We can identify the following rotational bands:

^{10}Be, $K^{\pi} = 1^{-}$: $E_x = 0.25[J(J+1) - 1\cdot 2] +$ 5.960 MeV;

^{11}Be, $K^{\pi} = \frac{3}{2}^{-}$: $E_x = 0.23\left[J(J+1) - \frac{3}{2}\cdot\frac{5}{2}\right] +$ 3.96 MeV;

^{12}Be, $K^{\pi} = 0^{+}$: $E_x = 0.21[J(J+1)] + 6.4$ MeV.

The slope parameter is inversely proportional to the moment of inertia of the rotating system. Assuming two α particles as the basic structure and additional neutrons distributed around, a distance of more than 5 fm between the α particles is estimated for all three cases. Such a large distance corresponds to separated α particles with rather small density overlap, since their rms radius is only about 1.7 fm [12]. These bands can really be termed molecular rotational bands.

In contrast to the large range of excitation energies populated on ^{9}Be, only a few low-lying states are

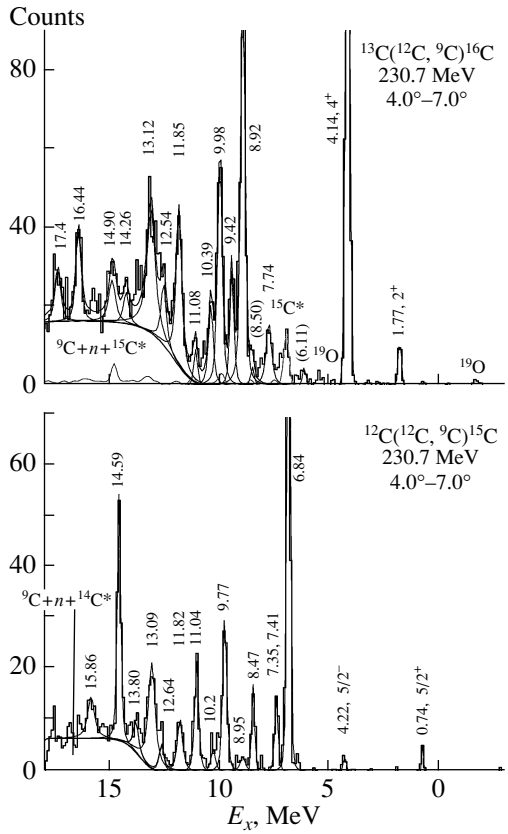

Fig. 5. Spectra of the ^{13}C(^{12}C, ^{9}C)^{16}C reaction (upper panel) and the ^{12}C(^{12}C, ^{9}C)^{15}C reaction (lower panel) measured at 230.7-MeV incident energy. In the upper panel, the dotted curve corresponds to the background from the ^{12}C contamination in the target. The broad distributions on the left show three-body contributions.

observed in the neutron transfer reactions on ^{10}Be to final states of ^{11}Be and ^{12}Be. It is more difficult in these spectra (Fig. 2) to identify weak states, because there is a strong background from oxygen in the target. Significant peaks could be analyzed so far only for the states at 0.32 and 1.78 MeV and the doublet at 2.7 and 3.4 MeV in ^{11}Be, and at 2.10, 4.56, and 5.7 MeV in ^{12}Be. These populated states can be characterized by a ^{10}Be core + particle structure without rotational band structure. The ^{11}Be states can be considered as single-particle states with the neutron in the open $1p1/2$, $1d5/2$, and $1d3/2$ orbits and also in the $1p3/2$ orbit, which is not occupied by about 30% in the ^{10}Be ground state through configuration mixing. In ^{12}Be, the same states are populated as in the ^{10}Be(t, p) reaction [13, 14]; they have a $(1p1/2)^{-1}(sd)^1$ and also a $(sd)^2$ structure. Theoretical calculations confirm the molecular structures in ^{11}Be [15] and ^{12}Be [16].

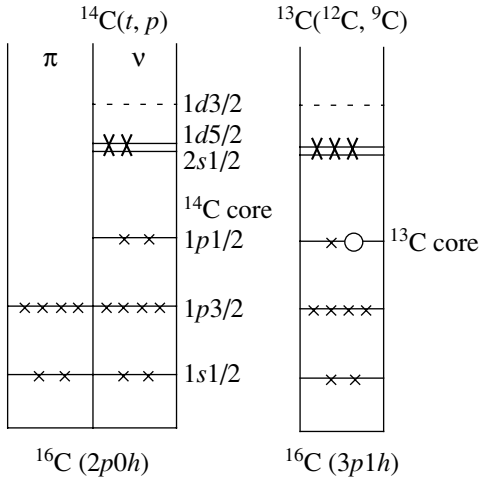

Fig. 6. Comparison of the main structures populated in ^{16}C in the first order by the (t, p) and the (^{12}C, ^{9}C) reactions: these are $2p0h$ and $3p1h$ configurations, respectively.

2.2. Spin-Parity Assignments in ^{11}Be below 4-MeV Excitation Energy

The spin parities of the low-lying states in ^{11}Be were assigned first in the ^{9}Be(t, p) reaction by Ajzenberg-Selove *et al.* [17], who assigned $3/2^-$ to the state at 3.96-MeV excitation energy due to its very characteristic shape of the measured angular distribution for an $\ell = 0$ transfer, and by Liu and Fortune [18], who analyzed the angular distributions up to 5.86 MeV by DWBA calculations and assigned $3/2^-$, $3/2^+$, and $3/2^-$ to the states at 3.41, 3.89, and 3.96 MeV, respectively.

In the $(d, 2p)$ reaction [19] and also in the $(t,$ ^{3}He) reaction [20], a strong state was observed at about 3.9 MeV (the 3.89/3.96 MeV doublet was not resolved) and an assignment of $5/2^-$ was given to the 3.89-MeV state. Furthermore, Millener [11] assigned $3/2^-$, $3/2^+$, and $5/2^-$ to the states at 3.41, 3.89, and 3.96 MeV, respectively, from the systematics in shell model calculations.

We performed two-neutron stripping and two-proton pickup reactions in order to contribute to the clarification of the situation. The reactions were chosen carefully in such a way that we should be able to observe characteristic shapes of the angular distributions. For this reason, reactions with the special feature of a $0^+ \to 0^+$ projectile transition were used, namely, the ^{9}Be(^{16}O, ^{14}O) reaction for the two-neutron transfer and the ^{13}C(^{12}C, ^{14}O) reaction for the two-proton pickup. The corresponding angular distributions are shown in Figs. 3 and 4, respectively. It should be emphasized that different peak positions were observed in the spectra for the two reactions

Table 1. Configurations and spin parities of ^{16}C basis states coupled from three neutrons in the $1p1/2$, $2s1/2$, and $1d5/2$ shells to a $^{13}C_{g.s}$ core (the true states will have strong configuration mixing)

Core	$1p1/2$		$2s1/2$		$1d5/2$		J^π	Config. (n, n, n)
	n	$(j^\pi)^n$	n	$(\gamma^\pi)^n$	n	$(j^\pi)^n$		
^{14}C	2	0^+	2	0^+	0	–	0^+	(220)
	2	0^+	0	–	2	0^+	0^+	(202)
						2^+	2^+	
						4^+	4^+	
	2	0^+	1	$1/2^+$	1	$5/2^+$	$2^+, 3^+$	(211)
^{13}C	1	$1/2^-$	2	0^+	1	$5/2^+$	$2^-, 3^-$	(121)
	1	$1/2^-$	1	$1/2^+$	2	0^+	$0^-, 1^-$	(112)
						2^+	$2^-, 3^-$	
						4^+	$4^-, 5^-$	
	1	$1/2^-$	0	–	3	$5/2^+$	$2^-, 3^-$	(103)
						$7/2^+$	$3^-, 4^-$	
						$9/2^+$	$4^-, 5^-$	

in the region of the doublet at 3.9 MeV, which indicates the population of mainly one member in either reaction: the 3.96(3)-MeV state in the $2n$-stripping reaction and the 3.90(3)-MeV state in the $2p$-pickup reaction. Therefore, we are able to determine from the phase of the observed angular distributions at least the parities of the considered states. The comparison with calculations of different ℓ transfers using the code Ptolemy [21] shows that the 3.96-MeV state has odd parity. Taking into account especially the deep structure in the (t, p) angular distribution of Ajzenberg-Selove, our result confirms the assignment of $3/2^-$ to this state.

The $2p$-pickup reaction populates the states at 0.32, 2.70, and 3.90 MeV. All three angular distributions show the same shape (see Fig. 4); therefore, the 3.90-MeV state must have odd parity. Here, the assignment of $5/2^-$ is supported by the results from the charge-exchange reactions [19, 20] and also from the systematics of the shell model calculations, where the $5/2^-$ assignment was originally given to the other doublet member at 3.96 MeV. The 3.41-MeV state is not at all populated in this reaction and only very weakly in the $2n$-stripping reaction (see Fig. 3); no significant conclusion can be drawn from these data for this state. However, there was an indication that it is populated in the one-neutron transfer on ^{10}Be; a $3/2^+$ state could be here. Liu and Fortune [18] used in the fit of the angular distribution of this state the ℓ-transfer value $\ell_t = 0$, although the calculation with $\ell_t = 1$, which is shown for the 3.89-MeV state, definitely fits the 3.41-MeV data better than the $\ell_t = 0$ calculation. In this situation, a $3/2^+$ spin parity is the most probable assignment to this state. This is also supported by the shell-model calculations, which predict in this excitation-energy region such a state [11].

We obtain as a result the spin-parity assignments $3/2^+$, $5/2^-$, and $3/2^-$ for the states at 3.41, 3.89, and 3.96 MeV, respectively.

3. SPECTROSCOPY OF ^{16}C STATES

The nucleus ^{16}C is interesting in connection with structure studies of more neutron-rich carbon isotopes, because two-particle configurations and also particle–hole excitations of one or two neutrons from the $1p$ shell to the sd shell are important. States of ^{16}C were investigated in the past only by the $^{14}C(t, p)$ reaction [22–24], where states up to 6.1-MeV excitation energy were populated. We now studied the states of ^{16}C using the $^{13}C(^{12}C, ^9C)$ reaction and observed excited states up to 17.4 MeV. The ^{16}C spectrum is shown in Fig. 5 (upper panel); 14 previously unknown states are identified. In the lower panel, the spectrum of the $^{12}C(^{12}C, ^9C)^{15}C$ reaction is shown, which could be used for a precise calibration, because states are known here up to 11.82 MeV (the five states observed at higher excitation energies were previously unknown).

Below 5-MeV excitation energy, four known states including the ground state are not observed, only the 2^+ state at 1.77 MeV and the 4^+ state at 4.14 MeV. The explanation for this can be found in the dynamical matching conditions of this three-neutron transfer, since final states with $\ell = 0$ (here, $2s1/2$) are suppressed by the transfer mechanism in the surface region at our incident energy, whereas states with $\ell = 2$ are favored. The effect is even enhanced when two neutrons are transferred into such orbits.

Above 6-MeV excitation energy, it is expected that states with one hole in the $1p1/2$ shell will appear, since the lowest negative-parity state in ^{14}C (1^- state) is located at 6.1 MeV and corresponds to the $(1p1/2)^{-1}(2s1/2)^1$ particle–hole configuration. These configurations cannot be directly excited in the $^{14}C(t, p)$ reaction (see Fig. 6), whereas the $^{13}C(^{12}C, ^9C)$ reaction is well suited for this purpose. Table 1 shows a compilation of possible configurations that can be obtained from the different spin couplings of three neutrons in the $1p1/2$, $2s1/2$, and $1d5/2$ shells on ^{13}C. The configurations are ordered according to the number n of neutrons in the $1p1/2$ shell (^{14}C and ^{13}C cores) and, furthermore, in the $2s1/2$ and $1d5/2$

Table 2. Results for ^{16}C: excitation energies, widths (only for resonances), differential cross sections, probable configurations (see Table 1), and spin parities (the last column shows the results obtained with the $^{14}C(t,p)$ reactions)

^{16}C states	$^{13}C(^{12}C,^{9}C)^{16}C$ 230.7 MeV, 4°–7°			$^{14}C(t,p)$ [22–24]
E_x, MeV	Γ_R, MeV	$d\sigma/d\Omega$, μb/sr	probable configuration	J^π
0.00		–	(220) + (202)	0^+
1.77		0.047	(202) + (211)	2^+
3.03		–	(202) + (220)	(0^+)
3.98		–	(211) + (202)	2
4.09		–	(211)	$3^{(+)}$
4.14		0.9	(202)	4^+
$S_n = 4.25$ MeV				
6.11	< 0.025	< 0.02	(121)	$(2^+, 3^-, 4^+)$
7.74	0.20	0.15	(112) + (103)	
(8.50)	(0.05)	0.023	(112)	
8.92	0.10	0.68	(103)	
9.42	0.10	0.18	(112) + (103)	
9.98	0.12	0.41	(103)	
10.39	0.15	0.16	(103)	
11.08	0.10	0.05		
11.85	0.22	0.36		
12.54	0.20	0.14		
13.12	0.40	0.47		
14.26	0.20	0.07		
14.90	0.30	0.13		
16.44	0.15	0.19		
17.4	0.2	0.12		

shells. For example, the $(1p1/2)^{-1}(2s1/2)^2(1d5/2)$ configuration is given by the label (121). The true states will have strong configuration mixing of these basis states.

In Table 2, our results for ^{16}C are summarized together with the (t, p) spin assignments [22–24]: excitation energies, widths of the resonances, and cross sections observed in the (^{12}C, ^{9}C) reaction are given. In the next column, the main configurations are given for known spin parities, and for the new states, possible configurations are estimated according to the observed cross sections and the expected localization of these configurations in a weak coupling model. Large cross sections indicate the population of a $(1d5/2)^3$ or at least a $(1d5/2)^2(2s1/2)$ configuration. The strong 8.92-MeV state is probably a 5^- state with the (103) configuration. The whole group of states between 7.74 and 10.39 MeV probably has this configuration (with further mixed-in (112) components), since, in a weak coupling between the $1p1h$ configuration at 6.7 MeV in ^{14}C and the 2^+ or 4^+ excitation at 1.77 and 4.14 MeV, respectively, we arrive in the designated region of excitation energy. Partial angular distributions, which we obtained for the strongest transitions, do not show very characteristic shapes for the ℓ transfer that would allow a unique spin assignment. A definite spin-parity assignment, also for the higher lying states, is diffuclt.

4. CONCLUSIONS

Specific cluster structures have been investigated in neutron-rich beryllium isotopes, and pronounced molecular structures with almost separated α particles have been found. Rotational bands are built on these structures, and the α–α distance in the core could be estimated from the corresponding moment of inertia. Spin-parity assignments have been given for states in ^{11}Be, where controversial values existed in the literature. This could be achieved by using selected reactions that populate the states by different mechanisms. Furthermore, we have populated states of ^{16}C in a three-neutron transfer reaction and investigated in this way, in particular, particle–hole states in this nucleus. The level scheme has been extended by 14 previously unknown states. New states have also been observed for the ^{15}C nucleus.

REFERENCES

1. W. von Oertzen, Z. Phys. A **357**, 355 (1997).
2. M. Freer and A. C. Merchant, J. Phys. G **23**, 261 (1997) (and references therein).
3. A. Ali and A. R. Bodmer, Nucl. Phys. **80**, 99 (1966).
4. D. Scharnweber, W. Greiner, and U. Mosel, Nucl. Phys. A **164**, 257 (1971); J. M. Eisenberg and W. Greiner, *Nuclear Theory* (North-Holland, Amsterdam, 1975), Vol. 1, p. 571.
5. F. Ajzenberg-Selove, Nucl. Phys. A **490**, 1 (1988); **506**, 1 (1990).
6. P. Descouvemont, Eur. Phys. J. A **12**, 413 (2001).
7. H. G. Bohlen *et al.*, Prog. Part. Nucl. Phys. **42**, 17 (1999).
8. H. G. Bohlen *et al.*, in *Proceedings of the ENPE99 Conference, Sevilla, 1999*, Ed. B. Rubio *et al.*; AIP Conf. Proc. **495**, 303 (1999).
9. M. Freer *et al.*, Phys. Rev. Lett. **82**, 1383 (1999).
10. M. Freer *et al.*, Phys. Rev. C **63**, 34301 (2001).
11. D. J. Millener, Nucl. Phys. A **693**, 394 (2001).
12. H. de Vries *et al.*, At. Data Nucl. Data Tables **36**, 495 (1987).
13. H. T. Fortune, G. B. Liu, and D. E. Alburger, Phys. Rev. C **50**, 1355 (1994).
14. D. E. Alburger *et al.*, Phys. Rev. C **17**, 1525 (1978).
15. Y. K. Kanada-Enyo and H. Horiuchi, Phys. Rev. C **66**, 024305 (2002).
16. P. Descouvemont and D. Baye, Phys. Lett. B **505**, 71 (2001).
17. F. Ajzenberg-Selove, R. F. Casten, O. Hansen, *et al.*, Phys. Lett. B **40**, 205 (1972); F. Ajzenberg-Selove, E. R. Flynn, and O. Hansen, Phys. Rev. C **17**, 1283 (1978).
18. G. B. Liu and H. T. Fortune, Phys. Rev. C **42**, 167 (1990).
19. H. Sakai *et al.*, Phys. Lett. B **302**, 7 (1993); T. Inomata, H. Akimune, I. Daito, *et al.*, Phys. Rev. C **57**, 3153 (1998).
20. I. Daito, H. Akimune, S. M. Austin, *et al.*, Phys. Lett. B **418**, 7 (1998).
21. M. Rhoades-Brown, M. H. Macfarlane, and S. C. Pieper, Phys. Rev. C **21**, 2417 (1980); **21**, 2436 (1980).
22. D. P. Balamuth, J. M. Lind, K. C. Young, Jr., and R. W. Zurmühle, Nucl. Phys. A **290**, 65 (1977).
23. H. T. Fortune, R. Middleton, M. E. Cobern, *et al.*, Phys. Lett. B **70B**, 408 (1977).
24. R. R. Sercely, R. J. Peterson, and E. R. Flynn, Phys. Rev. C **17**, 1919 (1978).

Physics of Atomic Nuclei, Vol. 66, No. 8, 2003, pp. 1501–1507. From Yadernaya Fizika, Vol. 66, No. 8, 2003, pp. 1546–1552.

Structure Studies of Exotic Nuclei Using (p,p') Reactions*

V. Lapoux[1)], N. Alamanos[1)], and E. Khan[2)]**

[1)] *DSM/DAPNIA/SPhN, CEA/Saclay, Gif-sur-Yvette, France*

[2)] *Institut de Physique Nucléaire, Orsay, France*

Received August 28, 2002

Abstract—The structure of radioactive beams is investigated using the simplest possible probe: the proton used as a target in inverse kinematic reactions. From (p,p') reactions, information on the neutron and proton transition densities is obtained through the comparison between the measured inelastic cross sections and the ones calculated using a microscopic potential and theoretical densities. (p,p') inelastic scattering data to the first excited state for the halo nucleus ^{6}He and for other nuclei ^{34}Ar and ^{34,36}S have been measured at GANIL using the MUST telescopes. This allows one to extract the global features of the transition densities, as shown for the halo nucleus ^{6}He. We can also probe the evolution of the shell structure along isotopic chains in moving towards the neutron or proton drip lines. The example of the sulfur isotopic chain is discussed. © *2003 MAIK "Nauka/Interperiodica"*.

1. MOTIVATIONS FOR STRUCTURE STUDIES

We perform structure studies using (p,p') reactions. Our aim is to obtain the spatial repartition of the nucleons of exotic nuclei, namely, the densities, ground-state and transition densities to excited states. The observables for the structure studies are angular cross sections of elastic and inelastic scattering.

The nuclear structure of stable nuclei is obtained through an electron scattering experiment, and this gives charge and then proton densities by unfolding the proton distribution. With electrons, we rely on the very well-known electromagnetic interaction to obtain the repartition of the protons. The neutron densities were deduced by using hadronic probes: proton, alpha, pions. Far from the valley of stability, the species are short-lived radioactive nuclei and cannot form targets, so we rely on the simplest probe, protons, used as a target in inverse kinematics experiments. Proton elastic scattering is a well-known tool for the study of ground-state densities, since the interaction potential can be related to the ground-state nuclear densities. In the case of radioactive nuclei, the interpretation of the data is complex, since we are dealing with nuclei having low threshold energies. They can easily couple to excited states or to continuum states during their interaction with a target, and the theoretical difficulty is to calculate the couplings accurately, to extract unambiguously information on the structure. Experimentally, the difficulty is to work with radioactive beams having lower and lower intensities in moving towards the drip lines. With high statistics, if a large transfer momentum is covered, it is possible to extract accurately from (p,p') data the radial structure of the nucleus as was done in the case of ^{18}O in [1]. For radioactive beams, generally the poor statistics do not allow one to give precisely the ground-state and transition densities as a function of the radial coordinate. Nevertheless, the (p,p') are a good tool to constrain the structure models proposed for the exotic nuclei: from (p,p'), we can deduce the features of the transition densities allowing one to reproduce the data and compare them to the theoretical data. During the last fifteen years, elastic and inelastic scattering direct reactions like Coulomb excitation (Coulex) and (p,p') were performed with radioactive beams to learn about the proton and neutron transition densities. Different scenarios, including core polarization mechanisms and neutron and proton interaction with the core, can be evoked to describe these transition densities. It is possible to know if we need a change in the description of the shells, deformation in neutron and proton densities, and large enhancement in proton and neutron transition probabilities.

For instance, in the case of light neutron-rich nuclei, we can test densities with neutron halo or skin developing "exotic" forms, compared to the stable nuclei. The halo is a direct consequence of the weak binding energies of the valence nucleons: in the case of ^{6}He, the two-neutron separation energy is small, 975 keV, which allows the wave functions to extend

*This article was submitted by the authors in English.

** e-mail: vlapoux@cea.fr

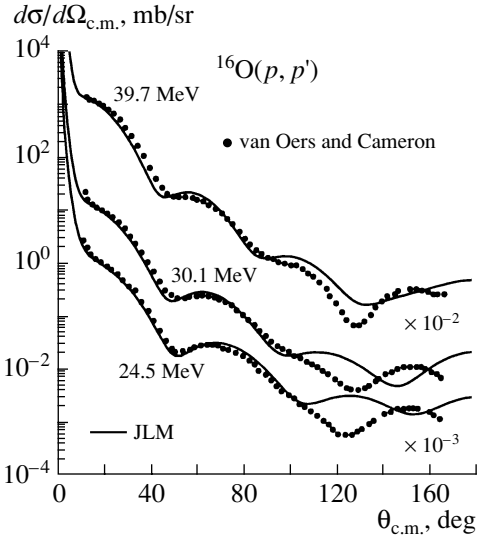

Fig. 1. Comparison between experimental data for the proton elastic scattering of ^{16}O and calculations done using the JLM potential as described in the text.

far from the core potential [2, 3]. These exotic nuclei are changing the normal rules of our textbooks of nuclear physics. Sizes are different from what is expected from the short range of the nuclear force and correlations play an important role [4], the decay to cluster states is favored, the proton and neutron may behave differently (see the report on neutron-rich boron isotopes by Oertzen [5]), and magicity may disappear.

By (p, p') reactions, we can probe the structure and test the prediction of models (either cluster or mean-field models) for the densities. Our tool to analyze the data is a microscopic potential that is introduced in the following section.

2. ANALYSIS OF (p, p') REACTIONS USING THE MICROSCOPIC POTENTIAL

2.1. The Microscopic JLM Potential

The nucleus–nucleon interaction for the elastic scattering on protons is taken as the microscopic, complex, and parameter-free JLM (Jeukenne, Lejeune, Mahaux) potential [6]. This potential is based upon infinite matter calculations, and it is built on the Reid hard-core nucleon–nucleon (NN) interaction, using the Brueckner–Hartree–Fock approximation. An improved local density approximation is applied to derive the potential in the case of a finite-range nucleus of density ρ and neutron and proton densities ρ_n and ρ_p. The complex local JLM potential depends only on incident energy E and on ρ_p and ρ_n. The JLM potential was parametrized for incident energies $E \leq 160$ MeV. In general, it is written using the normalization factors λ_V and λ_W for the real and imaginary parts:

$$U_{\rm JLM}(\rho, E)(r) = \lambda_V V(\rho, E)(r) + i\lambda_W W(\rho, E)(r) \quad (1)$$

for $A \geq 20$, λ_V and λ_W can be slightly modified (less than 10%) to fit the nucleus–nucleon data, but they are close to 1 for all $A \geq 20$ stable nuclei. It was shown that, usually in the case of light nuclei ($A \leq 20$), $\lambda_W = 0.8$ [7]. We adopt it as the standard normalization of JLM for light nuclei. This potential allows a good reproduction of large sets of nucleon–nucleus data [7–9]. Figure 1 shows it in the case of the light stable nucleus ^{16}O. The potential is calculated using a two-parameter Fermi (2pF) density for ^{16}O. The parameters of the 2pF proton density are fitted on the density extracted from the electron scattering.

The inelastic (p, p') angular cross sections are obtained through distorted wave Born Approximation (DWBA) calculations including the JLM potential. They are performed with the TAMURA code [10]. The entrance, transition, and exit channel potentials are defined with the ground-state and transition density. The normalization of the real and imaginary parts is fixed with the values obtained in the analysis of the elastic scattering. For a J_i to J_f transition, the density is written $\rho^{\rm tr} = \langle \Psi_f | \delta(\mathbf{r} - \mathbf{r}')) | \Psi_i \rangle$. The calculated inelastic (p, p') cross sections are sensitive to the M_n and M_p factors, which are the radial moments of the transition densities:

$$M_{p(n)} = \int dr r^{l+2} \rho^{\rm tr}_{p(n)}, \quad (2)$$

with l being the multipolarity of the transition. These factors can also be expressed as the matrix elements of the electromagnetic multipole operators $O^l_{p(n)}$ between nuclear states [11]:

$$M_{p(n)} = \langle J_f T T_z | O^l_{p(n)} | J_i T T_z \rangle. \quad (3)$$

The M_p factor is directly related to the $B(El)$ transition strength value obtained by the Coulex experiment. We adopt here the following convention for the relationship between $|M_p|$ and $B(El)$:

$$B(El, J_i \to J_f) = \frac{(2J_f + 1)}{(2J_i + 1)} |M_p|^2. \quad (4)$$

The models of elastic and inelastic scattering on a proton including the potential JLM were proven to be reliable to extract the fundamental quantities such as M_n/M_p without ambiguity for stable nuclei [8] as well as for exotic nuclei [9, 12]. $M_{p(n)}$ can be used as a signature for the modification of the shell structure

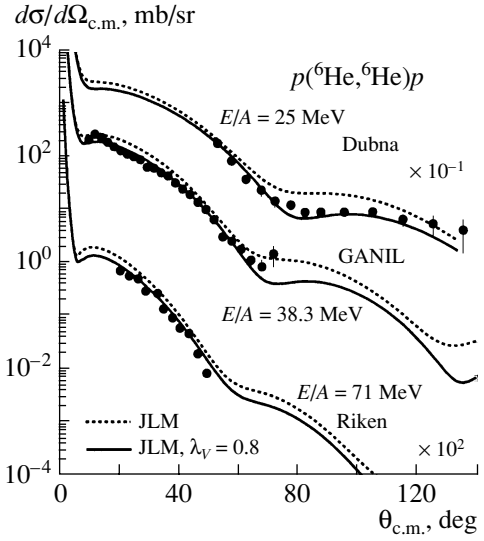

Fig. 2. The $^6\mathrm{He} + p$ GANIL data at 38.3 MeV/nucleon are plotted with previous data obtained at Dubna in the first experiment [19] at 25 MeV/nucleon and at Riken [20] at 71 MeV/nucleon. The dashed curves are calculated with the JLM potential. The solid curves reproduce the data with a reduction of the real part by a factor of 0.8.

and compared to the values predicted by different structure models.

A simple analysis of the (p, p') can be performed using the phenomenological Tassie form [13] for the densities. The proton (p) or neutron (n) transition density is obtained by deriving the ground-state density,

$$\rho^{\mathrm{tr},l}_{p(n)}(r) = -\alpha^l_{p(n)} r^{l-1} \frac{d\rho_{p(n)}}{dr}. \qquad (5)$$

The proton density is normalized with the α^l_p by requiring that its moment $|M_p|$ should satisfy Eq. (4) with $B(E2)$ obtained by Coulex. $|M_n|$ is then deduced by adjusting calculated (p, p') on the data.

2.2. Role of the Coupling to the Continuum in Elastic Scattering: The $^6He + p$ Entrance Channel

For the analysis of direct reactions, we need the potential of the entrance channel, namely, the potential deduced from elastic scattering. To study the effect of the weak binding on the interaction potential between a light exotic nucleus and a target, elastic scattering cross sections of the ^{6}He secondary beam at 38.3 MeV/nucleon on a proton have been measured at GANIL. The $^6\mathrm{He} + p$ results, as well as other existing data, are analyzed within the framework of the microscopic JLM potential [6]. A halo-type density given by few-body model calculations [14], with

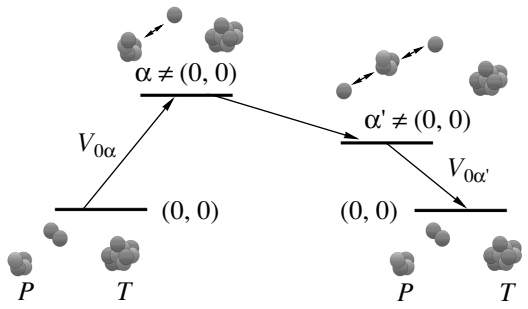

Fig. 3. Scheme of the virtual couplings occurring during an elastic scattering between projectile P and target T. They contribute to the DPP term in the total elastic optical potential.

a matter root-mean-square (rms) radius of 2.55 fm, was used to generate the potential. The rms value of this density corresponds to the value obtained by few-body analysis [15] of the high-energy $^6\mathrm{He} + p$ elastic scattering [16]. We have shown [17, 18] that the angular distributions of ^{6}He on a proton are better reproduced with a reduction of the real part of the JLM optical potential as seen in Fig. 2. The origin of this effect was discussed in [21] and may be explained within the theory developed by Feshbach [22]. According to this theory, the interaction potential should be written as $U = V + U_{\mathrm{pol}}$, where V is the usual real potential and U_{pol} is the dynamical polarization potential (DPP). V can be seen as the folding potential or the elastic potential described by microscopic or phenomenological models. It includes only the interaction between the projectile and the target ground states. The DPP is complex, nonlocal, and energy-dependent; it arises from couplings to inelastic channels. For well-bound nuclei, the probability of excitation during elastic scattering is weak, and the main contribution is imaginary, represented by the usual phenomenological imaginary part W. For weakly bound nuclei, the particle threshold is close to their ground state, which favors couplings to the excited states and to the continuum during their interaction with a target. This leads to a greater influence of the DPP and then to the reduction of the real part of the nuclear potential [23]. Therefore, one must take into account in the analysis the interaction potential term due to transitions going to the excited states and then back to the ground state [21]. However, the precise calculation of the DPP requires knowledge of the spectroscopy of the nucleus and also knowledge of low-lying resonant states and couplings to the continuum. The scheme for such a transition occurring during elastic scattering is presented in Fig. 3. It was explained in [23, 24] that a complex surface potential, with a repulsive real part, is expected to

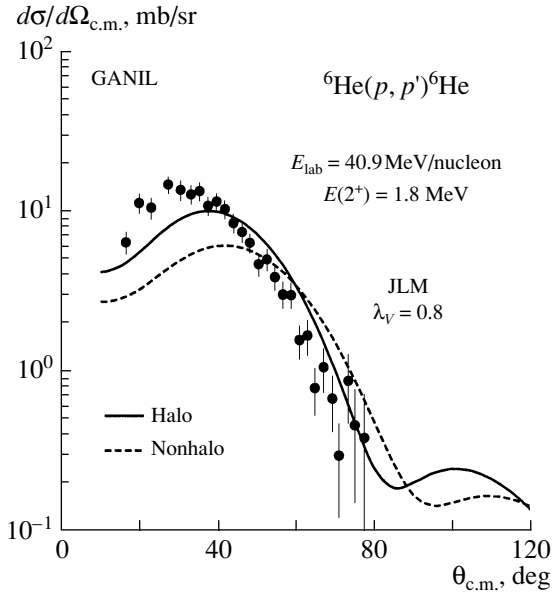

Fig. 4. Comparison between data [25] obtained at 40.9 MeV/nucleon using MUST and JLM calculations allowing one to test two kinds of phenomenological transition densities based on the Tassie model.

simulate the surface effects generated by the polarization potential and this corresponds to the reduction of the real part [17]. This effect is observed in ^{6}He + p scattering, analyzed with the JLM potential [18] and shown in Fig. 2. By taking it into account in the JLM calculation, we have successfully reproduced the data at 38.3 MeV/nucleon together with other data for ^{6}He on a proton measured at Riken [20] at $E/A =$ 71 MeV and at Dubna [19] at $E/A = 25$ MeV. The whole set of data is compared to the calculations in Fig. 2 [18].

Recently, the structure of the halo nucleus ^{6}He was explored through proton inelastic (p, p') scattering [25]. The interaction potential tested on elastic scattering will be used in the calculation of the (p, p') scattering.

2.3. Experimental Setup

For (p, p') reactions, the experimental apparatus MUST [26], an array of three-stage telescopes (a set of Si strips, SiLi and CsI telescopes) specifically designed to detect recoiling light charged particles, was used to measure angular distributions for elastic and inelastic scattering of radioactive beams on a proton target. Using MUST, (p, p') scattering data to the first excited state of ^{6}He at 1.8 MeV were measured with a 40.9-MeV/nucleon ^{6}He beam produced at GANIL [25]. The MUST detector detected the recoil proton in coincidence with a plastic scintillator measuring the heavy nucleus focused at a forward angle. The profile of the incident beam was given by two multiwire chambers, CATS [27], developed by the DAPNIA/SED. Energy, time of flight (between MUST and CATS), and position of the light charged particle were measured in the MUST detector, allowing for a full reconstruction of the (p, p') kinematics. Inelastic scattering on a proton, to the first excited states, below the proton separation threshold, for the nuclei ^{10,11}C was also measured at $E_{lab} \simeq$ 40 MeV/nucleon using the MUST device. A sketch of the experimental device can be found in [28], as well as a description of the analysis performed in this case.

By (p, p'), we can probe the structure and test the prediction of models (either cluster or mean-field models) for the densities.

3. DISCUSSION OF THE ^{6}He(p, p') REACTION

(p, p') scattering data to the first excited state of ^{6}He at 1.8 MeV have been measured at GANIL with the MUST telescopes. The results obtained at 40.9 MeV/nucleon [25] allow one to test different shapes for the transition densities. Here, we test two options for the ground-state and transition densities included in the JLM potential: one corresponding to a nonhalo case, with a matter rms radius equal to 2.2 fm, and the other one having the features of a halo density, namely, the large extension of the neutron density, and a larger matter rms radius of 2.5 fm. The transition densities are derived from ground-state densities by applying the Tassie model as was explained in Section 2.1. The calculations of the (p, p') cross sections for these two options are compared with the experimental data. We renormalized the theoretical proton transition in order to obtain a $B(E2)$ corresponding to the experimental value $(3.1 \pm 0.6 e^2$ fm$^4)$ given in [29]. The M_p value given by Eq. (4) is equal 0.79 fm^2. To reproduce the (p, p') data, we have to renormalize the neutron densities given by the Tassie model, and this corresponds to M_n/M_p equal to 4.4 or to 2.7 for the halo and nonhalo cases for the densities, respectively. In Fig. 4, the dashed and solid curves correspond to the nonhalo and halo options, respectively. The ^{6}He(p, p') analysis using JLM is in favor with the halo configuration for this nucleus. Here, we can provide a realistic shape for the neutron and proton ground-state and transition densities, which can be easily compared to the structure for ^{6}He predicted theoretically. A precise analysis including directly the effects of the couplings to the continuum was done using the discretized coupled-channel calculations (CDCC) and a dineutron model

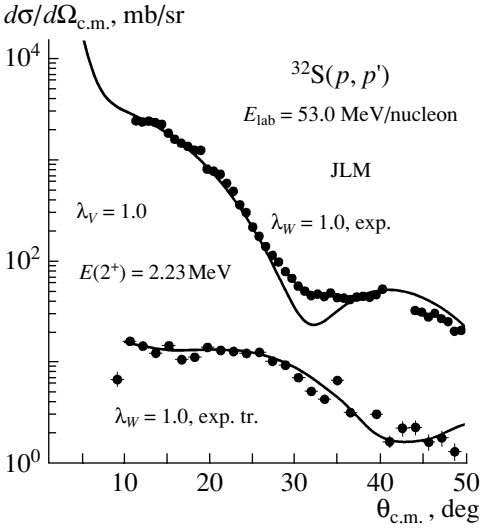

Fig. 5. Experimental $^{32}S(p, p')$ angular distributions measured at 53 MeV/nucleon are compared to calculations performed with the JLM potential and using experimental densities, as described in the text.

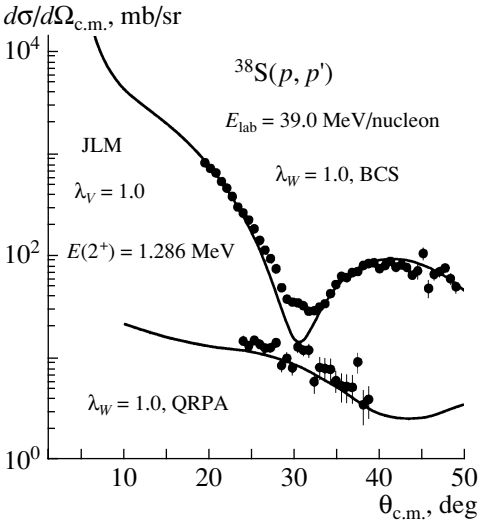

Fig. 6. Comparison between JLM calculations and experimental $^{38}S(p, p')$ elastic and inelastic distributions for the 2_1^+ state. The JLM potential is calculated using the ground-state densities obtained with HF + BCS and transition densities from QRPA model.

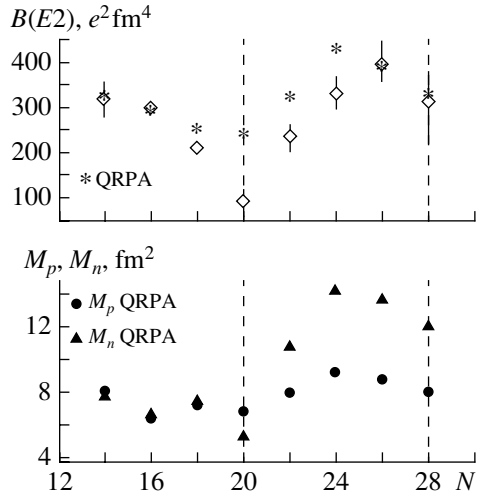

Fig. 7. (Top) Comparison for sulfur isotopes between calculated $B(E2)$ values (asterisks) and experimental ones (diamonds). (Below) M_n and M_p calculated values as a function of the neutron number N.

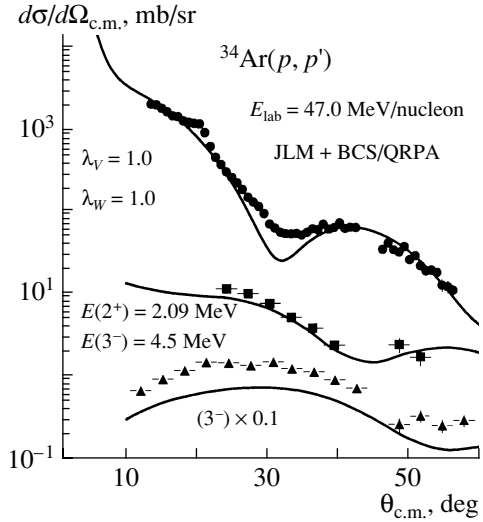

Fig. 8. (p, p') ^{34}Ar elastic and inelastic angular distributions for the 2^+ and 3^- states measured at 47 MeV/nucleon. Data are compared with calculations using the JLM potential and densities obtained with HF + BCS and QRPA models.

for ^{6}He [30]. It was applied to the ^{6}He + p elastic, inelastic, and transfer data measured at Dubna. It helps in determining the influence of the DPP. Nevertheless, through optical model calculations based on the JLM model, we directly test the densities. Both approaches are complementary: the CDCC to fix the couplings, and the JLM model to extract the densities.

$^{10,11}C(p, p')$ scattering data were also measured using the MUST detectors. These nuclei, like the other carbon isotopes described in the theory of the antisymmetrized molecular dynamics (AMD) [31] are expected to have a proton density with an oblate deformation. The aim of the experiment was to obtain structure information for these two neutron-deficient radioactive nuclei and to compare data to calculations performed with different models predicting the ground-state and transition densities. The analysis performed with the JLM potential is explained in these Proceedings [28].

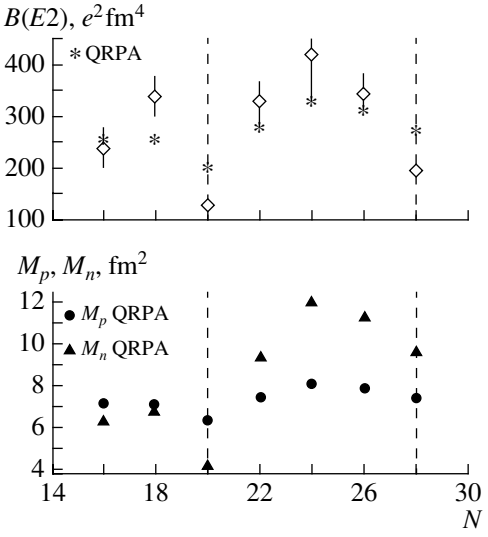

Fig. 9. Same as in Fig. 7, but for argon isotopes.

4. EVOLUTION OF THE SULFUR ISOTOPES

The ground-state neutron and proton densities are given from HF + BCS (*SGII*) calculations using the *SGII* parametrization of the effective Skyrme interaction. The transition densities are obtained through QRPA calculations with *SGII*. They are described in [32].

These calculations are well suited to interpret the excitations in terms of particle–hole (or two quasiparticles) configurations. To show the validity of the JLM interaction, we have performed a test calculation on the stable nucleus ^{32}S using the experimental ground-state and transition densities $0^+ \to 2^+$ of ^{32}S. The proton densities are deduced from the charge densities known from $(e,\ e')$ scattering, and we assume that the neutron densities are identical to the proton ones in performing the JLM calculations. The good agreement obtained with the MUST data measured at 53 MeV/nucleon is shown in Fig. 5. For this stable nucleus, no renormalization of the real part is needed, nor of the imaginary part, since we are in this intermediate-mass region. We also adopt for all sulfur isotopes the normalization factor $\lambda_W = 1$. For ^{38}S, the QRPA calculations give reasonable agreement with the data, as displayed by Fig. 6. As shown in Fig. 7, the trend of the $B(E2)$ values is well reproduced by the QRPA calculations. When crossing the shell gap, the shell closure $N = 20$ can be clearly seen as a minimum of the $B(E2)$ values (combined with the increase in the 2^+ excitation energies and decrease in S_{2n} separation energies). For the sulfur isotopes, the $N = 20$ closure is well seen on the $B(E2)$ and, correspondingly, in the evolution of the M_p. The trend of the M_n value is also interesting: the evolution of the neutron excitations is close to the one of the protons, which shows collective behavior of the densities. Proton elastic and inelastic scattering angular distributions to the 2_1^+ and 3_1^- states of ^{34}Ar were measured using the MUST Si-strip detector array with a secondary beam produced at GANIL. They are presented in Fig. 8. The agreement is good for the elastic and inelastic scattering to the 2^+, but the 3^- angular distribution is overestimated by the calculations. The measurement of the 3^- distribution is a good constraint on the models: we test the treatment of negative parity states in ^{34}Ar, implying particle–hole excitations across a shell gap. The calculated M_p and M_n values for the argon isotopes (see Fig. 9) show that $N = 20$ remains a good magic number, but for $N = 28$, the decreases in M_n and M_p are less pronounced, indicating a possible weakening of the shell effects. Coulex and (p, p') data are needed for ^{45,46}S and ^{47,48}Ar in order to clarify the picture.

As can be seen in the case of sulfur and argon isotopes, extracting the systematic behavior along isotopic chain from the neutron-deficient to neutron-rich side and combining the $B(E2)$ value (i.e., $|M_p|$) and M_n can provide a strong constraint on the theoretical shell structure models.

5. PERSPECTIVES USING THE (p, p') TOOL

The next generation facilities are expected to deliver radioactive beams at high intensities allowing one to extract precisely the nuclear transition densities, as was done in the past for stable beams [1], by leading model-independent analysis of the (p, p') reactions. At present, we can probe the transition densities predicted by shell model, HFB, QRPA, or cluster-model calculations. Since the elastic potential is the entrance channel of all more complicated direct reactions, like inelastic scattering and transfer reactions, it has to be correctly tuned on the elastic scattering. The measurement of the elastic scattering is required, if reliable information on structure has to be extracted from inelastic or transfer reactions. In our case, it has allowed us to probe the transition densities from the ground to the first excited state of the nuclei ^{6}He and ^{10}C, and for sulfur and argon isotopes.

REFERENCES

1. J. Kelly *et al.*, Phys. Rev. C **41**, 41 (1990).
2. P. G. Hansen and B. Jonson, Europhys. Lett. **4**, 409 (1987).
3. S. N. Ershov *et al.*, Phys. Rev. C **56**, 1483 (1997).
4. Y. Oganessian, this Conference.
5. W. von Oertzen, this Conference.

6. J. P. Jeukenne, A. Lejeune, and C. Mahaux, Phys. Rev. C **16**, 80 (1977).
7. J. S. Petler *et al.*, Phys. Rev. C **32**, 673 (1985).
8. S. Mellema, R. Finlay, F. Dietrich, and F. Petrovich, Phys. Rev. C **28**, 2267 (1983).
9. N. Alamanos, F. Auger, B. A. Brown, and A. Pakou, J. Phys. G **24**, 1541 (1998).
10. T. Tamura, W. R. Coker, and R. Rybicki, Comp. Phys. Comm. **2**, 94 (1971).
11. A. M. Bernstein, V. R. Brown, and V. A. Madsen, Phys. Rev. Lett. **42**, 425 (1979).
12. E. Khan *et al.*, Phys. Lett. B **490**, 45 (2000).
13. G. R. Satchler, *Direct Nuclear Reactions* (Clarendon Press, Oxford, 1983).
14. J. Al-Khalili, J. Tostevin, and I. Thompson, Phys. Rev. C **54**, 1843 (1996).
15. J. S. Al-Khalili and J. A. Tostevin, Phys. Rev. C **57**, 1846 (1998).
16. G. D. Alkhazov *et al.*, Phys. Rev. Lett. **78**, 2313 (1997).
17. V. Lapoux, PhD Thesis (Université d'Orsay, 1998).
18. V. Lapoux *et al.*, Phys. Lett. B **517**, 18 (2001).
19. R. Wolski *et al.*, Phys. Lett. B **467**, 8 (1999).
20. A. A. Korsheninnikov *et al.*, Nucl. Phys. A **617**, 45 (1997).
21. M. E. Brandan and G. R. Satchler, Phys. Rep. **285**, 143 (1997).
22. H. Feshbach, Ann. Phys. (N.Y.) **5**, 357 (1958).
23. Y. Sakuragi *et al.*, Prog. Theor. Phys. **70**, 1047 (1983).
24. Y. Sakuragi, Phys. Rev. C **35**, 2161 (1987).
25. A. Lagoyannis *et al.*, Phys. Lett. B **518**, 27 (2001).
26. The MUST Collab., Nucl. Instrum. Methods Phys. Res. A **421**, 471 (1999).
27. S. Ottini *et al.*, Nucl. Instrum. Methods Phys. Res. A **431**, 476 (1999).
28. C. Jouanne *et al.*, this Conference.
29. T. Aumann *et al.*, Phys. Rev. C **59**, 1252 (1999).
30. K. Rusek, K. W. Kemper, and R. Wolski, Phys. Rev. C **64**, 044602 (2001).
31. Y. Kanada-En'yo and H. Horiuchi, Phys. Rev. C **55**, 2860 (1997).
32. E. Khan *et al.*, Nucl. Phys. A **694**, 103 (2001).

Physics of Atomic Nuclei, Vol. 66, No. 8, 2003, pp. 1508–1514. From Yadernaya Fizika, Vol. 66, No. 8, 2003, pp. 1553–1559.

Structure of ^{10}C and ^{11}C from Elastic and Inelastic Scattering on a Proton Target*

C. Jouanne[1], N. Alamanos[1], F. Auger[1], A. Drouart[1], A. Gillibert[1], V. Lapoux[1], G. Lobo[1], L. Nalpas[1], E. C. Pollacco[1], J. L. Sida[1], Y. Blumenfeld[2], E. Khan[2], T. Suomijarvi[2], T. Zerguerras[2], A. Lagoyannis[3], A. Pakou[3], P. Roussel-Chomaz[4], H. Savajols[4], and A. Musumarra[5]**

[1] *DSM/DAPNIA/SPhN, CEA/Saclay, Gif-sur-Yvette, France*

[2] *Institut de Physique Nucléaire, Orsay, France*

[3] *Department of Physics, The University of Ioannina, Ioannina, Greece*

[4] *GANIL, Caen, France*

[5] *INFN–Laboratorio Nazionale del Sud, Catania, Italy*

Received February 18, 2003

Abstract—We measured elastic and inelastic scattering to the low-lying states of ^{10}C and ^{11}C isotopes on a proton target with respective incident energies 45.3 and 40.6 A MeV. Data are analyzed with a microscopic complex potential. Elastic data are sensitive to the rms matter radius, which has been deduced for both isotopes. The moment of the neutron transition density was deduced for ^{10}C from inelastic scattering.

1. INTRODUCTION

A renewed interest in clustering in light nuclei has been shown with the availibility of radioactive beams far from stability. The Antisymmetrized Molecular Dynamics (AMD) model [1] was applied to light neutron-rich nuclei from lithium to carbon. Due to the small values of the neutron and proton numbers N and Z, a very fast change in shape is expected from one nucleus to another. That behavior is strongly influenced by shell effects and the proximity of magic numbers like $Z = 8$ or $N = 8$. With $Z = 6$, the proton distribution of all the carbon isotopes is shown to be oblate deformed. The shape of the neutron distribution strongly depends on N: it rapidly varies from prolate to spherical or oblate. That is the case for the neutron-deficient isotopes ^{9}C and ^{10}C with a well-deformed prolate shape, while triaxiallity is predicted for the odd isotope ^{11}C. As a consequence, different shapes of the proton and neutron distributions may be expected [1]. Such a difference is not unique and was already predicted, e.g., in the case of magnesium isotopes [2]. However, it is not so easy to show experimental evidence for that difference, especially when it is not large or with opposite signs. An alternative way may be to validate with other experimental constraints the models predicting such an effect, which implies a better knowledge of the structure of ^{10}C and ^{11}C.

For that purpose, we performed elastic and inelastic scattering of ^{10}C and ^{11}C secondary beams on a proton target in inverse kinematics from 0° to 50° c.m. angles.

2. EXPERIMENTAL SETUP

The secondary beams were produced in the fragmentation of a primary ^{12}C projectile at 95 A MeV on the target of the SISSI device at Ganil. With the alpha spectrometer and an achromatic degrador, the

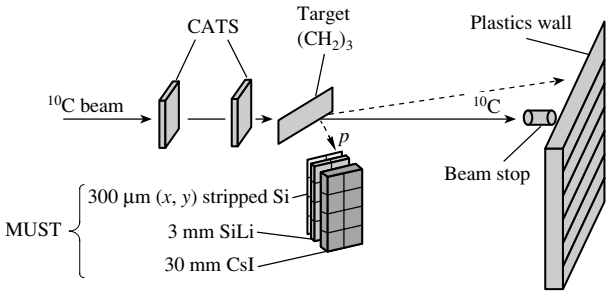

Fig. 1. Experimental setup.

*This article was submitted by the authors in English.

**e-mail: agillibert@cea.fr

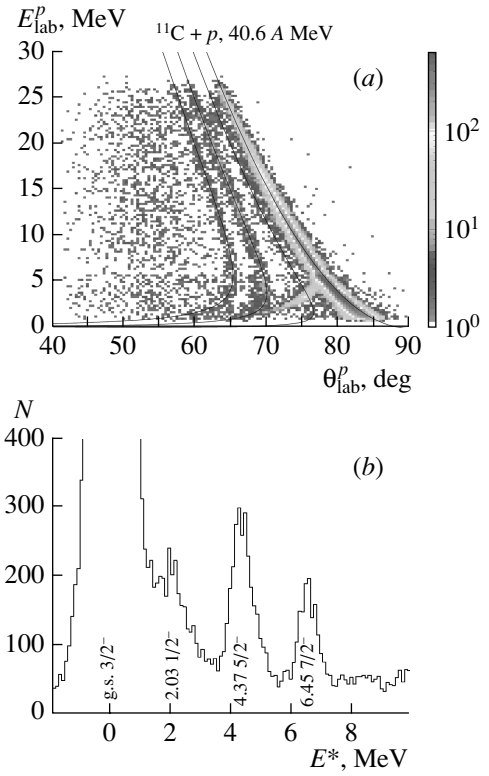

Fig. 2. Elastic and inelastic scattering $^{11}C + p$ at 40.6 A MeV. The thick lines superimposed in part (a) are the kinematical loci of the ^{11}C states. The calculated excitation energy spectrum is shown in part (b), without structure over the one-proton separation energy $S_p = 8.7$ MeV due to the imposed coincidence with ^{11}C in plastics. Higher energy structures are seen in coincidence with ^{10}B.

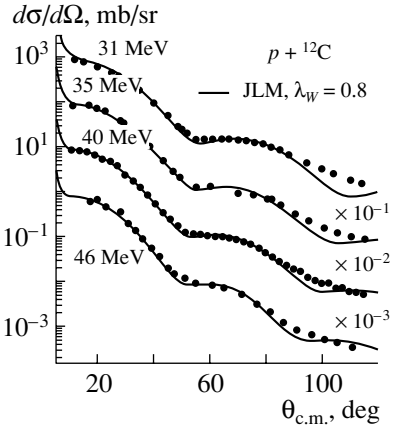

Fig. 3. JLM calculations for different incident proton energies on C target with the standard overall renormalization of the imaginary potential $\lambda_W = 0.8$.

selection of the beam results in very few contaminants. The experimental setup is described in Fig. 1. The optical qualities of the secondary beams require the reconstruction of the beam position and angle on the target with two beam tracking detectors (CATS). The proton target is a polypropylene film $(CH_2)_n$, the thickness of which is chosen according to the range and the angular straggling of the scattered protons in the target. The scattered protons are detected and identified by the MUST device [3], with the measurement of the angle, energy, and time of flight. Due to the inverse kinematics, the protons are measured from 90° to 40° relative to the beam in the laboratory frame for the elastic and quasi-elastic measurement. The beam and the ejectiles are detected in the forward direction in a small plastic scintillator at zero degrees or in the plastics wall for larger c.m. angles (Fig. 1). The selected events correspond to a kinematical coincidence between MUST and the plastic device with the additional information of the beam tracking detectors.

The excitation energy spectrum is calculated from the kinematical properties of the scattered protons (Fig. 2). The resolution depends on the target thickness, especially for low-energy protons emitted at small c.m. angles. We obtained $\delta E^* = 940$ keV for the slowed-down primary beam ^{12}C at 36.3 A MeV and an 8.25-mg/cm^2-thick target. The resolution was improved to $\delta E^* = 680$ keV with a 1.5-mg/cm^2-thick target for the secondary beams of interest.

3. DATA ANALYSIS AND SENSITIVITY OF THE METHOD

3.1. Elastic Scattering

For the analysis of the proton–nucleus elastic scattering data, we use a complex density and energy dependent potential $\mathcal{U}(\rho, E)$ which was parametrized with the nuclear matter properties [4]. Then, it is necessary to fix the ground-state density ρ of the A nucleus. It may be obtained either from theoretical calculations or by fitting to a given density. With the local density approximation, we obtain a microscopic complex potential used in DWBA calculations,

$$U(r, E) = \lambda_V V + i\lambda_W W, \qquad (1)$$

where λ_V and λ_W stand for the renormalization of the real and imaginary potential. An overall renormalization $\lambda_W = 0.8$ was shown to be necessary for light stable nuclei [5] and has been adopted for all our calculations. In Fig. 3 is shown the nice agreement obtained with previous data for elastic scattering of proton projectiles at various energies on a ^{12}C target, taking $\lambda_V = 1$. Other calculations with the JLM potential and comparisons to experimental data may be found in [6].

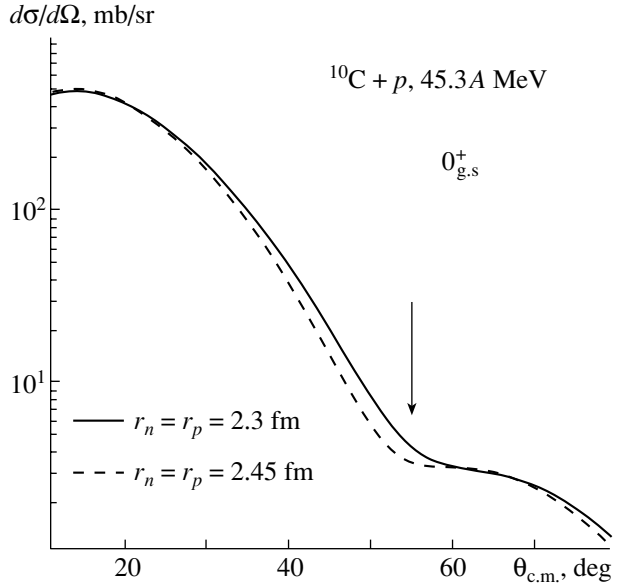

Fig. 4. Calculation of the elastic scattering cross section $^{10}C + p$ at 45.3 A MeV for a ^{10}C density with a Gaussian shape and two different rms radii. The proton and neutron densities and radii r_n and r_p are taken to be identical. The vertical arrow corresponds the maximum c.m. angle measured in our experiment.

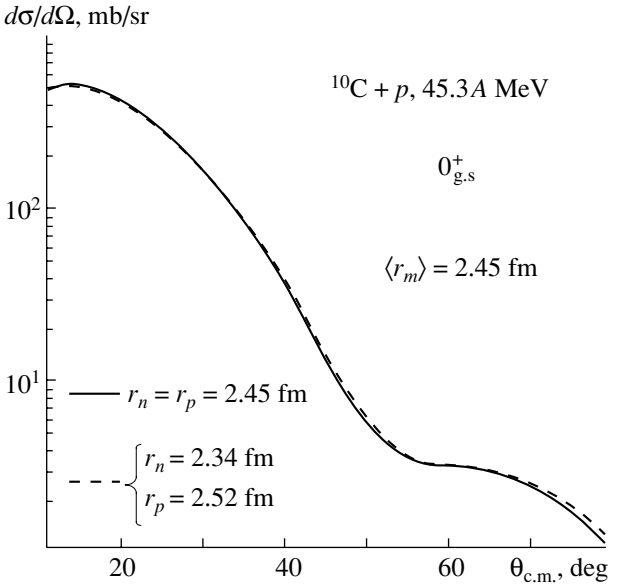

Fig. 5. Same as Fig. 4 for a given matter radius and equal and different neutron and proton radii.

3.2. Inelastic Scattering

Once the normalization set (λ_V, λ_W) of the proton–nucleus potential is fixed, it is possible to calculate the inelastic scattering from the ground state to excited states. Here, we define the matrix element M_p of the electromagnetic transition operator O_p^λ as

$$M_p = \langle J_f T T_z | O_p^\lambda | J_i T T_z \rangle \qquad (2)$$

related to $B(E\lambda)$ with

$$B(E\lambda, J_i \to J_f) = \frac{|M_p|^2}{2J_i + 1}. \qquad (3)$$

It is also connected to the proton transition density $\rho_p^{\rm tr}$ by

$$M_p = \int \rho_p^{\rm tr} r^{\lambda+2} dr. \qquad (4)$$

Equivalent definitions exist for the neutron matrix element M_n:

$$M_n = \langle J_f T T_z | O_n^\lambda | J_i T T_z \rangle = \int \rho_n^{\rm tr} r^{\lambda+2} dr. \qquad (5)$$

The transition densities are obtained within different models. The shape may also be obtained from the ground-state density with the Tassie prescription [7]

$$\rho_i^{{\rm tr},\lambda} = -\alpha_i^\lambda r^{\lambda-1} \frac{d\rho_i}{dr}. \qquad (6)$$

Finally, the cross section for inelastic scattering will be adjusted with the value of the ratio $|M_n|/|M_p|$. When $B(E\lambda)$ is known from other experiments like Coulomb excitation, $|M_p|$ is deduced from Eq. (3) and the inelastic cross section fixes the value of $|M_n|$.

3.3. Sensitivity of the Method

Elastic scattering was shown to be rather insensitive to details of the ground-state density, except for measurements at large c.m. angles. This is especially true in our case since the angular range does not exceed 60° c.m. In that angular range, the elastic cross section is mainly sensitive to the rms matter radius r_m. This is illustrated in Fig. 4 by a calculation done for a Gaussian density of ^{10}C and two different values of r_m, 2.3 and 2.45 fm. Figure 5 corresponds to the same calculation with $r_m = 2.45$ fm but the same (solid curve) or different (dashed curve) values for the neutron and proton radii. Obviously, elastic scattering data are not sensitive to these small differences in the neutron and proton densities.

4. RESULTS

4.1. ^{12}C

The primary ^{12}C beam was slowed down and used to check the setup. Elastic and inelastic scattering was also measured in a short run to test the analysis. ^{12}C is a well-known stable $N = Z$ nucleus which was studied with electron elastic scattering. We adopt the parametrization of [8] with a two-parameter Fermi density for the neutron and proton ground-state

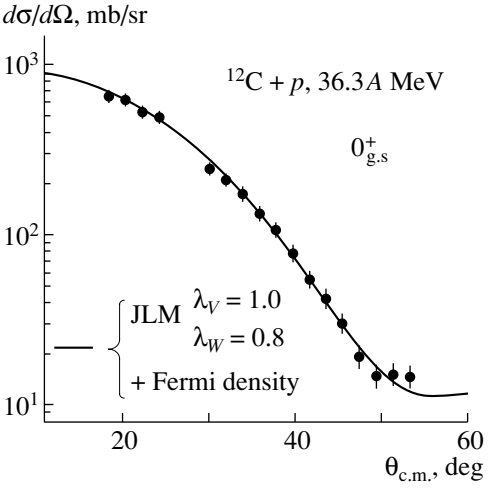

Fig. 6. Elastic scattering $^{12}\mathrm{C} + p$ at 36.3 A MeV. Data are compared to a calculation done with the JLM potential and the standard set $\lambda_V = 1.0$ and $\lambda_W = 0.8$. The same Fermi density is used for the neutron and proton densities with $r_m = 2.3$ fm.

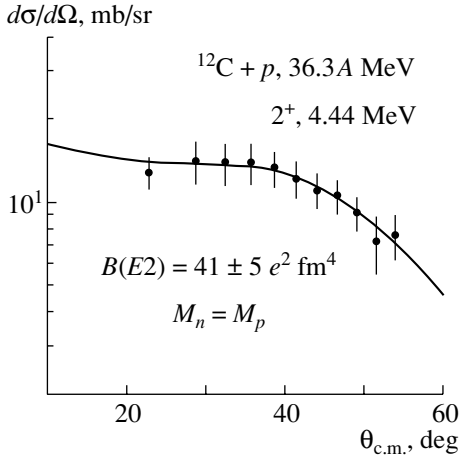

Fig. 7. Inelastic scattering cross section for $^{12}\mathrm{C} + p$ at 36.3 A MeV. The calculation is done with the adopted $B(E2)$ value and the assumption $|M_n| = |M_p|$.

densities assumed to be identical with an rms radius equal to 2.298 fm. We calculate the elastic scattering cross section $^{12}\mathrm{C} + p$ at 36. A MeV with the standard set $\lambda_V = 1.0$ and $\lambda_W = 0.8$. The result is compared to data in Fig. 6 with good agreement and no adjusted parameter. We also measured the inelastic scattering to the first 2^+ excited state at 4.44 MeV. The adopted $B(E2)$ value [9] is equal to $41 \pm 5\ e^2$ fm^4, corresponding to $|M_p| = 6.40 \pm 0.4$ fm^2. Like the ground state densities, the transition densities are assumed to be identical. They are deduced from Eq. (6) and normalized to the value of $|M_p|$. The inelastic cross

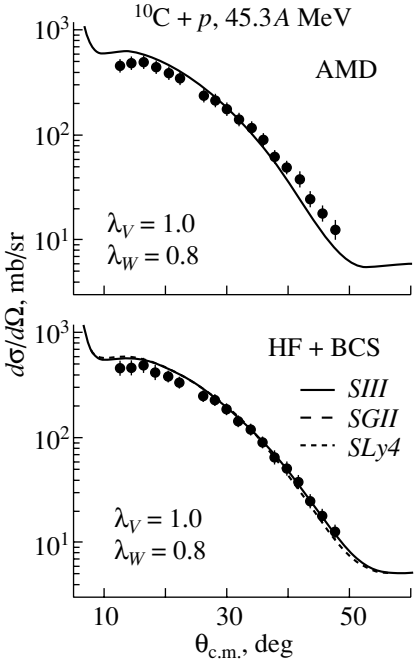

Fig. 8. Elastic scattering cross section for $^{10}\mathrm{C} + p$ with the standard set $\lambda_V = 1.0$ and $\lambda_W = 0.8$. The calculations were done with the ground-state densities from the AMD model (upper part) and HF + BCS densities (lower part) for three different Skyrme effective interactions.

section is reproduced within the error bars (Fig. 7) and the expected assumption $|M_n| = |M_p|$.

4.2. ^{10}C

In Fig. 8 are displayed several calculations with the standard set ($\lambda_V = 1.0$, $\lambda_W = 0.8$) and the ground-state densities from the AMD model [1] and HF + BCS calculations. The latter are performed with three different Skyrme effective interactions, as described in [10]. All of them overestimate the data at small c.m. angles: it is due to the couplings between the ground state and the continuum which remove flux from the elastic channel [6]. This effect is negligible for stable nuclei, but increases for exotic isotopes with lower particle thresholds. An exact calculation of such an effect is quite complex and involves terms that are not currently present in the JLM potential, like a real repulsive surface potential. For that reason, we prefer to simulate that correction [6] in a simpler way with a reduction of the real volume potential V, which gives λ_V smaller than 1. The best agreement with experimental data was obtained for $\lambda_V = 0.92$, as shown in Fig. 9.

With that renormalization, the angular distribution is correctly reproduced except for large c.m. angles, which are underestimated in the AMD model and HF + BCS with the *SLy4* effective interaction.

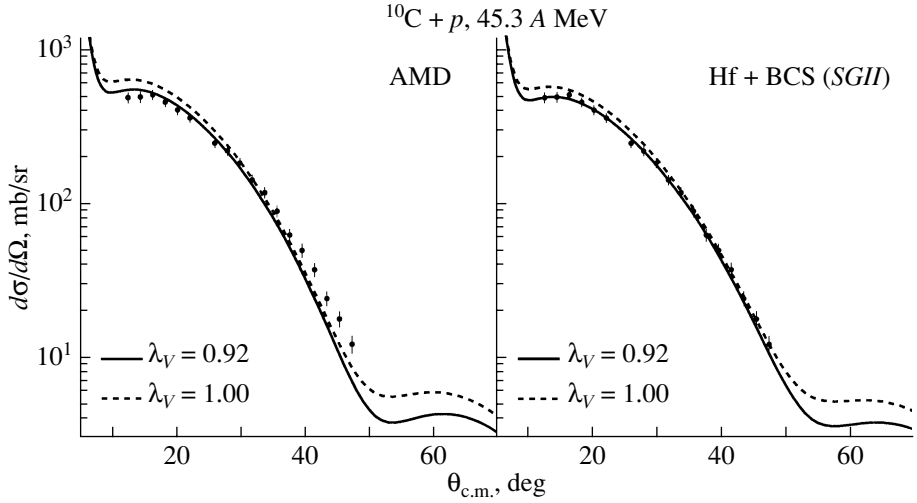

Fig. 9. Same as Fig. 8 with the renormalization $\lambda_V = 0.92$.

It is seen in Table 1 that these two calculations are associated with the largest rms matter radius, which is consistent with Fig. 4. From calculations that correctly reproduce the angular distribution, we can deduce $r_m = 2.42 \pm 0.10$ fm for ^{10}C. The error bar takes into account the statistical error on data, the uncertainty on λ_V, and the different values obtained in calculations that reproduce the data equally well. That value is larger than the one for ^{12}C, $r_m = 2.3$ fm, but still within the error bars. However, the QRPA (*SGII*) calculation, validated by the elastic data, predicts significantly larger values for r_p than for r_n in Table 1.

We have measured the inelastic scattering to the first 2^+ excited state at 3.35 MeV, already known with an adopted value [9] $B(E2) = 62 \pm 10\ e^2$ fm^4 corresponding to $M_p = 7.87 \pm 0.64$ fm^2. We see in Fig. 10 the predictions of the previous calculations for the inelastic scattering and the $|M_n|$, $|M_p|$, and $B(E2)$ corresponding values in Table 1. Except for the absolute value, the cross section is well reproduced. All of the calculations underestimate the $B(E2)$ value, even with the large error bars. If we renormalize the proton transition density to reproduce the adopted $B(E2)$ value, we may test a different assumptions for the $|M_n|$ value. Since the HF + BCS (*SGII*) calculation was validated by the elastic scattering data, we show in that case the results for a different $|M_n|$ value in Fig. 11. The solid curve corresponds to the $|M_n|$ value obtained with the mirror symmetry, that is, with the assumption $|M_n|(^{10}\mathrm{C}) = |M_p|(^{10}\mathrm{Be})$, this latter value being deduced from Eq. (3) and [9]. It clearly overestimates the data. This means that the mirror symmetry, if it is still valid, cannot be applied without care in such a matter. A better agreement is obtained with the

Table 1. Root-mean-squared neutron r_n, proton r_p, and matter r_m radii obtained for ^{10}C with the AMD model and HF + BCS calculations done with three Skyrme interactions (QRPA in case of inelastic scattering); an $E2$ transition from the ground state to the first 2^+ excited state is calculated within these models, and the $B(E2)$, $|M_p|$, and $|M_n|$ values are displayed on the lower part (the adopted value is $B(E2) = 62 \pm 10\ e^2$ fm^4)

	AMD	HF + BCS		
		SIII	*SGII*	*SLy4*
r_n (fm)	2.50	2.29	2.31	2.37
r_p (fm)	2.57	2.53	2.52	2.61
r_m (fm)	2.55	2.44	2.44	2.51
$B(E2)$ (e^2 fm^4)	45.0	21.6	30.3	22.1
$\lvert M_p\rvert$ (fm^2)	6.71	4.65	5.50	4.70
$\lvert M_n\rvert$ (fm^2)	7.42	5.15	6.01	5.96

Table 2. Root-mean-squared neutron r_n, proton r_p, and matter r_m radii obtained for ^{11}C with the AMD model and HF + BCS calculations done with three Skyrme interactions

	AMD	HF + BCS		
		SIII	*SGII*	*SLy4*
r_n (fm)	2.43	2.39	2.39	2.45
r_p (fm)	2.48	2.48	2.48	2.54
r_m (fm)	2.46	2.44	2.44	2.50

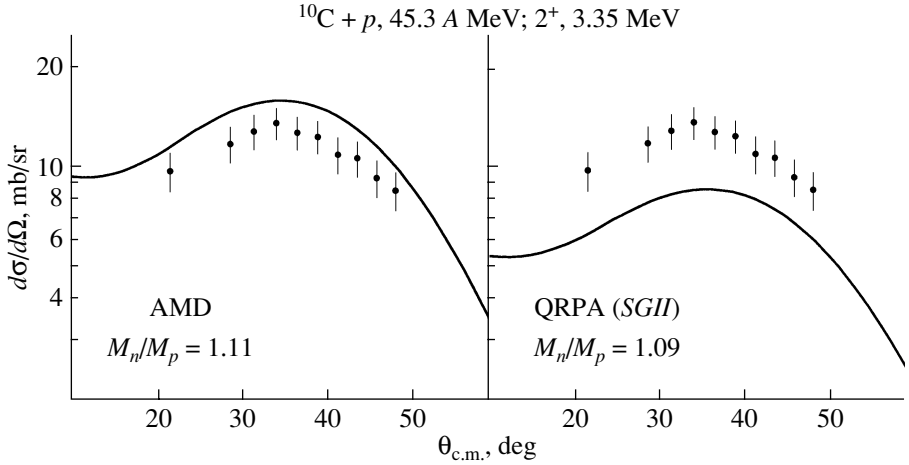

Fig. 10. Inelastic scattering to the first excited state of ^{10}C. The experimental angular distribution is compared to the calculations done with the densities from the AMD model (left part) or HF + BCS densities. The right part corresponds to the effective Skyrme interaction $SGII$; a similar behavior was obtained with $SIII$ and $SLy4$.

ratio $|M_n|/|M_p| = N/Z$ (long dashed curve), while the best agreement corresponds to $|M_n|/|M_p| = 0.70$ and $|M_n| = 5.51 \pm 1.07$ fm^2 (short dashed curve). The same conclusions may be obtained from the calculation done with the AMD density, although the elastic data are not so well reproduced. We see in Fig. 12 the ground-state neutron and proton densities for the AMD and HF + BCS ($SGII$) calculations of ^{10}C. AMD predicts a proton density not maximal at the origin, which is consistent with the clustering of ^{10}C in two α particles and two protons found in that model [1].

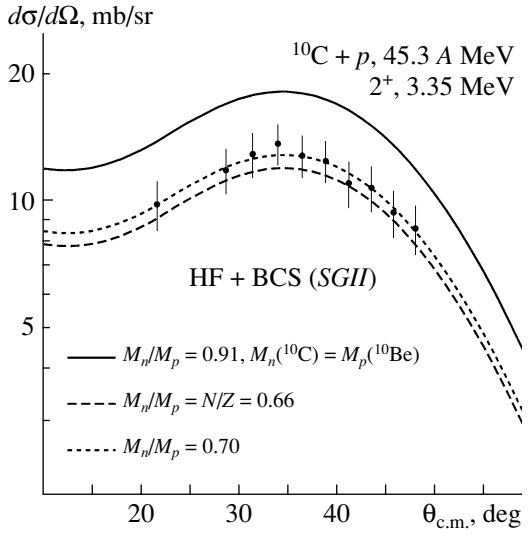

Fig. 11. Inelastic scattering cross section for ^{10}C + p.

4.3. ^{11}C

^{11}C was also studied with elastic and inelastic scattering on protons. In agreement with the ^{10}C data, we need a reduction of the real potential, corresponding to $\lambda_V = 0.90$, to reproduce the elastic scattering distribution at small c.m. angles. However, the data at larger angles are not reproduced in any calculation, suggesting a rms matter radius smaller than expected (Table 2). We may parametrize

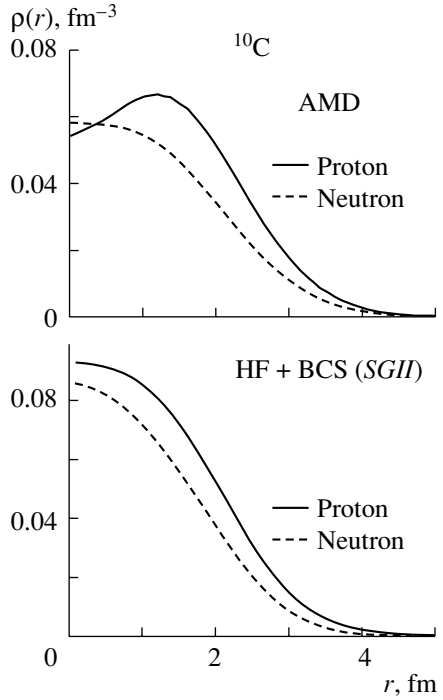

Fig. 12. Neutron and proton ground-state densities for ^{10}C from AMD and HF + BCS ($SGII$) calculations.

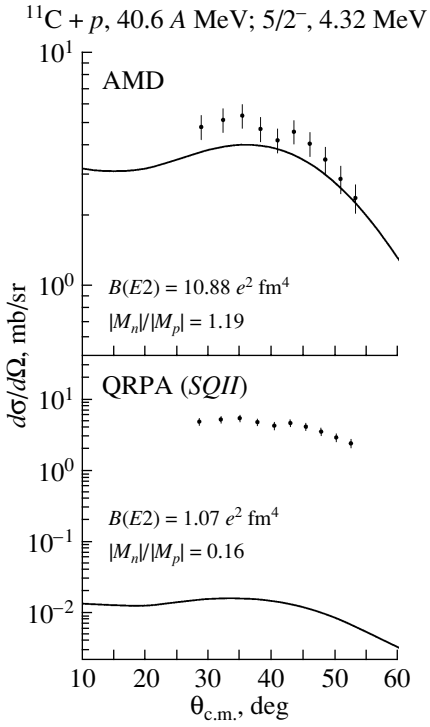

Fig. 13. Inelastic scattering of ^{11}C to the $5/2^-$ state at 4.32 MeV in the AMD and QRPA (*SGII*) calculations.

the ground-state density with a two-parameter Fermi density with the same geometry for the neutron and proton densities. The best agreement with the data is obtained for $r_m = 2.33$ fm, very close to the value for the neighbor ^{12}C, with the same error bar of 0.1 fm as for ^{10}C. Two peaks are clearly seen in Fig. 2 and correspond to the inelastic scattering from the $3/2^-$ ground state to a $5/2^-$ state at 4.32 MeV and a $7/2^-$ state at 6.48 MeV. These transitions are expected to be $E2$ transitions in the AMD and QRPA models, which is consistent with the shape of the experimental angular distribution (Fig. 13). The QRPA calculation fails to reproduce the experimental cross section, due to the very small $|M_n|$, $|M_p|$, and $B(E2)$ values. However, the experimental $B(E2)$ values are not known. In that case, the inelastic scattering data may only give access to the ratio $|M_n|/|M_p|$ without the individual values of $|M_n|$ and $|M_p|$. For the two transitions, the AMD model reproduces the angular distribution in spite of some disagreement with the elastic scattering data at large c.m. angles.

REFERENCES

1. Y. Kanada-En'yo and H. Horiuchi, Phys. Rev. C **55**, 2860 (1997).
2. J. Terasaki, H. Flocard, P. H. Heenen, and P. Bonche, Nucl. Phys. A **621**, 706 (1997).
3. Y. Blumenfeld *et al.*, Nucl. Instrum. Methods Phys. Res. A **421**, 471 (1999).
4. J. P. Jeukenne, A. Lejeune, and C. Mahaux, Phys. Rev. C **16**, 80 (1977).
5. J. S. Petler *et al.*, Phys. Rev. C **32**, 673 (1985).
6. V. Lapoux *et al.*, this Conference.
7. G. R. Satchler, *Direct Nuclear Reactions* (Clarendon Press, Oxford, 1983).
8. M. El-Azab Farid *et al.*, Nucl. Phys. A **438**, 525 (1985).
9. S. Raman *et al.*, At. Data Nucl. Data Tables **36**, 1 (1987).
10. E. Khan *et al.*, Phys. Lett. B **490**, 45 (2000).

Physics of Atomic Nuclei, Vol. 66, No. 8, 2003, pp. 1515–1518. From Yadernaya Fizika, Vol. 66, No. 8, 2003, pp. 1560–1562.

Proton Halos in Exotic Light Nuclei*

Z. Ren[1),2)], X. Z. Cai[3)], H. Y. Zhang[3)], and W. Q. Shen[3)]**

[1)] *Department of Physics, Nanjing University, Nanjing, China*

[2)] *Theoretical Center of Nuclear Physics, National Laboratory of Heavy-Ion Physics, Lanzhou, China*

[3)] *Shanghai Institute of Nuclear Research, Chinese Academy of Sciences, Shanghai, China*

Received August 28, 2002

Abstract—The current study on proton halos in exotic light nuclei is reviewed and discussed. We place emphasis on the newly discovered proton halo in ^{23}Al. A measurement of the reaction cross section of $N = 10$ isotones and $Z = 13$ isotopes is performed at Lanzhou in China. An abnormal increase in the reaction cross section is observed for ^{23}Al. This abnormal increase, combined with other data, strongly suggests that there is a proton halo in ^{23}Al. The possible cause for a proton halo in ^{23}Al is analyzed, and it is found that deformation can be important for it. Other candidates for proton halos are predicted.

1. INTRODUCTION

The development of radioactive beams has made it possible to study the structure of nuclei far from stability. A series of experiments [1–3] have shown that there exist neutron halos in exotic light nuclei near the neutron drip line. These studies change our views on nuclear structure and lead to a new impact on traditional nuclear physics along the isospin degrees of freedom.

At present, most of the studies in this field are on neutron-rich nuclei [1–7]. Studies on proton-rich nuclei are relatively few [8–13]. The study of the proton-rich nucleus ^{8}B has also led to an argument about the existence of a proton halo for some years. Borcea *et al.* [11] have systematically analyzed the experimental data on ^{8}B and pointed out that there is a pigmy halo in ^{8}B.

Morlock *et al.* [12] performed an experiment on ^{17}F and showed the existence of a proton halo in the first excited state $(1/2)^+$ in it. They observed in a proton-capture reaction on ^{16}O at low energies, i.e., $^{16}\mathrm{O}(p,\gamma)^{17}\mathrm{F}$, that the low-energy S factor is dominated by a transition to the first excited state $(1/2)^+$ in ^{17}F. They found that the S factor increases strongly with decreasing incident energies and this indicates the existence of a proton halo in the excited state $(1/2)^+$ in ^{17}F. The root-mean-square (rms) radius of the halo proton in the bound $(1/2)^+$ state is as large as 5.3 fm [5], while the rms radius of the ^{16}O core is approximately 2.6 fm. The relativistic mean-field (RMF) model is applied for the calculation of the properties of ^{17}F [14]. Its rms radius in the first excited state is $R_p(2s_{1/2}) \approx 5.0$ fm in the RMF model [14]. The theoretical value is close to the datum. Therefore, the theoretical model can reproduce the proton halo in the first excited state of ^{17}F.

Recently, the existence of proton halos in exotic light nuclei has been clearly established by several experiments on the $2s$–$1d$ shell nuclei. Simple mean-field calculations on the nuclei in the P and S isotopes predicted that there are proton halos in proton-drip-line nuclei [8, 9]. Experimentally, it is reported that there are proton halos in the ground state of ^{26,27,28}P [13]. The existence of a proton halo in ^{27}P is also confirmed by Shen's group in China [9]. A new candidate for proton halo is proposed for ^{23}Al based on the measurement of the reaction cross section [15].

In this paper, we will discuss the experimental results on proton-rich nuclei near ^{23}Al and point out that deformation should be important for the proton halo nucleus ^{23}Al.

2. THE PROTON HALO IN ^{23}Al

In this section, we report an experimental measurement of reaction cross section for proton-rich nuclei around ^{23}Al ($N = 10$ isotones and $Z = 13$ isotopes), and an abnormally large increase in σ_R for ^{23}Al is observed in the experiment. It is concluded that there is a proton halo in ^{23}Al based on the systematic analysis of experimental data.

*This article was submitted by the authors in English.

**e-mail: zren@nju.edu.cn;zren99@yahoo.com

1063-7788/03/6608-1515$24.00

Reaction cross section for $N = 10$ isotones and $Z = 13$ isotopes with ^{12}C target at intermediate energies

	Projectile energy, MeV/A	σ_R, mb
^{19}F	25.0	1620 ± 126
^{20}Ne	28.6	1668 ± 87
^{21}Na	31.0	1579 ± 100
^{22}Mg	33.4	1531 ± 125
^{23}Al	35.9	1892 ± 145
^{24}Al	32.8	1774 ± 94
^{25}Al	27.4	1629 ± 80
^{26}Al	24.7	1627 ± 108
^{27}Al	22.0	1733 ± 100
^{28}Al	19.0	1866 ± 121

The experiment was performed at the Heavy Ion Research Facility (HIRFL) of the Institute of Modern Physics (IMP) at Lanzhou. Secondary radioactive ion beams were produced by the Radioactive Ion Beam Line (RIBLL) in HIRFL through the projectile fragmentation of a 69-MeV/nucleon ^{36}Ar primary beam. A carbon target of thickness 109.7 mg/cm^2 was used. The isotopes were separated by means of magnetic rigidity ($B\rho$) and energy degradation (ΔE) [15]. The selected isotopes were further identified by the time of fight (TOF) and energy loss (ΔE) in a transmission Si surface barrier detector before incidence on a reaction target. Behind the reaction target, a telescope was installed, which consisted of five transmission Si surface barrier detectors and gave the energy losses (ΔE) and total energy of the reaction products. The thickness of the six Si detectors was 150, 150, 150, 700, 700, and 2000 μm, respectively, and the energy resolutions were not greater than 1.8%.

The reaction cross section σ_R is measured by the transmission-type experimental method, which relates the number of ions incident on the target ($N_{\rm inc}$) to the ions passing the target without interaction ($N_{\rm out}$) [15],

$$\sigma_R = \frac{A}{N_{\rm A} t} \ln \left[\frac{N_{\rm inc}}{N_{\rm out}} \right], \qquad (1)$$

where A is the mass number of the target, $N_{\rm A}$ is Avogadro's number, and t is the thickness of the target in units of g/cm^2. The incident energies of secondary ion beams in the middle of the carbon target vary from 25 to 36 MeV/nucleon. The total energy-deposition spectra after the reaction target is used to extract the noninteraction particles passing the target, where the peak near the total incident energy is defined as the noninteraction peak. In this case, the fragment is not identified uniquely. Inelastic scattering or any reaction not changing proton and/or neutron number in the incident nucleus is not included. The experimental data of σ_R for $N = 10$ isotones and $Z = 13$ isotopes are presented in the table and the figure. It is seen that there is a sudden increase in σ_R for ^{23}Al. In the table, the errors of σ_R refer to the statistical error plus the mean systematic error ($\pm 4\%$) of extrapolating the reaction events of low-Q-value reactions into the middle of the nonreacted ion's peak.

This anomalous behavior of σ_R is very similar to that of Li isotopes [1]. Tanihata *et al.* [1] concluded that there is an abnormally large radius of ^{11}Li and the neutron halo appears in this nucleus. In view of the very similar behavior for the Li isotope and the $N = 10$ isotone, we conclude that the abnormally large cross section in ^{23}Al may indicate an appearance of a proton halo in this nucleus. If we review the experimental proton separation energy of ^{23}Al, we notice that its proton separation energy is very small, $S_p = 0.125$ MeV [16]. This demonstrates that the last proton is very weakly bound in this nucleus. The proton separation energy in its neighboring nucleus ^{22}Mg is as high as $S_p = 5.497$ MeV [16]. Thus, ^{22}Mg is possibly a good inert core in ^{23}Al. This supports the view that there can be a proton halo in ^{23}Al.

The reaction cross section of ^{24}Al increases for a reference nucleus ^{25}Al. This indicates that there is possibly a proton skin in ^{24}Al. The proton separation energy of ^{24}Al is 1.871 MeV. This agrees with the assumption of proton skins. But for the nucleus ^{23}Al, the cross section is strongly enhanced compared with its neighboring nuclei. In particular, this happens even if its mass number is the smallest in this isotope series. This is evidence that there is a proton halo in ^{23}Al. Its proton separation energy is also small, $S_p = 0.125$ MeV. This is consistent with the picture of a proton halo.

After analyzing the experimental data around ^{23}Al and concluding that there is a proton halo in it, we now investigate the possible cause for the appearance of a proton halo.

The experimental ground-state spin and parity of ^{23}Al is not yet available. For its neighboring nucleus ^{22}Mg, there is a strong quadrupole deformation, $\beta_2 =$

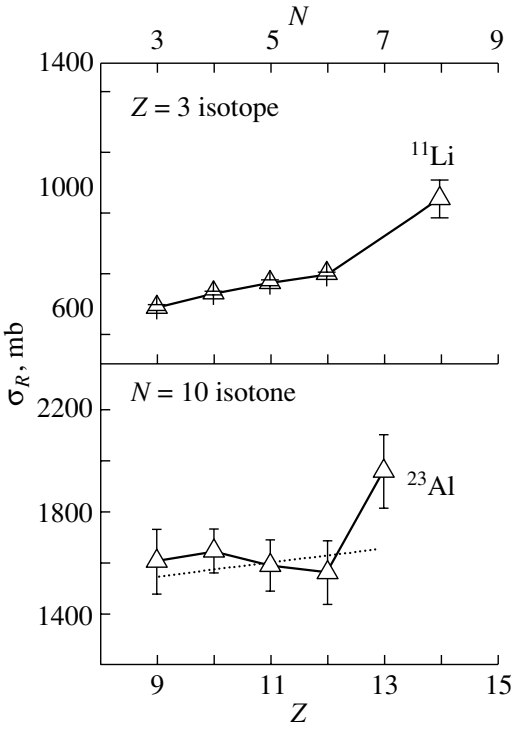

The reaction cross section of $N = 10$ isotones in this experiment. The old data from Tanihata *et al.* [1] are also drawn for comparison.

0.56 [17]. Because the last proton in ^{23}Al is very weakly bound, the deformation of ^{23}Al can be close to that of ^{22}Mg. According to the level sequence of deformed light nuclei by Bohr and Mottelson [18], the last proton in ^{23}Al should occupy the deformed state $(1/2)^+$ which is from the $2s_{1/2}$ state in a spherical case. This may suggest that the case of ^{23}Al is similar to that in ^{11}Be and ^{19}C. The core nuclei ^{10}Be and ^{18}C in both ^{11}Be and ^{19}C are strongly deformed according to experimental data and theoretical calculations. At present, a complete description of the neutron halo for both ^{11}Be and ^{19}C is still pending. Therefore, a correct description of the proton halo in ^{23}Al may bring a new challenge to the present theoretical models.

In the future, it will also be very interesting to measure the spin and parity of ^{23}Al to elucidate its ground-state properties. The measurement of its quadrupole moments and magnetic moments will shed the light on its ground-state deformation. In any event, the error bars of the present experiment are large. Thus, more measurements of σ_R at high or intermediate energies by more reliable and accurate methods are necessary.

3. SUMMARY

We have reviewed the present study on proton halos in the $2s$–$1d$ shell. This includes both experimental results and theoretical calculations on the proton halos of proton-rich nuclei in the $2s$–$1d$ shell. An experimental measurement of the reaction cross section was carried out at Lanzhou in China for proton-rich nuclei and the result is presented. Reaction cross sections σ_R of $N = 10$ isotones (^{19}F–^{23}Al) and $Z = 13$ isotopes (^{23}Al–^{28}Al) were measured at intermediate energies. An anomalous enhancement of σ_R for ^{23}Al was observed as compared with its neighboring nuclei. This result, together with the very small proton separation energy ($S_p = 0.125$ MeV), strongly suggests the existence of a proton halo in ^{23}Al. Further measurement of σ_R for Al isotopes was carried out and it confirms the abnormally large cross section for ^{23}Al. This again shows that there is a proton halo in ^{23}Al. The calculation of ^{23}Al with the relativistic density-dependent Hartree model manifests the existence of a proton halo in ^{23}Al when the last proton occupies the $2s_{1/2}$ level [15]. The appearance of a proton halo in ^{23}Al bridges the gap of halo phenomena between ^{17}Ne and ^{26,27}P. This is very important for elucidating the mechanism of the appearance of a halo in the $2s$–$1d$ shell. Further experiments and calculations will be necessary for a detailed study of the halo structure in ^{23}Al.

ACKNOWLEDGMENTS

This work is supported by a fund of the Ministry of Education in China under contract no. 20010284036, by the Major State Basic Research Development Program in China under contract no. G200077400, and by the National Natural Science Foundation of China under contract no. 10125521.

REFERENCES

1. I. Tanihata *et al.*, Phys. Lett. B **206**, 592 (1988).
2. W. Mittig *et al.*, Phys. Rev. Lett. **59**, 1889 (1987).
3. Z. Ren and G. Xu, Phys. Lett. B **252**, 311 (1990).
4. M. V. Zhukov, B. V. Danilin, D. V. Fedorov, *et al.*, Phys. Rep. **231**, 151 (1993).
5. T. Otsuka *et al.*, Phys. Rev. Lett. **70**, 1385 (1993).
6. L. Chulkov, E. Roeckl, and G. Kraus, Z. Phys. A **353**, 351 (1996).
7. Yu. Ts. Oganessian, V. I. Zagrebaev, and J. S. Vaagen, Phys. Rev. Lett. **82**, 4996 (1999).
8. Z. Ren, B. Chen, Z. Ma, and G. Xu, Phys. Rev. C **53**, R572 (1996).
9. D. Q. Fang, W. Q. Shen, *et al.*, Eur. Phys. J. A **12**, 335 (2001).
10. B. A. Brown and P. G. Hansen, Phys. Lett. B **381**, 391 (1996).

11. C. Borcea *et al.*, Nucl. Phys. A **616**, 231c (1997).
12. R. Morlock *et al.*, Phys. Rev. Lett. **79**, 3837 (1997).
13. A. Navin *et al.*, Phys. Rev. Lett. **81**, 5089 (1998).
14. Z. Ren, A. Faessler, and A. Bobyk, Phys. Rev. C **57**, 2752 (1998).
15. X. Z. Cai, H. Y. Zhang, W. Q. Shen, *et al.*, Phys. Rev. C **65**, 024610 (2002).
16. G. Audi and A. H. Wapstra, Nucl. Phys. A **565**, 1 (1993); private communications.
17. S. Raman *et al.*, At. Data Nucl. Data Tables **36**, 1 (1987).
18. A. Bohr and B. Mottelson, *Nuclear Structure* (Benjamin, New York, 1975), Vol. 2.

Physics of Atomic Nuclei, Vol. 66, No. 8, 2003, pp. 1519–1522. From Yadernaya Fizika, Vol. 66, No. 8, 2003, pp. 1563–1566.

Two-Proton Radioactivity Search*

I. G. Mukha**

Gesellschaft für Schwerionenforschung, GSI, Darmstadt, Germany[1)]

Received February 19, 2002

Abstract—Two-proton radioactivity, a spontaneous breakup of elements with emission of two protons, was predicted to exist near the proton drip line by V.I. Goldansky long time ago. The recent theoretical and experimental progress in a search for such an exotic nuclear decay is reviewed. In theory, the new three-body model which treats two-proton radioactivity as a genuine three-particle nuclear decay is considered. In experiment, the first evidence for two-proton decay of ^{45}Fe is described. Four atoms of ^{45}Fe, produced at the fragment separator of GSI, decayed via particle emission with a total energy of 1.1(1) MeV and a half-life of $3.2^{+2.6}_{-1.0}$ ms. A possible experiment for a direct observation of two-proton emission from the ground state of ^{19}Mg is considered for its decay in-flight. The half-life of ^{19}Mg, as well as proton–proton correlations, might be derived from the distribution of the ^{19}Mg decay vertices extrapolated from the measured trajectories of all fragments. © *2003 MAIK "Nauka/Interperiodica".*

1. TWO-PROTON RADIOACTIVITY LANDSCAPE

For the first time, two-proton radioactivity was considered theoretically by Goldansky in the early 1960s [1]. Near the proton drip line, where nuclear binding energies are almost zero, the pairing force is more important than in stable nuclei. This may result in a situation when a drip-line nucleus is bound with respect to single-proton decay but unbound to two-proton decay. Such a situation is similar to the Borromean property of bound halo nuclei (e.g., ^{6}He, ^{11}Li [2], or ^{17}Ne [3]), and it should regularly occur along the proton drip line. The calculations of atomic masses using shell model [4, 5] and the Coulomb energy systematics [6] have revealed dozens of candidates for a two-proton radioactivity.

2. THEORETICAL ADVANCE

Two-proton decay may be described via two alternative mechanisms: (i) sequential emission of protons via an intermediate state, which includes diproton emission, i.e., emission of a ^{2}He cluster with very strong *pp* correlations; (ii) simultaneous emission of protons. The latter case is adequate to a genuine three-particle disintegration (called true three-body decay in [1]), where resonances in the binary subsystems are located at higher energies than in the three-body system. Genuine three-body decay modes are measured in several light nuclei, e.g., ^{6}Be(0^{+})[7], ^{9}Be*($5/2^{-}$) [8], and ^{12}O [9]. The traditional idea of diproton (^{2}He) emission is that, due to the pairing effect, two protons form a quasiparticle under the Coulomb barrier, and this facilitates the penetration. Diproton models normally use the two-body R-matrix expression for the width (see, e.g., in [4, 10]) which combines two incompatible features, i.e., penetration of a pointlike particle along some trajectory below the Coulomb barrier and zero energy of relative motion for the constituents of this particle. However, the latter feature implies infinite size due to the uncertainty principle!

Recently, $2p$ emission was considered as a genuine three-particle nuclear decay in the rigorous basis of a realistic three-body model [11]. This method, which has been developed for quantitative studies of $2p$ emission, was first applied to the cases ^{19}Mg and ^{48}Ni. The results of calculations are in dramatic contrast to those obtained by using the traditional diproton model. In particular, the calculated half-life of ^{19}Mg is 1000 times larger in comparison with the respective estimate of the diproton model, which, in fact, provides only a low limit for the $2p$-decay half-life.

In Fig. 1, the half-lives of ^{19}Mg, ^{45}Fe, and ^{48}Ni calculated with the three-body model [11, 12] are shown as functions of $2p$-decay energy. The rectangles show the areas of predicted decay energies and respective half-life values. The ^{45}Fe- and ^{48}Ni-decay energies are taken from the systematics [13]. One can see that these nuclei are likely to decay within

*This article was submitted by the author in English.

** e-mail: I.Mukha@gsi.de

1) On leave from Russian Research Centre Kurchatov Institute, Moscow, Russia.

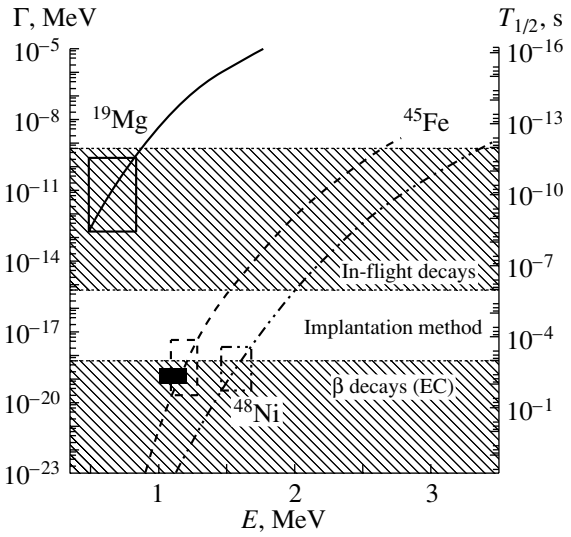

Fig. 1. Width (left ordinate) or half-life (right ordinate) as a function of decay energy for $2p$ emission candidates calculated with the three-body model. The parameters expected for decay of ^{19}Mg, ^{45}Fe, and ^{48}Ni are shown by rectangular frames. Dark box shows the experimental data obtained for ^{45}Fe.

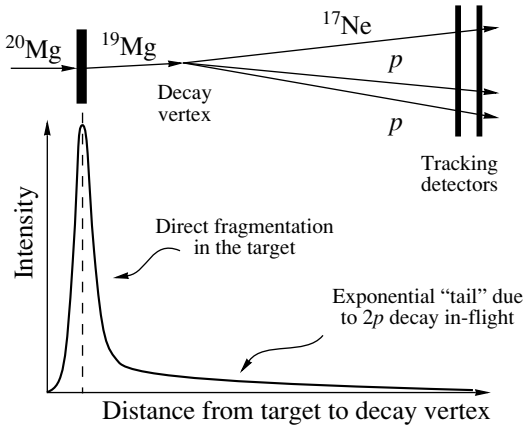

Fig. 2. Idea of measurements of two-proton decays in-flight. Upper panel: schematic layout of detectors. Lower panel: distribution of decay vertices reconstructed from tracking detector data.

the μs range or/and are β emitters. In experimental studies of these nuclei, the implantation method is an adequate technique. The ^{19}Mg-decay energy is carefully evaluated using the available data of its mirror, the ^{19}N nucleus, and the Coulomb displacement energy calculated with the three-body $^{17}\mathrm{Ne} + p + p$ model [14]. From Fig. 1, one may conclude that the ^{19}Mg decay cannot be measured using the implantation method; however, there is a chance to study this nucleus in an in-flight decay experiment.

3. EXPERIMENTAL PROGRESS IN A SEARCH FOR $2p$ RADIOACTIVITY

The experiments aimed at finding such an exotic nuclear decay generally use the ion-implantation or the in-flight decay method. In the former case, a radioactive nucleus is first stopped and the subsequent activity is measured. The latter method aims at detecting all fragments of a $2p$ precursor in missing-mass or invariant-mass measurements. Another type of in-flight decay experiment is possible as well, in which all fragments are tracked and the decay vertices are recovered from the measured trajectories. Such a tracking technique has proved to be a precise and effective tool in measurements of Coulomb fragmentation of ^{8}B with the KaoS spectrometer at GSI [15].

3.1. Evidence for Two-Proton Decay of ^{45}Fe Using an Implantation Method

No experimental evidence for the two-proton radioactivity has been obtained in the forty years since Goldansky's predictions. However, the recent results of decay measurements of the ^{45}Fe nucleus at GSI are very encouraging [16]. The iron isotopes have been produced by fragmentation reactions of a 650-MeV/u ^{58}Ni beam at the projectile fragment separator FRS of GSI. The production rate was one atom per day. The selected and identified ^{45}Fe nuclei have been implanted into a stack of silicon detectors mounted inside an NaI(Tl) barrel, and the subsequent activity has been measured. New fast-reset preamplifiers and digital front-end electronics allowing measurements a few microseconds after the moment of implantation have been applied. For five of the implanted ^{45}Fe atoms, decay signals have been recorded. Four decay events are consistent with $2p$ emission, and no β particles are registered in coincidences. The total energy released is 1.1(1) MeV, and the ^{45}Fe half-life is estimated to be $3.2^{+2.6}_{-1.0}$ ms. One decay event is consistent with a β-decay mechanism. These results are confirmed by the analysis of data obtained at GANIL [17]. Though two emitted protons are not identified in these experiments, the only explanation found is two-proton radioactivity [16].

The reported $2p$-decay energy and lifetime of ^{45}Fe are shown in Fig. 1 by the dark rectangular box. They are in a good agreement with the three-body model predictions [12]. Since the three-body model describes the ^{45}Fe data quantitatively, its predictions are reliable for other $2p$-emission candidates as well.

3.2. Possible Experiment Aimed for a Direct Observation of 2p Decay of ^{19}Mg

On the basis of the predicted $2p$-decay properties of ^{19}Mg, a new experiment of its in-flight decay

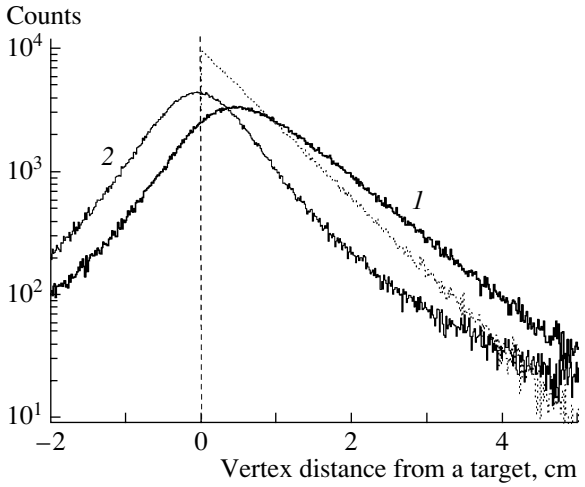

Fig. 3. Monte Carlo simulation of the ^{19}Mg decay vertex distributions with respect to the target. Dotted histogram is the simulated ^{19}Mg decay coordinates with assumed half-life $T_{1/2} = 20$ ps. The solid-line histogram *1* is result of reconstruction of the original distribution shown by dotted histogram. The solid-line histogram *2* shows the result of reconstructed prompt decay of ^{19}Mg within the target.

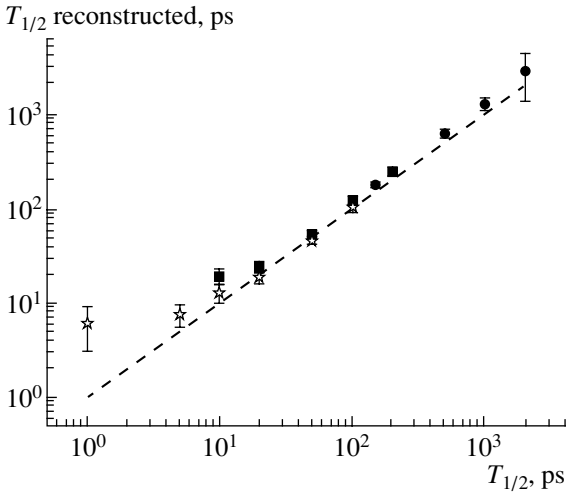

Fig. 4. The ^{19}Mg lifetime values derived from the reconstructed decay vertex distributions like the one shown in Fig. 3. For each half-life value $T_{1/2}$ assumed, 5000 decays of ^{19}Mg were simulated by GEANT. Stars, squares, and circles correspond to the different setup layouts with the multistrip detectors positioned from 4 to 60 cm after the target.

is proposed [18], where the decay protons might be observed directly. The idea of in-flight decay experiments is sketched in Fig. 2. Let us assume that the $2p$ precursor is produced in a nuclear reaction, e.g., one-neutron knock-out, and that the resulting state decays into the two protons and a heavy fragment after leaving a target area. If the direction of decay product is measured by a pair of tracking detectors, the coordinates of each decay can be defined as a vertex of three fragment momenta. Thus, the lifetime of the mother nucleus can be derived by fitting the measured vertex distribution by an exponential function. The measured vertex distribution should also contain a component from direct fragmentation of projectiles in the target, which is centered at the target position. The width of this component depends on the experimental resolution. A precise determination of all fragment trajectories is needed to reconstruct each decay vertex accurately and thus to disentangle the $2p$-radioactivity and the fragmentation components.

Ground states of ^{19}Mg can be populated via a secondary reaction with a radioactive beam of ^{20}Mg produced at the FRS facility at GSI. The ^{20}Mg radioactive nuclei can in turn be obtained in a fragmentation of a 350-MeV/u ^{24}Mg primary beam on a ^{9}Be target. The counting rate expected is $\sim$1 event per minute, with the total registration efficiency evaluated to be 10% [19]. Simulations of the radioactive beam production and passage of ions through the FRS magnets used the Monte Carlo program MOCADI [19]. The Monte Carlo program GEANT simulated nuclear decays and interactions of charged fragments with detectors and materials of the suggested setup. The main physics processes included in simulations are energy loss due to ionization, multiple scattering, hadronic interaction, fluctuations of energy loss, etc.

The geometry (target thickness, ion energies, distances of silicon detectors from the secondary target, etc.) was optimized in order to yield the maximum accuracy in half-life determination combined with a high registration efficiency. For example, the simulated distribution of ^{19}Mg decay vertices along the beam direction is shown in Fig. 3 by the dotted histogram. The assumed half-life value is $T_{1/2} = 20$ ps. The solid-line histogram *1* is the result of a reconstruction of the decay vertices using the coordinates provided by silicon microstrip detectors. The solid-line histogram *2* shows the result of reconstructed prompt decay of ^{19}Mg in the target which gives the spatial resolution of the suggested setup.

Fits of the reconstructed vertex distributions by an exponential function, being folded with the spatial resolution, can give reasonable estimates of the respective half-life values. For ^{19}Mg, the derived half-life values are shown in Fig. 4 as a function of the assumed half-lives. Stars, squares, and circles correspond to the different positions of the multistrip detectors, at distances ranging from 4 to 60 cm after the target. From Fig. 4, one can see that the shortest half-life accessible with the suggested setup is a few picoseconds. The best half-life accuracy can

be achieved by an optimal choice of corresponding positions of the tracking detectors.

In comparison with the implantation method, where heavier nuclei such as ^{45}Fe are produced with intensities of few events per day, ~1000 times more intensive production of ^{19}Mg is expected. The suggested method of measurements is also more informative because of a direct registration of protons and their correlations. It can provide a lifetime of $2p$ emitters. The range of accessible half-life overlaps reasonably well with the theoretical expectations. This method allows using a much thicker secondary target in comparison with the missing mass or invariant mass method, because a projectile struggling in a target does not affect the half-life precision. The suggested experiment requires high energies of beams, which allows a very thick secondary target to be used. For example, in comparison with the recent experiment at GANIL [20], one may expect a 15 times more intensive beam of ^{20}Mg produced. In addition, one may use a 15 times thicker secondary target. Moreover, the simulated efficiency of the suggested detector setup is higher by a factor of 5. All in all, the suggested experiment promises to be 1000 times more sensitive than the previous experiment at GANIL.

4. OUTLOOK

The recent experimental and theoretical advances in studies of two-proton radioactivity provide an optimistic prospective for further research of this long-predicted but unobserved phenomenon, which is expected to be regular near the proton drip line. The first evidence for two-proton radioactivity found in ^{45}Fe is indeed a breakthrough in studies of drip-line nuclei, though additional measurements of ^{45}Fe $2p$ decay providing data with better statistics and energy resolution are clearly needed. Decay properties of other $2p$ candidates may be efficiently studied with the implantation method in the mass region from 40 to 70. The in-flight decay method is expected to be effective for light nuclei, with masses ranging from 20 to 40. Future studies of other $2p$-decay candidates may benefit from accurate theoretical predictions provided reliable calculations of nuclear masses near the proton drip line are available.

ACKNOWLEDGMENTS

I am grateful to the collaborators of the S202 experiment at GSI. A particular credit is given to L.V. Grigorenko, who performed the three-body model calculations.

REFERENCES

1. V. I. Goldansky, Nucl. Phys. **19**, 482 (1960).
2. M. V. Zhukov *et al.*, Phys. Rep. **231**, 153 (1993).
3. M. V. Zhukov and I. J. Thompson, Phys. Rev. C **52**, 3505 (1995).
4. B. A. Brown, Phys. Rev. C **43**, R1513 (1991).
5. E. Ormand, Phys. Rev. C **53**, 214 (1996).
6. B. J. Cole, Phys. Rev. C **56**, 1866 (1997).
7. B. V. Danilin *et al.*, Yad. Fiz. **46**, 427 (1987) [Sov. J. Nucl. Phys. **46**, 225 (1987)]; O. V. Bochkarev *et al.*, Nucl. Phys. A **505**, 215 (1989).
8. O. V. Bochkarev *et al.*, Yad. Fiz. **52**, 1525 (1990) [Sov. J. Nucl. Phys. **52**, 964 (1990)]; G. Nyman *et al.*, Nucl. Phys. A **510**, 189 (1990).
9. R. A. Kryger *et al.*, Phys. Rev. Lett. **74**, 860 (1995).
10. W. Nazarewicz *et al.*, Phys. Rev. C **53**, 740 (1996).
11. L. V. Grigorenko, R. Johnson, I. G. Mukha, *et al.*, Phys. Rev. Lett. **85**, 22 (2000); Phys. Rev. C **64**, 054002 (2001).
12. L. V. Grigorenko, I. G. Mukha, and M. V. Zhukov, Nucl. Phys. A **713**, 372 (2003); **714**, 425 (2003).
13. G. Audi and A. H. Wapstra, Nucl. Phys. A **565**, 1 (1993); **595**, 409 (1995).
14. L. V. Grigorenko, I. G. Mukha, I. J. Thompson, and M. V. Zhukov, Phys. Rev. Lett. **88**, 042502 (2002).
15. N. Iwasa *et al.*, Phys. Rev. Lett. **83**, 2910 (1999).
16. M. Pfützner *et al.*, Eur. Phys. J. A **14**, 279 (2002).
17. J. Giovinazzo *et al.*, Phys. Rev. Lett. **89**, 102501 (2002).
18. I. G. Mukha, AIP Conf. Proc. **518**, 144 (2000); I. G. Mukha and G. Schrieder, Nucl. Phys. A **690**, 280c (2001).
19. N. Iwasa *et al.*, Nucl. Instrum. Methods Phys. Res. B **126**, 284 (1997).
20. T. Zerguerras, PhD Thesis (IPN, Orsay, 2001) (unpublished).

Physics of Atomic Nuclei, Vol. 66, No. 8, 2003, pp. 1523–1527. From Yadernaya Fizika, Vol. 66, No. 8, 2003, pp. 1567–1571.

The Present and Planned Recoil Mass Spectrometers at Nuclear Science Centre, New Delhi*

S. Nath[1)], A. Jhingan[1)], T. Varughese[1)], J. J. Das[1)], P. Sugathan[1)], N. Madhavan[1)], R. Kumar[1)], R. P. Singh[1)], S. Muralithar[1)], R. K. Bhowmik[1)], and A. K. Sinha[2)]**

[1)] *Nuclear Science Centre, New Delhi, India*
[2)] *InterUniversity Centre for DAE Facilities, Kolkata, India*

Received August 28, 2002

Abstract—Recoil mass spectrometers (RMS) are ideal instruments for identifying weakly populated reaction products in the forward angle from heavy-ion reactions amidst an intense beam background. The Heavy Ion Reaction Analyzer (HIRA) at the Nuclear Science Centre (NSC), New Delhi, is one of the few operating first generation RMSs. The features of and physics studies pursued using HIRA are covered in the paper. With the augmentation of the accelerator facilities at NSC, a second generation RMS combined with a gas-filled separator is planned. The design details of the new facility, Hybrid Recoil Mass Analyzer (HYRA), are presented. HYRA will be operated either stand-alone or in conjunction with a Large Gamma Array (LGA) at its target position. Physics studies planned with these forthcoming facilities are outlined.

1. INTRODUCTION

Recoil mass spectrometers have been used in a broad category of nuclear reaction and structure studies since early 1980s. These instruments are specially capable of identifying recoiling reaction products of interest in the very forward angle from the intense background of primary beam and other stronger reaction channels within a reasonably short time ($\sim \mu$s). The first generation recoil mass spectrometers [1–5] were optimized for identification of light and medium-heavy recoiling particles formed by collision of a light projectile on heavy targets. With the availability of augmented accelerator facilities and demand for investigation in new fields, the need for improvement of recoil separators was felt. The new generation separators are capable of identifying light recoiling particles from inverse kinematic reactions. Substantial improvement in the detection system also followed [6].

Recoil mass spectrometers, though they offer excellent beam rejection ($\sim 1 \times 10^{12}$, typically) and high mass resolution ($M/\Delta M \geq 300$, typically) and short separation time, are lacking in transport efficiency of the recoils. This results in a lower limit (few μb) for identifying a particular reaction channel. On the other hand, gas-filled separators [7–11], due to inherent charge state and velocity focusing [12, 13], offer very high transport efficiency, an order of magnitude enhancement with respect to their counterparts operating in vacuum. These instruments seem to be very effective for identifying heavy reaction products with very low formation probability (≤ 1 μb). However, the mass resolution is poor ($M/\Delta M \leq 50$) in gas-filled separators, and one has to rely upon efficient detection techniques (e.g., recoil decay tagging) for unambiguous identification of the recoils. The Heavy Ion Reaction Analyzer (HIRA) [4] at the Nuclear Science Centre (NSC), New Delhi, India, is one of the few operational first generation recoil mass spectrometers. The design specifications and operational experiences of HIRA are given in Section 2. The physics programs using this facility are outlined. The design details of the proposed recoil separator, Hybrid Recoil Mass Analyzer (HYRA), are presented in Section 3. HYRA is planned to be a unique combination of recoil mass spectrometer and gas-filled separator. The planned physics program is discussed subsequently.

2. HEAVY ION REACTION ANALYZER

2.1. Features of HIRA

HIRA has some unique features among the first generation recoil mass spectrometers. The electromagnetic configuration is Q–Q–ED–(M)–MD–ED–Q–Q, in which the dispersive elements are symmetric about the vertical plane through the middle of the magnetic dipole (MD). At the focal plane, space focusing, energy achromaticity, and

*This article was submitted by the authors in English.
**e-mail: subir@nsc.ernet.in

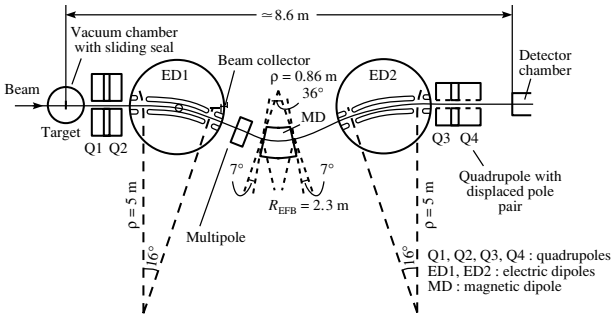

Fig. 1. Electromagnetic configuration of Heavy Ion Reaction Analyzer (see [4] for details).

mass dispersion are obtained. Here "M" stands for a magnetic multipole between the first electrostatic deflector (ED1) and MD, which helps in reducing angle and energy-related higher order aberrations. A horizontal slot in the anode plate of ED1 helps in achieving better beam rejection. The field distortion due to this slot is compensated by a "rose shim" design. The last quadrupole magnet Q4 has small components of hexapole and octupole fields (2.5 and 5.5% of quadrupole field, respectively), which reduce angle and mass related aberrations, resulting in a good mass spectrum in the focal plane. This is achieved by shifting the pole faces. The choice of the first higher order field before MD (i.e., before mass dispersion takes place) and the other after ED2 (i.e., after energy achromaticity is obtained) allows reducing energy and mass-dependent aberrations independently of each other. The ion-optical layout of HIRA is shown in Fig. 1. The table summarizes a few characteristic features of HIRA.

2.2. Studies with HIRA

HIRA, since it's commissioning, has been used in a variety of nuclear reaction and structure studies. Those include sub- and near-barrier fusion reaction, entrance channel dependence, spin and barrier distribution in fusion around barrier [14–17], transfer reactions (transfer to ground state, Z and A identification in transfer by kinematic coincidence) [18–21], evaporation residue tagged light charged particle emission [22] and gamma spectroscopy [23–25], and search for microsecond isomers around $N = 50$ closed shell nuclei and in the study of fission hindrance phenomenon [26] by evaporation residue detection and gamma multiplicity measurements. HIRA, in a mass dispersionless mode with x and y crossover at the MD center and with suitable hardware add-ons [27, 28], has been used to produce a high-purity ^{7}Be radioactive ion beam through (p, n) reaction in inverse kinematics with an intensity of 10^4–10^5 particles/s [29]. The secondary ^{7}Be beam has been used in experiments to extract the $S_{17}(0)$ astrophysical factor and in studying the modifications in the half-life of ^{7}Be in materials with different electronic environments. An experiment on ^{7}Be + ^{7}Li mirror nuclei scattering is currently being pursued.

Features of HIRA

(M/q) acceptance	±5%
(E/q) acceptance	±20%
Acceptance	0.1–10 msr (variable)
Mass dispersion	0–10 mm/% (variable)
Mass resolution	1/350 (typical for 1 msr)
Rotation angle	−10°–25°

3. HYBRID RECOIL MASS ANALYZER

The accelerator facility at NSC is being augmented by the installation of three modules of Superconducting (Nb based) LINAC with the Pelletron accelerator initially injecting the beam into it. An ECR ion source is being designed as a future injector to the LINAC. These upgrades will lead to beams in the energy range of 12 MeV/u for light ions such as ^{16}O and 8 MeV/u for medium-mass nuclei such as ^{58}Ni. To exploit the full potential of the enhanced energy, current, and the variety of beams (including the inert species), a new generation recoil separator has been planned, the details of which follow.

3.1. Layout and Ion Optics

The layout of the proposed recoil separator, HYRA, is shown in Fig. 2. It will consist of 11 quadrupole magnets, three dipole magnets, and one electrostatic deflector. The ion-optical design of the separator has been performed using the code GIOS [30]. The first section of the spectrometer will be used either as a gas-filled separator (for heavy residue detection) or as the initial momentum achromat in the vacuum mode of operation involving inverse kinematics. MD2 is designed to be able to bend ions in two mutually perpendicular directions for ease of operation in the two modes and to avoid disturbing the focal plane detector setup of the gas-filled separator. The entrance and exit angles of MD2 have been chosen accordingly. Q3 will have a provision for inserting a momentum-defining slit at its center to intercept the different charge states of the primary beam in the vacuum mode of operation. The entire separator is planned to be mounted on a

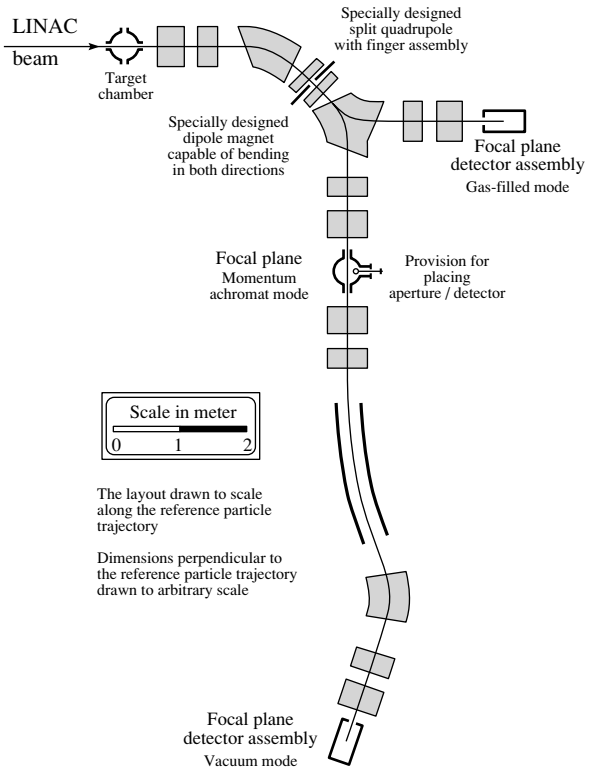

Fig. 2. Layout of the proposed recoil separator HYRA.

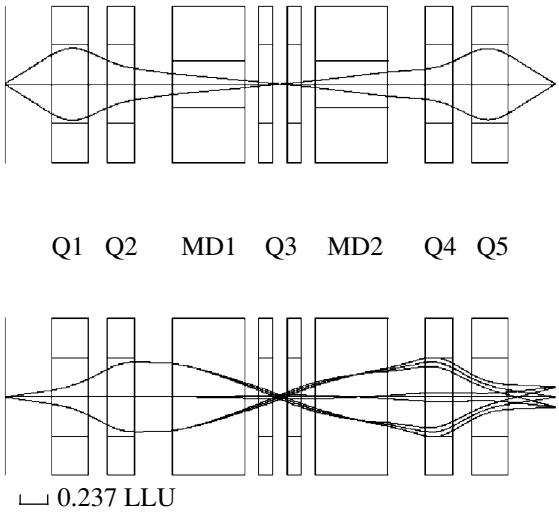

Fig. 3. First-order ion-optical layouts of the gas-filled part of HYRA in the dispersive (bottom) and transverse (top) planes (the figure shows GIOS simulation only; the effects of gas filling have not been considered here).

rotating platform with angles of rotation from $-2°$ to $+10°$ about the vertical line passing through the target.

Gas-filled mode. The hardware layout for the gas-filled mode will be Q1–Q2–MD1–Q3–MD2–Q4–Q5. The distance from the target position to the focal plane will be about 6 m. The maximum solid angle of acceptance is designed to be about 20 msr. The first-order ion-optical layout for this part is shown in Fig. 3.

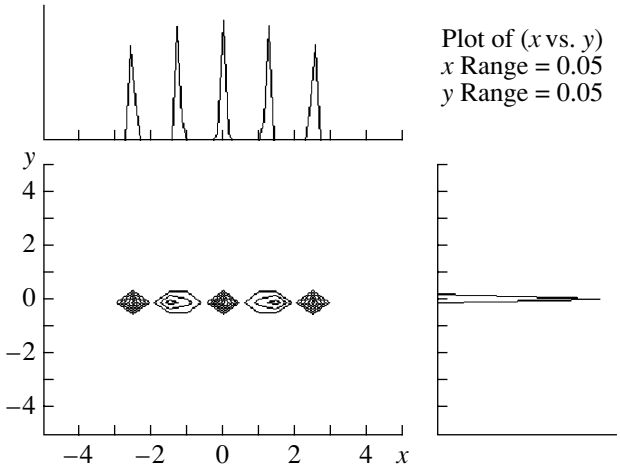

Fig. 4. A simulated mass spectrum at the focal plane of HYRA for the gas-filled part. The detector window is 100×100 mm. Mass dispersion (without gas filling) is 12.5 mm/% of (M/q).

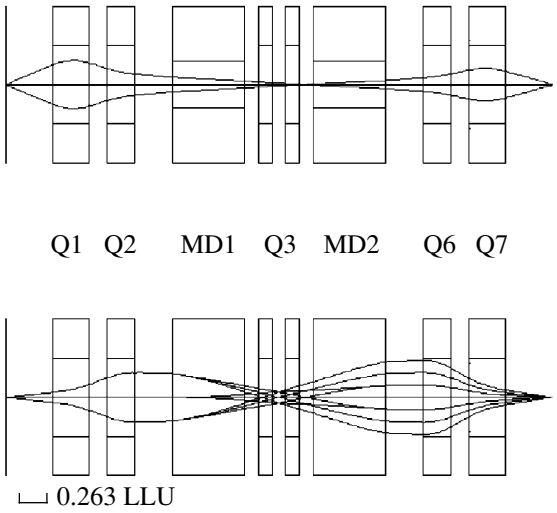

Fig. 5. First-order ion-optical layouts in the dispersive (bottom) and transverse (top) planes up to the momentum achromat position in the vacuum mode of HYRA.

The effects of charge changing collisions of ions with the gas molecules in a magnetic dipole field will result in the ions bending along an average radius of curvature determined by the effective charge state and independent of the initial velocity of the ion. Much the same way, the charge changing collisions of the ions in the quadrupole field is expected to provide focusing strength that depends on the effective charge state.

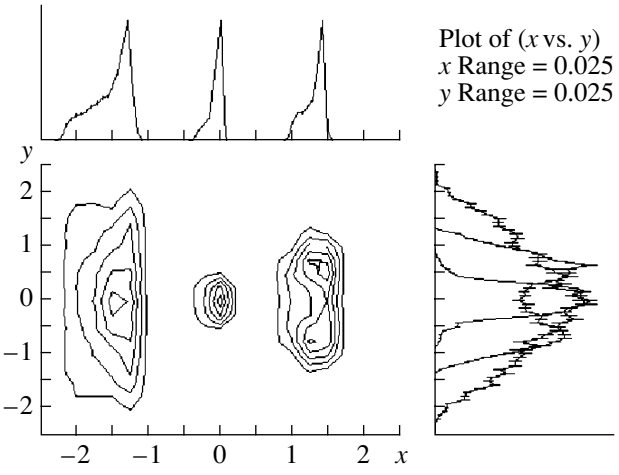

Fig. 6. Momentum separation at the center of Q3 in the vacuum mode of HYRA. The x–y window is 50×50 mm; 5% separation in magnetic rigidity causes 15-mm spatial separation. The simulation includes the effects of aberration up to third order in both x and y.

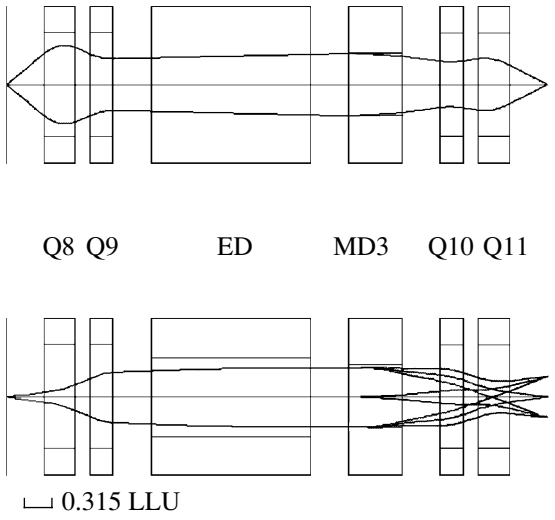

Fig. 7. First-order ion-optical layouts in the dispersive (bottom) and transverse (top) planes from the momentum achromat position up to the focal plane in the vacuum mode of HYRA.

This charge and velocity focusing leads to enhanced transport efficiency. The ion-optical dispersion is optimized to be 12.5 mm/%. First-order mass dispersion for this mode (without the effect of gas filling) is shown in Fig. 4.

Vacuum mode. The hardware layout for the vacuum mode is Q1–Q2–MD1–Q3–MD2–Q6–Q7–Q8–Q9–ED–MD3–Q10–Q11. The total length for this mode will be about 14 m. The solid angle of acceptance is designed to be varied up to 6 msr. The first part of HYRA, in this mode, will act as a momentum achromatic system with an intermediate x and y focus between Q7 and Q8. The ion-optical layout for the momentum achromat condition is shown in Fig. 5. Sufficient space has been kept around the intermediate focal plane to place collimator, detectors, etc.

At the center of Q3, particles of different momenta will be separated spatially. This will give the option of stopping the unwanted beam particles by inserting an appropriate slit assembly. Momentum separation at the center of Q3 is shown in Fig. 6.

Once momentum achromatic focus is achieved at the intermediate focal point between Q7 and Q8, the rest of the HYRA will act like a conventional RMS, though the second part deviates from the symmetric ED–MD–ED configuration. The ion-optical layout in the mass dispersive mode from the intermediate to the final focal plane of HYRA is shown in Fig. 7.

At the focal plane, final mass dispersion will be 10 mm/% of M/q. This can be increased up to 20 mm/%, but at the cost of slightly poorer mass resolution, as angle and mass-dependent higher order aberration terms tend to blow up. A small component of hexapole and octupole fields will be introduced in the last two quadrupoles by shift of the pole faces. This will help in achieving a cleaner mass spectrum. A simulated mass spectrum at the focal plane is shown in Fig. 8.

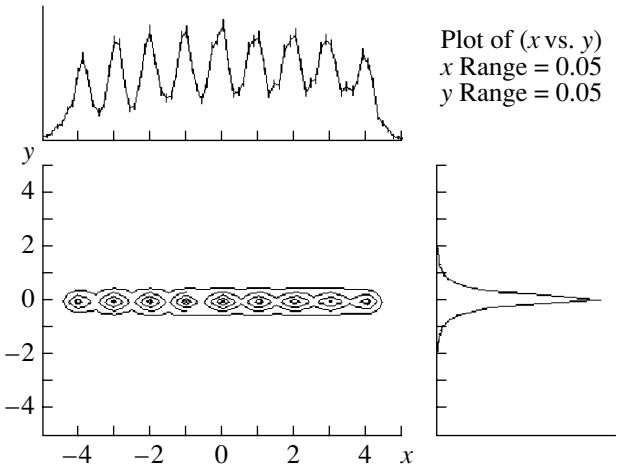

Fig. 8. (M/q) dispersion (10 mm/%) at the focal plane in the vacuum mode of HYRA. The detector window is 100×100 mm. Neighboring peaks differ by 1% of (M/q) with the central peak having $(M/q) = 107/31$. The simulation includes the effects of aberration up to third order in both x and y.

3.2. HYRA Coupled with a Large Gamma Array

The new mass separator HYRA, apart from being operated stand-alone in the two modes already discussed, would be used in conjunction with a

Large Gamma Array (LGA) for recoil-tagged spectroscopic studies. HYRA will act as the positive channel selector in the mode chosen, depending on the mass of the compound nucleus. The gamma-detector array will consist of 12 Compton-suppressed Clover detectors. With the Clover detectors pooled in from other institutes in India, the Indian National Gamma Array (INGA), consisting of 24 Compton-suppressed Clover detectors, will be realized. In the case of INGA, the geometrical solid angle of the array would be $\sim$20% of 4π and the total photopeak efficiency is estimated to be $\sim$5%.

3.3. Planned Physics Program

In the gas-filled mode, HYRA will be used for the study of fusion–fission and fission hindrance mechanism in the mass region $A \sim 200$, formation of very heavy systems, and recoil-tagged gamma spectroscopy of transuranium nuclei.

In the vacuum mode of operation, focus will be upon the $N = Z$ nuclei up to $A \sim 120$. Structures of these very neutron-deficient nuclei will be explored by recoil-tagged gamma spectroscopy.

The first section of HYRA sans the gas (i.e., QQ–D–Q–D–QQ) may also be used for extracting light and medium-mass radioactive ion beams using reactions such as (p, n) and (d, n) in inverse kinematics.

ACKNOWLEDGMENTS

The Hybrid Recoil Mass Analyzer project proposed by A.K. Sinha, N. Madhavan, P. Sugathan, J.J. Das (all from NSC), R. Singh (Delhi Univ.), K.M. Varier (Calicut Univ.), and M.C. Radhakrishna (Bangalore Univ.) is supported by the Department of Science and Technology (DST), Government of India (GOI), under grant no. SP/I2/PF-02/99. The Large Gamma Array (LGA) project, proposed by R.K. Bhowmik (NSC), S.C. Pancholi (Delhi Univ.), S.K. Datta (NSC), and S.B. Patel (Mumbai Univ.) is supported by the DST, GOI, under grant no. SP/S2/K-24/97.

REFERENCES

1. T. M. Cornier, M. G. Herman, B. S. Lin, and P. M. Stwertka, Nucl. Instrum. Methods Phys. Res. A **212**, 185 (1983).
2. P. Spolaore, J. D. Larson, C. Signorini, *et al.*, Nucl. Instrum. Methods Phys. Res. A **238**, 381 (1985).
3. C. N. Davids, B. B. Back, K. Bindra, *et al.*, Nucl. Instrum. Methods Phys. Res. B **70**, 358 (1992).
4. A. K. Sinha, N. Madhavan, J. J. Das, *et al.*, Nucl. Instrum. Methods Phys. Res. A **339**, 543 (1994).
5. H. Ikezoe, Y. Nagame, T. Ikuta, *et al.*, Nucl. Instrum. Methods Phys. Res. A **376**, 420 (1996).
6. C. J. Gross *et al.*, Nucl. Instrum. Methods Phys. Res. A **450**, 12 (2000).
7. K. Subotic, Y. T. Oganessian, V. K. Utyonkov, *et al.*, Nucl. Instrum. Methods Phys. Res. A **481**, 71 (2002).
8. M. Leino, J. Äystö, T Enqvist, *et al.*, Nucl. Instrum. Methods Phys. Res. B **99**, 653 (1995).
9. V. Ninov, P. Armbruster, F. P. Heßberger, *et al.*, Nucl. Instrum. Methods Phys. Res. A **357**, 486 (1995).
10. K. Morita, A. Yoshida, T. T. Inamura, *et al.*, Nucl. Instrum. Methods Phys. Res. B **70**, 220 (1992).
11. A. Ghiorso, S. Yashita, M. E. Leino, *et al.*, Nucl. Instrum. Methods Phys. Res. A **269**, 192 (1988).
12. B. L. Cohen and C. B. Fulmer, Nucl. Phys. **6**, 547 (1958).
13. C. B. Fulmer and B. L. Cohen, Phys. Rev. **109**, 94 (1958).
14. V. Tripathi, L. T. Baby, J. J. Das, *et al.*, Phys. Rev. C **65**, 014614 (2002).
15. L. T. Baby, V. Tripathi, J. J. Das, *et al.*, Phys. Rev. C **62**, 014603 (2000).
16. A. M. Vinodkumar, K. M. Varier, N. V. S. V. Prasad, *et al.*, Phys. Rev. C **53**, 803 (1996).
17. N. V. S. V. Prasad, A. M. Vinodkumar, A. K. Sinha, *et al.*, Nucl. Phys. A **603**, 176 (1996).
18. K. M. Varier, A. M. Vinodkumar, N. V. S. V. Prasad, *et al.*, Pramana, J. Phys. **53**, 167 (1999).
19. V. Tripathi, L. T. Baby, P. V. M. Rao, *et al.*, Pramana, J. Phys. **53**, 173 (1999).
20. L. T. Baby, V. Tripathi, D. O. Kataria, *et al.*, Phys. Rev. C **56**, 1936 (1997).
21. D. O. Kataria, A. K. Sinha, J. J. Das, *et al.*, Phys. Rev. C **56**, 1902 (1997).
22. I. M. Govil, R. Singh, A. Kumar, *et al.*, Phys. Rev. C **57**, 1269 (1998).
23. S. K. Tandel, S. B. Patel, R. K. Bhowmik, *et al.*, Phys. Rev. C **56**, R2358 (1997).
24. S. K. Tandel, S. B. Patel, R. K. Bhowmik, *et al.*, Nucl. Phys. A **632**, 3 (1998).
25. B. Mukherjee, S. Muralithar, G. Mukherjee, *et al.*, Acta Phys. Hung. New Ser.: Heavy Ion Phys. **11**, 189 (2000).
26. S. K. Hui, C. R. Bhuinya, A. K. Ganguly, *et al.*, Phys. Rev. C **62**, 054604 (2000).
27. J. J. Das, P. Sugathan, N. Madhavan, *et al.*, J. Phys. G **24**, 1371 (1998).
28. J. J. Das, P. Sugathan, N. Madhavan, *et al.*, Indian. J. Phys. **73S**, 136 (1999).
29. J. J. Das, P. Sugathan, and N. Madhavan, Indian. J. Pure Appl. Phys. **39**, 20 (2001).
30. H. Wollnik, J. Brezina, and M. Berz, Nucl. Instrum. Methods Phys. Res. A **258**, 408 (1987).

Physics of Atomic Nuclei, Vol. 66, No. 8, 2003, pp. 1528–1535. From Yadernaya Fizika, Vol. 66, No. 8, 2003, pp. 1572–1579.

The Characteristics of the Halo Neutron Preemission in the Fusion of ^{11}Li with Light Targets*

M. Petrascu**

Horia Hulubei National Institute for Physics and Nuclear Engineering, Bucharest, Romania

Received January 19, 2003

Abstract—The main characteristics of the halo neutron preemission in the fusion of ^{11}Li nuclei with light targets are reviewed. The recent experiment with a new array detector aimed at investigating neutron pair preemission is described. The position distribution measurement confirms the preemission of the halo neutrons in a very narrow forward cone of ~9 msrad. A novel approach for cross-talk rejection is described. By means of this approach, the true n–n coincidence sample was obtained. In view of obtaining the n–n correlation function, the crucial problem of the denominator construction is thoroughly analyzed. It was found that the single-product denominator built by a random coupling of single detected neutrons followed by cross-talk rejection, exceeds by up to 70% the denominator constructed by the event-mixing technique. We consider this behavior of the single-product denominator together with the large fluctuations seen when represented in small steps of relative momentum q as experimental evidence for residual correlation of single detected halo neutrons. © *2003 MAIK "Nauka/Interperiodica".*

1. INTRODUCTION

The neutron halo nuclei were discovered by Tanihata *et al.* [1]. These nuclei are characterized by very large matter radii, small separation energies, and small internal momenta of the valence neutrons.

Recently, it was predicted [2] that, due to the very large dimension of ^{11}Li, one may expect that, in a fusion process on a light target, the valence neutrons may not be absorbed together with the ^{9}Li core, but may be emitted in the early stage of the reaction. Indeed, the experimental investigations of neutron preemission in the fusion of ^{11}Li halo nuclei with Si targets [3–9] have shown that a fair amount of fusions (40 ± 12)% are preceded by one- or two-halo-neutron preemission.

In Fig. 1, it is illustrated why in the fusion process the preemission probability cannot be 100%. In some cases, both neutrons could escape (Fig. 1*a*) or both neutrons could be absorbed by the screening projectile and target nuclei (Fig. 1*b*). In other noncentral collision cases, it may happen that only one halo neutron could escape (Fig. 1*c*).

It was also found that, in the position distribution of the preemitted neutrons, a very narrow neutron group, leading to a transverse momentum distribution much narrower than that predicted by COSMA [10] model, is present (see Section 3.2 below). Some evidence based on preliminary n–n coincidence measurements, concerning the presence of neutron pairs within the narrow neutron group, has been mentioned in [8, 11]. In light of this evidence, the narrow neutron distribution could be caused by the final-state interaction between the two neutrons, preemitted in the fusion process. This view is supported by a more elaborated coincidence analysis of [8]. The results of this analysis are shown in Fig. 10 of [8]. Although the statistics of coincidences in Fig. 10 of [8] is poor, nevertheless it is an indication of neutron pair preemission within the narrow neutron group. Therefore, on the basis of these first results, it was decided to perform a new experiment aiming to investigate the neutron pair preemission in conditions of much higher statistics by means of a neutron array [12] detector.

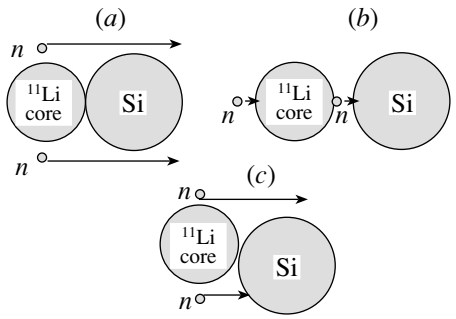

Fig. 1. Schematic representation of the halo neutron preemission in the fusion of ^{11}Li projectiles with Si targets.

*This article was submitted by the author in English.

**e-mail: mpetr@ifin.nipne.ro

In the following, first I will present the experimental setup and the results obtained for the neutron energy spectrum and position distribution. The criterion for selection of true n–n coincidences, some simulation by the aid of MENATE program, and the n–n true coincidence sample related to preemission, I will present afterwards. Finally, I will present an analysis concerning the building of the correlation function denominator.

2. THE EXPERIMENTAL SETUP

The experimental arrangement [13] is shown in Fig. 2. In this arrangement, a thin scintillator mounted at the F2 focus of RIPS, two position-sensitive parallel plate avalanche counters P1 and P2, a Veto1 scintillator having a 2×2 cm^2 hole, a MUSIC chamber with a Si-strip (SiS) detector-target and a Veto2 Si detector mounted inside, and an 81-component neutron array detector were used. As a trigger in this experiment, the $\mathrm{F2} \cdot \mathrm{P2} \cdot \overline{\mathrm{Veto1}} \cdot \mathrm{SiS} \cdot \overline{\mathrm{Veto2}}$ coincidences were chosen.

The array detector consists of 81 modules, made of $4 \times 4 \times 12$ cm^3 BC-400 crystals, mounted on XP2972 phototubes. This detector, placed in the forward direction at 138 cm from the target, was used for the energy (by time of flight) and position determination of the neutrons originating from the target. The crystals were wrapped with black paper. The numbering scheme of the neutron array detector is shown in the table. The detector labeled 1 was placed in the center. Detectors 2–9 are the closest detectors surrounding detector 1. Then follows the second circle formed by detectors 10–25, the third circle formed by detectors 26–49, and the fourth circle formed by detectors 50–81. Coincidences between some detector and the closest detectors are considered in this paper as first-order coincidences and so on.

3. THE MAIN RESULTS OBTAINED

3.1. The Energy Spectrum of Single Detected Neutrons

The neutron energy was determined by time of flight on a path of 1.38 m. In Fig. 3, the single-neutron energy spectrum detected by the detectors 1 to 9 is illustrated. The vertical lines *2*, *3* in Fig. 3 mark the time-of-flight gate between 12.2 and 14.2A MeV of the ^{11}Li beam, chosen in processing of the data. Vertical line *1* marks the 9-A MeV energy of the beam at the exit from the Si detector-target. By taking into account the energy resolution of ~6%, the neutron energy range related to the preemission process is ~8–15 MeV.

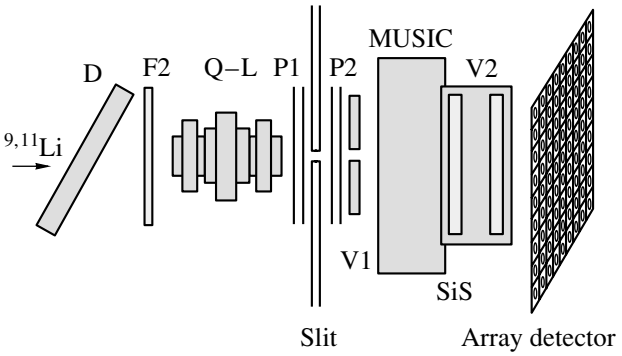

Fig. 2. General setup of the experiment. In this arrangement, a thin scintillator mounted at the F2 focus of RIPS, two position-sensitive parallel plate avalanche counters P1 and P2, a Veto1 scintillator having a 2×2 cm^2 hole, a MUSIC chamber with a Si-strip (SiS) detector-target and a Veto2 Si detector mounted inside, and an 81-component neutron array detector were used.

The dotted line represents the spectrum obtained by taking into account the detection efficiency correction calculated by using the Monte Carlo MENATE [14] program. One may observe some spikes in this spectrum at the energy $E = 9.25$ and 11.25 MeV. These types of spikes are also present in the neutron momentum spectrum at 132.5 and 147.5 MeV/c (see Section 4.1 below), but they are at the limit of statistical significance.

The neutron spectrum in Fig. 3 has a maximum near 11.25 MeV. It is broader than the energy of the beam at the entrance into the 0.5-mm Si detector-

The numbering scheme of the neutron array detector

54	53	52	51	50	81	80	79	78
55	29	28	27	26	49	48	47	77
56	30	12	11	10	25	24	46	76
57	31	13	3	2	9	23	45	75
58	32	14	4	1	8	22	44	74
59	33	15	5	6	7	21	43	73
60	34	16	17	18	19	20	42	72
61	35	36	37	38	39	40	41	71
62	63	64	65	66	67	68	69	70

Note: The detector labeled 1 was placed in the center. Detectors 2–9 are the closest detectors surrounding detector 1. Then follows the second circle, formed by detectors 10–25; the third circle, formed by detectors 26–49; and the fourth circle, formed by detectors 50–81. Coincidences between some detector and the closest detectors are considered in this paper as first-order coincidences and so on.

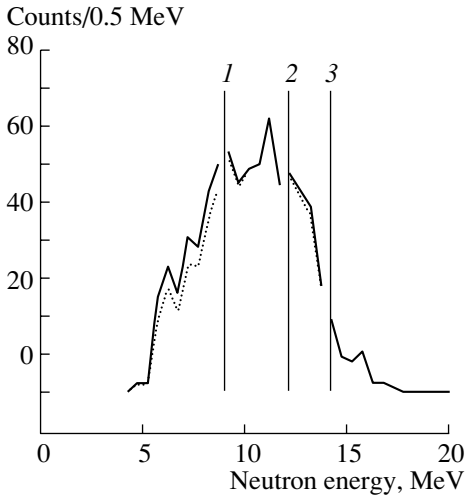

Fig. 3. This spectrum was obtained in event-by-event processing of the measured data and corresponds to detectors 1–9. Only the events with single neutrons are considered here. The vertical lines *2* and *3* mark the limits (lower and higher) of the ^{11}Li beam energy per nucleon entering the 0.5-mm-thick Si detector-target. The line *1* marks the lowest energy of the beam at the exit of the target.

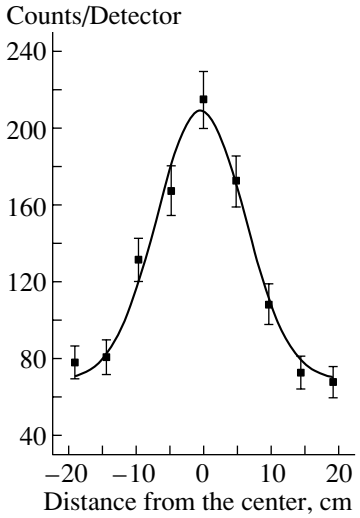

Fig. 4. The position spectrum measured along the horizontal line connecting detectors 58, 32, 14, 4, 1, 8, 22, 44, 74 (see the table) is shown. The neutron energy was selected between 6–16 MeV. The FWHM of this spectrum is ∼13 cm and corresponds to an aperture of ∼ 5.5° of the cone enveloping this forward neutron peak (solid angle ∼9 msrad).

target, due to the beam energy loss between the entrance point and the point where the fusion takes place. This means that the neutrons are flying with the energy corresponding to the beam velocity at the moment a fusion takes place in the Si target. This is an important characteristic of the halo neutron

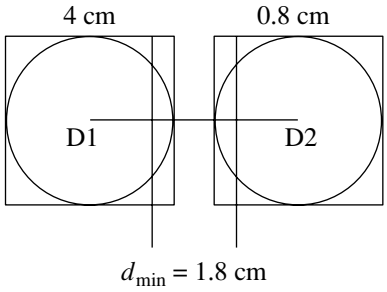

Fig. 5. The principle of c.t. rejection by using parameter $d_{\min}$ for first-order coincidences is shown. Represented here are two detectors, the distance between their centers being 4.8 cm. The distance $d_{\min} = 1.8$ cm for rejection is considered.

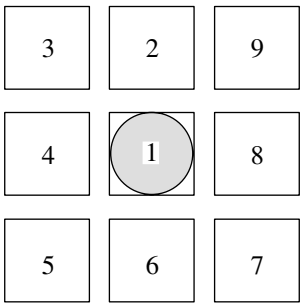

Fig. 6. Illustration of the simulation and rejection of c.t. by using the Monte Carlo program MENATE. Detector 1 is fired uniformly with 100 000 neutrons of given energy. The program gives the c.t. in each of the surrounding detectors 2–9 and the rejected c.t. as a function of $d_{\min}$.

preemission in the fusion of ^{11}Li halo nuclei with Si targets.

In the neutron spectrum, there is the zone between 4–8 MeV that apparently is not related to the preemission process. A possible process accounting for this part of the spectrum was described in [15].

3.2. The Position Distribution of the Preemitted Neutrons

The position spectrum measured along the horizontal line connecting detectors 58–74 is shown in Fig. 4. The neutron energy was selected between 6–16 MeV. The FWHM of this spectrum is ∼13 cm and corresponds to an aperture of ∼5.5° of the cone enveloping the forward neutron peak. The cone allowed by the internal momentum of the halo neutrons by taking into account the COSMA model is ∼150 msrad. It follows that a part of the preemitted neutrons is focused in a solid angle 15 times narrower than that predicted by the COSMA model [10]. This is another important characteristic of the neutron preemission. A possible explanation of this effect is presented in [16].

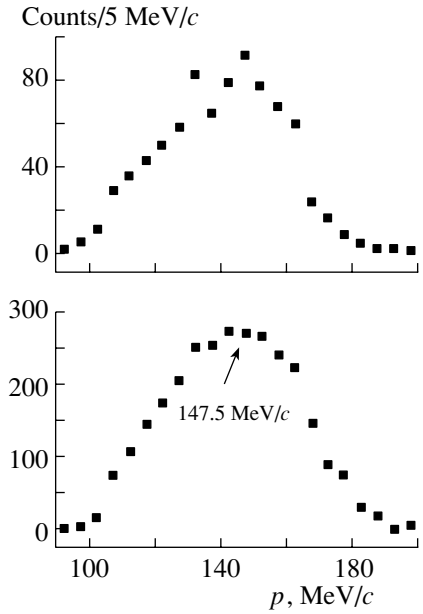

Fig. 7. The p-momentum spectrum of single detected neutrons by detectors 1 to 9 (upper part) and by detectors 1 to 49 (lower part). The total number of detected single neutrons is 783 in the upper part and 2865 in the lower part of the figure.

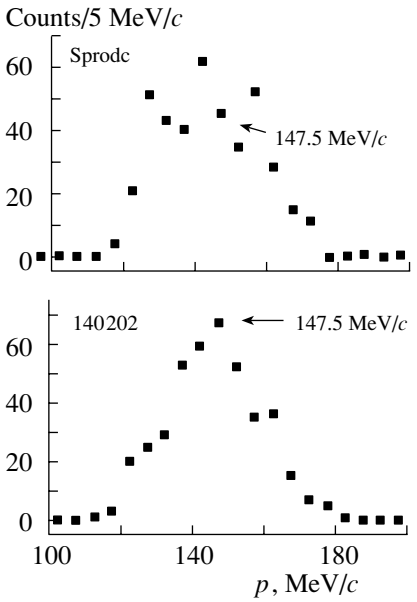

Fig. 8. The upper part of the spectrum corresponds to the distribution built by using condition (b). The lower part corresponds to the distribution built by using condition (a).

3.3. The n–n Coincidences

3.3.1. Selection of true coincidences and rejection of cross-talk

Here, the true n–n coincidences were selected by using the criterion of [17].

A coincidence between two detectors is rejected whenever the following condition is fulfilled:

$$E_1 > E_{\min} = \frac{1}{2} m \frac{d_{\min}^2}{\Delta t^2}, \qquad (1)$$

in which E_1 is the energy of the first arriving neutron in a time-of-flight measurement. $E_{\min}$ is the minimum energy required by the neutron scattered from the first detector to travel the minimum distance $d_{\min}$ to the second detector, in the time interval Δt. For the first rejection, $d_{\min}$ was considered as the distance between the centers of the detectors and Δt, the difference between the arrival times corresponding to the first and second neutrons. For example, by applying this criterion to the first-order coincidences, 118 coincidences were found from 447 coincidences. It follows that the rejection of coincidences by using formula (1) is up to 74%. For further rejection, we consider that it is more appropriate to use the parameter $d_{\min}$, because the distance between the adjacent detector centers is close to the detector dimension.

By taking $d_{\min}$ =1.8 cm as specified in Fig. 5, the number of first-order true coincidences is reduced from 118 to 46. Thus the rejection rises from 74 to 90%. From geometrical considerations, assuming a uniform distribution of the neutrons coming from the target over the surface of detector 1, in the 5-mm slice are about 12% of the incoming neutrons. Assuming also that these neutrons are scattered toward detector 2, it follows that the remaining c.t. is less than 1.5%. We tested the consistency of such data by using the MENATE program.

3.3.2. The simulation and rejection of cross-talk by using the Monte Carlo program MENATE

The author of MENATE, P. Desesquelles, has adapted the program [14] for calculation of cross-talk rejection for the case, when $d_{\min}$ is used as a rejection parameter.

One of the configurations used is shown in Fig. 6. Detector 1 is uniformly fired by neutrons of given energy. The cross-talk, cross-talk rejection, and diaphony are calculated as a function of the incoming energy of the neutron, the detector number, and the distance $d_{\min}$. For example, in the case of 100 000 neutrons with 15 MeV fired on detector 1, the total induced cross-talk on detectors 2–9 is 2815 counts, of which 2814 are rejected for $d_{\min}$ = 1.8 cm. This means that, in about 3000 counts, only one c.t. could pass as a true coincidence. In the case $d_{\min}$ = 4.8 cm, about 7% of c.t. could pass as true coincidences.

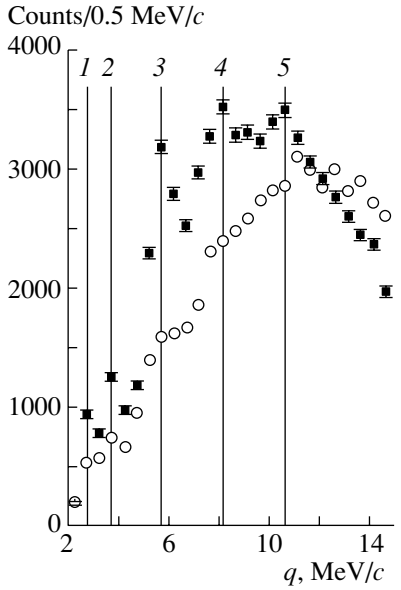

Fig. 9. The solid circles with error bars represent the denominator of the correlation function built by using the distribution obtained under condition (a). The open circles represent the denominator of the correlation function built by using the distribution obtained under condition (b).

3.3.3. The total number of true n–n coincidences within the narrow forward cone

After applying the above rejection procedure, 204 true coincidences remain (46 first-order, 71 second-order, 46 third-order, and 41 fourth-order coincidences). An approach for the percentage estimation of neutron pair preemission within the narrow cone, including also the neutrons within the 5–8 MeV range is presented in [13].

4. THE BUILDING OF THE CORRELATION FUNCTION DENOMINATOR

The two-neutron correlation function is given by [18]

$$C(q) = k\frac{N_c(q)}{N_{nc}(q)}, \qquad (2)$$

in which $N_c(q)$ represents the yield of n–n coincidence events and $N_{nc}(q)$ represents the yield of uncorrelated events. The variable q is the relative momentum $q = (1/2)|\mathbf{p}_1 - \mathbf{p}_2|$, in which $\mathbf{p}_1$ and $\mathbf{p}_2$ are the momenta of the two neutrons in l.s. The normalization constant k is obtained from the condition that $C(q) = 1$ at large relative momenta. A crucial problem for obtaining $C(q)$ is the construction of the denominator in formula (2), and therefore the main emphasis of my talk in the following is related to this problem. In general, two different approaches are commonly used. In the event-mixing technique, the denominator is generated by randomly mixing neutrons from the coincidence sample. This method ensures that the uncorrelated distribution includes the same class of collision and kinematic constraints as the numerator, but has the disadvantage that it may distort the correlations one wishes to measure, since the event-mixing technique may not completely succeed in decorrelating the events. In the single-product technique, the denominator is constructed from the product of single distributions. This method is preferred in [17], considering that the background yield is truly uncorrelated, but this is not valid for halo neutrons [19], due to the residual correlation of single neutrons. In fact, we will present in this paper experimental evidence for the residual correlation of single detected neutrons. The correlated background introduces a further complication, which is the dependence of the correlation function denominator on the energy or momentum distribution of the true n–n coincidence sample. We have proven this by using the single-product technique in two extreme cases: (a) by coupling randomly single neutrons and by applying afterwards the rejection [17] procedure; (b) by replacing the neutrons in the sample of coincidence events with neutrons from the sample of single neutrons. We will show in the following that the denominator A obtained with condition (a) gives large fluctuations when represented in small steps (0.5 MeV/c) of q. In the case when larger steps of q are used (2 MeV/c), the denominator A is significantly higher (up to 70%) than the denominator B obtained with condition (b).

We have also found that the denominator obtained with condition (b) is very close to the denominator obtained by using the event-mixing technique. In the following, the data supporting these conclusions are presented:

(1) The p momentum spectra of single neutrons detected by detectors 1 to 9 and 1 to 49.

(2) The p momentum distribution of single neutrons selected by conditions (a) and (b). These data are the input data into the program for the calculation of the correlation function denominator.

(3) The denominators of the correlation function (q in steps of 0.5 MeV/c) obtained with conditions (a) and (b).

(4) The denominators of the correlation functions (q in steps of 2 MeV/c) obtained with conditions (a) and (b).

(5) The denominators of the correlation function obtained with condition (b) and by event mixing.

(6) Discussion of the obtained results.

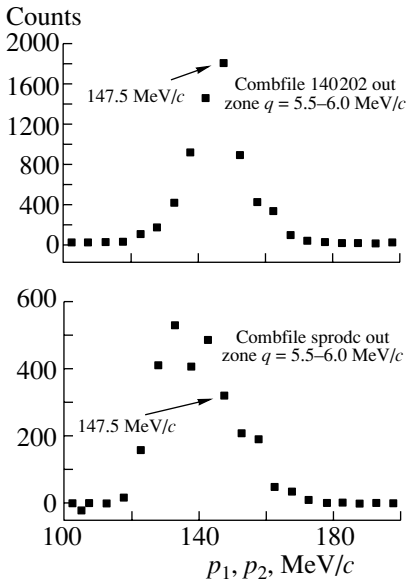

Fig. 10. p Distribution in the range $q = 5.5$–6.0 MeV/c for conditions (a) (upper part) and (b) (lower part). These distributions were extracted from the 6.21-Mb combination files containing the data for the two denominators.

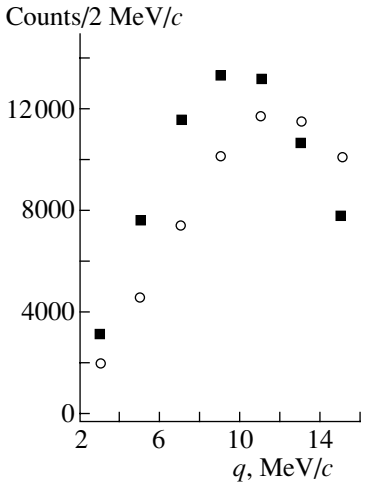

Fig. 11. The same denominators as in Fig. 9 are represented here as a function of q momentum in steps of 2 MeV/c.

4.1. The p-Momentum Spectra of Single Neutrons Detected by Detectors 1 to 9 and 1 to 49

One may see in Fig. 7 that the p spectrum corresponding to detectors 1 to 49 is smooth with no sign of an outside neutron source. The fluctuations seen in the spectrum corresponding to detectors 1 to 9 are at the limit of statistical significance.

4.2. The p-Momentum Distribution of Single Neutrons Selected by Conditions (a) and (b)

The lower spectrum in Fig. 8 corresponds to the distribution built by using condition (a), that is, by coupling randomly single neutrons and by applying afterwards the rejection [17] procedure. This spectrum appears to be narrower than the upper spectrum corresponding to condition (b), that is, by replacing the neutrons in the sample of coincidence events with neutrons from the sample of single neutrons. At the same time, the highest four points match the spectrum of Fig. 7, which is expected from a random grouping followed by a c.t. rejection of uncorrelated pairs. On the contrary, the spectrum corresponding to condition (b) is broader and displays irregularities, which is characteristic for somewhat low statistics of true n–n coincidences.

4.3. The Denominators of the Correlation Function (q in Steps of 0.5 MeV/c) Obtained with Conditions (a) and (b)

In Fig. 9, the solid circles with error bars represent the denominator A built by using condition (a), and the open circles represent the denominator B built by using condition (b). These representations are shown for relative momentum q in steps of 0.5 MeV/c between 2 and 15 MeV/c, to better see the difference between them. In the first case, there are present fluctuations marked 1 to 5, the largest one being fluctuation 3.

On the contrary, the denominator built by using condition (b) is much lower than the first one at least for q up to $\sim$12 MeV/c, the range, which is the most interesting for the correlation function. In Fig. 10, the p distributions picked up in the range $q = 5.5$–6.0 MeV/c corresponding to the largest fluctuation 3 in Fig. 9 are shown.

In the upper part of Fig. 10, the p distribution in the range $q = 5.5$–6.0 MeV/c for condition (a) and, in the lower part, this distribution for condition (b) are shown. These distributions were extracted from the 6.21-Mb combination files containing the final results for the correlation function denominators. One can see in Fig. 10 that the p distribution in the upper figure is narrower than in the lower figure. The number of counts due to momentum $p = 147.5$ MeV/c is 6 times larger than in the lower figure. The integrated number of counts in the upper figure is 3192, and in the lower figure, it is 1597. The ratio of these numbers is $\sim$2.

4.4. The Denominators of the Correlation Functions (q in Steps of 2 MeV/c) Obtained with Conditions (a) and (b)

In the next figure (Fig. 11), the same denominators are represented as a function of q in steps of 2 MeV/c.

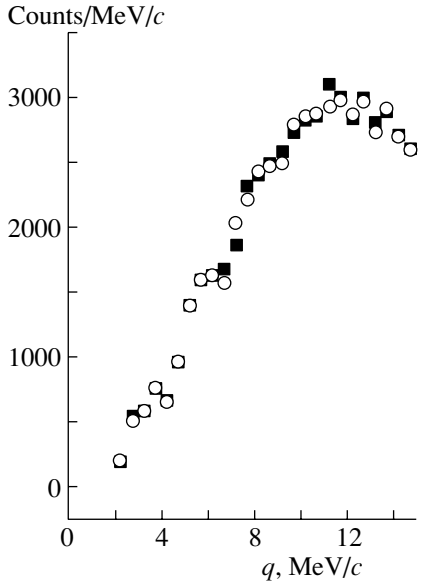

Fig. 12. By solid squares is represented the denominator of the correlation function obtained with condition (b). By open circles is represented the denominator obtained by the event-mixing technique.

In this figure, the solid squares represent the denominator built with condition (a) and the open circles represent the denominator built with condition (b). The ratio R between the two distributions integrated over 2 MeV/c remains large. For example, at $q =$ 3 MeV/c, $R = 1.54$; at $q = 5$ MeV/c, $R = 1.67$; at $q = 7$ MeV/c, $R = 1.54$; at $q = 9$ MeV/c, $R = 1.31$.

4.5. The Denominators of the Correlation Function Obtained with Condition (b) and by Event Mixing

One can see in Fig. 12 that the denominator obtained with condition (b) is quite similar to the denominator obtained with event-mixing technique. From this, it follows that probably the objection [17] that the event mixing after rejection denominator may be constructed with a biased spectrum in which a part of the true neutron coincidences have already been rejected is not very strict.

4.6. Discussion of the Obtained Results

Let us denote by A the denominator obtained under condition (a) and by B the denominator obtained under condition (b). These denominators correspond to different types of p-momentum distributions shown in Fig. 8. Denominator A corresponds to a narrow distribution peaking at 147.5 MeV/c. Denominator B corresponds to a broader p-momentum distribution. This denominator presents some small anomalies (fluctuations, changing of slope, etc.), as can be seen in Figs. 9 and 12, due to some couplings persisting in the event-mixing technique [17]. If in the case of denominator A the strength of these couplings were the same as in the case of B, there would be no reason for denominator A to be higher than denominator B. But in fact, denominator A is significantly higher than B due to the large fluctuations appearing in Fig. 9, replacing the small anomalies seen in the case of B. To these, one should also add the dramatic increase in the number of some momenta shown in Fig. 10. All these facts, we consider as a strong indication of residual correlation of single detected neutrons [19]. In the case of denominator B, the configuration of momenta favors less the manifestation of the residual correlation, and therefore one can see only the small anomalies, but in the case of denominator A, they are strongly evidenced by the fluctuations seen in Fig. 9. Consequently, the denominator B or the denominator built by event mixing could be a very useful tool in checking the correctness of the denominator obtained by using single products. If a type-A denominator is higher than a B denominator, this assuredly will be an indication that denominator A contains additional residual correlations.

In recent tests, the building of a denominator was also considered by using the detectors of the outer circle of the array (detectors 50 to 81). The reason for this was the assumption that the outer detectors should be less affected by the residual correlation. In this case, because the number of single neutrons was much lower than the number of single neutrons detected by the central detectors 1 to 49, it was not possible to apply rejection. Due to the fact that the denominator obtained in this case is, however, higher than B, it follows that the correlation function presented in [16] was underestimated especially in the range of second- to fourth-order coincidences. The effect of denominator B on the correlation function will be presented elsewhere [20].

The above results also underline the importance of higher statistics in experiments aiming to determine the intrinsic correlation function of the halo neutrons. Concerning preemission, one could increase significantly (up to 3.5 times) the number of n–n coincidences by using a C target instead of a Si target. This expected increase is due to the reduction of the screening effect of the target. In addition, we believe that it is very desirable to do combined measurements with ^{11}Li and ^{11}Be or ^{14}Be and ^{11}Be in order to obtain the intrinsic correlation function experimentally. ^{11}Be is a source for single halo neutrons and, therefore, one could construct the denominator of the correlation function free of residual correlation.

5. CONCLUSIONS

From the above presentation, it follows that the interaction of halo nuclei with usual nuclear matter is a rich field, in which new concepts, such as residual correlation, not known before may arise. At the same time, the studies in this field reveal, which approaches are the most effective for getting new information on the structure of the Borromean halo nuclei. In particular, complex experiments, in which Borromean together with ^{11}Be halo nuclei are used, are expected to lead to the intrinsic correlation function, that is, to the mapping of the spacetime structure of nuclei like ^{6}He, ^{11}Li, and ^{14}Be.

ACKNOWLEDGMENTS

This research has been performed jointly with I. Tanihata, T. Kobayashi, K. Morimoto, K. Katori, M. Chiba, Y. Nishi, S. Nishimura, A. Ozawa, T. Suda, and K. Yoshida from RIKEN; with A. Constantinescu, I. Cruceru, M. Giurgiu, A. Isbasescu, M. Isbasescu, and H. Petrascu from HH-NIPNE-Bucharest; and with C. Bordeanu from Weizmann Inst. Rehovot.

I am grateful to Prof. P. Desesquelles for the program MENATE. I also wish to thank Dr. F.M. Marques for sending him part of a paper prior to publication.

REFERENCES

1. Tanihata, H. Hamagaki, O. Hashimoto, *et al.*, Phys. Lett. B **160B**, 380 (1985).
2. M. Petrascu, A. Isbasescu, H. Petrascu, *et al.*, Balkan Phys. Lett. **3** (4), 214 (1995).
3. M. Petrascu, I. Tanihata, T. Kobayashi, *et al.*, Phys. Lett. B **405**, 224 (1997).
4. M. Petrascu, in *Proceedings of the International Summer School, Predeal, Romania, 1995*, Ed. by A. A. Raduta, D. S. Delion, and I. I. Ursu (World Sci., Singapore, 1996).
5. M. Petrascu, I. Tanihata, T. Kobayashi, *et al.*, Preprint RIKEN-AF-NP-237 (1996).
6. M. Petrascu, I. Tanihata, T. Kobayashi, *et al.*, Rom. J. Phys. **43**, 307 (1998).
7. M. Petrascu, C. Bordeanu, M. Giurgiu, and A. Isbasescu, J. Phys. G **25**, 799 (1999).
8. M. Petrascu, I. Tanihata, T. Kobayashi, *et al.*, Rom. J. Phys., Suppl. **44** (1–2), 83 (1999).
9. M. Petrascu, H. Kumagai, I. Tanihata, *et al.*, Rom. J. Phys., Suppl. **44** (1–2), 105 (1999).
10. M. V. Zhukov, V. Danilin, D. V. Fedorov, *et al.*, Phys. Rep. **231**, 151 (1993).
11. M. Petrascu, in *Proceedings of the International Summer School, Predeal, Romania, 1998*, Ed. by A. A. Raduta, S. S. Stoica, and I. I. Ursu (World Sci., Singapore, 1999), p. 268.
12. M. Petrascu, I. Tanihata, I. Cruceru, *et al.*, Rom. J. Phys., Suppl. **44** (1–2), 115 (1999).
13. M. Petrascu, I. Tanihata, T. Kobayashi, *et al.*, Preprint RIKEN-AF-NP-395 (2001).
14. P. Desesquelles, *The Monte Carlo Program MENATE*.
15. M. Petrascu, in *Proceedings of EXON International Symposium, Baikal-Lake, 2001*, Ed. by Yu. E. Penionzhkevich and E. A. Cherepanov (World Sci., Singapore, 2002), p. 256.
16. M. Petrascu *et al.*, in *Abstracts of the VII International School-Seminar*, p. 79.
17. R. Ghetti, N. Colonna, and J. Helgesson, Nucl. Instrum. Methods Phys. Res. A **421**, 542 (1999).
18. G. I. Kopylov, Phys. Lett. B **50B**, 472 (1974).
19. F. M. Marques *et al.,* Phys. Lett. B **476**, 219 (2000).
20. M. Petrascu *et al.*, to be published.

Physics of Atomic Nuclei, Vol. 66, No. 8, 2003, pp. 1536–1543. From Yadernaya Fizika, Vol. 66, No. 8, 2003, pp. 1580–1586.

New Neutron Magic Number $N = 16$ for Neutron-Rich Nuclei*

Z. Dlouhý, D. Baiborodin, J. Mrázek, and G. Thiamová**

(for GANIL–Orsay–Dubna–Řež–Bucharest Collaboration)

Nuclear Physics Institute, Academy of Sciences of the Czech Republic, Řež, Czech Republic

Received January 14, 2003

Abstract—A survey of experimental results obtained at GANIL (Caen, France) on the study of the properties of very neutron-rich nuclei ($Z = 6$–20, $A = 20$–60) near the neutron drip line and resulting in an appearance of further evidence for the new magic number $N = 16$ is presented. Very recent data on mass measurements of neutron-rich nuclei at GANIL and some characteristics of binding energies in this region are discussed. Nuclear binding energies are very sensitive to the existence of nuclear shells, and together with the measurements of instability of doubly magic nuclei ^{10}He and ^{28}O, they provide information on changes in neutron shell closures of very neutron-rich isotopes. The behavior of the two-neutron separation energies S_{2n} derived from mass measurements gives very clear evidence for the existence of the new shell closure $N = 16$ for $Z = 9$ and 10 appearing between the $2s_{1/2}$ and $1d_{3/2}$ orbitals. This fact, strongly supported by the instability of C, N, and O isotopes with $N > 16$, confirms the magic character of $N = 16$ for the region from carbon up to neon, while the shell closure at $N = 20$ tends to disappear for $Z \leq 13$. Decay studies of these hardly accessible short-lived neutron-rich nuclei from oxygen to silicon using in-beam γ-ray spectroscopy are also reported. © *2003 MAIK "Nauka/Interperiodica".*

1. INTRODUCTION

The study of the properties of extremely neutron- or proton-rich nuclei of light elements is a very important topic in modern nuclear physics. In extreme configurations of the nuclear matter, the higher sensitivity of the nuclear models to the choice of the nuclear potential parameters also gives us the opportunity to test different nuclear models. Research in this field has revealed the "halo" and/or "skin" nuclear structure [1, 2], phenomena quite different from the matter distribution of other particle-stable nuclei. The halo nucleus is supposed to consist of a core that is surrounded by one or two loosely bound neutrons moving far away from the core. The core has the same size as the bare nucleus forming the core and having a radius that corresponds to the mass of the core nucleus. Thus, by addition of one or two loosely bound valence neutrons to this core, the radius of the next neutron-rich isotope (i.e., the halo nucleus) can suddenly increase due to the relatively large distance of its valence neutrons from the core.

The nuclei near the drip line also exhibit other unique features such as deformations of nuclei near the drip line with magic neutron numbers, shape coexistence, or variations in the spin–orbit strength as a function of the N/Z ratio that could result in the modification of magic numbers in very neutron-rich nuclei [3, 4]. A breaking of magicity has already been observed at the $N = 20$ neutron shell closure, where an island of inversion in shell ordering has been shown to exist [5–8]. Such behavior has very wide consequences that have resulted in the instability of the doubly magic nuclei ^{10}He [9, 10] and ^{28}O [11, 12]. The anomalous behavior of the binding energies near the shell closure $N = 20$ close to the neutron drip line is also closely connected to this question.

Until recently, no experimental evidence about magic numbers, substituting $N = 20$, was available, though some theoretical calculations predict the existence of new magic number $N = 16$ [13]. Recently, two articles have appeared where evidence for existence of neutron magic number $N = 16$ for nuclei near the drip line has been presented. In our article [14], the evidence has been obtained from the dependence of two-neutron separation energy on Z and N; in the parallel experimental work of Ozawa *et al.* [15], information has been obtained from interaction cross sections and one-neutron separation energies.

Moreover, the determination of the lifetime [16] and of the deformation of ^{44}S [17] has indicated the existence of a similar effect at $N = 28$. This is the first shell closure that arises from the spin–orbit splitting and is responsible for the $1f_{7/2}$–$2p_{3/2}$ shell gap.

*This article was submitted by the authors in English.

**e-mail: dlouhy@ujf.cas.cz

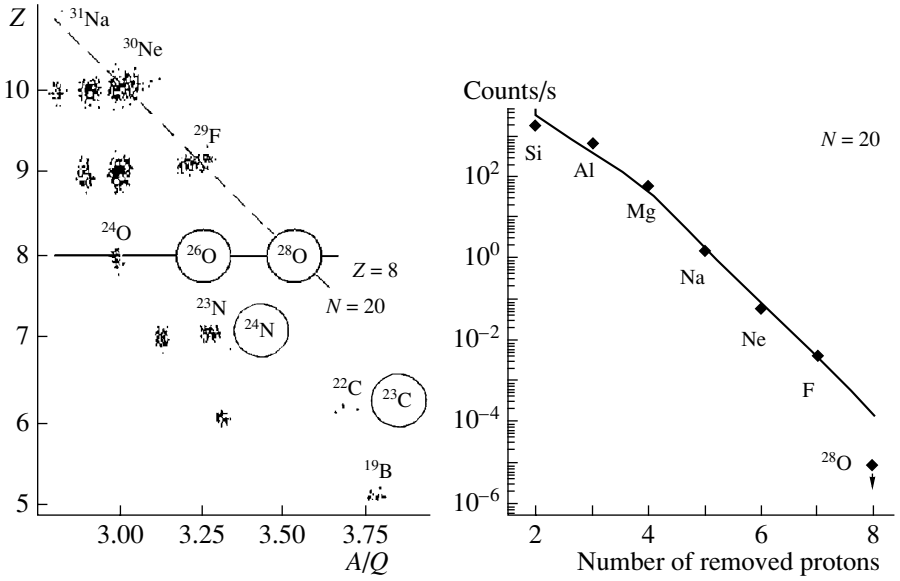

Fig. 1. Two-dimensional identification plot A/Q vs. Z (left); no counts have been observed for ^{24,25}N, ^{25,26,27,28}O. Yields of $N = 20$ isotones measured in experiment (right); the point with arrow for ^{28}O corresponds to the upper limit of one detected event.

The study of shell closures $N = 20$ and 28 is particularly interesting since the vanishing of the latter one could be the first evidence of the weakening of the spin–orbit force in neutron-rich nuclei. The determination of a neutron and proton drip line is also very important since it limits the particle stability region.

The properties of exotic nuclei have been studied in the GANIL–Orsay–Dubna–Řež–Bucharest collaboration. The radioactive nuclear beam facility at GANIL (France) with the LISE3 and SPEG spectrometers allows us to produce and study intense beams of very neutron-rich nuclei, previously unavailable. This equipment enables us to observe the unique properties of nuclei lying near the limit of the particle stability which possess extreme matter configurations.

The aim of the experiments was to study the particle stability of these nuclei; their masses, which constitute the basic knowledge of the nucleus; and their spectroscopic characteristics. Due to the inaccessibility of these short-lived nuclides, very little is known about their spectroscopy. Spectroscopic measurements can reveal details of the underlying microscopic structures and have proved essential for understanding these unexpected properties. Furthermore, they potentially provide a stringent test of the modern large-scale shell model calculations applied to elucidate these problems [8]. The investigation should also shed some light on the rearrangement of the magic numbers in neutron-rich nuclei at the drip line.

2. PARTICLE STABILITY OF NEUTRON-RICH NUCLEI AT AND AROUND DOUBLE MAGICITY

The experimental determination of the neutron drip line is very important for the understanding of nuclear stability in extreme values of isospin. During the last five years, our knowledge has been considerably extended concerning the stability of extremely neutron-rich isotopes; renewed efforts to search for new isotopes have been encouraged and many significant achievements have been obtained in the field.

For more than 30 years, a number of experiments [18] have been carried out to search for the doubly magic ^{10}He nucleus, which, if bound, would possess the highest N/Z ratio among all known nuclei. The experiments led to a conclusion, supported by fragmentation studies, that ^{10}He is probably unbound.

In 1994, Korsheninnikov *et al.* [9] investigated the ^{11}Li fragmentation using an invariant mass measurement, and at the same time, Ostrowski *et al.* [10] measured the mass and two excited states of ^{10}He with the ^{10}Be(^{14}C,^{14}O)^{10}He reaction. Both experiments led to the confirmation of the unbound ^{10}He ground state.

Recently, in our experiment on the LISE3 spectrometer at GANIL, we have used the fragmentation of the neutron-rich projectile ^{36}S to synthesize light very neutron-rich nuclei in the vicinity of the doubly magic nucleus ^{28}O, in order to determine the particle stability and to study the properties of these

nuclei [11]. The particle stability of ^{26}O has been predicted by many theoretical models, even though the particle instability of ^{25,26}O has been clearly shown in two experiments [19, 20]. On the other hand, the ^{28}O nucleus was predicted to be particle unstable despite its double magicity.

The fragmentation of a $^{36}S^{16+}$ ($E/A = 78.1$ MeV) beam on a ^{181}Ta (643 μm) target was used in the search for heavy oxygens. Passing the spectrometer (full flight distance 42 m), the reaction products were focused and separated by a system of quadrupole lenses, two dipole magnets operated in achromatic mode (with rigidity 4.3 and 3.2 T m), and a Wien filter. Products were identified unambiguously by the time-of-flight method, the energy loss, and the total kinetic energy measured by five planar surface barrier Si and Si(Li) detectors of different thickness mounted in a vacuum chamber at the achromatic focal point of LISE3.

In our experiment [11], no events corresponding to ^{26}O and ^{28}O were observed, as one can see from the identification matrix accumulated during 53 h of measurement shown in Fig. 1. Moreover, no events corresponding to the odd oxygen isotopes ^{25,27}O, to ^{24,25}N, or to ^{23}C were found. According to the experimental dependence of measured yield of light nuclei with $N = 20$ on the number of protons removed from ^{36}S also shown in Fig. 1, we expected to observe about 11 events of ^{28}O. Upper limits of the cross sections for the formation of the oxygen isotopes are estimated to be 0.7 and 0.2 pb for ^{26}O and ^{28}O, respectively. Thus, the unbound character of both ^{26}O and ^{28}O nuclei was firmly established. Therefore, at present, the heaviest experimentally found oxygen isotope remains the ^{24}O nucleus.

Our finding that ^{28}O is particle unstable fairly supports the idea that the onset of the deformation found in the Ne–Al region influences the breaking of magicity of $N = 20$ shell closure in the ^{28}O nucleus. The neutron drip line up to fluorine has also been investigated by Sakurai *et al.* [21] by the projectile fragmentation of a ^{40}Ar ($E/A = 94.1$ MeV) beam at the fragment separator RIPS at RIKEN. A new neutron-rich isotope ^{31}F has been observed for the first time, while the firm confirmation for the particle instability of ^{24,25}N and ^{25,26,27,28}O has been obtained. In both experiments [9, 16], the calculated and observed yields of isotopes are in a good agreement and provide strong evidence for the particle instability of ^{24,25}N, ^{26,27,28}O, and ^{30}F.

Thus, the heaviest experimentally found isotopes of carbon, nitrogen, and oxygen [11, 21] are ^{22}C, ^{23}N, and ^{24}O, respectively, with the same neutron number, $N = 16$, while the heaviest isotope of fluorine was found to be ^{31}F with $N = 22$. It should be noted that this is rather interesting behavior among the light nuclei. Usually, in the region further away from the shell closure, the neutron numbers of the heaviest isotopes of neighboring elements increase gradually with Z. Therefore, the sudden step in the largest neutron number from $N = 16$ for carbon, nitrogen, and oxygen to $N = 22$ for fluorine may correspond to a substantial change in shell structure.

3. MASS MEASUREMENT OF HEAVY ISOTOPES FROM Ne UP TO Ar

The question of particle stability is directly related to the masses and nuclear binding energies, which are very sensitive to the existence of shells and may provide clear signatures of shell closures [22]. An experiment on mass measurement using a direct time-of-flight technique was undertaken by Sarazin *et al.* [23] in order to investigate the $N = 20$ and 28 shell closures for nuclei from Ne ($Z = 10$) to Ar ($Z = 18$) and, thus, to bring some clarifications concerning the behavior of magic numbers far from stability. The nuclei of interest were produced by the fragmentation of an $E/A = 60$ MeV ^{48}Ca beam on a Ta target located in the SISSI device of the accelerator complex at GANIL. The mass was deduced from the relation $B\rho = \gamma m_0 v/q$, where $B\rho$ is the magnetic rigidity of a particle of rest mass m_0, charge q, and velocity v and γ is the Lorentz factor. This technique has already been used at GANIL to measure the masses of a large number of neutron-rich nuclei [24]. The 82-m-long flight path between a start detector located near the production target and a stop detector at the final focal plane of the high-resolution spectrometer SPEG facilitated the time-of-flight measurement. The magnetic rigidity was measured in the dispersive section of the SPEG spectrometer using a position-sensitive detector. Unambiguous particle identification was provided by a four-element silicon detector telescope.

The two-neutron separation energies S_{2n} derived from the measured masses are displayed in Fig. 2. Such systematics are of particular interest as the S_{2n} values correspond to a "derivative" of the mass surface. The new data [23] are presented with error bars, while the rest, except the encircled data, are taken from Audi and Wapstra [25]. The Ca, K, and Ar isotopes show a behavior typical of the filling of shells, with the two shell closures at $N = 20$ and $N = 28$ being evident at the corresponding sharp decrease in S_{2n} for the next two isotopes and a moderate decrease in S_{2n} for subsequent points as the filling of the next shell starts to influence S_{2n}. The sharp drop at

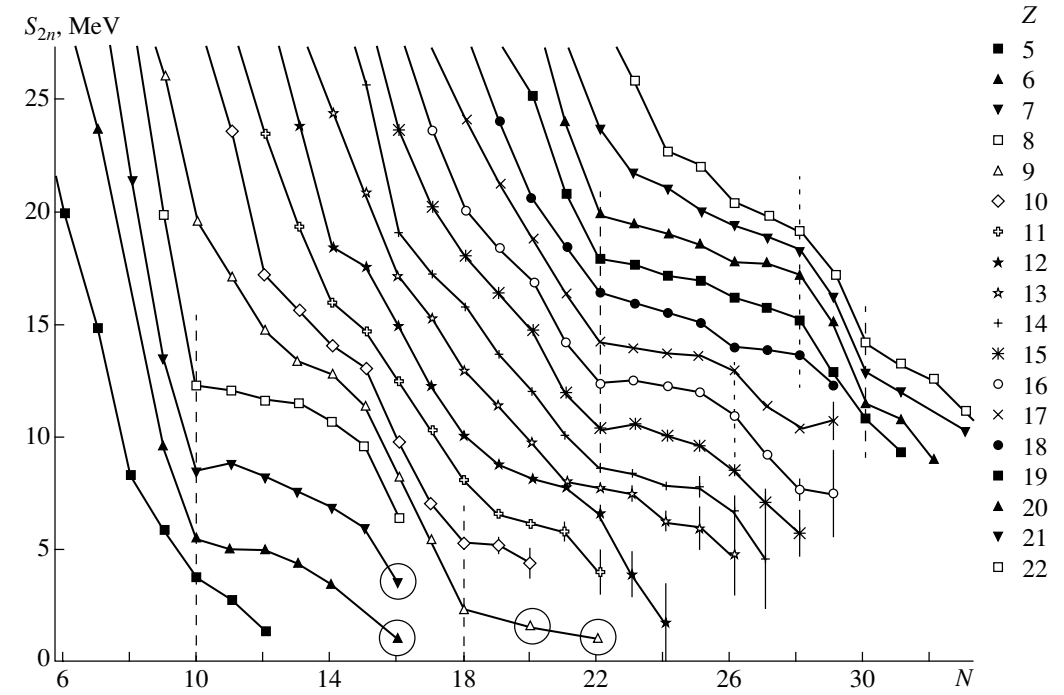

Fig. 2. Experimental S_{2n} values vs. neutron number N.

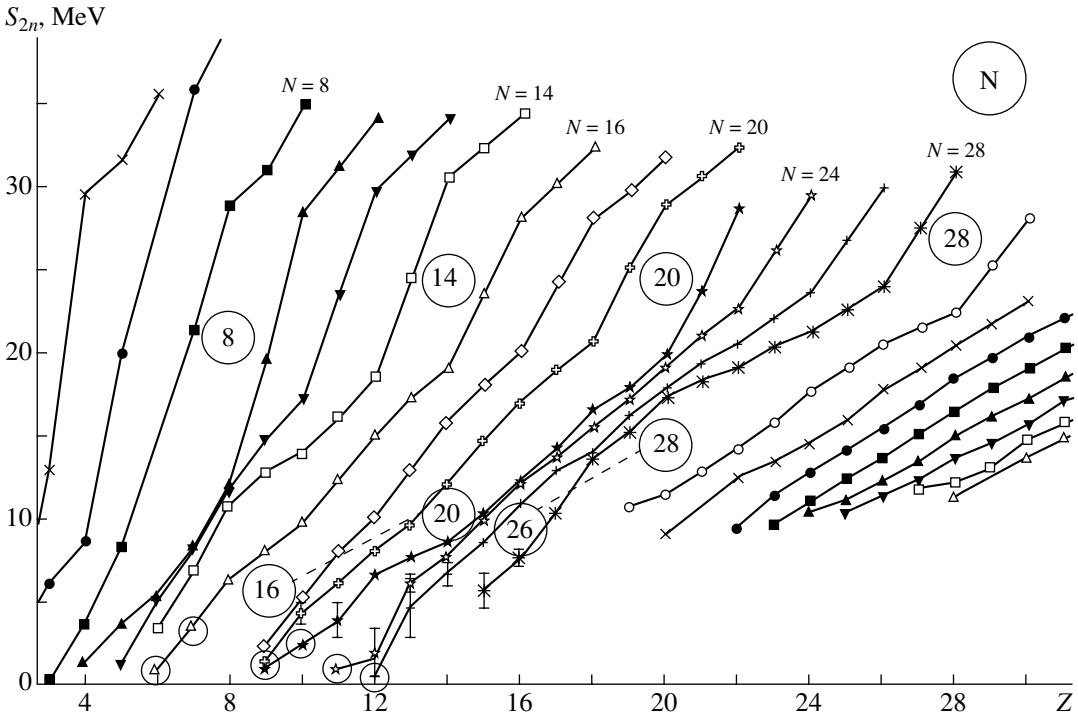

Fig. 3. Experimental S_{2n} values vs. proton number Z.

$N = 22$, shown by the dashed vertical line and corresponding to the shell $N_{sh} = 20$, is clearly visible through all the Si–Ca region, while going to lower Z to the Al–Na region, this drop seems to move towards lower N.

This was the reason why we made an attempt to clarify the situation of two-neutron separation en-

ergies in this region. We used the fact that several particle-stable nuclei [11, 21, 26] were found to exist in this region; however, their masses are not yet known. Nevertheless, their S_{2n} values must be positive, and therefore, we included the "expected" S_{2n} values of the heaviest particle-stable isotopes ^{23}N, ^{22}C, and ^{29,31}F in the graph, where they are marked by circles. The "expected" S_{2n} values for ^{29,31}F point out the region where they probably have to be located due to their experimentally found particle stability (positive S_{2n} values). Their values have been tentatively estimated as half of the S_{2n} value of the preceding particle-stable isotope to ensure the most probable decrease in S_{2n} values. The "expected" S_{2n} values of the heaviest particle-stable isotopes ^{23}N and ^{22}C have been placed in the plot to follow the trend seen in oxygen isotopes with $N \geq 14$. These values are not crucial for determination of the shell closure at $N = 16$; only the fact that particle-stable isotopes heavier than ^{23}N and ^{22}C do not exist is important.

The inclusion of the S_{2n} values for ^{29}F and ^{31}F was most important, because this allowed us to observe the sharp drop of the ^{27}F value followed by a moderate decrease in S_{2n} values for ^{29}F and ^{31}F, giving very clear evidence for the existence of the new shell closure at $N = 16$ for fluorine. A similar behavior confirming the $N = 16$ shell closure can be seen at the neon isotopes that exhibit a moderate decrease in S_{2n} values for ^{29}Ne and ^{30}Ne. We have already mentioned the sharp drop in S_{2n} values in the Al–Na region.

It should be noted that the evidence for a new magic number $N = 16$ follows also from Fig. 3, where the S_{2n} values are plotted vs. atomic number Z. The positions of various possible shells or pseudoshells are also shown in the figure. The shells $N = 20$ and 28 appearing in Fig. 2 are very clearly seen as large gaps in Fig. 3. The dashed lines in Fig. 3 symbolize the changes of neutron shell closures from 28 to 26 and from 20 to 16 in neutron-rich nuclei. However, both gaps narrow going to lower Z until, finally, at least the gap corresponding to $N = 20$ completely disappears at $Z = 13$, to emerge as the new $N = 16$ gap at $Z = 10$. This new gap governs over most of the light-Z neutron-rich nuclei and extends from carbon to neon. As one can see, only the even-N nuclei are plotted in Fig. 3. However, a detailed plot of odd-N nuclei vs. Z (not presented here) shows that a similar role as $N = 16$ for even-N nuclei is played by a gap $N = 15$ for odd-N nuclei.

Thus, we can state that a new shell closure at $N = 16$ has appeared in neutron-rich nuclei for $Z \leq 10$ between the $2s_{1/2}$ and $1d_{3/2}$ orbits in good agreement with Monte Carlo shell model calculations of Utsuno *et al.* [27] and Otsuka *et al.* [28] and also with the recently published work of Ozawa *et al.* [15], where, however, the information on the magicity of $N = 16$ is not so well pronounced. Mainly, it is due to the fact that one-neutron separation energies S_{1n} were plotted only for odd-N nuclei and the measurement of the interaction cross section of radioactive beams σ_I is not convincing enough.

As has already been pointed out by Sarazin *et al.* [23] the Cl, S, and P isotopes exhibit a pronounced change of slope around $N = 26$. Moreover, this change in the Cl and S isotopes is confirmed by the sharp drop at $N = 28$. The discontinuity observed at $N = 26$ in Fig. 2 appears in Fig. 3 as a rather large gap at $N = 26$ for $Z = 15$, 16, and 17. It is therefore evident that the representation of the S_{2n} values as a function of charge number Z is very useful. The observed trends are well reproduced by large-scale shell model calculations undertaken within the sd–fp model space [8]. A similar agreement was obtained in relativistic mean-field calculations [23] except for the odd–even staggering, which was not perfectly reproduced and may indicate a need to fine-tune the pairing force.

The discontinuity observed at $N = 26$ (Figs. 2 and 3) can now be understood in a simple Nilsson picture. For a prolate deformation of $\beta_2 \sim 0.2$, a large gap appears between the lowest three orbits and the fourth orbital arising from the $1f_{7/2}$ and higher orbitals. Consequently, a pseudoshell closure can be considered to appear at $N = 26$. Oblate deformations would not be compatible with these observations. Consequently, a pseudoshell closure can be considered to appear at $N = 26$.

As can be seen in Figs. 2 and 3, interesting new results have also been obtained for isotopes from Ne up to Al. In particular, the steep decrease in S_{2n} for ^{35,36}Mg suggests that the Mg isotopes may become unbound at much lower neutron number than the predicted value of $N \geq 28$. Confirmation of this fact could come from the gap opening at very low S_{2n} separation energies at $N = 22$ for $12 \geq Z \geq 9$ in Fig. 3. However, further experimental and theoretical work is required to confirm this conjecture.

4. IN-BEAM γ-RAY SPECTROSCOPY

Since the spectroscopic measurements can reveal details of the underlying microscopic structures, in-beam γ-ray spectroscopy is an effective tool to check for the shell closures in elements to Ar. The information on the energy of the first excited state and on $B(E2)(2^+ \rightarrow 0^+)$ represents only the first step to understanding the structure and estimating the deformation of the nucleus. Additional information on relative intensities and the $E(4^+)/E(2^+)$ ratio is also highly desirable. Such a measurement can

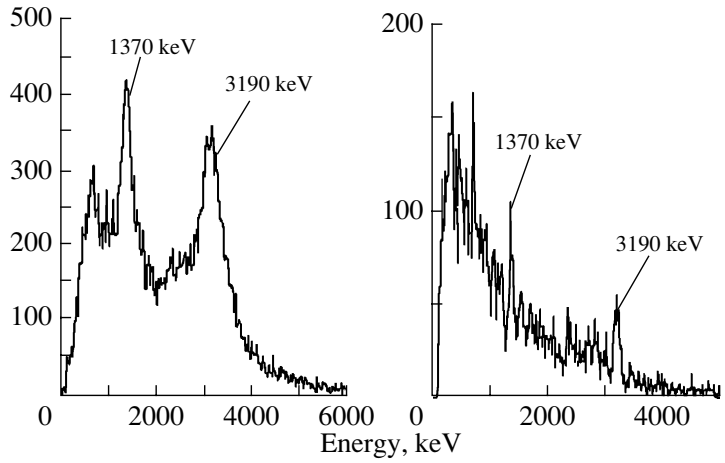

Fig. 4. Doppler-corrected γ spectra of ^{22}O in the BaF_2 (left) and in the germanium detectors (right).

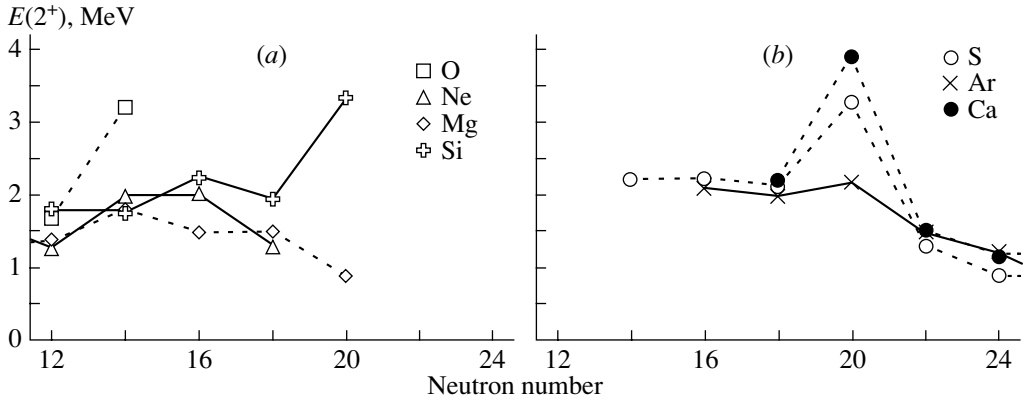

Fig. 5. Gamma-ray energy of the first 2^+ level for even–even nuclei.

probe important details of the underlying microscopic structures, determine the shape of the nuclei under study, and give new information on gaps between neighboring orbitals.

Recently, in-beam γ-ray spectroscopy measurements [29, 30] of a large number of exotic nuclei produced by the fragmentation of ^{36}S and ^{48}Ca projectiles on a thin Be target were performed at GANIL. In experiments, the coincidences between the outgoing fragments collected and identified at the focal plane of the SPEG spectrometer and γ rays measured using the array of 74 BaF_2 and four Ge segmented clover detectors, covering roughly 80% of the solid angle around the target location, were recorded.

Doppler-corrected γ-decay spectra of ^{22}O are shown in Fig. 4. From intensity argument, the line at 3.1 MeV, observed for the first time [30], represents the $2^+ \to 0^+$ transition in ^{22}O and thus extends the systematics of the first 2^+ state energies of oxygen isotopes up to $N = 14$. The dependence of the γ-ray energy of the first 2^+ excited state on neutron number for even–even nuclei is presented in Fig. 5. It should be noted that oxygen isotopes exhibit the lowest $E(2^+)$ energy of 1.7 MeV for ^{20}O, i.e., near the half-occupancy of the $d_{5/2}$ subshell ($N = 12$) just as the Ne and Mg isotopes do. However, the enhancement of $E(2^+)$ energy at $N = 14$ for Ne and Mg is much smaller than that for oxygen. If the enhancement seen in oxygen also appears in carbon, it will be additional confirmation of the existence of the $N = 16$ shell in the C–Ne region. Moreover, we should note that the nonexistence of a bound excited state in $N = 16$ isotones of carbon and oxygen would also indicate the existence of a shell at $N = 16$.

As one can see in Fig. 5*a*, the energy of the first 2^+ state for Ne isotopes rises from 1.25 MeV for ^{22}Ne to 2 MeV for ^{24}Ne and ^{26}Ne and then drops to 1.3 MeV for ^{28}Ne, showing a flat maximum for both 14 and 16 neutron numbers and suggesting a competition between the $1d_{5/2}$ and $2s_{1/2}$ orbits as well an elimination of the $N = 20$ shell. On the other hand, Mg isotopes show a steady decrease in the en-

ergy of the 2^+ state, confirming the weakening of the $N = 20$ shell after reaching the maximum at $N = 14$. However, Si isotopes exhibit maxima at $N = 16$ and 20 that suggest weakening of the $N = 14$ subshell closure.

In Fig. 5*b*, the γ-ray energies of the first 2^+ state for even isotopes of S, Ar, and Ca are plotted. These nuclides exhibit pronounced maxima at $N = 20$ shell; however, the strength of the $N = 16$ shell in these elements is very weak as these nuclides are no longer neutron-rich but lie on the proton-rich side of the valley of β stability. Thus, we can conclude that the strength of $N = 16$ shell can be observable by in-beam γ-ray spectroscopy mainly in the region from carbon up to neon.

The existence of the $N = 16$ gap should manifest itself in the shell correction ΔM, which reads

$$\Delta M = \Delta M_{\rm exp} - \Delta M^{\rm FRLDM}, \qquad (1)$$

where $\Delta M_{\rm exp}$ is the experimental mass excess and $\Delta M^{\rm FRLDM}$ is the spherical macroscopic energy calculated by Möller and Nix [31] in the finite range liquid-drop model. Well-pronounced minima in the shell corrections appear at $N = 16$ (or 15) for nuclei from oxygen up to aluminum. This gives further important evidence for the existence of the new shell closure at $N = 16$ in neutron-rich nuclei.

5. CONCLUSIONS

The synthesis and investigation of these extremely neutron-rich isotopes are crucial for better understanding of the nature of the nuclear interaction. The study of the shell closures $N = 20$ and 28 is particularly interesting since the vanishing of the latter one could be the first evidence of the weakening of the spin–orbit force in neutron-rich nuclei.

We can summarize that a new shell closure at $N = 16$ has appeared in neutron-rich nuclei for $Z \leq 10$ between the $2s_{1/2}$ and $1d_{3/2}$ orbits in good agreement with Monte Carlo shell model calculations. This fact is strongly supported by the instability of C, N, and O isotopes with $N > 16$ and confirms the magic character of $N = 16$ for the neutron-rich nuclei in the region $6 \leq Z \leq 10$, while the shell closure at $N = 20$ tends to disappear for $Z < 14$.

The existence of the new shell closure at $N = 16$ in neutron-rich nuclei is also supported by the behavior of the calculated shell correction in the O–Al region as well as the dependence of the energies of the first 2^+ states of Ne isotopes.

In particular, the ^{43}P, ^{44}S, and ^{45}Cl $N = 28$ nuclei appeared to be less bound than predicted, which constitutes new evidence of the weakening of the $N = 28$ shell closure. On the other hand, there appears a discontinuity in the slope at $N = 26$. Comparison with the shell model and relativistic mean-field calculations demonstrate that the observed effects arise from deformed prolate ground-state configurations associated with shape coexistence. Consequently, a pseudoshell closure can be considered to appear at $N = 26$.

In-beam γ-ray spectroscopy has proven itself to be an important tool to study low excited states in neutron-rich nuclei. The energy of the first 2^+ state of even–even nuclei exhibits maxima at $N = 20$ for Si, S, and Ca corresponding to doubly magic nuclei Z, N near the valley of stability. An enhancement at $N = 16$ for Ne, Si, and S corresponding to a new neutron shell closure in neutron-rich nuclei is also visible.

ACKNOWLEDGMENTS

The work was done in the GANIL–Orsay–Dubna–Řez–Bucharest collaboration and we are grateful to W. Mittig, D. Guillemaud-Mueller, Yu. Penionzhkevich, M. Lewitowicz, H.-G. Bohlen, C. Borcea, and J. Dobeš for fruitful discussions and help. We acknowledge support from French IN2P3 and GA of the Academy of Sciences of the Czech Republic, grant no. A1048102.

REFERENCES

1. I. Tanihata *et al.*, Phys. Rev. Lett. **55**, 2676 (1985).
2. P. G. Hansen and B. Jonson, Europhys. Lett. **4**, 409 (1987).
3. T. R. Werner *et al.*, Phys. Lett. B **335**, 259 (1994); Nucl. Phys. A **597**, 327 (1996).
4. Z. Ren *et al.*, Phys. Lett. B **380**, 241 (1996).
5. C. Thibault *et al.*, Phys. Rev. C **12**, 644 (1975).
6. N. A. Orr *et al.*, Phys. Lett. B **258**, 29 (1991).
7. E. K. Warburton *et al.*, Phys. Rev. C **41**, 1147 (1990).
8. J. Retamosa *et al.*, Phys. Rev. C **55**, 1266 (1997).
9. A. Korsheninnikov *et al.*, Phys. Lett. B **326**, 31 (1994).
10. A. N. Ostrowski *et al.*, Phys. Lett. B **338**, 13 (1994).
11. O. Tarasov, Z. Dlouhý, *et al.*, Phys. Lett. B **409**, 64 (1997).
12. Z. Dlouhý, Yu. Penionzhkevich, *et al.*, J. Phys. G (London) **25**, 859 (1999).
13. M. Beiner, R. J. Lombard, and D. Mas, Nucl. Phys. A **249**, 1 (1975).
14. Z. Dlouhý *et al.*, in *RNB-2000, 2000, Divonne, France*; Nucl. Phys. A **701**, 189 c (2002).
15. A. Ozawa *et al.*, in *RNB-2000, 2000, Divonne, France*; Phys. Rev. Lett. **84**, 5493 (2000).
16. O. Sorlin *et al.*, Phys. Rev. C **47**, 2941 (1993).
17. T. Glasmacher *et al.*, Phys. Lett. B **395**, 163 (1997).
18. J. Stevenson *et al.*, Phys. Rev. C **37**, 2220 (1988) (and references therein).
19. D. Guillemaud-Mueller *et al.*, Phys. Rev. C **41**, 937 (1990).

20. M. Fauerbach *et al.*, Phys. Rev. C **53**, 647 (1996).
21. H. Sakurai *et al.*, Phys. Lett. B **448**, 180 (1999).
22. W. Mittig, A. Lépine-Scilly, and N. Orr, Annu. Rev. Nucl. Sci. **47**, 27 (1997).
23. F. Sarazin *et al.*, Phys. Rev. Lett. **84**, 5062 (2000).
24. A. Gillibert *et al.*, Phys. Lett. B **192**, 39 (1987).
25. G. Audi and A. H. Wapstra, Nucl. Phys. A **624**, 1 (1997).
26. H. Sakurai *et al.*, Phys. Rev. C **54**, R2802 (1996).
27. Y. Utsuno *et al.*, Phys. Rev. C **60**, 054315-1 (1999).
28. T. Otsuka *et al.*, Nucl. Phys. A **685**, 100c (2001).
29. F. Azaiez, Phys. Scr. T **88**, 118 (2000).
30. M. Belleguic *et al.*, Phys. Scr. T **88**, 122 (2000).
31. P. Möller and J. R. Nix, At. Data Nucl. Data Tables **59**, 85 (1995).

Physics of Atomic Nuclei, Vol. 66, No. 8, 2003, pp. 1544–1551. From Yadernaya Fizika, Vol. 66, No. 8, 2003, pp. 1587–1594.

Resonance States of Hydrogen Nuclei ^{4}H and ^{5}H Obtained in Transfer Reactions with Exotic Beams*

G. M. Ter-Akopian[1)], D. D. Bogdanov †[1)], A. S. Fomichev[1)], M. S. Golovkov[1)], Yu. Ts. Oganessian[1)], A. M. Rodin[1)], S. I. Sidorchuk[1)], R. S. Slepnev[1)], S. V. Stepantsov[1)], R. Wolski[1),2)], V. A. Gorshkov[1)], M. L. Chelnokov[1)], A. A. Korsheninnikov[3)], E. Yu. Nikolski[3)], I. Tanihata[3)], F. Hanappe[4)], T. Materna[4)], L. Stuttge[5)], and A. H. Ninane[6)]**

[1)] *Flerov Laboratory of Nuclear Reactions, JINR, Dubna, Moscow oblast, 141980 Russia*

[2)] *Institute of Nuclear Physics, Cracow, Poland*

[3)] *RIKEN, Wako, Japan*

[4)] *Universite Libre de Bruxelles, Bruxelles, Belgium*

[5)] *Institut de Recherches Subatomiques, Strasbourg, France*

[6)] *Nuclear Physics Department Ch. du Cyclotron, University of Louvain, Louvain-la-Neuve, Belgium*

Received August 28, 2002

Abstract—To investigate ^{5}H resonance states with a better instrumental resolution, we utilized the two-neutron transfer reaction ^{3}H$(t,p)^5$H accomplished with the use of a cryogenic liquid-tritium target and 57.5-MeV triton beam. As a result of this study, a valuable fraction of protons detected at $\theta_{\rm lab} = 18°$–$32°$ in *ptn* coincidence events was attributed to the states of the ^{5}H nucleus. Two resonance states situated at 1.8 ± 0.1 and 2.7 ± 0.1 MeV above the $t+n+n$ decay threshold were obtained in the missing mass energy spectrum of the ^{5}H nucleus. The peak located close to $E_{^5{\rm H}} = 1.8$ MeV was clearly seen in the ^{5}H spectrum obtained from the energy distributions of ^{3}H nuclei emitted in the reaction ^{2}H(^{6}He, ^{5}H)^{3}He at $\theta_{\rm lab} = 17°$–$32°$. The width ($\Gamma_{\rm obs} \leq 0.5$ MeV) obtained for the two ^{5}H resonance states is surprisingly small. A state of ^{4}H with $E_{\rm res} = 3.3$ MeV and $\gamma^2 = 2.3$ MeV was obtained in the reaction ^{2}H$(t,p)^4$H from the spectra of protons leaving the target at $\theta_{\rm lab} = 18°$–$32°$ and detected in coincidence with neutrons emitted in the decay of ^{4}H nuclei. © *2003 MAIK "Nauka/Interperiodica".*

1. INTRODUCTION

The interest in the hydrogen isotopes heavier than tritium has continued over the last forty years. This is more than a mere part for the quest for neutron-drip nuclei: the interest in this problem has risen, because the superheavy isotopes of hydrogen seem to be candidates for nuclear systems with the most extreme excess of neutrons ever attained for a direct study.

All experimental data on ^{4}H reported to this day [1–13] suggest broad resonance states in this nucleus. The considerable dissimilarity seen between some of the reported data apparently reflects the difficulty and, perhaps, ambiguity inherent to the problem of revealing correct parameters for broad, overlapping resonances sought in nuclear reactions. The latest weighted estimates made for the ^{4}H levels [14] rely on the charge-symmetry reflection of ^{4}Li R-matrix parameters involving the Coulomb shift correction. The level diagram presented in this paper suggests for ^{4}H four resonance states at 3.19 MeV ($J^\pi = 2^-$), 3.50 MeV ($J^\pi = 1^-$), 5.27 MeV ($J^\pi = 0^-$), and 6.02 MeV ($J^\pi = 1^-$) above the $t+n$ decay threshold.

There were few experiments where the search for unbound ^{5}H was done. Young *et al.* [15] investigated the inclusive spectrum of protons emitted in the reaction ^{3}H$(t,p)^5$H accomplished with a 22.25-MeV triton beam. They observed a peak at 1.8 MeV relative to the $t+n+n$ threshold. However, they did not exclude a possibility that this peak could be attributed to the phase-space spectrum, which had at this beam energy the high-energy cutoff lying not far above 1.8 MeV. Gornov *et al.* [16] detected *pt* coincidence events from the reaction ^{9}Be$(\pi^-, pt)^5$H and reported on a bump in the ^{5}He spectrum centered

*This article was submitted by the authors in English.

†Deceased.

**e-mail: Gurgen.TerAkopian@jinr.ru

around 7 MeV. Recently, the same group observed four ^{5}H resonance states using the same reaction at 5, 10, 18, and 26 MeV above the $t + n + n$ threshold [13]. A bump at energy ~5 MeV was reported in [17], where the reaction ^{7}Li(^{6}Li, ^{8}B)^{5}H was studied.

Radioactive nuclear beams open favorable conditions for the study of such a neutron-rich system as ^{5}H. Since the projectiles are neutron-rich and loosely bound, the energy balance of relevant transfer reactions becomes more advantageous, the cross sections become higher, the reaction mechanisms turn out to be simpler, and the physical background is lower than it is with stable beams. The approach making use of a radioactive ^{6}He beam was realized in [18], where a search for ^{5}H quasi-bound states was made by studying the spectra of proton pairs emitted from the ^{2}H decay in the reaction ^{1}H(^{6}He, ^{5}H)^{2}He. The authors reported on the observation of a peak consistent with a ^{5}H resonance at 1.7 ± 0.3 MeV above the threshold for $t + n + n$ decay. The resonance was assumed to be the ^{5}H ground state. Its observable width was reported to be $\Gamma_{\rm obs} = 1.9 \pm 0.4$ MeV.

Different calculations made recently predicted the energy position of the ^{5}H ground state at 2.5 MeV [19], 3–4.5 MeV [20], 2.5–3.0 MeV [21], ≈3 MeV [22], and 1.14 MeV [23] above the decay threshold $t + n + n$. Keeping in mind the present state of such calculations, one could say that these predictions are consistent with the ground-state resonance position obtained for ^{5}H in [18]. The authors of papers [21, 22] predicted widths of 3–4 and 1–4 MeV, respectively, for the ^{5}H ground-state resonance. It is evident that one should continue experimental efforts to obtain more precise values for the energy and width of the ^{5}H resonance reported in [18] and, perhaps, to find excited states predicted for the ^{5}H nucleus [20, 21].

In this paper, we report on new results about the ^{4}H and ^{5}H nuclei, which we obtained in the reactions ^{2}H$(t,p)^4$H and ^{3}H$(t,p)^5$H with the use of a triton beam having an energy of 57.5 MeV. The ^{5}H investigation was complemented by the missing mass spectrum of this nucleus obtained from the study made for the reaction ^{2}H(^{6}He, ^{5}H)^{3}He. Preliminary results of experiments carried out with a triton beam were reported in 2001 at Berkeley [24], Lipary [25], and Sarov [26]. The present paper presents the latest status of the data analysis made for the reactions ^{2}H$(t,p)^4$H and ^{3}H$(t,p)^5$H. Results obtained from the study of the reaction ^{2}H(^{6}He, ^{5}H)^{3}He are presented here for the first time.

2. EXPERIMENTAL DETAILS

A 58-MeV triton beam delivered by the U-400M cyclotron was transported by the modified beam line of the separator ACCULINNA [27] to a shielded room, where a reaction chamber housing the tritium target and particle detectors was installed. This beam line was used also to reduce the angular and energy divergence of the primary triton beam, respectively, to 7 mrad and 0.3 MeV (FWHM). Finally, the triton beam with a typical intensity of 3×10^7 s^{-1} was focused in a halo-free 5-mm spot on the tritium target. Values of the beam energy, 57.5 MeV, and beam energy spread, 330 keV, obtained in the medium target plane, were estimated in two independent ways: from the separator tuning and by measuring tritons elastically scattered from different nuclei in the tritium target (tritium, hydrogen, and iron).

We produced ^{6}He nuclei in fragmentation reactions of a 32-MeV/nucleon beam of ^{11}B bombarding a thick beryllium target. The modified separator ACCULINNA [27] was used to cut off the secondary ^{6}He beam and to cleanse this beam of the primary ^{11}B ions and the majority of other reaction products. The ^{6}He beam obtained in the achromatic focal plane of this separator had an average energy of 24.5 MeV/nucleon. The beam energy spread and maximum angular divergence were, respectively, 7% (FWHM) and 15 mrad. A 9-m-long straight beam line was installed after the separator achromatic focal plane, providing that the beam was transported to the final focal plane, where the experimental target was located. Two plastic scintillator counters positioned between the achromatic and final focal planes measured the flight times of individual beam ions on a base of 850 cm. The energy was measured with a precision of 0.5% for individual ^{6}He ions. For individual ions hitting the target, the trajectory inclination angles towards the beam axis and the hit positions were fixed with a precision of 2 mrad and 1.25 mm, respectively. This was done with two pairs of multiwire proportional chambers, installed in front of the target. The secondary ^{6}He beam was focused on a deuterium gas target, in a 15-mm circle. Admixtures to this beam were tritons (35%) and ^{8}Li ions (1.5%). The measured flight times and amplitudes of the signals from one of the timing counters provided unambiguous separation of ^{6}He ions from these parasitic admixtures. Experiments were carried out with a typical beam intensity of 2×10^5 secondary ^{6}He ions per second on the deuterium target. After passing the TOF counters, the multiwire proportional chambers, and the target entrance window, the average energy of ^{6}He ions was 133 MeV in the target median plane. This energy value was estimated in two independent

ways: (i) from the separator tuning, supplemented with the calculated energy losses occurring in the detectors installed in front of the target and in the entrance windows of the target cell; (ii) by measuring the energy of recoil deuterium nuclei originating from the elastic scattering ^{6}He + ^{2}H observed around the c.m. angle $\theta_{\text{c.m.}} = 150°$.

In the study of reactions $^2\text{H}(t,p)^4\text{H}$ and $^3\text{H}(t,p)^5\text{H}$, we used the liquid-phase target cell described in [28]. The 0.4-mm-thick target cell had 12.5-μm-thick stainless steel entrance and exit windows hermetically welded to the cell casing. For the sake of safety, the target cell was embedded in a small protective volume also supplied with 12.5-μm stainless steel windows. High-purity deuterium gas or tritium gas of 92% purity with an admixture of hydrogen (1%) and deuterium (7%) was used to fill the target with liquid deuterium or tritium. The working temperature of the target cell was close to 20 K.

The gas target used in the study of the reaction $^2\text{H}(^6\text{He}, ^5\text{H})^3\text{He}$ had a cell of 4 mm in thickness and windows made of 6-μm stainless steel foils. The target was filled with a high-purity deuterium gas to a pressure of 10^5 Pa and cooled to a temperature of 25 K.

In the case of reactions $^2\text{H}(t,p)^4\text{H}$ and $^3\text{H}(t,p)^5\text{H}$, we used two detector telescopes for charged reaction products. In addition, we used 41 scintillation modules of the time-of-flight neutron spectrometer DEMON [29]. The first detector telescope intended for higher energy products (i.e., protons with $E \leq 40$ MeV) involved one 400-μm-thick and two 1-mm-thick Si strip detectors backed by a 6-mm thick Si(Li) detector. The data presented below were obtained with the telescope installed to detect protons emitted in a laboratory system angular range of $18° \leq \theta_{\text{lab}} \leq 32°$. The second telescope consisted of one 70-μm-thick, one 400-μm-thick, and two 1-mm-thick Si strip detectors. It was optimized to detect relatively slow tritons originating from the ^{5}H decay and, being installed on the other side with respect to the beam axis, covered an angular range of $15° \leq \theta_{\text{lab}} \leq 39°$. The DEMON modules were installed just behind the triton telescope at a distance of 2.5 m from the target and covered an angular range of $\theta_{\text{lab}} = 37° \pm 19°$ for neutrons emitted in the ^{5}H decay. Data acquisition was triggered, when time-correlated signals appeared either from the two telescopes or from the first telescope and any of the DEMON modules. The instrumental resolution obtained for ^{5}H resonance states lying in the energy range 1.5–5.0 MeV above the $t + n + n$ threshold was about 400 keV. This estimate was made for a resonance state showing up in a ^{5}H missing mass spectrum deduced from the proton energy and trajectory angles. Nearly the same resolution was attained for ^{4}H resonance states.

A detector telescope consisting of two Si strip detectors was used to register relatively low-energy ^{3}He product nuclei originating from the reaction $^2\text{H}(^6\text{He}, ^5\text{H})^3\text{He}$. In this telescope, the first and second Si detectors, respectively, were 70-μm and 1-mm thick. These detectors were 50×50 mm^2 and 60×60 mm^2 in area, respectively. A 13-mm-thick, large-area CsI(Tl) crystal was installed behind these two Si detectors in the telescope to detect long-range reaction products. The second detector telescope was intended for tritons originating from the ^{5}H decay. This telescope involved two Si strip detectors (both were 1-mm thick and 60×60 mm^2 in area) and one 13-mm thick, large-area CsI(Tl) crystal. The two telescopes were installed on opposite sides with respect to the beam axis at median angles of 25° and 16° chosen for the ^{3}He and triton telescopes, respectively. The distances from the target were 190 and 150 mm, respectively, for the ^{3}He and triton telescopes. Data acquisition was triggered by signals coming from the second, 1-mm, Si detector working in the ^{3}He telescope. The instrumental resolution obtained for ^{5}H resonance states lying in the energy range 1.5–5.0 MeV was about 600 keV. This estimate was made for a resonance state showing up in a ^{5}H missing mass spectrum deduced from the data (the energy and trajectory angles) obtained for ^{3}He nuclei.

Integral beam doses collected in these experiments were 3.2×10^{12} and 2.8×10^{13} for triton bombarding, respectively, the liquid-deuterium and liquid-tritium targets. In the case of the reaction $^2\text{H}(^6\text{He}, ^3\text{He})^5\text{H}$, the integral flux of ^{6}He ions was 3.5×10^{11}. The experiments were complemented by measurements made with empty target cells, assuring us that practically 100% of events in the spectra, which are shown below, were generated by interactions of bombarding ions with the filling gas nuclei, i.e., either with deuterium or with tritium.

3. RESULTS AND DISCUSSION

3.1. ^{4}H

The most thorough study of the reaction $^2\text{H}(t,p)^4\text{H}$ was done by Blagus *et al.* [11] working with a triton beam of around 35 MeV. These authors made special notes about the contribution of quasi-free scattering (QFS) in the proton spectra and studied this phenomenon separately [30].

Data obtained with the use of wide-aperture detector telescopes allowed us to reveal the contributions of various exit channels of the $t + t$ reaction in

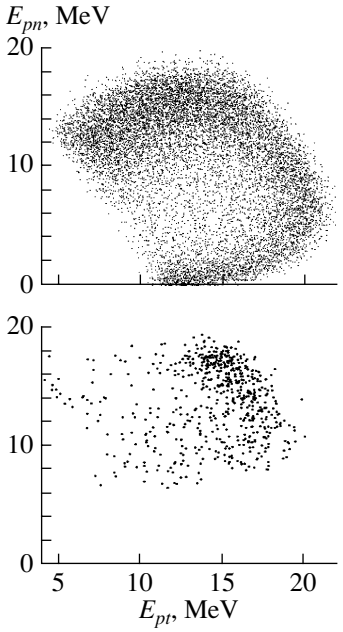

Fig. 1. Correlation plots E_{pn} vs. E_{pt} observed in the reaction ^{2}H$(t,p)^4$H. Plots shown in the upper and lower panels are produced, respectively, by *pt* and *pn* coincidence events observed in this reaction (for details, see text).

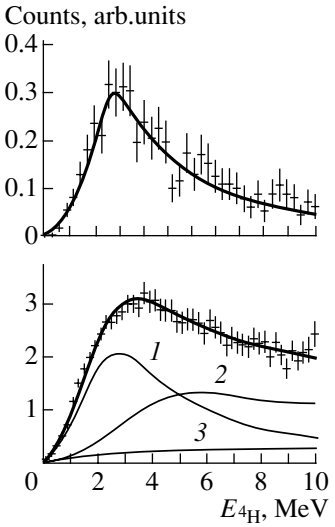

Fig. 2. Upper panel: The ^{4}H missing mass spectrum obtained from the data on *pn* coincidence events recorded in the reaction ^{2}H$(t,p)^4$H. The thick solid curve fits the spectrum resulting in $\chi^2 = 1.05$. It is a Breit–Wigner resonance curve with $E_R = 3.3$ MeV and $\gamma^2 = 2.3$ MeV. Lower panel: The same spectrum obtained from *pt* coincidence data. The thick solid curve shows a fit assuming a plain sum of a Breit–Wigner resonance (curve *1*) with continuum spectra originating from QFS (curve *2*) and phase space (curve *3*).

the proton spectra obtained from *pt* and *pn* coincidence events. Figure 1 shows two correlation plots drawn for kinetic energies *pt* and *pn* corresponding to the relative motion that *p*–*t* and *p*–*n* pairs show in their rest frames. The plot shown in the upper panel of this figure was drawn from the data recorded for *pt* coincidence events. In this plot, events exposing *pn* final-state interaction (FSI) populate a region below $E_{pn} \approx 3.5$ MeV. The area confined between $E_{pn} \approx 10$ and 15 MeV and $E_{pt} \approx 5.0$ and 11.0 MeV is populated mostly by the events that appeared as a result of *pt* FSI. Simulation assuming the formation of ^{4}He in its known excitation states models these events well. QFS events are described in PWIA to be confined mostly between $E_{pn} \approx 13$ and 18 MeV and $E_{pt} \approx$ 11.0 and 17.0 MeV, though some part of these events can be found in a zone lying below $E_{pt} \approx 11.0$ MeV.

In contrast to the *pt* coincidence events, the E_{pn} vs. E_{pt} correlation plot shown in the lower panel of Fig. 1 demonstrates a very low contribution (if any) from these interfering reaction channels: practically all the *pn* coincidence events occurred due to the reaction ^{2}H$(t,p)^4$H. Simulations made for the *pn* and *pt* FSI, as well as for QFS, supported the conclusion that very few events of this sort could be found when the *pn* coincidence triggers were in use.

Two missing mass spectra obtained for the ^{4}H nucleus on the basis of *pn* and *pt* coincidence events are shown in Fig. 2 (the upper and lower panels, respectively). Points showing the spectra in Fig. 2 are corrected for the energy-dependent detection efficiency, which was simulated for the real experimental array. The *pn* coincidence spectrum was fitted with one Breit–Wigner curve showing the resonance position at $E_R = 3.3$ MeV and reduced width $\gamma^2 = 2.3$ MeV.

The situation with the ^{4}H spectrum obtained from the *pt* coincidence events turns out to be more complex. The spectrum presented in the lower panel of Fig. 2 was drawn with the use of cuts eliminating zones densely populated by FSI and QFS events. Even after making these cuts, we had to assume contributions from QFS and the phase-space effect in the spectrum presented in the lower panel of Fig. 2. The reliability of fits made for a wide resonance mixed with these contributions is doubtful. One such fit showing $E_R = 3.7$ MeV and $\gamma^2 = 3.3$ MeV is presented in Fig. 2 in the lower panel.

At the present stage of the data analysis, we come to the conclusion that the most reliable results obtained in the present work for the position and width of the ^{4}H resonance state give $E_R = 3.3$ MeV and $\gamma^2 = 2.3$ MeV. One should more thoroughly analyze the *pt* coincidence data shown in Fig. 2 before making any inference about the ^{4}H resonance parameters based on these data. It seems to be quite probable

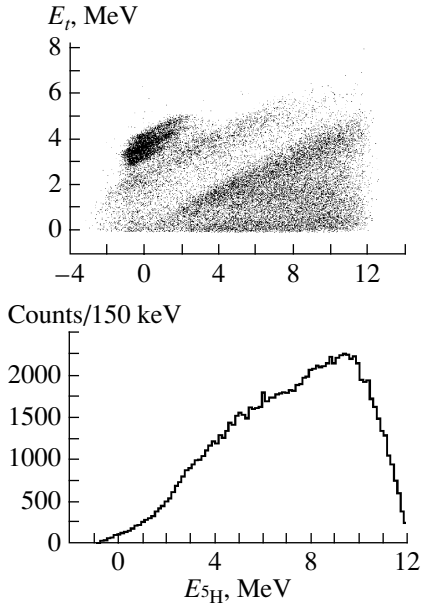

Fig. 3. Upper panel: Two-dimensional plot showing the distribution of pt coincidence events in coordinates E_t (triton energy seen in the ^{5}H rest frame) vs. $E_{^5\mathrm{H}}$ (the energy of the ^{5}H nucleus above the $t+n+n$ decay threshold). The data are obtained for the reaction $^3\mathrm{H}(t,p)^5\mathrm{H}$ at the triton beam energy of 57.5 MeV. Lower panel: The projection on the $\mathrm{E}_{^5\mathrm{H}}$ axis made for the ^{5}H locus seen in the upper panel.

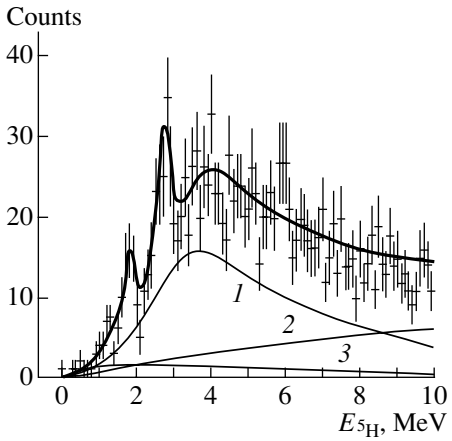

Fig. 4. Missing mass ^{5}H spectrum deduced from data on ptn coincidence events observed in the reaction $^3\mathrm{H}(t,p)^5\mathrm{H}$. The thick curve shows the best least-squares fit to the experimental points (for details, see text).

that the resonance seen at $E_R = 3.3$ MeV appears as a mixture of two resonances suggested in [14] for this nucleus at $E_R = 3.19$ and 3.50 MeV.

3.2. ^5H

Now, we turn to the ^{5}H data obtained in the experiment where the reaction $^3\mathrm{H}(t,p)^5\mathrm{H}$ was studied. The upper panel in Fig. 3 shows a correlation plot, where the triton kinetic energy observed in the rest frame of the ^{5}H nucleus is drawn vs. the missing mass energy of this nucleus. In this plot, one should look for ^{5}H events below and near the line given by the relation $E_t = (2/5)E_{^5\mathrm{H}}$. Thus, events associated with the ^{5}H decay should be confined inside the triangle contour occupying the lower right corner of the correlation plot. The most intense spot seen in the upper left part of this plot appears due to the elastic scattering of beam tritons on hydrogen residing in the tritium target and in water molecules deposited on the cold target windows. Other events seen outside the ^{5}H locus are due to the triton interactions with the deuterium admixture to the target.

The lower panel in Fig. 3 shows the projection on the $E_{^5\mathrm{H}}$ axis made for the ^{5}H locus seen in the upper panel. Evidently, one cannot see any prominent structure in this projection. An analysis made for events seen in Fig. 3 showed that the main contribution in the pattern, which one could ascribe to ^{5}H, is due to QFS of projectile tritons on protons bound in tritium target nuclei. The two spectator neutrons confined in the tritium nucleus acquire low energy in this process. This implies that one could select high-energy neutrons to get rid of QFS.

Following this indication, we analyzed triple, ptn, coincidence events taking into consideration neutrons with energy above 2.5 MeV. As compared to our early publications [24–26], the energy threshold for neutrons was raised by 1 MeV. The missing mass energy spectrum obtained for the ^{5}H system on the basis of ptn coincidence events is shown in Fig. 4. We note that the overwhelming majority of events showed a correct energy balance within error bars reasonable for the accuracy achieved in the ^{5}H mass measurement.

In the spectrum presented in Fig. 4, one can see two relatively narrow peaks rising above the continuum at 1.8 and 2.7 MeV. We fitted the spectrum extending in the ^{5}H energy from $E_{^5\mathrm{H}} = 0$ to 5 MeV, assuming that there are these two resonance peaks placed on a continuum spectrum. We revealed three continuum sources. These are (i) the phase-space spectrum originating from the reaction exit channel involving a triton and two free protons in the final state, (ii) the continuum spectrum obtained for events showing up in nn FSI, and (iii) similar events characterized with the nt FSI (the ^{4}H resonance parameters were used to simulate this source of the continuum). The thick solid curve shows the result of fitting obtained for experimental points in Fig. 4 with the assumption that two peaks with widths equal to our instrumental resolution (FWHM = 400 keV)

situated at $E_{^5\mathrm{H}} = 1.8 \pm 0.1$ and 2.7 ± 0.1 MeV are present in the spectrum. The curves in this figure show Monte Carlo simulations made for the three continuum sources. Curve *1* shows the simulated continuum spectrum obtained with regard to nt FSI, curve *2* shows the simulated phase-space spectrum for $t + n + n$ events in the final state, and the curve *3* shows the simulation made with regard to nn FSI. The amplitudes shown for these three continuum spectra were obtained as a result of χ^2 fitting. The resulting value $\chi^2 = 0.96$ gives a confidence level $\mathrm{CL} = 0.55$. The removal of the 1.8-MeV peak (while keeping the 2.7-MeV peak in the spectrum) reduces the confidence level to $\mathrm{CL} = 0.13$. Alternatively, if one removes the 2.7-MeV peak from the fitting procedure and restores the 1.8-MeV peak, the confidence level drops to $\mathrm{CL} = 0.25$. The best fit made with the simulated continuum spectrum (resonance peaks were excluded) resulted in $\chi^2 = 1.38$ and a confidence level $\mathrm{CL} = 4.3\%$.

This enables us to conclude that we have revealed in the ^{5}H nucleus two resonance states positioned at energies $E = 1.8 \pm 0.1$ and 2.7 ± 0.1 MeV above the threshold for the $^5\mathrm{H} \to t + n + n$ disintegration. A striking feature of these resonance states is their small width. The widths of both peaks in Fig. 4 are governed by instrumental resolution. Statistical deficiency leaves us with upper limits of ≤ 0.5 MeV, which one could estimate for the true widths of the two resonance states.

The position of the first peak, $E = 1.8 \pm 0.1$ MeV, coincides well with the ^{5}H ground-state resonance reported in [18] at 1.7 ± 0.3 MeV. Also, there is a room to conclude that the 0.5-MeV limit estimated in the present paper for the true resonance width is not in conflict with the width $\Gamma_{\mathrm{obs}} = 1.9 \pm 0.4$ MeV reported in [18]. The presence of the second, $E = 2.7$ MeV, peak makes a difference between the present paper and the ^{5}H spectrum of [18]. The observation of an excited state in the ^{5}H nucleus should not be a surprise, because theory (see [20, 21]) predicts that, in addition to the ground state, $J^\pi = 1/2^+$, the ^{5}H nucleus will have two excited states with spin/parity $J^\pi = 5/2^+$ and $3/2^+$. As noted in [18], the proton transfer reaction $p(^6\mathrm{He}, {}^5\mathrm{H})^2\mathrm{He}$ used in this work might be selective to the ^{5}H ground-state population. Moreover, the main contribution in the ^{5}H spectrum comes from the proton transfers occurring at small c.m. angles, where $L = 2$ transfers necessary to populate high-spin states are hindered. On the contrary, the $^3\mathrm{H}(t,p)^5\mathrm{H}$ reaction is also expected to populate excited states in ^{5}H. The ^{5}H spectrum shown in Fig. 4 is drawn using the data on the two-neutron transfer reaction detected in an angular range extending from 20° to 50° in the c.m. system. A drastic change in the probability ratio between $L = 0$ and $L = 2$ transfers occurs in this angular range. This supports the assumption that the second peak observed at the energy $E = 2.7 \pm 0.1$ MeV is associated with one of the excited states predicted for the ^{5}H nucleus. Taking into account the level sequence usual for spin–orbit splitting and the role of the spin factor in the transfer reaction cross section, we suppose that the $E = 2.7 \pm 0.1$ MeV peak displays the $5/2^+$ excited level in the ^{5}H nucleus.

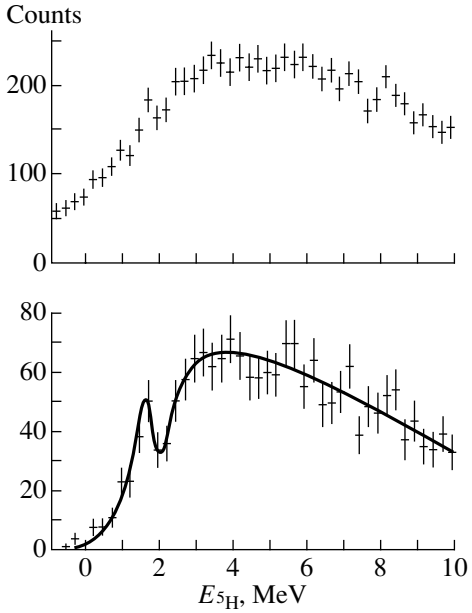

Fig. 5. Upper panel: The ^{5}H missing mass spectrum based on the data on energy and trajectory angle recorded for ^{3}He nuclei emitted in the reaction $^2\mathrm{H}(^6\mathrm{He}, {}^5\mathrm{H})^3\mathrm{He}$. Lower panel: The same spectrum built from the data on protons detected in coincidence with tritons emitted in the ^{5}H decay. The solid curve is drawn through the experimental points to guide the eye.

The cross sections averaged over the angular range covered by our measurements are estimated at 18^{+20}_{-10} and 34^{+30}_{-20} μb/sr for the two-neutron transfer reaction populating, respectively, the ground ($E = 1.8$ MeV) and excited ($E = 2.7$ MeV) ^{5}H states. The main contribution in the errors assigned to these cross-section values comes from the uncertainty in neutron detection efficiency.

The strikingly small width limits obtained for the two ^{5}H resonance states call for verification. The first experiment of this series were those dedicated to the reaction $^2\mathrm{H}(^6\mathrm{He}, {}^5\mathrm{H})^3\mathrm{He}$. We decided in favor of this reaction, because we could obtain a reasonably good energy resolution for the sought ^{5}H resonance states. Just as in the reaction $^1\mathrm{H}(^6\mathrm{He}, {}^2\mathrm{He})^5\mathrm{H}$, employed in [18], the use of the reaction $^2\mathrm{H}(^6\mathrm{He}, {}^5\mathrm{H})^3\mathrm{He}$ implies

the pickup of one proton from ^{6}He. Therefore, this reaction should selectively populate the ground state $J^\pi = 1/2^+$ in ^{5}H.

The ^{5}H missing mass spectra deduced from the ^{3}He energy distributions, measured in the laboratory system angular range $17^\circ \leq \theta_{\rm lab} \leq 32^\circ$, are presented in Fig. 5. In this figure, the upper and lower panels show, respectively, the ^{5}H spectra drawn with the use of inclusive ^{3}He data and data obtained for ^{3}He nuclei recorded in coincidence with tritons. These spectra were drawn with the selection of ^{3}He reaction products having lab. energy less than 25 MeV. Altogether, this limits to $17^\circ \leq \theta_{\rm c.m.} \leq 55^\circ$ the c.m. angular range for the reaction ^{2}H(^{6}He, ^{5}H)^{3}He.

One can say with confidence that the peak located close to $E_{^5{\rm H}} = 1.8$ MeV is clearly seen in the ^{5}H spectrum shown in the lower panel in Fig. 5. This peak shows up in the upper panel, i.e., in the inclusive spectrum. We roughly estimated at 5 μb/sr the cross section value for the reaction ^{2}H(^{6}He, ^{5}H)^{3}He populating ^{5}H in this resonance state. The resonance width seen in Fig. 5 is governed by the instrumental resolution, as was the case in the spectrum shown in Fig. 4, i.e., in the case of the reaction ^{3}H$(t,p)^5$H. This result once again supports the conclusion made earlier that the 1.8-MeV resonance in ^{5}H is rather narrow ($\Gamma \leq 500$ keV).

4. CONCLUSION

The missing mass energy spectrum has been obtained for ^{4}H nuclei formed in the reaction ^{2}H$(t,p)^4$H. The position and width of the ^{4}H resonance state, $E_R = 3.3$ MeV and $\gamma^2 = 2.3$ MeV, were deduced from the energy spectra of protons emitted at laboratory angles $18^\circ \leq \theta_{\rm lab} \leq 32^\circ$ and detected in coincidence with neutrons originating from the ^{4}H decay. The *pn* coincidence events turned out to be essentially free of interference made by backgrounds from final-state *pn* and *pt* interactions and quasi-free scattering resulting in knockout of protons from the deuterium target nuclei. On the contrary, *pt* coincidence events occurring in this reaction severely suffer from the background interference, giving ambiguous results for the ^{4}H energy spectrum. We note that the ^{4}H resonance parameters presented here are close to those reported in [11]. We consider our result to be satisfactory, as the resonance position obtained for ^{4}H is in accord with the weighted estimates made for the ^{4}H levels in [14]. Most probably, the ^{4}H spectrum observed in our work is the superposition of two resonances at $E_R = 3.19$ and 3.50 MeV suggested for this nucleus in [14]. We doubt that one will be able at some time to separate these two closely lying resonances populated either in transfer or fragmentation reactions or in reactions induced by the capture of slow pions. However, we do not exclude that a further study made for the reactions ^{2}H$(t,p)^4$H and ^{3}H$(t,d)^4$H will reveal the higher lying ^{4}H resonance pair supposed in [14] to be at 5.27 and 6.02 MeV.

Data obtained from the study of the reactions ^{3}H$(t,p)^5$H and ^{2}H(^{6}He, ^{5}H)^{3}He make us confident about the observation of a ^{5}H resonance state at energy $E_R = 1.8 \pm 0.1$ MeV above the $t+n+n$ decay threshold. This observation confirms the ground-state resonance position $E_R = 1.7 \pm 0.3$ MeV reported for this nucleus in [18]. Surprising is the small resonance width ($\Gamma_{\rm obs} \leq 0.5$ MeV) that showed up in the data obtained for both reactions. In the case of the reaction ^{3}H$(t,p)^5$H, the ^{5}H missing mass spectrum displays another narrow resonance state at $E_R = 2.7 \pm 0.1$ MeV. Evidently, it will be difficult to reconcile such small ^{5}H resonance widths with suggested theoretical concepts. This makes the further study of the ^{5}H nucleus intriguing.

ACKNOWLEDGMENTS

The work done in Dubna was partially supported by the Russian Foundation for Basic Research, project no. 02-02-16550.

REFERENCES

1. N. Jarmie *et al.*, Phys. Rev. **161**, 1050 (1967).
2. J. A. Bistirlich *et al.*, Phys. Rev. Lett. **25**, 950 (1970).
3. R. B. Weisenmiller *et al.*, Nucl. Phys. A **280**, 217 (1977).
4. T. C. Meyer, Nucl. Phys. A **324**, 335 (1979).
5. T. W. Phillips, B. L. Berman, and J. D. Seagrave, Phys. Rev. C **22**, 384 (1980).
6. U. Sennhauser *et al.*, Phys. Lett. B **103B**, 409 (1981); Nucl. Phys. A **386**, 429 (1982).
7. R. Franke *et al.*, Nucl. Phys. A **433**, 351 (1985).
8. A. V. Belozyorov *et al.*, Nucl. Phys. A **460**, 352 (1986).
9. D. Miljanic, S. Blagus, and M. Zadro, Phys. Rev. C **33**, 2204 (1986).
10. M. G. Gornov *et al.*, Pis'ma Zh. Éksp. Teor. Fiz. **45**, 205 (1987) [JETP Lett. **45**, 252 (1987)]; A. I. Amelin *et al.*, Pis'ma Zh. Éksp. Teor. Fiz. **51**, 607 (1990) [JETP Lett. **51**, 688 (1990)].
11. S. Blagus *et al.*, Phys. Rev. C **44**, 325 (1991).
12. D. V. Aleksandrov *et al.*, Pis'ma Zh. Éksp. Teor. Fiz. **62**, 18 (1995) [JETP Lett. **62**, 18 (1995)].
13. M. G. Gornov *et al.*, in *Abstracts of the International Conference "Features of Nuclear Excitation States and Mechanisms of Nuclear Reactions," Sarov, Russia, 2001,* p. 142.
14. D. R. Tilley, H. R. Weller, and G. M. Hale, Nucl. Phys. A **541**, 1 (1992).

15. P. G. Young *et al.*, Phys. Rev. **173**, 949 (1968).
16. M. G. Gornov *et al.*, Nucl. Phys. A **531**, 613 (1991).
17. D. V. Aleksandrov *et al.*, in *Proceedings of the International Conference "Exotic Nuclei and Atomic Masses (ENAM-95)", Arles, France, 1995* (Frontièrs, Gif-sur-Yvette, 1995), p. 329.
18. A. A. Korsheninnikov *et al.*, Phys. Rev. Lett. **87**, 092501 (2001).
19. J. J. Bevelacqua, Nucl. Phys. A **357**, 126 (1981).
20. N. A. F. M. Poppelier *et al.*, Phys. Lett. B **157B**, 120 (1985).
21. N. B. Shul'gina *et al.*, Phys. Rev. C **62**, 014312 (2000).
22. P. Discouvemont and A. Kharbach, Phys. Rev. C **63**, 027001 (2001).
23. N. K. Timofeyuk, Phys. Rev. C **65**, 064306 (2002).
24. G. M. Ter-Akopian *et al.*, AIP Conf. Proc. **610**, 920 (2002).
25. Yu. Ts. Oganessian *et al.*, in *Proceedings of the International Conference "Nuclear Physics at Border Lines", Lippari, Messina, Italy, 2001* (World Sci., Singapore, 2002), p. 372.
26. Yu. Ts. Oganessian *et al.*, Izv. Ross. Akad. Nauk, Ser. Fiz. **66**, 619 (2002).
27. A. M. Rodin *et al.*, Nucl. Instrum. Methods Phys. Res. B **126**, 236 (1996).
28. A. A. Yukhimchuk *et al.*, Preprint No. P13-2001-25, JINR (Dubna, 2001).
29. I. Tilquin *et al.*, Nucl. Instrum. Methods Phys. Res. A **365**, 446 (1995).
30. S. Blagus *et al.*, Z. Phys. A **337**, 297 (1990).

Physics of Atomic Nuclei, Vol. 66, No. 8, 2003, pp. 1552–1556. From Yadernaya Fizika, Vol. 66, No. 8, 2003, pp. 1595–1599.

Collective Excitations of the Element $Z = 120$*

Ş. Mişicu**, **T. Bürvenich, T. Cornelius, and W. Greiner**

Institut für Theoretische Physik, J. W. Goethe-Universität, Frankfurt am Main, Germany

Received January 19, 2003

Abstract—The low-lying vibrational excitations of superheavy even–even nuclei around $Z = 120$ and $N = 172$, predicted to be spherical by the relativistic mean-field (RMF) model, are studied within a phenomenological collective approach. In the framework of the macroscopic model for giant resonances, we compute the transition densities of the isoscalar monopole, quadrupole, and octupole and isovector dipole modes for the superheavy nucleus $^{292}120$, whose ground-state density is determined from the RMF model. The results are also compared to those for ^{208}Pb. © *2003 MAIK "Nauka/Interperiodica".*

INTRODUCTION

The superheavy nuclei owe their ephemeral existence solely to the shell effects and constitute a great challenge from both experimental [1] and theoretical [2] points of view. One of the most interesting questions in the study of the superheavy elements (SHE) is the possible appearance of new magic shell numbers. Within mean-field theories, several Skyrme forces and relativistic forces yield a spherical magic neutron number $N = 184$ [3]. Double-magic nuclei, i.e., the appearance of a magic-proton and a magic-neutron number in one and the same nucleus, occur in relativistic mean-field (RMF) calculations employing the forces NL-Z2 [4], NL3 [5], and PC-F1 [6] for the nucleus $^{292}120$ as a predominant case. A secondary case is realized with $^{304}120$. Compared to the next lighter double-magic nucleus ^{208}Pb, the nucleus $^{292}120$ presents a peculiarity related to its density profile. In the central region, calculations within several mean-field theories show a pronounced depletion of the density for protons and neutrons [4]. The confirmation of the double magicity of a superheavy nucleus could in future experiments be achieved by observing a vibrational pattern in its collective spectrum. Since the production cross sections of the elements are quite low, a way to observe collective states would be to investigate the α decay to vibrational states of a slightly deformed neighboring nucleus. Below, we explore qualitatively the consequences of the structure of the collective potential as predicted by modern self-consistent mean-field models for collective excitations.

We compute the potential energy surface (PES) within the RMF model, employing a selection of parametrizations to gain insight into the differences and uncertainties. We consider NL-Z2, NL3, and the force PC-F1, which corresponds to the RMF variant using pointlike interactions. The correction for spurious c.m. motion is performed by subtracting a posteriori

$$E_{\text{c.m.}} = \frac{\langle \hat{P}^2 \rangle}{2M}, \tag{1}$$

where $\hat{P}$ and M are total momentum and mass of the nucleus. Pairing is employed using the BCS model with a δ force (volume pairing) [7]. The pairing strengths for protons and neutrons are fitted to pairing gaps extracted from experimental data. The cuts through the PES are calculated in axial symmetry for reflection-symmetric shapes using a constraint on the total quadrupole moment Q_{20} of the nucleus. This is achieved by adding $-\lambda \hat{Q}_{20}$ to the Hamilton operator and minimizing $\langle \hat{H} - \lambda \hat{Q}_{20} \rangle$. All other multipole moments that are allowed by the symmetry of the calculation are not constrained and adjust themselves corresponding to the solution of minimal energy. The energy of the system is minimized using the damped gradient iteration method [8]. We do not correct for spurious rotational or vibrational motion, corresponding to zero-point energies, which would lower the total energy and modify the structure of the PES. The RMF code used in this study does not presently handle the nonaxiality, and therefore the γ-vibrational states are not included.

EXCITATIONS OF THE β-VIBRATIONAL BAND

In even–even spherical nuclei, the most prominent low-lying positive parity state is the vibrational one. For a pure harmonic quadrupole oscillator, the states

*This article was submitted by the authors in English.

**e-mail: misicu@th.physik.uni-frankfurt.de

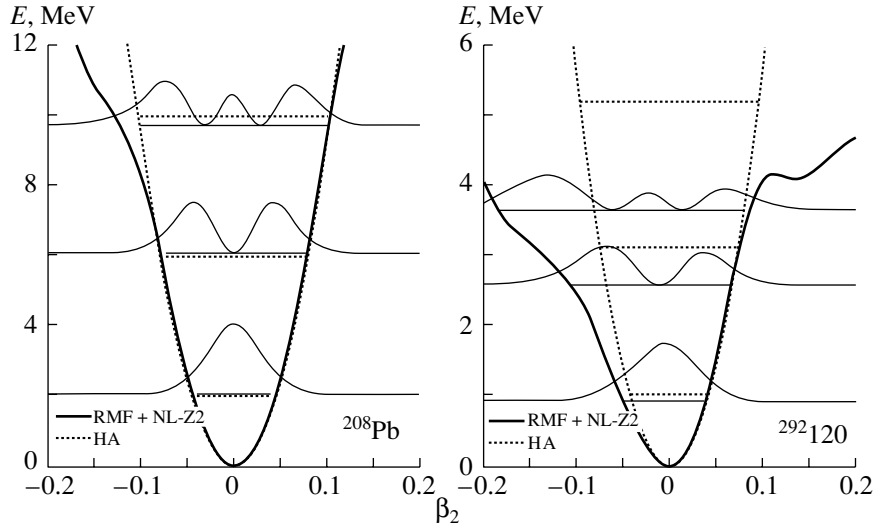

Fig. 1. Deformation potential computed in the framework of the RMF model with the NL-Z2 force (RMF + NL-Z2) and the first three vibrational states calculated within the collective model for two nuclei (solid curves). The HA is indicated by dotted curves. For each eigenvalue, we plotted its collective wave function. In the left panel, we represent the case of ^{208}Pb, where one sees that the HA works quite well, and in the right panel, the putative double-magic nucleus ^{292}120, for which the anharmonic distortions in the potential are already inducing a departure of the collective level spacing from the equidistant harmonic spacing.

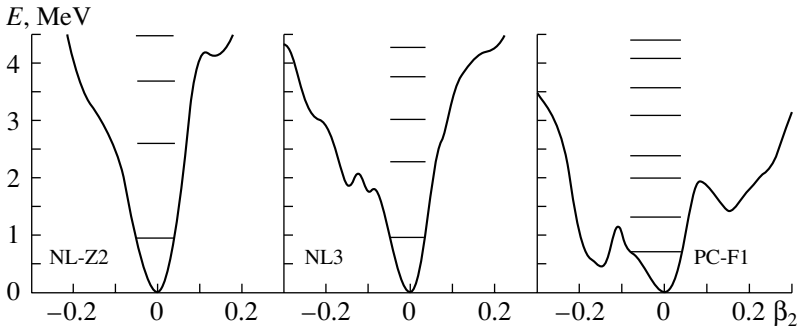

Fig. 2. Potential well and first eigenvalues of the collective model computed in the framework of the RMF with the forces NL-Z2, NL3, and PC-F1 for the isotope ^{292}120.

building the spectrum are equidistant and the three two-phonon states and the five three-phonon states are degenerated. The splitting of the triplet states and deviations from twice the one-phonon energy are indications of anharmonic terms in the collective Hamiltonian. If we consider only the β degree of freedom, the one-dimensional collective Hamiltonian reads

$$\hat{H}_\beta = -\frac{\hbar^2}{2B_2}\frac{\partial^2}{\partial\beta^2} + \hat{V}(\beta).$$

We solve numerically the corresponding stationary Schrödinger equation

$$\hat{H}_\beta\psi_n(\beta) = E_n\psi_n(\beta) \qquad (2)$$

by modifying the unbound potential $V(\beta)$ obtained in the RMF in a bound one. For the mass parameter B_2 of the collective motion, we use a phenomenological estimate [9] that reproduces quite well the experimental energies of the 2^+ and 4^+ energies in ^{208}Pb. We assume B_2 to be independent of deformation, which is an approximation reasonable for rather small deformations.

In Fig. 1, we display for the nuclei ^{208}Pb and ^{292}120 the vibrational states both in the potential emerging from a mean-field calculation using the force NL-Z2 and in the harmonic approximation (HA) of this potential. As one can see, the nucleus ^{208}Pb shows a pronounced harmonic behavior, at least for the first three vibrational states 0^+, 2^+, and 4^+. Consequently, the results within the HA, which work well up to an energy of 8 MeV, do not differ much from the calculation using the mean-field

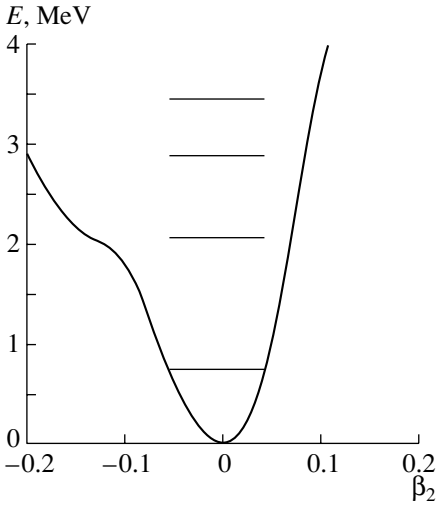

Fig. 3. Potential well and first eigenvalues from the collective model computed in the framework of the RMF model with the force NL-Z2 for $^{300}120$.

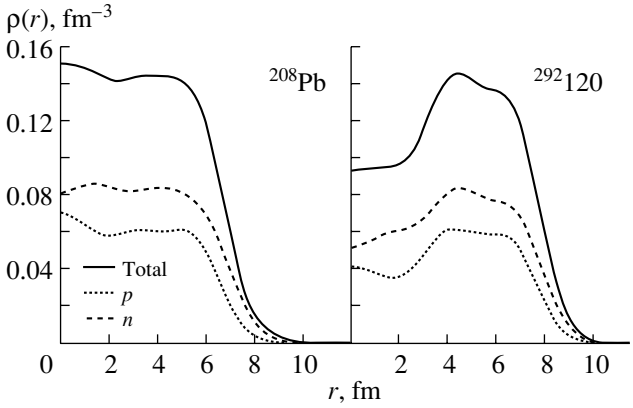

Fig. 4. Total density profiles of the heavy nucleus ^{208}Pb and the superheavy nucleus $^{292}120$. Both cases were computed in the framework of the RMF model with the force NL-Z2.

potential. We verified that this almost harmonic shape of the ^{208}Pb deformation energy is approximately the same when using NL-Z2, NL3, and PC-F1 forces. In contrast to that, the potential of the isotope $^{292}120$ exhibits a clear prolate–oblate asymmetry and the sequence of states follows a nonequidistant behavior. The collective wave function exhibits an asymmetric structure. This result was expected, because this isotope is unstable with respect to spontaneous fission (its barrier is up to 5 times smaller than the first symmetric barrier of ^{208}Pb) and, therefore, the departure of the deformation energy curve from the harmonic oscillator well is sensitively larger.

In Fig. 2, we compare the deformation energy curves and the eigenvalues of vibrational states for the isotope $^{292}120$ employing the forces NL-Z2, NL3, and PC-F1. The force NL-Z2 provides a curve (already sketched in the second panel of Fig. 1) that around the spherical minimum resembles a parabola, while anharmonicities become important for $\beta > 0.05$. The largest deviation from harmonicity is encountered for the force PC-F1, where the asymmetry with respect to the origin is very pronounced. The prediction employing NL3 lies somewhere between these extremes. Due to a softening of the PES for oblate shapes, states beginning with 2^+ have lower energy compared to the results with NL-Z2.

Calculations with NL-Z2 performed for the isotope $^{300}120$ provide a spherical minimum contrary to NL3 and PC-F1, which predict deformed minima. We again encounter deviations from a harmonic behavior (see Fig. 3).

All predictions discussed here lead to deviations from a harmonic spectrum, which is encountered, for example, for the double-magic lead nucleus. The details, however, depend significantly on the chosen mean-field force. The set of coupling constants PC-F1, corresponding to the RMF model with point couplings, leads to the highest density of states due to the softness of the PES. The NL-72 and NL3 forces have the same functional form. The distinction between them is determined by observables used in the fitting procedure.

ELECTRIC ISOSCALAR GIANT RESONANCES OF THE ELEMENT $^{292}120$

In Fig. 4, we compare the baryon densities of ^{208}Pb with the one for $^{292}120$. The obvious difference in the density profiles of the two nuclei will determine a different behavior in the collective excitations, where fluctuations of the density are involved. A typical example is given by giant resonances. The giant resonances are unlikely to be excited in SHE with external probes, such as photons or alphas, because of the small production cross sections. However, the superheavy elements could be created in an excited state, and thus the deexcitation mechanism may give additional information on its formation and structure. Giant resonances, especially of the electric dipole type, could be induced in the early stages of the formation of the compound nucleus due, for example, to the excitation of molecular radial vibrations of the projectile–target system.

Electric isoscalar giant resonances are well-known collective modes of nuclei, in which the disturbance is created by inelastically scattering a charged particle, e.g., an α particle, on a target nucleus. The transient electric field can excite an in-phase collective motion of protons and neutrons, which

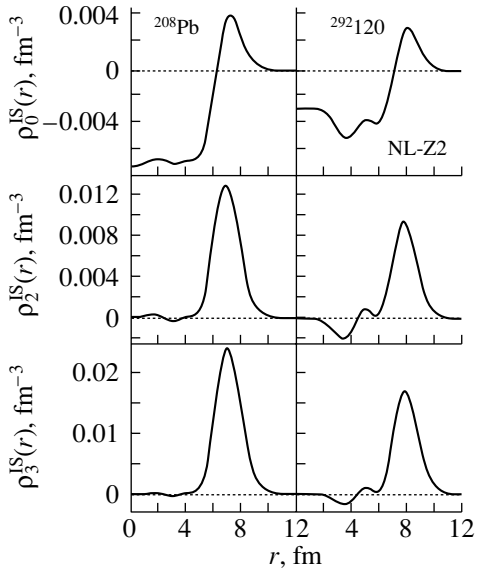

Fig. 5. Transition densities of ^{208}Pb and ^{292}120. The upper pair of figures corresponds to the giant monopole resonance (GMR), the middle one, to the quadrupole resonance (GQR), and the lowest one, to the octupole resonance (GOR).

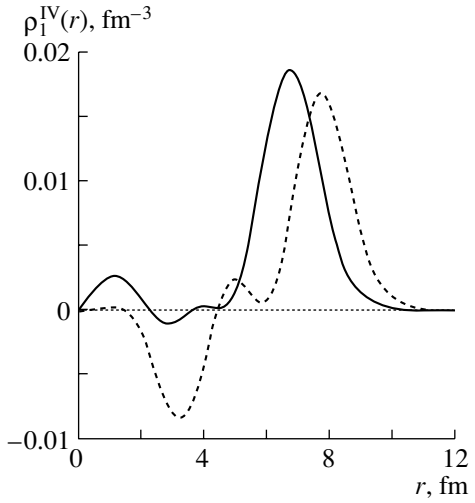

Fig. 6. Isovector dipole transition densities of ^{208}Pb (solid curve) and ^{292}120 (dashed curve) employing the NL-Z2 force.

eventually leads to the excitation of compressional waves of monopole (breathing, GMR), dipole (GDR), quadrupole (GQR), etc., type.

An important quantity in the investigation of giant resonances is provided by the so-called transition density, which is given by the multipole fluctuations of the nuclear density. In the folding model of hadronic interactions, the transition density multiplied to the corresponding multipolar component of the potential and integrated over the volume provides the form factor and the reduced electric transition probability [10].

We introduce the 2^λ-pole transition density, ρ_λ, of a target nucleus with projection μ

$$\rho_{\lambda\mu}(\mathbf{r}) = \langle\lambda\mu|\widehat{\rho}(\mathbf{r})|0\rangle = \frac{1}{\sqrt{2\lambda+1}}\rho_\lambda(r)Y^*_{\lambda\mu}(\theta,\phi),$$

where $\widehat{\rho}(\mathbf{r})$ is the density operator. If the energy-weighted sum rule, which measures the strength of giant resonances, is exhausted by a transition to a single state of excitation energy E_λ in a spherical nucleus, the corresponding isoscalar transition density is expressed in the so-called Tassie form:

$$\rho_\lambda^{\mathrm{IS}}(r) \approx \begin{cases} -\alpha_0\Big(3\rho(r) + rd\rho(r)/dr\Big), & \lambda = 0, \\ -\alpha_\lambda r^{\lambda-1}d\rho(r)/dr, & \lambda \geq 2, \end{cases}$$

where

$$\alpha_0^2 = \frac{2\pi\hbar^2}{mA\langle r^2\rangle E_0}, \qquad \alpha_\lambda^2 = \frac{2\pi\lambda\hbar^2}{mA\langle r^{2\lambda-2}\rangle E_\lambda}.$$

The kth moment of the total density is introduced through

$$\langle r^k\rangle = \int drr^{k+2}\rho(r). \tag{3}$$

For the dipole isovector transition density, we have

$$\rho_1^{\mathrm{IV}}(r) = -2\alpha_1\left(\frac{Z}{A}\frac{d\rho_n}{dr} - \frac{N}{A}\frac{d\rho_p}{dr}\right)$$

with

$$\alpha_1^2 = \frac{\pi\hbar^2}{2m}\frac{A}{NZE_1}.$$

For the excitation energy of the λ-pole giant resonance, we consider the ansatz

$$E_\lambda = K_{\mathrm{LT}}n_\lambda\hbar\omega, \quad \hbar\omega = 45A^{-1/3} - 25A^{-2/3},$$

where, as assumed above, we take only one phonon of excitation energy, i.e., $n_\lambda = 1$, and K_{LT} estimates are taken from [11]. With this ansatz, we obtain an estimate of 9.6 MeV for the GMR, 5 MeV for the GQR, 2.5 MeV for the GOR, and 13.4 MeV for the isovector giant dipole resonance. This means that the giant resonances could be triggered in the formation of the compound nucleus, because in cold fusion the excitation energy ranges in the interval 10–20 MeV.

In Fig. 5, we plotted the transition densities for ^{208}Pb and ^{292}120 for the cases $\lambda = 0$, 2, and 3. In all cases, the transition densities show a rather smooth behavior in the interior of the first nucleus and an oscillating one for the superheavy isotope. For monopole giant resonances, the breathing movement of the nuclear matter produces a region of lower and another one of higher density. The isotope ^{292}120 shows a sequence of compressed or expanded regions with

an overall amplitude smaller than that for ^{208}Pb. For the quadrupole and octupole resonances, the surface peak in the density will be attenuated at the surface in favor of compression–expansion waves in the interior. This former type of density oscillations is much less pronounced for ^{208}Pb.

The differences between the isovector transition densities of ^{208}Pb and ^{292}120 are depicted in Fig. 6. In the case of the superheavy isotope, a diminution of the density inside the nucleus corresponds to an expansion at the surface, similar to the GQR, but this time more pronounced.

CONCLUSIONS

We investigated the β-vibrational collective excitations of superheavy nuclei, which are predicted to be spherical by recent RMF calculations. Special attention was paid to the isotope ^{292}120, which is predicted to be doubly-magic. We compared the β-vibrational spectrum of this nucleus, in the absence of the γ deformations, to the one of the doubly magic ^{208}Pb. It turned out that ^{292}120 does not exhibit an equidistant spacing between the vibrational states as is the case for ^{208}Pb. For the same isotope, we used three different parametrizations of the effective nucleon–nucleon force, namely, NL-Z2, NL3, and PC-F1. Going from the first one to the last one, we obtain an increase by a factor of two in the vibrational level density. For another isotope, which is predicted to be spherical as well, namely ^{298}114, the qualitative differences between the deformation curves are less pronounced. The variation of the level density, when going from NL-Z2 to PC-F1 is softer in this case. As expected, the β-vibrational energies yield information about the potential and through that about the underlying forces. The reason for the discrepancies in the predictions of the collective potentials is not yet fully understood.

Assuming a dependence on A of the giant resonances centroids, similar to the one, which applies to known spherical nuclei such as ^{208}Pb, we computed the transition densities of the isoscalar monopole, quadrupole, octupole, and isovector dipole giant resonances in the isotope ^{292}120 and noticed some qualitative differences with respect to the transition densities of ^{208}Pb. It is interesting to note that, under such assumptions, the amount of energy necessary to excite a giant resonance is smaller than the average excitation energy present in the compound nucleus and therefore giant resonances could be candidates as deexcitation channels.

ACKNOWLEDGMENTS

One of us (Ş.M.) is grateful to the European Community for financial support through a Marie Curie fellowship.

REFERENCES

1. S. Hofmann and G. Münzenberg, Rev. Mod. Phys. **72**, 733 (2000).
2. W. Greiner, in *Proceedings of the International Workshop "Fusion Dynamics at the Extremes," Dubna, Russia, 2000*, Ed. by Yu. Ts. Oganessian and V. I. Zagrebaev (World Sci., Singapore, 2001), p. 1.
3. K. Rutz, M. Bender, T. Bürvenich, *et al.*, Phys. Rev. C **56**, 238 (1997).
4. M. Bender, K. Rutz, P.-G. Reinhard, *et al.*, Phys. Rev. C **60**, 34304 (1999).
5. G. A. Lalazissis, J. König, and P. Ring, Phys. Rev. C **55**, 540 (1997).
6. T. Bürvenich, D. G. Madland, J. A. Maruhn, and P.-G. Reinhard, Phys. Rev. C **65**, 044308 (2002).
7. M. Bender, K. Rutz, P.-G. Reinhard, and J. A. Maruhn, Eur. Phys. J. A **8**, 59 (2000).
8. P.-G. Reinhard and R. Y. Cusson, Nucl. Phys. A **378**, 418 (1982).
9. J. Eisenberg and W. Greiner, *Nuclear Theory* (North-Holland, Amsterdam, 1972), Vol. III.
10. G. R. Satchler, Nucl. Phys. A **472**, 215 (1987).
11. G. F. Bertsch and S. F. Tsai, Phys. Rep. C **18**, 125 (1975).

Physics of Atomic Nuclei, Vol. 66, No. 8, 2003, pp. 1557–1560. From Yadernaya Fizika, Vol. 66, No. 8, 2003, pp. 1600–1603.

Binding Energies of Even–Even Superheavy Nuclei*

Z. Ren**

Department of Physics, Nanjing University, Nanjing, China
Center of Theoretical Nuclear Physics, National Laboratory of Heavy-Ion Accelerator at Lanzhou, Lanzhou, China

Received August 28, 2002

Abstract—The structure of the even–even superheavy nuclei with the proton number $Z = 98$–110 is studied using the self-consistent relativistic mean-field theory. The calculated binding energies are in good agreement with the available experimental ones. An upper limit and a lower limit on the binding energies are set by the calculations. This is useful for future calculations of properties of superheavy nuclei and for the experimental synthesis of superheavy nuclei. The energy surface of some relevant superheavy nuclei is also given and it confirms the correctness of the calculations. © *2003 MAIK "Nauka/Interperiodica".*

Recent studies on superheavy nuclei attract many physicists in nuclear physics [1–5]. Since the report that the $Z = 114$ element was produced at Dubna in Russia in 1999 [4], more and more laboratories are participating in research on superheavy nuclei and new progress is being made [5–7]. For example, a new nuclide $^{270}110$ was produced at GSI (see [6]). A new nuclide $^{270}108$ was synthesized at PSI [7] and a new nuclide ^{259}Db was produced at the Institute of Modern Physics in Lanzhou [5].

In order to follow this new progress and to give a reliable prediction for further experiments, a reliable model is needed for the estimate of binding energies and alpha-decay energies of superheavy nuclei. In this paper, I study the ground-state properties of known even–even superheavy nuclei ($Z = 98$–110) and their neighboring nuclei. My objective is to make a systematic comparison of theoretical binding energies with all available data of binding energies for these isotope chains. An upper limit and a lower limit will be given by this comparison.

As the deformed relativistic mean-field (RMF) formulations can be found in some references [8–10], here we report the numerical results directly. Although there are some RMF calculations on superheavy nuclei [11–13], a systematic comparison on the predicting ability of the model is missing. In our previous paper, we investigated the properties of some odd nuclei [13]. Here, we study the even–even nuclei of $Z = 98$–110.

The numerical results are listed in Tables 1 and 2. The force parameters TMA and NLZ2 are used in the calculations. In Tables 1 and 2, the first column is for nuclei. $B_{\rm th}$ is the theoretical binding energy, whereas R_p and R_n are the root-mean-square radii for the proton- and neutron-density distributions, respectively. The symbols β_n and β_p in Tables 1 and 2 denote the quadrupole deformations of neutrons and protons, respectively. Further, the symbols Q_α(th.) and Q_α(exp.) are used for the calculated alpha-decay energies and the experimental ones. The experimental binding energies are obtained from the nuclear mass table [14] and the experimental alpha-decay energies can be deduced accordingly. They are listed in the last two columns for comparison.

It is seen from Table 1 that the theoretical binding energies are very close to the experimental data. The average difference between the theoretical binding energy and experimental one is approximately 2 MeV.

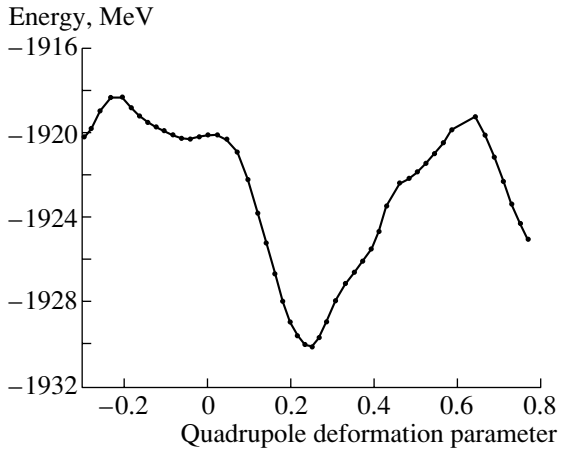

The energy surfaces of the nucleus $^{264}108$. The TMA force is used.

*This article was submitted by the author in English.

**e-mail: zren@nju.edu.cn;zren99@yahoo.com

1063-7788/03/6608-1557$24.00

Table 1. The ground-state properties of even–even superheavy nuclei with $Z \geq 98$ and $N \geq 150$. (The TMA force is inputted in the deformed RMF calculation. The last two columns are the experimental data of the alpha-decay energy and the total binding energy.)

Nucleus	$B_{\rm th}$, MeV	β_n	β_p	R_n	R_p	Q_α(th.)	Q_α(exp.)	$B_{\rm exp.}$, MeV
^{246}Cf	1846.30	0.27	0.27	6.12	5.92			1844.74
^{248}Cf	1858.95	0.26	0.27	6.14	5.93			1857.73
^{250}Cf	1870.97	0.26	0.26	6.16	5.94			1869.94
^{252}Cf	1882.44	0.26	0.26	6.19	5.95			1881.22
^{250}Fm	1867.01	0.26	0.27	6.15	5.96	7.59	7.56	1865.48
^{252}Fm	1880.07	0.26	0.27	6.17	5.97	7.18	7.16	1878.87
^{254}Fm	1892.47	0.26	0.27	6.19	5.98	6.80	7.31	1890.93
^{256}Fm	1903.71	0.26	0.26	6.21	5.99	7.03	7.03	1902.49
^{252}No	1873.17	0.26	0.27	6.15	5.98	8.59	8.55	1871.25
^{254}No	1887.22	0.26	0.27	6.17	5.99	8.09	8.24	1885.54
^{256}No	1900.69	0.26	0.27	6.19	6.00	7.68	8.57	1898.60
^{258}No	1912.85	0.26	0.27	6.21	6.01	7.92		
^{256}Rf	1892.63	0.25	0.26	6.17	6.01	8.84	8.96	1890.59
^{258}Rf	1906.98	0.26	0.27	6.20	6.02	8.54		
^{260}Rf	1919.99	0.23	0.23	6.21	6.02	9.00		
^{262}Rf	1932.67	0.22	0.22	6.23	6.03	8.48		
^{260}Sg	1911.85	0.25	0.26	6.20	6.04	9.08	9.93	1908.96
^{262}Sg	1925.90	0.25	0.26	6.22	6.06	9.38		
^{264}Sg	1939.26	0.22	0.23	6.23	6.06	9.03		
^{266}Sg	1952.40	0.22	0.22	6.25	6.07	8.57		
^{264}Hs	1930.17	0.24	0.25	6.23	6.07	9.98	10.54	1926.72
^{266}Hs	1944.46	0.24	0.24	6.24	6.08	9.74	10.18	
^{268}Hs	1958.42	0.22	0.23	6.26	6.09	9.14		
^{270}Hs	1971.80	0.22	0.22	6.28	6.10	8.90		
^{270}110	1961.39	0.22	0.22	6.26	6.11	11.34	10.954	

This corresponds to a relative difference of 0.1%. The maximum difference is 3.45 MeV for ^{264}108 and it corresponds to a relative difference of 0.2%. Considering the predicting ability of the RMF model for the binding energy of spherical nuclei ^{16}O, ^{40,48}Ca, ^{90}Zr, ^{116,124}Sn, and ^{208}Pb, which is also around 0.2%, we can say that the RMF model works well for the binding energy of the superheavy nuclei studied here. The theoretical alpha-decay energies agree well with the experimental ones within 1 MeV. This guarantees the good predicting ability of the RMF model for the alpha-decay properties. Calculations show that there is a prolate deformation in the ground state of these nuclei. In order to confirm the deformation, we carry out a constraint calculation [13] on the quadrupole moments and the result is drawn in the figure. This is a rather time-consuming calculation even for present-day computers.

The figure demonstrates the variation of the ground-state energy with the quadrupole deformation parameters for ^{264}108. The TMA force is inputted, and $N_f = N_b = 20$ is chosen. The pairing gaps are the same as before. The black points are numerical results and they are connected by solid lines. A minimum with $\beta_2 \approx 0.24$ appears on the energy curve. The valley around this minimum is wide and deep. This is the ground state of ^{264}108. The energy surface of other nuclei in Table 1 is very similar to that of ^{264}108. This confirms the reliability of the RMF results in Table 1. By the way, the other solutions in it lie higher in energy.

Table 2 is the RMF results with the NLZ2 force. It is seen again that the theoretical results agree well with the experimental data of the binding energies and alpha-decay energies. The precision of the force NLZ2 is as good as of the force TMA. A quadrupole deformation in the ground state of these nuclei is also obtained for NLZ2. Its value is close to that of the TMA force. This indicates that the RMF model is stable in this mass range. All previous discussions on Table 1 hold true for Table 2.

Table 2. The ground-state properties of even–even superheavy nuclei with $98 \leq Z$ and $N \geq 150$. (The NLZ2 force is inputted in the deformed RMF calculation. The last two columns are the experimental data of the alpha-decay energy and the total binding energy.)

Nucleus	$B_{\rm th}$, MeV	β_n	β_p	R_n	R_p	Q_α(th.)	Q_α(exp.)	$B_{\rm exp.}$, MeV
^{246}Cf	1843.06	0.31	0.31	6.24	6.01			1844.74
^{248}Cf	1855.48	0.31	0.32	6.27	6.02			1857.73
^{250}Cf	1866.84	0.31	0.31	6.30	6.03			1869.94
^{252}Cf	1877.73	0.30	0.31	6.32	6.05			1881.22
^{250}Fm	1863.65	0.30	0.31	6.27	6.04	7.71	7.56	1865.48
^{252}Fm	1876.03	0.30	0.31	6.30	6.06	7.75	7.16	1878.87
^{254}Fm	1887.90	0.30	0.31	6.32	6.07	7.24	7.31	1890.93
^{256}Fm	1899.60	0.29	0.30	6.35	6.08	6.43	7.03	1902.49
^{252}No	1870.69	0.30	0.32	6.27	6.07	7.86	8.55	1871.25
^{254}No	1884.14	0.30	0.32	6.30	6.08	7.81	8.24	1885.54
^{256}No	1896.98	0.30	0.31	6.33	6.09	7.35	8.57	1898.60
^{258}No	1909.53	0.30	0.31	6.35	6.11	6.67		
^{256}Rf	1890.73	0.30	0.32	6.30	6.10	8.26	8.96	1890.59
^{258}Rf	1904.50	0.30	0.31	6.33	6.11	7.94		
^{260}Rf	1917.87	0.30	0.31	6.35	6.13	7.41		
^{262}Rf	1930.84	0.29	0.30	6.38	6.14	6.99		
^{260}Sg	1909.01	0.30	0.31	6.33	6.14	10.02	9.93	1908.96
^{262}Sg	1923.35	0.29	0.30	6.35	6.15	9.45		
^{264}Sg	1937.25	0.29	0.30	6.38	6.16	8.92		
^{266}Sg	1950.47	0.28	0.29	6.40	6.17	8.67		
^{264}Hs	1926.63	0.28	0.29	6.35	6.17	10.68	10.54	1926.72
^{266}Hs	1941.35	0.28	0.29	6.38	6.18	10.30	10.18	
^{268}Hs	1955.59	0.27	0.28	6.40	6.19	9.96		
^{270}Hs	1969.22	0.27	0.28	6.42	6.20	9.55		
^{270}110	1958.86	0.26	0.26	6.40	6.21	10.79	10.954	

When we compare Table 1 and Table 2 together, we notice that the experimental binding energy is between the theoretical value with TMA and that with NLZ2. It seems that the obtained value with TMA sets the upper limit on the binding energy and the obtained value with NLZ2 sets the lower limit. This is very useful for the prediction of properties of superheavy nuclei, because both obtained values with TMA and NLZ2 are very close. Therefore, the theoretical results can be used as a guide for future experiments of superheavy nuclei. By the way, there are many sets of force parameters in the RMF model. The behavior of many force parameters for superheavy nuclei is similar to that of the TMA force. They also set the upper limit on the binding energy of a superheavy nucleus. Therefore, TMA is a typical force for the upper limit of the total binding energy and NLZ2 is a typical force for the lower limit.

Very recently, it was reported that the nucleus ^{270}110 has been produced at GSI [5]. The binding energy and alpha-decay energy of ^{270}110 are given in the last row of Tables 1 and 2, together with those of the nuclei on its alpha-decay chain. They can be directly compared with the experimental data.

Deformations may exist for many superheavy nuclei. In view of the fact that the nuclei in the actinium series are deformed, our conclusions are compatible with the present data on superheavy nuclei. Experimentally extracting information on deformation will be useful to test these views. One possible way is to investigate the rotational bands, and another way is to look for the isomer of superheavy nuclei. These will shed the light on deformation of superheavy nuclei.

In summary, we have investigated the structure of even–even superheavy nuclei with proton number $Z = 98$–110 in the RMF model. This is the systematic comparison between the theoretical binding energy of the RMF model and the available data. The calculated binding energy agrees well with the data. The biggest difference is 0.2% and this is also the precision of the RMF model for stable nuclei. The calculations also set an upper limit and a lower limit

on the binding energy based on the comparison with present data. This is useful as a guide for future experiments on superheavy nuclei. Experimental study of the deformation of superheavy nuclei will be very useful for understanding of the structure of superheavy nuclei and may also be possible with present facilities.

ACKNOWLEDGMENTS

This work was supported by the National Fund for Outstanding Young Scientists of the National Natural Science Foundation of China (10125521), the CAS Knowledge Innovation Project (no. KJCX2-SW-N02), and the 973 project of China (G2000077400).

REFERENCES

1. H. Q. Zhang, Nucl. Phys. Rev. **16**, 192 (1999) (in Chinese).
2. W. Q. Shen *et al.*, Phys. Rev. C **36**, 115 (1987).
3. Z. Ren *et al.*, Chin. Phys. Lett. **14**, 259 (1997).
4. Yu. Ts. Oganessian *et al.*, Nature (London) **400**, 242 (1999).
5. Z. G. Gan, Z. Qin, *et al.*, Eur. Phys. J. A **10**, 21 (2001).
6. S. Hofmann *et al.*, Eur. Phys. J. A **10**, 5 (2001).
7. A. Tuerler *et al.*, Phys. Rev. Lett. (in press).
8. Y. K. Gambhir *et al.*, Ann. Phys. (N.Y.) **198**, 132 (1990).
9. Z. Ren, Z. Y. Zhu, Y. H. Cai, and G. Xu, Phys. Lett. B **380**, 241 (1996).
10. B. Q. Chen, Z. Y. Ma, F. Gruemmer, and S. Krewald, Phys. Lett. B **455**, 13 (1999).
11. M. Bender *et al.*, Phys. Rev. C **60**, 034304 (1999).
12. S. K. Patra *et al.*, Nucl. Phys. A **651**, 117 (1999).
13. Z. Ren and H. Toki, Nucl. Phys. A **689**, 691 (2001).
14. G. Audi *et al.*, Nucl. Phys. A **624**, 1 (1997).

Physics of Atomic Nuclei, Vol. 66, No. 8, 2003, pp. 1561–1568. From Yadernaya Fizika, Vol. 66, No. 8, 2003, pp. 1604–1611.

Manifestation of Shell Effects in Quasifission Reactions*

E. A. Cherepanov** and **V. V. Volkov**

Flerov Laboratory of Nuclear Reactions, Joint Institute for Nuclear Research, Dubna, Moscow oblast, 141980 Russia

Received August 28, 2002

Abstract—In reactions used for the synthesis of superheavy elements, the shell effects manifested themselves in the mass distribution of quasifission products, i.e., in an increased yield of nuclei with a closed shell, such as ^{208}Pb and ^{132}Sn. A model for the description of this effect is proposed. © *2003 MAIK "Nauka/Interperiodica".*

1. INTRODUCTION

The nuclear-physical research with heavy ions at low energies, of approximately up to 10–15 MeV per nucleon, has resulted in the discovery of two new nuclear processes not known before for light bombarding particles, namely, deep inelastic transfer reactions (DITR) and quasifission. DITR have some characteristics of the energy spectra and angular distributions by which they can be distinguished from products of decay of excited compound nuclei or direct nuclear reactions [1–3]. The situation in the case of quasifission is more complicated. Mass and angular distributions of quasifission products have the same characteristics as fission of heavy nuclei. However, in quasifission, two nuclear fragments are formed as a result of the decay of an intermediate dinuclear system (DNS).

Quasi-fission is not realized in all the combinations of colliding nuclei. This nuclear process is characteristic of the interaction of massive heavy ions with heavy target nuclei.

Quasi-fission is the dominant channel in reactions of synthesis of superheavy elements (SHE). It reduces the cross section of the compound nucleus production a thousand or a million times. Quasi-fission is the main "threatening" process for the SHE production in reactions of cold synthesis, in which ^{208}Pb and ^{209}Bi targets are used. Quasi-fission reduces, by some orders of magnitude, the cross section of fusion in reactions of warm synthesis of SHE in which an actinide target and ^{48}Ca ions are used. In the mass distribution of quasifission products, the shell effects unambiguously manifest themselves: there is an increased yield of nuclei with closed proton and neutron shells.

2. MECHANISM OF THE QUASIFISSION PROCESS

2.1. Quasifission in Terms of a Macroscopic Dynamic Model

The existence of the quasifission process was predicted by Swiatecki in 1972 [4], though the term "quasifission" was introduced by him later, in 1980. Analyzing the evolution of the form of two colliding drops of nuclear liquid as a function of the kinetic energy and their total charge, mass, and mass asymmetry, he obtained the following result: for light and average nuclear drops, complete fusion with formation of an excited compound nucleus is more favorable from the point of view of the potential energy. In contrast, in collisions of massive nuclei, evolution of the DNS to the symmetric form is more favorable. For large values of Z^2/A, the nuclear system in such a form is unstable and decays into two fragments with close masses, without formation of a compound nucleus.

In 1980, Swiatecki proposed a macroscopic dynamic model (MDM) for the description of nuclear reactions between massive nuclei [5, 6]. The model was based on liquid drop representations of nuclei and classical equations of motion. In the MDM, quasifission has a definite energy interval. Since nuclear drops have high viscosity, there is a need for additional kinetic energy (the extra push E_x) for fusing into a strongly deformed mononucleus. More additional kinetic energy (the extra–extra push E_{xx}) is necessary for the deformed mononucleus to overcome the nuclear friction and to reach a compact form of a compound nucleus. If the collision kinetic energy E_i is within the interval from $B_C + E_x$ to $B_C + E_{xx}$, the mononucleus following the potential energy of the system comes to the quasifission channel.

*This article was submitted by the authors in English.

**e-mail: cher@jinr.ru

1063-7788/03/6608-1561$24.00

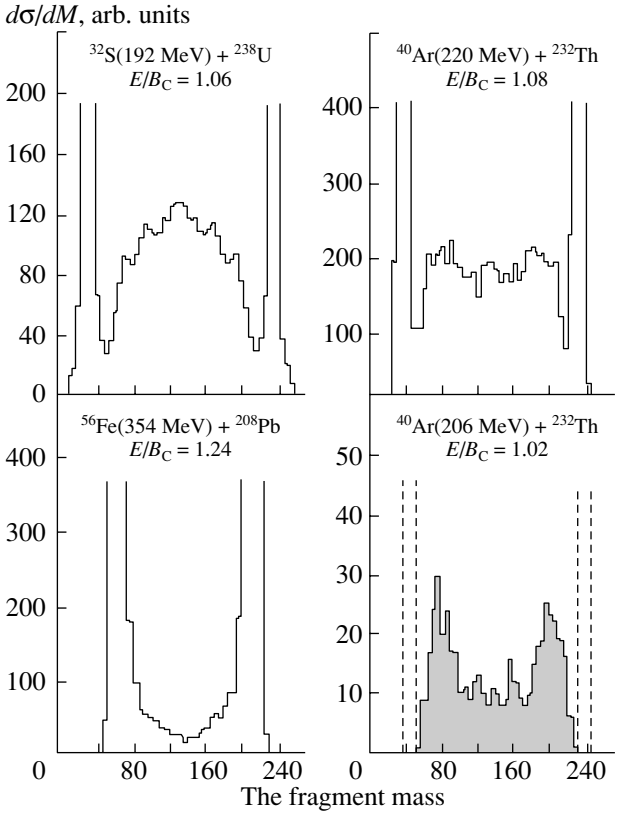

Fig. 1. The fragment mass distribution for the three reactions with various mass asymmetries in the entrance channel [8].

2.2. Quasifission in Terms of the Dinuclear System Concept

The DNS concept (DNSC) was proposed and elaborated in Dubna for the description of the complete fusion process [7]. This concept is based on the experimental information on the nuclear interaction obtained in the study of DITR [1–3]. These reactions yield unique information on the interaction of nuclei which turn out to be in close contact after the full dissipation of the collision kinetic energy. The DNSC allows us to give a realistic description for the mechanism of complete fusion of nuclei and quasifission. According to the DNSC, these processes proceed as follows:

At the capture of a heavy ion by the target nucleus, complete dissipation of the collision kinetic energy occurs and a DNS is formed.

The DNS evolves in time by transfer of nucleons to a compound nucleus, or to the symmetric form. In the symmetric form, the Coulomb repulsion between the DNS nuclei reaches the maximal value and the system breaks up into two fragments, i.e., comes to the quasifission channel. As the evolution of a DNS is a statistical process, there is a competition between the complete fusion and quasifission channels.

The nuclei of the DNS keep their individuality during the whole process of evolution of the DNS. This important feature of the DNS evolution is a consequence of the shell structure of nuclei.

In the framework of the model [7], quasifission is considered as a process of evolution of the DNS, formed at the capture stage, in the direction of decreasing its charge and mass asymmetry, accompanied by the decay of the system into two fragments via all intermediate and final configurations. The evolution of the DNS is governed by the potential energy of the DNS, which is a function of its charge (mass) asymmetry and the angular momentum of the collision. In the reactions of synthesis of SHE, the DNS excitation energy is low. For this reason, in calculations of the potential energy, the real (table) masses of the interacting nuclei rather than the liquid drop values are used. On the potential energy curve, quite deep minima occur for those DNS configurations for which one of the system nuclei is a doubly magic one. The DNS evolution is retarded at these minima, which in turn leads to an increased yield of the corresponding fragment nuclei.

The DNSC for the complete fusion of nuclei makes it possible to interpret this shell effect and to create a model for the description of the mass distribution in the quasifission process.

3. MANIFESTATION OF SHELL EFFECTS IN QUASIFISSION (EXPERIMENTAL DATA)

Shell effects in quasifission were first observed in Dubna, at the FLNR [8], in the irradiation of ^{232}Th with ^{40}Ar ions at a bombardment energy of 206 MeV. In the mass distribution of quasifission products, a maximum was found, which corresponded to the decay of the DNS into two fragments, one of which was a nucleus close in mass to the Pb nucleus, and the other, the complimentary nucleus (see Fig. 1).

This "lead peak" manifests itself very strongly in reactions of warm synthesis of SHE. The mass spectra of quasifission and fission products and their energy spectrum were studied at the FLNR (Dubna) using a ^{48}Ca beam. Two nuclei—quasifission or fission fragments—were registered in coincidences under kinematical conditions appropriate to the DNS decay or fission of a compound nucleus. In Fig. 2, the mass spectra of nuclear fragments measured in the reactions, ^{48}Ca + ^{238}U, ^{48}Ca + ^{244}Pu, and ^{48}Ca + ^{248}Cm are presented. In the mass spectra of all three reactions, a high peak is seen which corresponds to the DNS decay to the Pb nucleus and a complimentary nucleus.

The fission and quasifission fragments in reactions of the SHE synthesis were investigated in [9, 10].

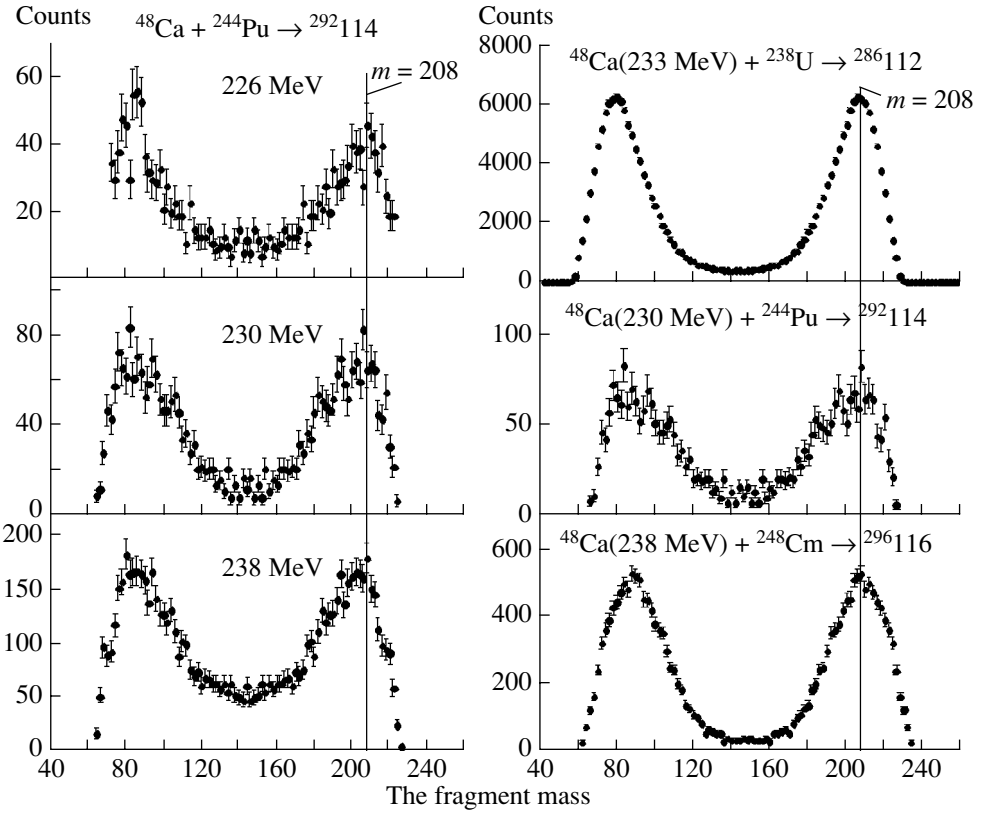

Fig. 2. The fragment mass distribution in the reactions ^{48}Ca + ^{244}Pu = ^{292}114, ^{48}Ca + ^{238}U = ^{286}112, and ^{48}Ca + ^{248}Cm = ^{296}116 [9, 10].

The experiments were carried out at energies near the entrance Coulomb barrier B_C. Insignificant variations of collision energy did not change the picture of the fragment mass distribution. In the reaction ^{48}Ca + ^{238}U, for the collision energy corresponding to the excitation of a compound nucleus equal to 21–33 MeV, one more maximum was observed, which corresponded to the nuclei with closed proton ($Z = 50$) and neutron ($N = 82$) shells (see Fig. 3).

In another series of experiments [9, 10], ^{232}Th, ^{244}Pu, and ^{248}Cm targets were irradiated with heavier ^{58}Fe ions. The high "lead" maximum in the mass distribution of products of quasifission was also observed.

Existing theoretical models do not give an explanation of the appearance of the shell effects in the quasifission process. Only the DNSC allows one to reveal the nature of their manifestation.

4. INTERPRETATION OF SHELL EFFECTS IN QUASIFISSION IN TERMS OF THE DNSC

The synthesis of SHE was carried out at heavy-ion energies close to the entrance Coulomb barrier. It provides favorable conditions for the survival of an excited compound nucleus during the decay process. Figure 4 shows the three-dimensional proximity potential (a qualitative picture) as a function of the distance between the centers of the nuclei and the charge number of one of the DNS nuclei. After the capture of a heavy ion by a target nucleus, the DNS is formed in the potential energy pocket. Then, the DNS will move along the valley in the direction of increasing symmetry and to complete fusion. During the evolution, the DNS may be broken up into two fragments without formation of a compound nucleus. In Fig. 4, the corresponding processes are indicated by arrows. In Fig. 5, two profiles of the potential energy are shown: the profiles along the minimum and the maximum of the potential energy surface calculated for the reaction ^{48}Ca + ^{244}Pu. The curve $V(Z, L = 0)$ (for the quantity R corresponding to the pocket) has a few local minima, which reflect the shell structure in the interacting nuclei. Heavy and superheavy elements are typically produced at ion energies corresponding to the minimally possible excitation energy of the compound nucleus. This ensures a higher survival probability for the compound nucleus during its deexcitation.

The excitation energy of the initial DNS, formed at

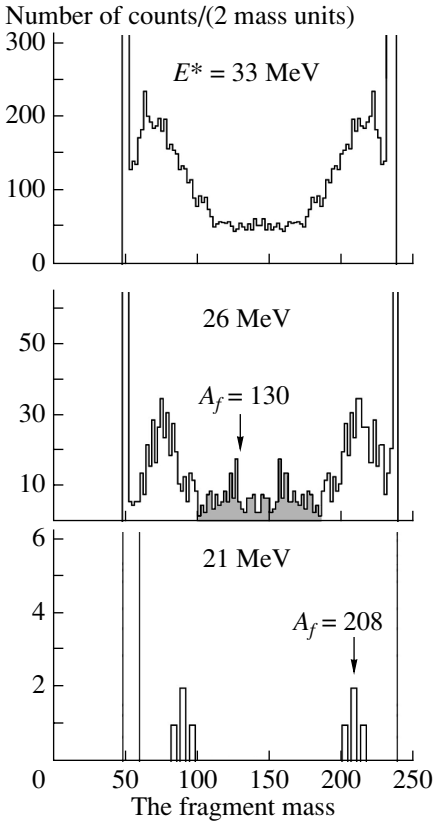

Fig. 3. The fragment mass distribution in the reactions $^{48}Ca + {}^{238}U = {}^{286}112$ for three different excitation energies of the compound nucleus [11].

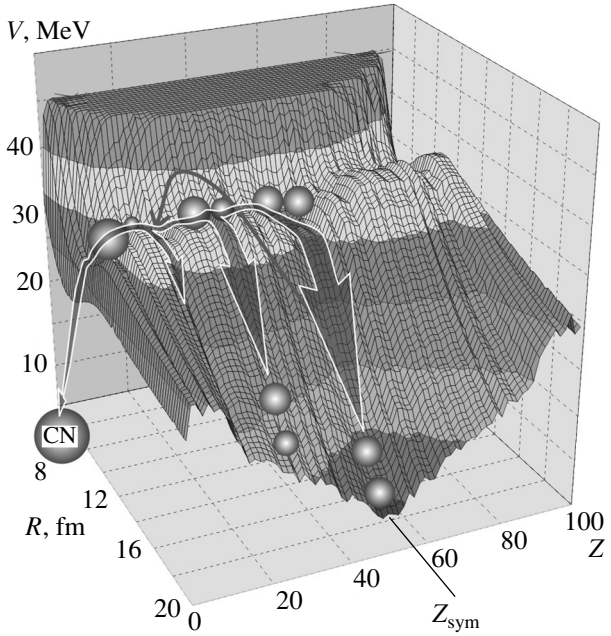

Fig. 4. Proximity potential as a function of the charge number of one of the DNS nuclei and the distance between the centers of the nuclei. The entrance channel and probable ways for the DNS evolution are shown by arrows.

the capture of the ^{48}Ca nucleus by the nucleus of an actinide target, is about 10 MeV. Figure 5, in which the potential energy of the DNS and its excitation energy in the $^{48}Ca + {}^{244}Pu$ reaction are presented, illustrates this situation. At such a low DNS excitation energy, the structure of the nuclei included in the system will be retained to a great extent; therefore, in calculations of the system potential energy, it is necessary to use real (not liquid drop) tabulated nuclear masses. In the DNS potential energy, there are features caused by the shell structure of the constituent nuclei. For a configuration in which one of the DNS nuclei is the ^{208}Pb nucleus, in the potential energy of the system, there is quite a deep minimum, and a potential barrier appears on the way of the DNS evolution to a symmetric configuration. Further on, in the reactions of SHE synthesis, the pocket in the nucleus–nucleus potential $V(R)$, holding the two nuclei of the system in contact, is not deep, and its depth decreases together with decreasing DNS asymmetry (see Fig. 5).

When one of the nuclei of the system is the ^{208}Pb nucleus, the quasifission barrier B_{qf}, holding the DNS from decay, turns out to be below this potential barrier. Due to the statistical properties of the DNS evolution, the decay of the system into two fragments becomes more probable than its transition to the following more symmetric configurations, and in the mass distribution of quasifission products, a typical "lead" maximum appears.

In reactions of warm SHE synthesis, the nuclei of actinide elements ^{238}U, ^{244}Pu, and ^{248}Cm are bombarded with ^{48}Ca ions. Weakly bound nucleons of these heavy nuclei are transferred with high probability to the nucleus of the doubly magic ^{48}Ca. For the formation of the "lead" configuration of the DNS, 30, 36, and 40 nucleons, accordingly, should be transferred to the ^{48}Ca nucleus. Thus, the "lead" configuration of the DNS in these reactions essentially differs from the initial configuration, and its extraction does not present a problem in the experiment.

In contrast, in reactions of cold synthesis, in which a ^{208}Pb target is used, the minimum in the potential energy of the system corresponds to the initial configuration of the DNS. The main contribution to the quasifission channel is provided by the DNS decay from the initial configuration, but in this case it is difficult to separate the products of quasifission and the products of deep inelastic scattering.

The use of warm fusion reactions allowed synthesizing the superheavy elements 114 and 116. Using the same reactions, the effect of the nuclear shell

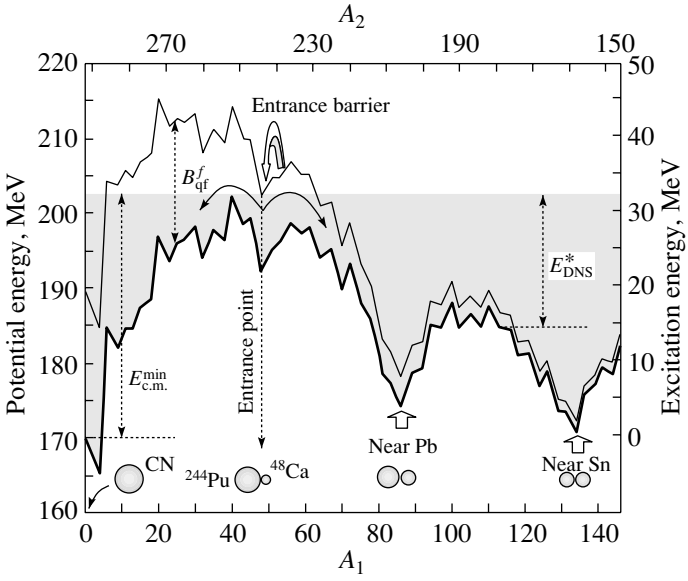

Fig. 5. Potential energy of the system of two interacting nuclei at the top of the entrance barriers (upper curve) and the driving potential of the DNS (lower curve) as a function of the atomic number of one of the fragments for the ^{48}Ca + ^{244}Pu reaction [12]. The difference between these two curves is the quasifission barriers for each stage of the DNS evolution.

structure on the mass distribution of quasifission products was revealed.

4.1. Model for the Description of the Mass Distribution of Quasifission Products

In the reactions used for the synthesis of SHE, the excitation energy of a DNS is low and DNS nuclei retain their individuality. This peculiarity of the DNS dictates the way for the calculation of its potential energy. Description of the fusion of two nuclear drops in terms of the Macroscopic Dynamic Model (MDM) [4–6] does not take into account the shell structure of the nuclei, and complete fusion does not compete with quasifission. These two processes are considered to be distinctly separated in energy space.

The main factor that determines the way of the DNS evolution is the system's potential energy $V(Z, L)$ where nucleus–nucleus part is

$$V(R, L) = V_N(R) + V_C(R) + V_{rot}(R, l). \quad (1)$$

We took the proximity potential (for details, see [13]) as the nuclear potential $V_N(R)$:

$$V_N(R) = 4\pi\gamma\bar{R}b\Phi(\xi), \quad (2)$$

where

$$\gamma = 0.951\left[1 - 1.7826\left(\frac{N-Z}{A}\right)^2\right] \text{ [MeV fm}^2\text{]};$$

$$\bar{R} = \frac{C_P C_T}{C_P + C_T}, \quad C_k = R_k\left[1 - (b/R_k)\right],$$

$$\xi = s/b, \quad s = r - (C_P + C_T);$$

$$\Phi(\xi) = \begin{cases} -1.7817 + 0.9270\xi + 0.14300\xi^2 - 0.09000\xi^3, \\ \xi < 0; \\ -1.7817 + 0.9270\xi + 0.01696\xi^2 - 0.05148\xi^3, \\ 0 < \xi < 1.9475; \\ -4.41\exp\left(-\xi/0.7176\right), \xi > 1.9475, \end{cases}$$

where the index $k = P$ or T. The Coulomb energy was calculated from the following formula:

$$V_C = Z_P Z_T e^2 \begin{cases} 1/r, & r > R_C, \\ \dfrac{1}{2R_C}\left(3 - \dfrac{r^2}{R_C^2}\right), & r < R_C. \end{cases}$$

The rotational energy $V_{rot}(R, l)$ was calculated with the rigid momentum of inertia. Our estimates show that the rotational component affects very insignificantly the results of calculating the quasifission–fusion competition at an ion energy close to the Coulomb barrier. In Fig. 5, the DNS excitation energy, which corresponds to the minimum possible excitation energy of the compound nucleus, is shown by cross-hatching. As follows from Fig. 5, the system obtains the greater part of the excitation energy while descending from the Businaro–Gallone (BG) point to the point of the compound nucleus formation. Only at this stage of the DNS evolution will most of the potential energy of the DNS be transformed into the excitation energy of the compound nucleus.

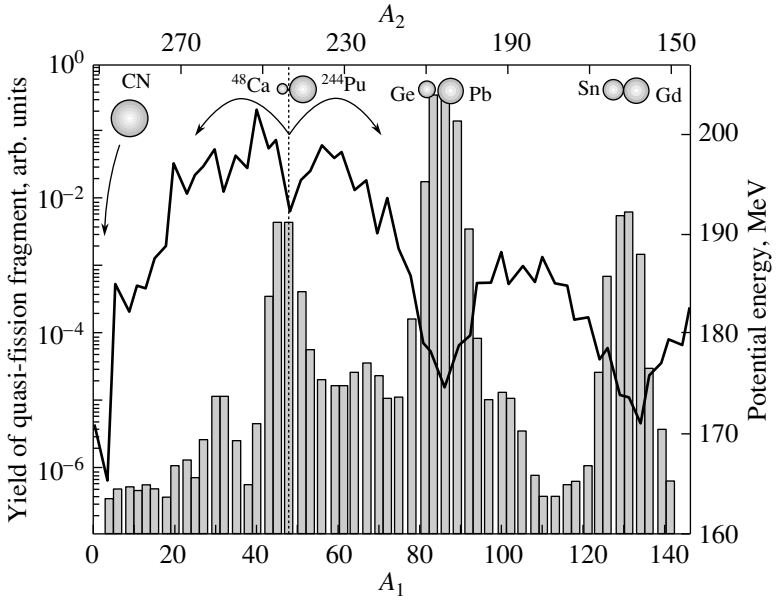

Fig. 6. The driving potential of the DNS as a function of the mass number of one of the reaction fragments. The calculated total spectrum in the fragment mass distribution for the reaction ^{48}Ca + ^{244}Pu is shown also.

This peculiarity of the DNS evolution, characteristic of SHE fusion reactions, requires the use of experimental masses for the calculation of the potential energy $V(Z, L)$. On the way to the compound nucleus formation, the DNS has to overcome the inner potential barrier B^*_{fus}, which is the difference between the magnitudes of the potential $V(Z, L)$ at the BG point and at the entrance reaction point. The inner potential barrier B^*_{fus} in a massive DNS has an endothermic nature, when the system is evaluated in the direction of the compound nucleus formation. Evolution of the DNS in the reverse direction, to a more symmetric shape, may result in its leaving the potential pocket (with a breakup into two fragments—the movement in the direction of increasing R) after overcoming the quasifission barrier, which was taken as the difference between the magnitudes of the driving potential and the point of scission into two fragments. The energy necessary for overcoming these barriers is taken from the excitation energy E^* of the DNS. A compound nucleus is unlikely to be formed if the DNS excitation energy is lower than the value of B^*_{fus}. The more symmetric the entrance channel combination of nuclei, the higher the inner fusion barrier B^*_{fus} that the DNS has to overcome on the way to compound nucleus formation; and the lower the quasifission barrier B_{qf}, the stronger the competition offered by quasifission.

4.2. Competition between Complete Fusion and Quasifission in Reactions of SHE Production

Nucleon transfer between the nuclei in a DNS is statistical in nature, and there is a possibility that the system may reach and overcome the BG point, and thus a compound nucleus will be formed. An alternative to that process is the breakup of the system into two fragments (quasifission). In order to calculate the probability of proton transfer from one

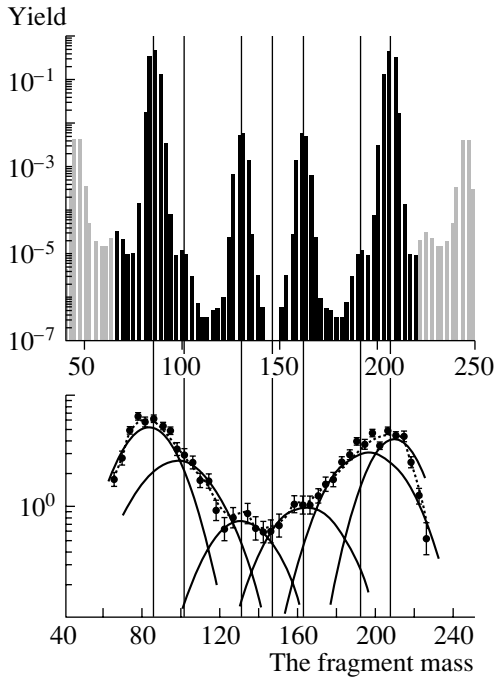

Fig. 7. Calculations of the quasifission mass distribution in the reaction ^{48}Ca + ^{244}Pu = ^{292}114 (upper panel) and the fragment mass distribution for the same reaction measured experimentally (bottom panel) [10].

nucleus to another in a DNS, we used an expression from [14] and assumed that the macroscopic nucleon transfer probability P_z can be expressed in terms of the microscopic probability λ_z and the level density ρ_z as $P_z = \lambda_z \rho_z$. The level density can be written using the DNS potential energy, $\rho_z = \rho(E^*)$, where E^* is the excitation energy of the DNS. Finally, the proton capture probability can be written as follows:

$$P^+ = \left\{1 + \exp\left[\frac{V(Z+1,L) - V(Z-1,L)}{2T}\right]\right\}^{-1}, \quad (3)$$

$$P^- = \left\{1 + \exp\left[\frac{V(Z-1,L) - V(Z+1,L)}{2T}\right]\right\}^{-1},$$

where $T = (E^*/\alpha)^{1/2}$ is the nuclear temperature; $\alpha = 0.093A$ is the level density parameter. Knowing these relative ($P^+ + P^- = 1$) probabilities and using a random value uniformly distributed over the interval between 0 and 1, we randomly chose the direction for the DNS to move: either the direction to a symmetric system or the direction to the compound nucleus. The procedure may be repeated as many times as necessary for obtaining the necessary statistics. Figure 6 shows the calculated results—the mass distribution of quasifission products for the reaction ^{48}Ca + ^{208}Pb. It is seen from this figure that the spectrum for the mass distribution of reaction fragments strongly correlates with the structure of the driving potential. The maxima of the mass distribution are matched by the position of the local minima of the potential. It reflects our approach to the calculations of the DNS decay for the case when there exist quasi-stationary states (local minima), which gives grounds for the application of the statistical model.

On the basis of the DNSC, a model of mass distribution of quasifission products in reactions of SHE synthesis was developed. Mass distribution in quasifission is the result of competition between two nuclear processes during the evolution of a DNS, which has been formed at the capture stage. One way of the evolution is the evolution of a DNS to the symmetric form; another way is the decay of the system into two fragments from all intermediate and final configurations. The DNS evolution proceeds under conditions of partial statistical equilibrium. Thus, it is possible to assume that the probability of the DNS transition from a given configuration into the neighboring one and the probability of its decay into two fragments are proportional to the level density of the DNS in the neighboring configuration and at the top of the quasifission barrier B_{qf}.

The DNS level density is determined by the DNS excitation energy E^*, which is the difference between the collision kinetic energy and the potential energy of the system. The height of the quasifission barrier B_{qf} is determined by the nucleus–nucleus potential $V(R)$.

Thus, the basic components of the model are the potential energy of the DNS, $V(Z,L)$, and the nucleus–nucleus potential, $V(R)$. As the model is focused on the reactions of synthesis of SHE, in which the DNS excitation energy is low, masses of the system's nuclei in the calculation of $V(Z,L)$ were taken in their ground states. The deformation of the nuclei of the system was also taken into account for their ground states. In the case of the deformed nuclei, their orientations corresponding to the minimum of the potential energy of the system were used. As the masses of quasifission fragments in reactions of the synthesis of SHE are significant, for the calculation of the nuclear part of the potential $V(R)$, we took the proximity potential [13].

The most suitable method for the description of the DNS evolution and decay is the Monte Carlo method. Using this method it is possible to trace the fate of a large number of DNS and obtain information on the mass distribution of quasifission products. Figure 7 presents the calculation of the mass distribution of quasifission products in the reaction ^{48}Ca + ^{244}Pu. The experimental data are shown by points [10]. Approximating Gaussian curves are drawn though the points. From Fig. 7, it can be seen that our model reproduces an enhanced yield of fragments with mass numbers 208 and 132 observed in the experiment. However, the yield of nuclei with closed shells appeared to be rather high in the model. During the DNS evolution to the symmetric form, its excitation energy grows substantially. It leads to the weakening of the influence of shells effects and accordingly to decreasing the maxima in the mass spectrum.

5. CONCLUSION

Quasi-fission is a nuclear process that is realized in collisions of two massive nuclei. Quasi-fission is the disintegration of a DNS, which is formed at the capture stage and evolves into the symmetric form. Quasi-fission is the dominant channel in nuclear reactions used for the synthesis of superheavy elements.

In reactions of warm synthesis of superheavy elements, there are indications of the influence of the nuclear structure of the DNS nuclei on the probability of the system disintegration observed in the mass distribution of quasifission products—nuclear fragments with closed shells have the greatest yield.

The concept of the DNS offers a clear and realistic interpretation of the quasifission process and occurrence of shell effects in the mass distributions. The

model based on this concept allows one to reproduce the shell effects in experimental mass distributions of quasifission products.

ACKNOWLEDGMENTS

We would like to thank V.I. Zagrebaev for his program of calculating the driving potential and also for the numerous fruitful discussions and Yu.Ts. Oganessian and M.G. Itkis for their support of and attention to this work.

This work was partially supported by INTAS, grant no. 00-655.

REFERENCES

1. V. V. Volkov, Phys. Rep. **44**, 99 (1978).
2. V. V. Volkov, *Nuclear Reaction Deep Inelastic Transfer* (Énergoizdat, Moscow, 1982).
3. W. U. Schröder and J. R. Huizenga, *Treatise on Heavy-Ion Science*, Ed. by D. A. Bromley (Plenum Press, New York, 1984), Vol. 2, p. 984.
4. W. J. Swiatecki, J. Phys. (Paris) C **33**, 5 (1972).
5. W. J. Swiatecki, Phys. Scr. **24**, 113 (1981).
6. S. Bjornholm and W. J. Swiatecki, Nucl. Phys. A **391**, 471 (1982).
7. V. V. Volkov, Izv. Akad. Nauk SSSR, Ser. Fiz. **50**, 1879 (1986); N. V. Antonenko *et al.*, Phys. Rev. C **51**, 2635 (1995).
8. P. Gippner *et al.*, Z. Phys. A **325**, 335 (1986).
9. M. G. Itkis *et al.*, in *Proceedings of the 7th International Conference on Clustering Aspects of Nuclear Structure and Dynamics, Rab, Croatia, 1999,* Ed. by M. Korolija, Z. Basrak, and R. Caplar (World Sci., Singapore, 2000), p. 386.
10. M. G. Itkis *et al.*, in *Proceedings of the International Workshop "Fusion Dynamics at the Extremes," Dubna, 2000*, Ed. by Yu. Ts. Oganessian and V. I. Zagrebaev (World Sci, Singapore, 2001), p. 93.
11. Yu. Ts. Oganessian, M. G. Itkis, and V. K. Utyonkov, in *Proceedings of the International Workshop "Fission Dynamics of Atomic Cluster and Nuclei," Portugal, 2000,* Ed. by J. do Providencia, *et al.* (World Sci., Singapore, 2000), p. 275.
12. E. A. Cherepanov, in *Proceedings of the International Workshop "Fusion Dynamics at the Extremes", Dubna, 2000,* Ed. by Yu. Ts. Oganessian and V. I. Zagrebaev (World Sci., Singapore, 2001), p. 186.
13. J. Blocki, J. Randrup, W. Swiatecki, and C. F. Tsang, Ann. Phys. (N.Y.) **105**, 427 (1977).
14. L. G. Moretto and J. S. Sventek, Phys. Lett. B **58**, 26 (1975).

Physics of Atomic Nuclei, Vol. 66, No. 8, 2003, pp. 1569–1573. From Yadernaya Fizika, Vol. 66, No. 8, 2003, pp. 1612–1616.

On Search and Identification of Relatively Short-Lived Superheavy Nuclei ($Z \geq 110$) by Fossil Track Studies of Meteoritic and Lunar Olivine Crystals*

V. P. Perelygin †[1], Yu. V. Bondar[2], R. Brandt[3], W. Ensinger[3], R. L. Fleischer[4], L. I. Kravets[1], M. Rebetez[5], R. Spohr[6], P. Vater[3], and S. G. Stetsenko[1]**

[1] *Joint Institute for Nuclear Research, Dubna, Moscow oblast, 141980 Russia*
[2] *Ukraine State Scientific Centre on Environmental Radiogeochemistry, Kiev, Ukraine*
[3] *Philipps University, Kernchemie, Marburg, Germany*
[4] *Department of Geology, Union College, Schenectady, NY, USA*
[5] *Laboratoire de Microanalyses Nucleares, Université de Besancon, France*
[6] *GSI, Darmstadt, Germany*

Received August 28, 2002

Abstract—The main goal of the present work is the search for and identification of relatively stable nuclei of superheavy elements (SHE) ($Z > 110$) in galactic matter by fossil track study of nonconducting crystals from the surface of meteorites and rocks from the lunar regolith. Nuclei of SHE are thought to be the products of nucleosynthesis in explosive processes in our Galaxy (supernova r-process nucleosynthesis and, especially, neutron-star formation, etc.). When accelerated to relativistic energies in the Galaxy, they can produce extended trails of damage in nonconducting extraterrestrial crystals. The lifetime of such SHE in galactic cosmic rays will range from 10^3 to 10^7 yr to be registered in extraterrestrial crystals. To search for and to identify the superheavy nuclei in the galactic cosmic rays, it was proposed to use the ability of nonconducting extraterrestrial crystals such as olivines, pyroxenes, and feldspars to detect and to store for many millions of years the trails of damage produced by fast $Z \geq 23$ nuclei coming to rest in the crystalline lattice. The track lengths of fast $Z \geq 23$ nuclei are directly proportional to Z^2 of these nuclei. The nuclei of SHE produce, when coming to rest in a crystal volume, tracks that are a factor of 1.6–1.8 longer than the tracks due to cosmic-ray Th and U nuclei. To identify the tracks due to superheavy nuclei, calibrations of the same crystals were performed with accelerated Au, Pb, and U nuclei. For visualization of these tracks inside the crystal volume, proper controlled annealing and chemical etching procedures were developed. Since 1980, fossil tracks due to Th and U nuclei have observed and unambiguously identified (1988) by subsequent calibrations of the olivine crystals with accelerated U, Au, and Pb ions. The number of tracks of Th and U nuclei measured in olivine crystals totaled more than 1600, as compared with the prior 30 events. The other approach to identifying SHE in nature is to search for tracks in phosphate crystals from spontaneous fission of $Z \geq 110$ nuclei; these produce two-prong and three-prong fission fragment tracks and differ significantly from the tracks from spontaneous fission of ^{238}U and ^{244}Pu nuclei. Extraterrestrial phosphate crystals of lunar and meteoritic origin will be investigated. Such SHE nuclei can survive in crystals of extraterrestrial rocks and produce spontaneous fission tracks, if the lifetime is more than 5×10^7 yr. © *2003 MAIK "Nauka/Interperiodica"*.

1. INTRODUCTION—BACKGROUND AND JUSTIFICATION

The existence of relatively stable superheavy elements (SHE) in nature was predicted theoretically in the mid-1960s by S.G. Nilsson, J.R. Nix, and A. Sobiczewski (see [1]). On the basis of the nuclear shell model it was estimated that doubly magic nuclei with atomic number $110 \leq Z \leq 114$ and neutron number $N = 184$ can possess lifetimes between 10^3 and 10^9 yr. Thus, these elements, like Th and U, could have survived in the Earth and meteorites since the formation of the Solar System, about 4.6×10^9 yr ago.

Experimental attempts to discover long-lived SHE nuclei with lifetimes $\geq 2 \times 10^8$ yr in natural

*This article was submitted by the authors in English.
†Deceased.
**e-mail: kravets@lnr.jinr.ru

samples undertaken from the late 1960s to the late 1970s provided limited evidence of their existence in both terrestrial samples and meteorites. These experiments were done by studying alpha radioactivity and spontaneous fission, which can significantly exceed the effect of spontaneous fission of ^{238}U. Still, no decisive information on the existence of SHE in nature was obtained.

In the early 1970s, a completely new approach was proposed to identify SHE nuclei in galactic matter. It was based on the ability of nonconducting crystals to register and to store trails of damage due to fast, heavy cosmic-ray nuclei for many millions of years. The pioneering work was conducted by R.L. Fleischer, P.B. Price, R.M. Walker, and colleagues, who discovered tracks due to transiron ($Z \geq 36$) very very heavy cosmic-ray nuclei. In spite of many subsequent attempts by Price, D. Lal, M. Maurette, Walker, and V.P. Perelygin (see [1]) during the 1960s and 1970s, no quantitative information was obtained on the charge spectra and the abundance of $Z \geq 36$ nuclei in cosmic rays.

A new approach [2–4] first demonstrated in 1980 was based on (i) partially controlled annealing of both fossil cosmic ray tracks and fresh ones from accelerated Kr, Xe, Au, Pb, and U nuclei, and (ii) revealing the volume etchable track length (VETL) of these nuclei in olivine crystals from meteorites. Specifically, olivine-rich meteorites—the pallasites Marjalahti, Eagle Station, and Lipovsky Khutor—were chosen for such study. It is worth noting the incredible collecting power of extraterrestrial "natural orbital stations," i.e., meteorites. For example, through every square centimeter of the Marjalahti meteorite preatmospheric surface during its radiation exposure—180×10^6 yr—the fluence of $Z \geq 70$ nuclei corresponds to an exposure of about 20 000 m^2 of plastic track detectors in space for one year.

Unfortunately, the ablation of meteorites in the terrestrial atmosphere erased about 90% of such track information for the aforementioned Marjalahti and Lipovsky meteorites. Lunar crystals have a great advantage, the absence of ablation; we propose to choose individual lunar crystals that were situated in the upper 2 cm of the lunar regolith for many millions of years.

Such crystals can be used to search not only for SHE nuclei ($Z \geq 110$–114, $N = 184$) but also for SSHE nuclei (Z about 160–180, $N \approx 320$–360)—the possible long-lived doubly magic nuclear remnants of disintegration and decay of pure neutron matter, ejected during the formation of neutron stars.

Freshly formed nuclei with $Z \geq 36$, up to $Z \approx 110$ and above, as has been recently stated by Slavatinsky [5], are accelerated by the intense electromagnetic fields of exploding neutron stars to energies of 10^6 GeV/nucleon. These nuclei can reach the Solar System in as little as 10^3 yr and produce very long latent tracks in nonconducting crystals.

Thus, we can seek SHE nuclei with a lifetime $\geq 10^3$ yr in extraterrestrial crystals that have been exposed for many millions of years at the surface of meteorites and the lunar regolith. Another way to identify SHE in nature is to search in phosphate crystals for tracks from spontaneous fission of $Z \geq 110$ nuclei; they produce two-prong and three-prong tracks and differ significantly from the spontaneous fission tracks of ^{238}U and ^{244}Pu nuclei.

Extraterrestrial phosphate crystals of lunar and meteoritic origin will be investigated in future studies, because these crystals began to register fission fragment tracks about 4.2–4.3 billion years ago—after the parent body of these extraterrestrial objects cooled [6]. Such nuclei of SHE can survive in extraterrestrial rocks and produce tracks from spontaneous fission if their lifetime is more than 5×10^7 yr.

2. EXPERIMENT

2.1. Milestones

Recent synthesis and discoveries of very stable isotopes of elements 110–116 stimulated the present project. During 1999–2000 in the Flerov Laboratory of Nuclear Reactions, JINR, Dubna, Yu.Ts. Oganessian and his colleagues succeeded in obtaining a number of rather neutron-rich isotopes of elements 112, 114, and 116 in reactions of high-intensity beams of ^{48}Ca with monoisotopic targets of ^{238}U, ^{244}Pu, and ^{248}Cm, respectively [7]. The most stable isotope obtained was the odd–even nuclide ^{285}112, which has a lifetime between 10 and 30 min, compared to 10–60 s for neighboring nuclei of $Z =$ 110, 114 and milliseconds to seconds for $Z = 116$ or $Z = 106$–109 nuclei. Still, the isotope ^{285}112 has only 173 neutrons—11 less than the magic number $N = 184$.

For the known actinide nuclei ($Z = 89$–98), such a neutron difference for the lightest and most stable isotopes provides a stabilization factor of 10^{10}–10^{13} in lifetime. The discovery of a new very stable isotope of element 112 provides final, unambiguous proof of the existence of a new island of relatively stable SHE nuclei; the island was predicted theoretically much earlier. Now, we point out that there is no way to produce a neutron number of 184 using present-day accelerators and target nuclei. The only way to find doubly magic SHE nuclei is to seek these nuclei in natural samples.

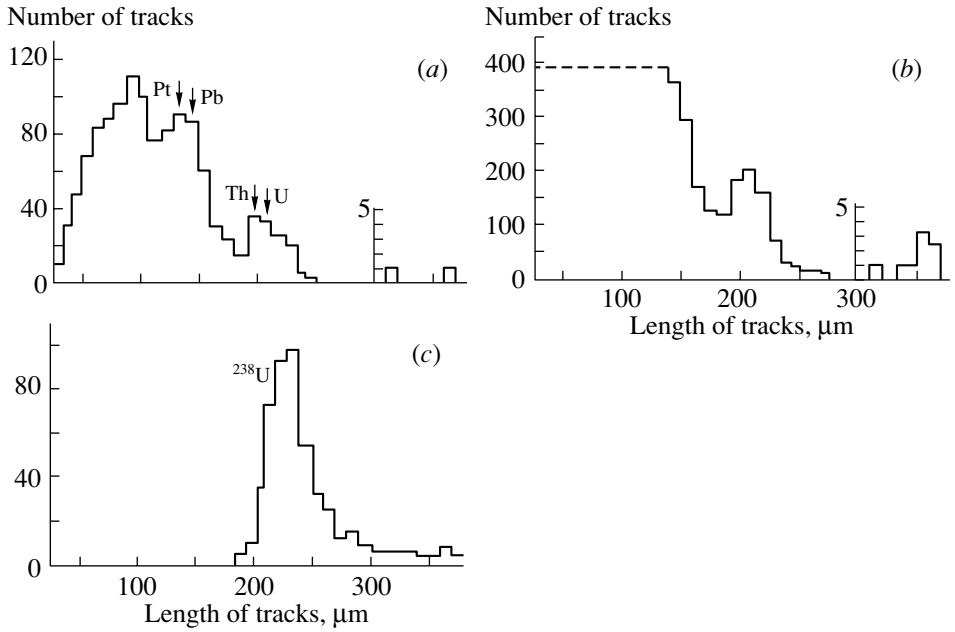

Fig. 1. The VETL spectrum of fossil tracks due to galactic cosmic-ray nuclei and due to accelerated ^{238}U in meteoritic olivine crystals annealed at 430°C for 32 h before etching; 90% of the tracks were measured in crystals from the Marjalahti meteorite: (*a*) fossil track-length spectra [2]; (*b*) fossil track-length spectra [3, 4]; (*c*) track-length spectra due to accelerated ^{238}U nuclei [3].

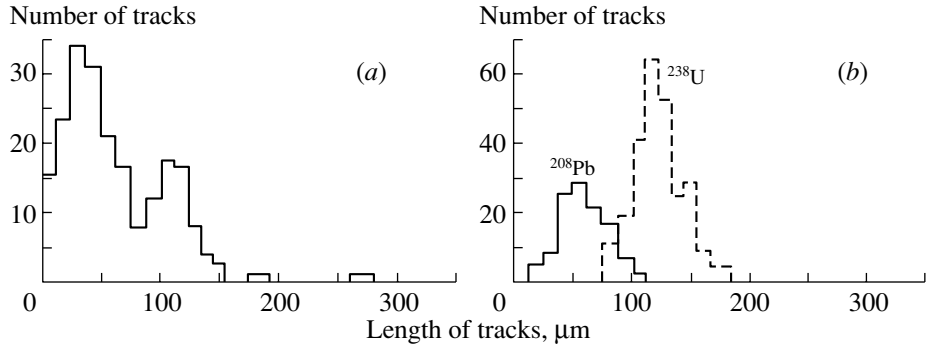

Fig. 2. VETL spectrum of fossil tracks due to galactic cosmic-ray nuclei and due to accelerated ^{208}Pb and ^{238}U in Marjalahti olivine crystals annealed at 450°C for 32 h before etching: (*a*) fossil track-length spectra; (*b*) track-length spectra due to accelerated ^{208}Pb and ^{238}U nuclei [4].

2.2. Detection of the Heaviest Cosmic-Ray Nuclei

There are two approaches to detection of ultraheavy ($Z \geq 36$) galactic cosmic-ray nuclei. The traditional investigation of ultraheavy nuclei in galactic cosmic rays was based on present-day detection of these nuclei in space using large-area stacks of nuclear emulsions and/or plastic track detectors. Historically, the study of the heaviest cosmic-ray component was initiated by P.H. Fowler, R.A. Adams, and V.C. Gowen in 1967, using a 4.5-m^2 stack of nuclear emulsions exposed near the top of the atmosphere with a balloon for a few days.

Then, from the late 1960s to the mid-1970s, a number of research groups exposed large stacks of nuclear emulsions and plastic detectors on balloons and on the orbital station Skylab. From the start of the 1980s, two systems of big electronic detectors started to detect cosmic-ray nuclei on the orbital stations Ariel-6 and HEAO-3 [2–4]. The main disadvantage of that approach is the very low flux of the heaviest cosmic-ray nuclei. As a result, during 1981–1984, only three cosmic-ray nuclei with $Z \geq 89$ were definitely detected with the two electronic detectors. During 1985–1990, using the NASA LDEF, a large stack of plastics was exposed by the Dublin–ESTEC

group [7]. In spite of an exposure for 69 months of 46 m^2 of plastic track detectors, only 27 actinide nuclei were detected (see [4]). No track of $Z \geq 110$ cosmic-ray nuclei was found.

The other type of galactic cosmic-ray investigation used the ability of nonconducting meteoritic crystals—pyroxenes, olivine, feldspars, phosphates—to detect and to store for many tens and hundreds of millions of years the tracks due to the nuclei with $Z \geq 20$ (the Fe group and heavier nuclei). But obtaining quantitative information on the charge and energy spectra of ultraheavy cosmic-ray nuclei from fossil tracks in extraterrestrial crystals encounters methodological problems. One is the very high background of Fe-group nuclei (10^{10}–10^{12} tracks per cm^2); another problem is partial annealing of tracks in silicate crystals that occurs under the conditions of outer space. This annealing prevents direct comparison of the etchable track lengths of fossil tracks and those of fresh tracks (used to calibrate the same crystals using accelerated heavy ions ($Z = 20$–92). Thus, attempts made in the late 1960s to the early 1970s to study the heaviest galactic cosmic-ray nuclei by tracks in meteoritic and lunar crystals yielded only qualitative results for cosmic-ray nuclei with $Z > 83$ (for a review, see [1]).

Freshly synthesized SHE nuclei in our Galaxy, accelerated to relativistic energies, can produce extended trails of damage in meteoritic and lunar crystals. The VETL of these nuclei is proportional to Z^2. Thus, the $Z = 110$–114 superheavy nuclei produce tracks that are a factor of 1.6–1.8 longer than tracks due to fast Th or U ions. The main advantage of fossil track studies in extraterrestrial olivine crystals is the very long exposure time—about 200×10^6 yr for the Marjalahti and Lipovsky meteorites. Crystals in these meteorites contain up to 10^2 Th and U cosmic-ray tracks per cm^3.

For quantitative information, the technique of controlled annealing of tracks in crystals prior to etching was originally applied to olivines from the Marjalahti and Eagle Station meteorites. The procedure chosen for annealing olivine, at 430°C for 32 h, erased fossil tracks from Fe nuclei (10^{10}–10^{11} cm^{-3}) and shortened tracks of $Z > 50$ nuclei by a factor of 6–8. More importantly, differences were removed in the thermal history of the tracks, which had been recorded during the space exposure of these meteorites, over a few tens to hundreds of millions of years.

In 1980, Perelygin [2] found that the VETL of Pt–Pb and Th, U galactic cosmic-ray nuclei in meteoritic olivine crystals annealed at 430°C for 32 h were about 100–130 and 160–180 μm, respectively (Fig. 1*a*).

These tracks of different lengths were unambiguously identified in 1988 by calibrations of the same olivine crystals with accelerated Au, Pb, and U nuclei. In further studies, more than 1600 fossil tracks of Th and U nuclei were measured (Fig. 1*b*). For these annealing conditions, 11 extralong tracks ($L = 340$–380 μm) were found [3, 4]. The correspondence of fossil and fresh ^{208}Pb and ^{238}U tracks was clear after annealing at 450°C for 32 h, as seen in Fig. 2. In spite of the limited statistics in Fig. 2, a single fossil track with the length of ≥ 250 μm was seen. The maximum track length of Th or U nuclei cannot exceed 200 μm under these annealing conditions at any orientation in olivine. Detailed x-ray and optical analysis shows that five of the 11 anomalously long tracks could not be from Th or U cosmic rays. Thus, we have evidence of SHE nuclei; their abundance relative to the actinide elements is $\sim(3$–$10) \times 10^{-3}$.

The proposed main goal of future studies is to obtain conclusive necessary and sufficient proof of the existence of SHE nuclei in galactic matter for lifetime $\geq 10^3$ yr.

2.3. Spontaneous Fission of $Z \geq 110$ Nuclei

The other possibility for study is the search for and identification of fossil tracks from spontaneous fission of $Z \geq 110$ nuclei in extraterrestrial phosphate crystals. There are two possibilities:

(i) The annealing behavior of tracks from spontaneous fission differs drastically in phosphates for actinides and for SHE. The proper annealing (for instance, at 450°C for 32 h for Marjalahti whitlockite) provides separation of fission fragment tracks of ^{238}U and ^{244}Pu spontaneous fission from those due to the spontaneous fission of $Z \geq 110$ nuclei. The volume etchable track lengths differ by a factor of 2. The fossil track-length spectra must be compared with those from thermal-neutron-induced fission of ^{235}U in the same crystals annealed under the same conditions. Such tracks should provide proof of spontaneous fission of $Z \geq 110$ nuclei, if present.

(ii) The estimated probability of ternary spontaneous fission of $Z = 110$–114 nuclei as compared with binary fission is 10^{-3} to 10^{-4}. For actinide nuclei, that ratio is $\leq 10^{-7}$. These three-prong tracks will also have a mean length 20% greater than those of binary tracks due to spontaneous fission of actinide nuclei. Thus, the observation and measurements of such three-prong spontaneous fission tracks in phosphate crystals would provide unambiguous proof of SHE nuclei in the Solar System.

In both cases, we must reveal spontaneous fission tracks on polished surfaces of the crystals. For such a study, we shall use accelerated $Z \geq 30$ ions with

energy ≥10 MeV/nucleon at 90° to the surface. The fluence of accelerated ions will be 5×10^5–2×10^6 ions/cm^2. Such bombardments could be performed at the cyclotrons U-400 (FLNR, JINR, Dubna), GSI UNILAC (Darmstadt), and GANIL Tandem Cyclotrons (Caen).

3. RESEARCH MILESTONES

The basic method of the proposed studies is the controlled partial annealing of both fossil cosmic-ray tracks and fresh ones of accelerated Kr, Xe, Au, Pb, and U nuclei; the revelation of these tracks inside meteoritic and lunar silicates and phosphates; and measurement and analysis of the VETL spectra.

For that purpose, the etching solution must be delivered inside the crystal volume either by artificial cracks, produced by a well-focused Nd laser beam, or (better) by bombardment of polished crystals with $Z \geq 26$ nuclei accelerated at the cyclotrons of JINR (Dubna), GANIL (Caen), and GSI (Darmstadt). Also, these facilities will be used for calibrating the sensitivity of meteoritic and lunar silicates with accelerated ^{197}Au, ^{208}Pb, and ^{238}U of energies 20–50 MeV/nucleon. There are two main ways to realize the proposed goal of unambiguous discovery and identification of long-lived SHE nuclei in natural samples.

First is the search for and identification of anomalously long tracks produced by $Z \geq 110$ galactic cosmic-ray nuclei in extraterrestrial olivine crystals. For that purpose, the main object of study will be the Eagle Station pallasite, which contains positions that were only 2–3 cm from the preatmospheric surface. Olivine crystals from these locations are very rich in $Z \geq 50$ nuclei, many more than were found in the Marjalahti pallasite. We estimate that, in 10–12 cm^3 of these olivines, we shall be able to find and identify up to ten anomalously long tracks. The annealing of these crystals at 440–450°C will eliminate the background of the Th and U nuclei at any orientation in olivine, but not the $Z \geq 110$ nuclei.

Second, we plan to identify of tracks from spontaneous fission of SHE in extraterrestrial phosphate crystals. These will be in the presence of a significant background from spontaneous fission of ^{238}U. Also, in old extraterrestrial samples, ^{244}Pu must be dealt with. To distinguish the SHE tracks, we shall use the track-in-track technique to reveal three-prong spontaneous fission tracks and shall employ controlled annealing of these crystals (in the case of two-prong events). In our study, we shall choose whitlockite and stanfildite crystals from the Marjalahti, Lipovsky Khutor, and Omolon meteorites and phosphates from the Luna-16 and Luna-24 probes.

ACKNOWLEDGMENTS

We are very grateful to the Russian Foundation for Basic Research for providing us with support under project no. 01-02-16410.

REFERENCES

1. R. L. Flescher, P. B. Price, and R. M. Walker, *Nuclear Tracks in Solids. Principles and Applications* (Univ. of California Press, Berkeley, 1975), p. 605.
2. V. P. Perelygin and S. G. Stetsenko, Pis'ma Zh. Éksp. Teor. Fiz. **32**, 622 (1980) [JETP Lett. **32**, 608 (1980)].
3. V. P. Perelygin, S. G. Stetsenko, H. J. Crawford, and T. J. M. Symons, Z. Phys. A **388**, 435 (1991).
4. V. P. Perelygin, R. I. Petrova, S. G. Stetsenko, *et al.,* Radiat. Meas. **31**, 609 (1999).
5. S. A. Slavatinsky, Soros Teach. Mag. **10**, 68 (1999).
6. V. P. Perelygin, R. I. Petrova, L. Enkhjin, *et al.,* Radiat. Meas. **25**, 525 (1995).
7. Yu. Ts. Oganessian, V. K. Utyonkov, and Yu. V. Lobanov, JINR Commun. No. E7-99-53 (Dubna, 1999).

Physics of Atomic Nuclei, Vol. 66, No. 8, 2003, pp. 1574–1577. From Yadernaya Fizika, Vol. 66, No. 8, 2003, pp. 1617–1620.

Nuclear Mean Field from Chirally Symmetric Effective Theory*

A. Staszczak**

Institute of Physics, Maria Curie-Skłodowska University, Lublin, Poland

Received August 28, 2002

Abstract—The mean-field theory of the nuclear many-body problem proposed recently by Furnstahl, Serot, and Tang (FST) is discussed. The FST chiral Lagrangian is derived in terms of an effective field theory. This new approach allows one to construct in a controlled manner the universal nuclear Lagrangian consistent with symmetries of QCD. The FST Lagrangian is constructed by using power counting, i.e., the expansion in powers of the lowest lying hadronic fields and their derivatives. Terms in the Lagrangian are organized by applying Georgi's naive dimensional analysis and "naturalness" condition. The relevant degrees of freedom are nucleons, pions, an isoscalar-vector field (ω meson), an isoscalar-scalar field (σ meson), and an isovector-vector field (ρ meson). The chiral symmetry is realized nonlinearly using a standard WCCWZ procedure. © *2003 MAIK "Nauka/Interperiodica".*

1. EFFECTIVE FIELD THEORIES (INSTEAD OF INTRODUCTION)

The basic idea underlying the effective field theory approach [1] is relevant to the appearance of disparate characteristic energy scales, $E \ll E_0$, in quantum field theories. Suppose that we are interested in the physics at lower scale E; then, we can choose a cutoff scale Λ at or slightly below E_0 and divide the generic fields ϕ into low- and high-energy parts: ϕ_L and ϕ_H ($\phi = \phi_L + \phi_H$); accordingly, their momenta are smaller or greater than Λ. The effective Lagrangian is obtained by path integration over the high-energy part ϕ_H in the generating functional Z:

$$Z = \int [d\phi_L][d\phi_H] e^{i\int d^4x \mathcal{L}(\phi_L,\phi_H)} = \int [d\phi_L] e^{i\int d^4x \mathcal{L}_{\text{eff}}(\phi_L)}, \quad (1)$$

where

$$\int d^4x \mathcal{L}_{\text{eff}}(\phi_L) = -i \ln \int [d\phi_H] e^{i\int d^4x \mathcal{L}(\phi_L,\phi_H)}. \quad (2)$$

The next step is to write $\mathcal{L}_{\text{eff}}$ in terms of local operators $\mathcal{L}_{\text{eff}}(\phi_L) = \sum_i^\infty g_i(\Lambda) O_i(\phi_L)$, where $g_i(\Lambda)$ are the coupling constants absorbing the contribution of the integrated-out high-energy degrees of freedom. The effective Lagrangian is represented by a tower of interactions; to make this procedure useful, we need some dimensional analysis. In units $\hbar = c = 1$, the action $S_{\text{eff}} = \int d^4x \mathcal{L}_{\text{eff}}(\phi_L)$ is dimensionless. If an operator O_i has dimension $[O_i] = [m]^{\delta_i} \equiv \delta_i$, in mass units, then its coupling constant has dimension $[g_i] = 4 - \delta_i$. We can also define dimensionless coefficients $c_i = \Lambda^{\delta_i - 4} g_i$, which are additionally assumed to be "natural," i.e., of order $\mathcal{O}(1)$.

For a process at scale $E \ll \Lambda$, we can estimate dimensionally the magnitude of the ith operator in the action as $\int d^4x O_i \sim E^{\delta_i - 4}$, so that the ith term is of order

$$\int d^4x \frac{c_i}{\Lambda^{\delta_i - 4}} O_i \sim c_i \left(\frac{E}{\Lambda}\right)^{\delta_i - 4}. \quad (3)$$

Now, we can see that, at energies below Λ, the behavior of the different operators is determined by their dimension. If $\delta_i < 4$, the operator is more and more important when $E \to 0$ and is termed *relevant*. Similarly, if $\delta_i > 4$, the operator is less and less important, and is termed *irrelevant*. An operator with $\delta_i = 4$ is equally important at all scales and is called *marginal*.

The general form of the effective Lagrangian is obtained by setting the operators O_i according to their dimensions,

$$\mathcal{L}_{\text{eff}}(\phi_L) = \mathcal{L}_{\delta \le 4} + \sum_{\delta_i > 4} \frac{c_i}{\Lambda^{\delta_i - 4}} O_i(\phi_L), \quad (4)$$

where $\mathcal{L}_{\delta \le 4}$ contains the potentially renormalizable (relevant and marginal) terms. At energies much below Λ, corrections due to the nonrenormalizable parts (irrelevant) are suppressed by powers of E/Λ.

There are at least two relevant energy scales in nuclear physics: the pion-decay constant $f_\pi \approx 93$ MeV and a larger scale $\Lambda \sim 4\pi f_\pi \sim 1$ GeV, which characterizes the mass scale of physics beyond Goldstone

*This article was submitted by the author in English.

** e-mail: stas@tytan.umcs.lublin.pl

1063-7788/03/6608-1574$24.00

bosons. Using a naive dimensional analysis, as originally proposed for low-energy QCD by H. Georgi and A.V. Manohar, the effective Lagrangian describing interactions of nucleons N, pions $\boldsymbol{\pi}$, and non-Goldstone bosons (scalar ϕ and/or vector V mesons) takes the general form

$$\mathcal{L}_{\text{eff}} = \sum_{\{ndpb\}}^{\infty} c_{ndpb} \left(\frac{\bar{N}\Gamma N}{f_\pi^2 \Lambda}\right)^{n/2} \left(\frac{D_\mu, m_\pi}{\Lambda}\right)^d \quad (5)$$

$$\times \left(\frac{\boldsymbol{\pi}}{f_\pi}\right)^p \frac{1}{b!} \left(\frac{\phi, V}{f_\pi}\right)^b f_\pi^2 \Lambda^2 = \sum_{\Delta=0}^{\infty} \mathcal{L}^{(\Delta)},$$

$$\Delta \equiv \frac{n}{2} + d + b - 2, \quad (6)$$

where Γ is a product of Dirac matrices, D_μ is a covariant derivative, and m_π is a pion mass (treated the same as a derivative). The dimensionless low-energy constants (LECs), $\{c_{ndpb}\}$, are assumed to be natural, of $\mathcal{O}(1)$.

In Eq. (5), the interactions are grouped in sets $\mathcal{L}^{(\Delta)}$ of a common index Δ (6); each of them carries a factor of the form $(1/\Lambda)^\Delta$. This formula has profound implications if we invoke chiral symmetry [2]. For strong interactions (in absence of external gauge fields, e.g., photons), the chiral constraint guarantees that $\Delta \geq 0$ and the large-scale Λ does not occur with positive powers in Eq. (5).

2. NONLINEAR REALIZATION OF CHIRAL SYMMETRY

In the hadronic world, the chiral group $G \equiv SU(2)_L \times SU(2)_R$ is spontaneously broken in vacuum to the vectorial (isospin) subgroup $H \equiv SU(2)_{V=L+R}$ with the appearance of pseudoscalar Goldstone bosons (pions: π^0, π^+, π^-). The nonlinear realization of chiral symmetry has been suggested by S. Weinberg and developed further by C. Callan, S. Coleman, J. Wess, and B. Zumino (WCCWZ). In the WCCWZ formalism, the Goldstone bosons, $\boldsymbol{\pi}(x)$, being coordinates of the coset space G/H, are naturally represented by elements $\xi(x) = \xi(\pi(x))$ of this coset space. The chiral symmetry is defined by specifying the action of G on the representative $\xi(x)$,

$$\xi(x) \xrightarrow{g} g_R \xi(x) h^\dagger(g, \pi(x)) = h(g, \pi(x))\, \xi(x) g_L^\dagger, \quad (7)$$

where $g \equiv (g_L, g_R) \in G$. The equality in Eq. (7) is due to parity and it defines the so-called compensator (field) $h(g, \pi(x)) \in H$. Its dependence on the Goldstone boson fields $\pi(x)$ is a characteristic feature of the nonlinear realization of chiral symmetry. Applying an exponential parametrization, we can write a coset representative $\xi(x) = \xi(\pi(x))$ as $U(x) \equiv \xi^2(x) = \exp(2i\pi(x)/f_\pi)$, where the isotriplet of pions is collected in a 2×2 special unitary matrix $\pi(x) \equiv \boldsymbol{\pi}(x) \cdot \frac{1}{2}\boldsymbol{\tau}$, with $\boldsymbol{\tau}$ being Pauli matrices.

The other relevant degrees of freedom needed for the construction of the effective Lagrangian are an isospinor nucleon field $N(x) = \begin{pmatrix} p(x) \\ n(x) \end{pmatrix}$ and the low-lying non-Goldstone bosons: an isovector-vector $\rho(770)$ meson $\rho_\mu(x) \equiv \boldsymbol{\rho}_\mu(x) \cdot \frac{1}{2}\boldsymbol{\tau}$; an isoscalar-vector meson $\omega(782)$ represented by a vector field $V_\mu(x)$; and an effective isoscalar-scalar field $S(x)$ (σ meson) described by the shifted field $\phi(x) \equiv S_0 - S(x)$, where S_0 is the vacuum expectation value of the scalar field S. We can also define the additional needed ingredients: an axial vector field $a_\mu \equiv -\frac{i}{2}(\xi^\dagger \partial_\mu \xi - \xi \partial_\mu \xi^\dagger)$; a polar vector field $v_\mu \equiv -\frac{i}{2}(\xi^\dagger \partial_\mu \xi + \xi \partial_\mu \xi^\dagger)$; and a covariant strength tensor $v_{\mu\nu} = \partial_\mu v_\nu - \partial_\nu v_\mu + i[v_\mu, v_\nu] = -i[a_\mu, a_\nu]$, associated with the polar vector v_μ. The covariant derivative of ρ meson $D_\mu \rho_\nu = \partial_\mu \rho_\nu + i[v_\mu, \rho_\nu]$ can be used to construct the covariant field tensor $\rho_{\mu\nu} = D_\mu \rho_\nu - D_\nu \rho_\mu + i g_\rho [\rho_\mu, \rho_\nu]$.

3. FST EFFECTIVE LAGRANGIAN

The low-energy effective Lagrangian of Furnstahl, Serot, and Tang (FST) [3, 4] incorporates the symmetries of QCD: Lorentz invariance, parity conservation, and nonlinear realization of chiral $SU(2)_L \times SU(2)_R$ symmetry; this Lagrangian is also invariant under the electromagnetic $U(1)_{\text{em}}$ and isospin $SU(2)$ group. The FST Lagrangian is expanded in powers of fields and their derivatives in the procedure of power counting with index $\tilde{\Delta} = n/2 + d + b$, where n is the number of nucleon fields, d is the number of derivatives, and b the number of non-Goldstone boson fields in each term. Taking as the large energy scale Λ in Eq. (5) the nucleon mass $M = 939$ MeV, we may write the effective chiral Lagrangian through quartic order ($\tilde{\Delta} \leq 4$) as the sum

$$\mathcal{L}_{\text{eff}}(x) = \mathcal{L}_N^{(4)}(x) + \mathcal{L}_M^{(4)}(x) + \mathcal{L}_{\text{EM}}^{(4)}(x). \quad (8)$$

The part of the Lagrangian involving nucleons takes the form

$$\mathcal{L}_N^{(4)}(x) = \bar{N}[i\gamma^\mu (\partial_\mu + i v_\mu + i g_\rho \rho_\mu + i g_v V_\mu) \quad (9)$$

$$+ g_A \gamma^\mu \gamma_5 a_\mu - M + g_s \phi] N - \frac{f_\rho g_\rho}{4M} \bar{N} \rho_{\mu\nu} \sigma^{\mu\nu} N$$

$$-\frac{f_v g_v}{4M}\bar{N}V_{\mu\nu}\sigma^{\mu\nu}N-\frac{\kappa_\pi}{M}\bar{N}v_{\mu\nu}\sigma^{\mu\nu}N,$$

where $\sigma_{\mu\nu}=\frac{i}{2}[\gamma_\mu,\gamma_\nu]$; $V_{\mu\nu}\equiv\partial_\mu V_\nu-\partial_\nu V_\mu$ is the covariant tensor of the ω meson; $g_A\approx 1.26$ is the axial coupling constant; g_ρ f_ρ, and g_v, f_v are vector and so-called tensor couplings for ρ and ω mesons; g_s is a Yukawa coupling for the effective scalar field ϕ; and under the assumption of vector-meson dominance (VMD), $\kappa_\pi=f_\rho/4$ is the coupling for higher order πN interaction.

The mesonic part of the effective Lagrangian is

$$\begin{aligned}\mathcal{L}_M^{(4)}(x)&=\frac{1}{2}\Big(1+\alpha_1\frac{g_s\phi}{M}\Big)\partial_\mu\phi\partial^\mu\phi \qquad (10)\\ &+\frac{f_\pi^2}{4}\mathrm{tr}(\partial_\mu U\partial^\mu U^\dagger)-\frac{1}{2}\mathrm{tr}(\rho_{\mu\nu}\rho^{\mu\nu})\\ &-\frac{1}{4}\Big(1+\alpha_2\frac{g_s\phi}{M}\Big)V_{\mu\nu}V^{\mu\nu}-g_{\rho\pi\pi}\frac{2f_\pi^2}{m_\rho^2}\mathrm{tr}(\rho_{\mu\nu}v^{\mu\nu})\\ &+\frac{1}{2}\Big(1+\eta_1\frac{g_s\phi}{M}+\frac{\eta_2}{2}\frac{g_s^2\phi^2}{M^2}\Big)m_v^2V_\mu V^\mu\\ &+\frac{1}{4!}\zeta_0 g_v^2(V_\mu V^\mu)^2+\Big(1+\eta_\rho\frac{g_s\phi}{M}\Big)m_\rho^2\mathrm{tr}(\rho_\mu\rho^\mu)\\ &-m_s^2\phi^2\Big(\frac{1}{2}+\frac{\kappa_3}{3!}\frac{g_s\phi}{M}+\frac{\kappa_4}{4!}\frac{g_s^2\phi^2}{M^2}\Big),\end{aligned}$$

where $m_v=782$ MeV; $m_\rho=770$ MeV; m_s are ω, ρ, and σ meson masses; and $g_{\rho\pi\pi}$ is the coupling of $\rho\pi\pi$ interaction, which is $g_{\rho\pi\pi}=g_\rho$, assuming VMD. The electromagnetic interactions are described by

$$\begin{aligned}\mathcal{L}_{\mathrm{EM}}^{(4)}(x)&=-\frac{1}{4}F^{\mu\nu}F_{\mu\nu} \qquad (11)\\ &-\frac{1}{2}e\bar{N}\gamma^\mu(1+\tau_3)NA_\mu-\frac{e}{4M}F_{\mu\nu}\bar{N}\lambda\sigma^{\mu\nu}N\\ &-\frac{e}{2M^2}\bar{N}\gamma_\mu(\beta_s+\beta_v\tau_3)N\partial_\nu F^{\mu\nu}\\ &-2ef_\pi^2A^\mu\mathrm{tr}(v_\mu\tau_3)-\frac{e}{2g_\gamma}F_{\mu\nu}\Big[\mathrm{tr}(\tau_3\rho^{\mu\nu})+\frac{1}{3}V^{\mu\nu}\Big],\end{aligned}$$

where A_μ is the electromagnetic field and $F_{\mu\nu}$ is the electromagnetic-field-strength tensor. According to VMD and phenomenology, one can find that $g_\gamma=5.01$. The Lagrangian $\mathcal{L}_{\mathrm{EM}}^{(4)}$ is invariant under the $U(1)_{\mathrm{em}}$ group. The composite structure of the nucleon is included through an anomalous moment $\lambda\equiv\frac{1}{2}\lambda_p(1+\tau_3)+\frac{1}{2}\lambda_n(1-\tau_3)$, where $\lambda_p=1.793$ and $\lambda_n=-1.913$ are the anomalous magnetic moments of the proton and the neutron, respectively.

The effective chiral Lagrangian Eq. (8) at a given order contains certain parameters that are not constrained by the symmetries. Apart from the isoscalar (β_s) and isovector (β_v) electromagnetic form factors and the tensor coupling for ρ meson (f_ρ), which are fixed from the free-space-charge radii of the nucleon [3, 4], the remaining thirteen LECs $\{g_s/(4\pi)$, $g_v/(4\pi)$, $g_\rho/(4\pi)$, $\eta_1,\eta_2,\eta_\rho,\kappa_3,\kappa_4,\zeta_0,m_s/M,f_v,\alpha_1,\alpha_2\}$ have to be determined from experimental data. These LECs are defined applying the naive dimensional analysis, so that they are assumed to be of order $\mathcal{O}(1)$, i.e., natural.

4. RELATIVISTIC HARTREE APPROXIMATION

The mean-field approximation dismisses (ignores) all quantum fluctuations of the meson fields and treats them by their expectation values. Under the assumption of time reversal invariance, the spatial components of the 4-vector fields vanish; also, since the ground state is assumed to have well-defined parity, the pseudoscalar pion field does not contribute in this approximation. This results in a set of coupled equations, namely, the Dirac equation with meson mean potentials for the nucleons and the Klein–Gordon-type equations with sources for the mesons and the photon. If we restrict consideration to the static and spherically symmetric case, the equations get simplified. The resulting coupled one-dimensional differential equations may be solved by an iterative procedure (for details, see [3]). Once the solution has been found, the ground-state energy of the system is given by

$$E=\sum_a^{\mathrm{occ}}E_a(2j_a+1)-\int d^3xU_m, \qquad (12)$$

where the superscript "occ" means that the summation of the single-particle nucleon energies E_a runs only over occupied (valence) orbitals and U_m is a functional depending on the various nucleon densities and the meson mean potentials.

The binding energy of a system of $A=Z+N$ nucleons is defined by

$$E_B=E-E_{\mathrm{c.m.}}-AM, \qquad (13)$$

where $E_{\mathrm{c.m.}}$ is the center-of-mass correction, which can be estimated nonrelativistically; its empirical estimate is $E_{\mathrm{c.m.}}\approx 17.2A^{-0.2}$ MeV. The mean-square radius of the charge distribution (with the c.m. motion correction) is given by

$$\langle r^2\rangle_{\mathrm{chg}}=\langle r^2\rangle-\frac{3}{4\langle\hat{P}^2_{\mathrm{c.m.}}\rangle}, \qquad (14)$$

where

$$\langle r^2\rangle=\frac{1}{Z}\int d^3x\mathbf{r}^2\rho_{\mathrm{chg}}(\mathbf{r}),\quad \langle\hat{P}^2_{\mathrm{c.m.}}\rangle=2AME_{\mathrm{c.m.}}. \qquad (15)$$

Since the additional nonrenormalizable interactions between the nucleon and electromagnetic field are included in $\mathcal{L}_{\mathrm{EM}}$ [Eq. (11)], the charge density $\rho_{\mathrm{chg}}(\mathbf{r})$ automatically contains the long-range electromagnetic structure of the nucleon, and it is unnecessary to introduce an ad hoc form factor.

In summary, the discussed FST model has been formulated in modern language of effective field theories. This new approach is considered to offer a natural and useful framework to establish a connection between the nuclear many-body problem and the underlying QCD. The values of fitted parameters (LECs) obtained by the authors are all of $\mathcal{O}(1)$, which mean that the applied procedure of power counting is robust and naive dimensional analysis is compatible with the nuclear phenomenology. For a further summary and outlook, the interested reader is referred to [5].

ACKNOWLEDGMENTS

I am grateful to the Bogolyubov–Infeld Programme for financial support during the VII International School–Seminar on Heavy Ion Physics in Dubna.

REFERENCES

1. S. Weinberg, *The Quantum Theory of Fields* (Cambridge University Press, Cambridge, 1995, 1996), Vols. 1, 2.
2. S. Weinberg, Physica A **96**, 327 (1979); Phys. Lett. B **251**, 288 (1990); Nucl. Phys. B **363**, 3 (1991); Phys. Lett. B **295**, 114 (1992).
3. R. J. Furnstahl, B. D. Serot, and H.-B. Tang, Nucl. Phys. A **615**, 441 (1997); Nucl. Phys. A (Erratum) **640**, 505 (1998).
4. B. D. Serot and J. D. Walecka, Int. J. Mod. Phys. E **6**, 515 (1997).
5. R. J. Furnstahl and B. D. Serot, Commun. Nucl. Part. Phys. **2**, A23 (2000); nucl-th/0005072v2.

Physics of Atomic Nuclei, Vol. 66, No. 8, 2003, pp. 1578–1581. From Yadernaya Fizika, Vol. 66, No. 8, 2003, pp. 1621–1624.

Application of the Program LISE to Fusion–Evaporation*

O. B. Tarasov[1),2)**] **and D. Bazin**[1)]

[1)] *National Superconducting Cyclotron Laboratory, Michigan State University, East Lansing, MI 48824-1321, USA*

[2)] *Flerov Laboratory of Nuclear Reactions, Joint Institute for Nuclear Research, Dubna, Moscow oblast, 141980, Russia*

Received August 28, 2002

Abstract—A new fusion–evaporation model LisFus for fast calculation of fusion residue cross sections has been developed in the framework of the code LISE. This model can calculate very small cross sections quickly compared to programs using the Monte Carlo method. Such type of the fast calculations is necessary to estimate fusion residue yields. Using this model, the program LISE now has the possibility of calculating the transmission of fusion residues through a fragment separator. It is also possible to use fusion residue cross sections calculated by the program PACE, which has been incorporated in the LISE package. The code PACE is a modified version of JULIAN—the Hillman–Eyal evaporation code using a Monte Carlo code coupling angular momentum. A comparison between PACE and the LisFus model is presented. © *2003 MAIK "Nauka/Interperiodica".*

1. INTRODUCTION

The program LISE [1] is intended to calculate the transmission and yields of fragments produced and collected in a fragment separator. It allows one to fully simulate the production of radioactive beams, from the parameters of the reaction mechanism to the detection of nuclei selected by the fragment separator. Among the goals of this program is a highly user-friendly environment, designed not only to forecast intensities and purities for planning experiments, but also as a tuning tool during experiments, where its results can be quickly compared to on-line data.

So far, the only the production reaction mechanism used in the program was only the projectile fragmentation. Further development of the program is directed towards lower energies down to the Coulomb barrier and involves other types of reactions. With the occurrence of new facilities producing high-intensity radioactive beams of low energies (for example SPIRAL [2] and DRIBs project [3]), a fast calculation of reaction-product transmission through a fragment separator at these energies (in particular fusion–evaporation reactions) has become necessary. To fulfil this need, a new model with a fast algorithm for calculating residue formation cross sections must be built. More problematic is the question of calculating cross sections of nuclei far from stability, since programs based on the Monte Carlo method such as PACE, CASCADE are very time consuming. To avoid this problem the LisFus model using the analytical approach was developed within the framework of the program LISE. The basic principles of model, as well as its advantages and disadvantages, are given in the following section.

The program LISE offers the possibility of comparing the LisFus model with the program PACE ported to Windows from FORTRAN to C++ and incorporated in the LISE package under the name PACE4. The code PACE [4] (Projection Angular-momentum Coupled Evaporation] is a modified version of JULIAN—the Hillman–Eyal evaporation code using a Monte Carlo code coupling angular momentum. In the LISE framework, the program PACE4 has several new features:

A user-friendly interface, where the user can enter information in a dialog box, in which the explanation for each parameter is displayed. A convenient output of results is available too.

The possibility of plotting the calculated cross sections using the LISE tools.

A database of recommended values for binding energies [5] was added to the program.

2. LisFus—FUSION RESIDUE CROSS-SECTION FAST CALCULATIONS

The new fusion–evaporation model LisFus is based on the Bass fusion cross-section algorithm [6],

*This article was submitted by the authors in English.

**e-mail: tarasov@nscl.msu.edu

Comparison of the performance between different kinds of low-energy fusion residue selection

Selection	Yield of $^{42}Ca^{19+}$, 10^5 s^{-1}	Transmission, %	Yields of all ions, 10^5 s^{-1}	Purification, %
Dipole ($dp/p = 3\%$)	14	2.34	49	28
Dipole & Wien velocity filter	6.8	1.14	8.9	76
Wien velocity filter	7.0	1.17	28	25
Wien velocity filter ⊗ Dipole	60	10.0	65	93

the evaporation cascade algorithm of the abrasion–ablation model [7], and the LISE code mathematical apparatus of probability distributions using the transport integral theory [8]. The evaporation stage is treated in a macroscopic way on the basis of a master equation that leads to diffusion equations as proposed by Campi and Hüfner [9] and lately reexamined by Gaimard and Schmidt [7]. For each i point of excitation-energy (E_i) distribution (P) of a parent nucleus, the LisFus model calculates the probabilities (W_k) of eight possible decay channels (n, $2n$, p, $2p$, d, t, ^{3}He, α) and a daughter excitation-energy distribution function $D_k(E_i)$. Using these definitions it is possible to express the i segment of the parent excitation function as follows:

$$\int_{E_i}^{E_{i+1}} P(E)\,dE = \sum_{k=1}^{8} W_k(E_i) D_k(E_i).$$

The fast speed of the LisFus calculations allows one to build and inspect fusion residue excitation functions quickly. The analytic approach of this model permits one to calculate the cross section for nuclei far from stability. However, the model does not take into account the contribution of the angular momentum, nor the deexitation channels by gamma emission and fission. Despite these approximations, the calculations obtained with this model are in good agreement with other programs using more complicated algorithms shown, for example, in the case of an excited ^{215}At nucleus evaporation process (see Fig. 1). Comparison of LisFus's and PACE's calculations with experimental data [10, 11] are shown in Fig. 2.

3. FUSION RESIDUE TRANSMISSION THROUGH A FRAGMENT SEPARATOR

In order to calculate a fusion residue yield through a fragment separator, it is also necessary to calculate their kinematics: velocity distribution (mean velocity and widths of longitudinal and transverse momentum distributions) and angular distribution. The residue velocity after the reaction (fusion and evaporation of light particles) is assumed to be equal to the compound nucleus recoil velocity. A Maxwell distribution of velocities is used to calculate the root-mean-square velocity after evaporation of light particles. In order to simplify the calculations and obtain the result in an analytic form it was assumed that

each step represents only one-nucleon evaporation;

the excitation energy of the daughter nucleus on each step is a delta function;

the one nucleon separation energy is averaged out between the compound and the residue.

Under these assumptions, it is possible to consider the final distribution as a convolution of N Gaussian distributions with $\sigma_i = \sqrt{\tau_i/\mathrm{amu}}/A_i$, where N is the number evaporated nucleons, A_i is the mass number of intermediate nucleus, and τ_i is its temperature. Angular distributions in the c.m. system are assumed

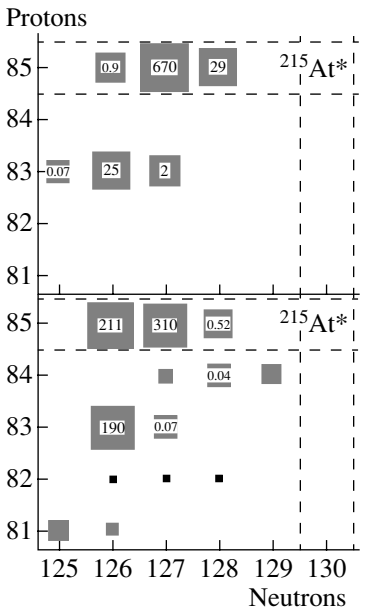

Fig. 1. Evaporation products following the fusion ^{6}He + ^{209}Bi for the c.m. energy 25 MeV. The PACE4 calculations are shown in the upper frame; the LisFus calculations, on the bottom frame. Cross section values (in mb) are shown inside squares.

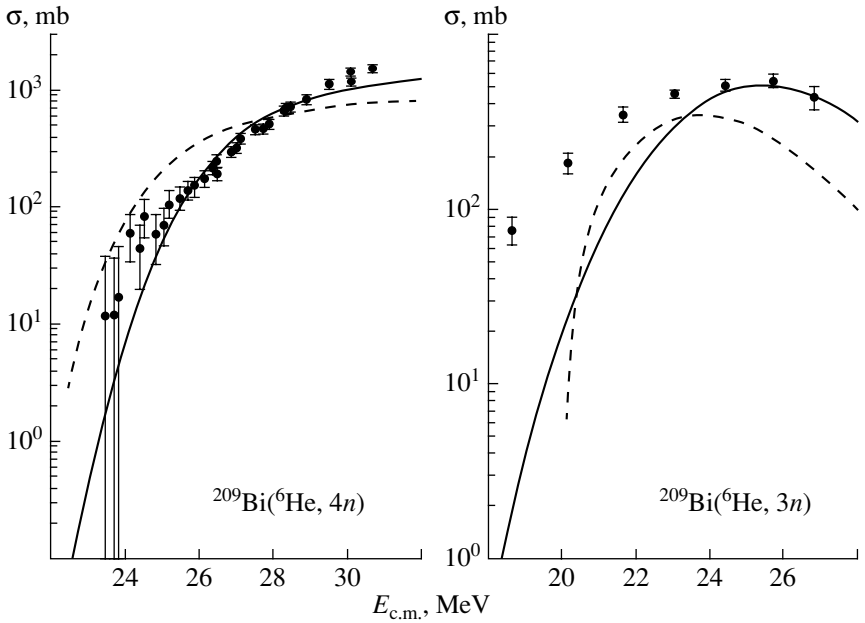

Fig. 2. The measured four-neutron evaporation cross section [10] (left panel) and three-neutron evaporation cross section [11] (right panel) as a function of the c.m. energy. The solid curve is the prediction of the statistical model code PACE and the dashed curve is the LisFus code calculations accordingly.

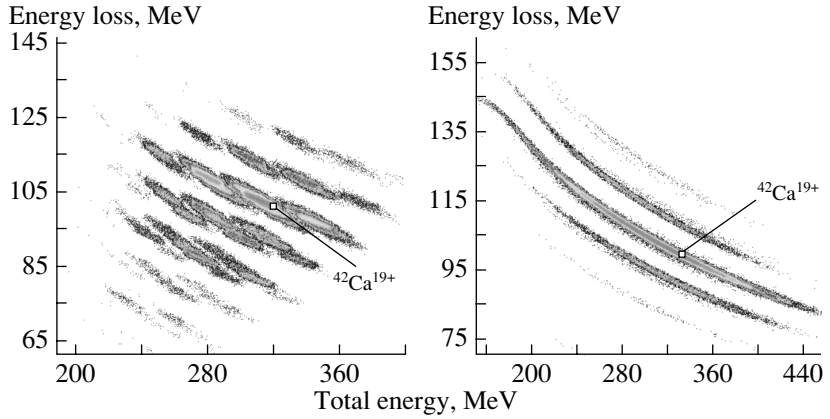

Fig. 3. $\Delta E-E$ selection plots for two different selection methods. The left plot shows the selection by a magnetic dipole, and the right plot shows a combination of Wien velocity filter and a dipole that compensates the filter's dispersion. Both devices are tuned on $^{42}Ca^{19+}$.

isotropic. The calculated widths of longitudinal and transverse momentum distributions are used to obtain the angular distributions.

In the case of fusion reactions, attention should be paid to the ionic charge of the residue, as fusion reactions take place at lower energies than fragmentation. For this purpose a fusion residue calculator has been developed and incorporated in the LISE package.

The last step is selection of a chosen fusion residue by the separation devices to maximize transmission and purity. In today's version, four methods of separation are available in the program LISE: magnetic rigidity, energy loss in a wedge located at the dispersive focal plane, Wien velocity filter, and combination of a Wien filter and a dipole. The most popular method of separation for low energies is velocity separation (velocity filter). At small energies, using energy loss in a wedge is ruled out. Electrostatic and gas-filled separators will be available as well in the program LISE in the future. Comparisons between different selection methods of fusion residues in the reaction ^{40}Ar(15 MeV/u) + Be(64.4 μm) are shown in Fig. 3 and in the table, where it is apparently that the combination of a Wien velocity filter and a dipole (as in the spectrometer VAMOS [12]) gives the best

results: best purification and largest transmission of the chosen fusion residue.

REFERENCES

1. D. Bazin, M. Lewitowicz, O. Sorlin, and O. Tarasov, Nucl. Instrum. Methods Phys. Res. A **482**, 314 (2002); program LISE; http://dnr080.jinr.ru/lise; http://www.nscl.msu.edu/lise.
2. A. C. Mueller, Z. Phys. A **358**, 153 (1997); http://www.ganil.fr/spiral.
3. DRIBs project: http://159.93.28.88/dribs/home.html.
4. A. Gavron, Phys. Rev. C **21**, 230 (1980).
5. G. Audi and A. H. Wapstra, Nucl. Phys. A **595**, 409 (1995).
6. R. Bass, Phys. Rev. Lett. **39**, 265 (1977).
7. J.-J. Gaimard and K.-H.Schmidt, Nucl. Phys. A **531**, 709 (1991).
8. D. Bazin and B. Sherrill, Phys. Rev. E **50**, 4017 (1994).
9. X. Campi and J. Hüfner, Phys. Rev. C **24**, 2199 (1981).
10. P. A. De Young *et al.*, Phys. Rev. C **58**, 3442 (1998).
11. P. A. De Young *et al.*, Phys. Rev. C **62**, 047601 (2000).
12. http://www.ganil.fr/vamos/ (Spectrometer VAMOS).

Physics of Atomic Nuclei, Vol. 66, No. 8, 2003, pp. 1582–1585. From Yadernaya Fizika, Vol. 66, No. 8, 2003, pp. 1625–1628.

New Mechanism for the Production of Extremely Fast Light Particles in Heavy-Ion Collisions in the Fermi Energy Domain*

A. S. Denikin** **and V. I. Zagrebaev**

Joint Institute for Nuclear Research, Dubna, Moscow oblast, 141980 Russia

Received August 28, 2002

Abstract—Employing a four-body classical model, various mechanisms responsible for the production of fast light particles in heavy-ion collisions at low and intermediate energies have been studied. It has been shown that, at energies lower than 50 A MeV, light particles of velocities of more than two times the projectile velocities are produced due to the acceleration of the target light particles by the mean field of the incident nucleus. It has also been shown that precision experimental reaction research in normal and inverse kinematics is likely to provide vital information about which mechanism is dominant in the production of fast light particles. © *2003 MAIK "Nauka/Interperiodica".*

The production of preequilibrium light particles (n, p, t, α) in nucleus–nucleus collisions depends on the way that the nuclear system evolves at the initial stage of the reaction. For heavy-ion collisions, the light-particle cross section is known to be a noticeable fraction of the total reaction cross section even at low energies on the order of 10 A MeV; i.e., light-particle production is a distinctive feature of all nuclear reactions involving heavy ions. This means that studying the production mechanisms for those particles is likely to provide direct information on both the dynamics of the initial stage of the reaction and the potential and dissipative forces of nucleus–nucleus interaction.

Vast bodies of data [1–6] demonstrate that, in heavy-ion reactions at energies per nucleon on the order of the Fermi energy, light particles are produced in a wide angular range, their velocities being two or more times higher than the velocities of the beam particles. Figure 1 shows the measured differential proton cross section at $\theta_{\text{lab}} = 20°$ in the case of the ^{16}O (20 A MeV) + ^{197}Au collision [1]. What is the mechanism of the production of these extremely fast light particles? The ultimate answer to that question has not been provided yet. Circumstantial evidence suggests that they are of a preequilibrium nature. This makes them more difficult to study by a direct experiment since there is currently no way of studying processes taking place in time intervals on the order of 10^{-20} s.

Attempts to interpret the experimental picture have resulted in the creation of a number of theoretical models and approaches. Among these, in particular, are the models of moving sources [7], Fermi jet [8–10], dissipative breakup and massive transfer [11], etc. A comprehensive survey of experimental and theoretical works related to this problem is given in [12]. Applying these approaches, the authors have succeeded in qualitatively describing the energy and angular dependences of the spectra of emitted light particles as well as revealing some production mechanisms for them. Among the latter, in particular, is the mechanism of "splashing" nucleons out of a retarding projectile nucleus, the high velocities of the

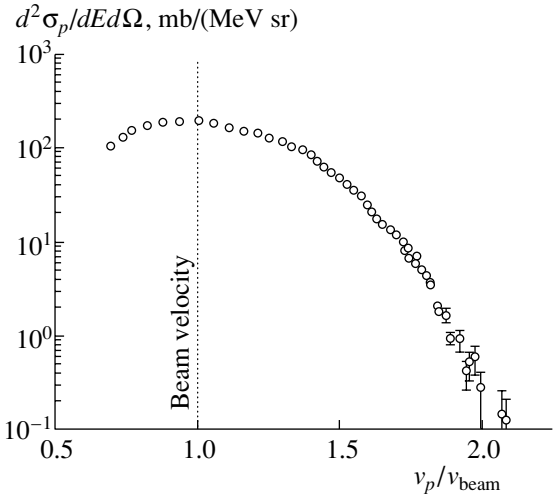

Fig. 1. Measured differential cross section of protons emitted at the angle $\theta_{\text{lab}} = 20°$ in the reaction $^{16}\text{O} + {}^{197}\text{Au} \to p + X$ at the energy 20A MeV plotted vs. the proton velocity in units of the beam velocity. The experimental data are taken from [1].

*This article was submitted by the authors in English.

**e-mail: denikin@jinr.ru

light particles being due to the addition of the velocity of Fermi motion within the projectile nucleus and the velocity of its center of mass. The importance of taking this mechanism into account was shown [9, 11], when describing the spectra of the α particles produced in projectile breakup and massive transfer at collision energies on the order of several tens of MeV per nucleon. Nucleon–nucleon collisions are also likely to result in a fast light particle being emitted due to scattering on nucleons of high velocities. The Fermian shape of nucleon momentum distributions explains the existence of such nucleons in a heated nuclear system.

The first mechanism, capable of qualitatively describing the experimental results in a transparent way, fails to provide satisfactory quantitative agreement. The nucleon–nucleon collision model is adequate at high energies ($\geq 100\,A$ MeV), but in the region of energies $E_0 < 50\,A$ MeV, the nucleon–nucleon interaction cross section for heavy-ion collisions decreases due to the Pauli principle. Therefore, this mechanism influences the formation of the hard part of the spectrum of light particles to a smaller degree.

Recent advances in instrumentation have made possible the precise measurement of the angular and energy spectra of light particles [4–6], which is likely to shed light upon still unresolved problems.

In [13], we proposed a four-body classical model of nucleus–nucleus collisions, which permits establishing the role of mean nuclear fields and nucleon–nucleon collisions in the production of light particles. This model considers the projectile and target nuclei to be bound two-body systems that are composed of a heavy core and a light fragment moving in its field. The interactions of the fragments, which follow classical trajectories, define six pair potentials. The interaction between the light fragments and the cores was described by the Woods–Saxon potential with compilation-based parameters [14]. The interaction between the heavy cores was described by the proximity potential or the Woods–Saxon potential, the parameters of the latter being chosen so as to reproduce the height and position of the Coulomb barrier. The coupling with the reaction channels, which were not taken into account explicitly, was introduced by means of dissipative forces acting between the heavy cores of the target and projectile. The choice of friction coefficients and form factors for the dissipative forces was based on [15]. To provide a more correct estimate of the channel differential cross sections, the description of the relative motion of the projectile (target) light particle and the target (projectile) core has an absorption probability for them that has been introduced as $P_{ij}^{\mathrm{abs}} = 1 - \exp\left(-s_{ij}/\lambda_{ij}\right)$, where s_{ij} is the distance traveled by particle i in the nucleus j, and λ_{ij} is the corresponding free path length, which is, as is well known, related to the imaginary part of the optical potential, the parameters of which were chosen according to [14].

Specifying the relative distance vector $\mathbf{r}_{ij}$ for the projectile components and the binding energy E_{ij}^{sep}, known by experiment, as well as the orbital momentum $\mathbf{l}_{ij}$ for their relative motion, completely defines the projectile inner spatial configuration. The components of the vector $\mathbf{r}_{ij}$ were chosen randomly and equiprobably in the classically allowed region. To have the relative motion momentum $\mathbf{p}_{ij}$ uniquely determined, one of the components of the vector $\mathbf{l}_{ij}$ must also be specified (by a random choice) in addition to the $\mathbf{r}_{ij}$ and E_{ij}^{sep} values. Repeating the same operations for the target nucleus and specifying the relative motion of the centers of mass of the nuclei depending on the reaction allow one to determine the initial conditions that are required for solving the set of classical equations of motion.

The model outlined above has 15 reaction channels with a different combination of particles in the final fragments. Eight of these channels contribute to the total cross section for preequilibrium light particles, which can be divided into two groups: particles emitted from the projectile and from the target. Taking into account all the pair potentials allows us to study the whole range of processes that result in light-particle emission as well as to establish the role played in them by one or another type of interaction.

We have investigated heavy-ion collisions at energies of several tens of MeV per nucleon and thoroughly studied the production mechanisms for fast light particles. It is remarkable and unexpected that the hardest part of the energy spectrum of emitted light particles corresponds to particles emitted from the target nucleus rather than from the projectile nucleus, as has been assumed up to now. There is a simple enough explanation for this phenomenon, which appears to be unusual at first sight.

Let us assume for simplicity that the heavy cores have masses much larger than those of the light particles; the light particle moves in the nucleus at a velocity equal to the Fermi velocity v_{F}; the nuclei move relative to one another at the velocity $v_0 \approx v_{\mathrm{F}}$; the trajectories of the heavy fragments are taken to be undistorted; the binding energy of the light particle in the nucleus is assumed to be much smaller than the collision energy $E_{ij}^{\mathrm{sep}} \ll E_0 = mv_0^2/2$, where m is the mass of the light particle. Then, as has been shown in [13], for example, the neutrons emitted from the projectile ("splashing out") will have a maximum laboratory system energy expressed as

$$E_n^{\max} \approx \frac{m}{2}\left(v_0^2 + 2v_0 v_{\mathrm{F}}\right) = 3\frac{mv_0^2}{2} = 3E_0. \qquad (1)$$

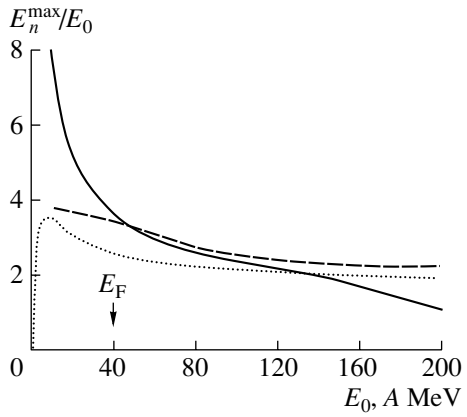

Fig. 2. The ratio of maximum energy E_n^{max} of preequilibrium neutron to the beam energy E_0 calculated for the reaction $^{20}Ne + {}^{165}Ho \to n + X$ as a function of the beam energy. The curves correspond to the maximum energy of neutrons originating from target (solid curve), emitted from the projectile (dotted curve), and emitted after nucleon–nucleon collisions (dashed curve). The arrow represents the beam energy per nucleon approximately equal to the Fermi energy.

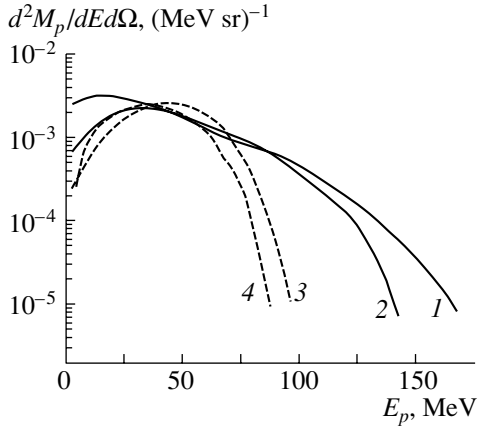

Fig. 3. Calculated differential multiplicity of preequilibrium protons emitted at the angle $\theta_{lab} = 51°$ in the reactions $^{40}Ar + {}^{51}V$ and $^{132}Xe + {}^{51}V$ at the incident energy 44 A MeV. Curves *1* and *2* correspond to the protons originating from the target ^{51}V bombarded with ^{132}Xe and ^{40}Ar projectiles, respectively; curves *3* and *4* correspond to the protons emitted from the ^{132}Xe and ^{40}Ar projectiles, respectively.

In the framework of this model under the same assumptions, the maximum energy of the neutrons emitted both from the projectile and from the target in elastic nucleon–nucleon collisions is limited by the value

$$E_n^{max} \approx \frac{m}{2}(v_0 + v_F)^2 = 4\frac{mv_0^2}{2} = 4E_0. \qquad (2)$$

However, such a mechanism of emitting a fast nucleon suggests that the recoil nucleon should impart all of its kinetic energy to the particle knocked out and, consequently, pass into an occupied lower energy state, which is forbidden by the Pauli principle. Therefore, this mechanism does not manifest itself in full measure at low and intermediate collision energies and comes into play as the collision energy increases, when states lower and lower in energy become unoccupied in the process of the system becoming excited.

The production mechanism for the fast light particles emitted form the target is more complicated. To begin with, let us consider the elastic scattering of a target light particle on a moving infinitely heavy repulsing wall. If, before colliding, the light particle and the heavy wall have been moving collinearly in opposite directions with parallel velocities v_F and v_0 respectively, then the c.m. velocity of the light particle is $v_{c.m.} = -(v_0 + v_F)$. After elastically colliding, the light particle will have the velocity $v'_{c.m.} = -v_{c.m.} = (v_0 + v_F)$, the lab velocity being $v' = v'_{c.m.} + v_0 = 2v_0 + v_F$. Thus the maximum energy of a neutron emitted from the target will be

$$E_n^{max} \approx 4\frac{m}{2}\left(v_0^2 + v_0 v_F\right) = 8\frac{mv_0^2}{2} = 8E_0; \qquad (3)$$

i.e., the fastest neutrons will have a velocity of more than 2.5 times that of the beam particles. Now, suffice it to say that an elastic collision with a repulsing wall is kinematically equivalent to elastic scattering at the angle $\theta_{c.m.} = -180°$ (i.e., orbiting) in the attractive field of an incident nucleus. However, orbiting is possible at quite low relative motion energies. At higher energies, a light particle can be deflected only due to the field of the projectile at a certain c.m. angle θ_R called an angle of rainbow scattering. Therefore, the maximum energy of a preequilibrium light particle emitted will be a function of collision energy, light-particle–incident-nucleus interaction potential, particle binding energy, and dissipative forces.

More accurate calculations of the maximum energy of the preequilibrium neutrons produced in the reaction $^{20}Ne + {}^{165}Ho \to n + X$ are presented in Fig. 2. Given here is the E_n^{max}/E_0 ratio as a function of the beam energy E_0 for the above mechanisms: the solid curve is for the energy of the neutrons emitted from the target; the dotted curve is for the energy of the neutrons emitted from the projectile; the dashed curve is for the energy of neutrons produced in nucleon–nucleon collisions, which was calculated with regard to the Pauli principle. Thus, it is seen that, at collision energies per nucleon smaller than E_F (indicated with an arrow in Fig. 2), the mechanism involving acceleration of neutrons by the moving

mean field of the projectile is dominant in the formation of the high-energy portion of neutron spectra. In the high-energy region, the key role is played by nucleon–nucleon collisions. It should also be noted that the curves in Fig. 2 do not represent $E_n^{\max}$ in a strict way since our calculations did not take into account the nonzero probability of there existing nucleons of velocities much higher than v_F. Therefore, the boundaries indicated by the curves in Fig. 2 will shift to higher energies.

How should the predictions made by our model be tested, and how should the yields of preequilibrium light particles emitted from a projectile and target be separated? There is currently no direct solution. However, the above analysis of various processes of light-particle production in heavy-ion collisions shows that the mechanism of emission of fast nucleons from the target is only slightly sensitive to the projectile nucleus mass, and, consequently, the maximum energy of light particles is not likely to change greatly upon replacing one projectile by another. On the other hand, the maximum energy of the target nucleons accelerated by the attractive field of the incident nucleus is defined by the corresponding rainbow scattering angle, which depends on the dimensions of the deflecting mean field [16],

$$\theta_R \approx \left(V_C - 0.7U_0\sqrt{R_U/a_U}\right)/E_{\text{c.m.}},$$

where V_C is the height of the Coulomb barrier for the emitted light particle; U_0, R_U, and a_U are the depth, radius, and diffusiveness of the light-particle–projectile interaction potential, and $R_U \approx 1.3A^{1/3}$. Now, it is evident that the energy distribution of emitted light particles must be more elongated for a reaction with a heavy projectile than for a reaction with a light one. This conclusion is supported by Fig. 3, in which the calculated differential preequilibrium proton cross sections are shown for the angle $\theta_{\text{lab}} = 51^\circ$ for the $^{40}\text{Ar} + {}^{51}\text{V}$ and $^{132}\text{Xe} + {}^{51}\text{V}$ reactions (in normal and inverse kinematics) at the energy $E_0 = 44\,A$ MeV. It is seen, first, that the key role in the formation of the high-energy part of the spectrum is played by the protons emitted from the target nuclei (curves *1* and *2* in Fig. 3). Second, the distribution of the protons emitted from projectiles of different masses (curves *3* and *4*) only changes its shape to a large degree at small energies; i.e., a more massive ^{132}Xe projectile loses less energy in a collision with a ^{51}V target than does ^{40}Ar. Therefore, these two reactions have projectile proton distributions with shifted maxima. Third, the ^{40}Ar-induced reaction in normal kinematics has a preequilibrium proton spectrum that is several tens of MeV shorter than that for the reaction with the heavier ^{132}Xe projectile. Thus, comparing precisely measured data on the distributions of the light particles produced in heavy-ion collisions in reactions of normal and inverse kinematics will give us vital information about which mechanism is dominant in emission of a fast light particle.

REFERENCES

1. T. C. Awes *et al.*, Phys. Rev. C **25**, 2361 (1982).
2. D. Sackett *et al.*, Phys. Rev. C **44**, 384 (1991).
3. G. Lanzano *et al.*, Phys. Rev. C **58**, 281 (1998).
4. Yu. E. Penionzhkevich *et al.*, Preprint No. E7-98-282, Joint Inst. Nucl. Res. (Dubna, 1998).
5. R. Alba *et al.*, Phys. Lett. B **322**, 38 (1994).
6. P. Sapienza *et al.*, Nucl. Phys. A **630**, 215c (1998).
7. T. C. Awes *et al.*, Phys. Rev. C **24**, 89 (1981).
8. J. P. Bondorf *et al.*, Nucl. Phys. A **333**, 285 (1980).
9. K. Mohring, W. J. Swiatecki, and M. Zielinska-Pfabe, Nucl. Phys. A **440**, 89 (1985).
10. J. Randrup and R. Vanderbosch, Nucl. Phys. A **474**, 219 (1987).
11. V. I. Zagrebaev, Ann. Phys. (N.Y.) **197**, 33 (1990).
12. V. Zagrebaev and Yu. Penionzhkevich, Prog. Part. Nucl. Phys. **35**, 575 (1995).
13. A. S. Denikin and V. I. Zagrebaev, Yad. Fiz. **65**, 1494 (2002) [Phys. At. Nucl. **65**, 1459 (2002)].
14. C. M. Perey and F. G. Perey, At. Data Nucl. Data Tables **13**, 293 (1974).
15. D. H. E. Gross and H. Kallinowski, Phys. Rep. **45**, 175 (1978).
16. J. Knoll and R. Schaeffer, Ann. Phys. (N.Y.) **97**, 307 (1976).

Physics of Atomic Nuclei, Vol. 66, No. 8, 2003, pp. 1586–1589. From Yadernaya Fizika, Vol. 66, No. 8, 2003, pp. 1629–1632.

Multidimensional Langevin Approach to Description of Near-Barrier Heavy-Ion Fusion and Deep-Inelastic Collisions*

M. A. Naumenko**, **A. S. Denikin, and V. I. Zagrebaev**

Joint Institute for Nuclear Research, Dubna, Moscow oblast, 141980 Russia

Received August 28, 2002

Abstract—A six-dimensional Langevin approach is developed for the analysis of near-barrier heavy-ion fusion and deep-inelastic collisions. In its framework, vibrational and rotational degrees of freedom of both nuclei are taken into account explicitly. Calculated fusion cross sections, compound nuclei spin distributions, and angular and energy distributions of deep-inelastic products show satisfactory agreement with experimental data. © *2003 MAIK "Nauka/Interperiodica".*

1. INTRODUCTION

Fokker–Planck and Langevin equations may be successfully applied for the description of low-energy fusion and deep-inelastic collisions. These equations are based on the concepts of nuclear friction and stochastic behavior of the system with many degrees of freedom. The solution of the Langevin equations is less difficult compared to the Fokker–Planck equation and does not require additional simplifying assumptions. It is well known that the deformations of nuclear surfaces and the rotation of deformed nuclei seriously affect the dynamics of nuclear interaction. Therefore, taking them into account is important for the description of low-energy nucleus–nucleus collisions. But this dramatically increases the calculation time and difficulty, which is the main reason why up to now only two- or four-dimensional calculations have been performed [1]. In the present work, vibrational and rotational degrees of freedom of both nuclei are taken into account explicitly in the framework of the six-dimensional Langevin approach. Fusion cross sections, compound nuclei spin distributions, and angular and energy distributions of deep-inelastic products are calculated and compared with experimental data.

2. THEORETICAL MODEL

Collective degrees of freedom play a significant role in low-energy ($\leq$10 MeV/nucleon) fusion and deep-inelastic collisions. For the description of these processes, a six-dimensional Langevin model may be applied. The geometry of collision is shown schematically in Fig. 1. Let us assume for simplicity that the symmetry axes of nuclei belong to the plane of reaction. We shall use the following notation: r is the distance between centers of mass of nuclei, θ is the polar angle, φ_i are the angles between the symmetry axes of the nuclei and the beam direction, β_i are the dynamic quadrupole deformations, β_{i0} are the static quadrupole deformations of the ground states, $q = \{r, \theta, \varphi_i, \beta_i\}$ is the complete set of six variables, and $p_r, p_\theta, p_{\varphi_i}$, and p_{β_i} are the conjugated momenta. We suppose that the index $i = 1$ corresponds to the projectile, and $i = 2$ to the target. Let us also introduce angles $\alpha_1 = \varphi_1 + \theta$ and $\alpha_2 = \varphi_2 - \theta$.

The surface of the deformed axially symmetric nucleus taking into account volume conservation may be described by the formula

$$R_i(\alpha_i, \beta_i) = \frac{R_{i0}(1 + \beta_i Y_{20}(\alpha_i))}{\sqrt[3]{1 + \frac{3}{5}\delta_i^2 + \frac{2}{35}\delta_i^3}}, \qquad (1)$$

where $R_{i0} = r_{i0}A_i^{1/3}$, $\delta_i = \sqrt{5/(4\pi)}\beta_i$, and $Y_{20}(\alpha_i)$ is a spherical harmonic of the second order. In our calculations, we chose the parameter $r_0 = 1.2$ fm for both nuclei.

To describe surface vibrations of nuclei we will use the harmonic oscillator model. The corresponding Lagrangians may be written in the form

$$L_i^{\text{vib}} = \frac{p_{\beta_i}^2}{2B_i} - C_i\frac{(\beta_i - \beta_{i0})^2}{2}, \qquad (2)$$

where C_i are the rigidity parameters and B_i are the mass parameters; they may be calculated in the framework of the liquid drop model or from experimental data about vibrational states of nuclei.

*This article was submitted by the authors in English.

**e-mail: naumenko@lnr.jinr.ru

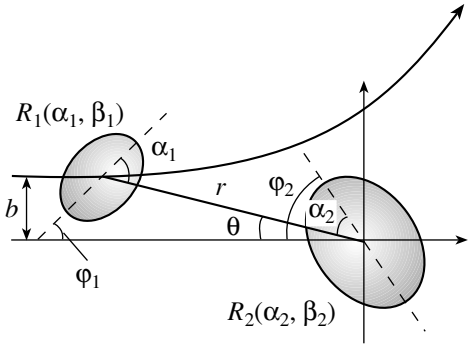

Fig. 1. The geometry of the collision process.

The full Lagrangian is then

$$L = \frac{p_r^2}{2\mu} + \frac{p_\theta^2}{2\mu r^2} + \sum_i \frac{p_{\varphi_i}^2}{2J_i} + \sum_i \left(\frac{p_{\beta_i}^2}{2B_i} - C_i \frac{(\beta_i - \beta_{i0})^2}{2} \right) - V(q), \tag{3}$$

where μ is the reduced mass of the system; J_i are the inertia momenta of nuclei; and V is the interaction potential, which consists of Coulomb and nuclear parts.

The Coulomb interaction is a sum of monopole–monopole and monopole–quadrupole interactions, $V_C = V_C^{(mm)} + V_C^{(mq)}$. The monopole–monopole one was chosen in the form

$$V_C^{(mm)} = Z_1 Z_2 e^2 \begin{cases} 1/r, & r > R_C, \\ (3 - r^2/R_C^2)/(2R_C), & r < R_C, \end{cases} \tag{4}$$

where $R_C = R_{01} + R_{02}$. We shall denote the quadrupole momenta of nuclei by Q_i; then,

$$V_C^{(mq)} = \frac{Z_1 Q_2 e^2}{2R^2} P_2(\cos\alpha_2) f(q) + \frac{Z_2 Q_1 e^2}{2R^2} P_2(\cos\alpha_1) f(q), \tag{5}$$

where

$$Q_i \approx \frac{3}{\sqrt{5\pi}} Z_i \widetilde{R}_i^2 \beta_i, \quad R = \widetilde{R_1} + \widetilde{R_2},$$

$$\widetilde{R_i} = R_{0i} \Big/ \sqrt[3]{1 + \frac{3}{5}\delta_i^2 + \frac{2}{35}\delta_i^3},$$

$$f(q) = \begin{cases} R^2/r^3, \; r > \widetilde{R_1}(1+\delta_1) + \widetilde{R_2}(1+\delta_2), \\ r^2/R^3, \; r < \widetilde{R_1}(1-\delta_1/2) + \widetilde{R_2}(1-\delta_2/2), \\ s^2(q)R^2/r^3 + c^2(q)r^2/R^3, \text{ in other cases.} \end{cases}$$

Here, $s^2(q) + c^2(q) = 1$, and functions $s(q)$ and $c(q)$ are chosen so that $f(q)$ is continuous together with its first derivative.

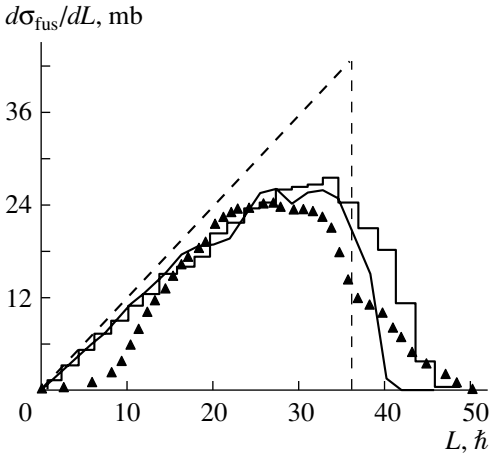

Fig. 2. The compound nuclei spin distribution for the reaction $^{16}O(E_{c.m.} = 80.4$ MeV$) + {}^{144}Nd \rightarrow {}^{160}Er^*$. The experimental data (triangles) are compared with theoretical calculations by Fröbrich [5] (histogram) and our results obtained with and without fluctuations (solid and dashed lines, respectively).

Woods–Saxon potentials with volume or surface form factors or a "proximity" potential [2] may be chosen as the nuclear part of the interaction. We must note that all potentials will give almost the same fusion cross sections, compound nuclei spin distributions, and angular and energy distributions of deep-inelastic products if positions and heights of their barriers are the same. In our calculations, the Woods–Saxon volume potential

$$V_N(q) = V_0 \frac{1}{1 + \exp[(r - R_V)/a]} \tag{6}$$

is used, where $R_V = R_1(\alpha_1, \beta_1) + R_2(\alpha_2, \beta_2)$ and the diffuseness parameter $a = 0.5$ fm.

Phenomenological nuclear friction is introduced to describe the dissipation of kinetic energy into degrees of freedom that are not taken into account explicitly within this model (mostly single-particle ones). The Rayleigh function is written in the standard form

$$D = \frac{1}{2} \sum_{k,n=1}^{6} \gamma_{kn}(q) \dot{q}_k \dot{q}_n, \tag{7}$$

where $\gamma_{kn}(q)$ is the friction tensor calculated within the surface friction model [3].

Friction leads to the heating of nuclei and appearance of stochastic forces $F_k(t) = \sqrt{\gamma_{kk} T}\Gamma(t)$, where $\Gamma(t)$ is a Gaussian-distributed random value with the following properties: $\langle \Gamma(t) \rangle = 0$ and $\langle \Gamma(t)\Gamma(t') \rangle = 2\delta_\varepsilon(t - t')$ (see, for example, [1]); the temperature of the nuclei $T = \sqrt{E^*/d}$ is determined by the excitation energy E^* and the level density parameter $d = (A_1 + A_2)/8$ MeV^{-1} [4].

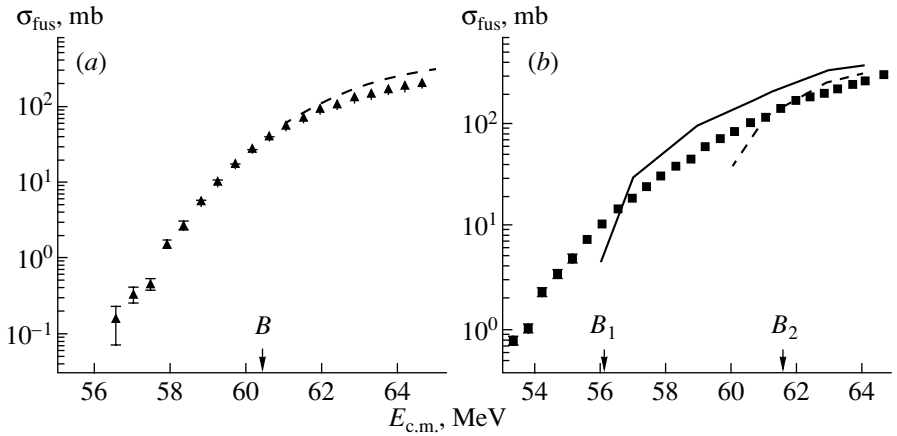

Fig. 3. (*a*) The excitation function for the reaction $^{16}O + {}^{144}Sm$. Triangles represent experimental data [6], and the dashed line is our calculation for spherical nuclei. (*b*) The excitation function for the reaction $^{16}O + {}^{154}Sm$. Squares represent experimental data [6]; the dashed line is our calculation for spherical nuclei; the solid line is our calculation taking into account static deformation of ^{154}Sm with averaging over initial orientations.

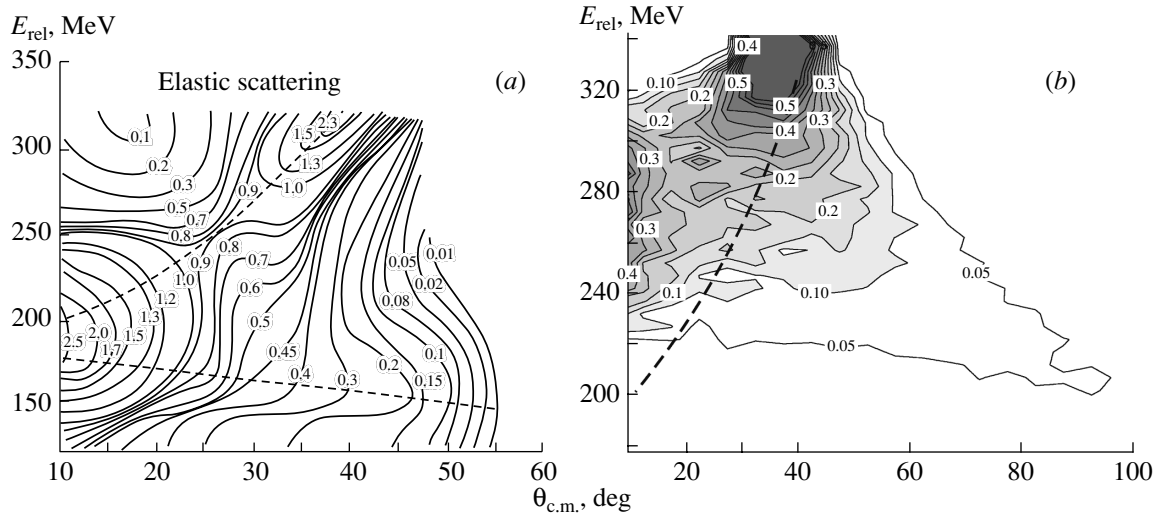

Fig. 4. Double differential cross section (in mb/(sr MeV)) for the reaction $^{56}Fe(E_{c.m.} = 345\ MeV) + {}^{165}Ho$. (*a*) Experiment [7]; projectile-like fragments with $12 \le Z \le 35$ were detected. (*b*) Calculation; stochastic forces were taken into account.

The set of Langevin equations

$$\frac{d}{dt}\left(\frac{\partial L}{\partial \dot{q}_k}\right) - \frac{\partial L}{\partial q_k} = -\frac{\partial D}{\partial \dot{q}_k} + \sqrt{\gamma_{kk}(q)\,T(E^*)}\,\Gamma(t),\ k = \overline{1,6}, \tag{8}$$

is solved numerically. The incident energy, impact parameter, deformations, and orientations of the nuclei are the initial conditions that we need for its solution. In case of stochastic forces, for each impact parameter, a number of trajectories are calculated. Those of them that go far enough behind the potential barrier cannot go outside and contribute to the fusion cross section. Others go outside or even may be reflected from the barrier without overcoming it, which leads the system to deep-inelastic, quasi-elastic, or elastic channels. In the case of deformed ground states, averaging over randomly chosen initial orientations is performed.

3. RESULTS OF OUR CALCULATIONS

The feature mentioned above results in smearing-out of calculated compound nuclei spin distributions, which allows us to reproduce the corresponding experimental data successfully. The compound nuclei spin distribution for the reaction $^{16}O(E_{c.m.} = 80.4\ MeV) + {}^{144}Nd \rightarrow {}^{160}Er^*$ is given in Fig. 2. The experimental data (triangles) are compared with theoretical calculations by Fröbrich [5] (histogram)

and with our results obtained with and without fluctuations (solid and dashed lines, respectively). In spite of the fact that only relative motion degrees of freedom were included in our calculations, the results show good agreement with experiment and Fröbrich's calculations performed taking into account dynamic deformations and using "nose-to-nose" geometry.

Rotational degrees of freedom are very important in the case of highly deformed nuclei collisions. A good example of this fact is a significant difference in the fusion cross sections of ^{16}O with two isotopes ^{144}Sm and ^{154}Sm. The ground state of ^{144}Sm is spherically symmetric, but ^{154}Sm is highly deformed with quadrupole deformation $\beta_{20} = 0.27$. In the latter case, instead of one Coulomb barrier, we obtain a multidimensional potential surface strongly depending on the orientation of the colliding nuclei. The excitation functions for the fusion reactions ^{16}O + ^{144}Sm and ^{16}O + ^{154}Sm are given in Fig. 3. Triangles and squares represent experimental data [6], dashed lines are calculations for spherical nuclei, and the solid line in Fig. 3*b* is a calculation taking into account the static deformation of ^{154}Sm with averaging over initial orientations. In Fig. 3*a*, the Coulomb barrier for spherical nuclei is marked with an arrow, and in Fig. 3*b*, the barriers B_1 and B_2 correspond to the different orientations of the target $\alpha_2 = 0°$ and 90°, respectively. The role of rotation and dynamic deformation is much less in this case; including them hardly changes the results. We can see that static deformation of ^{154}Sm plus averaging over initial orientations allows one to obtain fusion events at subbarrier energies, which leads to better agreement with experimental data. The Langevin forces do not significantly influence the fusion cross section in this case because of the low excitation energy, i.e., low temperature of the touching nuclei.

In calculation of deep-inelastic processes with energies about 10 MeV/nucleon, stochastic forces play a much more noticeable role and taking them into account is necessary for a realistic description of energy and angular distributions of fragments. The experimental double differential cross section (Wylczynski plot) for the reaction ^{56}Fe($E_{cm} = 345$ MeV) + ^{165}Ho is given in Fig. 4*a*. In the experiment projectile-like fragments with $12 \leq Z \leq 35$ were detected. The results of our calculation are shown in Fig. 4*b*. Here, stochastic forces were taken into account without dynamic rotations and deformations. A pronounced ridge is observed in the experimental data. It is shown as a dashed line in both figures. We see that the model properly reproduces the position of the maximum in the double differential cross section corresponding to so-called grazing collisions. The main reason for the discrepancy between theoretical calculations and experiment for large energy losses is the nucleon exchange in the collision process, which we did not take into account. This will be our immediate task for the future.

4. CONCLUSION

A six-dimensional Langevin approach is proposed for description of near-barrier fusion and deep-inelastic collisions. The role of vibrational and rotational degrees of freedom in the dynamics of nucleus–nucleus collisions was investigated. It was shown that taking them into account is important for reproducing the experimental data because the interaction potential strongly depends on these degrees of freedom. Taking into account fluctuations allows one to reproduce compound nuclei spin distributions without influencing much the value of the fusion cross section. Stochastic forces also play an important role in forming angular and energy distributions of the fragments formed in deep-inelastic processes.

The solution of the Langevin equations gives us important information about the dissipated energy, dynamic deformations, and orientations of nuclei at the moment of their contact, which is important for the analysis of the system's further evolution into channels of complete fusion and deep-inelastic scattering.

Nucleon exchange plays an important role in the dynamics of heavy-ion collision. Taking into account additional degrees of freedom describing nucleon exchange is our immediate task for the future.

REFERENCES

1. P. Fröbrich and I. I. Gontchar, Phys. Rep. **292**, 131 (1998).
2. J. Blocki, J. Randrup, W. J. Swiatecki, and C. F. Tsang, Ann. Phys. (N.Y.) **105**, 427 (1977).
3. D. H. E. Gross and H. Kalinowski, Phys. Rep. C **45**, 175 (1978).
4. A. V. Ignatyuk, *Statistical Properties of Excited Atomic Nuclei* (Énergoizdat, Moscow, 1983).
5. P. Fröbrich, Springer Proc. Phys. **58**, 93 (1991).
6. J. R. Leigh *et al.*, Phys. Rev. C **52**, 3151 (1995).
7. A. D. Hoover *et al.*, Phys. Rev. C **25**, 256 (1982).